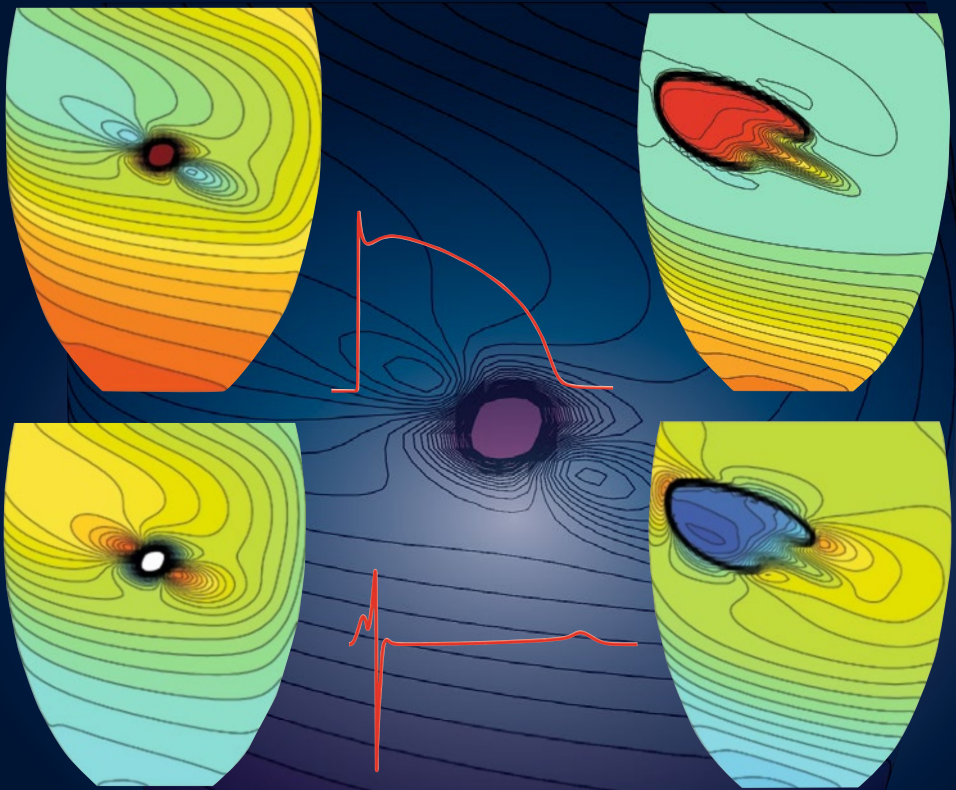Volume 13

Mathematical Cardiac Electrophysiology

Piero Colli Franzone • Luca F. Pavarino • Simone Scacchi

MS&A
Modeling, Simulation & Applications

Springer

MS&A

Volume 13

More information about this series at
http://www.springer.com/series/8377

Piero Colli Franzone • Luca F. Pavarino •
Simone Scacchi

Mathematical Cardiac Electrophysiology

Springer

Piero Colli Franzone
Dipartimento di Matematica
Università degli Studi di Pavia
Pavia
Italy

Luca F. Pavarino
Dipartimento di Matematica
Università degli Studi di Milano
Milano
Italy

Simone Scacchi
Dipartimento di Matematica
Università degli Studi di Milano
Milano
Italy

Preface

The goal of this book is to present some of the most successful and advanced mathematical and numerical models used in the field of cardiac electrophysiology. The bioelectric activity of the heart is the subject of a vast and still growing interdisciplinary literature in medicine, physiology, bioengineering, mathematical biology, chemistry, physics and bioinformatics. The long history and diversity of this field of research is shown e.g. by the earlier monographs by Jack, Noble and Tsien [250], Peskin [383], Nelson and Gezelowitz [346], Pilkington and Plonsey [386], by the reference works by Pilkington et al. [387], Panfilov and Holden [369], Keener and Sneyd [273], Gulrajani [215], Plonsey and Barr [393], Efimov et al. [158], and by some of the periodic review books by Zipes and Jalife [588–590]. In the last decade, more specific monographs on computational electrocardiology were published by Sachse [446], Pullan at el. [406], Sundnes et al. [502]; see also Macfarlane et al. [312]. Since the emphasis of this book is on mathematical and numerical aspects of the models and algorithms presented, we hope that this monograph will present new elements and will complement the works above.

Electrocardiology deals with the description of both intracardiac bioelectric phenomena and the extracardiac electric field generated in the animal or human body. The practice of modern medicine relies on noninvasive imaging technologies, such as CT, MRI and PET, for diagnostic purposes and for driving therapeutic procedures. Even though cardiac arrhythmias are among the major causes of death and disability, a noninvasive imaging technique yielding an accurate and reliable diagnosis of the electrophysiological state of the heart is not yet available. Clinic Electrocardiography deals with the detection and interpretation of noninvasive potential measurements collected from the time course of the usual electrocardiograms (ECG) at a few points on the body surface or from the evolution of body surface maps, i.e. potential distribution maps on the body surface reconstructed from measures at numerous electrodes (100 or more, see the surveys by [504, 511]). Since the electrode location of the ECG is centimeters away from the heart surface and the current conduction from heart to thorax yields a strong signal

attenuation and smoothing, the information content of ECGs and body maps is limited and it is a difficult task to extract from these signals detailed information on pathological heart states associated with ischemia or sudden death. Indeed, the origin of arrhythmogenic activity or the existence of abnormal electrophysiological substrates in many cases may not be easily inferred from the sequence of cardiac excitation.

The scientific base of Electrocardiology is the so-called *Forward Problem of Electrocardiology*, i.e. modeling the bioelectric cardiac sources and the conducting media in order to derive the potential field. Of considerable applicative interest are also the so-called *Inverse Problems of Electrocardiography* in terms of potentials (see e.g. the review [216, 442] and [68, 69, 415]) or in terms of the cardiac sources (see e.g. [110, 439]).

In the past few decades, experimental electrophysiology has been increasingly supported by the mathematical and numerical models of computational electrocardiology. The formulation of models at both cellular and tissue levels provide essential tools in order to integrate the increasing knowledge of the bioelectrochemical phenomena occurring through cardiac cellular membranes. Detailed cellular phenomena are described in microscopic membrane models and the latter are then inserted in macroscopic tissue models in order to investigate their effects at tissue level. These coupled models are then validated by comparing simulated results with experimental in vitro and in vivo data, generating a feedback loop that may lead to improved and more detailed models and/or the redesign of new experiments. As a further step, these electrophysiological models are being increasingly coupled and integrated with mechanical models of tissue deformation, hemodynamical models of cardiac blood flow and more in general with models of the cardiovascular system. This complex integrative effort is the current focus of several research projects, for example such as the Physiome Project (www.physiome.org.nz) and the EC-sponsored Virtual Physiological Human (VPH) Initiative (www.vph-noe.eu). Ultimately, the integration of these models should provide new tools enabling the biomedical community to link genetic and proteomic databases to anatomy and to functions at the cellular, tissue and organ level.

From a macroscopic point of view, the Forward Problem of Electrocardiology is described by the so-called Bidomain model for the evolution of the intra, extracellular and extracardiac potential fields. The two main components of the Bidomain model are: (a) the dynamics of the ionic current flow through the cardiac cellular membrane, modeled by a system of ordinary differential equations and (b) a macroscopic representation of the cardiac tissue modeled as a bidomain superposition of the intra and extra cellular media characterized by anisotropic conductivity tensors associated with the fiber architecture of the myocardium. The Bidomain model is computationally expensive because of the involvement of different space and time scales. In fact, meaningful portions of cardiac tissue have sizes on the order of centimeters, while the steep potential gradient is localized in a thin layer about 1 mm thick, requiring discretizations on the order of a tenth of millimeter. Moreover, a normal heartbeat can last on the order of 1 s, while the time constants of the rapid kinetics involved range from 0.1 to 500 ms, requiring in

some phases time steps on the order of the hundredths of milliseconds (or less when currents or shocks are applied). Therefore, in realistic three-dimensional models it is possible to have discrete problems with more than $O(10^7)$ unknowns at every time step and simulations have to be run for many thousands of time steps.

A simplified cardiac tissue model is the anisotropic Monodomain system, i.e. a parabolic reaction-diffusion equation describing the evolution of the transmembrane potential coupled with an ionic membrane model. This model has been widely used for three-dimensional simulations due to its reduced computational costs.

Current large-scale simulations of whole heartbeats using Bidomain and Monodomain models require adaptive and parallel tools in order to reduce their high computational cost. While both tools can in principle be applied to both space and time, most studies employ adaptive methods in time and parallel solvers in space, since the other alternatives are still the subject of current research even for simpler model problems in two dimensions. Therefore in this book, we present the main numerical techniques for efficiently simulating cardiac reaction-diffusion models. In particular, we focus on scalable parallel Bidomain solvers that are capable of efficiently scaling their performance for increasing processor counts in current and future multicore parallel computers.

Among the important aspects of cardiac modeling not covered in this book are cardiac mechanics, blood flow, electro-mechanical and fluid-mechanical coupling, and cardiac imaging. Research in these fields is also growing tremendously and a separate book would be necessary to properly present the main mathematical and numerical models available. For an overview of these related fields, we refer to e.g. the monographs [47, 140, 242, 369, 446], the works [138, 232, 246, 384, 385, 491] with the references therein, and the recent proceedings of the conferences FIMH (Functional Imaging and Modeling of the Heart) [21, 180, 266, 316, 327, 366, 447], CINC (Computing in Cardiology, http://cinc.org/archives/2013/, http://cinc.org/archives/2012/), STACOM (Statistical Atlases and Computational Models of the Heart) [74–76].

The book is structured in the following chapters.

In Chap. 1, we give a brief review of the basic physiology and anatomy of the heart, including the specialized cells of the cardiac conduction system, working cardiomyocytes, fibroblasts, extracellular matrix, collagen, gap junctions, connexin, cardiac stem cells and the fiber and laminar architecture of the ventricular myocardium. We then present the main phases of a cardiac action potential, its spatial and temporal heterogeneity, and continue by describing the main features of an electrocardiogram (ECG), with its leads, deflections, intervals and main alterations. The chapter concludes with a review of the main cardiac imaging techniques currently available.

Chapter 2, introduces the fundamental tools for modeling the bioelectric activity of excitable cells: the Nernst – Planck equation, the Goldman-Hodgkin-Katz (GHK) current-voltage relation, and the Nernst equilibrium potential, together with its thermodynamical derivation. Next, the Poisson-Nernst-Planck (PNP) electrodiffusion model is derived and two classical current – voltage relations are obtained in the short and long channel limits. With these tools, we can define the basic electrical

circuit model of the cellular membrane, where the transmembrane current, modeled as the sum of the capacitive and ionic currents through the membrane, must balance the given applied current. The ionic currents are then described by using the classical ion channel gating models, allowing us to build cardiac action potential models. We start with the celebrated Hodgkin-Huxley (H-H) model and briefly review some of the historical ventricular models based on the H-H formalism, such as the Beeler-Reuter, Luo-Rudy I and Luo-Rudy dynamic models, examining also how these ionic models satisfy the principle of charge conservation and how to derive the so-called restitution curve for the action potential duration of a given ionic model. Reduced models, such as the minimal FitzHugh-Nagumo model are also presented, together with their phase-plane analysis, bifurcation and frequency diagrams.

Chapter 3 presents mathematical models of periodic cardiac cells arrangements, beginning with one-dimensional fibers, deriving the cable equation, showing a one-dimensional homogenization technique and the main results on one-dimensional traveling waves, namely traveling fronts for the bistable equation and traveling pulses for the FitzHugh-Nagumo system with a diffusion term. We then move to models of cardiac tissue in more dimensions, illustrating a two-scale homogenization technique that allow us to derive an averaged Bidomain model, proving both well-posedness results for the cellular and the averaged models and convergence results based on Γ-convergence techniques. We then present an heuristic derivation of the anisotropic Bidomain model in both parabolic-parabolic and parabolic-elliptic forms. Well-posedness results are derived using different techniques, such as time semi-discretization, Faedo-Galerkin techniques, and fixed point arguments.

Chapter 4 presents the main reduced macroscopic cardiac models: the linear anisotropic Monodomain model, Eikonal models (both Eikonal-curvature and Eikonal-diffusion models), and the relaxed non-linear anisotropic Monodomain model. These model are then given in dimensional form and some well-posedness results are summarized. The chapter is concluded by a numerical comparison between activation time maps computed with these reduced models and the full Bidomain model.

Chapter 5 is devoted to the modeling of anisotropic cardiac sources, presenting both the differential and integral formulations of the potential field. Approximate representations of cardiac sources such as the heart surface and oblique dipole source models are given, as well as the cardiac sources splitting into axial and conormal components in both axially symmetric and orthotropic media. The chapter concludes with a numerical example illustrating this source splitting and its comparison with experimental results.

Chapter 6 briefly reviews the Inverse problem of Electrocardiology, in terms of cardiac sources, in terms of wavefront and in terms of potential alone, presenting the mathematical models of the cardiac electric sources and their numerical approximations.

Chapter 7 presents the main numerical techniques employed in the space and time discretizations of the Monodomain and Bidomain cardiac models. In particular, we apply the finite element method in space and finite difference methods in time. The latter can be fully implicit or semi-implicit, and can employ

decoupling techniques and operator splitting methods between the ordinary and partial differential equation components of the cardiac models. The chapter is concluded by a review of numerical methods for the eikonal–diffusion equation.

Chapter 8 is devoted to the construction and analysis of parallel solvers for the discrete Bidomain systems arising at each time step of an implicit or semi-implicit time discretization. Our parallel solvers are based on domain decomposition methods, more specifically on overlapping Schwarz methods, which provide scalable preconditioners accelerated with a Krylov space iterative method such as PCG or GMRES. After recalling the main results of the abstract Schwarz theory, we derive scalable convergence rate bounds for two-level and multilevel additive Schwarz preconditioners for the Bidomain system. We then present the results of several numerical tests with these Schwarz preconditioners in additive, multiplicative and hybrid form, showing their scalability on different parallel machines and investigating their performance with respect to the different discretization parameters. We also present how these Schwarz preconditioners can be combined with block-diagonal and block-factorized preconditioners suggested by the 2×2 block structure of discrete Bidomain systems.

Chapter 9 illustrates how to apply the Bidomain and Monodomain solvers developed in the previous chapters to simulate and study some of the most important phenomena in cardiac electrophysiology. More precisely, we present detailed simulations of: (1) the genesis of cardiac excitation and virtual electrode phenomena, in particular anode/cathode make/break and strength-interval (S-I) curves; (2) the anisotropic propagation of excitation and recovery fronts in three dimensional domains; (3) the effects of cardiac heterogeneities (transmural and apico-basal) on fronts propagation and APD distribution; (4) the morphology of electrograms, in particular of the QRS complex and the T wave; (5) the computation of excitation and repolarization time markers; (6) the presence of ischemic regions and effects such as ST-segment depression and elevation; (7) the simulation of cardiac reentry phenomena.

An Appendix lists some of the main cardiac simulation research projects, software libraries, some related monographs and tables of physical units and constants used in the book.

The authors would like to thank Prof. Bruno Taccardi for introducing them to the field of Mathematical Physiology and for many stimulating discussions, Prof. Alfio Quarteroni for his encouragement throughout this project, Dr. Fabrizio del Bianco and Dr. Lara Charawi for their help in proofreading the manuscript.

Pavia, Italy   Piero Colli Franzone
Milano, Italy   Luca F. Pavarino
Milano, Italy   Simone Scacchi
April 2014

Contents

Chapter 1
Basic Cardiac Anatomy and Electrocardiology

In this chapter, we briefly review the basic physiology and anatomy of the heart; a more complete treatment with many more details can be found in standard textbooks such as [189,267]. The heart is a double pump consisting of four chambers, two atria in the upper part, separated by the interatrial septum and two ventricles in the lower part, separated by the interventricular septum. Atria and ventricles are separated by the atrioventricular septum, which contains the tricuspid valve in the right heart and the mitral valve in the left heart. The right ventricle is connected to the pulmonary artery via the pulmonary valve and the left ventricle is connected to the aorta via the aortic valve, see Fig. 1.1 for a schematic view and [189] for more details. The ventricular walls are externally lined by a thin connective layer called epicardium and internally by the endocardium, with the cardiac muscle called myocardium in between. The left ventricular wall is about three times thicker than the right one, while the atrial walls are considerably thinner. The right heart functions as a pump driving blood through the pulmonary circulation, to the lungs and then back to the heart, while the left heart functions as another pump driving the oxygenated blood through the systemic circulation around the body. These two main cardiac functions, mechanical and haemodynamical, are driven and coordinated by the electrical activity of the heart, which is the main focus of this monograph. In this chapter, we will briefly review the essential features of the cardiac bioelectrical activity. The main events in a normal cardiac cycle are often described by a Wiggers diagram, see Fig. 1.2, showing the simultaneous time course of blood pressure (aortic, atrial, ventricular), ventricular volume, electrocardiogram, and phonocardiogram during a normal cardiac cycle.
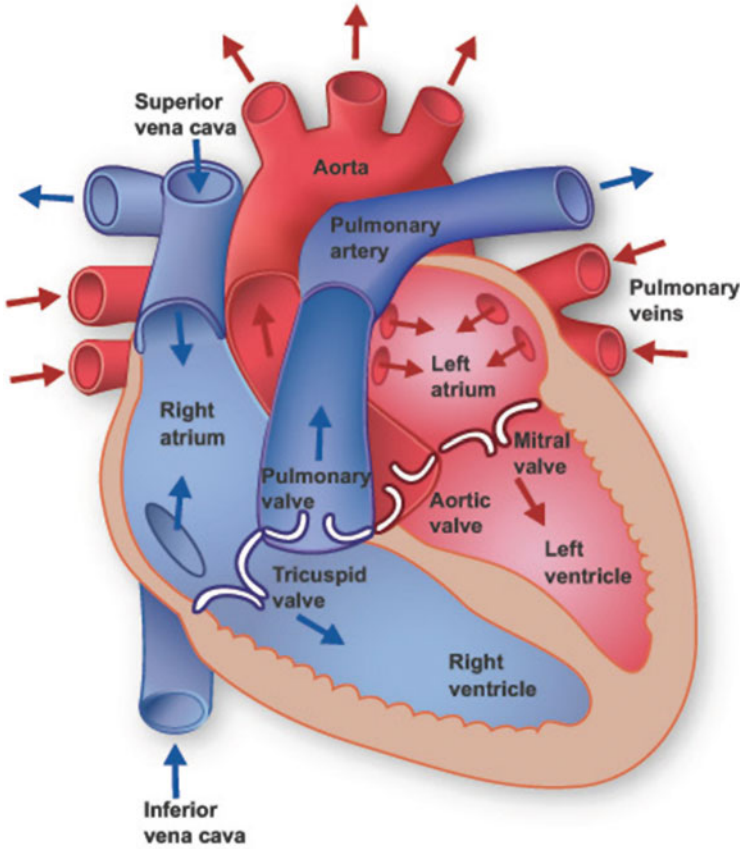
Fig. 1.1 Schematic diagram of the heart anatomy (From [240])

1.1   Conduction System: SA and AV Node, Purkinje Network

As in other muscle cells, the contraction of cardiac cells is initiated by an electrical activation due to an action potential, a depolarizing transitory membrane current that raises the transmembrane potential of an excitable cell from its resting value ranging between -90 and -80 mV to slightly positive values, followed by a repolarizing current that returns the transmembrane potential to its resting value. Differently from skeletal muscle cells, cardiac cells are able to autonomously activate, independently of a nervous stimulus. The electrical activity of the heart originates at the sinoatrial node (SAN), a group of cardiac pacemaker cells located on the right atrium, see Fig. 1.3 and [444] for more details. SAN cells have the fastest spontaneous depolarization speed of the cardiac conduction system and therefore they control the cardiac frequency in normal conditions. The autonomic nervous system and the endocrine system have direct influence over the SAN
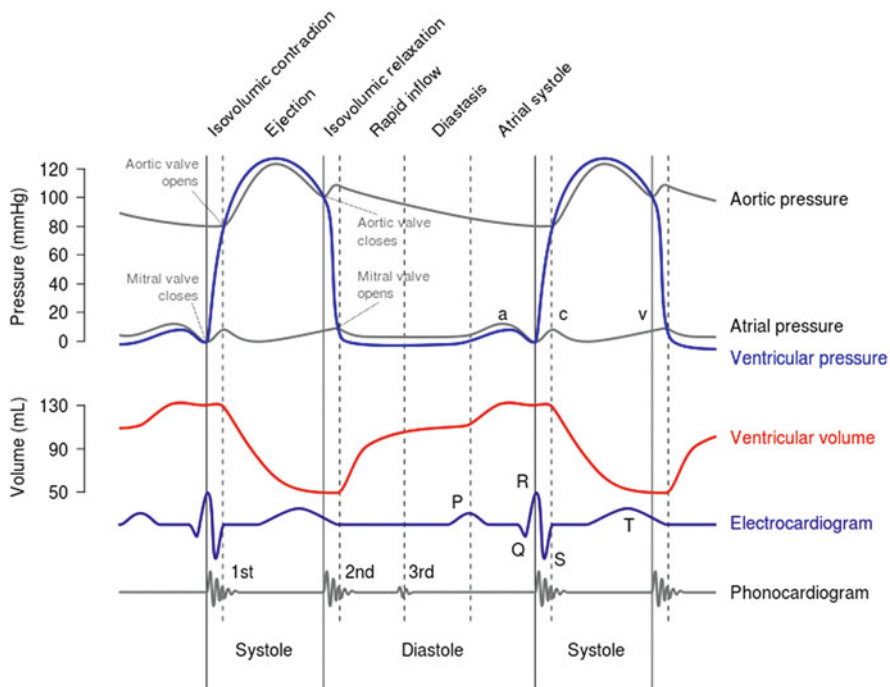
Fig. 1.2 Wiggers diagram of a normal cardiac cycle (From [239])
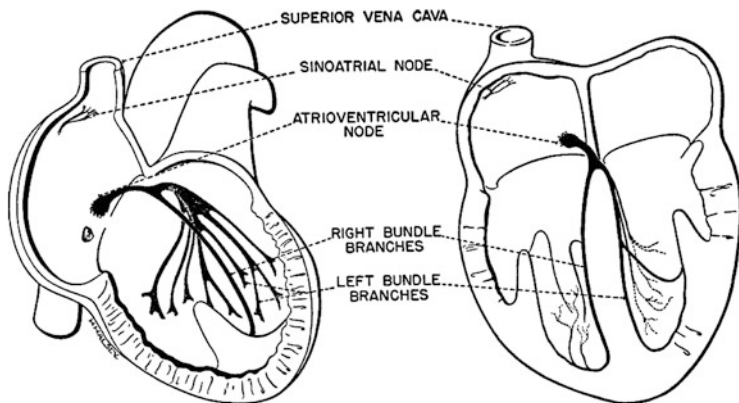
Fig. 1.3 Schematic diagram of the heart conduction system

cells and they can modulate both beat-to-beat and long-term variations of the cardiac frequency. In normal conditions, SAN cells generate an action potential that propagates throughout the right atrium and through Bachmann's bundle to the left atrium, stimulating the myocardium of both atria to contract. The activation front reaches the atrioventricular node (AVN) located at the base of the atria

where the interatrial septum and interventricular septum meet. AVN cells have a relatively slow conduction velocity and they are responsible for the major part of normal conduction delays between atrial and ventricular contractions. Such delays are properly timed in order to optimize the atrial pump activity and to protect the ventricles from too early stimulation. The AVN conducts the action potential through the nonexcitable atrioventricular septum, activating the specialized fibers of the bundle of His and the Purkinje network that spread as a tree-like left and right bundle branches ending on the endocardial surface of the ventricles. These Purkinje terminations transmit the action potentials to the ventricular walls and cardiac excitation then propagates throughout the ventricles. The electrical activation of the left ventricle, the largest cardiac chamber, normally starts at the interventricular septum, propagates towards the anteroapical region and reaches the posterobasal region. The electrical activation of the right ventricle starts shortly after the left ventricle activation; see e.g. [462].

1.2 Cardiac Tissue Organization

Cardiac muscle presents specific features different from the other two main types of muscle, skeletal and smooth muscles. The two fundamental features of cardiac muscle are its cyclical activity of contraction/relaxation, where the individual myocytes contract and relax according to a precise sequence and its homeostatic regulation in order to maintain a relatively constant circulatory pressure in spite of large flow variations. While skeletal myocytes are functionally separated and individually innervated, cardiac myocytes are electrically connected in order to form a single functional unit, known as cardiac syncytium. While skeletal muscle strength is modulated mostly by recruiting a variable number of motor units, in the cardiac syncytium recruitment is not possible and strength modulation relies on the myocytes strength modulation. Moreover, while in skeletal muscle cells a sequence of action potentials can generate an increasing force just by a temporal sum of single pulses, in cardiac myocytes each cycle of contraction/relaxation is activated by a single action potential that has a duration about 100 times longer.

In cardiac tissue are present three fundamental cell types with different structural and functional characteristics: working, nodal, and conduction cells.

Working cardiomyocytes. These form the mass of atrial and ventricular tissues and are responsible for force development. Their morphology is tubular (with possible branches), with a length of about 50–150 μm and a diameter of about 10–20 μm. Myocytes volume and shape can be complex and variable, according to the tissue region, species, developmental stage and disease processes. They are enclosed by a lipid membrane, the sarcolemma, and contain one or more nuclei, mitochondria, myofibrils, the sarcoplasmic reticulum, sarcomeres, the cytoskeleton anchoring the different organelles and an aqueous solution, the sarcoplasm, filling the intracellular space. The sarcolemma is a semi-permeable barrier and contains ion channels, pumps and exchangers that allow the inward and outward

currents involved in the action potential, as well as other proteins involved in cell adhesion and signalling. Cardiomyocytes exhibit a periodic structure with cross striations formed by alternating segments of thick and thin protein filaments. Their sarcolemma presents deep invagination along the Z-discs known as T-tubules, that allow depolarization of the membrane to quickly penetrate to the interior of the cell and play a critical role in the excitation-contraction coupling. Cardiomyocytes are mechanically coupled at specialized region of the membrane known as intercalated disks, which also include gap junction channels providing electrical coupling (see below).

Nodal cells. These cells constitute the SA and AV nodes and are able to autonomously activate due to the presence of specific ionic channels. Compared with working myocytes, they are smaller, more tortuous, have limited contractile activity and lack T-tubules. Nodal cells are richly innervated by parasympathetic and sympathetic nervous system fibers, that make them susceptible to autonomic influences. The SA and AV nodes also contain some transitional cells with intermediate features between nodal and atrial myocytes.

Conduction cells. These are also called Purkinje cells and have a morphology similar to working myocytes but with a larger diameter (up to $80\,\mu m$), reduced contractile proteins and a few T-tubules. They also have the ability of automaticity, but at a slower rate than SA or AV node cells.

Table 1.1 reports the average values of diastolic potential, upstroke velocity, overshoot, action potential duration (APD) and propagation velocity for different mammalian cardiomyocytes. For detailed measurements of conduction velocities in canine cardiac tissue, see [586, Table 16-1, p. 148].

Fibroblasts. Cardiac tissue is composed by myocytes that are arranged in a complex three-dimensional fiber and laminar architecture, described below. In areas between and surrounding cardiac myocytes there are cardiac fibroblasts, that constitute the major non-myocyte cell population in the ventricles [206]. Although cardiomyocytes occupy the largest volume fraction of the normal heart, they are outnumbered by the smaller fibroblasts. These are responsible for the synthesis of extracellular matrix proteins such as different types of collagen. Fibroblasts can

Table 1.1 Average values of diastolic potential, upstroke velocity, overshoot, action potential duration (APD) and propagation velocity for different mammalian cardiomyocytes

Cell types	Diastolic potential (mV)	Upstroke velocity (mV/ms)	Overshoot (mV)	APD (ms)	Propagation velocity (mm/ms)
SAN	−50, −60	1–10	30	100–200	0.03–0.05
Atria	−80	100–200	30	100–200	0.3–0.7
AVN	−60, −70	5–15	20	100–300	0.1
His budle/Purkinje	−80, −90	800	40	200–500	2–4
Ventricles	−80	100–200	40	200–500	0.5–0.8 along
					0.15–0.25 across

develop into myofibroblasts and both cell types are involved in the development of fibrosis in injured cardiac tissue. The structural arrangement of fibroblasts is still not well understood, but some authors have suggested that they are organized in sheets that follow closely the myocardial sheets, with some fibroblasts forming strands that bridge cleavage planes between sheets [206]. Cardiac fibroblasts are electrically non-excitable cells, but they are efficient mechano-electrical transducers. The possibility that fibroblasts may actively contribute to cardiac electrophysiology has been considered only recently, see [77, 192, 330, 424].

Extracellular matrix and collagen. The extracellular matrix (ECM) is an extensive and highly organized network of fibrous proteins, collagen and elastin, and is the major determinant of passive mechanical properties of cardiac tissue. The ECM plays important roles in muscle development, myoblast differentiation and in maintaining functional integrity of the myocardium [576]. Collagen and elastin have relative densities that can vary with tissue type, species and age. The ECM structure differs at different cardiac locations. In the endomysium, the collagen network surrounds single myocytes and interconnects neighboring myocytes. In the perimysium, bundles of collagen fibers envelope groups of adjacent myocytes, providing the laminar cardiac structure and long perimysal collagenous tendons can link adjacent laminae. In the epimysium, layers of collagen and elastin are found at the epicardium and endocardium.

Gap junctions and connexin. Cardiac myocytes are mechanically connected by junctions anchored to the cytoskeleton, known as intercalated disks, and are electrically connected by electrical synapses, known as gap junctions, connecting myocytes mostly end-to-end (longitudinal gap junctions) but also laterally (transverse gap junctions) [423]. Gap junctions are small ionic channels with low selectivity, with a diameter of about 2 nm and length of about 2–12 nm. They are composed of two adjoint connexons, located in the membranes of the two coupled cells, and each connexon is formed by six channel proteins known as connexins (Cx40, Cx43, Cx45). Cx43 is the main cardiac connexin and is mostly present in ventricular tissue. Cx40 is present in atrial tissue and in the conduction system, while Cx45 is present only in the conduction system. Longitudinal gap junctions are prevalent in ventricular myocardium, yielding a macroscopic electrical coupling that is anisotropic.

Cardiac stem cells. The human heart has been traditionally viewed as a terminally differentiated postmitotic organ, with cardiomyocytes established in number at birth and persisting throughout the lifespan of the organism. This view has been recently changed by the discovery that cardiac stem cells live in the heart and differentiate into the various cardiac cell lineages; see e.g. [41, 46, 190, 289, 296] and the references therein. Cardiac stem cells regulate myocyte turnover and condition myocardial recovery after injury. The initial enthusiasm triggered by the discovery of endogenous cardiac stem cells was then followed by some controversy over the nature of myocyte renewal in the human heart. Intense research studies are underway to explore this new field of cardiac regeneration. Several categories of cardiac progenitors have been described and diverse experimental strategies to remuscularize the injured heart using adult stem cells and pluripotent stem cells,

cellular reprogramming and tissue engineering are in progress. The novel results that are rapidly appearing in the literature impose a reconsideration of the mechanisms involved in myocardial aging and the progression of cardiac hypertrophy to heart failure. Even if controversial experimental issues are still present, cardiac regeneration studies have great potentials and could soon lead to new understanding and treatments of infarcted hearts and to restoration of myocardial mass and ventricular function; see e.g. [190].

1.3   Fiber and Laminar Architecture of Ventricular Myocardium

In addition to the complex extracellular network of fibroblasts and collagen described above, the ventricular myocardium exhibits a complex three-dimensional spatial organization where myocytes are connected mostly end-to-end to form cardiac fibers with varying orientation. This ventricular fiber orientation rotates smoothly between endocardium and epicardium, see Streeter [498]. Cardiac fibers are also known to have an additional laminar organization consisting of muscle sheets, typically 4–6 myocytes thick, running radially from epi- to endocardium, with surface orientation varying throughout the ventricles. These sheets are separated by gaps called cleavage planes and by layers of connective tissue, see e.g. [138, 234, 292–294, 465, 530].

Diffusion tensor magnetic resonance imaging (DT-MRI) has been used to measure fiber orientation as the principal eigenvector of the diffusion tensor measured at each image voxel in formaldehyde-fixed hearts [465]. In DT-MRI, the pattern of diffusion is represented mathematically by a symmetric second-rank tensor in three-dimensional space, which can be written as a 3×3 matrix. The three orthogonal eigenvectors of this tensor (ranked in order of the magnitudes of their corresponding eigenvalues) have been related to cardiac structure, with the eigenvalues representing the diffusion along three principal axes. Theory suggests that the direction of greatest proton diffusion, i.e. the eigenvector with the largest eigenvalue (primary eigenvector) will be along the fiber long axis, intermediate diffusion (the secondary eigenvector) will lie in the myolaminar plane, orthogonal to the fiber long axis. The third and minor direction of diffusion (the tertiary eigenvector) is by definition orthogonal to the primary and secondary eigenvectors, so it is normal to the myolaminar plane. The correspondence between the primary eigenvector and fiber orientation, and the secondary and tertiary eigenvectors and sheet orientation has been validated by combined DT-MRI and three-dimensional histological reconstruction of fiber and sheet structure.

Therefore, at any myocardial point $\mathbf{x}$, it is possible to identify a triplet of orthonormal principal axes $\mathbf{a}_l(\mathbf{x})$, $\mathbf{a}_t(\mathbf{x})$, $\mathbf{a}_n(\mathbf{x})$, with $\mathbf{a}_l(\mathbf{x})$ parallel to the local fiber direction, $\mathbf{a}_t(\mathbf{x})$ and $\mathbf{a}_n(\mathbf{x})$ tangent and orthogonal to the radial laminae, respectively, and both being transversal to the fiber axis [34, 137, 292, 293]; see Fig. 1.4 for a
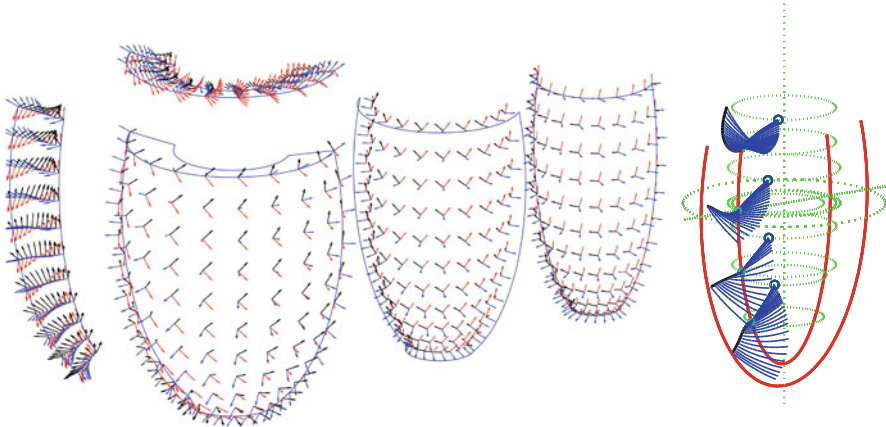
Fig. 1.4 *Left*: schematic representation of ventricular fiber architecture with orthonormal triplets of vectors along fiber (*red*), and two orthogonal vectors (*blue* and *black*) on intramural, epi-, mid-, endocardial sections. *Right*: schematic view of a few laminae (*blue*) on selected sections (outlined in *green*) of the ventricular wall (outlined in *red*)

schematic representation of ventricular fiber architecture of triplet of orthonormal principal axes (left) and laminar organization (right).

1.4 Cardiac Action Potentials

Cardiac cells are excitable cells, some autonomously (SAN pacemaker cells) and some after a proper electrical stimulus. The excitation of a cardiac cell causes a rapid variation of its potential difference across the cell membrane, the so-called transmembrane potential. If the stimulus is below a certain threshold value, the transmembrane potential quickly returns to its resting value after the stimulus ends. On the other hand, if the stimulus is above threshold, the cell membrane depolarizes and the transmembrane potential increases from the negative resting value to a value around or above zero, remains around this value for a certain interval and then returns to the resting value after the membrane repolarizes. This event is called an action potential.

1.4.1 Action Potential Phases

The main phases of a typical ventricular action potential are displayed in Fig. 1.5.

Phase 0. In this phase, myocytes undergo a rapid depolarization due to the opening of the fast Na^+ channels. This causes a rapid increase in the membrane
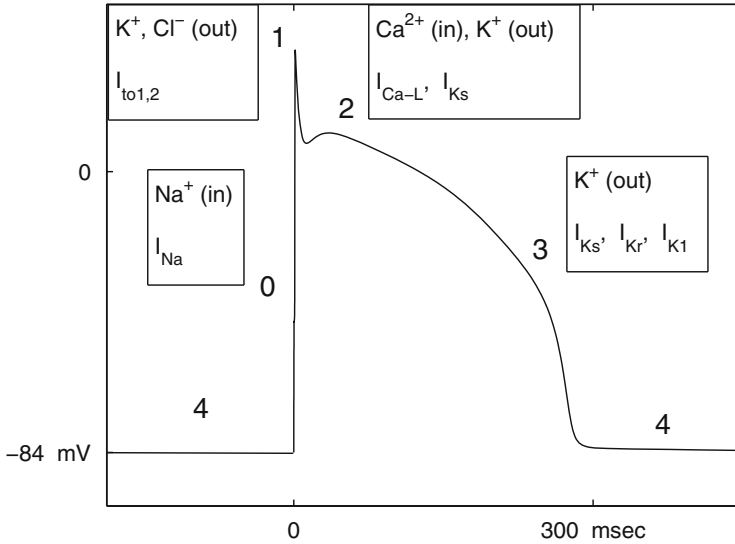
Fig. 1.5 Schematic plot of a cardiac action potential with its phases 0 (depolarization or upstroke), 1 (peak or notch), 2 (plateau), 3 (repolarization or recovery), 4 (resting) and main ions and currents involved in each phase

conductance and thus a rapid influx of Na^+ ions into the cell, the I_{Na} current, through sodium channels formed by alpha-subunits with channel proteins of the $NA_V 1.\#$ family encoded by SCN genes (mostly $Na_V 1.5$ channel protein encoded by the SCN5A gene associated with Long QT and Brugada syndrome channelopathies) and by beta-subunits with $Na_V \beta\#$ channel proteins encoded by SCN#B genes.

Phase 1 occurs with the inactivation of the fast Na^+ channels. The transient net outward current causing the small downward deflection of the action potential is due to K^+ and Cl^- ions carried by the I_{to1} and I_{to2} currents, respectively.

Phase 2 is the plateau phase sustained by a balance between inward movement of Ca^{2+}, the I_{Ca} current through L-type calcium channels ($Ca_V 1.2$ channel protein encoded by CACNA1C gene) and outward movement of potassium ions K^+, the I_{Ks} current through the slow delayed rectifier potassium channels (KvLQT1 channel protein encoded by the KCNQ1 gene). The sodium-calcium exchanger current $I_{Na,Ca}$ and the sodium/potassium pump current $I_{Na,K}$ also play minor roles during phase 2.

Phase 3. This is the "rapid repolarization" phase of the action potential, when the L-type Ca^{2+} channels close while the slow delayed rectifier (I_{Ks}) K^+ channels are still open. This ensures a net outward current, corresponding to negative change in membrane potential, thus allowing more types of K^+ channels to open. These are primarily the rapid delayed rectifier K^+ channels (I_{Kr} current, $K_V 11.1$ channel protein encoded by hERG or KCNH2 genes) and the inwardly rectifying K^+ current I_{K1}. This net outward, positive current causes the cell to repolarize. The delayed

rectifier K^+ channels close when the membrane potential is restored to about -80 to -85 mV, while I_{K1} is maintained throughout phase 4, contributing to set the resting membrane potential.

Phase 4 is the resting phase, during which the transmembrane potential remains at the resting value of about -84 mV until it is stimulated by an external electrical stimulus.

1.4.2   Action Potential Heterogeneity

Cardiac action potentials differ significantly in different regions of the heart. Indeed, action potentials from atrial, ventricular and specialized conduction myocytes exhibit different waveforms, see Fig. 1.6. Moreover, isolated myocytes with different action potential morphologies have been observed in the epicardial, midmyocardial (M-cells), and endocardial regions (transmural heterogeneity) and also along the apex-to-base direction of the ventricle (apex-to-base heterogeneity). When these myocytes are embedded in the ventricular wall, their heterogeneous properties affect the sequence of repolarization and the actual APD distribution in the entire wall (spatial dispersion of APD).

Right and left ventricle heterogeneity. Right ventricular myocytes from dog hearts show action potentials with shorter APD and deeper notches than in left ventricular myocytes. Some authors have related these features to larger I_{to} and I_{Ks} currents in the right ventricle and have suggested that arrhythmogenic gradients could arise at the interventricular septum.
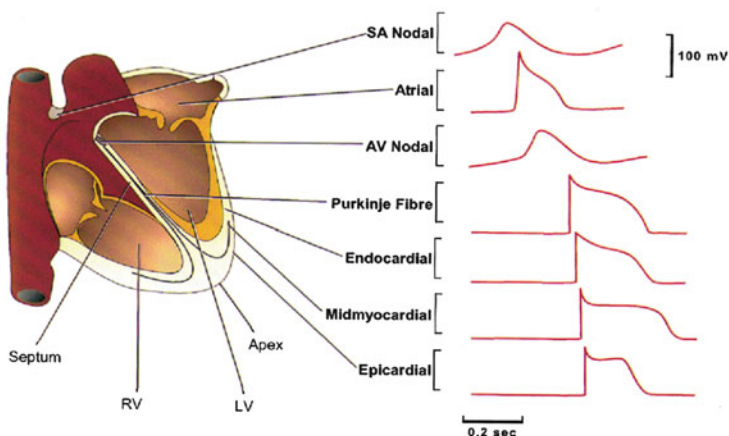
Fig. 1.6 Heterogeneity of cardiac action potentials from different regions of the heart

Apex-to-base dispersion. Rabbit ventricular myocytes from the basal region show action potential with shorter APD than myocytes from the apex region. Moreover, I_{Kr} and I_{Ks} currents are smaller in apical than in basal myocytes, with I_{Kr} the largest in apical cells and I_{Ks} the largest in basal cells. The shorter basal APD causes ventricular repolarization to proceed from the basal toward the apical region. Transmural and apex-to-base APD dispersion have been shown to be arrhythmogenic in many heart preparations.

Transmural dispersion. Studies in isolated tissues and myocytes in several animal species have found differences in action potentials shapes and APD across the ventricular wall, showing a transmural dispersion with shorter APD in subepicardial than in subendocardial cells and with the longest APD in midmyocardial cells, the so-called M-cells; see e.g. [7–10, 553, 572]. Studies have found transmural heterogeneity in the expression of ionic channels, in particular in the I_{Na}, I_{Kr}, I_{Ks}, I_{to1} currents and in the Na^+/Ca^{2+} exchanger. There has been some controversy whether transmural repolarization gradient are present in vivo and in particular in human heart, since cell coupling and electrotonic currents tend to mask APD heterogeneity. Since the T wave in the ECG (described in the next section) marks ventricular repolarization and the APD determines the QT interval, transmural dispersion of repolarization contributes to amplitude, polarity and duration of the T wave and to the QT interval duration. It can also contribute to ST segment elevation, QT dispersion and pathological U waves.

Temporal dispersion of APD. In addition to spatial dispersion, APD can also show temporal dispersion due to beat-to-beat changes alternating between short and long action potentials. For example, T wave alternans (beat-to-beat changes of the T wave amplitude) are associated with reentrant ventricular tachycardia. Moreover, spatial and temporal dispersion together seem to be associated with a broad range of cardiac arrhythmias. For example, spatial dispersion of APD and refractoriness can lead to temporal dispersion of repolarization after a premature stimulus, and the resulting spatio-temporal dispersion can generate a functional conduction block initiating reentry.

1.5   The Electrocardiogram (ECG)

The ECG is the registration of the extracellular potential on the body surface due to the propagation of cardiac action potentials. The registering electrodes are usually placed at standard positions described below.

1.5.1 ECG Leads

Einthoven leads. Given the potentials at the left arm Φ_L, at the right arm Φ_R and at the left foot Φ_F, Einthoven standard limb leads are defined as

$$V_I = \Phi_L - \Phi_R$$
$$V_{II} = \Phi_F - \Phi_R$$
$$V_{III} = \Phi_F - \Phi_L.$$

By Kirchhoff's law, we have $V_I + V_{III} = V_{II}$. Einthoven assumed that the heart is located at the center of a homogeneous spherical conductor representing the torso, and that the three vectors associated with these three leads form an equilateral triangle in the vertical frontal plane of the body, see Fig. 1.7.

Augmented leads. In addition to the three Einthoven leads, three additional leads, denoted by aV_R, aV_L, aV_F and known as augmented leads, are defined on the frontal plane in the directions that bisect the sectors associated with each pair of Einthoven leads. For example, the augmented aV_F lead is defined by

$$V_{aV_F} = \Phi_F - \frac{\Phi_L + \Phi_R}{2}.$$
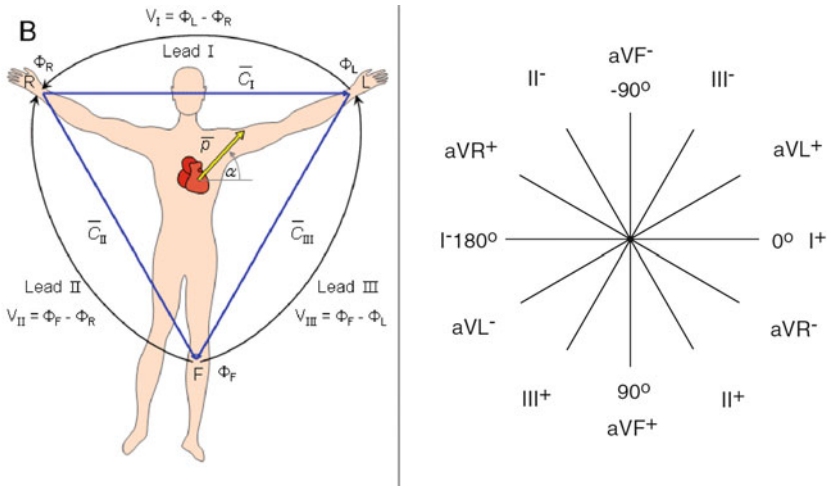
Fig. 1.7 Schematic view of Einthoven standard limb leads (*left*) and augmented leads (*right*)
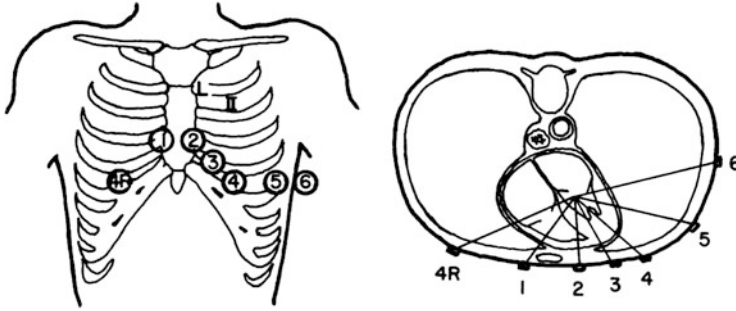
Fig. 1.8 The six precordial leads $V_1, \ldots, V_6$ in a frontal view (*left*) and horizontal cross-section (*right*) of the thorax

In this way, we obtain six leads that divide the frontal plane into equal 30° sectors, see Fig. 1.7. In order to measure potentials close to the heart, six additional leads are defined on a horizontal plane by using the Wilson central terminal

$$\Phi_{CT} = \frac{\Phi_R + \Phi_L + \Phi_F}{3}.$$

Precordial leads. The six precordial (or chest) leads, denoted by $V_1, \ldots, V_6$, are obtained by comparing the Wilson central terminal with unipolar electrode readings taken from six different locations on the chest, see Fig. 1.8 and [444] for more details. V_1 and V_2 are located at the fourth intercostal space on the right and left side of the sternum, and the other four proceed around the left chest just below the fourth rib, ending with V_6 under the armpit. The 12 leads $I, II, III, aV_R, aV_L, aV_F, V_1, \ldots, V_6$ form the most commonly used clinical ECG system.

1.5.2 ECG Deflections and Intervals

A schematic view of a normal electrocardiogram is shown in Fig. 1.9, while an example of a 12-lead recording is shown in Fig. 1.10. The various deflections in the ECG signal are commonly denoted in alphabetic order as P, Q, R, S, T, U. The temporal sequence of these waves remains constant, but their amplitude and sign can vary depending on the recording electrode position on the thorax.

P wave. The P wave is associated with atrial depolarization, that continues during the subsequent PQ segment. The completion of atrial repolarization generates an atrial Ta wave not visible in normal ECGs because hidden by the QRS complex. The PQ segment is also associated with the delay between the beginning of atrial and ventricular activation (atrioventricular conduction time).
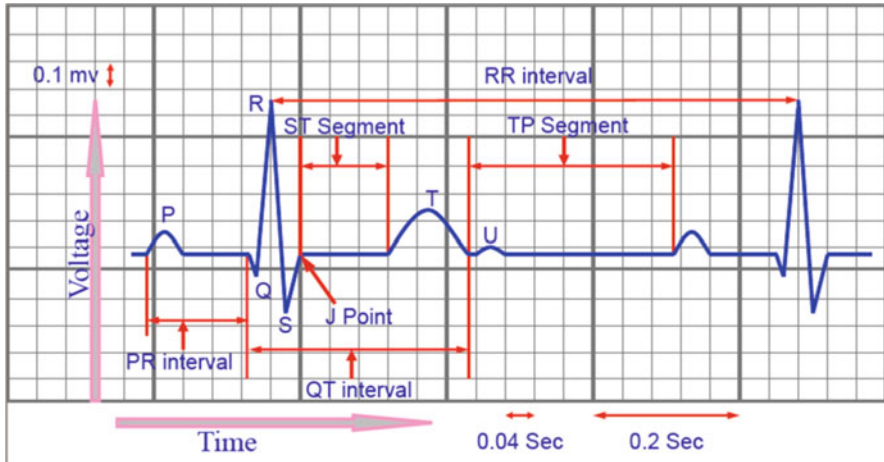
Fig. 1.9 Schematic view of a normal ECG waveform
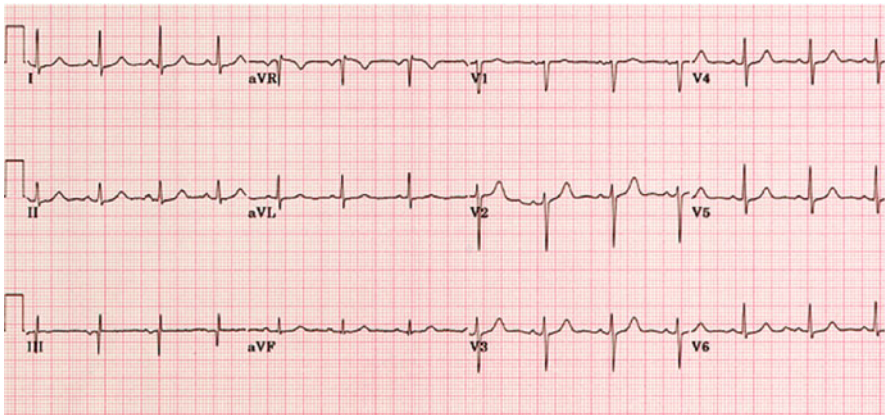
Fig. 1.10 Sample of actual ECG waveforms

QRS complex. The subsequent QRS complex, usually the largest deflection in the ECG, is associated with the complex activation sequence of the ventricles, resulting in upward and downward deflections and multiple peaks in most of the leads. The Q wave corresponds to the activation of the interventricular septum, the R wave corresponds to the septum activation completion and the apex activation, the S wave corresponds to the activation of the ventricular free walls and the basal region. These three waves are not always detectable and can sometimes merge, yielding a quite variable morphology of the QRS complex.

ST segment. The QRS complex in normal ventricular myocytes is followed by a rather long period where all cells are depolarized during the plateau of the action potential. This isoelectric interval, known as ST segment, lasts a few hundreds

milliseconds, starting at the end of the QRS complex (the so-called J point) and ending at the beginning of the T wave.

T wave. The T wave signals ventricular repolarization and its morphology depends on the repolarization sequence through the ventricles. In normal hearts, the start of the T wave is thought to correlate with the plateau ending of the epicardial cells, the T wave peak with the full repolarization of the epicardium, the end of the T wave with the repolarization of the midmyocardial M-cells.

QT interval. The QT interval is measured from the beginning of the QRS complex to the end of the T wave. Since the QT interval is strongly frequency dependent, a corrected QT interval QTc is sometimes defined, for example by normalizing it as $QTc = QT/\sqrt{RR}$.

U wave. After the T wave, it is sometimes present a smaller diastolic deflection known as U wave. Some authors explain the U wave as due to repolarization of the papillary muscles or Purkinje fibers, while others explain it as due to late repolarization of M-cells or yet to afterpotentials caused by ventricular stretch.

Other important cardiac events too weak to be detected on the ECG include atrial repolarization, SA nodal activation, AV nodal conduction and Purkinje network propagation. An example of a normal 12-lead ECG recording is shown in Fig. 1.10.

1.5.3 ECG Diagnosis

We briefly review here some of the main ECG alterations. For a more complete treatment see [189] and [317].

Normal sinus rhythm. The normal sinus rhythm of a healthy normal heart has an ECG with all three P, QRS, T complexes normal, distinguishable and with a frequency between 60 and 100 bpm (beats per minute).

Sinus bradycardia and tachycardia. A sinus rhythm of less than 60 bpm is called sinus bradycardia and may be a consequence of increased vagal or parasympathetic tone. A sinus rhythm of higher than 100 bpm is called sinus tachycardia; most often it is due to physiological response to physical exercise or psychical stress, but may also result from congestive heart failure.

Sinus arrhythmia. If the sinus rhythm is irregular such that the longest PP or RR interval exceeds the shortest interval by 0.16 s, then it is called sinus arrhythmia, a very common situation in all age groups and not considered a heart disease in young people.

Nonsinus atrial rhythm and wandering pacemaker. If the origin of atrial contraction is located somewhere else in the atria other than the sinus node (nonsinus atrial rhythm) or wanders in the atria (wandering pacemaker), then the P waves can have variable polarity and the PQ interval variable duration.

Paroxysmal atrial tachycardia (PAT). Paroxysmal atrial tachycardia describes the condition when the P waves are a result of a reentrant activation front (circus movement) in the atria, usually involving the AV node. This leads to a high rate of activation, usually between 160 and 220 bpm. In the ECG the P wave is regularly

followed by the QRS complex. The isoelectric baseline may be seen between the T wave and the next P wave.

Atrial flutter. When the heart rate is sufficiently elevated so that the isoelectric interval between the T wave ending and the P wave beginning disappears, the arrhythmia is called atrial flutter. The origin is also believed to involve a reentrant atrial pathway. The frequency of these fluctuations is between 220 and 300 bpm. The AV node and, thereafter, the ventricles are generally activated by every second or every third atrial impulse (2:1 or 3:1 heart block).

Atrial fibrillation. The activation in the atria may also be fully irregular and chaotic, producing irregular fluctuations in the baseline called atrial fibrillation. A consequence is that the ventricular rate is rapid and irregular, though the QRS contour is usually normal.

Ventricular tachycardia. Slower conduction in ischemic ventricular muscle that leads to circular activation (reentry) causes activation of the ventricular muscle at a high rate (over 120 bpm) and generates rapid, bizarre, and wide QRS complexes. This arrythmia is called ventricular tachycardia and is often a consequence of ischemia and myocardial infarction.

Ventricular fibrillation. When ventricular depolarization occurs chaotically, the situation is called ventricular fibrillation. The ECG has coarse irregular deflections without QRS-complexes. The cause of fibrillation is the establishment of multiple re-entry loops usually involving diseased heart muscle. The contraction of the ventricular muscle is irregular and is ineffective at pumping blood, with a result of almost immediate loss of consciousness and death within minutes.

Atrioventricular blocks. In normal sinus rhythm, the P waves always precede the QRS-complex with a PR-interval of 0.12–0.2 s. When the P wave always precedes the QRS complex but the PR interval is prolonged over 0.2 s, first-degree atrioventricular block is diagnosed. If the PQ interval is longer than normal and the QRS complex sometimes does not follow the P wave, the atrioventricular block is of second-degree. If the PR interval progressively lengthens, leading finally to the dropout of a QRS complex, the second degree block is called a Wenkebach phenomenon. Complete lack of synchronism between the P wave and the QRS complex is diagnosed as third-degree (or total) atrioventricular block.

Bundle-branch blocks. In right bundle-branch block (RBBB), the right bundle-branch is defective so that the electrical impulse cannot travel through it to the right ventricle, but activation reaches the right ventricle by proceeding from the left ventricle. This can be seen in the ECG as a QRS complex wider than 0.1 s, or a broad terminal S wave in lead I, or a double R wave in lead V1. The situation in left bundle-branch block (LBBB) is similar, but activation proceeds in a direction opposite to RBBB. The ECG has a broad and tall R wave, usually in leads I, aVL, V5 or V6.

Wolff-Parkinson-White (WPW) syndrome. In this syndrome, the QRS complex initially exhibits an early upstroke called the delta wave. The interval from the P wave to the R spike is normal, but the early ventricular excitation forming the delta wave shortens the PQ time. The cause of the WPW syndrome is the passage of activation from the atrium directly to the ventricular muscle via an abnormal route,

called the bundle of Kent, which bypasses the AV junctions. This activates part of the ventricular muscle before normal activation reaches it via the conduction system (after a delay in the AV junction), a process called pre-excitation.

Atrial hypertrophy. Right atrial hypertrophy is a consequence of right atrial overload, due to tricuspid valve disease (stenosis or insufficiency), pulmonary valve disease, or pulmonary hypertension. An unusually large (i.e. 0.25 mV) P wave is seen in leads aVF and III. Left atrial hypertrophy is a consequence of left atrial overload, due to mitral valve disease (stenosis or insufficiency), aortic valve disease, or hypertension in the systemic circulation. The P wave exhibits two phases with the same polarities in lead I but opposite polarities in V1. This typical P wave form is called the mitral P wave.

Ventricular hypertrophy. Right ventricular hypertrophy is a consequence of right ventricular overload, due to pulmonary valve stenosis, tricuspid insufficiency, pulmonary hypertension or many congenital cardiac abnormalities, such as a ventricular septal defect. The ECG shows a tall R wave of 0.7 mV in lead V1. Left ventricular hypertrophy is a consequence of left ventricular overload, due to mitral valve disease, aortic valve disease, or systemic hypertension. The ECG has a tall R wave in leads I, III, V5, V6 and has a tall S wave in leads III, V1 and V2.

Myocardial ischemia and infarction. The decreased transport of oxygen to the cardiac muscle due to occlusion of a coronary artery is called ischemia. Ischemia causes changes in the resting potential and in the repolarization of the muscle cells, which are seen as changes in the T wave. If the oxygen transport is terminated in a certain area, the heart muscle dies in that region. This is called an infarction.

1.6 Cardiac Imaging

As part of the rapidly evolving fields of medical and biological imaging, also the field of cardiac imaging is currently experiencing tremendous progresses that are producing better imaging techniques seeking to reveal, diagnose, or examine both cardiac diseases and the normal cardiac anatomy and physiology. Among the many techniques available, we mention the following ones and refer the interested readers to some of the recent monographs [83, 291, 475, 554] and reviews [2, 83] in the field.

Angiocardiography is a technique for radiographic examination of the heart chambers and thoracic veins and arteries. A liquid radiocontrast agent, typically containing iodine, is injected into the bloodstream, then the tissues are examined using X-rays. To avoid dilution, the radiopaque material is typically introduced with a catheter, a process known as selective angiocardiography. The X-ray image is normally captured on high speed serial media that allow the motion to be observed, such as a 35 mm film. The process requires fasting before the test, with a sedative and an antihistamine being administered before the test. Angiocardiography can be used to detect and diagnose congenital defects in the heart and adjacent vessels. The use of angiocardiography has declined with the introduction of echocardiography.

However, angiocardiography is still in use for selected cases as it provides a higher level of anatomical detail than echocardiography.

Coronary catheterization uses pressure monitoring and blood sampling through a catheter inserted into the heart through blood vessels in the leg to determine the functioning of the heart, and, following injections of radiocontrast dye, uses X-ray fluoroscopy, typically at 30 frames per second, to visualize the position and size of blood within the heart chambers and arteries. Coronary angiography is used to determine the patency and configuration of the coronary artery lumens.

Echocardiogram. Transthoracic echocardiogram uses ultrasonic waves for continuous heart chamber and blood movement visualization. In recent times, it has become one of the most commonly used tools in diagnosis of heart problems, as it allows non-invasive visualization of the heart and the blood flow through the heart, using a technique known as Doppler.

Transoesophageal echocardiogram uses a specialized probe containing an ultrasound transducer at its tip, that is passed into the patient's esophagus. It is used in diagnosis of various thoracic defects or damage, i.e. heart and lung imaging. It has some advantages and disadvantages over thoracic or intravascular ultrasound.

Percutaneous echocardiogram, also known as intravascular ultrasound, is an imaging methodology using specially designed, long, thin, complex manufactured catheters attached to computerized ultrasound equipment to visualize the lumen and the interior wall of blood vessels.

3D echocardiography (also known as 4D echocardiography when the picture is moving) is now possible, using a matrix array ultrasound probe and an appropriate processing system. This enables detailed anatomical assessment of cardiac pathology, particularly valvular defects, and cardiomyopathies. The ability to slice the virtual heart in infinite planes in an anatomically appropriate manner and to reconstruct three-dimensional images of anatomic structures makes 3D echocardiography unique for the understanding of the congenitally malformed heart. Real Time 3-Dimensional echocardiography can be used to guide the location of bioptomes during right ventricular endomyocardial biopsies, placement of catheter delivered valvular devices, and in many other intraoperative assessments. The 3D Echo Box developed by the European Association of Echocardiography offers a complete review of Three Dimensional Echocardiography; see http://www.escardio. org/communities/EACVI/education/echo-box/3d-echobox-2/Pages/welcome.aspx.

Computed Tomography Angiography (CTA), an imaging methodology using a ring-shaped machine with an X-Ray source spinning around the circular path so as to bathe the inner circle with a uniform and known X-Ray density. Cardiology uses are growing with the incredible developments in CT technology. Currently, multidetector CT, specially the 64 detector-CT are allowing to make cardiac studies in just a few seconds (less than 10 s, depending on the equipment and protocol used). These images are reconstructed using algorithms and software. Great development and growth will be seen in the short term, allowing radiologists to diagnose cardiac artery disease without anesthesia and in a non-invasive way.

Magnetic Resonance Imaging (MRI) (originally called nuclear magnetic resonance imaging), an imaging methodology based on aligning the spin axis of nuclei within molecules of the object being visualized using both powerful superconducting magnets and radio frequency signals and detectors. Cardiology uses are growing, especially since MRI differentiates soft tissues better than CT and allows for comprehensive exams including the quantitative assessment of size, morphology, function, and tissue characteristics in one single session. Current implementations for cardiology uses are sometimes limited by lengthy protocols, claustrophobia and contraindications based on some complex metallic implants (pacemakers, defibrillators, insulin pumps), while artificial valves and coronary stents are generally not problematic. Image quality can be reduced by the continuous movement of heart structures. There is a promising future in cardiac MRI by more efficient scans, increasing availability of scanners and more widespread knowledge about its clinical application.

Optical mapping. Traditionally, surface electrodes have been, and continue to be used to measure extracellular cardiac electric potentials. Arrays of electrodes are placed on the heart's surface and electrical activities are recorded simultaneously from a limited number (a few hundred) of sites. These surface contact mapping techniques may suffer from low spatial and temporal resolution, low depth field, and far-field effects.

Rapid technical innovations during the last decades of the twentieth century have led to the development of sophisticated optical mapping techniques, see e.g. [18, 227]. Optical mapping is performed by using voltage sensitive dyes and imaging systems with high temporal and spatial resolutions (i.e., acquiring thousands of pixels in a few milliseconds) and can be used in a variety of settings from the subcellular level in vitro to the whole heart in vivo. Both activation and repolarization times can be measured directly from different sites in both normal and diseased heart (e.g., ischemic heart).

Numerical studies of optical mapping techniques have been carried out using the Bidomain equations coupled with a photon diffusion equation, see e.g. [50,404,433] and the references therein.

Chapter 2
Mathematical Models of Cellular Bioelectrical Activity

In this chapter, we briefly review the main mathematical models used in cellular electrophysiology, and we refer to [212, 273] for a more complete treatment and additional topics.

2.1 Excitable Cellular Membranes

A fundamental topic in molecular biophysics is the study of ionic currents through protein channels of excitable cellular membranes as a function of the ionic concentrations, applied voltage and channel structure.

The cellular membrane is a lipid bilayer in which are immersed proteins. The membrane contains water-filled pores and protein-lined pores, called *ionic channels*, which allow the flow of specific ions, primarily Na^+, K^+, Cl^-, and Ca^{2+}. The membrane acts as a barrier to the free flow of ions and maintains concentration differences of these ions. The concentration gradients produce a potential difference across the membrane, the *transmembrane potential*, that drives the ionic currents.

Concentration differences are set up and maintained by active transport mechanisms that use energy to pump ions against their concentration gradients.

One of the most important of these pumps is the $Na^+ - K^+$ *ATPase* sodium-potassium pump: it uses energy stored in *ATP* (adenosine triphosphate) molecules to pump Na^+ out of the cell and K^+ in

$$ATP + 3[Na^+]_i + 2[K^+]_e \rightarrow ADP + P_i + 3[Na^+]_e + 2[K^+]_i,$$

releasing *ADP* (adenosine diphosphate) and inorganic phosphate P_i. For example, in the squid giant axon: $[Na^+]_i = 50$ mM $< [Na^+]_e = 437$ mM, $[K^+]_i = 397$ mM $> [K^+]_e = 20$ mM. At the equilibrium, this biochemical pump maintains a potential jump between the intra- and extracellular space of $v_{rest} = -65$ mV.

2.2   The Nernst-Planck Equation

In general, the flux across the membrane of the generic ion K with valence z is the sum of two contributions, the diffusion flux J_{diff} and the electric flux J_{elect}, all measured in $mol\,cm^{-2}\,s^{-1}$. The constitutive law describing this total flux is known as the Nernst-Planck equation.
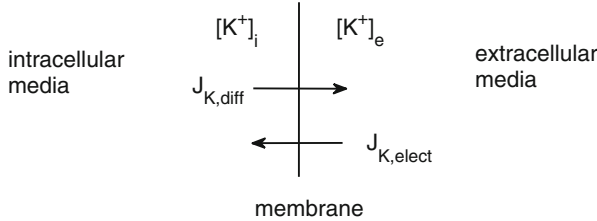
Due to the ion motion by diffusion, down the concentration gradient, the diffusion flux J_{diff} satisfies *Fick law*:

$$J_{diff} = -D\nabla c,$$

where D is the diffusion coefficient $(cm^2\,s^{-1})$ and c is the concentration $(mol\,cm^{-3})$.

Due to the ion motion by electric field, the electric flux J_{elect} satisfies the *Planck equation*:

$$J_{elect} = -\frac{z}{|z|}\mu c\nabla u,$$

where u is the electric potential (V), μ is the mobility of the ion $(cm^2\,V^{-1}\,s^{-1})$, z is the valence of the ion, so that $\frac{z}{|z|} = \begin{cases} +1 \text{ for positive ions} \\ -1 \text{ for negative ions}. \end{cases}$

We note that if the concentration gradient is zero then $J_{diff} = 0$, while if the potential gradient is zero then $J_{elect} = 0$.

In both the electric and the diffusion fluxes, the ions collide with the solvent and therefore the diffusion coefficient D and the ion mobility μ should be related. Indeed, Einstein [159] found that this relationship is given by

$$D = \frac{\mu RT}{|z|F}, \tag{2.1}$$

where R is the gas constant $(8.314\,J/(K\cdot mol))$, T the absolute temperature (K), $F = eN_A$ the Faraday's constant $(9.6485e + 4\,C/mol)$, e the elementary charge and N_A the Avogadro's number, see Tables A.1 and A.2. Then it follows that the total ionic flux J is given by

$$J = J_{diff} + J_{elect} = -D\nabla c - \frac{z}{|z|}\mu c\nabla u,$$

hence, using (2.1), we obtain the *Nernst-Planck equation*

$$J = -D\left(\nabla c + \frac{zF}{RT}c\nabla u\right). \tag{2.2}$$

Let us assume now that the ion flux J and the electric potential u are transverse to the cell membrane, which extends from $x = 0$ (inside) to $x = L$ (outside), and the diffusion coefficient D is constant. Moreover, if we are at the steady state $\partial_t c = 0$, thus the conservation law

$$\partial_t c + \partial_x J = 0$$

implies that J is constant. Hence, we can reduce Eq. (2.2) to the one-dimensional problem

$$\frac{dc}{dx}(x) + \frac{zF}{RT}\frac{du}{dx}(x)c(x) + \frac{J}{D} = 0. \tag{2.3}$$

Equation (2.3) is clearly a linear differential equation in $c(x)$, whose solution can be obtained in terms of $u(x)$ and J by multiplying by

$$\exp\left(\frac{zF}{RT}\int_0^x \frac{du}{ds}(s)ds\right)$$

and integrating on $(0, x)$, yielding

$$c(x) = \exp\left(-\frac{zF}{RT}(u(x) - u(0))\right)\left(c(0) - \frac{J}{D}\int_0^x \exp\left(\frac{zF}{RT}(u(s) - u(0))\right)ds\right). \tag{2.4}$$

2.3 The Goldman-Hodgkin-Katz (GHK) Current-Voltage Relation

If we suppose the electric field constant across the membrane, then

$$\frac{du}{dx} = -\frac{v}{L},$$

where $v = u(0) - u(L) = u_i - u_e$ and we have adopted the standard notation with indexes i, e denoting intra- and extracellular quantities. In this case, setting $c(0) = c^i$, the solution (2.4) of the Nernst-Planck equation is

$$c(x) = \frac{JRTL}{DzvF}\left(1 - \exp\left(\frac{zvF}{RTL}x\right)\right) + c^i \exp\left(\frac{zvF}{RTL}x\right).$$

In order to satisfy $c(L) = c^e$, it must be that

$$J = \frac{DzFv}{LRT} \frac{c^i - c^e \exp\left(\frac{-zvF}{RT}\right)}{1 - \exp\left(\frac{-zvF}{RT}\right)}.$$

The *electrical current density* in $C\,s^{-1}\,cm^{-2} = A\,cm^{-2}$ is defined by $I := zFJ$, hence we obtain the *Goldman-Hodgkin-Katz (GHK)* current-voltage relation

$$I = P \frac{z^2 F^2}{RT} v \frac{c^i - c^e \exp\left(\frac{-zvF}{RT}\right)}{1 - \exp\left(\frac{-zvF}{RT}\right)}, \tag{2.5}$$

where $P = \frac{D}{L}$ is the permeability of the membrane to the ion K.

The GHK flux equation is applied in several fields, one of the most important being in modeling the L-type channels in calcium dynamics, see e.g. [47].

2.4   Nernst Equilibrium Potential

We consider a membrane separating two neutral solutions with different ionic concentrations, e.g. the salt KCl composed by the ions potassium K^+ and chloride Cl^-. Moreover, we suppose that the membrane is permeable only to one of the two ions, that we denote by K, with generic valence z.

At thermodynamical equilibrium, each local process and its reverse proceed at the same rate, hence $J = 0$ and the solution (2.4) of the Nernst-Planck equation becomes

$$c(x) = \exp\left(-\frac{zF}{RT}(u(x) - u(0))\right) c(0),$$

from which it follows that in $x = L$

$$\log\left(\frac{c(L)}{c(0)}\right) = -\frac{zF}{RT}(u(L) - u(0)).$$

Using the standard notation with indexes i, e denoting intra- and extracellular quantities, respectively, we then obtain the *Nernst equation* for the equilibrium (reversal) potential

$$v_K := u_i - u_e = -\frac{RT}{zF} \log\left(\frac{c^i}{c^e}\right).$$

Table 2.1 Intra- and extracellular concentration and Nernst potential values for ventricular myocytes

	Extracellular concentration (mM)	Intracellular concentration (mM)	Nernst potential (mV)
Na^+	145	15	60
Cl^-	100	5	−80
K^+	4.5	160	−95
Ca^{2+}	1.8	1e−4	130
H^+	1e−4	2e−4	−18

This derivation is based on the constitutive Nernst-Planck law for the total flux. For a thermodynamical derivation from electrochemical potentials that shows the universal character of the Nernst potential, see the next Section.

For ventricular myocytes, the typical intra- and extracellular concentrations and Nernst potential values are given in Table 2.1.

2.5 Thermodynamical Derivation of the Nernst Potential

We recall that the first law of Thermodynamics states that for a closed system the change dU of internal energy equals the difference between the amount of heat dQ supplied to the system and the amount of external work dW performed by the system,

$$dU = dQ - dW.$$

Since the work performed by the system can be written in terms of the increase dV in its volume V and the external pressure p as $dW = pdV$, the first law can also be written as

$$dU = dQ - pdV.$$

The second law of Thermodynamics states that the change dS of the entropy S of the system is

$$dS = dS_{rev} + dS_{irr},$$

where dS_{rev} is the change due to the reversible interaction of the system with its environment and dS_{irr} is the irreversible internal change within the system that is always ≥ 0. Since $dS_{rev} = dQ/T$ with T the absolute temperature, this law can also be written as

$$dS_{irr} = dS - dQ/T.$$

The Gibbs free energy is defined as

$$G = U + pV - TS,$$

i.e. as the difference between the enthalpy $H = U + pV$ and the product TS. Differentiating and using the first and second laws of Thermodynamics, we obtain

$$dG = Vdp - SdT - TdS_{irr}.$$

For reversible processes, $dS_{irr} = 0$, hence the second law implies $dQ = TdS$ and the first law

$$dU = TdS - pdV,$$

which is a fundamental relationship expressing the change in internal energy dU of a closed system in terms of reversible changes in its entropy S and volume V. On the other hand, for open systems the internal energy can also increase due to an increase dn_i of its i-th component

$$dU = \left(\frac{\partial U}{\partial n_i}\right)_{S,V,n_j} dn_i,$$

where S, V and the other components n_j, with $j \neq i$, are kept constant. Hence, the first law of Thermodynamics becomes

$$dU = TdS - pdV + \sum_i \mu_i dn_i,$$

where $\mu_i = \left(\frac{\partial U}{\partial n_i}\right)_{S,V,n_j}$ is the chemical potential of the i-th component, and the Gibbs free energy becomes

$$dG = Vdp - SdT + \sum_i \mu_i dn_i. \tag{2.6}$$

This last equation shows that the chemical potential for the i-th component can also be defined as $\mu_i = \left(\frac{\partial G}{\partial n_i}\right)_{T,p,n_j}$.

For charged ions with valence z_i, the electrochemical potential is defined as

$$\tilde{\mu}_i = \mu_i + z_i Fu, \tag{2.7}$$

where F is the Faraday constant and u the electric potential.

The chemical potential μ_g for an ideal gas can be derived using the equation of state $pV = nRT$, relating the pressure p, volume V, number of moles n, gas constant R, temperature T. If we consider $n = 1\,\text{mol}$ of ideal gas expanding at constant temperature, then Eq. (2.6) gives us

$$dG = Vdp = RT\frac{dp}{p},$$

and by integration

$$G = G_0 + RT\log\frac{p}{p_0},$$

where p_0 is a reference pressure and G_0 the associated Gibbs free energy. Since for a mole of pure substance the chemical potential is given by the Gibbs free energy, the last equation can be rewritten as

$$\mu_g = \mu_g^0 + RT\log\frac{p}{p_0}, \tag{2.8}$$

with μ_g^0 the chemical potential of the gas at the reference pressure p_0. If we take the reference pressure equal to 1 atmosphere, Eq. (2.8) becomes

$$\mu_g = \mu_g^0 + RT\log p. \tag{2.9}$$

The chemical potential of a solute can be derived by considering a solute dissolved in a solvent to be similar to gas molecules present in free space. Since the ideal gas equation can be written as $p = \frac{n}{V}RT = cRT$, with c the molar concentration of the solute, we see that, at constant temperature, the pressure is proportional to the concentration c. Therefore, by the analogy with a gas, the chemical potential of a solute s dissolved in a solvent is given by Eq. (2.9) with the pressure replaced by the concentration c_s of the solute:

$$\mu_s = \mu_s^0 + RT\log c_s. \tag{2.10}$$

For an ion species in solution, Eq. (2.10) generalizes to the case of an electrochemical potential $\tilde{\mu}_s$ as in (2.7)

$$\tilde{\mu}_s = \mu_s + z_s Fu = \mu_s^0 + RT\log c_s + z_s Fu. \tag{2.11}$$

The Nernst equilibrium potential can be derived from this equation by considering an ion species s in equilibrium across a membrane and denoting by c_s^i, c_s^e the intracellular and extracellular concentrations, respectively. Since at equilibrium we must have $\tilde{\mu}_s^i = \tilde{\mu}_s^e$, Eq. (2.11) yields

$$\mu_s^0 + RT\log c_s^i + z_s Fu_i^s = \mu_s^0 + RT\log c_s^e + z_s Fu_e^s,$$

so that

$$z_s F(u_i^s - u_e^s) = -RT \log \frac{c_s^i}{c_s^e},$$

i.e. the Nernst equilibrium potential $v_s = u_i^s - u_e^s = -\dfrac{RT}{z_s F} \log \dfrac{c_s^i}{c_s^e}.$

2.6   Electrodiffusion Models: The Poisson-Nernst-Planck (PNP) Equation

We now suppose to have two types of ions, a cation S_1 and an anion S_2, with concentrations c_1 and c_2, valences $z_1 = z > 0$ and $z_2 = -z < 0$. We consider the flux through a channel Ω connecting the intra- and extracellular neutral spaces. The Nernst-Planck equations for the fluxes J_1, J_2 of S_1 and S_2 state that

$$J_1 = -D_1 \left(\nabla c_1 + \frac{zF}{RT} c_1 \nabla u \right),$$
$$J_2 = -D_2 \left(\nabla c_2 - \frac{zF}{RT} c_2 \nabla u \right),$$

and the conservation law (continuity equation)

$$\partial_t c_1 + \operatorname{div} J_1 = 0 \ \ \text{in } \Omega,$$
$$\partial_t c_2 + \operatorname{div} J_2 = 0 \ \ \text{in } \Omega.$$

Furthermore, by Gauss law

$$\operatorname{div} D = \rho \ \ \text{in } \Omega,$$

where $D = \epsilon_a E$ is the dielectric displacement associated to the electric field E, ϵ_a the dielectric constant in the ionic solution, ρ the charge density. Since $E = -\nabla u$ with u the electric potential, we have $D = -\epsilon_a \nabla u$ and since in one mole there are $q N_A z = Fz$ charges, we have $\rho = N_a q(z_1 c_1 + z_2 c_2) = Fz(c_1 - c_2)$. Hence, inside the channel Ω

$$-\Delta u = \frac{Fz}{\epsilon_a}(c_1 - c_2).$$

We denote by S the lateral surface of the channel Ω and by $\partial \Omega_i, \partial \Omega_e$ the two channel openings in contact with the intra and extracellular media, respectively. Then, we make the following additional assumptions, yielding boundary conditions for the ionic concentrations, fluxes and the electric potential:

(a) The cation and anion concentrations on both sides of the membrane are constant, so that the intra- and extracellular spaces are in electrical equilibrium

$$c_1(x,t)|_{\partial \Omega_i} = c_2(x,t)|_{\partial \Omega_i} = c^i, \quad c_1(x,t)|_{\partial \Omega_e} = c_2(x,t)|_{\partial \Omega_e} = c^e;$$

(b) Since the dielectric constants ϵ_a of the channel's solution and ϵ_m of the membrane satisfy $\epsilon_m \ll \epsilon_a$, we assume that the channel wall is electrically insulated,

$$n^T E|_S = 0, \quad \text{i.e.} \quad n^T \nabla u|_S = 0;$$

(c) The channel wall prevents the movement of ions toward the lipidic regions,

$$n^T J_i|_S = 0, \quad n^T J_e|_S = 0;$$

(d) The electric potentials at the channel openings in contact with the extracellular and intracellular media are constant and equal to u_i and u_e, respectively, but, since the potential is given up to an additive constant, we set

$$u|_{\partial \Omega_i} = u_i - u_e = v, \quad u|_{\partial \Omega_e} = 0.$$

The *Poisson-Nernst-Planck* (PNP) equation treats discrete ions in a channel as a continuum charge distribution, representing the average ion fluxes in terms of densities and potential gradients. For a derivation of the PNP system from the Langevin model of ionic motion, see Schuss et al. [464]. For a singular perturbation analysis of the steady-state PNP system, see e.g. [26, 212, 438, 484] and the references therein. In addition to continuum PNP equations, more detailed approaches have been studied, such as all-atom Molecular Dynamics (MD), non-linear Poisson-Boltzmann (PB) equation, Brownian Dynamics (BD), see Roux et al. [437]. For a multiscale model linking MD and electrophysiology for the cardiac I_{Ks} channel, see Silva et al. [482].

Since the channel has a diameter of a few Angstroms, it can be assumed cylindrical and the membrane around the channel planar. Then the ionic concentrations c_1, c_2, fluxes J_1, J_2 and potential u are constant on each cross section of the cylindrical channel Ω and depend only on the position x across the cylindrical channel Ω, that we assume to range from 0 (intracellular media) to L (extracellular media).

We now consider the steady-state of the 1-D model, assuming that the ion concentrations are constant across the channel section. Collecting the previous equations and boundary conditions, we find the one-dimensional *Poisson-Nernst-Planck* (PNP) system:

$$
\begin{cases}
\partial_t c_1 + \partial_x J_1 = 0 \quad \text{with} \quad J_1 = -D_1\left(\partial_x c_1 + \dfrac{zF}{RT}c_1\partial_x u\right) \\[2mm]
\partial_t c_2 + \partial_x J_2 = 0 \quad \text{with} \quad J_2 = -D_2\left(\partial_x c_2 - \dfrac{zF}{RT}c_2\partial_x u\right) \\[2mm]
\partial^2_{xx} u = -\dfrac{zF}{\epsilon_a}(c_1 - c_2) \\[2mm]
\text{with boundary conditions:} \\
c_1(0,t) = c_2(0,t) = c^i \quad c_1(L,t) = c_2(L,t) = c^e \\
u(0,t) = v \quad u(L,t) = 0 \\
\text{and initial conditions:} \\
u(x,0) = 0 \quad c_1(x,0) = c_2(x,0) = 0.
\end{cases}
$$

At steady state $\partial_t c_1 = \partial_t c_2 = 0$, hence the stationary PNP system becomes

$$
\begin{cases}
\dfrac{d}{dx}D_1\left(\dfrac{dc_1}{dx} + \dfrac{zF}{RT}c_1\dfrac{du}{dx}\right) = 0, \\[2mm]
\dfrac{d}{dx}D_2\left(\dfrac{dc_2}{dx} - \dfrac{zF}{RT}c_2\dfrac{du}{dx}\right) = 0, \\[2mm]
\dfrac{d^2u}{dx^2} = -\dfrac{zF}{\epsilon_a}(c_1 - c_2) \\[2mm]
c_1(0) = c_2(0) = c^i \\
c_1(L) = c_2(L) = c^e \\
u(0) = v \quad u(L) = 0.
\end{cases}
\tag{2.12}
$$

This one-dimensional non-linear boundary value system admits a unique solution $c_1(x)$, $c_2(x)$, $u(x)$, see [370] and for a perturbation analysis [26]. Multidimensional existence results follow from the theory of semiconductor equations, see e.g. [320], and exploiting the gradient flow structure of the PNP system, see e.g. [6]. The system can be written in dimensionless form by rescaling the variables and functions as

$$
y = x/L, \quad \phi = uzF/RT, \quad p = \frac{c_1}{c^i + c^e}, \quad n = \frac{c_2}{c^i + c^e},
$$
$$
J_p = J_1\frac{L}{(c^i + c^e)D_1}, \quad J_n = J_2\frac{L}{(c^i + c^e)D_2}, \quad \hat{c}^{i,e} = \frac{c^{i,e}}{c_i + c_e}, \quad \hat{v} = \frac{vzF}{RT},
$$

so that

$$\frac{d^2\phi}{dy^2} = \frac{zFL^2}{RT}\frac{d^2u}{dx^2} = -\frac{z^2F^2L^2}{RT\epsilon_a}(c^i + c^e)(p - n),$$
$$-J_p = \frac{dp}{dy} + p\frac{d\phi}{dy},$$
$$-J_n = \frac{dn}{dy} - n\frac{d\phi}{dy}.$$

The first two equations of (2.12) require that $\dfrac{dJ_p}{dy} = \dfrac{dJ_n}{dy} = 0$, i.e. that J_p and J_n are constant. Therefore, the dimensionless one-dimensional stationary PNP system becomes:

find $\{p(x), n(x), \phi(x)\}$ and constants $\{J_p, J_n\}$ such that

$$\begin{cases} -J_p = \dfrac{dp}{dy} + p\dfrac{d\phi}{dy}, \\ -J_n = \dfrac{dn}{dy} - n\dfrac{d\phi}{dy} \\ \dfrac{d^2\phi}{dy^2} = -\lambda^2(p - n), \\ \text{with boundary conditions:} \\ p(0) = n(0) = \hat{c}^i, \quad p(1) = n(1) = \hat{c}^e, \quad \phi(0) = \hat{v}, \quad \phi(1) = 0, \end{cases} \tag{2.13}$$

with $\lambda^2 = \dfrac{z^2F^2L^2}{\epsilon_a RT}(c^i + c^e)$.

Since no analytical solutions of this system are known, we will look for approximate solutions obtained by perturbation techniques with respect to the parameter λ.

2.6.1   PNP: The Short Channel or Low Concentrations Limit

We look first for approximate solutions when the parameter $\lambda = \dfrac{zF}{\sqrt{\epsilon_a RT}}L\sqrt{c^i + c^e}$ is small, corresponding to *short channels* or *low ionic concentrations*. This is a regular perturbation problem and in order to obtain an approximation with error of order $O(\lambda)$ we solve the reduced problem in the limit case of $\lambda = 0$. Thus

$$\frac{d^2\phi}{dy^2} = 0$$

implies that the electric field $E = -\dfrac{d\phi}{dy}$ is constant and the potential $\phi(y)$ is linear, so from the boundary conditions we obtain

$$\phi(y) = \hat{v} - \hat{v}y, \quad \frac{d\phi}{dy} = -\hat{v}.$$

Then the differential equation for p becomes

$$-J_p = \frac{dp}{dy} - \hat{v}p.$$

Integrating between 0 and y and using the left boundary condition $p(0) = \hat{c}^i$, we obtain

$$p(y) = \hat{c}^i e^{\hat{v}y} + J_p \frac{1 - e^{\hat{v}y}}{\hat{v}}.$$

The right boundary condition $p(1) = \hat{c}^e$ then determines

$$J_p = \hat{v} \frac{\hat{c}^i - \hat{c}^e e^{-\hat{v}}}{1 - e^{-\hat{v}}}.$$

Analogously, the differential equation for n becomes

$$-J_n = \frac{dn}{dy} + \hat{v}n,$$

so, by integrating and imposing the boundary conditions, we obtain

$$n(y) = \hat{c}^i e^{-\hat{v}y} - J_n \frac{1 - e^{-\hat{v}y}}{\hat{v}},$$

$$J_n = -\hat{v} \frac{\hat{c}^i - \hat{c}^e e^{\hat{v}}}{1 - e^{\hat{v}}}.$$

Returning to the original variables, we then determine the dimensional fluxes J_1, J_2, hence the ionic density currents

$$I_1 = zFJ_1 = \frac{z^2 F^2}{RT} \frac{D_1}{L} v \frac{c^i - c^e e^{-\frac{zF}{RT}v}}{1 - e^{-\frac{zF}{RT}v}},$$

$$I_2 = zFJ_2 = \frac{z^2 F^2}{RT} \frac{D_2}{L} (-v) \frac{c^i - c^e e^{\frac{zF}{RT}v}}{1 - e^{\frac{zF}{RT}v}}.$$

These are GHK current-voltage relations (2.5), with $P_K = D_K/L, \ \ K = 1,2$.

2.6.2 PNP: The Long Channel or High Concentrations Limit

We now look for approximate solutions when the parameter λ is large. We define the small parameter $\eta = 1/\lambda = \dfrac{\sqrt{\epsilon_a RT}}{zF} \dfrac{1}{L\sqrt{c^i + c^e}}$ and consider the singular perturbation problem for the potential

$$\eta^2 \frac{d^2\phi}{dy^2} = n - p.$$

The reduced problem obtained in the limit case for $\eta = 0$ implies that $p(y) = n(y)$, so by adding or subtracting the equations for J_p and J_n in (2.13) we have

$$\begin{cases} -J_p - J_n = \dfrac{dp}{dy} + \dfrac{dn}{dy} = 2\dfrac{dp}{dy}, \\ -J_p + J_n = p\dfrac{d\phi}{dy} + n\dfrac{d\phi}{dy} = 2p\dfrac{d\phi}{dy} \\ p(0) = n(0) = \hat{c}^i, \quad p(1) = n(1) = \hat{c}^e, \quad \phi(0) = \hat{v}, \quad \phi(1) = 0. \end{cases} \tag{2.14}$$

The first equation requires $\dfrac{dp}{dy}$ to be constant and from the boundary conditions we obtain $p(y) = \hat{c}^i + (\hat{c}^e - \hat{c}^i)y$, therefore system (2.14) becomes

$$\begin{cases} \dfrac{J_p + J_n}{2} = (\hat{c}^e - \hat{c}^i) \\ \dfrac{d\phi}{dy} = \dfrac{\hat{J}}{p(y)} = \dfrac{\hat{J}}{\hat{c}^i + (\hat{c}^e - \hat{c}^i)y}, \end{cases} \tag{2.15}$$

with $\hat{J} = (J_n - J_p)/2$, yielding

$$\phi(y) = \hat{v} + \frac{\hat{J}}{\hat{c}^e - \hat{c}^i} \log \frac{\hat{c}^i + (\hat{c}^e - \hat{c}^i)y}{\hat{c}^i}.$$

Then the boundary condition $\phi(1) = 0$ gives us the condition $\hat{v} + \dfrac{\hat{J}}{\hat{c}^e - \hat{c}^i} \log \dfrac{\hat{c}^e}{\hat{c}^i} = 0$, that determines $\hat{J} = (\hat{c}^e - \hat{c}^i)\dfrac{-\hat{v}}{\log \frac{\hat{c}^e}{\hat{c}^i}}$, which coupled with (2.15) implies

$$\begin{cases} -J_p = (\hat{c}^e - \hat{c}^i)(\dfrac{-\hat{v}}{\log \frac{\hat{c}^e}{\hat{c}^i}} + 1), \\ J_n = (\hat{c}^e - \hat{c}^i)(\dfrac{-\hat{v}}{\log \frac{\hat{c}^e}{\hat{c}^i}} - 1). \end{cases}$$

Returning to the dimensional fluxes $J_1 = \dfrac{c^i + c^e}{L} D_1 J_p$, $J_2 = \dfrac{c^i + c^e}{L} D_2 J_n$, we find that the dimensional currents $I_1 = zF\dfrac{c^i + c^e}{L} D_1 J_p$, $I_2 = -zF\dfrac{c^i + c^e}{L} D_2 J_n$ are

$$
\begin{aligned}
I_1 &= \frac{zF}{L}(c^e - c^i)D_1 \left(\frac{v}{\frac{RT}{zF} \log \frac{c^e}{c^i}} - 1 \right) = \frac{zFD_1}{L} \frac{c^e - c^i}{v_1}(v - v_1), \\
I_2 &= -\frac{zF}{L}(c^e - c^i)D_2 \left(\frac{v}{\frac{RT}{zF} \log \frac{c^e}{c^i}} - 1 \right) = \frac{-zFD_2}{L} \frac{c^e - c^i}{v_2}(v - v_2),
\end{aligned}
\tag{2.16}
$$

where $v_k = \dfrac{RT}{z_k F} \log \dfrac{c^e}{c^i}$, $k = 1, 2$ are the Nernst potentials of the two ions considered.

These linear current-voltage relations are derived using the approximation of a constant diffusive gradient.

2.6.3 Equilibrium Potential for Multi-ion Fluxes

The Nernst equilibrium potential has a derivation based on universal thermodynamic principles only in the simple case of a single-ion flux. If we consider two or more ions, the situation is more complex and in general there is no potential that zeros each individual ionic current. However, we can still compute a reverse potential that zeros the total ionic current.

For example, if we consider the two ions Na^+, K^+ and we assume that their channels obey GHK current-voltage relations

$$
\begin{aligned}
I_{Na^+} &= \frac{F^2}{RT} v P_{Na} \frac{c^i_{Na} - c^e_{Na} e^{-\frac{F}{RT} v}}{1 - e^{-\frac{F}{RT} v}}, \\
I_{K^+} &= \frac{F^2}{RT} v P_K \frac{c^i_K - c^e_K e^{-\frac{F}{RT} v}}{1 - e^{-\frac{F}{RT} v}},
\end{aligned}
$$

with $P_{Na} = \frac{D_{Na}}{L}$, $P_K = \frac{D_K}{L}$, then the reverse potential at which $I_{Na^+} + I_{K^+} = 0$ is

$$
v_r = -\frac{RT}{F} \log \frac{P_{Na} c^i_{Na} + P_K c^i_K}{P_{Na} c^e_{Na} + P_K c^e_K}.
$$

If instead the channels obey linear current-voltage relations

$$
I_{Na^+} = G_{Na}(v - v_{Na}), \quad I_{K^+} = G_K(v - v_K),
$$

then the reverse potential that zeros the total current is

$$v_r = \frac{G_{Na}v_{Na} + G_K v_K}{G_{Na} + G_K}.$$

Analogously, if we consider the three ions Na^+, K^+, Cl^- with GHK channels, we have

$$v_r = -\frac{RT}{F} \log \frac{P_{Na}c_{Na}^i + P_K c_K^i + P_{Cl}c_{Cl}^i}{P_{Na}c_{Na}^e + P_K c_K^e + P_{Cl}c_{Cl}^e},$$

while with linear channels we have

$$v_r = \frac{G_{Na}v_{Na} + G_K v_K + G_{Cl}v_{Cl}}{G_{Na} + G_K + G_{Cl}}.$$

2.7   Electrical Circuit Model of the Cellular Membrane

Since the cell membrane separates charges that accumulate at its intra- and extracellular surfaces, it can be viewed as a capacitor. The capacitance is defined as the ratio between the charge Q across the capacitor and the voltage potential drop v necessary to hold the charge

$$C_m = \frac{Q}{v}.$$

Since the capacitive current is $I_{cap} = dQ/dt$, if C_m is constant, we have

$$I_{cap} = \frac{dQ}{dt} = C_m \frac{dv}{dt}.$$

The cellular membrane is modeled as a capacitor in parallel with a resistor (ionic current), as shown in Fig. 2.1, so by the current conservation law, the transmembrane current given by the sum of the capacitative and ionic currents, must be equal to the applied current I_{app}

$$C_m \frac{dv}{dt} + I_{ion} = I_{app}. \tag{2.17}$$

The structure of the total ionic current will be described by the specific ionic membrane model adopted. In order to discuss these models, we need to introduce the formalism for modeling ion channel gating. For more properties about ionic channels of excitable membranes see [228].
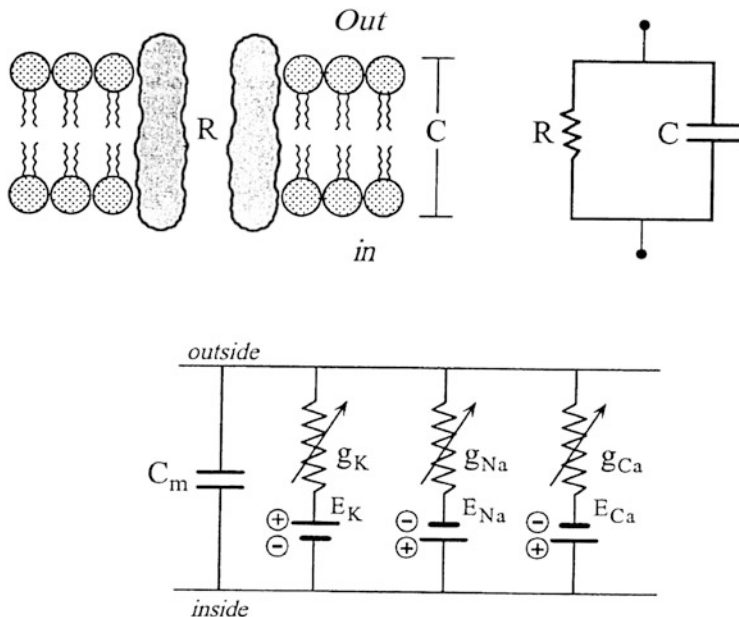
Fig. 2.1 Electrical circuit model of the cellular membrane

2.8   Ion Channel Gating

In general, for a given transmembrane potential drop, the ionic current through a population of ionic channels is given in a unit area of membrane surface and can be modeled as a product

$$I_{ion} = g(v, t)\phi(v),$$

where $g(v, t)$ is the proportion of open channels in a unit area of the membrane surface and $\phi(v)$ is the current-voltage (I-V) relation of a single open channel. In the previous sections on electrodiffusion models, we have seen different models for $\phi(v)$. For example, in the long channel limit (2.16), we have $\phi(v) = g_c(v - v_r)$, where g_c and v_r are the channel conductance and resting potential, respectively. The proportion of open channels in a unit area of the membrane surface can be written as $g(v, t) = \dfrac{N}{S} = \dfrac{N_{tot}}{S}\dfrac{N}{N_{tot}}$, where N is the number of open channels on the membrane surface, N_{tot} is the total number of membrane channels, S is the membrane surface area. Hence, in the long channel limit we have $I_{ion} = \overline{G}_c w(v - v_r)$, where $\overline{G}_c = \dfrac{N_{tot} g_c}{S}$ is the maximal channel conductance per unit

area of the membrane surface and $w = \dfrac{N}{N_{tot}}$ is the percentage of open channels. We now show how to model this percentage w, also known as gating variable, starting with the simplest case of a single-unit two-state channel.

One unit protein with two states. Consider a membrane portion of unit area containing a given type of ionic channels that behave independently and that assume two states S_0 (close) or S_1 (open), with transition rate constants α, β (in general dependent on the transmembrane potential v) as indicated in the first order kinetic diagram

$$\text{close state} = S_0 \underset{\beta}{\overset{\alpha}{\rightleftarrows}} S_1 = \text{open state} .$$
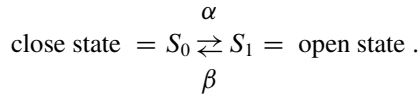
If $S_0(t), S_1(t)$ are the average numbers of channels that at time t are in the state S_0, S_1, respectively, then

$$\begin{cases} \dfrac{dS_1(t)}{dt} = \alpha\, S_0(t) - \beta\, S_1(t) \\ S_1(t) + S_0(t) = S. \end{cases}$$

By setting $s_0 = S_0(t)/S, s_1 = S_1(t)/S$, the percentages of close and open channels per unit area of the surface membrane, we then have

$$\begin{cases} \dfrac{ds_1}{dt} = \alpha\, s_0 - \beta\, s_1 \\ s_0 + s_1 = 1. \end{cases}$$

Eliminating s_0 and denoting by $w = s_1$ the gating variable, we have

$$\dfrac{dw}{dt} = \alpha\, (1 - w) - \beta\, w .$$

By setting $w_\infty = \frac{\alpha}{\alpha+\beta}$ and $\tau_w = \frac{1}{\alpha+\beta}$, this equation can be rewritten as

$$\dfrac{dw}{dt} = \dfrac{w_\infty - w}{\tau_w}, \tag{2.18}$$

where w_∞ and τ_w are the equilibrium state and the time constant, respectively.

By voltage-clamp or patch-clamp techniques, it is possible to apply an external current that balances the membrane current in such a way that the transmembrane potential v is kept at a fixed value in time. In this case, the capacitive current

$I_{cap} = C_m \frac{dv}{dt}$ is zero and in the circuit model equation (2.17) in the long-channel limit we have $I_{ion}(t, v) = \overline{G}\, w(t, v)\, (v - v_r) = I_{app}$, hence the membrane conductance can be obtained as

$$\overline{G}\, w(t, v) = \frac{I_{app}(t, v)}{v - v_r}.$$

For each fixed value of v, these experimental curves can be plotted in time and compared with the theoretical curves predicted by solving the gating equation (2.18) in the voltage-clamp setting: if at time $t = 0$ v is increased from 0 to v_0 and held fixed at such value, the time behavior is given by

$$w(t) = w_\infty(v_0)(1 - e^{-t/\tau_w(v_0)}), \tag{2.19}$$

while if at time $t = T$ we return v back to 0, we obtain the evolution

$$w(t) = w_\infty(v_0)e^{-(t-T)/\tau_w(v_0)}), \tag{2.20}$$

see Fig. 2.2. If the experimental conductance curves do not agree with these exponential curves, then the single-unit two-state channel model is not adequate and more complex models must be considered. Such models are introduced in the next sections and indeed they will be needed to correctly describe the ionic currents in the membrane models developed in the literature, starting with the classical Hodgkin-Huxley model presented in Sect. 2.9.1.
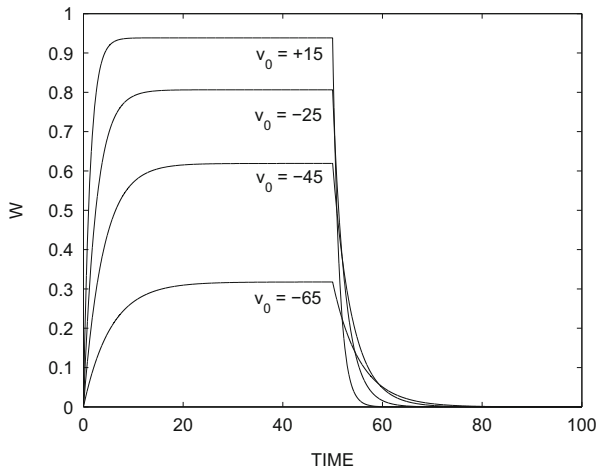
Fig. 2.2 Plots of voltage-clamp solutions (2.19) on the interval $[0\ T]$ and (2.20) on $[T\ 100]$, with $T = 50$ ms, for $v_0 = -65, -45, -25, 15$ mV

Two subunits with two states. Analogously, if we consider ionic channels with two equal and independent subunits, which can open and close according to the following kinetic diagram

$$\text{close state } S_0 \underset{\beta}{\overset{2\alpha}{\rightleftarrows}} S_1 \underset{2\beta}{\overset{\alpha}{\rightleftarrows}} S_2 = \text{ open state },$$
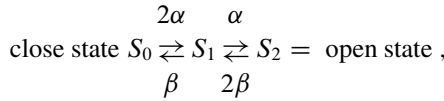
we have

$$\begin{cases} \dfrac{ds_0}{dt} = \beta s_1 - 2\alpha s_0 \\[2mm] \dfrac{ds_1}{dt} = -\beta s_1 + 2\alpha s_0 - \alpha s_1 + 2\beta s_2 \\[2mm] \dfrac{ds_2}{dt} = \alpha s_1 - 2\beta s_2. \end{cases}$$

From the condition $\frac{d}{dt}(s_0 + s_1 + s_2) = 0$ it follows $s_0 + s_1 + s_2 = 1$, hence

$$\begin{cases} \dfrac{ds_0}{dt} = \beta s_1 - 2\alpha s_0 \\[2mm] \dfrac{ds_2}{dt} = \alpha s_1 - 2\beta s_2 \\[2mm] s_1 = 1 - s_0 - s_2, \end{cases}$$

and after a change of variable

$$s_2 = n^2, \quad s_1 = 2n(1-n), \quad s_0 = (1-n)^2$$
$$\frac{dn}{dt} = \alpha(1-n) - \beta n.$$

k subunits with two states. Consider now an ionic channel with k equal and independent subunits, which can open and close according to the following kinetic diagram
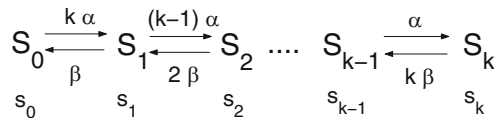
As in the case with two subunits, after a change of variable, we obtain

$$s_2 = n^k, \quad s_j = \binom{k}{j} n^j (1-n)^{k-j}$$

$$\frac{dn}{dt} = \alpha(1-n) - \beta n.$$

Two different subunits. We consider now two subunits of different type, that we will denote by m and h. The transition rate constants are α, β for m and γ, δ for h, as indicated in the following kinetic diagram
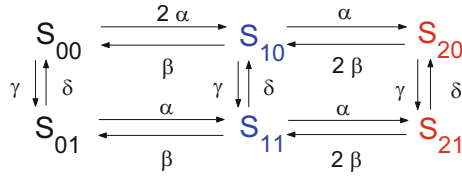
After a change of variable in the associated system of differential equations, we obtain

$$s_{00} = (1-m)^3(1-h), \ s_{10} = 3m(1-m)^2(1-h),$$
$$s_{20} = 3m^2(1-m)(1-h), \ s_{30} = m^3(1-h)$$
$$s_{01} = (1-m)^3 h, \ s_{11} = 3m(1-m)^2 h, \ s_{21} = 3m^2(1-m)h, \ s_{31} = m^3 h$$

$$\frac{dm}{dt} = \alpha(1-m) - \beta m, \qquad \frac{dh}{dt} = \gamma(1-h) - \delta h. \tag{2.21}$$

2.9 Cardiac Action Potential Models

The first mathematical model that describes accurately the action potential waveform and the associated permeability changes was proposed by Hodgkin and Huxley in [229]. Although the Hodgkin-Huxley (HH) model was developed specifically for nerve action potentials, the ideas and the mathematical formalism have been used later in a number of models describing cardiac action potentials, see the survey papers [356, 443] and also [141, 215, 282].

2.9.1   Hodgkin-Huxley Model

The celebrated Hodgkin-Huxley (HH) model consists of the following system, coupling the equation of the equivalent circuit model (2.17) with the equations of channel gating as in (2.18)–(2.21) for three gating variables m, h, n

$$
\begin{cases}
C_m \dfrac{dv}{dt} + I_{ion}(v, m, h, n) = I_{app} \\
\dfrac{dm}{dt} = \dfrac{m_\infty(v) - m}{\tau_m(v)} \\
\dfrac{dh}{dt} = \dfrac{h_\infty(v) - h}{\tau_h(v)} \\
\dfrac{dn}{dt} = \dfrac{n_\infty(v) - n}{\tau_n(v)}
\end{cases}
$$

where the ionic current is the sum of sodium, potassium and leakage currents

$$
I_{ion} = I_{Na} + I_K + I_L.
$$

Each of these currents has a linear current-voltage structure as in (2.16), with three equal activation and one inactivation independent subunits for the sodium channel

$$
I_{Na} = \bar{G}_{Na} m^3 \, h \, (v - v_{Na}),
$$

four equal activation independent subunits for the potassium channel

$$
I_K = \bar{G}_K \, n^4 \, (v - v_K),
$$

and no units for the leakage current

$$
I_L \;\; = \bar{G}_L \, (v - v_L).
$$

Here $\bar{G}_{Na}, \bar{G}_K, \bar{G}_L$ are the maximal conductances and v_{Na}, v_K, v_L are the Nernst potentials of each channel type, respectively.

We recall that the coefficients of the gating variables equations are given by

$$
\begin{aligned}
m_\infty &= \frac{\alpha_m}{\alpha_m + \beta_m}, & \tau_m &= \frac{1}{\alpha_m + \beta_m}, \\
h_\infty &= \frac{\alpha_h}{\alpha_h + \beta_h}, & \tau_h &= \frac{1}{\alpha_h + \beta_h}, \\
n_\infty &= \frac{\alpha_n}{\alpha_n + \beta_n}, & \tau_n &= \frac{1}{\alpha_n + \beta_n},
\end{aligned}
$$

with

$$\alpha_m = \frac{0.1(25 - v)}{\exp[0.1(25 - v)] - 1}, \quad \beta_m = 4 \exp\left(\frac{-v}{18}\right),$$
$$\alpha_h = 0.07 \exp\left(\frac{-v}{20}\right), \quad \beta_h = \frac{1}{\exp[0.1(30 - v)] + 1},$$
$$\alpha_n = \frac{0.01(10 - v)}{\exp[0.1(10 - v)] - 1}, \quad \beta_n = 0.125 \exp\left(\frac{-v}{80}\right).$$

The remaining parameters are

$$\bar{G}_{Na} = 120, \ \bar{G}_K = 36, \ \bar{G}_L = 0.3, \ v_{Na} = 115, \ v_K = -12, \ v_L = 10.6.$$

2.9.2   General Structure of Cardiac Cellular Membrane Models

The ionic current through channels of the membrane is modulated by the transmembrane potential $v = u_i - u_e$, by gating variables $w := (w_1, \ldots, w_M)$ and by ionic intracellular concentration variables $c := (c_1, \ldots, c_S)$. In the membrane models considered in the remainder of this chapter, the ionic current has the following general structure

$$I_{ion}(v, w, c) = \sum_{k=1}^{N} G_k(v, c) \prod_{j=1}^{M} w_j^{p_{jk}} (v - v_k(c)) + I_n(v, w, c),$$

where N is the number of ionic currents, G_k is the membrane conductance and v_k is the reversal potential for the k-th current, p_{jk} are integers and I_n accounts for time independent ionic fluxes.

The dynamics of the gating variables w is described in the Hodgkin-Huxley formalism by a system of ODEs having the following structure

$$\begin{cases} \dfrac{dw_j}{dt} = R_j(v, w) = \alpha_j(v)(1 - w_j) - \beta_j(v)w_j \\ w_j(0) = w_{j,0} \\ \alpha_j, \ \beta_j > 0, \ 0 \leq w_j \leq 1, \ j = 1, \ldots, M. \end{cases} \qquad (2.22)$$

The dynamics of the ionic concentration variables c is described by the additional system of ODEs

$$\begin{cases} \dfrac{dc_j}{dt} = S_j(v, w, c) = -\dfrac{I_{c_j}(v, w) \cdot A_{cap}}{V_{c_j} \cdot z_{c_j} \cdot F} \\ c_j(0) = c_{j,0} \\ j = 1, \ldots, S, \end{cases} \qquad (2.23)$$

where I_{c_j} is the sum of ionic currents carrying ion c_j, A_{cap} is the capacitive membrane area, V_{c_j} is the volume of the compartment where c_j is updated, z_{c_j} is the valence of ion c_j and F is the Faraday constant.

The transmembrane current I_m is the sum of the capacitive current, associated with the membrane lipidic bilayer and of the ionic current I_{ion}. Since I_m must balance the applied current I_{app} (see e.g. [250]), then the evolution of the transmembrane potential of a single myocyte is given by the following system of ODEs

$$
\begin{cases}
C_m \dfrac{dv}{dt} + I_{ion}(v, w, c) = I_m = I_{app}, \\
\dfrac{dw}{dt} - R(v, w) = 0, \qquad \dfrac{dc}{dt} - S(v, w, c) = 0, \\
v(0) = v_0, \qquad w(0) = w_0, \qquad c(0) = c_0,
\end{cases}
\tag{2.24}
$$

where C_m, I_{ion}, and I_{app} are the surface capacitance, the ionic current of the membrane and the applied current per unit area of the membrane surface, respectively.

2.9.3 Ionic Models of Purkinje Fibers, Sinoatrial Node (SAN), Atria

In this work, we will focus on cardiac ionic models of ventricular cells. Among the many other cardiac ionic models, we mention the Punkinje fiber models by Noble [355], McAllister-Noble-Tsien [323], DiFrancesco-Noble [149], the Sinoatrial node (SAN) models by Zhang et al. [585], Severi et al. [472], and the references therein, the atrial models by Nygren et al. [360], Kneller et al. [280] and the references therein. For many additional models, we refer e.g. to Pullan et al. [406].

2.9.4 Ventricular Models

The first ventricular membrane model was formulated by Beeler and Reuter in 1977 [33]. This model, as the McAllister-Noble-Tsien model [323] developed in 1975 for Purkinje fibers, relied on the Hodgkin-Huxley formalism and, similarly to the Hodgkin-Huxley model, assumed that sodium and potassium intracellular concentrations ($[Na^+]_i$, $[K^+]_i$) remain constant during the action potential. However, in cardiac myocytes entry of Ca^{2+} through the L-type calcium channel $I_{Ca(L)}$ produces a significant change in the calcium intracellular concentration $[Ca^{2+}]_i$, mainly by triggering Ca^{2+} release from the sarcoplasmic reticulum (SR) via the calcium-induced calcium-release (CICR) process. A first attempt to take into account the $[Ca^{2+}]_i$ dynamics necessary to reproduce action potential morphology was introduced in the earliest ventricular cell models, such as the Beeler-Reuter

[33] and the Luo-Rudy phase I [308], but only at a phenomenological level. More biophysically detailed $[Ca^{2+}]_i$ models were introduced in later models, see e.g. [254, 306, 405, 473].

Changes in $[Na^+]_i$ and $[K^+]_i$ can also influence the action potential morphology when cells are paced at a fast rate. The first model incorporating detailed information regarding $[Na^+]_i$ and $[K^+]_i$ dynamic concentration changes was the DiFrancesco-Noble model [149] of the Purkinje fibers. Rasmusson et al. [418] developed a similar model for a bullfrog atrial cell. The Luo-Rudy dynamic (LRd) model [309, 310] of the guinea pig ventricular action potential formulated these processes for the ventricular myocytes. These models were founding members in a new class of *second generation* models that account for dynamic ion concentration changes. Several such models for ventricular myocytes in different species have been published since that time (see Table 2.2) and in particular Rudy's group has recently published a detailed ionic model for human ventricular myocytes, see [361].

Table 2.2 Some of the most used ventricular ionic models for different species and dimensions of the associated dynamical systems of differential equations

Reference	Species	Equations
Beeler and Reuter [33]	Mammalian	8
Ebihara and Johnson [154]	Chick embrio	
Luo and Rudy [308]	Guinea pig	8
Noble et al. [357]	Guinea pig	17
Luo and Rudy [309, 310]	Guinea pig	19
Fenton and Karma [170]	Mammalian	3
Jafri, Rice and Winslow [254]	Guinea pig	31
Noble et al. [358]	Guinea pig	22
Priebe and Beuckelmann [402]	Human	22
Winslow et al. [563]	Canine	33
Clancy and Rudy [93, 94]	Guinea pig	
Pandit et al. [367]	Rat	26
Puglisi et al. [405]	Rabbit	
Bondarenko et al. [53]	Mouse	41
ten Tusscher et al. [521]	Human	17
Hund and Rudy [243]	Canine	29
Shannon et al. [473]	Rabbit	46
Cortassa et al. [136]	Mammalian	50
Livshitz and Rudy [306]	Canine	18
Niederer and Smith [351]	Rat	
Bueno-Orovio, Cherry and Fenton [65]	Human	4
Mahajan et al. [315]	Rabbit	26
Li et al. [299]	Mouse	36
O'Hara and Rudy [361]	Human	41

More recently, detailed ionic models have been coupled with detailed signaling pathways models; see for example [224] for a simulation study of beta-adrenergic signaling and its whole-cell effects in ventricular myocytes by incorporating receptor isoforms, multiple pathways and phosphorylation.

2.9.4.1   The Beeler-Reuter Model

In 1977, Beeler and Reuter developed the first mathematical model of a mammalian ventricular muscle cell (see [33]) based on the Hodgkin-Huxley formalism. The ionic current I_{ion} is given by the sum of $N = 4$ currents

$$I_{ion} = I_{Na} + I_s + I_{K1} + I_{x_1}.$$

The fast inward sodium current I_{Na} is primarily responsible for the rapid upstroke of the action potential, while the other currents determine the configuration of the plateau and repolarization phases. The slow inward current I_s, primarily carried by calcium ions, influences the duration of the action potential. The time-dependent and time-independent outward potassium currents I_{x1} and I_{K1} are instead responsible for the repolarization phase. It was also discovered that the intracellular calcium concentration changes significantly during the course of an action potential, hence this was included in the model as an additional dynamic variable.

Fast inward sodium current I_{Na}. In addition to the activation gate m and the inactivation gate h of the Hodgkin-Huxley model, Beeler and Reuter added a slow inactivation gate j. All the three gating variables follow the dynamics governed by Eq. (2.22). The expression of the sodium current is given by

$$I_{Na} = (\bar{g}_{Na} m^3 h j + \bar{g}_{NaC})(v - E_{Na}),$$

where E_{Na} is the sodium reversal potential (50 mV), $\bar{g}_{Na}$ is the maximal sodium conductance (0.04 mS/mm^2) and $\bar{g}_{NaC}$ is the constant background sodium conductance ($3 \cdot 10^{-5}$ mS/mm^2).

Slow inward current I_s. This current is controlled by an activation gate d and an inactivation gate f, both following the dynamics of (2.22). The magnitude of the current is given by

$$I_s = \bar{g}_s d f (v - E_s),$$

where $\bar{g}_s$ is the maximal channel conductance $9 \cdot 10^{-4}$ mS/mm^2. The reversal potential E_s depends on the intracellular calcium concentration $[Ca^{2+}]_i$, precisely

$$E_s = -82.3 - 13.0287 \log(0.001 [Ca^{2+}]_i).$$

The time dependence of the intracellular calcium concentration depends in turn on the current I_s, according to

$$\frac{d[Ca^{2+}]_i}{dt} = -0.01 I_s + 0.07(10^{-4} - [Ca^{2+}]_i).$$

Time-dependent outward potassium current I_{x_1}. As in the Hodgkin-Huxley model, this current is controlled by a single gating variable x_1, following (2.22). The expression of the current is

$$I_{x_1} = 8 \cdot 10^{-3} x_1 \left(\frac{\exp(0.04(v+77)) - 1}{\exp(0.04(v+35))} \right).$$

Time-independent outward potassium current I_{K1}. The experimental evidence suggested the presence of a time-independent background potassium current with magnitude given by

$$I_{K1} = 0.0035 \left(\frac{4(\exp(0.04(v+85)) - 1)}{\exp(0.08(v+53)) + \exp(0.04(v+53))} \right) +$$
$$0.035 \left(\frac{0.2(v+23)}{1 - \exp(-0.04(v+23))} \right).$$

2.9.4.2 The Luo Rudy I Model (LR1)

In 1991, Luo and Rudy developed a new mammalian ventricular membrane model [308], based on the Beeler-Reuter model, adjusting some parameters to reproduce more recent experimental results and including additional potassium currents. In the LR1 model, the ionic current I_{ion} is given by the sum of $N = 6$ currents

$$I_{ion} = I_{Na} + I_{si} + I_K + I_{K1} + I_{Kp} + I_b,$$

two inwards (I_{Na}, I_{si}) and four outwards (I_K, I_{K1}, I_{Kp}, I_b). The first three currents depend on six gating variables and one ion (intracellular calcium) concentration, while the last three are time-independent. The reversal potentials are set to the Nernst potentials for the ions involved, allowing the reversal potentials to vary according to ionic concentrations gradients. Figure 2.3 reports the time evolution of the transmembrane potential v, the gating variables m, h, j, d, f, X and the intracellular calcium concentration $[Ca^{2+}]_i$.

Fast inward sodium current I_{Na}. The expression of this current is the same as in the Beeler-Reuter model with the omission of the constant background sodium conductance, thus

$$I_{Na} = \bar{g}_{Na} m^3 h j (v - E_{Na}),$$

where $g_{Na} = 0.23 \, \text{mS/mm}^2$.
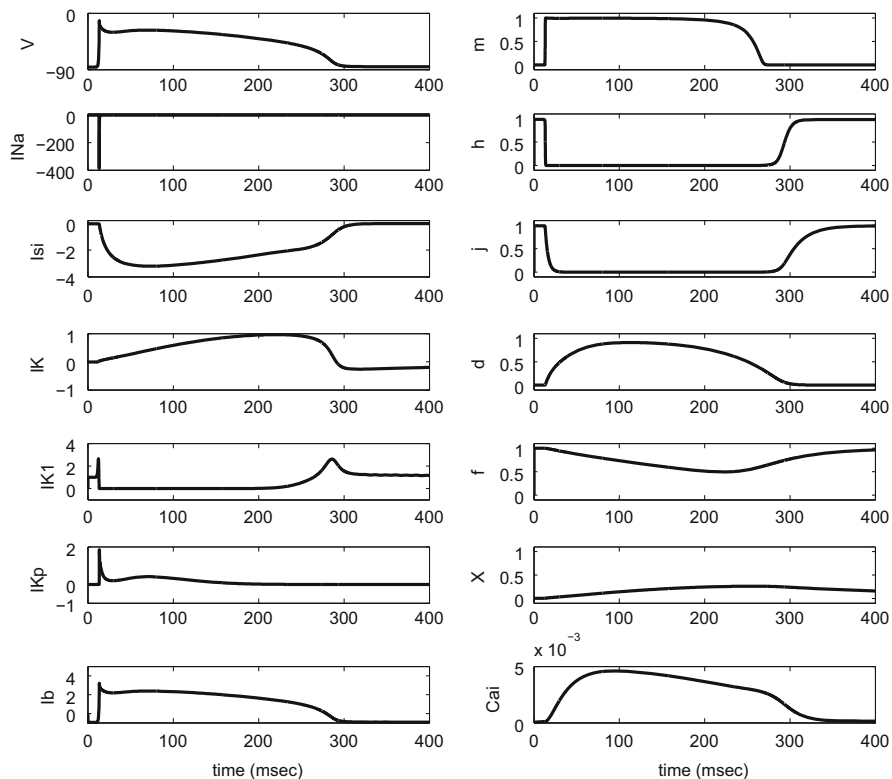
Fig. 2.3 LR1 model: Transmembrane potential v, ionic currents I_{Na}, I_{si}, I_K, I_{K1}, I_{Kp}, I_b, gating variables m, h, j, d, f, X and intracellular calcium concentration $[Ca^{2+}]_i$ as functions of time

Slow inward current I_{si}. The general form of this current is the same as the one of the I_s current in the Beeler-Reuter model

$$I_{si} = \bar{g}_{si}df(v - E_{si}),$$

where the reversal potential E_{si} is given by

$$E_{si} = 7.7 - 13.0287 \log([Ca^{2+}]_i).$$

The dynamics of the gating variable d, f and the intracellular calcium concentration $[Ca^{2+}]_i$ is the same as in the Beeler-Reuter model.

Time-dependent potassium current I_K. Unlike in the Beeler-Reuter model, this current is controlled not only by an activation gate X, but also by an inactivation gate X_i. The magnitude of the current is given by

$$I_K = \bar{g}_K X X_i (v - E_K),$$

where the maximal potassium conductance depends on the extracellular potassium concentration according to

$$\bar{g}_K = 2.82 \cdot 10^{-3} \sqrt{\frac{[K^+]_o}{5.4}} \text{ mS/mm}^2.$$

The reversal potential E_K is dependent on the concentration of both K^+ and Na^+ ions and is given by

$$E_K = \frac{RT}{F} \log \left(\frac{[K^+]_o + PR_{NaK}[Na^+]_o}{[K^+]_i + PR_{NaK}[Na^+]_i} \right),$$

where PR_{NaK} is a dimensionless permeability ratio for Na^+ that is expressed relative to K^+. The activation gate X follows the classical Hodgkin-Huxley dynamics (2.22), while the new inactivation gate X_i is given by

$$X_i = \begin{cases} 2.837 \dfrac{\exp(0.04(v + 77)) - 1}{(v + 77)\exp(0.04(v + 35))} & v > -100 \text{ mV} \\ 1 & v \le -100 \text{ mV}. \end{cases}$$

Time-independent potassium current I_{K1}. This current was reformulated using one gating variable with a time constant small enough that it may be approximated by a steady-state formulation. The magnitude of the current is

$$I_{K1} = \bar{g}_{K1} K1_\infty (v - E_{K1}),$$

where the maximal channel conductance is

$$\bar{g}_K = 6.047 \cdot 10^{-3} \sqrt{\frac{[K^+]_o}{5.4}} \text{ mS/mm}^2$$

and the reversal potential is the Nernst potential for potassium ions. The steady-state gate is given by

$$K1_\infty = \frac{\alpha_{K1}}{\alpha_{K1} + \beta_{K1}},$$

where

$$\alpha_{K1} = \frac{1.02}{1 + \exp(0.2385(v - E_{K1} - 59.215))},$$

$$\beta_{K1} = \frac{0.49124 \exp(0.08032(v - E_{K1} + 5.476)) + \exp(0.06175(v - E_{K1} - 594.31))}{1 + \exp(-0.5143(v - E_{K1} + 4.753))}.$$

Plateau potassium current I_{Kp}. This current, given by

$$I_{Kp} = \bar{g}_{Kp} K_p (v - E_{Kp}),$$

plays a role during the plateau phase of the action potential, restoring the cell to its resting state. The maximal current conductance is $\bar{g}_{Kp} = 1.83 \cdot 10^{-4}\,\mathrm{mS/mm^2}$, the reversal potential is the same of the time-independent potassium current, thus $E_{Kp} = E_{K1}$ and

$$K_p = \frac{1}{1 + \exp((7.488 - v)/5.98)}.$$

Background current I_b. This current is a linear function of the transmembrane potential with magnitude given by

$$I_b = \bar{g}_b (v - E_b),$$

where $\bar{g}_b = 0.03921\,\mathrm{mS/cm^2}$ and $E_b = -59.87\,\mathrm{mV}$.

2.9.4.3   The Luo Rudy Dynamic Model (LRd)

In 1994, Luo and Rudy developed a new mammalian ventricular membrane model [309, 310], mainly based on data from the guinea pig. The new model includes a detailed phenomenological description of calcium-induced calcium-release, intracellular calcium cycling and calcium buffering. The ionic current I_{ion} is given by the sum of $N = 11$ currents

$$I_{ion} = I_{Na} + I_{Ca(L)} + I_K + I_{K1} + I_{Kp} + I_{NaCa} + I_{NaK} + I_{nsCa} + I_{pCa} + I_{bCa} + I_{bNa}.$$

Figure 2.4 reports the time evolution of the transmembrane potential v, the gating variables m, h, j, d, f, X_{s1}, X_{s2}, X_r and the intracellular calcium concentration $[Ca^{2+}]_i$.

Fast inward sodium current I_{Na}. The formulation of this current is the same as the LR1 model, but the maximum conductance was decreased to $\bar{g}_{Na} = 16\,\mathrm{mS/cm^2}$.

L-type calcium current $I_{Ca(L)}$. This current, equivalent to the slow inward current I_{si} from the LR1 model, is the sum of the currents through the L-type calcium channel that is permeable to Ca^{2+}, Na^+ and K^+. The name is due to its activity, which is *long lasting* in comparison to other calcium currents, such as the T-type *transient* calcium current. The magnitude of the current is given by

$$I_{Ca(L)} = I_{Ca(L)Ca} + I_{Ca(L)Na} + I_{Ca(L)K},$$
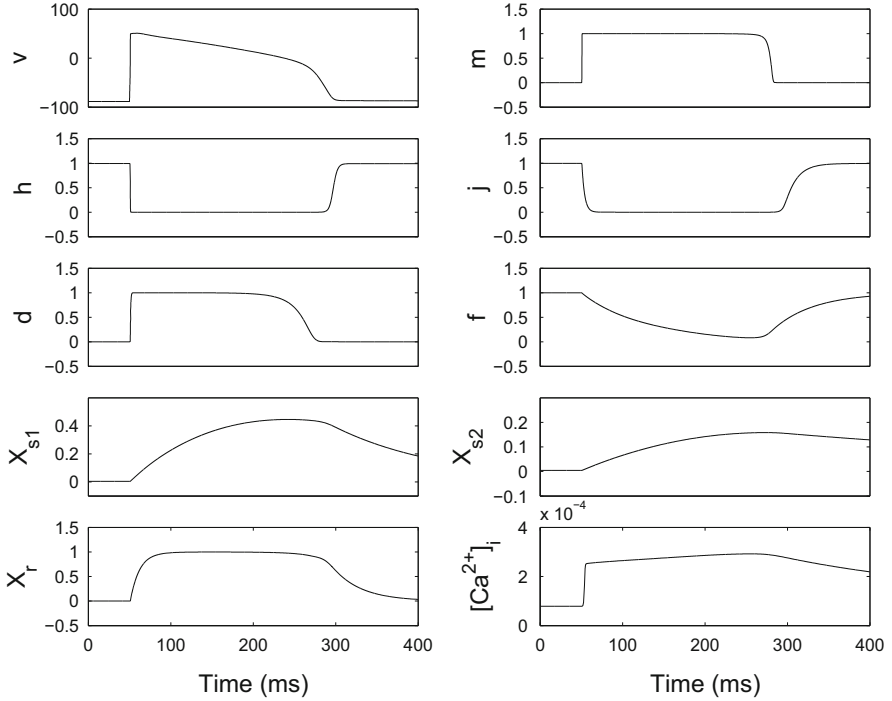
Fig. 2.4 LRd model: Transmembrane potential v, gating variables $m, h, j, d, f, X_{s1}, X_{s2}, X_r$ and the intracellular calcium concentration $[Ca^{2+}]_i$ as functions of time

where

$$I_{Ca(L)Ca} = d \cdot f \cdot f_{Ca} \cdot \bar{I}_{Ca(L)Ca}$$

$$I_{Ca(L)Na} = d \cdot f \cdot f_{Ca} \cdot \bar{I}_{Ca(L)Na}$$

$$I_{Ca(L)K} = d \cdot f \cdot f_{Ca} \cdot \bar{I}_{Ca(L)K}.$$

The $\bar{I}_{Ca(L)Ca}$, $\bar{I}_{Ca(L)Na}$ and $\bar{I}_{Ca(L)K}$ terms represent the maximum currents through the channel for each ion species. Because there is only one physical channel, each of these equations is governed by the same gating variables. The activation gate d and the inactivation gate f follow the Hodgkin-Huxley formalism (2.22), while the further inactivation gate f_{Ca} is governed by the following equation

$$f_{Ca} = \cfrac{1}{1 + \left(\cfrac{[Ca^{2+}]_i}{K_{mCa}} \right)^2},$$

where K_{mCa} is the half activation concentration for Ca^{2+} set to $0.6 \cdot 10^{-3}$ mM. The three fully activated current terms follow the *short channel limit*, thus

$$\bar{I}_S = P_S z_S^2 \frac{vF^2}{RT} \frac{\gamma_{Si}[S]_i \exp(z_S vF/RT) - \gamma_{So}[S]_o}{\exp(z_S vF/RT) - 1},$$

where $S = Ca^{2+}$, Na^+, K^+. P_S is the permeability of the membrane to ion S with valence z_S and γ_{Si}, γ_{So} are the intracellular and extracellular activity coefficients of ion S.

Time-dependent potassium current I_K. The kinetics of the gating variables was updated from the LR1 model and an additional pair of activation gates was added, thus

$$I_K = \bar{g}_K X^2 X_i (v - E_K),$$

where

$$X_i = \frac{1}{1 + \exp\left(\frac{v-56.26}{32.1}\right)}.$$

Time-independent potassium current I_{K1}. The formulation of this current is the same as the one in the LR1 model, but the maximum channel conductance was changed to

$$g_{K1} = 0.75 \sqrt{[K^+]_o/5.4}\, \text{mS/cm}^2.$$

Plateau potassium current I_{Kp}. The formulation of this current is the same as the one in the LR1 model.

Sodium-calcium exchanger I_{NaCa}.

$$\begin{aligned}
I_{NaCa} = k_{NaCa} &\cdot \frac{1}{K_{m,Na}^3 + [Na^+]_o^3} \cdot \frac{1}{K_{m,Ca} + [Ca^{2+}]_o} \cdot \frac{1}{1 + k_{sat} \exp((\eta - 1)vF/RT)} \\
&\cdot \left(\exp(\eta vF/RT)[Na^+]_i^3[Ca^{2+}]_o - \exp((\eta - 1)vF/RT)[Na^+]_o^3[Ca^{2+}]_i \right),
\end{aligned}$$

where $k_{NaCa} = 2\,000\,\mu\text{A}/\mu\text{F}$, $K_{m,Na} = 87.5$ mM, $K_{m,Ca} = 1.38$ mM, $k_{sat} = 0.1$ and $\eta = 0.35$.

Sodium-potassium pump I_{NaK}.

$$I_{NaK} = \bar{I}_{NaK} \cdot f_{NaK} \cdot \frac{1}{1 + (K_{m,Nai}/[Na^+]_i)^{1.5}} \cdot \frac{[K^+]_o}{[K^+]_o + K_{m,Ko}},$$

where $\bar{I}_{NaK} = 1.5\,\mu A/\mu F$, $K_{m,Nai} = 10\,mM$, $K_{m,Ko} = 1.5\,mM$ and

$$f_{NaK} = \frac{1}{1 + 0.1245\exp(-0.1vF/RT) + 0.0365\sigma\exp(-vF/RT)}$$

$$\sigma = 1/7\left(\exp([Na^+]_o/67.3) - 1\right).$$

Non-specific calcium-activated current I_{nsCa}. Although activated by calcium, this current arises from the transport of sodium and potassium ions.

$$I_{nsCa} = (\bar{I}_{nsNa} + \bar{I}_{nsK})\frac{1}{1 + \left(\frac{K_{mnsCa}}{[Ca^{2+}]_i}\right)^3},$$

where $K_{mnsCa} = 1.2\,\mu M$ and $\bar{I}_{nsNa}$, $\bar{I}_{nsK}$ are computed according to the *short channel limit* formula.

Sarcolemmal calcium pump I_{pCa}.

$$I_{pCa} = \bar{I}_{pCa}\frac{[Ca^{2+}]_i}{K_{m,p(Ca)} + [Ca^{2+}]_i},$$

where $\bar{I}_{pCa} = 1.15\,\mu A/\mu F$ and $K_{m,p(Ca)} = 0.5\,mM$.

Calcium background current I_{bCa}.

$$I_{bCa} = g_{bCa}(v - E_{Ca,N}),$$

where $g_{bCa} = 0.003016\,mS/\mu F$ and

$$E_{Ca,N} = (RT/2F)\log([Ca^{2+}]_o/[Ca^{2+}]_i).$$

Sodium background current I_{bNa}.

$$I_{bNa} = g_{bNa}(v - E_{Na,N}),$$

where $g_{bNa} = 0.00141\,mS/\mu F$ and $E_{Na,N} = E_{Na}$.

Intracellular potassium dynamics. The evolution of the intracellular K^+ concentration is described by the following ODE

$$\frac{d[K^+]_i}{dt} = -\frac{A_{cap}}{V_{myo}F}(I_{K,t} - 2I_{NaK}), \qquad (2.25)$$

where A_{cap} is the capacitative area of the membrane, V_{myo} is the volume of the myoplasm, F is the Faraday constant and $I_{K,t}$ is the total K^+ current through all ion channels, i.e.

$$I_{K,t} = I_K + I_{K1} + I_{Kp}.$$

Intracellular sodium dynamics. The evolution of the intracellular Na^+ concentration is described by the following ODE

$$\frac{d[Na^+]_i}{dt} = -\frac{A_{cap}}{V_{myo}F}(I_{Na,t} + 3I_{NaK} + 3I_{NaCa}),$$

where $I_{Na,t}$ is the total Na^+ current through all ion channels, i.e.

$$I_{Na,t} = I_{Na} + I_{bNa}.$$

Intracellular calcium buffering. The formulation of the intracellular calcium handling is based on the concepts detailed in the DiFrancesco-Noble model [149], but includes two additional features. The first is a calcium leakage current from the Sarcoplasmic Reticulum back into the cytosol and the second is the inclusion of calcium buffers within the intracellular spaces. Therefore, the evolution of the free calcium $[Ca^{2+}]_i$, junctional sarcoplasmic reticulum (JSR) free calcium $[Ca^{2+}]_{jsr}$ and network sarcoplasmic reticulum (NSR) calcium $[Ca^{2+}]_{nsr}$ concentrations are described by the following ODEs:

$$\frac{d[Ca^{2+}]_i}{dt} = -\beta_{myo}\left(\frac{A_{cap}}{2V_{myo}F}(I_{Ca,t} - 2I_{NaCa}) + \frac{V_{nsr}}{V_{myo}}(I_{up} - I_{leak}) - \frac{V_{jsr}}{V_{myo}}I_{rel}\right), \tag{2.26}$$

$$\frac{d[Ca^{2+}]_{jsr}}{dt} = \beta_{jsr}(I_{tr} - I_{rel}), \tag{2.27}$$

$$\frac{d[Ca^{2+}]_{nsr}}{dt} = I_{up} - I_{leak} - \frac{V_{jsr}}{V_{nsr}}I_{tr}, \tag{2.28}$$

where $I_{Ca,t}$ is the total Ca^{2+} current through all ion channels, i.e.

$$I_{Ca,t} = I_{Ca(L)} + I_{nsCa} + I_{pCa} + I_{bCa},$$

and the buffering of Ca^{+2} is modeled by incorporating instantaneous buffering to troponin C in the myoplasm and to calmodulin in JSR binding sites (see e.g. [547]) by means of

$$\beta_{myo} = \left(1 + \frac{[\overline{trpn}]K_{m,trpn}}{([Ca^{2+}]_i + K_{m,trpn})^2} + \frac{[\overline{cmdn}]K_{m,cmdn}}{([Ca^{2+}]_i + K_{m,cmdn})^2}\right)^{-1},$$

$$\beta_{jsr} = \left(1 + \frac{[\overline{csqn}]K_{m,csqn}}{([Ca^{2+}]_{jsr} + K_{m,csqn})^2}\right)^{-1}.$$

All the other symbols are defined in Table 2.3.

Table 2.3 Abbreviations used in the description of the LRd model

A_{cap}	Capacitative area of membrane	cm^2
C_m	Membrane capacitance	$\mu F/cm^2$
F	Faradays constant 96 485	C/mol
$I_{K,t}$	Total K^+ current through all ion channels	$\mu A/cm^2$
$I_{Na,t}$	Total Na^+ current through all ion channels	$\mu A/cm^2$
$I_{Ca,t}$	Total Ca^{2+} current through all ion channels	$\mu A/cm^2$
I_{NaCa}	$Na^+ - Ca^{2+}$ exchanger	$\mu A/cm^2$
I_{NaK}	$Na^+ - K^+$ pump	$\mu A/cm^2$
JSR	Junctional sarcoplasmic reticulum	
NSR	Network sarcoplasmic reticulum	
I_{leak}	Ca^{2+} leak from NSR	mM/ms
I_{rel}	Ca^{2+} release from JSR	mM/ms
I_{tr}	Ca^{2+} transfer from NSR to JSR	mM/ms
I_{up}	Ca^{2+} uptake into NSR	mM/ms
V_{myo}	Volume of myoplasm	μL
V_{jsr}	Volume of JSR	μL
V_{nsr}	Volume of NSR	μL
$[K^+]_i$	Intracellular concentration of K^+	mM
$[Na^+]_i$	Intracellular concentration of Na^+	mM
$[Ca^{2+}]_i$	Intracellular concentration of free Ca^{2+}	mM
$[Ca^{2+}]_{i,t}$	Total intracellular concentration of bound and free Ca^{2+}	mM
$[Ca^{2+}]_{jsr}$	JSR concentration of free Ca^{2+}	mM
$[Ca^{2+}]_{jsr,t}$	Total JSR concentration of bound and free Ca^{2+}	mM
$[Ca^{2+}]_{nsr}$	NSR concentration of free Ca^{2+}	mM

2.9.4.4   LRd Model Updates

The development of the LRd model continued after 1994 and the latest version is described in the 2007 work [306] by Livshitz and Rudy. Among the major updates, we recall those introduced in 1995 by [583], in particular the original formulation of the T-type transient calcium current $I_{Ca(T)}$ and the introduction of the rapid and slow potassium currents I_{Kr}, I_{Ks}, replacing the obsolete time-dependent potassium current I_K.

T-type calcium current $I_{Ca(T)}$. The magnitude of this current is given by

$$I_{Ca(T)} = g_{Ca(T)} b^2 g (v - E_{Ca}),$$

where $g_{Ca(T)} = 0.05 \, mS/cm^2$ and

$$E_{Ca} = (RT/2F) \log([Ca^{2+}]_o/[Ca^{2+}]_i).$$

The gating variables b and g follow the Hodgkin-Huxley formalism (2.22).

Time-dependent rapid potassium current I_{Kr}.

$$I_{Kr} = g_{Kr} X_r r (v - E_{Kr}),$$

with

$$g_{Kr} = 0.02614 \sqrt{[K^+]_o/5.4}, \quad E_{Kr} = (RT/F) \log([K^+]_o/[K^+]_i),$$

$$r = \frac{1}{1 + \exp((v + 9)/22.4)}$$

and X_r following (2.22).

Time-dependent slow potassium current I_{Ks}.

$$I_{Ks} = g_{Ks} X_{s1} X_{s2} (v - E_{Ks}),$$

where

$$g_{Ks} = 0.433 \left(1 + \frac{0.6}{1 + (0.000038/[Ca^{2+}]_i)^{1.4}} \right),$$

$$E_{Ks} = (RT/F) \log \left(\frac{[K^+]_o + P_{Na,K}[Na^+]_o}{[K^+]_i + P_{Na,K}[Na^+]_i} \right).$$

and X_{s1}, X_{s2} satisfying (2.22).

With these updates, the total K^+ and Ca^{2+} currents become

$$I_{K,t} = I_{Kr} + I_{Ks} + I_{K1} + I_{Kp}$$

and

$$I_{Ca,t} = I_{Ca(L)} + I_{Ca(T)} + I_{nsCa} + I_{pCa} + I_{bCa},$$

respectively.

2.9.5 Charge Conservation in Ionic Models

Membrane models have proven to be a useful and widely accepted tool for studying the electrophysiology and contractility of excitable cells. The second-generation of membrane ionic models incorporates the dynamics of the cytoplasmic concentrations of Na^+, K^+ and Ca^{2+} and in the literature concerns regarding their behavior in response to prolonged periods of rapid pacing have been reported, see e.g. [163, 213, 244, 307, 417, 573]. In particular, drift of intracellular ion concentrations and transmembrane potential v and the existence of an infinite number of steady

states, are often cited as problems with such models, see [213, 573]. In order to address these concerns, models based on the principle of charge conservation have been formulated. In this formulation, the differential equation computing v from the transmembrane current, i.e. the first equation in (2.24), is replaced with an algebraic equation relating v to intracellular ion concentrations, see [163, 539]. This algebraic approach has proven to be stable with respect to drift in the computed ion concentrations and v. We present here the algebraic approach applied to the LRd model, as done in [244].

Introducing the total intracellular calcium concentration $[Ca^{2+}]_{i,t}$, given by the sum of troponin (trpn) and calmodulin (cmdn) bound and free Ca^{2+}, i.e.

$$[Ca^{2+}]_{i,t} = [Ca^{2+}]_i + \frac{[\overline{trpn}][Ca^{2+}]_i}{[Ca^{2+}]_i + K_{m,trpn}} + \frac{[\overline{cmdn}][Ca^{2+}]_i}{[Ca^{2+}]_i + K_{m,cmdn}},$$

and the total JSR calcium concentration $[Ca^{2+}]_{jsr,t}$, given by the sum of calsequestrin (csqn) bound and free JSR Ca^{2+}, i.e.

$$[Ca^{2+}]_{jsr,t} = [Ca^{2+}]_{jsr} + \frac{[\overline{csqn}][Ca^{2+}]_{jsr}}{[Ca^{2+}]_{jsr} + K_{m,csqn}},$$

we have that

$$\frac{d[Ca^{2+}]_{i,t}}{dt} = \beta_{myo}^{-1} \frac{d[Ca^{2+}]_i}{dt}, \qquad \frac{d[Ca^{2+}]_{jsr,t}}{dt} = \beta_{jsr}^{-1} \frac{d[Ca^{2+}]_{jsr}}{dt}. \qquad (2.29)$$

Substituting (2.29) into Eqs. (2.26) and (2.27), we obtain

$$\frac{d[Ca^{2+}]_{i,t}}{dt} = -\frac{A_{cap}}{2V_{myo}F}(I_{Ca,t} - 2I_{NaCa}) - \frac{V_{nsr}}{V_{myo}}(I_{up} - I_{leak}) + \frac{V_{jsr}}{V_{myo}}I_{rel}, \qquad (2.30)$$

$$\frac{d[Ca^{2+}]_{jsr,t}}{dt} = I_{tr} - I_{rel}. \qquad (2.31)$$

Combining (2.28), (2.30) and (2.31), we have

$$\frac{d[Ca^{2+}]_{i,t}}{dt} = -\frac{A_{cap}}{2V_{myo}F}(I_{Ca,t} - 2I_{NaCa}) - \frac{V_{nsr}}{V_{myo}}\frac{d[Ca^{2+}]_{nsr}}{dt} - \frac{V_{jsr}}{V_{myo}}\frac{d[Ca^{2+}]_{jsr,t}}{dt},$$

and we finally derive the system

$$\begin{cases} \dfrac{V_{myo}F}{A_{cap}}\dfrac{d[K^+]_i}{dt} = -(I_{K,t} - 2I_{NaK}), \\[3mm] \dfrac{V_{myo}F}{A_{cap}}\dfrac{d[Na^+]_i}{dt} = -(I_{Na,t} + 3I_{NaK} + 3I_{NaCa}), \\[3mm] \dfrac{2V_{myo}F}{A_{cap}}\left(\dfrac{d[Ca^{2+}]_{i,t}}{dt} + \dfrac{V_{nsr}}{V_{myo}}\dfrac{d[Ca^{2+}]_{nsr}}{dt} + \dfrac{V_{jsr}}{V_{myo}}\dfrac{d[Ca^{2+}]_{jsr,t}}{dt}\right) = -(I_{Ca,t} - 2I_{NaCa}). \end{cases} \qquad (2.32)$$

The total transmembrane ionic current I_{ion}, given by

$$I_{ion} = I_{K,t} + I_{Na,t} + I_{Ca,t} + I_{NaK} + I_{NaCa},$$

provides the change in the transmembrane potential v according to the current conservation law applied to the cell membrane modeled as a capacitor in parallel with the ionic current

$$C_m \frac{dv}{dt} + I_{ion} = 0. \tag{2.33}$$

Combining (2.32) and (2.33), we have

$$
\begin{aligned}
C_m \frac{dv}{dt} &= -I_{ion} \\
&= -(I_{K,t} + I_{Na,t} + I_{Ca,t} + I_{NaK} + I_{NaCa}) \\
&= \frac{V_{myo}F}{A_{cap}} \left(\frac{d[K^+]_i}{dt} + \frac{d[Na^+]_i}{dt} + 2\frac{d[Ca^{2+}]_{i,t}}{dt} \right. \\
&\quad \left. +2\frac{V_{nsr}}{V_{myo}}\frac{d[Ca^{2+}]_{nsr}}{dt} + 2\frac{V_{jsr}}{V_{myo}}\frac{d[Ca^{2+}]_{jsr,t}}{dt} \right),
\end{aligned}
\tag{2.34}
$$

hence it holds

$$C_m v - \frac{V_{myo}F}{A_{cap}} \left([K^+]_i + [Na^+]_i + 2[Ca^{2+}]_{i,t} + 2\frac{V_{nsr}}{V_{myo}}[Ca^{2+}]_{nsr} + 2\frac{V_{jsr}}{V_{myo}}[Ca^{2+}]_{jsr,t} \right) = C_0,$$

with C_0 constant. This equation can be interpreted as a relationship between the electric potential and the charge across a capacitor; indeed, applying the Gauss law to the membrane as a capacitor in an electric circuit, we have $C_m(u_i - u_e) = \rho$ with ρ the net charge difference between the intra- and extracellular charge densities given by $\rho_i - \rho_e$. In the previous model, we have considered only Na^+, K^+ and Ca^{2+}, which are the most important ions for the generation of the action potential, disregarding the contribution of other ions and we have implicitly assumed that the extracellular ionic concentrations are constant. Therefore, the constant C_0 is given by

$$C_0 = -\rho_e = -\frac{V_{myo}F}{A_{cap}} \left([K^+]_e + [Na^+]_e + 2[Ca^{2+}]_e \right),$$

yielding the latent algebraic conservation relationship

$$
\begin{aligned}
v = &\frac{V_{myo}F}{A_{cap}C_m}([K^+]_i - [K^+]_e + [Na^+]_i - [Na^+]_e + 2([Ca^{2+}]_{i,t} + \\
&\frac{V_{nsr}}{V_{myo}}[Ca^{2+}]_{nsr} + \frac{V_{jsr}}{V_{myo}}[Ca^{2+}_{jsr,t}] - [Ca^{2+}]_e)).
\end{aligned}
\tag{2.35}
$$

As a consequence, it is clear from this conservation law that the initial values of v and of the ion concentrations can not be selected arbitrarily.

Summarizing, we have two equivalent mathematical formulations:

- The common *full-differential approach*, composed of the differential system for the state variables transmembrane potential, gating variables and concentrations of $[Na^+]_i$, $[K^+]_i$, $[Ca^{2+}]_i$, $[Ca^{2+}]_{nsr}$, $[Ca^{2+}]_{jsr}$, where due to the latent conservation relationship, the state variables are not linearly independent, requiring that the initial condition must satisfy the conservation law;
- The *differential-algebraic approach*, composed of the differential system for the concentrations of $[Na^+]_i$, $[K^+]_i$, $[Ca^{2+}]_i$, $[Ca^{2+}]_{nsr}$, $[Ca^{2+}]_{jsr}$ and gating variables, that is coupled with the algebraic relationship for the transmembrane potential.

We remark that in the former approach, as a consequence of the linear dependence of the state variables, the resulting jacobian matrix is singular. Therefore, the study of stability of equilibrium points and cycles as functions of relevant parameters should be performed using the differential-algebraic formulation.

When an external current is applied, Eq. (2.33) becomes

$$C_m \frac{dv}{dt} + I_{ion} = I_{app}.$$

To satisfy the algebraic conservation relation between the transmembrane potential and ionic concentrations, it is required that charges carried by a stimulation current are accounted for a specific ionic species. Usually, in many simulation studies of periodical pacing, K^+ is chosen as a charge ion for the stimulus current. Therefore Eq. (2.25) is modified as follows:

$$\frac{d[K^+]_i}{dt} = -\frac{A_{cap}}{V_{myo}F}(I_{K,t} - 2I_{NaK} - I_{app}).$$

In this way, we eliminate the drift behavior of ion concentrations. Otherwise, proceeding as in (2.34) and integrating on $[0, t]$, the drift term

$$V_{drift} = \int_0^t I_{app}(s)\, ds,$$

would be added at the right hand side of Eq. (2.35), which might alter the membrane dynamics for long-term pacing, see [244].

2.9.6 Action Potential Duration Restitution Curve

The restitution function is a mesoscopic characteristic of cardiac tissue. It describes the duration of an action potential (APD), which is the time interval when the cardiac cell is in an excited state, as a function of the diastolic interval (DI), which is the time interval when the cardiac cell is in an unexcited state. At large DIs, the ionic currents in the cell have time to go back to the resting state and the corresponding APD is close to the maximum APD. If the DI is decreased, some of the ionic currents are still activated and the corresponding APD is smaller. There is a minimum DI for which the ionic currents are so activated that is not possible to elicit another action potential. This produces a minimum APD different from zero in the restitution curve of the APD. Figure 2.5 reports the restitution curve calculated using the LRd model.

2.9.7 Reduced Ionic Models

2.9.7.1 The FitzHugh-Nagumo Model and Other Cubic-Like Models for the Excitation Phase

In order to investigate phenomena on larger spatial and temporal scales, and also for theoretical purposes, several reduced membrane models have been developed that do not seek to model sub-cellular processes, but only to provide an action potential
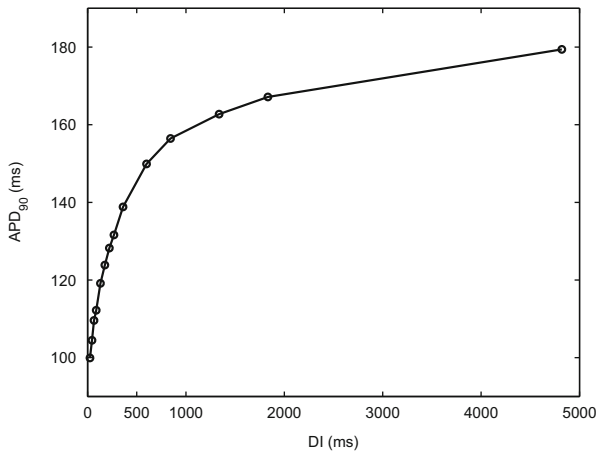
Fig. 2.5 Action potential duration restitution curve computed with the LRd model

at a minimal computational cost. The unknowns of these models are a normalized transmembrane potential v and a gating variable w, following the general kinetics

$$\begin{cases} \dfrac{dv}{dt} = f(v, w) \\ \dfrac{dw}{dt} = g(v, w). \end{cases}$$

- FitzHugh-Nagumo model [178]:

$$f(v, w) = -kv(v - a)(v - 1) - w, \quad g(v, w) = \epsilon(v - \gamma w);$$

- Roger-McCulloch model [422]:

$$f(v, w) = -kv(v - a)(v - 1) - vw, \quad g(v, w) = \epsilon(v - \gamma w);$$

- Aliev-Panfilov model [1]:

$$f(v, w) = -kv(v - a)(v - 1) - w, \quad g(v, w) = \epsilon(\gamma v(v - 1 - a) + w);$$

- Mitchell-Schaeffer model [333]:

$$f(v, w) = -\frac{w}{\tau_{in}}v^2(v - 1) - \frac{v}{\tau_{out}}, \quad g(v, w) = \begin{cases} \dfrac{1 - w}{\tau_{open}} & \text{if } v \leq v_{gate}, \\ \dfrac{-w}{\tau_{close}} & \text{if } v > v_{gate}. \end{cases}$$

Here $0 < a < 1$, k, ϵ, γ, τ_{in}, τ_{out}, τ_{open}, τ_{close}, $0 < v_{gate} < 1$ are given constants;

- Morris-Lecar model [337]:

$$\begin{aligned} -f(v, w) &= \frac{g_{Ca}m_\infty(v - v_{Ca}) + g_K w(v - v_K) + g_L(v - v_L)}{C_m} \\ g(v, w) &= \phi \frac{w_\infty - w}{\tau_w} \end{aligned} \qquad (2.36)$$

where

$$\begin{aligned} m_\infty(v) &= 0.5[1 + \tanh((v - v_1)/v_2)] \\ w_\infty(v) &= 0.5[1 + \tanh((v - v_3)/v_4)] \\ \tau_w(v) &= 1/\cosh((v - v_3)/(2v_4)). \end{aligned}$$

Table 2.4 Three calibrations of the Morris-Lecar parameters g_{Ca}, v_3, v_4, ϕ

	g_{Ca} (mS/cm^2)	v_3 (mV)	v_4 (mV)	ϕ (ms^{-1})
ML1	4.4	2.	30.	0.04
ML2	4	12	17.4	0.066
ML3	4	12	17.4	0.23

The parameters of the Morris-Lecar model are: $C_m = 20\,\mu\text{F/cm}^2$, $v_{Ca} = 120\,\text{mV}$, $v_K = -84\,\text{mV}$, $g_K = 8\,\text{mS/cm}^2$, $v_L = -60\,\text{mV}$, $g_L = 2\,\text{mS/cm}^2$, $v_1 = -1.2\,\text{mV}$, $v_2 = 18\,\text{mV}$. For the remaining parameters, we consider three different calibrations denoted by **ML1**, **ML2**, **ML3** in Table 2.4 and used later in the section on bifurcation diagrams.

2.9.7.2 The Fenton-Karma Model

This reduced model, proposed in [170], consists of three ordinary differential equations for the transmembrane potential v and two gating variables u and w:

$$
\begin{cases}
\dfrac{dv}{dt} = f(v, u, w) \\[2mm]
\dfrac{du}{dt} = H(v - v_c)(1 - u)/\tau_{u(v)}^- - H(v - v_c)u/\tau_u^+ \\[2mm]
\dfrac{dw}{dt} = H(v_c - v)(1 - w)/\tau_w^- - H(v - v_c)w/\tau_w^+ ,
\end{cases}
$$

where H is the Heaviside function centered at zero and the ionic current $f(v, u, w) = -I_{fi} - I_{so} - I_{si}$ is the sum of the three currents

$$I_{fi}(v, u) = -uH(v - v_c)(1 - v)(v - v_c)/\tau_d$$

$$I_{so}(v) = H(v - v_c)/\tau_o + H(v - v_c)/\tau_r$$

$$I_{si}(v, w) = -w(1 + tanh(k(v - v_c^{si})))/(2\tau_{si}).$$

The values of the parameters in the previous expressions can be found in Table I of [170].

2.9.8   Phase-Plane Analysis of the FitzHugh-Nagumo (FHN) Model

The FitzHugh-Nagumo model can be derived from a simplified electrical circuit model of the cell membrane. The circuit consists of a capacitor (with current i_c) in parallel with a nonlinear current–voltage device (with current $j = F(u)$) and a serial system with a resistor, an inductance, and a battery (with current i). Let $u = u_i - u_e$ be the transmembrane potential and v_R, v_L, v_0 be the resistor, inductance, and battery potentials, respectively. Given an applied current I_a, Kirchhoff's laws state that

$$\begin{cases} i_c + i + j = I_a, \\ u = v_0 + v_L + v_R. \end{cases}$$

From $i_c = C\frac{du}{dt}$, $v_R = Ri$ (Ohm's law), $v_L = L\frac{di}{dt}$ (Faraday's law), we have

$$\begin{cases} C\dfrac{du}{dt} = -i - F(u) + I_a, \\ L\dfrac{di}{dt} = u - Ri - v_0. \end{cases}$$

In order to write this system in dimensionless form, we scale the time as $\tau = R_m t/L$, where $R_m = 1/F'(0)$ and we define the dimensionless variables $v(\tau) = u(L\tau/R_m)/v_m$, $w(\tau) = R_m i(L\tau/R_m)/v_m$, where v_m is the maximal value of u. Then

$$\begin{cases} \dfrac{dv}{d\tau} = \dfrac{L}{v_m R_m}\dfrac{du}{dt} = \dfrac{L}{v_m R_m C}(-i - F(u) + I_a) = \dfrac{L}{R_m^2 C}\left(-\dfrac{R_m i}{v_m} - \dfrac{R_m F(u)}{v_m} + \dfrac{R_m}{v_m}I_a\right), \\ \dfrac{dw}{d\tau} = \dfrac{R_m L}{v_m R_m}\dfrac{di}{dt} = \dfrac{L}{v_m L}(v - Ri - v_0) = \dfrac{u}{v_m} - \dfrac{R}{R_m}\dfrac{R_m i}{v_m} - \dfrac{v_0}{v_m}. \end{cases}$$

Defining $\hat{v}_0 = v_0/v_m$, $\hat{F}(v) = \frac{R_m}{v_m}F(v_m v)$, $\hat{I}_a = \frac{R_m}{v_m}I_a$, $\gamma = R/R_m$, $\epsilon = CR_m^2/L$, we have

$$\begin{cases} \epsilon\dfrac{dv}{d\tau} = -w - \hat{F}(v) + \hat{I}_a, \\ \dfrac{dw}{d\tau} = v - \gamma w - \hat{v}_0. \end{cases}$$

This system is a particular instance of the generalized FitzHugh-Nagumo planar dynamical system

$$\begin{cases} \epsilon\dfrac{dv}{d\tau} = f(v, w) + \hat{I}_a, \\ \dfrac{dw}{d\tau} = g(v, w). \end{cases} \tag{2.37}$$
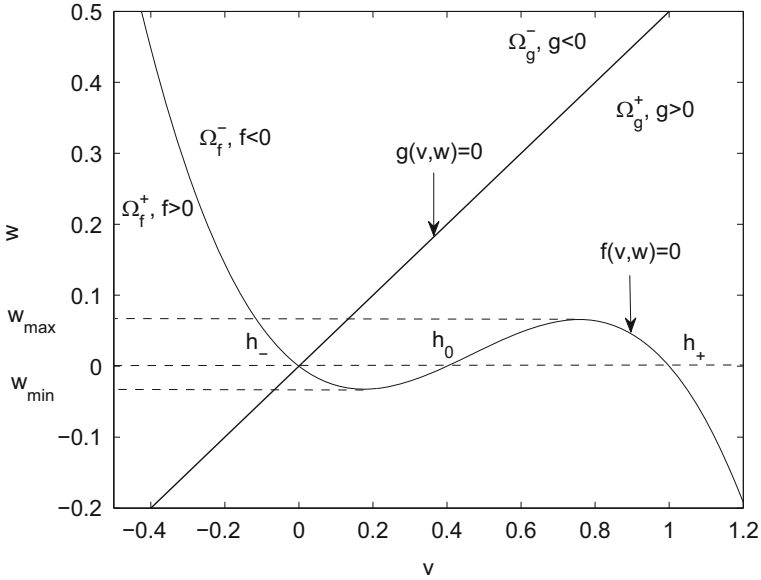
Fig. 2.6 v, w-phase plane, nullclines and notations for the FHN model

We assume a situation as the one in Fig. 2.6, where the nullcline $f(v, w) = 0$ is a cubic-like function in v with 3 distinct zeros, local maximum value w_{max}, local minimum value w_{min} and the nullcline $g(v, w) = 0$ has only one intersection point (v^*, w^*) with $f = 0$ (for an example with more than one intersection, see Fig. 2.9).

More precisely, we assume that it exists an interval (w_{min}, w_{max}) such that:

- For $w > w_{max} \exists ! v : f(v, w) = 0$, defining a function $v = h_-(w)$;
- For $w < w_{min} \exists ! v : f(v, w) = 0$, defining a function $v = h_+(w)$;
- For $w_{min} < w < w_{max}$ there are three real roots $h_-(w) < h_0(w) < h_+(w)$ of $f(v, w) = 0$.

The cubic-like nullcline $f(v, w) = 0$ partitions the v, w-plane into two regions, $\Omega_f^- = \{(v, w) : w > \overline{w}, \text{ where } f(v, \overline{w}) = 0\}$ and $\Omega_f^+ = \{(v, w) : w < \overline{w}, \text{ where } f(v, \overline{w}) = 0\}$. We assume that $f < 0$ in Ω_f^- and $f > 0$ in Ω_f^+. Analogously, the other nullcline $g(v, w) = 0$ partitions the plane into two regions $\Omega_g^- = \{(v, w) : w > \overline{w}, \text{ where } g(v, \overline{w}) = 0\}$ and $\Omega_g^+ = \{(v, w) : w < \overline{w}, \text{ where } g(v, \overline{w}) = 0\}$, and we assume that $g < 0$ in Ω_g^- and $g > 0$ in Ω_g^+. These assumptions guarantee that the partial derivatives of f and g are nonpositive or nonnegative but we will make the stronger assumptions $\partial_w f(v, w) < 0$, $\partial_v f(v, w) > 0$, and $\partial_v g(v, w) > 0$, $\partial_w g(v, w) < 0$.

According to the chosen initial conditions (v_0, w_0) and the applied current $\hat{I}_a$, the generalized FitzHugh-Nagumo system (2.37) admits solutions with quite different dynamics. The intersection point (v^*, w^*) between the nullclines $f = 0$, $g = 0$ is an equilibrium point and its stability is determined by the eigenvalues λ_1, λ_2 of the Jacobian matrix evaluated at (v^*, w^*)

$$J = \begin{bmatrix} \partial_v f & \partial_w f \\ \partial_v g & \partial_w g \end{bmatrix} :$$

– We have stability if λ_1, λ_2 are both real and negative (stable node or sink) or if they are a complex conjugate pair with negative real part (stable spiral);
– We have instability if λ_1, λ_2 are both real positive (unstable node or source) or they have opposite signs (saddle) or they are a complex conjugate pair with positive real part (unstable spiral).

Equivalently, the stability of a planar dynamical system is often described in terms of the trace $tr(J) = \lambda_1 + \lambda_2$ and determinant $det(J) = \lambda_1 \lambda_2$ of the Jacobian matrix.

For our generalized FitzHugh-Nagumo system (2.37), we have stability if (v^*, w^*) lies on the lower branch $h_-(w)$ or upper branch $h_+(w)$ of the nullcline $f = 0$, while we have instability if (v^*, w^*) lies on its middle branch $h_0(w)$. In Fig. 2.7, we consider first some examples without applied current, $\hat{I}_a = 0$. We will then vary $\hat{I}_a$ in Figs. 2.8 and 2.9 we will consider a case with three equilibrium points. In each figure, the left panel shows the nullclines (dashed lines) and the trajectory (continuous line) in the phase plane v, w starting from the initial point (v_0, w_0) (marked with $\diamond$); the equilibrium point (v^*, w^*) is marked with $\star$.

(a) **FHN dynamics with zero applied current $\hat{I}_a$ (Fig. 2.7).**

(a1) Stable equilibrium: subthreshold response. Consider first $w_0 \in (w_{min}, w_{max})$ and $v_0 < h_0(w_0)$. Then v returns to the equilibrium point v^* (Fig. 2.7 top, stable spiral), because in the region where $f < 0$ if the initial point (v_0, w_0) is above the nullcline $g = 0$, then here $g < 0$ and (v, w) returns to the equilibrium point (v^*, w^*), and if (v_0, w_0) is below the nullcline $g = 0$, then here $g > 0$ so w initially increases until the trajectory crosses $g = 0$ into the region where $g < 0$ and (v, w) again returns to (v^*, w^*). Analogous considerations apply when $w_0 \in (w_{min}, w_{max})$ and $v_0 < h_0(w_0)$ in the region where $f > 0$.

(a2) Stable equilibrium: action potential (Fig. 2.7 middle, stable spiral). If instead $v_0 > h_0(w_0)$ (for simplicity we still assume $w_0 \in (w_{min}, w_{max})$), then we have an action potential. First, we have an excitation phase during a time $\tau = O(\epsilon)$, where v tends to the upper branch $h_+(w)$ of the nullcline $f = 0$,
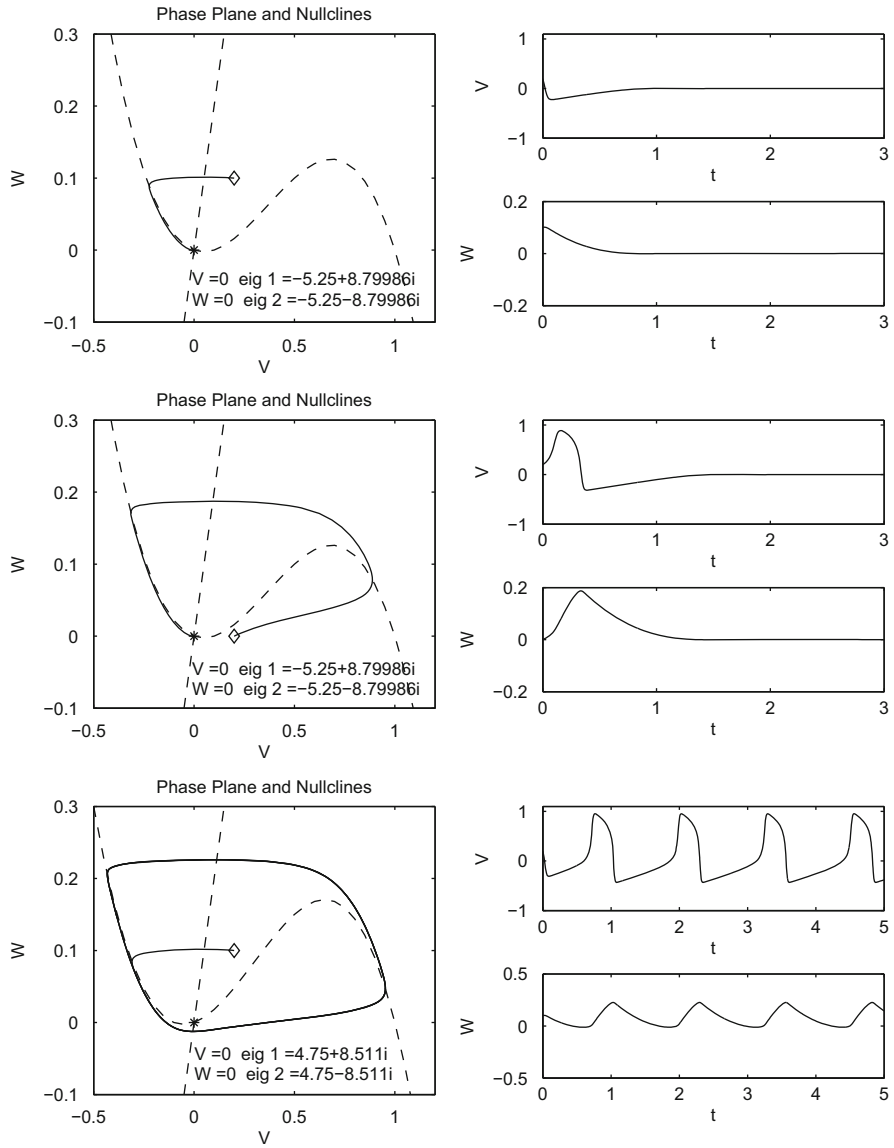
Fig. 2.7 FHN model (2.37) with $\hat{I}_a = 0$, $\epsilon = 0.01$. In *top* and *middle panels* $f(v, w) = v(v - 0.1)(1 - v) - w$, $g(v, w) = v - w/2$, while in *bottom panels* $f(v, w) = v(v + 0.1)(1 - v) - w$, $g(v, w) = v - w/2$. Phase plane trajectories, nullclines, coordinates of the marked equilibrium point $\star$ and associated eigenvalues (*left*), solutions v, w as functions of time (*right*)
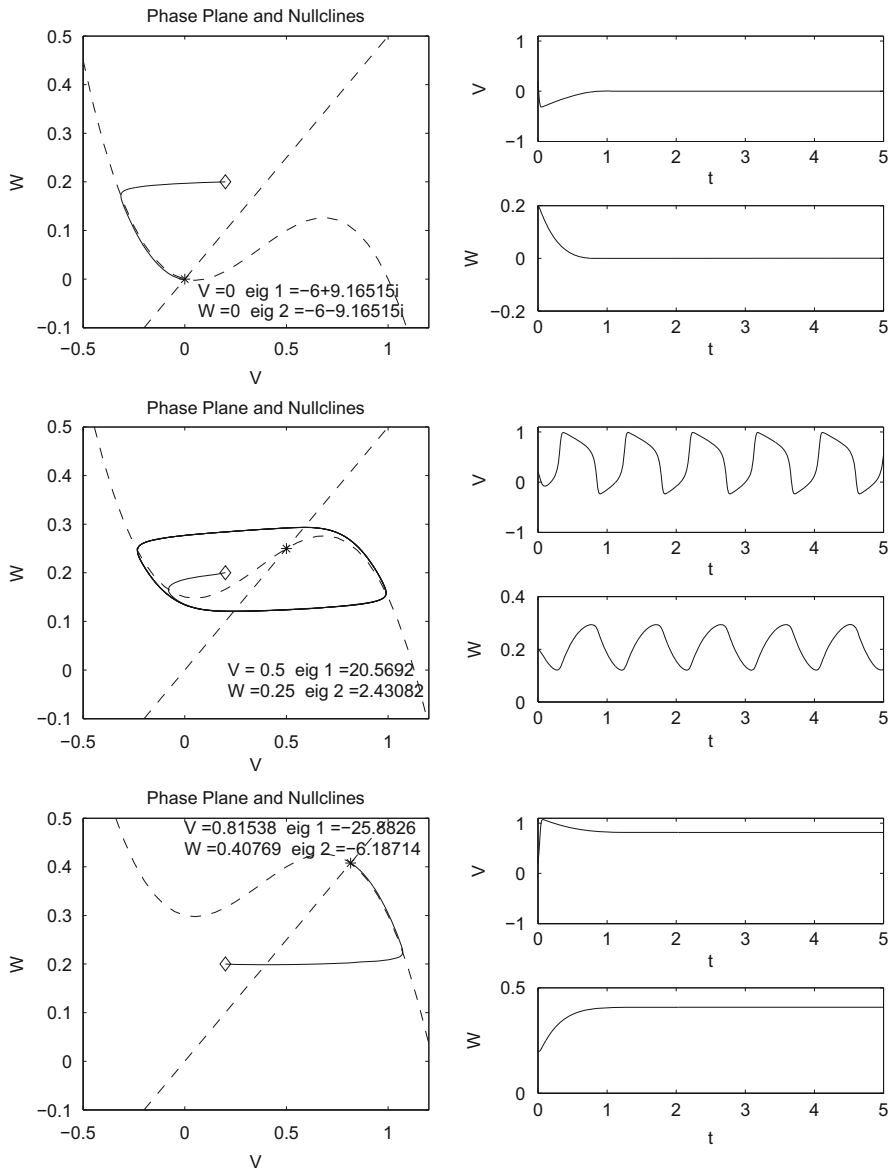
Fig. 2.8 FHN model (2.37) with varying $\hat{I}_a$, with $f(v, w) = v(v - 0.1)(1 - v) - w$, $g(v, w) = v - 2w$, $\epsilon = 0.01$. $\hat{I}_a = 0$ (*top*), 0.15 (*middle*), 0.3 (*bottom*). Phase plane trajectories, nullclines, coordinates of the marked equilibrium point $\star$ and associated eigenvalues (*left*), solutions v, w as functions of time (*right*)

Phase Plane and Nullclines

V =0.77016 eig 1 =−24.0703
W =0.15403 eig 2 =−10.2438

V = 0.12984 eig 1 = 24.9783
W =0.025969 eig 2 =−1.66426

V =0 eig 1 =2.5+6.6144i
W =0 eig 2 =2.5−6.6144i
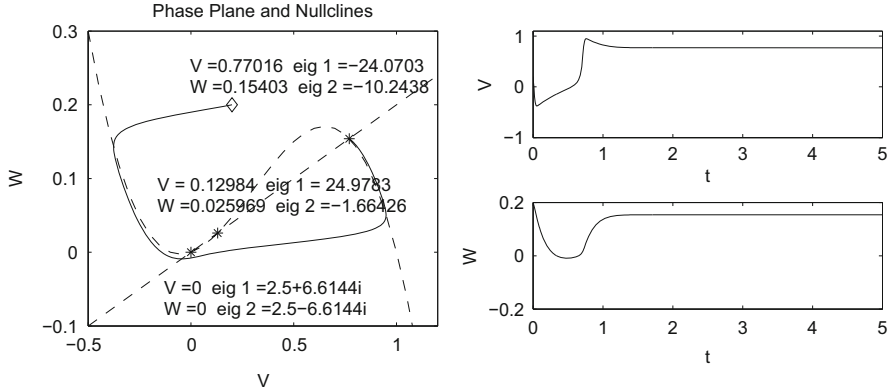
Fig. 2.9 FHN model (2.37) with nullclines intersecting in three points: $f(v, w) = v(v + 0.1)(1 - v) - w$, $g(v, w) = v - 5w$, $\epsilon = 0.01$, $\hat{I}_a = 0$. Phase plane trajectories, nullclines, coordinates of the marked equilibrium points $\star$ and associated eigenvalues (*left*), solutions v, w as functions of time (*right*)

because in this region $f > 0$. Indeed, if we scale time as $\tau' = \tau/\epsilon$ and define $\hat{v}(\tau') = v(\epsilon\tau')$, $\hat{w}(\tau') = w(\epsilon\tau')$, we have $\partial_{\tau'}\hat{v} = \epsilon\partial_\tau v$, $\partial_{\tau'}\hat{w} = \epsilon\partial_\tau w$, and

$$\begin{cases} \dfrac{d\hat{v}}{d\tau'} = f(\hat{v}, \hat{w}), \\ \dfrac{d\hat{w}}{d\tau'} = \epsilon g(\hat{v}, \hat{w}). \end{cases}$$

Therefore, for small ϵ, $\hat{w} \approx w_0$ is approximately constant and $\hat{v}$ evolves toward $h_+(w_0)$. Then for $\tau > O(\epsilon)$ we have an excited state where (v, w) tends to stay on the upper branch, where $f = 0$ and w evolves approximately according to $\dfrac{dw}{d\tau} = g(h_+(w), w)$. This "plateau" lasts approximately up to the finite time

$$\int_{w_{min}}^{w_{max}} \frac{dw}{g(h_+(w), w)},$$

when w reaches w_{max} at the local maximum of $f = 0$. After this time, we have a recovery phase, where w is again approximately constant and v now evolves toward the lower branch $h_-(w)$ since we are again in the region where $f < 0$. Once the lower branch is reached, (v, w) tends to return to the equilibrium point (v^*, w^*) since the latter lies on the lower branch, i.e. $g(h_-(w^*), w^*) = 0$.

(a3) Unstable equilibrium: limit cycle associated with a periodic solution (Fig. 2.7 bottom, unstable spiral). If otherwise (v^*, w^*) lies on the middle branch $h_0(w)$, the equilibrium is unstable and the trajectory of (v, w) starts another excitation phase generating another action potential and so on. In this case, we have a limit cycle associated with a periodic solution.

(b) Effect of increasing the applied current $\hat{I}_a$ (Fig. 2.8).

  (b1) Stable equilibrium: subthreshold response (Fig. 2.8 top, stable spiral). For $\hat{I}_a = 0$, we have a subthreshold response as in case (a1) shown in Fig. 2.7, top.

  (b2) Unstable equilibrium: periodic limit cycle (Fig. 2.8 middle, source). For $\hat{I}_a = 0.15$, the nullcline $f = 0$ is shifted upward and (v^*, w^*) becomes a source point, yielding a periodic limit cycle corresponding to a periodic train of action potentials.

  (b3) Stable equilibrium (Fig. 2.8 bottom, sink). For $\hat{I}_a = 0.3$, the nullcline $f = 0$ is further shifted upward and (v^*, w^*) becomes a sink point quickly attracting the trajectory to the equilibrium.

(c) Multiple equilibrium points (Fig. 2.9). A FHN system with $f(v, w) = v(v + 0.1)(1 - v) - w$, $g(v, w) = v - 5w$, $\hat{I}_a = 0$, having three equilibrium points is shown in Fig. 2.9: from left to right, they are an unstable spiral, a saddle point, and a sink. The trajectory quickly tends to the lower branch of the $f = 0$ nullcline, follows it until it is repelled by the two unstable equilibrium points, tends to the upper branch of the $f = 0$ nullcline and terminates in the sink.

(d) Cathodal and anodal current pulses (Figs. 2.10 and 2.11).

  In the previous simulations, the action potentials were generated by appropriate choices of initial conditions v_0, w_0 for the transmembrane potential and recovery variables. A more physiological technique to generate an action potential consists in starting from resting initial conditions v_0, w_0 and applying an appropriate current pulse $\hat{I}_a$ for a sufficiently long time interval T_{stim}. In the FitzHugh-Nagumo model (2.37), the application of such current pulse shifts the $f = 0$ nullcline upward if $\hat{I}_a > 0$ (see Fig. 2.10) or downward if $\hat{I}_a < 0$ (see Fig. 2.11). This shift changes temporarily the equilibrium point for the duration of the stimulation interval T_{stim} so that v_0, w_0 is no longer an equilibrium point
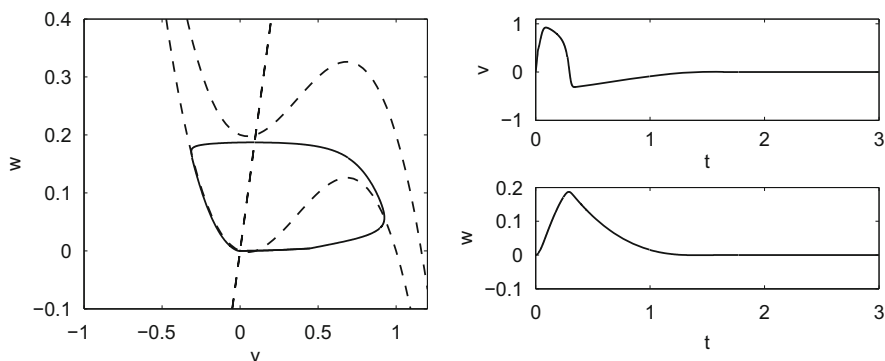
Fig. 2.10 Cathode make due to current pulse $I_a = 0.2$ lasting 0.02 ms for FHN model (2.37) with $f(v, w) = v(v - 0.1)(1 - v) - w$, $g(v, w) = v - w/2$, $\epsilon = 0.01$. Phase plane trajectories and nullclines (*left*), solutions v, w as functions of time (*right*)
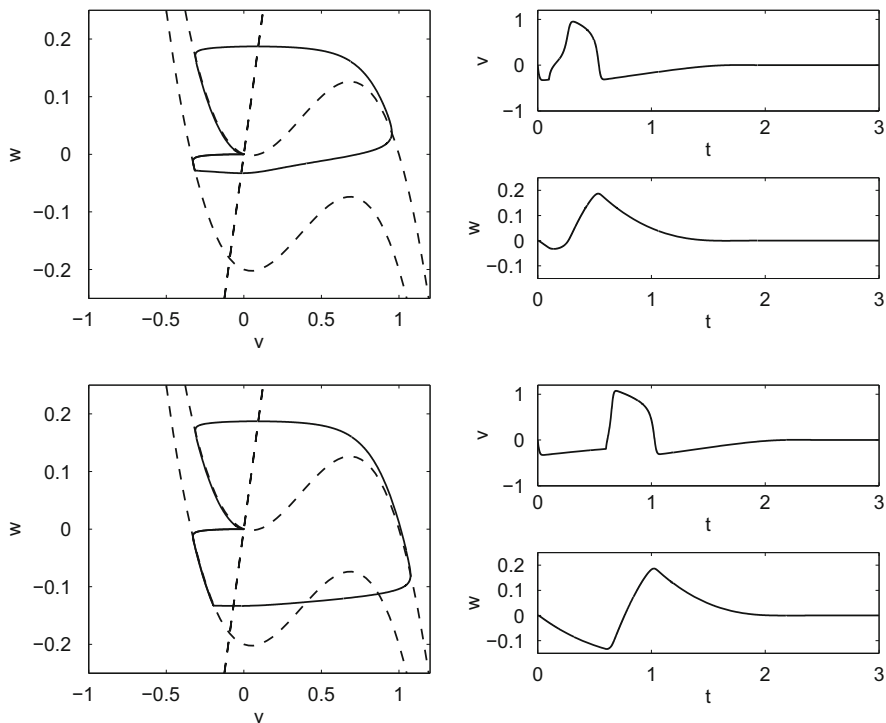
Fig. 2.11 Anode break due to current pulse $I_a = -0.2$ lasting 0.1 ms (*top*) or 0.6 ms (*bottom*) for FHN model (2.37) with $f(v, w) = v(v - 0.1)(1 - v) - w$, $g(v, w) = v - w/2$, $\epsilon = 0.01$. Phase plane trajectories and nullclines (*left*), solutions v, w as functions of time (*right*)

and the variables v, w start a trajectory toward the closest nullcline branch. When the pulse is turned off at time T_{stim}, the f nullcline returns to the original curve $f = 0$. By this time, v and w have reached a point in phase-space that, for proper choices of pulse amplitude and interval duration, belongs to the excitable region, so that an action potential is generated. Figure 2.10 shows such an action potential generated by a pulse with $I_a = 0.2$, $T_{stim} = 0.02$, known as cathode make mechanism. Instead Fig. 2.11 shows two cases with action potentials generated by pulses with $I_a = -0.2$, $T_{stim} = 0.1$ (top) or $I_a = -0.2$, $T_{stim} = 0.6$ (bottom), known as anode break mechanism. Additional activation mechanisms (known as cathode break and anode make) are present in space-time cardiac domains, in particular in three-dimensional domains, where more complex virtual electrode polarization (VEP) activation patterns are present, see Chap. 9.1.

2.9.9 Bifurcation Diagrams

There are several mechanisms from which limit cycles arise in models of excitable cells. A periodic behavior of the transmembrane potential can be thought of as a transition back and forth between hyperpolarized and depolarized states. We review here four main mechanisms that govern the onset of oscillations in some of the previous ionic models. For more details we refer to e.g. [288, 419].

A possible motivation for studying the dynamical response of an ionic model to a sustained injection of a constant current, i.e. a bias current, is for example the fact that during ischemia there is an accumulation of extracellular potassium in the ischemic zone, leading to an increase of the membrane potential. This creates a current flow between the injured and healthy zone. We study here this effect by modeling the injury current as a time- and voltage-independent *bias* current, and considering simple membrane models. We illustrate the first two mechanisms considering the simplest FHN model.

The dynamics of the FHN system as a function of an applied *bias* current $\hat{I}_a$, i.e. a continuous constant current, can be summarized by a bifurcation diagram with respect to $\hat{I}_a$. We present now some bifurcation and frequency diagrams computed by the XPPAUT software [165].

(a) Choosing $\epsilon = 0.1$, i.e. modifying the time scale of the v variable, we find in Fig. 2.12 that by increasing $\hat{I}_a$, a periodic solution appears through a supercritical Hopf-Bifurcation (HB) point near $\hat{I}_a = 0.075$, leading to a branch of small-amplitude periodic orbits of nonzero frequencies. By increasing $\hat{I}_a$ further, we find that the periodic orbits have decreasing amplitudes and then disappear at another HB point near $\hat{I}_a = 0.17$. This type of dynamical phenomenon, with oscillations arising with arbitrary small amplitude via a supercritical HB point and with nonzero oscillation frequency, is also called *soft excitation* by some authors.
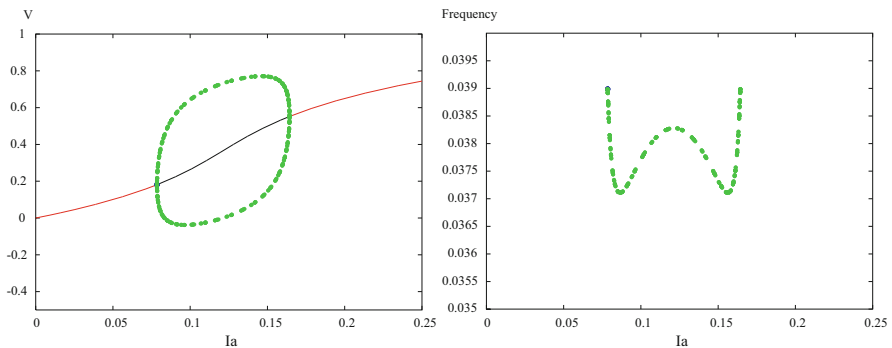
Fig. 2.12 *Left*: bifurcation diagram for FHN model with $f(v, w) = v(v - 0.1)(1 - v) - w + \hat{I}_a$, $g(v, w) = v - 2w$, $\epsilon = 0.1$ with respect to $\hat{I}_a$. *Right*: associated frequency diagram

(b) Choosing $\epsilon = 0.01$, i.e. shortening the time constant of v, we find in Fig. 2.13 that for all values of $\hat{I}_a \geq 0$ there is a unique equilibrium point (EP), which loses its asymptotical stability for values of $\hat{I}_a$ between two subcritical Hopf bifurcation points, HB1 and HB2 and we see also the presence of a stable limit cycle for values of $\hat{I}_a$ ranging approximately between 0.03 and 0.22. Near the subcritical HB1 point there is a large-amplitude stable limit cycles and bistability between stable oscillations and a stable equilibrium point, separated by an unstable small-amplitude periodic orbit. The unstable limit cycle turns back and coalesces at a turning bifurcation point with the stable limit cycle at a value of $\hat{I}_a$ that is smaller than the one associated to the subcritical HB point. A zoom of the left part of this interval is shown in Fig. 2.13, right panel, revealing a subcritical HB1 near $\hat{I}_a = 0.0319$. The branch of unstable periodic orbits comes out near HB1 and lies on the side of HB1 where there is a stable branch of EP. Decreasing $\hat{I}_a$ from the HB1 value, a *saddle-node periodic bifurcation* (SNPB) point appears, connecting a stable and an unstable branch of limit cycles. Above it two stable structures appear, a stable EP and a stable limit cycle, as well as an unstable limit cycle.

The frequency of the limit cycle as a function of $\hat{I}_a$, also computed with XPPAUT, is shown in Fig. 2.14, left panel, together with a zoom near the Hopf bifurcation point shown in the right panel.

This type of onset of oscillations arising abruptly with stable large-amplitude oscillations and with relatively high frequencies it is also called *hard excitation* mechanism or also *saddle-node bifurcation of limit cycles* (SNBLC), since for increasing $\hat{I}_a$ there is the creation of a pair of limit cycles, one stable and the other unstable with non zero frequencies.

An analogous reflected situation happens at the right part of the bifurcation interval (zoom not shown), where unstable small-amplitude periodic orbits now appear on the stable equilibrium branch on the right side of the right HB point.
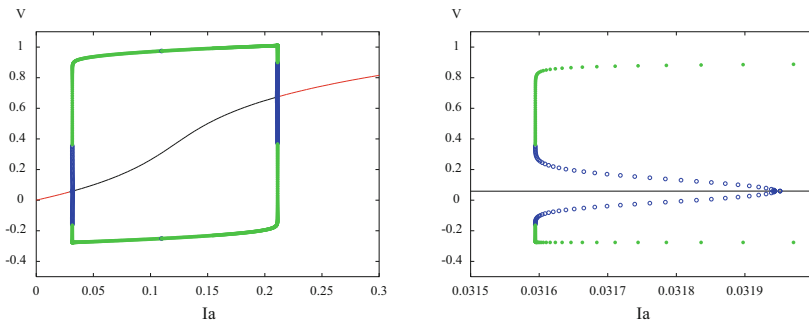
Fig. 2.13 *Left*: bifurcation diagram for FHN model with $f(v, w) = v(v - 0.1)(1 - v) - w + \hat{I}_a$, $g(v, w) = v - 2w$, $\epsilon = 0.01$ with respect to $\hat{I}_a$. *Right*: zoom of the left bifurcation point
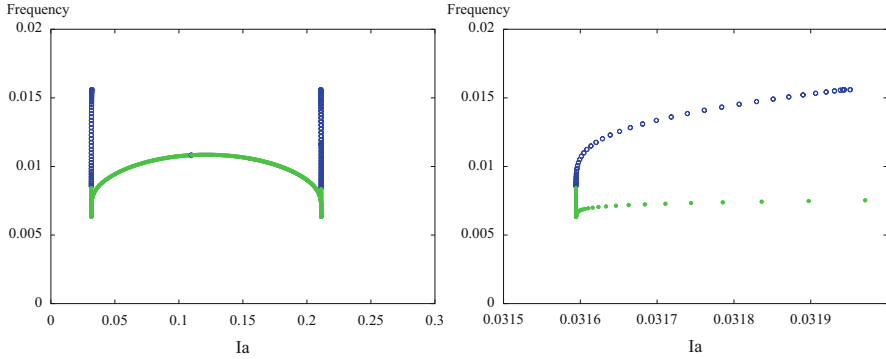
Fig. 2.14 *Left*: frequency diagram for FHN model with $f(v, w) = v(v-0.1)(1-v)-w$, $g(v, w) = v - 2w$, $\epsilon = 0.01$. *Right*: zoom of the left interval
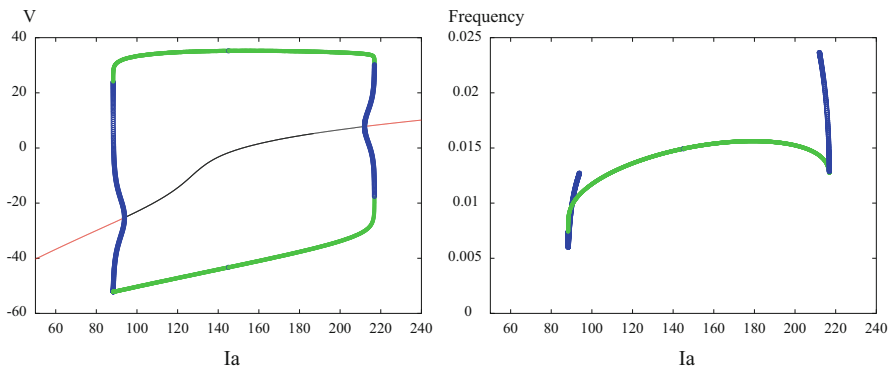
Fig. 2.15 *Left*: bifurcation diagram for the Morris-Lecar model (2.36) with respect to $\hat{I}_a$ with the parameter calibration **ML1** in Table 2.4. *Right*: frequency diagram

The previous mechanisms (a) and (b) of onset of oscillations are associated with local bifurcations that are local phenomena where limit cycles originate with small amplitude when a single equilibrium state changes from stable to unstable or viceversa. A bifurcation diagram of the same local type (b) is also obtained for the Morris-Lecar model using the parameter calibration (ML1) reported in Table 2.4; see Fig. 2.15.

Moreover, the bifurcation diagram of the Hodgkin-Huxley model, displayed in Fig. 2.16, shows the same bistable behavior between a SNPB and a HB1. Differently from the other models, a second supercritical Hopf bifurcation point appears, where stable periodic orbits of small amplitude come out lying near the unstable branch. See Fig. 2.17 for the associated frequency diagram.
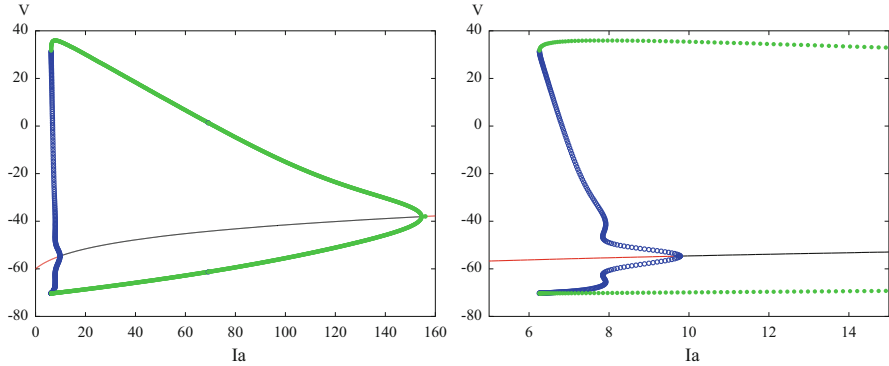
Fig. 2.16 *Left*: bifurcation diagram for HH model with respect to $\hat{I}_a$. *Right*: zoom of the left bifurcation point
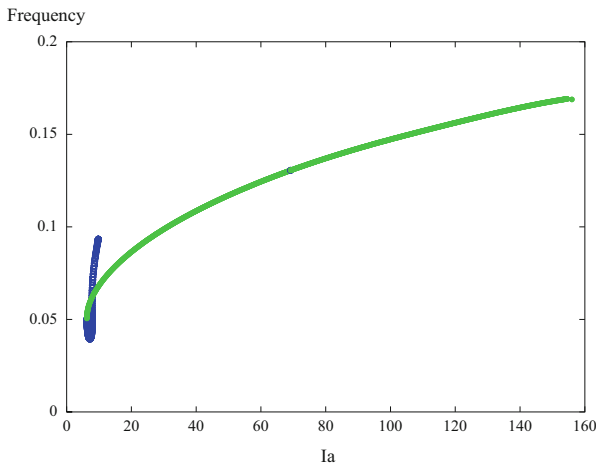
Fig. 2.17 *Left*: frequency diagram for HH model with respect to $\hat{I}_a$

(c) We now look at two other mechanisms of onset of oscillations that are very different from the previous mechanisms (a) and (b) since they are associated with global bifurcations and show that it is possible to create or destroy spiking with arbitrary low frequencies when the amplitude of the sustained injected current is increased. A type of global bifurcation is related to the appearance of homoclinic bifurcation. We recall that an homoclinic orbit is a closed curve that has a single equilibrium point located along the curve and the period of the orbit is infinite. Figure 2.18 displays the bifurcation diagram with respect to the injected current $\hat{I}_a$ for the Morris-Lecar model using the calibration parameter
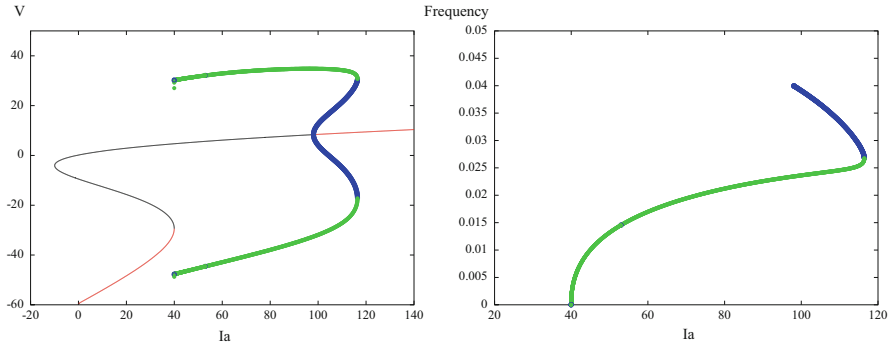
Fig. 2.18 Transmembrane potential (*left*) and frequency (*right*) bifurcation diagrams with respect to $\hat{I}_a$ for Morris-Lecar model (2.36) with the parameter calibration **ML2** in Table 2.4

(ML2) reported in Table 2.4, still computed with XPPAUT. The diagram starts on the left with a stable node branch but by increasing $\hat{I}_a$ two unstable branches of equilibrium points appear, the upper one associated with unstable spirals, and the intermediate with saddle points. By increasing $\hat{I}_a$ further, the unstable saddle and stable nodes coalesce at a HB bifurcation point and subsequently disappear. A limit cycle then emerges as a homoclinic orbit that has a finite (large) amplitude with zero frequency as shown in Fig. 2.18, right panel. This type of dynamical behavior associated with saddle-node on a limit cycle is sometimes called a *saddle-node homoclinic orbit*. By increasing $\hat{I}_a$ further, the stable limit cycle disappears through a saddle-node bifurcation of limit cycles.

(d) We now increase the constant ϕ from 0.066 to 0.23, yielding a decrease of the time constant of the potassium gating variable w, thus increasing its changing rate. Figure 2.19 displays the bifurcation diagram for the Morris-Lecar model using the parameter calibration (ML3) reported in Table 2.4. After an initial branch of stable node, we have again two saddle node bifurcation points connecting two unstable branches and a subcritical HB appears on the upper branch, but now with a value between the two saddle node bifurcation points. As in the previous case (c), the stable branch of limit cycles terminates again with an homoclinic orbit which is now on the middle branch before the right saddle node bifurcation point. For $\hat{I}_a$ ranging between the subcritical HB values and the right saddle node bifurcation there are two stable equilibrium points and a stable limit cycle, yielding a *twistable* dynamics.

This type of global bifurcation is called *saddle-homoclinic bifurcation*. The frequency of the stable limit cycles approaches the zero frequency of the homoclinic orbit more rapidly than in the previous SNBLC diagram.
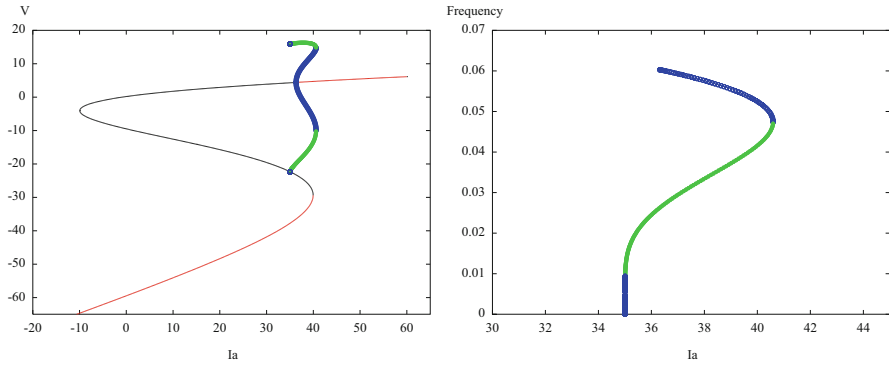
Fig. 2.19 Transmembrane potential (*left*) and frequency (*right*) bifurcation diagrams with respect to $\hat{I}_a$ for Morris-Lecar model (2.36) with the parameter calibration **ML3** in Table 2.4
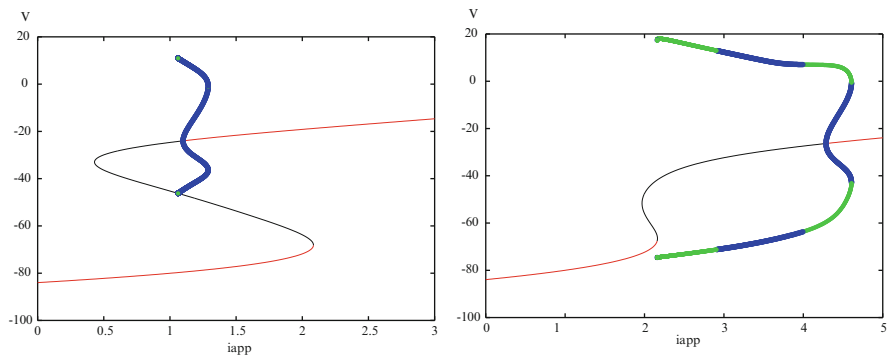
Fig. 2.20 Bifurcation diagram for LR1 model with the original calibration parameters (*left*) and the with the I_K current scaled by a factor 3 (*right*)

We have also computed the bifurcation diagrams for the LR1 model with both the original calibration parameters and with the I_K current scaled by a factor 3. The results obtained with the XPPAUT software display bifurcation diagrams of Fig. 2.20, left and right panels, similar to the diagram of Figs. 2.19 and 2.18, respectively, but with different stability properties.

For bifurcation diagrams related to second generation models, we refer e.g. to [57].

Chapter 3
Mathematical Models of Cardiac Cells Arrangements: The Bidomain Model

3.1 Models of Cardiac Fibers

3.1.1 Cable Equation

We model an excitable cell as a long cylindrical cable and assume the so-called core conduction assumption, stating that the potential along the cable depends only on the length variable and not on radial or angular variables, so that the cable model is one-dimensional. Then we assume that the cable is composed of a number of short sections of length dx with isopotential membrane, and that in each section we have only the transmembrane and axial currents, as illustrated in the following diagram
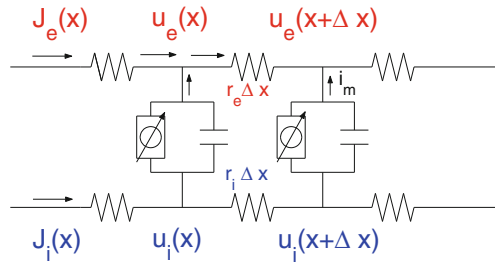
The relationship between the intra- and extracellular current fluxes $J_{i,e}$ ($\mathrm{A\,cm}^{-2}$) and the intra- and extracellular potentials $u_{i,e}$ (V) is given by *Ohm's law*

$$J_i = -\frac{1}{r_i}\partial_x u_i = -\sigma_i \partial_x u_i,$$
$$J_e = -\frac{1}{r_e}\partial_x u_e = -\sigma_e \partial_x u_e,$$

where $\sigma_{i,e}$ are the intra- and extracellular conductivities (Ω^{-1} cm^{-1}) and $r_{i,e}$ are the intra- and extracellular resistances per unit space (Ω cm).

We denote by i_m the current across the membrane; it is an outward current, i.e. it is considered positive when directed toward the extracellular space. By *Kirchhoff's law* of conservation of electric charges, we have

$$J_i(x) = J_i(x + \Delta x) + \int_x^{x+\Delta x} i_m(s)ds,$$

$$J_e(x + \Delta x) = J_e(x) + \int_x^{x+\Delta x} i_m(s)ds,$$

as illustrated in the following diagram
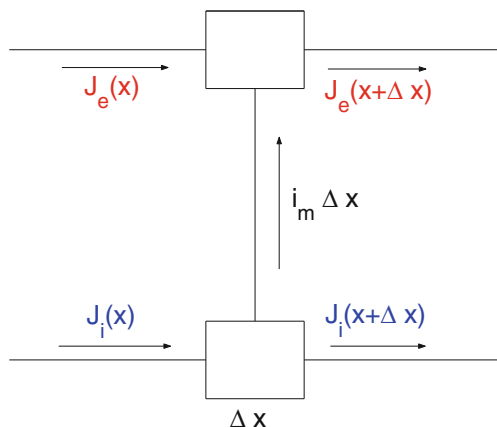
Assuming J_i, J_e differentiable, in the limit $\Delta x \to 0$ we obtain the following current conservation laws

$$\partial_x J_i = -i_m,$$
$$\partial_x J_e = i_m,$$

which imply

$$\partial_x(J_i + J_e) = 0, \quad \text{i.e.} \quad J_i + J_e = const.$$

We consider a fiber of length L, cut and healed at the two ends, leading to insulating boundary conditions for the intracellular medium

$$J_i = 0 \quad \text{at} \quad x = 0, \ x = L.$$

Moreover, we inject a cathodal extracellular current and eject an anodal extracellular current of strength $I_{app}(t)$ at the two ends of the fiber, i.e.

$$J_e = I_{app}(t) \quad \text{at} \quad x = 0, \ x = L,$$

thus we finally obtain

$$J_i(0) + J_e(0) = J_i(L) + J_e(L) = I_{app}(t), \quad \text{i.e.} \quad J_i(x,t) + J_e(x,t) = I_{app}(t).$$

The membrane current per unit area of the membrane surface is given by

$$I_m = C_m \partial_t v + I_{ion}.$$

This can be expressed as a current i_m per unit volume by multiplying by the ratio χ between the membrane surface area for a given length of fiber and the volume enclosed by this surface, i.e.

$$i_m = \chi\, I_m = \chi\,(C_m \partial_t v + I_{ion}).$$

Collecting together this last equation with Kirchhoff's and Ohm's laws, we have the system

$$\begin{cases} v = u_i - u_e \\ -\sigma_i \partial_x u_i - \sigma_e \partial_x u_e = I_{app}(t) \\ \partial_x(\sigma_i \partial_x u_i) = i_m \\ i_m = \chi(C_m \partial_t v + I_{ion}). \end{cases}$$

By setting $u_e = u_i - v$ in the second equation, we obtain

$$-\sigma_i \partial_x u_i - \sigma_e \partial_x u_i + \sigma_e \partial_x v = I_{app}(t) \;\Rightarrow\; \partial_x u_i = \frac{1}{\sigma_i + \sigma_e}(\sigma_e \partial_x v - I_{app}(t)),$$

and from the third and fourth equation, we finally obtain the *cable equation*

$$\partial_x(\sigma \partial_x v) - \partial_x\left(\frac{\sigma_i}{\sigma_i + \sigma_e}\right) I_{app}(t) = i_m = \chi(C_m \partial_t v + I_{ion}), \qquad (3.1)$$

where

$$\sigma = \frac{\sigma_i \sigma_e}{\sigma_i + \sigma_e}$$

is the conductivity of the bulk medium, corresponding to the conductivity of the intra- and extracellular media connected in series. Due to the presence of gap junctions between two subsequent myocytes, the conductivity $\sigma_i(x)$ is practically constant in the interior of the cell, with value given by the cytosolic conductivity, but in the small length of the gap junctions it undergoes a strong reduction due to the high resistivity of the gap junctions.

3.1.2 Homogenization

Let us consider an infinite fiber composed by cells connected by end-to-end junctions and embedded in an extracellular equipotential conductor medium, i.e. u_e is constant. Supposing that the cytoplasmic fluid and the junctions are ohmic conductors and applying the current conservation law, in the *stationary regime* the intracellular current density $J_i(x)$ satisfies

$$J_i(x) = -\sigma_i \frac{du_i}{dx}, \qquad \frac{d}{dx} J_i(x) = -i_m(x), \tag{3.2}$$

where i_m is the membrane current. Since the extracellular medium is assumed equipotential, the extracellular flux vanishes and, from $v = u_i - u_e$, we have $\frac{\partial v}{\partial x} = \frac{\partial u_i}{\partial x}$. Setting $\sigma = \sigma_i$ and combining the two equations in (3.2), we get

$$\frac{d}{dx}\left(\sigma \frac{dv}{dx}\right) = i_m. \tag{3.3}$$

The junctions are more resistive than the cytoplasmic fluid, therefore we assume that σ varies periodically with period equal to the distance ϵ between two subsequent junctions. Hence, $\sigma = \sigma(\frac{x}{\epsilon})$ is periodic with period ϵ, or, defining $\xi = \frac{x}{\epsilon}, \sigma = \sigma(\xi)$ is periodic with period 1.

In general, if the cells present some kinds of heterogeneities, we suppose that

$$\sigma = \sigma(x, \xi) \geq \sigma_0 > 0, \tag{3.4}$$

periodic in ξ with period 1.

Combining (3.3) and (3.4), we obtain the following equation, describing the profile of the electric potential along the one-dimensional fiber,

$$\frac{d}{dx}\left(\sigma\left(x, \frac{x}{\epsilon}\right) \frac{dv}{dx}(x)\right) = i_m(x). \tag{3.5}$$

We have two spatial scales:

- x, varying from 0 to L, the length of the fiber, is the macroscopic variable;
- $\xi = \frac{x}{\epsilon}$, varying in $[0, 1]$, describes the singular cellular element and is the adimensional microscopic variable.

Assume now that the solution of Eq. (3.5) has the following structure

$$v_\epsilon(x) = V\left(x, \frac{x}{\epsilon}\right),$$

i.e. it is a function depending on the macro- and microscopic scales, periodic with respect to $\xi = \frac{x}{\epsilon}$ with period 1.

If $\epsilon \ll 1$, we can let $\epsilon \to 0$ and expand v_ϵ in powers of ϵ

$$v_\epsilon(x) = V\left(x, \frac{x}{\epsilon}\right) = V_0\left(x, \frac{x}{\epsilon}\right) + \epsilon V_1\left(x, \frac{x}{\epsilon}\right) + \epsilon^2 V_2\left(x, \frac{x}{\epsilon}\right) + O(\epsilon^3),$$

with the coefficients $V_i(x, \frac{x}{\epsilon})$ periodic in $\xi = \frac{x}{\epsilon}$ of period 1.
   We suppose that the coefficients V_i have zero mean value on $\xi \in (0, 1)$ for $i \geq 1$,

$$\int_0^1 V_i(x, \xi)\, d\xi = 0 \text{ for } i \geq 1,$$

then it holds

$$v_\epsilon(x) = \int_0^1 V(x, \xi)\, d\xi = \int_0^1 V_0(x, \xi)\, d\xi.$$

The derivative of v_ϵ with respect to x is given by

$$\begin{aligned}
\frac{d}{dx} v_\epsilon(x) = \frac{d}{dx} V\left(x, \frac{x}{\epsilon}\right) &= \frac{\partial}{\partial x} V\left(x, \frac{x}{\epsilon}\right) + \frac{\partial}{\partial \xi} V\left(x, \frac{x}{\epsilon}\right) \frac{d\xi}{dx} \\
&= \frac{\partial}{\partial x} V\left(x, \frac{x}{\epsilon}\right) + \frac{\partial}{\partial \xi} V\left(x, \frac{x}{\epsilon}\right) \frac{1}{\epsilon},
\end{aligned}$$

thus

$$\frac{d\cdot}{dx} = \frac{\partial\cdot}{\partial x} + \frac{1}{\epsilon} \frac{\partial\cdot}{\partial \xi}$$

and

$$\begin{aligned}
\frac{d}{dx}\left(\sigma \frac{dv_\epsilon}{dx}\right) &= \frac{d}{dx}\left(\sigma\left(\frac{\partial V}{\partial x} + \frac{1}{\epsilon}\frac{\partial V}{\partial \xi}\right)\right) \\
&= \frac{\partial}{\partial x}\left(\sigma\left(\frac{\partial V}{\partial x} + \frac{1}{\epsilon}\frac{\partial V}{\partial \xi}\right)\right) + \frac{1}{\epsilon}\frac{\partial}{\partial \xi}\left(\sigma\left(\frac{\partial V}{\partial x} + \frac{1}{\epsilon}\frac{\partial V}{\partial \xi}\right)\right) \\
&= \frac{\partial}{\partial x}\left(\sigma \frac{\partial V}{\partial x}\right) + \frac{1}{\epsilon}\frac{\partial}{\partial x}\left(\sigma \frac{\partial V}{\partial \xi}\right) + \frac{1}{\epsilon}\frac{\partial}{\partial \xi}\left(\sigma \frac{\partial V}{\partial x}\right) + \frac{1}{\epsilon^2}\frac{\partial}{\partial \xi}\left(\sigma \frac{\partial V}{\partial \xi}\right).
\end{aligned}$$

Imposing that v_ϵ is solution of (3.5) and expanding in powers of ϵ, we get

$$\begin{aligned}
\frac{d}{dx}\left(\sigma \frac{dv_\epsilon}{dx}\right) = &\; \frac{1}{\epsilon^2}\left\{\frac{\partial}{\partial \xi}\left(\sigma \frac{\partial V_0}{\partial \xi}\right)\right\} \\
&+ \frac{1}{\epsilon}\left\{\frac{\partial}{\partial \xi}\left(\sigma \frac{\partial V_1}{\partial \xi}\right) + \frac{\partial}{\partial x}\left(\sigma \frac{\partial V_0}{\partial \xi}\right) + \frac{\partial}{\partial \xi}\left(\sigma \frac{\partial V_0}{\partial x}\right)\right\} \\
&+ \left\{\frac{\partial}{\partial \xi}\left(\sigma \frac{\partial V_2}{\partial \xi}\right) + \frac{\partial}{\partial x}\left(\sigma \frac{\partial V_1}{\partial \xi}\right) + \frac{\partial}{\partial \xi}\left(\sigma \frac{\partial V_1}{\partial x}\right) + \frac{\partial}{\partial x}\left(\sigma \frac{\partial V_0}{\partial x}\right)\right\} \\
&+ O(\epsilon^3) = i_m(x).
\end{aligned}$$

If we equal the terms of order $\frac{1}{\epsilon^2}$, $\frac{1}{\epsilon}$, 1, we get the following differential problems

$$(P0) \quad \begin{cases} \dfrac{\partial}{\partial \xi}\left(\sigma(x,\xi)\dfrac{\partial}{\partial \xi}V_0(x,\xi)\right) = 0 \ \ \text{for } \xi \in (0,1) \\ V_0(x,0) = V_0(x,1), \end{cases} \tag{3.6}$$

$$(P1) \quad \begin{cases} \dfrac{\partial}{\partial \xi}\left(\sigma(x,\xi)\dfrac{\partial}{\partial \xi}V_1(x,\xi)\right) = -\dfrac{\partial}{\partial x}\left(\sigma(x,\xi)\dfrac{\partial}{\partial \xi}V_0(x,\xi)\right) + \\ \hphantom{\dfrac{\partial}{\partial \xi}} -\dfrac{\partial}{\partial \xi}\left(\sigma(x,\xi)\dfrac{\partial}{\partial x}V_0(x,\xi)\right) \quad \text{for } \xi \in (0,1) \\ V_1(x,0) = V_1(x,1) \\ \displaystyle\int_0^1 V_1(x,\xi)\, d\xi = 0, \end{cases}$$

$$(3.7)$$

$$(P2) \quad \begin{cases} \dfrac{\partial}{\partial \xi}\left(\sigma(x,\xi)\dfrac{\partial}{\partial \xi}V_2(x,\xi)\right) = i_m(x,\xi) - \dfrac{\partial}{\partial x}\left(\sigma(x,\xi)\dfrac{\partial}{\partial x}V_0(x,\xi)\right) + \\ \hphantom{\dfrac{\partial}{\partial \xi}aaa} -\dfrac{\partial}{\partial x}\left(\sigma(x,\xi)\dfrac{\partial}{\partial \xi}V_1(x,\xi)\right) + \\ \hphantom{\dfrac{\partial}{\partial \xi}aaa} -\dfrac{\partial}{\partial \xi}\left(\sigma(x,\xi)\dfrac{\partial}{\partial x}V_1(x,\xi)\right) \quad \text{for } \xi \in (0,1) \\ V_2(x,0) = V_2(x,1) \\ \displaystyle\int_0^1 V_2(x,\xi)\, d\xi = 0. \end{cases}$$

All the previous problems have the following general structure

$$\begin{cases} \dfrac{\partial}{\partial \xi}\left(\sigma(x,\xi)\dfrac{\partial}{\partial \xi}v(x,\xi)\right) = S(x,\xi) \ \ \text{for } \xi \in (0,1) \\ v(x,0) = v(x,1). \end{cases} \tag{3.8}$$

If v is a solution of (3.8), then integrating both the sides of the equation we get

$$\int_0^1 \frac{\partial}{\partial \xi}\left(\sigma\frac{\partial}{\partial \xi}v\right)\, d\xi = \sigma(x,1)\frac{\partial}{\partial \xi}v(x,1) - \sigma(x,0)\frac{\partial}{\partial \xi}v(x,0) = \int_0^1 S(x,\xi)\, d\xi.$$

Since v is periodic, it must hold

$$\sigma(x,1)\frac{\partial}{\partial \xi}v(x,1) - \sigma(x,0)\frac{\partial}{\partial \xi}v(x,0) = 0,$$

from which it follows

$$\int_0^1 S(x,\xi)\, d\xi = 0. \tag{3.9}$$

It can be proved that (3.9) is also a sufficient condition for the solvability of (3.8), i.e.:

if $\int_0^1 S(x, \xi)\, d\xi = 0$, then $\exists!$ solution $v(x, \xi)$ periodic in ξ with period 1 of (3.8). v is unique up to a constant, that can be fixed by imposing zero mean value for $\xi \in (0, 1)$,

$$\int_0^1 v(x, \xi)\, d\xi = 0.$$

Problem (P0).   If we multiply both the sides of (3.6) times V_0 and integrate on $(0, 1)$, we get

$$0 = \int_0^1 \frac{\partial}{\partial \xi}\left(\sigma \frac{\partial V_0}{\partial \xi}\right) V_0\, d\xi = -\int_0^1 \sigma \left(\frac{\partial V_0}{\partial \xi}\right)^2 d\xi$$

and

$$0 = \int_0^1 \sigma \left(\frac{\partial V_0}{\partial \xi}\right)^2 d\xi \geq \sigma_0 \int_0^1 \left(\frac{\partial V_0}{\partial \xi}\right)^2 d\xi,$$

hence

$$\frac{\partial V_0}{\partial \xi} = 0.$$

This means that $V_0 = V_0(x)$ is constant with respect to ξ.

Problem (P1).   Since $\frac{\partial V_0}{\partial \xi} = 0$, Eq. (3.7) becomes

$$\frac{\partial}{\partial \xi}\left(\sigma \frac{\partial V_1}{\partial \xi}\right) = -\frac{\partial}{\partial \xi}\left(\sigma \frac{\partial V_0}{\partial x}\right) \Rightarrow \frac{\partial}{\partial \xi}\left(\sigma \frac{\partial V_1}{\partial \xi} + \sigma \frac{\partial V_0}{\partial x}\right) = 0,$$

implying that

$$\sigma \left(\frac{\partial V_1}{\partial \xi} + \frac{\partial V_0}{\partial x}\right) = \phi(x)$$

is constant with respect to ξ. Integrating the resulting equation

$$\frac{\partial V_1}{\partial \xi} + \frac{\partial V_0}{\partial x} = \frac{\phi(x)}{\sigma(x, \xi)} \tag{3.10}$$

over $(0, 1)$, we get

$$\frac{\partial}{\partial x} V_0(x) = \phi(x) \frac{1}{\bar{\sigma}(x)},$$

where we have introduced the harmonic average of σ with respect to ξ

$$\bar{\sigma}(x) = \frac{1}{\int_0^1 \frac{1}{\sigma(x,\xi)} \, d\xi}.$$

Equation (3.10) becomes

$$\frac{\partial}{\partial \xi} V_1(x,\xi) = \left(\frac{\bar{\sigma}(x)}{\sigma(x,\xi)} - 1 \right) \frac{\partial}{\partial x} V_0(x).$$

Setting

$$V_1(x,\xi) = w(x,\xi) \frac{\partial}{\partial x} V_0(x),$$

it follows

$$\frac{\partial V_1}{\partial \xi} = \frac{\partial w}{\partial \xi} \frac{\partial V_0}{\partial x} = \left(\frac{\bar{\sigma}}{\sigma} - 1 \right) \frac{\partial V_0}{\partial x},$$

and then

$$\frac{\partial w}{\partial \xi} = \frac{\bar{\sigma}}{\sigma} - 1.$$

Let us introduce now the cellular problem

$$\begin{cases} \frac{\partial}{\partial \xi} w(x,\xi) = \frac{\bar{\sigma}(x)}{\sigma(x,\xi)} - 1 \quad \text{for } \xi \in (0,1) \\ w(x,0) = w(x,1) \\ \int_0^1 w(x,\xi) \, d\xi = 0, \end{cases}$$

whose solution is given by

$$w(x,\xi) = w(x,0) + \int_0^\xi \left(\frac{\bar{\sigma}(x)}{\sigma(x,s)} - 1 \right) ds.$$

In order to have

$$\int_0^1 w(x,\xi) \, d\xi = 0,$$

$w(x, 0)$ must satisfy

$$w(x, 0) = -\int_0^1 \left(\bar{\sigma}(x) \int_0^\xi \frac{1}{\sigma(x, s)} \, ds - \xi \right) d\xi$$

$$= -\bar{\sigma}(x) \int_0^1 \int_0^\xi \frac{1}{\sigma(x, s)} \, ds \, d\xi + \frac{1}{2}.$$

Therefore

$$V_1(x, \xi) = w(x, \xi) \frac{\partial}{\partial x} V_0(x)$$

with

$$w(x, \xi) = \bar{\sigma}(x) \int_0^\xi \frac{1}{\sigma(x, s)} \, ds - \xi - \bar{\sigma}(x) \int_0^1 \int_0^\xi \frac{1}{\sigma(x, s)} \, ds \, d\xi + \frac{1}{2}.$$

Problem (P2).   To ensure the solvability, it must hold that

$$0 = \int_0^1 S(x, \xi) \, d\xi$$

$$= \int_0^1 \left(i_m(x) - \frac{\partial}{\partial x} \left(\sigma(x, \xi) \frac{\partial}{\partial x} V_0(x) + \sigma(x, \xi) \frac{\partial}{\partial \xi} V_1(x, \xi) \right) \right.$$

$$\left. - \frac{\partial}{\partial \xi} \left(\sigma(x, \xi) \frac{\partial}{\partial x} V_1(x, \xi) \right) \right) d\xi$$

$$= i_m(x) - \frac{\partial}{\partial x} \int_0^1 \sigma(x, \xi) \left(1 + \frac{\partial}{\partial \xi} w(x, \xi) \right) \frac{\partial}{\partial x} V_0(x) \, d\xi$$

$$- \int_0^1 \frac{\partial}{\partial \xi} \left(\sigma(x, \xi) \frac{\partial}{\partial x} V_1(x, \xi) \right) d\xi.$$

Since

$$\frac{\partial}{\partial \xi} w(x, \xi) = \frac{\bar{\sigma}(x)}{\sigma(x, \xi)} - 1$$

and the last term

$$\int_0^1 \frac{\partial}{\partial \xi} \left(\sigma(x, \xi) \frac{\partial}{\partial x} V_1(x, \xi) \right) d\xi = \sigma(x, 1) \frac{\partial}{\partial x} V_1(x, 1) - \sigma(x, 0) \frac{\partial}{\partial x} V_1(x, 0) = 0$$

because of the periodicity of σ and V_1, we finally get the equation

$$\frac{d}{dx} \left(\bar{\sigma}(x) \frac{d}{dx} V_0(x) \right) = i_m(x).$$

We recall that

$$\int_0^1 V(x,\xi)\,d\xi = \int_0^1 V_0(x,\xi)\,d\xi = \int_0^1 V_0(x)\,d\xi = V_0(x),$$

hence V_0 is denoted as the average potential.

In order to give a detailed approximation of the microscopic scale, one can consider the first order correction

$$v_\epsilon(x) = V\left(x,\frac{x}{\epsilon}\right) = V_0(x) + \epsilon w\left(x,\frac{x}{\epsilon}\right)\frac{d}{dx}V_0(x) + O(\epsilon^2).$$

3.1.3 Traveling Waves

A *traveling wave* is a solution of a PDE on an infinite domain that travels at constant velocity with fixed shape. Traveling waves are mainly divided into two types. The first is a *traveling front*, where the wave consists of a transition between two different levels: if v denotes the wave variable, then in front of the wave, v is steady at some low value, and behind the wave, v is steady at a higher value. The second type of traveling wave is a *traveling pulse*, where the wave begins and ends at the same value of v and resembles a moving bump. Thus, the main difference between traveling fronts and traveling pulses is that the former do not present recovery, while in the latter recovery plays an important dynamic role; see e.g. [63, 273].

3.1.3.1   Traveling Fronts

The cable equation (3.1) has been extensively studied in the special version known as the *bistable equation*

$$\partial_t v = \partial_{xx} v + f(v), \tag{3.11}$$

where

- $f(v)$ has three zeros at $v = 0, \alpha, 1$, with $0 < \alpha < 1$;
- $f'(0) < 0$ and $f'(1) < 0$.

The values $v = 0$ and $v = 1$ are stable steady solutions of the ODE $\partial_t v = f(v)$. For existence, uniqueness and stability of traveling wavefront solutions and long time behavior of the solution of (3.11), see [173–175].

An example of f often used in this context is the cubic polynomial

$$f(v) = av(v-1)(\alpha - v), \qquad 0 < \alpha < 1.$$

A traveling wave is a translation-invariant solution of (3.11), providing a transition between the two stable rest states (zeros of $f(v)$) and it travels with a constant speed c, i.e. a solution of the form

$$v(x, t) = V(x + ct) = V(\xi), \tag{3.12}$$

for a suitable value of c. When written as a function of the new traveling wave variable ξ, the wave appears stationary. Because we use $\xi = x + ct$, a solution with a positive c corresponds to a wave moving from right to left, while a solution with a negative c moves from left to right.

By imposing that $v(x, t)$ given in (3.12) satisfies the bistable equation (3.11), one obtains that any traveling wave solution solves the following second order ODE

$$V_{\xi\xi} - cV_\xi + f(V) = 0. \tag{3.13}$$

If $V(\xi)$ provides a transition between rest values, it must hold that

$$\lim_{\xi \to -\infty} V(\xi) = 0 \text{ and } \lim_{\xi \to +\infty} V(\xi) = 1, \quad \text{implying} \quad \lim_{\xi \to \pm\infty} f(V(\xi)) = 0.$$

From (3.13), it follows that a traveling wave solution of the bistable equation is a solution of the first order ODE system

$$
\begin{aligned}
V_\xi &= W \\
W_\xi &= cW - f(V),
\end{aligned}
$$

connecting the steady states $(V, W) = (0, 0)$ and $(V, W) = (1, 0)$ in the (V, W) phase plane. Such a trajectory, connecting two different steady states, is called a *heteroclinic trajectory* and it approaches $(0, 0)$ as $\xi \to -\infty$ and $(1, 0)$ as $\xi \to +\infty$. Beyond the steady states $(0, 0)$ and $(1, 0)$, which are saddle points, the other steady state is $(\alpha, 0)$, which is a node, if c is positive, or a spiral point, if c is negative. Because $(0, 0)$ and $(1, 0)$ are saddle points, in order to find a traveling wave solution, we determine whether a parameter c exists such that the trajectory leaving $(0, 0)$ at $\xi = -\infty$ reaches $(1, 0)$ at $\xi = +\infty$.

We first determine the sign of the velocity c. Supposing a monotone increasing $(V_\xi > 0)$ connecting trajectory exists, multiplying (3.13) by V_ξ and integrating from $\xi = -\infty$ to $\xi = +\infty$, one obtains the following relationship

$$c \int_{-\infty}^{+\infty} W(\xi)^2 d\xi = \int_0^1 f(u) du. \tag{3.14}$$

Thus, if the integral of $f(u)$ between $u = 0$ and $u = 1$ is positive, the traveling waves move from right to left and the state variable V moves from $V = 0$ to $V = 1$, while if the integral is negative viceversa.

Theorem 3.1. *Suppose $\int_0^1 f(u)du > 0$. Then there exists a unique velocity $c > 0$ with a corresponding traveling wave solution of the bistable equation.*

Proof. To verify uniqueness, from

$$\frac{dW}{dV} = c - \frac{f(V)}{W},$$

we observe that the slope $\frac{dW}{dV}$ of trajectories in the (V, W) phase plane is a monotone increasing function of the parameter c. Let $c = c_0$ be a velocity value for which a connecting trajectory exists. Suppose now that for a value $c_1 > c_0$, another connecting trajectory exists. The trajectory leaving the saddle point $(0, 0)$ for c_1 must lie above the connecting trajectory for c_0. For the same reason, the trajectory approaching the saddle point $(1, 0)$ for c_1 must lie below the connecting trajectory for c_0. A single trajectory cannot lie above and below another one, thus there cannot be a connecting trajectory for $c > c_0$. Analogously, there cannot be a connecting trajectory for $c < c_0$. Hence the connecting trajectory is unique.

To verify existence, we first suppose c large. Let K be the smallest positive number for which $\frac{f(u)}{u} \leq K$, $\forall u : 0 < u \leq 1$ and let σ be any fixed positive number. On the line $W = \sigma V$ the slope of trajectories satisfies

$$\frac{dW}{dV} = c - \frac{f(V)}{W} = c - \frac{f(V)}{\sigma V} \geq c - \frac{K}{\sigma}.$$

With c large enough, it is assured that $c - \frac{K}{\sigma} > \sigma$. Therefore once trajectories are above the line $W = \sigma V$, they stay above it. Because the slope of the unstable trajectory leaving the saddle point $(V, W) = (0, 0)$ is the positive root of $\lambda^2 - c\lambda + f'(0) = 0$, which is always larger than c, this trajectory starts above the curve $W = \sigma V$. Thus is stays always above $W = \sigma V$ and consequently passes above the saddle point $(V, W) = (1, 0)$.

With $c = 0$, by multiplying (3.13) by V_ξ and integrating, one obtains that the trajectory leaving $(V, W) = (0, 0)$ satisfies

$$\frac{W^2}{2} + \int_0^V f(u)du = 0,$$

and if it reaches $V = 1$ for some value of W, then

$$\frac{W^2}{2} + \int_0^1 f(u)du = 0,$$

which can occur only if $\int_0^1 f(u)du \leq 0$. Since this is in contradiction with the hypothesis that $\int_0^1 f(u)du > 0$, it follows that the trajectory cannot reach $V = 1$ and neither it can remain in the first quadrant, because $W > 0$ implies that V increases.

As a consequence, this trajectory must intersect $W = 0$ for some $V < 1$, thus it cannot be the connecting trajectory.

Summarizing, we have found two trajectories, one with c large, which misses the saddle point $(V, W) = (1, 0)$ staying above it, and one with $c = 0$, which intersects the $W = 0$ axis for some $V < 1$. Because trajectories depend continuously on the parameters of the problem, there is a family of trajectories depending continuously on c between these two special trajectories, and therefore there must be at least one trajectory reaching $(V, W) = (1, 0)$.

Example. Suppose $f(v)$ is the cubic polynomial

$$f(v) = v(v - \alpha)(1 - v).$$

Our goal is to find a heteroclinic connection between 0 and 1, so we guess that

$$W = BV(1 - V). \tag{3.15}$$

By substituting (3.15) into (3.13), it follows that it must hold

$$(-2B^2 + 1)V + (B^2 - cB - \alpha) = 0,$$

which is identically zero only if we choose

$$B = \frac{1}{\sqrt{2}} \qquad c = \frac{1}{\sqrt{2}}(1 - 2\alpha),$$

showing that the velocity is a decreasing function of α and the direction of propagation changes at $\alpha = 1/2$, according to the change of sign of $\int_0^1 f(u)du$. From the solution of (3.15), we obtain the profile of the traveling wave

$$V(\xi) = \frac{1}{2}\left[1 + \tanh\left(\frac{x}{2\sqrt{2}}\right)\right].$$

3.1.3.2   Traveling Pulses

A *traveling pulse* is a traveling wave solution that starts and ends at the same steady state of the governing equations. In the previous section, we have seen that a traveling front solution of the bistable equation corresponds to a *heteroclinic trajectory* in the (V, W) phase plane, i.e. a trajectory that connects two different steady states of the system. Analogously, a traveling pulse corresponds to a trajectory that starts and ends at the same steady state in the (V, W) phase plane. Such trajectories are called *homoclinic orbits*.

In order to study wave propagation in excitable media, we first consider the following FitzHugh-Nagumo system

$$\epsilon \partial_t v = \epsilon^2 \partial_{xx} v + f(v, w)$$
$$\partial_t w = g(v, w), \tag{3.16}$$

where ϵ is a small positive number and, without any loss of generality, the space variable x has been scaled so that the diffusion coefficient is ϵ^2, see e.g. [173–175, 532]. This type of reaction-diffusion singular perturbation problem develops in a short time a sharp propagating interface, i.e. a steep wavefront. In fact, in [85, 86], it was shown that, after a time period of order $O(\epsilon \log \epsilon)$, a sharp transition layer of thickness of order $O(\epsilon)$ appears. Let us recall that the variable v represents the transmembrane potential, while w represents a slow gating variable.

We now proceed further in understanding the structure of traveling wave solutions of (3.16), by performing a singular perturbation analysis, see e.g. [79]. Starting from smooth initial data $(v_0(x), w_0(x))$, the diffusion term $\epsilon \partial_{xx} v$ and the variation of w from its initial data can be neglected for a short time. In fact, setting $\tau = \frac{t}{\epsilon}$, $\hat{v}(x, \tau) = v(x, \epsilon t)$ and $\hat{w}(x, \tau) = w(x, \epsilon t)$, then

$$\partial_t \hat{v} = \epsilon^2 \partial_{xx} \hat{v} + f(\hat{v}, \hat{w})$$
$$\partial_t \hat{w} = \epsilon g(\hat{v}, \hat{w}). \tag{3.17}$$

An approximation of order ϵ is obtained by setting ϵ to zero in (3.17), i.e.

$$\partial_t \hat{v} = f(\hat{v}, \hat{w})$$
$$\partial_t \hat{w} = 0.$$

Thus $\hat{w}(x) = w_0(x)$ and, using the notations introduced in Sect. 2.9.8 (see also Fig. 2.6), in a short time ($t = O(\epsilon)$) $\hat{v} \to h_\pm(w_0)$, if $v_0(x) \gtrless h_0(w_0)$. The region of space where $v = h_+(w)$ is called *excited region*, while the region where $v = h_-(w)$ is called *recovered region*. In these two regions, it holds

$$f(\hat{v}, \hat{w}) = 0$$
$$\partial_t \hat{w} = g(\hat{v}, \hat{w}), \tag{3.18}$$

thus

$$\hat{v} = h_\pm(\hat{w})$$
$$\partial_t \hat{w} = G_\pm(\hat{w}) = g(h_\pm(\hat{w}), \hat{w}).$$

However, there are regions of space, called *interfaces*, where diffusion is large and (3.18) cannot be applied. To understand what happens when diffusion is large, we rescale space and time by setting $\tau = t$ and $\xi = \frac{x - y(t)}{\epsilon}$, where $y(t)$ denotes the position of the wavefront, i.e. the points

$$y(t) : v(y(t), t) = h_0(w_0(x)).$$

The original system of equations (3.16) becomes

$$\hat{v}_{\xi\xi} + y'(\tau)\hat{v}_\xi + f(\hat{v}, \hat{w}) = \epsilon\partial_\tau\hat{v}$$
$$y'(\tau)\hat{w}_\xi = \epsilon(g(\hat{v}, \hat{w}) - \partial_\tau\hat{w}),$$

and, after setting $\epsilon = 0$, it reduces to

$$\hat{v}_{\xi\xi} + y'(\tau)\hat{v}_\xi + f(\hat{v}, \hat{w}) = 0$$
$$y'(\tau)\hat{w}_\xi = 0. \tag{3.19}$$

It follows from (3.19) that $\hat{w}$ is independent of ξ, but not necessarily of τ, i.e. $\hat{w}(\tau) = \hat{w}(y(\tau), \tau)$. Because (3.19) describes the transition layer between regions where (3.18) holds, we require the *matching condition*

$$\lim_{\xi \to \pm\infty} f(\hat{v}(\xi, \tau), w(\tau)) = 0,$$

i.e.

$$\hat{v}(\pm\infty, \tau) = h_\mp(\hat{w}(\tau)).$$

Since $y(\tau)$ represents the position of the wavefront, $y'(\tau)$ is the wave velocity.

The first equation in (3.19) is a *bistable equation*, in the form (3.13), thus, for fixed $\hat{w}$, there exists $c = c(\hat{w})$ for which the equation

$$\hat{v}_{\xi\xi} + c(\hat{w})\hat{v}_\xi + f(\hat{v}, \hat{w}) = 0 \tag{3.20}$$

has a *heteroclinic orbit* connecting two stable roots of $f(\hat{v}, \hat{w}) = 0$. This means that $c(\hat{w})$ is the unique value for which (3.20) has a solution with $\hat{v} \to h_+(\hat{w})$ as $\xi \to -\infty$ and $\hat{v} \to h_-(\hat{w})$ as $\xi \to +\infty$.

Summarizing, in most of space, (3.18) holds. At any transition between the two types of (3.18), a sharp transition in v occurs, with a wavefront traveling at the speed $y'(t) = c(w)$ if $v = h_+(w)$ on the left and $v = h_-(w)$ on the right, or $y'(t) = -c(w)$ if $v = h_-(w)$ on the left and $v = h_+(w)$ on the right. We now suppose that far to the right the medium is at rest, i.e. $\exists\, w_+ : G_-(w_+) = 0$, and that a wavefront of excitation moves from left to right with velocity $y'(t) = c(w_+) > 0$. Following the same procedure used to derive (3.14), one obtains

$$c(w) = \frac{\int_{h_-(w)}^{h_+(w)} f(v, w)dv}{\int_{-\infty}^{+\infty} v_\xi^2 d\xi},$$

and thus $c(w_+) > 0$ if and only if

$$\int_{h_-(w)}^{h_+(w)} f(v, w)dv > 0. \tag{3.21}$$

If (3.21) fails to hold, then the medium is not sufficiently excitable to sustain a traveling pulse.

3.1.4   Conduction Velocity Restitution Curve

Conduction block is a key arrhythmogenic mechanism. It can result from a reduction of inward membrane currents, a reduction of gap junctional coupling and from tissue inhomogeneities. Conduction velocity (CV) of the propagating electric impulse in the cardiac tissue depends, as the action potential duration (see Sect. 2.9.6), on one or several previous diastolic or interbeat intervals. This dependence, called *restitution*, is an important determinant of the stability of conduction and is involved in the generation of arrhythmias. The CV restitution function describes this dependence of the conduction velocity on the diastolic interval (DI). Figure 3.1
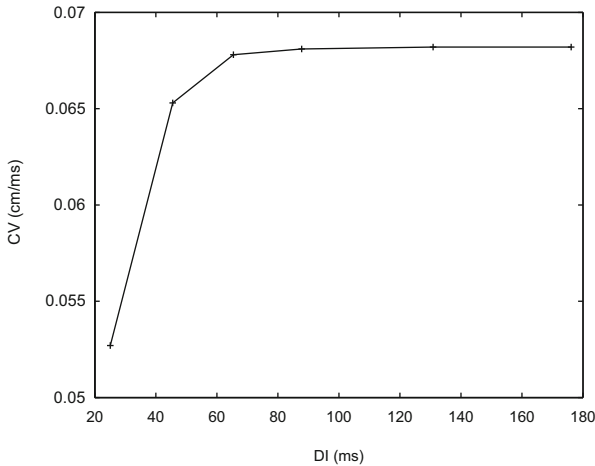
Fig. 3.1 Conduction velocity (CV) restitution curve computed with the cable equation coupled with the LRd model

reports the CV restitution curve calculated using the cable equation coupled with the LRd model, i.e. the following system of PDEs

$$
\begin{cases}
c_m \dfrac{\partial v}{\partial t} - \sigma \dfrac{\partial^2 v}{\partial x^2} + i_{ion}(v, w, c) = i_{app}, \\[2mm]
\dfrac{dw}{dt} - R(v, w) = 0, \\[2mm]
\dfrac{dc}{dt} - S(v, w, c) = 0,
\end{cases}
$$

with $c_m = \chi C_m$, $i_{ion} = \chi I_{ion}$, $\sigma = 1.2 \cdot 10^{-3}\,\Omega^{-1}\,\mathrm{cm}^{-1}$ and the functions I_{ion}, S, R given by the LRd model.

3.2   Models of Cardiac Tissue

The cardiac tissue is composed of a collection of elongated cardiac cells having roughly a cylindrical form with a diameter $d_c \approx 10\,\mu\mathrm{m}$ and length $l_c \approx 100\,\mu\mathrm{m}$. The cells are coupled together mainly in end-to-end and also in side–to–side apposition by gap junctions, [237, 448]. These specialized membrane regions of densely packed channels provide direct intercellular communication between the cytoplasmatic compartments of two adjacent cells; they are large at the longitudinal cell ends and small along the lateral borders. The end-to-end contacts form the long fiber structure of the cardiac muscle whereas the presence of lateral junctions establishes a connection between the elongated fibers.

At a cellular level the structure of the cardiac tissue can be viewed as composed by two ohmic conducting media: the intracellular space Ω_i (inside the cells) and the extracellular space Ω_e (outside) separated by the active membrane Γ_m. Due to the presence of gap junctions connecting the cardiac cells end-to-end and side-to-side, Ω_i and Ω_e are regarded as two simply-connected open sets of $\mathbb{R}^3$. The effects of the microstructure on the current flow are also included in the conductivity tensors $\Sigma_i(\mathbf{x})$, $\Sigma_e(\mathbf{x})$ as inhomogeneous functions of space that reflect the local variations of conductances because of the presence of structural intra and extracellular inhomogeneities of resistance associated with e.g. gap junctions, connective tissue, collagen and blood vessels. Let u_i, u_e be the intra and extracellular potentials and $\mathbf{J}_{i,e} = -\Sigma_{i,e}\nabla u_{i,e}$ their current densities. Let $\mathbf{n}_i$, $\mathbf{n}_e$ denote the unit exterior normals to the boundary of Ω_i and Ω_e respectively, satisfying $\mathbf{n}_i = -\mathbf{n}_e$ on Γ_m. Under the quasi-static assumption (see [394] and [215, Ch. 5.3] for the validity of this condition for biological fields), due to the current conservation law, the normal current flux through the membrane is continuous, thus $\mathbf{J_i} \cdot \mathbf{n}_i = \mathbf{J_e} \cdot \mathbf{n}_i$, i.e in terms of potentials

$$
\mathbf{n}_i^T\, \Sigma_i\, \nabla u_i + \mathbf{n}_e^T\, \Sigma_e\, \nabla u_e = 0, \quad \text{on } \Gamma_m.
$$

On the other hand, since the only active source elements lie on the membrane Γ_m, each flux equals the membrane current per unit area I_m, which consists of a capacitive and an ionic term (see [250, 317]):

$$- \mathbf{n}_i^T \, \Sigma_i \, \nabla u_i = \mathbf{n}_e^T \, \Sigma_e \, \nabla u_e = I_m = C_m \, \frac{\partial v}{\partial t} + I_{ion}. \tag{3.22}$$

Here C_m is the surface capacitance of the membrane per unit area and $v := u_i|_{\Gamma_m} - u_e|_{\Gamma_m}$ is the transmembrane potential evidencing that Γ_m is a discontinuity surface for the potential (in the following, we will simply write $v = u_i - u_e$).

Denoting by I_i^s, I_e^s the stimulation currents applied to the intra and extracellular space, we have

$$- \operatorname{div}(\Sigma_i \nabla u_i) = I_i^s, \quad \text{in } \Omega_i, \qquad - \operatorname{div}(\Sigma_e \nabla u_e) = I_e^s, \quad \text{in } \Omega_e. \tag{3.23}$$

Assuming $\Omega_H := \Omega_i \cup \Omega_e \cup \Gamma_m$ embedded into an insulating medium, then homogeneous Neumann boundary conditions for u_i, u_e on the remaining part of the boundaries $\Gamma_{i,e} = \partial\Omega_{i,e} \setminus \Gamma_m$ must be assigned

$$\mathbf{n}_{i,e}^T \Sigma_{i,e} \nabla u_{i,e} = 0.$$

Finally, the system (3.22), (3.23) must be supplemented by the initial conditions

$$v(\cdot, 0) = v_0, \quad w(\cdot, 0) = w_0, \quad \text{on } \Gamma_m.$$

For the electric potentials u_i, u_e we can consider two characteristic length scales: a *micro* scale related to typical cell dimensions $\{d_c, l_c\}$ and a *macro* scale determined by a suitable length constant of the tissue. At the latter scale length, i.e. at a macroscopic level, in spite of the discrete cellular structure, the cardiac tissue can be represented by a continuous model. To identify this macroscopic scale, following [348], we consider a suitable non-dimensional form of the cellular mathematical model.

The cellular conductivity matrices $\Sigma_i(\mathbf{x})$ and $\Sigma_e(\mathbf{x})$ are symmetric positive definite matrices; setting $\bar{\mu} = \bar{\mu}_i + \bar{\mu}_e$, with $\bar{\mu}_i$, $\bar{\mu}_e$ the average eigenvalues on a cell element, we consider the dimensionless conductivity matrices

$$\sigma_{i,e} = \Sigma_{i,e}/\bar{\mu}.$$

Let R_m be an estimate of the passive membrane resistance near the equilibrium point v_r, i.e. the resting transmembrane potential. Multiplying by $R_m/\bar{\mu}$ both sides of Eq. (3.22), we obtain

$$- \sigma_i \, R_m \, \mathbf{n}_i^T \nabla u_i = \frac{C_m R_m}{\bar{\mu}} \, \frac{\partial v}{\partial t} + \frac{R_m}{\bar{\mu}} I_{ion}. \tag{3.24}$$

We introduce the membrane time constant $\tau_m = R_m C_m$, the length scale unit $\Lambda = \sqrt{l_c \bar{\mu} R_m}$ and we consider the following scaling of the space and time variables

$$\hat{\mathbf{x}} = \mathbf{x}/\Lambda, \quad \hat{t} = t/\tau_m.$$

Disregarding the presence of applied current terms, rescaling Eqs. (3.23) and (3.24) in the intra and extracellular media, we obtain:

$$\text{div}_{\hat{\mathbf{x}}}(\sigma_i \nabla_{\hat{\mathbf{x}}} u_i) = 0 \quad \text{in } \Omega_i \qquad \text{div}_{\hat{\mathbf{x}}}(\sigma_e \nabla_{\hat{\mathbf{x}}} u_e) = 0 \quad \text{in } \Omega_e,$$

$$-\mathbf{n}_i^T \sigma_i \nabla_{\hat{\mathbf{x}}} u_i = \mathbf{n}_e^T \sigma_e \nabla_{\hat{\mathbf{x}}} u_e = \varepsilon \frac{\partial v}{\partial \hat{t}} + I_{ion}(v, w, c) \qquad \text{on } \Gamma_m,$$

where the dimensionless parameter is the ratio $\varepsilon = l_c/\Lambda$ between the *micro* and the *macro* length constants.

The two-scale method of homogenization can be applied to the previous current conservation equations. The microscopic space variable measured in unit cell is defined by $\boldsymbol{\xi} := \mathbf{x}/l_c$; then with respect to the dimensionless macroscopic coordinates, the micro and macro scales are related to each other by the scaling parameter ε

$$\boldsymbol{\xi} := \hat{\mathbf{x}}/\varepsilon$$

For convenience, we will omit in the following the superscripts ^ of the dimensionless variables.

Following the standard approach of homogenization theory, we are assuming that the cells are distributed according to an ideal periodic organization similar to a regular lattice of interconnected cylinders. Due to the longitudinal and transverse intercellular interconnections, in the modeled periodic cellular aggregate the intra and extracellular media are connected regions. If $\{\boldsymbol{e}_1, \boldsymbol{e}_2, \boldsymbol{e}_3\}$ is an orthogonal basis of $\mathbb{R}^3$, we denote by

$$E_i, \quad E_e := \mathbb{R}^3 \setminus \overline{E}_i, \quad \text{with common boundary } \Gamma_m := \partial E_i \cap \partial E_e,$$

two reference open, connected and periodic subsets of $\mathbb{R}^3$ with Lipschitz boundary, i.e. satisfying

$$E_{i,e} + \boldsymbol{e}_k = E_{i,e}, \quad k = 1, 2, 3.$$

The elementary periodicity region

$$Y := \left\{ \sum_{k=1}^{3} \alpha_k \boldsymbol{e}_k : 0 \leq \alpha_k < 1, \quad k = 1, 2, 3 \right\}$$

is composed of the intra and extracellular volumes $Y_{i,e} = Y \cap E_{i,e}$ and represents a reference volume box containing a single cell Y_i with cell membrane surface $S_m = \Gamma_m \cap Y_i$.

The main geometrical assumption is that the physical intra or extracellular regions are the ε-dilation of the reference lattices $E_{i,e}$, defined as

$$\varepsilon E_{i,e} = \{\varepsilon \xi : \xi \in E_{i,e}\}, \quad \text{with} \quad \varepsilon \Gamma_m := \{\varepsilon \xi : \xi \in \Gamma_m\}.$$

Therefore, the decomposition of the physical region Ω_H, occupied by the cardiac tissue, into the intra and extracellular domains $\Omega_{i,e}^{\varepsilon}$ (see e.g. Fig. 3.2) can be obtained simply by intersecting Ω_H with $\varepsilon E_{i,e}$, i.e.

$$\Omega_i^{\varepsilon} = \Omega_H \cap \varepsilon E_i, \quad \Omega_e^{\varepsilon} = \Omega_H \cap \varepsilon E_e, \quad \Gamma_m^{\varepsilon} = \partial \Omega_i^{\varepsilon} \cap \partial \Omega_e^{\varepsilon} = \Omega_H \cap \varepsilon \Gamma_m.$$

The common boundary Γ_m^{ε} models the cellular membrane.
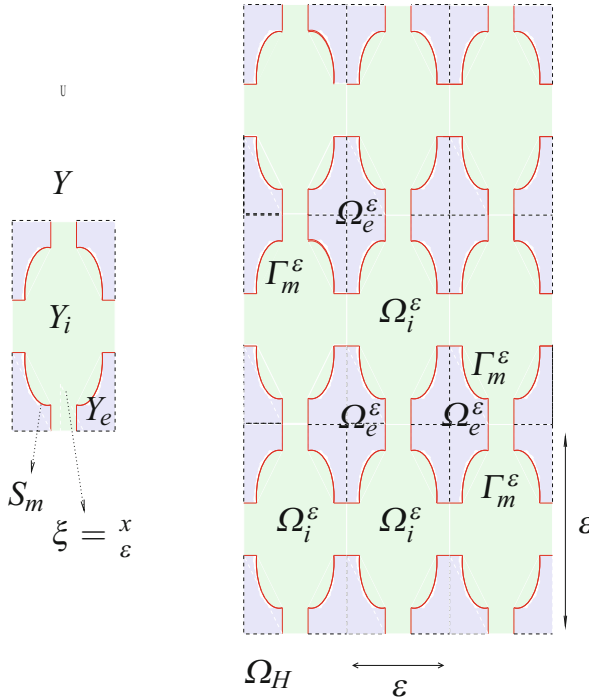
Fig. 3.2 *Right*: The ideal periodic geometry in a bidimensional section of the simplified 3–D periodic network of interconnected cells. *Left*: Unit cell in the microscopic variable $\xi = x/\varepsilon$

Since the cardiac tissue exhibits a number of significant inhomogeneities, such as those related to cell-to-cell communications, the conductivity tensors are considered dependent on both the slow and fast variables, i.e. $\sigma_{i,e}(x, \frac{x}{\varepsilon})$. The dependence of σ_i on $\frac{x}{\varepsilon}$ models the inclusion of gap-junction effects. We then define the rescaled symmetric conductivity matrices

$$\sigma_{i,e}^{\varepsilon}(x) = \sigma_{i,e}(x, \frac{x}{\varepsilon}),$$

where $\sigma_{i,e}(x, \xi) : \Omega_H \times E_{i,e} \to \mathbb{M}^{3 \times 3}$ are continuous functions satisfying the usual uniform ellipticity and periodicity conditions

$$\left.\begin{array}{c} \sigma|y|^2 \leq \sigma_{i,e}(x, \xi) y \cdot y \leq \sigma^{-1}|y|^2 \\ \sigma_{i,e}(x, \xi + e_k) = \sigma_{i,e}(x, \xi) \end{array}\right\} \quad \forall \, (x, \xi) \in \Omega_H \times E_{i,e}, \ y \in \mathbb{R}^3,$$

for a given constant $\sigma > 0$.

3.2.1   The Dimensionless Cellular Model $\mathbf{P}^{\varepsilon}$

Summarizing, we formulate the full reaction-diffusion system associated with the cellular model $\mathbf{P}^{\varepsilon}$ as follows:

Let $\Omega_H := \Omega_i^{\varepsilon} \cup \Omega_e^{\varepsilon} \cup \Gamma_m^{\varepsilon}$ be the cardiac tissue volume,

$\Omega_i^{\varepsilon} :=$ the intracellular space with dimensionless conductivity $:= \sigma_i^{\varepsilon}$,

$\Omega_e^{\varepsilon} :=$ the extracellular space with intracellular conductivity $:= \sigma_e^{\varepsilon}$,

$\mathbf{n}_i, \mathbf{n}_e :=$ the exterior unit normals to $\partial \Omega_i^{\varepsilon}, \partial \Omega_e^{\varepsilon}$,

$\Gamma_m^{\varepsilon} :=$ the surface cellular membrane,

$\boldsymbol{n} = \mathbf{n}_i = -\mathbf{n}_e$ the normal to Γ_m^{ε} pointing toward Ω_e^{ε}.

Then the vector $(u_i^{\varepsilon}, u_e^{\varepsilon}, w^{\varepsilon}, c^{\varepsilon})$, with $v^{\varepsilon} = u_i^{\varepsilon} - u_e^{\varepsilon}$ satisfies the problem:

$$\begin{cases} -\operatorname{div} \sigma_i^{\varepsilon}(x) \nabla u_i^{\varepsilon} = 0 & \text{in } \Omega_i^{\varepsilon} \\ -\operatorname{div} \sigma_e^{\varepsilon}(x) \nabla u_e^{\varepsilon} = 0 & \text{in } \Omega_e^{\varepsilon} \end{cases} \tag{3.25}$$

$$I_m^{\varepsilon} = \begin{cases} -\sigma_i^{\varepsilon}(x) \, \boldsymbol{n}^T \nabla u_i^{\varepsilon} = \varepsilon \, [\, \dfrac{\partial v^{\varepsilon}}{\partial t} \, + \, I_{ion}(v^{\varepsilon}, w^{\varepsilon}, c^{\varepsilon}) \,] \\[4mm] -\sigma_e^{\varepsilon}(x) \, \boldsymbol{n}^T \nabla u_e^{\varepsilon} = \varepsilon \, [\, \dfrac{\partial v^{\varepsilon}}{\partial t} \, + \, I_{ion}(v^{\varepsilon}, w^{\varepsilon}, c^{\varepsilon}) \,] \end{cases} \tag{3.26}$$

$$\frac{\partial w^{\varepsilon}}{\partial t} - R(v^{\varepsilon}, w^{\varepsilon}) = 0 \quad \text{on } \Gamma_m^{\varepsilon}, \qquad \frac{\partial c^{\varepsilon}}{\partial t} - S(v^{\varepsilon}, w^{\varepsilon}, c^{\varepsilon}) = 0,$$

supplemented by the following boundary conditions of Neumann type (assuming for instance that the cellular aggregate is embedded in an insulated medium)

$$\mathbf{n}^T \nabla u_i^\varepsilon = 0 \quad \text{on} \quad \partial \Omega_i^\varepsilon / \Gamma_m^\varepsilon \quad \text{and} \quad \mathbf{n}^T \nabla u_e^\varepsilon = 0 \quad \text{on} \quad \partial \Omega_e^\varepsilon / \Gamma_m^\varepsilon,$$

and the following degenerate initial conditions on $v^\varepsilon, w^\varepsilon, c^\varepsilon$

$$v^\varepsilon(\mathbf{x}, 0) = v_0^\varepsilon(\mathbf{x}), \quad w^\varepsilon(\mathbf{x}, 0) = w_0^\varepsilon(\mathbf{x}), \quad c^\varepsilon(\mathbf{x}, 0) = c_0^\varepsilon(\mathbf{x}) \quad \text{su } \Gamma_m^\varepsilon.$$

The variables $v^\varepsilon, w^\varepsilon, c^\varepsilon$ and I_m^ε are defined only on the surface of the cellular membrane Γ_m^ε.

3.2.2   Formal Two-Scale Homogenization

We briefly indicate how to use the two–scale method (see [23, 44, 260, 362, 454]) and formal asymptotic expansions to convert the microscopic model of the periodic cellular aggregate into an averaged continuum representation of the cardiac tissue, neglecting the presence of stimulation currents. We seek a solution $(u_i^\varepsilon, u_e^\varepsilon, w^\varepsilon, c^\varepsilon)$ where each component has an asymptotic form in powers of ε of the following type:

$$u = u_0(\mathbf{x}, \boldsymbol{\xi}, t) + \varepsilon u_1(\mathbf{x}, \boldsymbol{\xi}, t) + \varepsilon^2 u_2(\mathbf{x}, \boldsymbol{\xi}, t) + \cdots$$

with coefficients u_k Y–periodic functions of $\boldsymbol{\xi}$. Considering the full derivative operators

$$\nabla u = \varepsilon^{-1} \nabla_\xi u + \nabla_x u,$$

$$\operatorname{div} \sigma \nabla u = \varepsilon^{-2} \operatorname{div}_\xi \sigma \nabla_\xi u + \varepsilon^{-1} \operatorname{div}_\xi \sigma \nabla_x u + \varepsilon^{-1} \operatorname{div}_x \sigma \nabla_\xi u + \operatorname{div}_x \sigma \nabla_x u,$$

substituting the asymptotic forms into the first equations of (3.25, 3.26) and equating the coefficients of the powers -1, 0, 1, of ε to zero, we obtain the following equations for the functions $u_k(\mathbf{x}, \boldsymbol{\xi}, t)$, $k = 0, 1, 2$ associated with $u = u_i^\varepsilon$:

$$\begin{cases} \text{Find } u_k \ Y\text{–periodic in } \xi \text{ such that:} \\ -\operatorname{div}_\xi \sigma_i(\mathbf{x}, \boldsymbol{\xi}) \nabla_\xi u_k = f_k(\mathbf{x}, \boldsymbol{\xi}) - \operatorname{div}_\xi \sigma_i \mathbf{F}_k(\mathbf{x}, \boldsymbol{\xi}) & \text{in} \quad E_i \\ \mathbf{n}_\xi^T \sigma_i(\mathbf{x}, \boldsymbol{\xi}) \nabla_\xi u_k = g_k(\mathbf{x}, \boldsymbol{\xi}) + \mathbf{n}_\xi^T \sigma_i \mathbf{F}_k(\mathbf{x}, \boldsymbol{\xi}) & \text{on} \quad \Gamma_m, \end{cases} \quad (3.27)$$

with

$$\begin{cases} f_0 = 0, \ \mathbf{F}_0 = \mathbf{0} & \text{in} \quad E_i \\ g_0 = 0 & \text{on} \quad \Gamma_m, \end{cases} \quad (3.28)$$

$$\begin{cases} f_1 = 2\text{div}_x \sigma_i \nabla_\xi u_0, \quad \mathbf{F}_1 = \mathbf{0} \quad in \quad E_i \\ g_1 = \mathbf{n}_\xi^T \sigma_i \nabla_x u_0 \qquad\qquad on \quad \Gamma_m, \end{cases} \tag{3.29}$$

$$\begin{cases} f_2 = \text{div}_x \sigma_i \nabla_\xi u_1 + \text{div}_x \sigma_i \nabla_x u_0, \quad \mathbf{F}_2 = -\sigma_i \nabla_x u_1, \quad in \quad E_i \\ g_2 = -\left(\dfrac{\partial v_0}{\partial t} + I_{ion}(v_0, w_0, c_0) \right), \quad on \quad \Gamma_m \\ v_0 = u_0^i - u_0^e, \qquad \partial_t w_0 - R(v_0, w_0) = 0, \qquad \partial_t c_0 - S(v_0, w_0, c_0) = 0. \end{cases} \tag{3.30}$$

In problem (3.27), the variable $\mathbf{x}$ appears as a parameter. Let $f_k(\mathbf{x}, \boldsymbol{\xi})$, $\mathbf{F}_k(\mathbf{x}, \boldsymbol{\xi})$, $g_k(\mathbf{x}, \boldsymbol{\xi})$ be Y–periodic functions in ξ. Then the problems for $k = 0, 1, 2$ admit a unique solution u_k, apart from an additive constant (consequence of an easy extension of the result in [23] Th. 2 or [362] Th. 6.1) if and only if

$$\int_{Y_i} f_k d\xi + \int_{S_m} g_k ds_\xi = 0, \quad k = 0, 1, 2. \tag{3.31}$$

From the first cellular problem (3.28) for $k = 0$, it follows that the Y–periodic solution u_0 is independent of $\boldsymbol{\xi}$ and $u_0(\mathbf{x})$, depending only on the macroscopic variable $\mathbf{x}$, represents a potential average over Y_i if the subsequent terms $u_k(\mathbf{x}, \boldsymbol{\xi}, t)$ are determined with zero mean value on Y_i. Since $f_1 = 0$ and $\int_{S_m} \mathbf{n}_\xi^T \sigma_i \nabla_x u_0 \, ds_\xi = 0$ the solvability of problem (3.28) related to the data (3.29) is assured and it is easy to check that the solution with zero mean on Y_i, i.e. $\int_{Y_i} u_1 d\xi = 0$, can be represented as

$$u_1(\mathbf{x}, \boldsymbol{\xi}, t) = -\mathbf{w}(\mathbf{x}, \boldsymbol{\xi})^T \nabla_x u_0, \tag{3.32}$$

where $\mathbf{w}(\mathbf{x}, \boldsymbol{\xi}) = (w_1, w_2, w_3)^T$ is the unique zero mean value solution on Y_i satisfying

$$\begin{cases} \text{div}_\xi \sigma_i(\mathbf{x}, \boldsymbol{\xi}) \nabla_\xi w_k = 0, \quad in \ Y_i, \\ \mathbf{n}_\xi^T \sigma_i(\mathbf{x}, \boldsymbol{\xi}) \nabla_\xi w_k = n_{\xi_k} \qquad on \ S_m, \quad k = 1, 2, 3. \end{cases} \tag{3.33}$$

Then problem (3.27) related to the data (3.30) becomes

$$\begin{cases} -\text{div}_\xi \sigma_i \nabla_\xi u_2 = -\text{div}_\xi \sigma_i \nabla_x (\mathbf{w}^T \nabla_x u_0) \\ \qquad\qquad\qquad + \text{div}_x \sigma_i \nabla_x u_0 - \text{div}_x \sigma_i \nabla_\xi (\mathbf{w}^T \nabla_x u_0) \quad in \quad Y_i \\ n_\xi^T \sigma_i \nabla_\xi u_2 = -\left(\dfrac{\partial v_0}{\partial t} + I_{ion}(v_0, w_0) \right) + n_\xi^T \sigma_i (\mathbf{w}^T \nabla_x u_0) \qquad on \quad S_m. \end{cases}$$

In order to assure its solvability, the following compatibility relation must be satisfied

$$-\int_{Y_i} \mathrm{div}_x \, \sigma_i \, \nabla_\xi (\mathbf{w}^T \nabla_x u_0) \, d\xi + \int_{Y_i} \mathrm{div}_x \, \sigma_i \, \nabla_x u_0 \, d\xi - \int_{S_m} (\frac{\partial v_0}{\partial t} + I_{ion}(v_0, w_0)) \, ds_\xi = 0.$$

Considering that u_0 is independent of $\boldsymbol{\xi}$ and using (3.32) it follows that

$$\mathrm{div}_x \left[\int_{Y_i} \sigma_i (\mathbf{x}, \boldsymbol{\xi}) \{ I - \nabla_\xi \mathbf{w}(\mathbf{x}, \boldsymbol{\xi})^T \} \, d\xi \right] \nabla_x u_0 = |S| (\frac{\partial v_0}{\partial t} + I_{ion}(v_0, w_0)),$$

where I is the identity matrix, $\nabla_\xi \mathbf{w}^T = [\nabla_\xi w_1, \nabla_\xi w_2, \nabla_\xi w_3]$ and $|Y_i|$, $|S_m|$ denote the volume and the area of Y_i and S_m, respectively.

Let $\beta = |S_m|/|Y|$ be the ratio between the surface membrane and the volume of the reference cell and $\beta_{i,e} = |Y_{i,e}|/|Y|$. With reference to medium (i) $u_0 = u_0^i$, $\mathbf{w} = \mathbf{w}^i$ we set

$$D_i(\mathbf{x}) = \frac{1}{|Y|} \int_{Y_i} \sigma_i(\mathbf{x}, \boldsymbol{\xi}) \{ I - \nabla_\xi (\mathbf{w}^i)^T \} \, d\xi.$$

Hence, we obtain the following "*averaged equation*" for the intracellular potential

$$\mathrm{div} \, D_i(\mathbf{x}) \nabla_x u_0^i = \beta \left(\frac{\partial v_0}{\partial t} + I_{ion}(v_0, w_0) \right).$$

Following [44], it is easy to verify that the macroscopic conductivity tensor of the intracellular D_i is symmetric and positive definite.

Proceeding similarly for $u = u_e$ and taking into account that the unit normal $\mathbf{n}$ points inside Ω_e, we obtain the following averaged equations for the extracellular potential

$$\mathrm{div} \, D_e(\mathbf{x}) \nabla_x u_0^e = -\beta \left(\frac{\partial v_0}{\partial t} + I_{ion}(v_0, w_0) \right).$$

3.2.3 The Dimensionless Averaged Model P

Summarizing, for a periodic network of interconnected cells, the governing dimensionless equations of the macroscopic intra and extracellular potentials at zero order in ε are given by

$$\begin{cases} \mathrm{div} \, D_i(\mathbf{x}) \nabla_x u_i = \beta \left(\dfrac{\partial v}{\partial t} + I_{ion}(v, w) \right) \\[2mm] \mathrm{div} \, D_e(\mathbf{x}) \nabla_x u_e = -\beta \left(\dfrac{\partial v}{\partial t} + I_{ion}(v, w) \right) \\[2mm] v = u_i - u_e, \quad \dfrac{\partial w}{\partial t} - R(v, w) = 0, \quad \dfrac{\partial c}{\partial t} - S(v, w, c) = 0. \end{cases} \qquad (3.34)$$

Here the effective conductivity tensors are given by

$$D_{i,e}(\mathbf{x}) = \frac{1}{|Y|} \int_{Y_{i,e}} \sigma_{i,e}(\mathbf{x}, \boldsymbol{\xi}) \left\{ I - \nabla_{\xi}(\mathbf{w}^{i,e})^T \right\} d\xi$$

and $\mathbf{w}^{i,e} = (w_1^{i,e}, w_2^{i,e}, w_3^{i,e})^T$ are solutions of

$$\begin{cases} \operatorname{div}_{\xi} \sigma_{i,e}(\mathbf{x}, \boldsymbol{\xi}) \nabla_{\xi} w_k^e = 0, & \text{in } Y_{i,e} \\ \mathbf{n}_{\xi}^T \sigma_{i,e}(\mathbf{x}, \boldsymbol{\xi}) \nabla_{\xi} w_k^{i,e} = n_{\xi_k}, & \text{on } S, \quad k = 1, 2, 3. \end{cases}$$

The previous derivation based on the two-scale method is only formal, but the averaged model can be rigorously justified in the framework of Γ-convergence theory as a limit problem of the cellular model for $\varepsilon \to 0$, see [4].

3.2.4 Theoretical Results for the Cellular and Averaged Models

We introduce the functional space

$$\mathbb{V}^{\varepsilon} = \left\{ H^1(\Omega_i^{\varepsilon}) \times H^1(\Omega_e^{\varepsilon}) \right\} / \left\{ (\gamma, \gamma) : \gamma \in \mathbf{R} \right\} \times L^2(\Gamma_m^{\varepsilon})^M \times L^2(\Gamma_m^{\varepsilon})^R, \quad (3.35)$$

the vector variables $\boldsymbol{U} := (u_i, u_e, w, c) \in \mathbb{V}^{\varepsilon}$, $\hat{\boldsymbol{U}} := (\hat{u}_i, \hat{u}_e, \hat{w}, \hat{c}) \in \mathbb{V}^{\varepsilon}$, the vector time derivative $\partial_t \boldsymbol{U} := (\dfrac{\partial u_i}{\partial t}, \dfrac{\partial u_e}{\partial t}, \dfrac{\partial w}{\partial t}, \dfrac{\partial c}{\partial t})$ and we set $v = u_i - u_e$, $\hat{v} = \hat{u}_i - \hat{u}_e$. Then we introduce the forms

$$b^{\varepsilon}(\boldsymbol{U}, \hat{\boldsymbol{U}}) := \varepsilon \int_{\Gamma_m^{\varepsilon}} [\, v\,\hat{v} + w\,\hat{w} + c\,\hat{c}\,] \, d\gamma,$$

$$a^{\varepsilon}(\boldsymbol{U}, \hat{\boldsymbol{U}}) := \sum_{i,e} \int_{\Omega_{i,e}^{\varepsilon}} \sigma_{i,e}^{\varepsilon} \, \nabla u_{i,e} \cdot \nabla \hat{u}_{i,e} \, d\mathbf{x},$$

$$F^{\varepsilon}(\boldsymbol{U}, \hat{\boldsymbol{U}}) := \varepsilon \int_{\Gamma_m^{\varepsilon}} [I_{ion}(v, w, c)\,\hat{v} - R(v, w)\,\hat{w} - S(v, w, c)\,\hat{c}\,] \, d\gamma,$$

and we consider the variational formulation of the differential problem $\mathbf{P}^{\varepsilon}$:

Find $\boldsymbol{U}^{\varepsilon} : [0, T] \to \mathbb{V}^{\varepsilon} : b^{\varepsilon}(\partial_t \boldsymbol{U}^{\varepsilon}, \hat{\boldsymbol{U}}) + a^{\varepsilon}(\boldsymbol{U}^{\varepsilon}, \hat{\boldsymbol{U}}) + F^{\varepsilon}(\boldsymbol{U}^{\varepsilon}, \hat{\boldsymbol{U}}) = 0 \; \forall \, \hat{\boldsymbol{U}} \in \mathbb{V}^{\varepsilon},$
$$(3.36)$$

where the parabolic b^{ε} and elliptic a^{ε} forms are degenerate, but their sum is coercive on $\mathbb{V}^{\varepsilon}$. The variational formulation is supplemented by the initial conditions:

$$v^{\varepsilon}(\cdot, 0) = v_0^{\varepsilon}, \quad w^{\varepsilon}(\cdot, 0) = w_0^{\varepsilon}, \quad c^{\varepsilon}(\cdot, 0) = c_0^{\varepsilon}, \quad \text{on } \Gamma_m{}^{\varepsilon},$$

We consider the functional space

$$\mathbb{V} := \left\{ H^1(\Omega_H) \times H^1(\Omega_H) \right\} / \left\{ (\gamma, \gamma) : \gamma \in \mathbf{R} \right\} \times L^2(\Omega_H)^M \times L^2(\Omega_H)^R$$

and we introduce the following bilinear and nonlinear forms associated with the averaged model (3.34): for $\boldsymbol{U} = (u_i, u_e, w, c) \in \mathbb{V}$, $\hat{\boldsymbol{U}} = (\hat{u}_i, \hat{u}_e, \hat{w}, \hat{c}) \in \mathbb{V}$, and $v = u_i - u_e$, $\hat{v} = \hat{u}_i - \hat{u}_e$, we set

$$b(\boldsymbol{U}, \hat{\boldsymbol{U}}) := \beta \int_{\Omega_H} [\partial_t v \, \hat{v} + \partial_t w \, \hat{w} + \partial_t c \, \hat{c}] \, dx,$$

$$a(\boldsymbol{U}, \hat{\boldsymbol{U}}) := \sum_{i,e} \int_{\Omega_{i,e}} D_{i,e} \nabla u_{i,e} \cdot \nabla u_{i,e} \, d\mathbf{x}$$

$$F(\boldsymbol{U}, \hat{\boldsymbol{U}}) := \beta \int_{\Omega_H} [I_{ion}(v, w, c) \, \hat{v} - R(v, w) \, \hat{w} - S(v, w, c) \, \hat{c}] \, dx.$$

The homogenized conductivity tensors $D_{i,e}$ can be characterized by solving the following variational cellular problems for every $y \in \mathbb{R}^3$:

$$y^T D_{i,e}(x) \, y := \min \left\{ \frac{1}{|Y|} \int_{Y_{i,e}} \left(\nabla u(\xi) + y \right)^T \sigma_{i,e}(x, \xi) \left(\nabla u(\xi) + y \right) d\xi : \right.$$

$$\left. u \in H^1_{loc}(\mathbb{R}^d), \, uY\text{-periodic} \right\}.$$

These tensors are symmetric and positive definite matrices, and the bilinear form $a(\cdot, \cdot)$ is coercive on $\mathbb{V}$.

The variational formulation of the averaged problem $\mathbf{P}$, related to the macroscopic model (3.34), is given by:

Find $\boldsymbol{U} : [0, T] \to \mathbb{V} : b(\partial_t \boldsymbol{U}, \hat{\boldsymbol{U}}) + a(\boldsymbol{U}, \hat{\boldsymbol{U}}) + \mathscr{F}(\boldsymbol{U}, \hat{\boldsymbol{U}}) = 0 \; \forall \hat{\boldsymbol{U}} \in \mathbb{V},$

(3.37)

supplemented with the initial conditions

$$v(\cdot, 0) = v_0, \quad w(\cdot, 0) = w_0, \quad c(\cdot, 0) = c_0, \quad \text{in} \;\; \Omega_H.$$

We now focus on the FitzHugh-Nagumo membrane model [178, 179]: the ionic current is a cubic like function in v and is linear in the recovery variable w. In this simplified model, the unknown is the vector $(u_i^\varepsilon, u_e^\varepsilon, w^\varepsilon)$ and it was shown in [105] that both the cellular and the averaged models share the same variational structure and yield well posed problems. More precisely, introducing the quotient space as in (3.35)

$$\mathbb{V}^\varepsilon = \left\{ H^1(\Omega_i^\varepsilon) \times H^1(\Omega_e^\varepsilon) \right\} / \left\{ (\gamma, \gamma) : \gamma \in \mathbf{R} \right\} \times L^2(\Gamma_m^\varepsilon), \tag{3.38}$$

we have the following result for problem $\mathbf{P}^\varepsilon$.

Theorem 3.2. *Assuming Γ^ε is regular and supposing that the initial data satisfy*

$$(v_0^\varepsilon, w_0^\varepsilon) \in L^2(\Gamma_m^\varepsilon) \times L^2(\Gamma_m^\varepsilon),$$

then there exists a unique solution $\boldsymbol{U}^\varepsilon = (u_i^\varepsilon, u_e^\varepsilon, w^\varepsilon) \in C^0(]0, T]; \mathbb{V}^\varepsilon)$ of the variational formulation (3.36) of Problem $\boldsymbol{P}^\varepsilon$ with

$$\frac{\partial v^\varepsilon}{\partial t}, \quad \frac{\partial w^\varepsilon}{\partial t} \in L^2(0, T; L^2(\Gamma_m^\varepsilon));$$

$\underline{u}^\varepsilon := (u_i^\varepsilon, u_e^\varepsilon)$ *solves the differential equations $\boldsymbol{P}^\varepsilon$ in the standard distributional sense.*

Introducing the quotient space

$$\mathbb{V} := \left\{ H^1(\Omega_H) \times H^1(\Omega_H) \right\} / \left\{ (\gamma, \gamma) : \gamma \in \mathbf{R} \right\} \times L^2(\Omega_H)$$

we have the following result for problem $\mathbf{P}$.

Theorem 3.3. *Assuming that the initial data satisfy*

$$(v_0, w_0) \in L^2(\Omega_H) \times L^2(\Omega_H),$$

then there exists a unique solution $\boldsymbol{U} = (u_i, u_e, w) \in C^0(]0, T]; \mathbb{V})$ of the variational formulation (3.37) of the averaged Problem $\mathbf{P}$ with

$$\frac{\partial v}{\partial t}, \quad \frac{\partial w}{\partial t} \in L^2(0, T; L^2(\Omega_H));$$

$\underline{u} := (u_i, u_e)$ *solves the differential equations $\boldsymbol{P}$ in the standard distributional sense.*

We remark that the above abstract variational framework of the cellular (3.36) and averaged (3.37) models in terms of the forms $a^\varepsilon, b^\varepsilon, F^\varepsilon$ and a, b, F respectively, share the same structural properties, see [105].

Well-posedness results for the cellular and the averaged models with ionic current membrane dynamics, described by the classical Hodgkin-Huxley model [229] or by the Luo-Rudy Phase I model [308], can be found in [540, 541].

3.2.5 Γ-Convergence Result for the Averaged Model with FHN Dynamics

We now present a convergence result for the homogenization process related to the Bidomain model with Nagumo membrane model (i.e. FHN without the recovery variable); see [378] for details of the general FHN case.

The problem P^ε is not a standard parabolic homogenization problem and its main difficulties are associated with the fact that b^ε depends explicitly on ε, it is *degenerate* and the boundaries of $\Omega_{i,e}^\varepsilon$ could be quite irregular. For $z^\varepsilon \in L^2(\Gamma^\varepsilon)$, $\underline{u}^\varepsilon = (u_i^\varepsilon, u_e^\varepsilon) \in H^1(\Omega_i^\varepsilon) \times H^1(\Omega_e^\varepsilon)$, and $z \in L^2(\Omega_H)$, $\underline{u} = (u_i, u_e) \in (H^1(\Omega_H))^2$, we define the energy-like functionals

$$b^\varepsilon(z^\varepsilon) := \varepsilon \int_{\Gamma_m^\varepsilon} |z^\varepsilon|^2 d\gamma, \quad a^\varepsilon(\underline{u}^\varepsilon) := \sum_{i,e} \int_{\Omega_{i,e}^\varepsilon} \sigma_{i,e}^\varepsilon \nabla u_{i,e}^\varepsilon \cdot \nabla u_{i,e}^\varepsilon dx,$$

$$b(z) := \beta \int_{\Omega_H} |z|^2 dx, \quad a(\underline{u}) := \sum_{i,e} \int_{\Omega_H} D_{i,e} \nabla u_{i,e} \cdot \nabla u_{i,e} \, dx,$$

$$\mathscr{G}^\varepsilon(z^\varepsilon) := \varepsilon \int_{\Gamma_m^\varepsilon} G(z^\varepsilon) d\gamma, \quad \mathscr{G}(z) := \beta \int_{\Omega_H} G(z) dx, \tag{3.39}$$

where G is a positive primitive of g in the FHN model.

Theorem 3.4. *Let us assume that* $v_0^\varepsilon = u_{i,0}^\varepsilon - u_{e,0}^\varepsilon$, w_0^ε *are converging to* $v_0 = u_{i,0} - u_{e,0}$, w_0 *in the following "distributional" sense, i.e.*

$$\lim_{\varepsilon \downarrow 0} \varepsilon \int_{\Gamma_m^\varepsilon} v_0^\varepsilon(x) \zeta(x) \, d\gamma = \beta \int_{\Omega_H} v_0(x) \zeta(x) \, dx, \quad \forall \zeta \in C_0^\infty(\Omega_H)$$

$$\lim_{\varepsilon \downarrow 0} \varepsilon \int_{\Gamma_m^\varepsilon} w_0^\varepsilon(x) \zeta(x) \, d\gamma = \beta \int_{\Omega_H} w_0(x) \zeta(x) \, dx, \quad \forall \zeta \in C_0^\infty(\Omega_H)$$

$$\lim_{\varepsilon \downarrow 0} \int_{\Omega_{i,e}^\varepsilon} u_{i,e}^\varepsilon(x) \zeta(x) \, dx = \beta_{i,e} \int_{\Omega_H} u_{i,e}(x) \zeta(x) \, dx, \quad \forall \zeta \in C_0^\infty(\Omega_H)$$

and the related energies satisfy

$$\lim_{\varepsilon \downarrow 0} b^\varepsilon(v_0^\varepsilon) = b(v_0), \ \lim_{\varepsilon \downarrow 0} b^\varepsilon(w_0^\varepsilon) = b(w_0), \quad \limsup_{\varepsilon \downarrow 0} \left(a^\varepsilon(u_0^\varepsilon) + \mathscr{G}^\varepsilon(v_0^\varepsilon) \right) < +\infty.$$

Let $\Omega_0 \subset\subset \Omega_H$ *be a reference open subdomain with positive measure,* $\underline{u}^\varepsilon = (u_i^\varepsilon, u_e^\varepsilon)$, $v^\varepsilon = u_i^\varepsilon - u_e^\varepsilon$, w^ε *and* $\underline{u} = (u_i, u_e)$, $v = u_i - u_e$, w *be the solutions of the cellular and averaged models with* $\int_{\Omega_0 \cap \Omega^\varepsilon} u_e^\varepsilon dx = 0$, *and* $\int_{\Omega_0 \cap \Omega_H} u_e dx = 0$, *respectively. Then for every time* $t \in [0, T]$

$$(u_{i,e}^\varepsilon, v^\varepsilon, w^\varepsilon) \to (u_{i,e}, v, w) \quad \text{as } \varepsilon \downarrow 0, \text{ in the distributional sense,}$$

with

$$a^\varepsilon(\boldsymbol{u}^\varepsilon) \to a(\boldsymbol{u}), \quad b^\varepsilon(v^\varepsilon) \to b(v), \quad b^\varepsilon(w^\varepsilon) \to b(w).$$

Moreover, there exist extensions $\mathcal{T}_i^\varepsilon u_i^\varepsilon, \mathcal{T}_e^\varepsilon u_e^\varepsilon$ of $u_i^\varepsilon, u_e^\varepsilon$ in the whole domain Ω_H, solution of the cellular problem $\mathbf{P}^\varepsilon$, which converge in $L^2(0, T; H_{loc}^1(\Omega_H))$ to the unique solution $(u_i, u_e) \in \mathbb{V}$ of the averaged model $\boldsymbol{P}$.

The variational approach for the convergence of the evolution problem is based on the introduction of the time-semidiscrete approximation by the implicit Euler method, which reduces the evolution system to discrete families of stationary problems. More precisely, given $\boldsymbol{U}_0^\varepsilon$, we introduce the sequence of variational problems:

Find $\boldsymbol{U}_{\tau,n}^\varepsilon \in \mathbb{V}$, $n = 1, \dots, N$ such that

$$b^\varepsilon\left(\frac{\boldsymbol{U}_{\tau,n}^\varepsilon - \boldsymbol{U}_{\tau,n-1}^\varepsilon}{\tau}, \hat{\boldsymbol{U}}\right) + a^\varepsilon(\boldsymbol{U}_{\tau,n}^\varepsilon, \hat{\boldsymbol{U}}) + F^\varepsilon(\boldsymbol{U}_{\tau,n}^\varepsilon, \hat{\boldsymbol{U}}) = 0, \quad \forall \hat{\boldsymbol{U}} \in \mathbb{V}.$$

For $\tau = T/N$ sufficiently small, the coercivity of $a + b$ and the one-sided Lipschitz condition on F^ε guarantee the recursive solvability of these equations.

The previous Theorem follows by combining Γ−convergence and uniform error estimates for the Euler discretization; assuming, for simplicity, an instantaneous ionic current without recovery, i.e. $I_{ion}(v) = g(v)$, the discrete solution $\boldsymbol{U}_{\tau,1}^\varepsilon, \dots \boldsymbol{U}_{\tau,N}^\varepsilon$ of the Euler scheme solves the iterated (convex) minimization problem

$$\boldsymbol{U}_{\tau,n}^\varepsilon = \arg\min_{\boldsymbol{V} \in \mathbb{V}} \left\{ \frac{1}{2\tau} b^\varepsilon(\boldsymbol{V} - \boldsymbol{U}_{\tau,n-1}^\varepsilon) + \Phi^\varepsilon(\boldsymbol{V}) \right\}, \tag{3.40}$$

where Φ^ε is the Lyapunov functional

$$\Phi^\varepsilon(\boldsymbol{U}^\varepsilon) := a^\varepsilon(\underline{\boldsymbol{u}}^\varepsilon) + \mathcal{G}^\varepsilon(v^\varepsilon)$$

and $a^\varepsilon, b^\varepsilon, \mathcal{G}^\varepsilon$ have been defined in (3.39). Analogously, we can define the same quantities for the limit case $\varepsilon = 0$, obtaining a discrete solution $\boldsymbol{U}_{\tau,n}$ that solves an iterated convex minimization problem (3.40) without ε involving the Lyapunov functional

$$\Phi(\boldsymbol{U}) := a(\underline{\boldsymbol{u}}) + \mathcal{G}(v),$$

with $a, b, \mathcal{G}$ again defined in (3.39).

The general strategy for passing to the limit (see [378]) can be summarized in the following diagram

$$
\boxed{\begin{array}{c} \textbf{Evolution Problem} \\ P^{\varepsilon} \;\; : \;\; U^{\varepsilon} \end{array}} \quad \rightarrow \quad \boxed{\begin{array}{c} \textbf{Stationary Problem} \\ U^{\varepsilon,n+1}_{\tau} : \\ \min_W \frac{1}{2\tau} b^{\varepsilon}(W - U^{\varepsilon,n}_{\tau}) + \Phi^{\varepsilon}(W) \end{array}}
$$

$$
\varepsilon \downarrow 0
$$

$$
\boxed{\begin{array}{c} \textbf{Limit of the Evolution} \\ \textbf{Problem } P \;\; : \;\; U \end{array}} \quad 0 \leftarrow \tau \quad \boxed{\begin{array}{c} \textbf{Limit of the Stationary Problem} \\ U^{n+1}_{\tau} : \min_W \frac{1}{2\tau} b(W - U^{n}_{\tau}) + \Phi(W) \end{array}}
$$
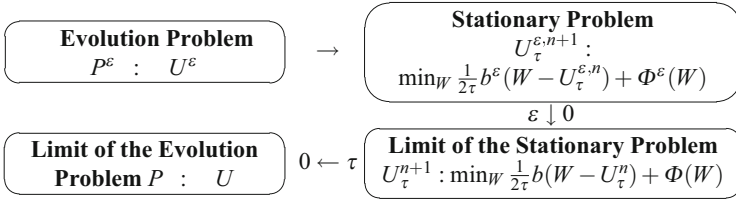
3.3 The Macroscopic Anisotropic Bidomain Model

The macroscopic Bidomain representation of the cardiac tissue (3.34) has been derived in the previous chapter using homogenization techniques.

We now present a heuristic derivation of the Bidomain model, based on the notion of the *interpenetrating domains* introduced in [463], formalized by [199, 329, 531], see also [225, 391]. We denote by Ω_H the cardiac tissue volume that we assume represented as the superposition of two anisotropic continuous media, the intra- (i) and extra- (e) cellular media, coexisting at every point of the tissue and separated by a distributed continuous cellular membrane.

Given a point $\mathbf{x} \in \Omega_H$, we denote by $\mathbf{J}_i(\mathbf{x}, t), \mathbf{J}_e(\mathbf{x}, t)$ the local average current densities per unit area in the intra- and extracellular media and by i_m the transmembrane current per unit volume flowing across the membrane surface. Consider a volume V surrounding $\mathbf{x}$ and denote by $|V|$ its volume, ∂V its smooth surface, $\mathbf{n}$ the outward normal on ∂V. Then the current conservation law on the volume V states that

$$
\frac{1}{|V|} \int_{\partial V} \mathbf{J}_e \cdot \mathbf{n} d\sigma = -\frac{1}{|V|} \int_{\partial V} \mathbf{J}_i \cdot \mathbf{n} d\sigma = c_m \frac{1}{|V|} \int_V i_m \cdot dx,
$$

i.e. the flux entering the extracellular volume must equal the flux exiting the intra-cellular volume, and both must equal the transmembrane current across the membrane (directed from the intra- to the extracellular media). Taking the limit as $|V| \to 0$, it then follows

$$
div\mathbf{J}_e(x, t) = -div\mathbf{J}_i(x, t) = i_m.
$$

We recall that the cardiac tissue consists of an arrangement of fibers that rotate counterclockwise from epi- to endocardium, and that have a laminar organization modeled as a set of muscle sheets running radially from epi- to endocardium.

The anisotropy of the intra- and extracellular media, related to the macroscopic arrangement of the cardiac myocytes in the fiber structure, is described by the anisotropic conductivity tensors $D_i(\mathbf{x})$ and $D_e(\mathbf{x})$, defined as

$$\begin{cases} D_{i,e}(\mathbf{x}) = \sigma_l^{i,e}\, \mathbf{a}_l(\mathbf{x})\mathbf{a}_l^T(\mathbf{x}) + \sigma_t^{i,e}\, \mathbf{a}_t(\mathbf{x})\mathbf{a}_t^T(\mathbf{x}) + \sigma_n^{i,e}\, \mathbf{a}_n(\mathbf{x})\mathbf{a}_n^T(\mathbf{x}) = \\ \quad = \sigma_l^{i,e} I + (\sigma_t^{i,e} - \sigma_l^{i,e})\mathbf{a}_t(\mathbf{x})\mathbf{a}_t^T(\mathbf{x}) + (\sigma_n^{i,e} - \sigma_l^{i,e})\mathbf{a}_n(\mathbf{x})\mathbf{a}_n^T(\mathbf{x}). \end{cases}$$
(3.41)

Here $\mathbf{a}_l(\mathbf{x})$, $\mathbf{a}_t(\mathbf{x})$, $\mathbf{a}_n(\mathbf{x})$, is a triplet of orthonormal principal axes with $\mathbf{a}_l(\mathbf{x})$ parallel to the local fiber direction, $\mathbf{a}_t(\mathbf{x})$ and $\mathbf{a}_n(\mathbf{x})$ tangent and orthogonal to the radial laminae, respectively, and both being transversal to the fiber axis (see e.g. LeGrice et al. [292]). Moreover, $\sigma_l^{i,e}$, $\sigma_t^{i,e}$, $\sigma_n^{i,e}$ are the conductivity coefficients in the intra- and extracellular media measured along the corresponding directions $\mathbf{a}_l, \mathbf{a}_t, \mathbf{a}_n$. For *axisymmetric* anisotropic media $\sigma_n^{i,e} = \sigma_t^{i,e}$. Since the anisotropic intra- and extracellular media are ohmic, currents and potentials are related by

$$\mathbf{J}_i = -D_i \nabla u_i, \quad \mathbf{J}_e = -D_e \nabla u_e,$$

and we obtain the following parabolic - parabolic (PP) formulation of the Bidomain system.

PP-formulation. Given the applied intra- and extracellular currents per unit volume $I_{i,e}^s : \Omega_H \times (0,T) \to \mathbb{R}$, and initial conditions $v_0 : \Omega_H \to \mathbb{R}$, $\mathbf{w}_0 : \Omega_H \to \mathbb{R}^k$, $\mathbf{z}_0 : \Omega_H \to (0,+\infty)^m$, find the intra- and extracellular potentials $u_{i,e} : \Omega_H \times (0,T) \to \mathbb{R}$, the transmembrane potential $v = u_i - u_e : \Omega_H \times (0,T) \to \mathbb{R}$, the gating variables $\mathbf{w} : \Omega_H \times (0,T) \to \mathbb{R}^k$ and the ionic concentrations variables $\mathbf{z} : \Omega_H \times (0,T) \to \mathbb{R}^m$ such that

$$\begin{cases} c_m \dfrac{\partial v}{\partial t} - \mathrm{div}(D_i \nabla u_i) + I_{ion}(v, \mathbf{w}, \mathbf{z}) = I_i^s & \text{in } \Omega_H \times (0,T) \\[2mm] -c_m \dfrac{\partial v}{\partial t} - \mathrm{div}(D_e \nabla u_e) - I_{ion}(v, \mathbf{w}, \mathbf{z}) = I_e^s & \text{in } \Omega_H \times (0,T) \\[2mm] \dfrac{\partial \mathbf{w}}{\partial t} - \mathbf{F}(v, \mathbf{w}) = 0, & \text{in } \Omega_H \times (0,T) \\[2mm] \dfrac{\partial \mathbf{z}}{\partial t} - \mathbf{G}(v, \mathbf{w}, \mathbf{z}) = 0, & \text{in } \Omega_H \times (0,T) \\[2mm] \mathbf{n}^T D_{i,e} \nabla u_{i,e} = 0 & \text{in } \partial\Omega_H \times (0,T) \\[2mm] v(\mathbf{x}, 0) = v_0(\mathbf{x}), \quad \mathbf{w}(\mathbf{x},0) = \mathbf{w}_0(\mathbf{x}), \quad \mathbf{z}(\mathbf{x},0) = \mathbf{z}_0(\mathbf{x}), & \text{in } \Omega_H, \end{cases}$$
(3.42)

where we have assumed an insulated cardiac boundary $\partial\Omega_H$. The nonlinear reaction term I_{ion} and the ODE system for the gating variables $\mathbf{w}$ and the ionic concentrations $\mathbf{c}$ are given by the ionic membrane model.

PE-formulation. System (3.42) can be equivalently rewritten in terms of the transmembrane and extracellular potentials $v(\mathbf{x}, t)$ and $u_e(\mathbf{x}, t)$, thus obtaining the parabolic-elliptic (PE) formulation of the Bidomain model

$$
\begin{cases}
c_m \dfrac{\partial v}{\partial t} - \text{div}(D_i \nabla v) - \text{div}(D_i \nabla u_e) + I_{ion}(v, \mathbf{w}, \mathbf{z}) = I_i^s & \text{in } \Omega_H \times (0, T) \\[2mm]
-\text{div}(D_i \nabla v) - \text{div}((D_i + D_e)\nabla u_e) = I_i^s + I_e^s & \text{in } \Omega_H \times (0, T) \\[2mm]
\dfrac{\partial \mathbf{w}}{\partial t} - \mathbf{F}(v, \mathbf{w}) = 0, & \text{in } \Omega_H \times (0, T) \\[2mm]
\dfrac{\partial \mathbf{z}}{\partial t} - \mathbf{G}(v, \mathbf{w}, \mathbf{z}) = 0, & \text{in } \Omega_H \times (0, T) \\[2mm]
\mathbf{n}^T D_i \nabla(v + u_e) = 0 & \text{in } \partial\Omega_H \times (0, T) \\[2mm]
\mathbf{n}^T (D_i + D_e)\nabla u_e + \mathbf{n}^T D_i \nabla v = 0, & \text{in } \partial\Omega_H \times (0, T) \\[2mm]
v(\mathbf{x}, 0) = v_0(\mathbf{x}), \;\; \mathbf{w}(\mathbf{x}, 0) = \mathbf{w}_0(\mathbf{x}), \;\; \mathbf{z}(\mathbf{x}, 0) = \mathbf{z}_0(\mathbf{x}), & \text{in } \Omega_H.
\end{cases}
\tag{3.43}
$$

We note that, in the previous models, we have not included many anatomical components, such as:

- The specialized ventricular conduction system, composed of the bundle of His, the left and right bundle branches, and an extensive Purkinje network, which connects to the myocardium at discrete sites known as Purkinje-ventricular junctions, see e.g. [22, 55, 425, 520];
- The presence of the coronary vasculature, see [51, 52, 490];
- The deformation of the cardiac tissue induced by the mechanical contraction and relaxation process [232, 245, 246, 527].

3.4 Well-Posedness Results Based on Semi-discretization in Time

Following [105], we first consider the well-posedness of the variational formulation of the macroscopic PP Bidomain model (3.42) coupled with a Fitzhugh-Nagumo-like membrane dynamics.

Let us suppose that

$$\Omega_H \text{ is a Lipschitz domain of } \mathbb{R}^3, \tag{3.44}$$

$D_i(x)$ and $D_e(x)$ are measurable and satisfy the uniform ellipticity condition

$$\exists \alpha, \ m > 0 : \quad \alpha |\xi|^2 \leq D_{i,e}(x) \xi \cdot \xi \leq m |\xi|^2, \quad \forall \xi \in \mathbb{R}^3, \ x \in \Omega_H, \tag{3.45}$$

and finally f is a continuous function with

$$f(0) = 0; \quad \exists \lambda_f \geq 0 : \quad \frac{f(x) - f(y)}{x - y} \geq -\lambda_f, \quad \forall x, y \in \mathbb{R}, \quad \text{with } x \neq y. \tag{3.46}$$

We will also require that f has a cubic growth at infinity, i.e.

$$0 < \liminf_{|s| \to +\infty} \frac{f(s)}{s^3} \leq \limsup_{|s| \to +\infty} \frac{f(s)}{s^3} < +\infty. \tag{3.47}$$

Then consider the following Bidomain problem:

Problem (M). Given

$$I_{i,e}^s : \Omega_h \times (0, T) \to \mathbb{R}, \quad \text{and} \quad v_0, \ w_0 : \Omega_H \to \mathbb{R},$$

we seek

$$u_i, \ u_e, \ w : \Omega_H \times (0, T) \to \mathbb{R}, \quad \text{with} \quad v := u_i - u_e,$$

which solve

$$\begin{cases} c_m \dfrac{\partial v}{\partial t} - \text{div}(D_i \nabla u_i) + f(v) + \theta w = I_i^s & \text{in } \Omega_H \times (0, T) \\[2mm] -c_m \dfrac{\partial v}{\partial t} - \text{div}(D_e \nabla u_e) - f(v) - \theta w = I_e^s & \text{in } \Omega_H \times (0, T) \\[2mm] \dfrac{\partial w}{\partial t} + \gamma w - \eta v = 0, & \text{in } \Omega_H \times (0, T) \\[2mm] \mathbf{n}^T D_{i,e} \nabla u_{i,e} = 0 & \text{in } \partial \Omega_H \times (0, T) \\[2mm] v(\mathbf{x}, 0) = v_0(\mathbf{x}), \ w(\mathbf{x}, 0) = w_0(\mathbf{x}), & \text{in } \Omega_H, \end{cases} \tag{3.48}$$

with θ positive parameter.

Let us now introduce the Hilbert spaces

$$\mathbf{X} := H^1(\Omega_H) \times H^1(\Omega_H) \times L^2(\Omega_H), \quad \mathbf{V} := \mathbf{X}/\{(c, c, 0) : c \in \mathbb{R}\}, \qquad (3.49)$$

whose generic element (u_i, u_e, w) we denote by $\mathbf{u}$, the bilinear forms on $\mathbf{V} \times \mathbf{V}$

$$b(\mathbf{u}, \hat{\mathbf{u}}) := \int_{\Omega_H} [c_m(u_i - u_e)(\hat{u}_i - \hat{u}_e) + \rho w \hat{w}]dx, \quad \text{with } \rho := \frac{\theta}{\eta}, \qquad (3.50)$$

$$a(\mathbf{u}, \hat{\mathbf{u}}) := \sum_{i,e} \int_{\Omega_H} D_{i,e} \nabla u_{i,e} \cdot \nabla \hat{u}_{i,e} \, dx + \theta \int_{\Omega_H} [w(\hat{u}_i - \hat{u}_e) - (u_i - u_e)\hat{w}]dx,$$
$$\qquad (3.51)$$

the functionals on $\mathbf{X}$

$$\begin{cases} \langle \mathbf{L}(t), \hat{\mathbf{u}} \rangle := \sum_{i,e} \int_{\Omega_H} I_{i,e}^s \hat{u}_{i,e} \, dx, \\ \langle \ell^0, \hat{\mathbf{u}} \rangle := \int_{\Omega_H} (c_m v_0 \hat{v} + \rho w_0 \hat{w}) \, dx, \end{cases} \qquad (3.52)$$

and the operator $\mathscr{F} : D(\mathscr{F}) \subset \mathbf{V} \to \mathbf{V}'$

$$\langle \mathscr{F}\mathbf{u}, \hat{\mathbf{u}} \rangle := \int_{\Omega_H} f(u_i - u_e)(\hat{u}_i - \hat{u}_e) \, dx, \qquad (3.53)$$

with domain

$$D(\mathscr{F}) := \{\mathbf{u} \in \mathbf{V} : f(u_i - u_e) \in L^1(\Omega_H) \cap (H^1(\Omega_H))'\};$$

this means that for every $\mathbf{u} \in D(\mathscr{F})$ there exists a constant $C > 0$ such that

$$\int_{\Omega_H} f(u_i - u_e)\zeta \, dx \le C ||\zeta||_{H^1(\Omega_H)}, \quad \forall \zeta \in H^1(\Omega_H) \cap L^\infty(\Omega_H).$$

Again we observe that all these definitions are compatible with the quotient space $\mathbf{V}$, provided that

$$\int_{\Omega_H} (I_i^s + I_e^s) \, dx = 0 \quad \text{for a.e. } t \in (0, T). \qquad (3.54)$$

We can give now the precise statement of Problem (**M**) in a variational abstract form.

Problem (AM). Let us assume that

$$I_{i,e}^s \in L^2(\Omega_H \times (0, T)) \quad \text{and} \quad v^0, \, w^0 \in L^2(\Omega_H), \tag{3.55}$$

and (3.54) is satisfied. Then, if $\mathbf{V}$, b, a, $\mathbf{L}$, $\boldsymbol{\ell}^0$, $\mathscr{F}$ are defined by (3.49), …, (3.53) respectively, and A, B are defined as

$$\langle A\mathbf{u}, \hat{\mathbf{u}} \rangle := a(\mathbf{u}, \hat{\mathbf{u}}), \quad \langle B\mathbf{u}, \hat{\mathbf{u}} \rangle := b(\mathbf{u}, \hat{\mathbf{u}}) \qquad \forall \mathbf{u}, \, \hat{\mathbf{u}} \in \mathbf{V},$$

we seek $\mathbf{u}(t) := (u_i(\cdot, t), \, u_e(\cdot, t), \, w(\cdot, t))$, with

$$\mathbf{u} \in L^2(0, T; \mathbf{V}), \quad B\mathbf{u} \in W_{loc}^{1,1}(0, T; \mathbf{V}') \cap C^0([0, T]; \mathbf{V}'),$$

satisfying

$$(B\mathbf{u})' + A\mathbf{u} + \mathscr{F}\mathbf{u} = \mathbf{L} \qquad \text{in } \mathbf{V}', \quad \text{a.e. in } (0, T),$$

together with the initial condition

$$(B\mathbf{u})(0) = \boldsymbol{\ell}^0.$$

It holds the following theorem, proved in [105] by applying the theory developed in [457] for abstract evolution inequalities, based on semi-discretization in time, a-priori error estimates and compactness properties.

Theorem 3.5. *Assume that (3.54) and (3.55) are satisfied, together with*

$$I_i^s + I_e^s \in W^{1,1}(0, T; L^2(\Omega_H)).$$

Then Problem (AM) admits a unique solution $\mathbf{u}$*. In particular there exist a couple*

$$u_i, \, u_e \in L^2(0, T; H^1(\Omega_H)),$$

uniquely determined up to a family of additive constants $c(t)$, and a unique couple (v, w) with

$$v \in C^0([0, T]; L^2(\Omega_H)) \cap L^2(0, T; H^1(\Omega_H)), \quad \partial_t v \in L_{loc}^2(0, T; L^2(\Omega_H)),$$

$$w, \, \partial_t w \in C^0([0, T]; L^2(\Omega_H)),$$

which solve Problem (M). Moreover, if

$$v^0 \in H^1(\Omega_H) \qquad \text{and} \qquad v^0 f(v^0) \in L^1(\Omega_H),$$

then

$$u_{i,e} \in C^0([0, T]; H^1(\Omega_H)), \quad \partial_t v \in L^2(\Omega_H \times (0, T)), \quad w \in C^0([0, T]; H^1(\Omega_H)).$$

3.5   Well-Posedness Results Based on Faedo-Galerkin Techniques

In this section, we will review the well-posedness results for weak solutions of the PE-formulation of the Bidomain model, established in [60] by using a Faedo-Galerkin technique. See also [42, 59] for a similar approach, based on a parabolic regularization technique.

The result in [60] holds for simple membrane models, which neglect the ionic concentrations **z**. In the following, assume for sake of simplicity that the membrane model takes into account only one gating variable, thus $k = 1$, $\mathbf{w} = w$ and $\mathbf{F} = F$. With the previous assumptions, the PE-formulation of the Bidomain model becomes

$$
\begin{cases}
c_m \dfrac{\partial v}{\partial t} - \operatorname{div}(D_i \nabla v) - \operatorname{div}(D_i \nabla u_e) + I_{ion}(v, w) = I_i^s & \text{in } \Omega_H \times (0, T) \\[2mm]
-\operatorname{div}(D_i \nabla v) - \operatorname{div}((D_i + D_e)\nabla u_e) = I_i^s + I_e^s & \text{in } \Omega_H \times (0, T) \\[2mm]
\dfrac{\partial w}{\partial t} - F(v, w) = 0, & \text{in } \Omega_H \times (0, T) \\[2mm]
\mathbf{n}^T D_i \nabla(v + u_e) = 0 & \text{in } \partial\Omega_H \times (0, T) \\[2mm]
\mathbf{n}^T (D_i + D_e)\nabla u_e + \mathbf{n}^T D_i \nabla v = 0, & \text{in } \partial\Omega_H \times (0, T) \\[2mm]
v(\mathbf{x}, 0) = v_0(\mathbf{x}), \quad w(\mathbf{x}, 0) = w_0(\mathbf{x}), & \text{in } \Omega_H.
\end{cases}
\tag{3.56}
$$

Preliminary variational results. Denote by $V = H^1(\Omega_H)$, $H = L^2(\Omega_H)$, $U = V/\mathbb{R}$ and, for any $u \in V$, $[u] = u - \int_{\Omega_H} u \in U$. Consider now the following variational problem:

find $(u, u_e) \in U \times U$ such that

$$
a_i(u, v) + a_i(u_e, v) + a_i(u, v_e) + (a_i + a_e)(u_e, v_e) = <s_i, v> + <s_i + s_e, v_e>
\tag{3.57}
$$

$\forall (v, v_e) \in U \times U$. The bilinear forms $a_{i,e}(\cdot, \cdot)$ on $U \times U$ are

$$
a_i(u, v) = \int_{\Omega_H} D_i \nabla u \cdot \nabla v \, dx, \qquad a_e(u, v) = \int_{\Omega_H} D_e \nabla u \cdot \nabla v \, dx, \quad \forall (u, v) \in U \times U,
$$

s_i, $s_e \in V'$ are given source terms and $< \cdot, \cdot >$ is the V'-duality.

Under the hypothesis of uniform ellipticity of the conductivity tensors $D_{i,e}$, the bilinear forms $a_{i,e}(\cdot, \cdot)$ are symmetric, continuous and coercive. Define now the bilinear form

$$
b((u, u_e), (v, v_e)) = a_i(u, v) + a_i(u_e, v) + a_i(u, v_e) + (a_i + a_e)(u_e, v_e)
$$

on $(U \times U) \times (U \times U)$, which is also symmetric, continuous and coercive. We have the following

Theorem 3.6. *Let $s_{i,e} \in V'$ and $u \in U$ be given. The variational equations*

$$(a_i + a_e)(\tilde{u}_e, v_e) = -a_i(u, v_e) \quad \forall v_e \in U, \tag{3.58}$$

$$(a_i + a_e)(\bar{u}_e, v_e) = < s_i + s_e, v_e > \quad \forall v_e \in U, \tag{3.59}$$

have unique solutions $\tilde{u}_e$, $\bar{u}_e \in U$. For any $u, v \in U$, we can define the mappings

$$\bar{a}(u, v) = b((u, \tilde{u}_e), (v, 0)), \qquad < s, v > = < s_i, v > -a_i(\bar{u}_e, v).$$

The mapping $\bar{a}$ is bilinear, symmetric, continuous and coercive on $U \times U$, and the mapping s is bilinear and continuous on U.

Equation (3.57) has a unique solution (u, u_e) where u is also the unique solution of

$$\bar{a}(u, v) = < s, v > \qquad \forall v \in U,$$

and $u_e = \tilde{u}_e + \bar{u}_e$.

We can now define the bilinear form $a(\cdot, \cdot)$ on $V \times V$

$$a(u, v) = \bar{a}([u], [v]) \qquad \forall (u, v) \in V \times V.$$

The following theorem holds.

Theorem 3.7. *The bilinear form $a(\cdot, \cdot)$ is symmetric, continuous and coercive on V. There exists an increasing sequence $0 = \lambda_0 < \ldots \leq \lambda_i \leq \ldots$ in $\mathbb{R}$ and an orthonormal Hilbert basis of H of eigenvectors $\{\psi_i\}_{i \in \mathbb{N}}$ such that for all $i \in \mathbb{N}$, $\psi_i \in V$ and*

$$\forall v \in V \qquad a(\psi_i, v) = \lambda_i(\psi_i, v).$$

Specific assumptions and notations. The existence of weak solutions of Problem (3.56) hold under minimal regularity assumptions:

- Ω_H has a Lipschitz boundary $\partial \Omega_H$;
- $D_{i,e}$ have $L^\infty(\Omega_H)$ coefficients;
- $I_{i,e}^s : [0, +\infty) \to V'$ and $\int_{\Omega_H} (I_i^s(x, t) + I_e^s(x, t))dx = 0$ for *a.e.* $t > 0$.

In addition assume that there exists $p \geq 2$ such that:

(H1)   The Sobolev embedding $V = H^1(\Omega_H) \subset L^p(\Omega_H)$ holds: $p \geq 2$ if $d = 2$, $2 \leq p \leq 6$ if $d = 3$ (see [62]);

(H2)   The functions I_{ion} and F are affine with respect to w:

$$I_{ion}(v, w) = I_{ion}^1(v) + I_{ion}^2(v)w, \qquad F(v, w) = F_1(v) + F_2 w,$$

where I_{ion}^1, I_{ion}^2, $F_1 : \mathbb{R} \to \mathbb{R}$ are continuous functions and $F_2 \in \mathbb{R}$;

(H3)   There exist constants $c_i \geq 0$ $(i = 1, \ldots, 6)$ such that for any $v \in \mathbb{R}$

$$|I_{ion}^1(v)| \leq c_1 + c_2 |v|^{p-1}$$
$$|I_{ion}^2(v)| \leq c_3 + c_4 |v|^{p/2-1}$$
$$|F_1(v)| \leq c_5 + c_6 |v|^{p/2};$$

(H4)   There exist constants $a, \ \lambda > 0, b, \ c \geq 0$ such that for any $(v, w) \in \mathbb{R}^2$

$$\lambda v I_{ion}(v, w) + w F(v, w) \geq a|v|^p - b(\lambda |v|^2 + |w|^2) - c.$$

Remark 3.1. Three examples of membrane models that satisfy these assumptions are the FitzHugh-Nagumo model [273], the Aliev-Panfilov model [1] and the Roger-McCulloch model [422].

Existence for the initial value problem. Under the minimal regularity assumptions on the data Ω_H, $D_{i,e}$, $I_{i,e}^s$ and defining $D(0, T)$ as the space of real functions C^∞ on $\mathbb{R}$ with compact support in $(0, T)$, it is possible to write the

Definition 3.1. (Weak solutions). Consider $\tau > 0$ and the three functions $v : t \in [0, \tau) \to v(t) \in H$, $u_e : t \in [0, \tau) \to u_e(t) \in H$, $w : t \in [0, \tau) \to w(t) \in H$. Given $(u_0, w_0) \in H$, we say that (v, u_e, w) is a weak solution of (3.56) if, for any $T \in (0, \tau)$,

1. $v : [0, T] \to H$ and $w : [0, T] \to H$ are continuous, and $u(0) = u_0$, $w(0) = w_0$ in H;
2. For a.e. $t \in (0, \tau)$, we have $v(t) \in V$, $u_e(t) \in V/\mathbb{R}$, $v \in L^2(0, T; V) \cap L^p(Q_T)$ where $Q_T = \Omega_H \times [0, T]$, and (v, u_e, w) verify in $D'(0, T)$

$$\frac{d}{dt}(v(t), \hat{v}) + \int_{\Omega_H} D_i \nabla(v(t) + u_e(t)) \cdot \nabla \hat{v} + \int_{\Omega_H} I_{ion}(v(t), w(t))\hat{v} = <I_i^s(t), \hat{v}>$$
$$\frac{d}{dt}(w(t), \hat{w}) + \int_{\Omega_H} F(v(t), w(t))\hat{w} = 0$$

respectively for all $\hat{v} \in V$ and for all $\hat{w} \in H$, and

$$\int_{\Omega_H} D_i \nabla v(t) \cdot \nabla \hat{u}_e + \int_{\Omega_H} (D_i + D_e) \nabla u_e(t) \cdot \nabla \hat{u}_e = <I_i^s(t) + I_e^s(t), \hat{u}_e> \qquad \forall \hat{u}_e \in V/\mathbb{R}.$$
$$(3.60)$$

Lemma 3.1. *The functions v, u_e, w are a weak solution of (3.56) if conditions 1–2 of Definition 3.1 hold and (u, w) verify in $D'(0, T)$*

$$\frac{d}{dt}(v(t), \hat{v}) + a(v, \hat{v}) + \int_{\Omega_H} I_{ion}(v(t), w(t))\hat{v} = \; < s(t), \hat{v} > \quad \forall \hat{v} \in V$$

$$\frac{d}{dt}(w(t), \hat{w}) + \int_{\Omega_H} F(v(t), w(t))\hat{w} = 0 \quad \forall \hat{w} \in H$$

where $a(\cdot, \cdot)$ and $s \in V'$ are defined in Theorem 3.6. The function u_e is then recovered from (3.60).

Theorem 3.8 (Global existence of a weak solution). *Let Ω_H, $D_{i,e}$ satisfy the minimal regularity specified previously and suppose that the hypotheses (H1)–(H4) on I_{ion} and F hold for some $p \geq 2$. Let then be given u_0, $w_0 \in H$ and $I_{i,e}^s \in L^2(\mathbb{R}_+; V')$ such that $\int_{\Omega_H}(I_i^s(x, t) + I_e^s(x, t))dx = 0$ for a.e. $t > 0$. Then the system (3.56) has a weak solution (v, u_e, w) in the sense of Definition 3.1 with $\tau = +\infty$.*

Sketch of the proof. The proof consists of three steps:

- Construction of an approximate solution using the Faedo-Galerkin technique, based on the special orthonormal Hilbert basis (in H) $\{\psi_i\}_{i \in \mathbb{N}}$ of eigenvectors defined in Theorem 3.7;
- A priori estimates on the approximate solution;
- Compactness results and convergence of the approximate solution towards a weak solution.

Uniqueness. Consider the function $G : \mathbb{R}^2 \rightarrow \mathbb{R}^2$ defined by

$$G(v, w) = \begin{bmatrix} \mu I_{ion}(v, w) \\ F(v, w) \end{bmatrix} \quad \forall (v, w) \in \mathbb{R}^2, \quad \text{for some } \mu > 0.$$

Let $z = (v, w) \in \mathbb{R}^2$, $Q(z) = \frac{1}{2}(\nabla G(z)^T + \nabla G(z))$ be the symmetric part of ∇G and denote by $\lambda_1(z) \leq \lambda_2(z)$ its eigenvalues. Suppose that

$$(U1) \quad \exists C \in \mathbb{R} : \forall z \in \mathbb{R}^2 \quad \lambda_2(z) \geq \lambda_1(z) \geq C.$$

Theorem 3.9 (Uniqueness). *If the condition (U1) is satisfied, then the solution obtained in Theorem 3.8 is unique.*

A different proof based on a regularization argument has been given in [59] for the PP-formulation of the Bidomain model. The proof holds true for the Bidomain model coupled with the Laplace equation for the torso and, in addition to the

generalized FitzHugh-Nagumo models considered in [60], a regularized version of the Mitchell-Scheffer membrane model has been also taken into account. In this ionic model, the functions I_{ion} and F are given by:

$$I_{ion}(v, w) = \frac{w}{\tau_{in}} v^2 (v - 1) - \frac{v}{\tau_{out}},$$
$$F(v, w) = \left(\frac{1}{\tau_{close}} + \frac{\tau_{close} - \tau_{open}}{\tau_{close} \tau_{open}} h_\infty(v) \right) (v - h_\infty),$$

where

$$h_\infty(v) = \frac{1}{2} \left(1 - \tanh \left(\frac{v - v_{gate}}{\eta_{gate}} \right) \right)$$

and τ_{in}, τ_{out}, $\tau_{open} < \tau_{close}$, v_{gate}, η_{gate} are positive constants.

The regularized finite dimensional problems used in the Faedo-Galerkin procedure are constructed by adding the terms

$$\frac{1}{n} \frac{\partial u_{i,n}}{\partial t} \quad \text{and} \quad \frac{1}{n} \frac{\partial u_{e,n}}{\partial t} \quad \text{with } n \in \mathbb{N}$$

into the first and second equations of the PP-formulation of the Bidomain system, respectively.

3.6 Well-Posedness Results Based on Fixed Point Arguments

In this section, we will review the well-posedness result for the PP-formulation of the Bidomain model, obtained in [541] using a fixed point argument. This result covers a wide range of complex membrane models.

The ionic current. Assume that the ionic current

$$I_{ion} : \mathbb{R} \times \mathbb{R}^k \times (0, +\infty)^m \to \mathbb{R}$$
$$(v, \mathbf{w}, \mathbf{z}) \qquad \qquad \to I_{ion}(v, \mathbf{w}, \mathbf{z})$$

has the general structure:

$$I_{ion}(v, \mathbf{w}, \mathbf{z}) := \sum_{i=1}^{m} J_i (v, \mathbf{w}, \log z_i) + \tilde{H}(v, \mathbf{w}, \mathbf{z}), \qquad (3.61)$$

where, $\forall i = 1, \ldots, m$,

$$
\begin{aligned}
&J_i \in C^1(\mathbb{R} \times \mathbb{R}^k \times \mathbb{R}), \\
&0 < \underline{G}(\mathbf{w}) \le \frac{\partial}{\partial \zeta} J_i(v, \mathbf{w}, \zeta) \le \overline{G}(\mathbf{w}), \\
&\left| \frac{\partial}{\partial v} J_i(v, \mathbf{w}, 0) \right| \le L_v(\mathbf{w}),
\end{aligned}
\tag{3.62}
$$

$\underline{G}, \overline{G}, L_v$ belong to $C^0(\mathbb{R}^k, \mathbb{R}_+)$ and

$$
\tilde{H} \in C^0(\mathbb{R} \times \mathbb{R}^k \times (0, +\infty)^m) \cap \mathrm{Lip}(\mathbb{R} \times [0, 1]^k \times (0, +\infty)^m).
\tag{3.63}
$$

Remark 3.2. The functions $\tilde{H}$ (and H_i in the following) do not have a precise physical meaning, but allow some currents which differ from J_i to be included in the model, e.g. they could represent the Na-K pump and the non-specific Ca-activated currents in [309].

The dynamics of the gating variables is described by the system of ODEs

$$
\frac{\partial w_j}{\partial t} = F_j(v, w_j), \quad j = 1, \ldots, k.
\tag{3.64}
$$

Assume that

$$
\begin{aligned}
&F_j : \mathbb{R}^2 \to \mathbb{R} \quad \text{is locally Lipschitz continuous,} \\
&F_j(v, 0) \ge 0 \quad \forall v \in \mathbb{R} \\
&F_j(v, 1) \le 0 \quad \forall v \in \mathbb{R},
\end{aligned}
\tag{3.65}
$$

$\forall j = 1, \ldots, k$.

In the membrane models considered, F_j has the particular form

$$
F_j(v, w_j) := \alpha_j(v)(1 - w_j) - \beta_j(v)w_j, \quad j = 1, \ldots, k,
$$

where α_j and β_j are positive rational functions of exponentials in v. A general expression for both α_j and β_j is given by

$$
\frac{C_1 \exp(\frac{v - v_n}{C_2}) + C_3(v - v_n)}{1 + C_4 \exp(\frac{v - v_n}{C_5})},
$$

where C_1, C_3, C_4, v_n are non-negative constants and C_2, C_5 are positive constants.

The dynamics of the ionic concentrations is described by the system of ODEs

$$
\frac{\partial z_i}{\partial t} = G_i(v, \mathbf{w}, \mathbf{z}) := -J_i(v, \mathbf{w}, z_i) + H_i(v, \mathbf{w}, \mathbf{z}) \quad i = 1, \ldots, m,
\tag{3.66}
$$

where J_i is the function described in (3.62) and

$$H_i \in C^0(\mathbb{R} \times \mathbb{R}^k \times (0, +\infty)^m) \cap \text{Lip}(\mathbb{R} \times [0,1]^k \times (0, +\infty)^m), \quad i = 1, \dots, m. \tag{3.67}$$

Adding the two equations in (3.42), we have

$$-\operatorname{div}(D_i \nabla u_i) - \operatorname{div}(D_e \nabla u_e) = I_i^s + I_e^s.$$

Integrating on Ω_H and applying the divergence theorem and the Neumann boundary conditions, we have the following compatibility condition for the system to be solvable

$$\int_{\Omega_H} (I_i^s + I_e^s)dx = 0. \tag{3.68}$$

We recall that the electric potentials in bounded domains are defined up to an additive constant. In our case, u_i and u_e are determined up to the same additive time-dependent constant, while v is uniquely determined. This common constant is related to the choice of the reference potential. The usual choice consists in selecting this constant so that u_e has zero average on Ω_H, i.e.

$$\int_{\Omega_H} u_e \, dx = 0. \tag{3.69}$$

Suppose then that $D_i(x)$ and $D_e(x)$ are measurable and satisfy the uniform ellipticity condition (3.45).

The condition on the initial datum. In view of the result of continuity for the solution v of the Bidomain model, we must ask for the initial datum v_0 to be compatible, in a sense to specify, with the Neumann homogeneous boundary conditions. Intuitively, if $v_0 = u_i^0 - u_e^0$, then we should have

$$D_i \nabla u_i^0 \cdot \mathbf{n} = 0 = D_e \nabla u_e^0 \cdot \mathbf{n}, \quad \text{on } \partial\Omega_H,$$

but fixing both $u_i(x, 0)$ and $u_e(x, 0)$, as initial data, may render the problem unsolvable, because the time derivative involves only the difference $u_i - u_e$. The correct assumption may seem abstract, see [541, Sec. 3]: let $v \in H^1(\Omega_H)$ be given, then the following minimization problem has a unique solution:

$$\min\left\{ \sum_{i,e} \int_{\Omega_H} D_{i,e} \nabla \bar{u}_{i,e} \cdot \bar{u}_{i,e} \, dx : \bar{u}_{i,e} \in H^1(\Omega_H), \int_{\Omega_H} \bar{u}_e \, dx = 0, \ \bar{u}_i - \bar{u}_e = v \right\}. \tag{3.70}$$

Now, if $I_i^s(0) + I_e^s(0) \in L^2(\Omega_H)$, then the following elliptic problem admits a unique solution $u_b^0 \in H^2(\Omega_H)$:

$$\begin{cases} -\operatorname{div}((D_i + D_e)\nabla u_b^0) = I_i^s(0) + I_e^s(0) & \text{in } \Omega_H, \\ ((D_i + D_e)\nabla u_b^0) \cdot \mathbf{n} = 0 & \text{on } \partial\Omega_H, \\ \displaystyle\int_{\Omega_H} u_b^0 \, dx = 0. \end{cases}$$

Finally, we say that an initial datum v_0 satisfies the *admissibility property* if

$$\begin{cases} \text{the couple } (\bar{u}_i, \bar{u}_e) \text{ solution of (3.70) w.r.t. } v_0, \text{ satisfies} \\ D_i(\nabla\bar{u}_i + u_b^0) \cdot \mathbf{n} = D_e(\nabla\bar{u}_e + u_b^0) \cdot \mathbf{n} = 0 \text{ on } \partial\Omega_H. \end{cases} \tag{3.71}$$

We can now state the main result of [541], concerning the existence of a variational solution for (3.42).

Theorem 3.10. *Assume that*

$$\Omega_H \text{ is of class } C^{1,1}, \qquad D_{i,e} \text{ are Lipschitz in } \Omega_H.$$

Let us take as given data

$v_0 \in H^2(\Omega_H)$, *satisfying the admissibility property (3.71)*,
$\mathbf{w}_0 : \Omega_H \to [0,1]^k$, *measurable*,
$\mathbf{z}_0 \in (L^2(\Omega_H))^m$, *with* $\log(\mathbf{z}_0) \in (L^2(\Omega_H))^m$,
$I_{i,e}^s \in L^p(0,T;L^2(\Omega_H))$, *for* $p > 4$, *satisfying (3.68) and*
$I_i^s + I_e^s \in H^1(0,T;L^2(\Omega_H))$.

Let us also take as given the ionic currents satisfying (3.61)–(3.63), the dynamics of the gating variables $\mathbf{F}(v, \mathbf{w})$, *satisfying (3.64) and (3.65), the dynamics of the ionic concentrations* $\mathbf{G}(v, \mathbf{w}, \mathbf{z})$, *satisfying (3.66) and (3.67).*

Then there exists a unique solution of Problem (3.42), given by $k + m + 2$ *functions* $w_1, \ldots, w_k, z_1, \ldots, z_m, u_i, u_e$ *satisfying*

$u_{i,e} \in L^p(0,T;H^2(\Omega_H))$,
$v := u_i - u_e \in W^{1,p}(0,T;L^2(\Omega_H)) \cap L^p(0,T;H^2(\Omega_H)) \cap C^0([0,T];C^0(\Omega_H))$,
$\mathbf{w} : Q \to [0,1]^k$ *measurable*, $\quad \mathbf{z} : Q \to (0,+\infty)^m$ *measurable*,
$w_j(x,\cdot) \in C^1(0,T) \cap C^0([0,T])$ *for a.e.* $x \in \Omega_H$, $j = 1, \ldots, k$,
$z_i(x,\cdot) \in C^1(0,T) \cap C^0([0,T])$ *for a.e.* $x \in \Omega_H$, $i = 1, \ldots, m$,
$\mathbf{z} \in H^1(0,T;L^2(\Omega_H))^m \cap L^\infty(Q)^m$, $\quad \log \mathbf{z} \in L^\infty(Q)^m$,

where we have defined $Q = \Omega_H \times (0,T)$.

Sketch of the proof. The proof of Theorem 3.10 is divided into three parts. In a first step, one fixes v and solves the ODE systems of the gating and ionic concentrations variables, obtaining suitable a priori estimates and qualitative properties of the solution.

In the second step, a reduction technique is used in order to split the degenerate parabolic system into an elliptic equation coupled with a non-degenerate parabolic equation in $L^2(\Omega_H)$, governed by the generator of an analytic semigroup. Considering $I_{ion}(v, \mathbf{w}, \mathbf{z})$ as a known function, we apply a result of maximal regularity in L^p, obtaining the existence and uniqueness of, and estimates for, the potentials u_i, u_e (and thus for $v = u_i - u_e$) in $L^p(0, T; H^2(\Omega_H)) \cap W^{1,p}(0, T; L^2(\Omega_H))$.

These estimates, owing to classical interpolation techniques, provide a crucial bound for v in $L^\infty(Q)$. Then, by choosing the correct functional spaces for $\mathbf{w}, \mathbf{z}$ and v, it is possible to establish the existence and uniqueness of a solution $(v, \mathbf{w}, \mathbf{z})$ for Problem (3.42), using Banach's Fixed Point Theorem.

The main difficulties in the parabolic equation reside in its degenerate structure, which reflects the differences in the anisotropy of the intra- and extracellular tissues, and in the lack of a maximum principle. Moreover, the concentration variables z_i appear as arguments of a logarithm, both in the dynamics of the concentrations and in the ionic currents, and therefore it is necessary to bound $\mathbf{z}$ far from zero.

3.7 Semi-discrete Approximation of the Bidomain Model with FHN Dynamics

We conclude this section mentioning some examples of approximation results for the averaged model $\boldsymbol{P}$; for other approximation results in the context of reaction-diffusion problems, see e.g. [230, 259, 321, 334].

At first, we consider a semi-discrete scheme in space obtained using conforming linear finite elements, (see e.g. [414] for a general introduction to the finite element method). Assuming that Ω_H is a polygonal convex domain in R^3 and $\mathscr{T}_h$ is a family of triangulations associated with a reference polyhedron $\hat{E}$ by an invertible affine maps T_E, for every $E \in \mathscr{T}$; we denote by V_h the finite dimensional space of continuous functions whose restriction to each element of $\mathscr{T}$ are polynomial of degree 1. A semidiscrete problem is obtained by applying a standard Galerkin procedure on V_h to the averaged model (3.34). In [455] various stability results are shown and the following error estimate:

Theorem 3.11. *For a regular and quasi-uniform mesh and a regular initial datum $w_0 \in H^1(\Omega_H)$, denoting by $\boldsymbol{U}_h(t)$ the finite element approximation of the semidiscrete approximation of (3.37) with FitzHugh-Nagumo dynamics, then the following optimal a priori error estimate holds*

$$\mathrm{e}_h^2 := \max_{t \in (0,T)} b\big(\boldsymbol{U}(t) - \boldsymbol{U}_h(t)\big) + \int_0^T a\big(\boldsymbol{U}(t) - \boldsymbol{U}_h(t)\big) \, dt \le Ch^2.$$

We now consider a semi-discrete approximation in time of the averaged model applying the implicit Euler scheme. More precisely, we choose a partition of the time interval $[0, T]$ into N subintervals

$$\mathscr{P} = \{0 = t_0 < t_1 < t_2 < \dots t_{N-1} < t_N = T\}, \text{ with variable step } \tau_n = t_n - t_{n-1}$$

and we set $\tau = max_{1 \leq n \leq N} \ \tau_n$.
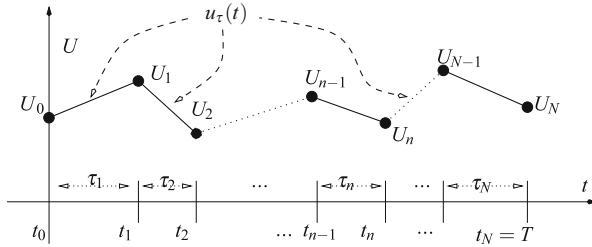
Given $\boldsymbol{U}_0$, we introduce the sequence of variational problems: Find $\boldsymbol{U}_n \in V_h$, $n = 1, \dots, N$ such that

$$b(\frac{\boldsymbol{U}_n - \boldsymbol{U}_{n-1}}{\tau_n}, \hat{\boldsymbol{U}}) + a(\boldsymbol{U}_n, \hat{\boldsymbol{U}}) + F(\boldsymbol{U}_n, \hat{\boldsymbol{U}}) = 0, \quad \forall \hat{\boldsymbol{U}} \in V_h. \qquad (3.72)$$

Considering the discrete solution $\boldsymbol{U}_\tau(t)$ given by the continuous piecewise linear function interpolating the values $\{\boldsymbol{U}_n\}_{n=0}^N$ on the grid $\mathscr{P}$, we have the following error estimate

Theorem 3.12. *For sufficiently regular initial data, the following a priori error estimate between $\boldsymbol{u}$ and $\boldsymbol{U}_\tau$, measured by the natural variational (semi)norms holds:*

$$e_\tau^2 := \max_{t \in (0,T)} b\big(\boldsymbol{U}(t) - \boldsymbol{U}_\tau(t)\big) + \int_0^T a\big(\boldsymbol{U}(t) - \boldsymbol{U}_\tau(t)\big) \, dt \leq C \tau^2,$$

or equivalently

$$\|\sqrt{b(\boldsymbol{U} - \boldsymbol{U}_\tau)}\|_{L^\infty(0,T)} + \|\boldsymbol{U} - \boldsymbol{U}_\tau\|_{L^2(0,T;\mathbb{V})} \leq C \tau,$$

with C independent of τ.

We conclude presenting a result related to a posteriori error estimates. In [32], resorting to the theory developed in [359] for evolution variational problems, a posteriori error estimates were derived for general degenerate evolution equations.

Theorem 3.13. *For sufficiently regular initial data, let e_τ be the error between U and U_τ measured by the natural variational (semi)norm*

$$e_\tau^2 := \max\left[\max_{t\in(0,T)} e^{-2\lambda_g t} b\big(U(t) - U_\tau(t)\big), \int_0^T e^{-2\lambda_g t} a\big(U(t) - U_\tau(t)\big)\, dt\right]$$

with $\lambda_g = \left(\inf_{v\in R} g'(v)\right)^{-}$.

Then applying the theory of [32] to the Bidomain model, the error e_τ can be estimated a posteriori by

$$e_\tau^2 \leq \sum_n \tau_n^2 \mathscr{D}_n + \frac{\lambda_g^2}{2} \sum_n \tau_n^2 \sqrt{b\big(\delta U^n\big)},$$

where $\mathscr{D}_n = a\big(U_n - U_{n-1}\big) + F\big(U_n, U_n - U_{n-1}\big) - F\big(U_{n-1}, U_n - U_{n-1}\big)$,

$$\delta U^n = \frac{U_n - U_{n-1}}{\tau_n}.$$

Chapter 4
Reduced Macroscopic Models: The Monodomain and Eikonal Models

In the Bidomain model (3.42), the transmembrane potential v during the excitation phase of the heartbeat exhibits a steep propagating layer spreading throughout the myocardium with a thickness of about 0.5 mm. At every point of the cardiac domain, this upstroke phase lasts about 1 ms. Therefore, the simulation of the excitation process requires the numerical solution of problems with small space and time steps (of the order of 0.1 mm and 0.01 ms). A further inconvenient of the Bidomain model is its severe ill-conditioning, mainly due to the pure Neumann boundary conditions, of the linear systems deriving from its discretization. The solution of such linear systems with iterative methods such as the Conjugate Gradient, preconditioned by standard cheap preconditioners (ILU or SSOR), is not effective, thus more sophisticated computational demanding preconditioners are required (see Chaps. 7 and 8).

All these facts constraint 3–D simulations to limited blocks with dimensions of a few cm, see [101, 102, 104, 226]. For large scale simulations involving the whole ventricles, the computer memory and time requirements become excessive and less demanding approximations have been developed, such as Monodomain and Eikonal models.

4.1 Linear Anisotropic Monodomain Model

In order to reduce further the computational load many large scale simulations have been performed using the so-called Monodomain model; it is well known that if the two media have the same anisotropy ratio then the Bidomain system reduces to the Monodomain model. We remark that this is not a physiological case, as it clearly follows from well established experimental evidence. We shall present an interesting derivation of a reduced Bidomain model, which does not make such a priori assumption (see also [99, 269]) and that we will still call Monodomain model.

Denoting by $J_{tot} = \mathbf{j_i} + \mathbf{j_e}$ the total current flowing in the two media and by $D = D_i + D_e$ the conductivity of the bulk medium, since $J_{tot} = -D_i \nabla u_i - D_e \nabla u_e$, substituting $u_i = v + u_e$, we obtain

$$\nabla u_e = -D^{-1} D_i \nabla v - D^{-1} J_{tot}. \tag{4.1}$$

Therefore, the second equation in the Bidomain system (3.42) can be written as

$$-c_m \frac{\partial v}{\partial t} + \text{div}(D_e D^{-1} D_i \nabla v) + \text{div}(D_e D^{-1} J_{tot}) - i_{ion}(v, w, c) = I_{app}^e. \tag{4.2}$$

Since the conductivity tensors are given by (3.41), then

$$D_e D^{-1} = \mu_l^e I + (\mu_t^e - \mu_l^e)\mathbf{a}_t(\mathbf{x})\mathbf{a}_t^T(\mathbf{x}) + (\mu_n^e - \mu_l^e)\mathbf{a}_n(\mathbf{x})\mathbf{a}_n^T(\mathbf{x}), \tag{4.3}$$

with $\mu_{l,t,n}^e = \sigma_{l,t,n}^e/(\sigma_{l,t,n}^e + \sigma_{l,t,n}^i)$. Assuming constant conductivity coefficients and taking into account that $\text{div} J_{tot} = I_{app}^i + I_{app}^e$, we have

$$\begin{aligned}
\text{div}(D_e D^{-1} J_{tot}) &= \mu_l^e \, \text{div} \, J_{tot} + (\mu_t^e - \mu_l^e) \, \text{div}[\mathbf{a}_t(\mathbf{x})\mathbf{a}_t^T(\mathbf{x}) J_{tot}] \\
&\quad + (\mu_n^e - \mu_l^e) \, \text{div}[\mathbf{a}_n(\mathbf{x})\mathbf{a}_n^T(\mathbf{x}) J_{tot}] \\
&= \mu_l^e(I_{app}^i + I_{app}^e) + (\mu_t^e - \mu_l^e) \, \text{div}[\mathbf{a}_t(\mathbf{x})\mathbf{a}_t^T(\mathbf{x}) J_{tot}] \\
&\quad + (\mu_n^e - \mu_l^e) \, \text{div}[\mathbf{a}_n(\mathbf{x})\mathbf{a}_n^T(\mathbf{x}) J_{tot}].
\end{aligned} \tag{4.4}$$

From (4.1) it follows $-D_e D^{-1} D_i \nabla v = D_e D^{-1} J_{tot} + D_e \nabla u_e$, so we have the flux relationship

$$-\mathbf{n}^T D_e D^{-1} D_i \nabla v = \mathbf{n}^T D_e D^{-1} J_{tot} + \mathbf{n}^T D_e \nabla u_e. \tag{4.5}$$

Using the split form (4.3), the first term on the right hand side can be written as

$$\begin{aligned}
\mathbf{n}^T(D_e D^{-1} J_{tot}) =&\mu_l^e \mathbf{n}^T J_{tot} + (\mu_t^e - \mu_l^e)(\mathbf{n}^T \mathbf{a}_t)(\mathbf{a}_t^T J_{tot}) \\
&+ (\mu_n^e - \mu_l^e)(\mathbf{n}^T \mathbf{a}_n)(\mathbf{a}_n^T J_{tot}).
\end{aligned} \tag{4.6}$$

The insulating conditions $\mathbf{n}^T \mathbf{j_i} = \mathbf{n}^T \mathbf{j_e} = 0$ imply $\mathbf{n}^T J_{tot} = 0$, i.e. J_{tot} is tangent to Γ_H, and assuming that fibers are also tangent to Γ_H we have $\mathbf{n}^T \mathbf{a}_n = 0$ and $\mathbf{a}_t^T J_{tot} = 0$; substituting these conditions in (4.6), it follows

$$\mathbf{n}^T D_e D^{-1} D_i \nabla v = 0. \tag{4.7}$$

We remark that for media having equal anisotropic ratio, i.e. $\sigma_l^e/\sigma_l^i = \sigma_t^e/\sigma_t^i = \sigma_n^e/\sigma_n^i$, we have $\mu_l^e = \mu_t^e = \mu_n^e$. Thus, the two additional terms in (4.4), related to the projections of J_{tot} on the directions across fiber, disappear. Disregarding these two additional source terms $\mathbf{a}_t^T J_{tot}$ and $\mathbf{a}_n^T J_{tot}$, we have $\text{div}(D_e D^{-1} J_{tot}) \approx$

$\mu_l^e(I_{app}^i + I_{app}^e)$. Substituting this approximation in (4.2) and considering the boundary condition (4.7), we obtain an approximate model consisting in a single parabolic reaction-diffusion equation for v and coupled with the same gating system

$$\begin{cases} c_m \dfrac{\partial v}{\partial t} - \operatorname{div}(D_m \nabla v) + i_{ion}(v, w, c) = I_{app}^m & \text{in } \Omega_H \times (0, T) \\ \dfrac{\partial w}{\partial t} - R(v, w) = 0, \dfrac{\partial c}{\partial t} - S(v, w, c) = 0 & \text{in } \Omega_H \times (0, T) \\ \mathbf{n}^T D_m \nabla v = 0 & \text{in } \Gamma_H \times (0, T) \\ v(\mathbf{x}, 0) = v_0(\mathbf{x}), \quad w(\mathbf{x}, 0) = w_0(\mathbf{x}), \quad c(\mathbf{x}, 0) = c_0(\mathbf{x}) & \text{in } \Omega_H, \end{cases}$$
(4.8)

with the conductivity tensor $D_m = D_e D^{-1} D_i$, $I_{app}^m = \left(I_{app}^i \sigma_l^e - I_{app}^e \sigma_l^i \right) / (\sigma_l^e + \sigma_l^i)$. The evolution equation determines the distribution of $v(\mathbf{x}, t)$ and then the extracellular potential distribution u_e is derived by solving the elliptic boundary value problem

$$\begin{cases} -\operatorname{div}(D \nabla u_e) = \operatorname{div}(D_i \nabla v) + I_{app}^i + I_{app}^e & \text{in } \Omega_H, \\ -\mathbf{n}^T D \nabla u_e = \mathbf{n}^T D_i \nabla v & \text{on } \Gamma_H. \end{cases}$$
(4.9)

We refer to the system consisting of Eqs. (4.8) and (4.9) as the anisotropic Monodomain model. We remark that the Bidomain and the Monodomain model are described by a system of a parabolic equation coupled with an elliptic equation, but in the latter the evolution equation is fully uncoupled with the elliptic one in the case of an insulated domain Ω_H.

4.2 Eikonal Models

Another route to avoid the high computational costs of the full Bidomain model is based on the use of *eikonal models* for the evolution of the excitation wavefront surface.

With these models the simulation of the activation sequence in large volumes of cardiac tissue has become computationally practical but at the price of a loss of fine details concerning the thin layer where the upstroke of the action potential occurs. These numerical simulations are based on laws describing the macroscopic kinetic mechanism of the spreading of the excitation wavefronts, and do not require a fine spatial and temporal resolution.

We now outline the derivation of this kind of approximated models. The FitzHugh–Nagumo approximation of the membrane kinetics is very useful for a qualitative analysis of the non-linear dynamics of the R-D system. As we shall focus only the excitation phase, we can neglect the recovery variable w hence $i_{ion} = g(v)$.

The resulting simplified ionic model is widely used for gaining general insight into wave propagation in the cardiac excitable medium. Although this model is not suitable in a quantitative detailed study, at a fine scale, of the upstroke of the action potential v through the excitation wavefront, it is nevertheless appropriate if we are interested in the large scale behavior of the front-like solution. We note that during the excitation phase of the heart beat the main feature, at a macroscopic level, is the excitation wavefront configuration and its motion. In order to investigate the propagation of this wavefront we must analyze more deeply the internal layer of v which affects the spreading.

Denoting by χ the membrane surface area per unit volume of the tissue, by C_m the membrane capacitance per unit area of the membrane surface, and by I_{ion} the ionic current per unit area of the membrane surface, that is carried by the flow of ions across the membrane, then the transmembrane current i_m per unit volume is given by

$$i_m = \left(C_m \frac{\partial v}{\partial t} + I_{ion} \right) \chi.$$

We recall that the so-called fast sodium current I_{Na} is the main current responsible for the depolarization of cardiac cells during the excitation phase of the transmembrane action potential. Experimental findings in measuring I_{Na} in different cardiac preparations justify the modeling of the sodium current mechanisms by means of gating equations of the Hodgkin-Huxley type, see e.g. [193, 308] for guinea pig, [367] for rat, [473] for rabbit, [209, 521] for human myocytes. Hence I_{Na} is represented by

$$I_{Na} = \bar{G}_{Na} \, m^3 \, h \, j \, (v - v_{Na}),$$

where the m, h, j variables, modeling the sodium conductance dynamics, referred to as the sodium activation and inactivation, satisfy the equations

$$\frac{dm}{dt} = \frac{m_\infty(v) - m}{\tau_\infty(v)}, \quad \frac{dh}{dt} = \frac{h_\infty(v) - h}{\tau_\infty(v)}, \quad \frac{dj}{dt} = \frac{j_\infty(v) - j}{\tau_\infty(v)}. \tag{4.10}$$

In the depolarization phase the time constant of the activation gate m for ventricular cells is about 0.2 ms, whereas the inactivation time constants are of order 50 and 300 ms for h and j gates, respectively. Thus, we assume that the membrane obeys the simplified time-independent ionic current-voltage relation, obtained by considering an instantaneous change of sodium conductance, i.e. taking $m = m_\infty(v)$, $h = h_\infty(v_r) \simeq 0.98$, $j = j_\infty(v_r) \simeq 0.99$, where v_r is the resting potential. In this simplified approximation, the ionic current model is given by the non-linear current-voltage law

$$I_{ion}(v) = I_{Na}(v) + I_L(v),$$
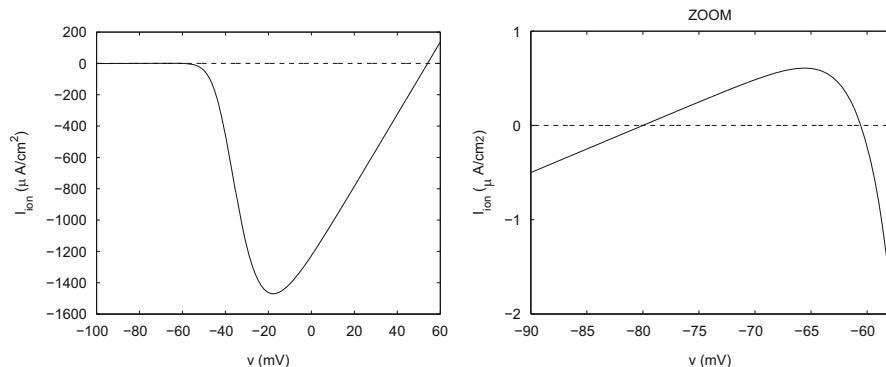
Fig. 4.1 Cubic-like behavior of the ionic current per unit area of membrane surface I_{ion} (μA/cm^2) as a function of the transmembrane potential v (mV)

with

$$I_{Na}(v) = \bar{G}_{Na} m_\infty(v)^3 (v - v_{Na}), \quad I_L = \bar{G}_L (v - v_L),$$

where I_L is the leakage current. Using the $\bar{G}_{Na}$, v_{Na} and $m_\infty(v)$ expressions in the sodium current of the LR1 model [308] and choosing $\bar{G}_L = 0.05 \, \text{mS/cm}^2$, $V_l = -80 \, \text{mV}$, the behavior of $I_{ion}(v)$ is of cubic-like type as displayed in Fig. 4.1, i.e. it has the following properties:

1. $I_{ion} \in C^1(\mathbb{R})$;
2. There exist only three zeros $v_r < v_{th} < v_p$;
3. $I'_{ion}(v_r) > 0$ and $I'_{ion}(v_p) < 0$;
4. $\int_{v_r}^{v_p} I_{ion}(v) dv < 0$.

We want to investigate the approximate kinematic properties of traveling wavefront solutions of the Bidomain system (3.42), neglecting some details of the transmembrane action potential, but retaining its essential features. In order to gain this information, we carry out a singular perturbation analysis of an appropriately scaled form of system (3.42). Our interest concerns the description of the *stationary* or *regular* propagation of the excitation wavefronts, that is, the spreading away from the initial phase related to the starting stimuli or from front-front or front-boundary collisions.

In the *stationary* propagation, we can scale the **x** and t variables, taking spatial (L) and temporal (T) scale factors in such a way that the corresponding mean wavefront velocity becomes of unitary order. In this phase of the excitation process, the velocity varies between 0.3 and 0.7 mm/ms, according as it is measured longitudinally of transversally to the fiber direction. Since the upstroke of the transmembrane potential lasts about 2 ms, for an average propagation velocity of $\theta = 0.5$ mm/ms, we estimate an average thickness of the excitation layer 1 mm. It follows that a characteristic time $T = 20$ ms is the average time required by the

traveling impulse to cover a characteristic distance of $L = 1\,\mathrm{cm}$ corresponding to the transmural thickness of the ventricular wall. Therefore, rescaling the x and t variables using L and T as

$$\hat{x} = \frac{x}{L} \qquad \hat{t} = \frac{t}{T},$$

and setting

$$\bar{g}_{Na} = \chi \bar{G}_{Na} \qquad g(v) = -\frac{I_{ion}}{\bar{g}_{Na}},$$

the rescaled Bidomain system becomes

$$\begin{cases} \dfrac{c_m}{\bar{g}_{Na}T} \dfrac{\partial \hat{v}}{\partial \hat{t}} = \mathrm{div}_{\hat{x}} \left(\dfrac{1}{\bar{g}_{Na}L^2} D_i \nabla_{\hat{x}} \hat{u}_i \right) + g(\hat{v}) & \text{in } \Omega_H \\[3mm] -\dfrac{c_m}{\bar{g}_{Na}T} \dfrac{\partial \hat{v}}{\partial \hat{t}} = \mathrm{div}_{\hat{x}} \left(\dfrac{1}{\bar{g}_{Na}L^2} D_e \nabla_{\hat{x}} \hat{u}_e \right) - g(\hat{v}) & \text{in } \Omega_H. \end{cases} \qquad (4.11)$$

Using the following typical parameters values

$$C_m = 1\,\mu\mathrm{F/cm^2}, \ \bar{G}_{Na} = 20\,\mathrm{ms/cm^2}, \ \chi = 10^3\,\mathrm{cm^{-1}},$$

and recalling that the conductivity coefficients $\sigma_{l,t,n}^{i,e}$ are in the range $0.1\text{–}2\,\mathrm{mS/cm^2}$, we obtain

$$\frac{c_m}{\bar{g}_{Na}T} = \epsilon\tau_m, \qquad \frac{\sigma_{l,t,n}^{i,e}}{\bar{g}_{Na}L^2} = \epsilon^2 \hat{\sigma}_{l,t,n}^{i,e},$$

with ϵ of order 10^{-2}, τ_m of unitary order and $\hat{\sigma}_{l,t,n}^{i,e}$ in the range $0.1\text{–}1$.

Hence, the macroscopic dimensionless form of the Bidomain model can be written as the following singularly perturbed reaction-diffusion (R-D) system

$$\begin{cases} \epsilon\tau_m \dfrac{\partial \hat{v}}{\partial \hat{t}} = \epsilon^2 \,\mathrm{div}_{\hat{x}}(\hat{D}_i \nabla_{\hat{x}} \hat{u}_i) + g(\hat{v}) & \text{in } \Omega_H \\[3mm] -\epsilon\tau_m \dfrac{\partial \hat{v}}{\partial \hat{t}} = \epsilon^2 \,\mathrm{div}_{\hat{x}}(\hat{D}_e \nabla_{\hat{x}} \hat{u}_e) - g(\hat{v}) & \text{in } \Omega_H. \end{cases} \qquad (4.12)$$

In the following, we will denote by $v^\varepsilon = \hat{v}$, $u_{i,e}^\varepsilon = \hat{u}_{i,e}$, and for the sake of simplicity in the notations, we will drop all the ˆsymbols out elsewhere.

The R-D systems with excitable dynamics are studied by mathematical tools from singular perturbation theory, see e.g. [174, 273]. Given the previous singular perturbation structure, u_i^ε, u_e^ε diffuse quite slowly, while the reaction takes place much faster; hence, the development of a moving layer associated with a traveling wavefront solution is to be expected. Exploiting the singular perturbation approach,

we can derive anisotropic geometric evolution laws capturing the asymptotic behavior of traveling wavefront solutions of the R-D system (4.12) (see [37, 39, 112, 113, 268, 271–273] and for isotropic media [492]).

Assuming that the excitation propagates in fully recovered tissue, a monotonic temporal behavior of v^ε is expected; then the excitation wavefront $S_\varepsilon(t)$ can be represented by the level surface of the transmembrane potential of value $(v_r + v_p)/2$, i.e.:

$$S_\varepsilon(t) = \{\mathbf{x} \in \Omega_H, \ v_\varepsilon(\mathbf{x}, t) = (v_r + v_p)/2\}. \tag{4.13}$$

We define the *activation time* $\psi_\varepsilon(\mathbf{x})$ as the time instant at which the potential v^ε at $\mathbf{x}$ reaches the value $(v_r + v_p)/2$. Then the excitation wavefront $S_\varepsilon(t)$ is also represented by the level surface of the activation time at the time instant t, i.e.:

$$S_\varepsilon(t) = \{\mathbf{x} \in \Omega_H, \ \psi_\varepsilon(\mathbf{x}) = t\}. \tag{4.14}$$

Let

$$q_{i,e}(\mathbf{x}, \boldsymbol{\xi}) = \boldsymbol{\xi}^T D_{i,e}(\mathbf{x}) \boldsymbol{\xi} \tag{4.15}$$

be the conductivity coefficient at a point $\mathbf{x}$ in the intra- and extracellular media, respectively, measured along the direction of the unit vector $\boldsymbol{v}$. We define the harmonic mean of the quadratic forms associated with the conductivity tensors $D_{i,e}$ by

$$q(\mathbf{x}, \boldsymbol{\xi}) = (q_i(\mathbf{x}, \boldsymbol{\xi})^{-1} + q_i(\mathbf{x}, \boldsymbol{\xi})^{-1})^{-1}. \tag{4.16}$$

The non-linear form $q(\mathbf{x}, \boldsymbol{\xi})$ admits the following representation

$$q(\mathbf{x}, \boldsymbol{\xi}) = \boldsymbol{\xi}^T Q(\mathbf{x}, \boldsymbol{\xi}) \boldsymbol{\xi} \quad \text{with} \quad Q(\mathbf{x}, \boldsymbol{\xi}) = \frac{q_i(\mathbf{x}, \boldsymbol{\xi})^2 D_e(\mathbf{x}) + q_e(\mathbf{x}, \boldsymbol{\xi})^2 D_i(\mathbf{x})}{[q_i(\mathbf{x}, \boldsymbol{\xi}) + q_e(\mathbf{x}, \boldsymbol{\xi})]^2}, \tag{4.17}$$

which gives the conductivity measured along the direction $\boldsymbol{\xi}$ of the bulk medium composed by coupling in series the media (i) and (e). Then we introduce the following indicatrix function

$$\Phi(\mathbf{x}, \boldsymbol{\xi}) = \sqrt{q(\mathbf{x}, \boldsymbol{\xi})}. \tag{4.18}$$

Under the assumptions 1, 2, 3, 4 let (c,a) be the unique bounded solution of the eigenvalue problem (see Sect. 3.1.3):

$$\begin{cases} a'' + c\, a' + g(a) = 0 \\ a(-\infty) = v_p\,, \quad a(\infty) = v_r\,, \quad a(0) = (v_p + v_r)/2. \end{cases} \tag{4.19}$$

A formal inner asymptotic expansion in powers of ε of $(u_i^\varepsilon, u_e^\varepsilon)$ solution of (4.12) and $v^\varepsilon = u_i^\varepsilon - u_e^\varepsilon$ can be performed using two different types of variable stretching. Let $\boldsymbol{\nu}$ be the Euclidean unit vector normal to the wavefront $S_\varepsilon(t)$ oriented toward the resting tissue and for $\mathbf{s}(t) \in S_\varepsilon(t)$ we define the vector $\mathbf{n}_\Phi(\mathbf{s}) = \Phi_\xi(\mathbf{s}, \boldsymbol{\nu})$. As in [39] we use a Lagrangian point of view and we consider the moving reference $(\mathbf{s}, y, \tau)$ defined by

$$y = \frac{\eta}{\varepsilon} \quad , \quad \mathbf{x} = \mathbf{s}(t) + \eta\, \mathbf{n}_\Phi(\mathbf{s}(t)), \quad \tau = t, \quad \forall \mathbf{s}(t) \in S_\varepsilon(t), \tag{4.20}$$

i.e. stretching the space coordinate along the $\mathbf{n}_\Phi$ direction.

Using the moving frame (4.20) the asymptotic expansion for the Bidomain model (4.12) shows that (see [39], Appendix B), at least formally, the front associated with (4.13) moves along the relative normal vector $\mathbf{n}_\Phi$ with velocity $\theta_\varepsilon(\mathbf{n}_\Phi)$ given at any $\mathbf{s}(t) \in S_\varepsilon(t)$ by:

$$\theta_\varepsilon(\mathbf{n}_\Phi) = \frac{c - \varepsilon\, \mathrm{div}\, \mathbf{n}_\Phi}{\tau_m} + \mathcal{O}(\varepsilon^2), \tag{4.21}$$

where c is related to the traveling wave solution a of (4.19). Since $\mathbf{n}_\Phi \cdot \boldsymbol{\nu} = \Phi(\mathbf{s}, \boldsymbol{\nu})$, the velocity $\theta_\epsilon(\boldsymbol{\nu})$ in the Euclidean normal direction $\boldsymbol{\nu}$ of $S_\varepsilon(t)$ is given by $\Phi(\mathbf{s}, \boldsymbol{\nu})\theta_\epsilon(\mathbf{n}_\Phi)$ then:

$$\theta_\epsilon(\boldsymbol{\nu}) = \frac{\Phi(\mathbf{s}, \boldsymbol{\nu})}{\tau_m}(c - \varepsilon\, \mathrm{div}\, \Phi_\xi(\mathbf{s}, \boldsymbol{\nu})) + \mathcal{O}(\varepsilon^2). \tag{4.22}$$

Therefore dropping $\mathcal{O}(\varepsilon^2)$ terms, the front behaves as an hypersurface $S(t)$, propagating with the anisotropic geometric law with normal velocity $\theta(\boldsymbol{\nu})$ given by:

$$\theta(\boldsymbol{\nu}) = \frac{\Phi(\mathbf{s}, \boldsymbol{\nu})}{\tau_m}(c - \varepsilon\, \mathrm{div}\, \Phi_\xi(\mathbf{s}, \boldsymbol{\nu})). \tag{4.23}$$

Equations of this type are also called *eikonal-curvature models* since $k_\Phi = \mathrm{div}\, \mathbf{n}_\Phi = \mathrm{div}\, \Phi_\xi(\mathbf{s}, \boldsymbol{\nu})$ is the anisotropic mean curvature with respect to a suitable Finsler metric; see [15, 37–39] for definitions and properties.

A formal derivation based on an Eulerian point of view was developed in [112, 113]; in this approach the new frame $(\boldsymbol{\chi}, \tau)$ is defined by stretching the time variable with respect to the activation time, i.e.:

$$\boldsymbol{\chi} = \mathbf{x}, \qquad \tau = \frac{t - \psi_\epsilon(\mathbf{x})}{\varepsilon}. \tag{4.24}$$

Using the fixed Eulerian frame (4.24) and developing the asymptotic expansion of the Bidomain model (4.12), we obtain the following expression, equivalent to formulae (59) and (61) derived in [113]:

$$\frac{1}{\Phi(\mathbf{x}, \nabla \psi_\varepsilon)} \left(\tau_m + \varepsilon \operatorname{div} \left(\Phi(\mathbf{x}, \nabla \psi_\varepsilon) \Phi_\xi(\mathbf{x}, \nabla \psi_\varepsilon) \right) \right) = c + \mathcal{O}(\varepsilon^2). \qquad (4.25)$$

Since

$$\boldsymbol{v} = \frac{\nabla \psi_\varepsilon}{|\nabla \psi_\varepsilon|} \quad \text{and} \quad \theta_\varepsilon(\boldsymbol{v}) = \frac{1}{|\nabla \psi_\varepsilon|},$$

we obtain

$$\frac{\theta_\varepsilon(\boldsymbol{v})}{\Phi(\mathbf{x}, \boldsymbol{v})} \left(\tau_m + \varepsilon \operatorname{div} \left(\frac{\Phi(\mathbf{x}, \boldsymbol{v}) \Phi_\xi(\mathbf{x}, \boldsymbol{v})}{\theta_\varepsilon(\boldsymbol{v})} \right) \right) = c + \mathcal{O}(\varepsilon^2), \qquad (4.26)$$

or equivalently

$$\tau_m \frac{\theta_\varepsilon(\boldsymbol{v})}{\Phi(\mathbf{x}, \boldsymbol{v})} = c - \varepsilon \operatorname{div} \Phi_\xi(\mathbf{x}, \boldsymbol{v}) + \varepsilon \frac{\Phi(\mathbf{x}, \boldsymbol{v})}{\theta_\varepsilon(\boldsymbol{v})} \nabla \left(\frac{\theta_\varepsilon(\boldsymbol{v})}{\Phi(\mathbf{x}, \boldsymbol{v})} \right) \cdot \Phi_\xi(\mathbf{x}, \boldsymbol{v}) + \mathcal{O}(\varepsilon^2). \qquad (4.27)$$

Since both Eqs. (4.22)–(4.27) imply $\dfrac{\theta_\varepsilon(\boldsymbol{v})}{\Phi(\mathbf{x}, \boldsymbol{v})} = c + \mathcal{O}(\varepsilon)$, then the two eikonal equations (4.22), (4.27) are equivalent up to second order terms. Equations (4.23) and (4.27), disregarding the $\mathcal{O}(\varepsilon^2)$ term, are called respectively *eikonal–curvature* and *eikonal–diffusion* equations, [121, 522].

The rigorous justification of the connection between the evolution of a suitable level set of v and the surface flowing under geometric evolution law, remains to our knowledge an open problem. A partial rigorous characterization in the Γ−convergence framework was obtained for the stationary Bidomain model in [4]. We introduce the family of vectorial integral Lyapunov functionals dependent on the couple $\boldsymbol{u}^\varepsilon := (u_i, u_e)$

$$\mathcal{F}^\varepsilon(\boldsymbol{u}) := \varepsilon \int_\Omega \left(D_i \nabla u_i \cdot \nabla u_i + D_e \nabla u_e \cdot \nabla u_e \right) dx \\ + \frac{1}{\varepsilon} \int_\Omega G(u_i - u_e) \, dx, \qquad (4.28)$$

where $G' = g$.

The degenerate reaction-diffusion system associated with (4.12) in the couple of unknowns $\boldsymbol{u} := (u_i^\varepsilon, u_e^\varepsilon)$ can be obtained by taking the gradient flow of the Lyapunov functional with respect to the positive but degenerate bilinear form in $L^2(\Omega; \mathbb{R}^2)$

$$b(\boldsymbol{u}, \boldsymbol{w}) := \int_{\Omega} (u_i - u_e) \, (w_i - w_e) \, dx, \quad \boldsymbol{u} = (u_i, u_e), \quad \boldsymbol{w} = (w_i, w_e).$$

This yields the following system of variational evolution equations

$$b(\partial_t \boldsymbol{u}^{\varepsilon}, \boldsymbol{v}) + \delta \mathscr{F}^{\varepsilon}(\boldsymbol{u}^{\varepsilon}, \boldsymbol{v}) = 0 \quad \forall \boldsymbol{v} \in H^1(\Omega; \mathbb{R}^2), \tag{4.29}$$

where $\partial_t \boldsymbol{u}^{\varepsilon} = \left(\dfrac{\partial u_i}{\partial t}, \dfrac{\partial u_e}{\partial t} \right)$ and $\delta \mathscr{F}^{\varepsilon}(\boldsymbol{u}, \cdot)$ is the Euler-Lagrange first variation of the functional $\mathscr{F}^{\varepsilon}$ [201], which is the variational formulation of (4.12). Since the anisotropic curvature k_{Φ} corresponds to the first variation of the anisotropic surface energy integral functional associated with Φ given by (4.18) see [38], in order to justify the form of the anisotropic curvature term, we have studied in [4] the asymptotic limit, as $\varepsilon \downarrow 0$, of the stationary problem associated with the singular reaction–diffusion system (4.12) for a function $g = G'$, where now G is a potential having wells of equal depth. More precisely, the $\Gamma-$limit of Lyapunov functionals associated with the family (4.28) is a surface integral functional whose energy density is a continuous family of norms $\Phi^*(\mathbf{x}, \cdot)$ characterized by solving a localized minimization problem, see [4] for details.

Formal asymptotic results in the Bidomain case (see [39, 112, 113]) suggest that $\Phi^*(\mathbf{x}, \nu) = \Phi(\mathbf{x}, \nu) = \sqrt{q(x, \nu)}$. On the other hand, in some pathophysiological setting, such as regional ischemia and a healed infarction, the corresponding conductivity tensors D_i, D_e yield a nonconvex Φ: since Φ^* is always convex, in this case the previous equality does not hold. It would be interesting to check if the convex envelope of Φ is a good substitute in this case.

4.3   Relaxed Non-linear Anisotropic Monodomain Model

We can easily see that, rescaling as in (4.12) the reaction-diffusion equation related to the Monodomain model (4.8) and using formal asymptotic expansions as before, the anisotropic evolution law of the front does not coincide with that derived from the Bidomain model. In fact, although the eikonal-curvature equation up to terms of order $O(\varepsilon^2)$ presents the same structure

$$\theta(\boldsymbol{v}) = \frac{\Phi(\mathbf{s}, \boldsymbol{v})}{\tau_m} (c - \varepsilon \operatorname{div} \Phi_{\xi}(\mathbf{s}, \boldsymbol{v})), \tag{4.30}$$

the non-linear function $\Phi(\mathbf{x}, \boldsymbol{\xi}) = \sqrt{q(\mathbf{x}, \boldsymbol{\xi})}$ for the Monodomain model is defined by

$$q(\mathbf{x}, \boldsymbol{\xi}) = \boldsymbol{\xi}^T D_m(\mathbf{x}) \boldsymbol{\xi} \quad \text{where} \quad D_m(\mathbf{x}) = D_e(\mathbf{x})(D_i(\mathbf{x}) + D_e(\mathbf{x}))^{-1} D_i(\mathbf{x}), \tag{4.31}$$

i.e. D_m is the harmonic mean tensor associated with $D_{i,e}$.

We now consider the following Monodomain model with non-linear diffusion term, which we call the *relaxed Monodomain model*

$$\frac{\partial v}{\partial t} - \frac{1}{\varepsilon}\, g(v) - \varepsilon \, \text{div} \, (Q(\mathbf{x}, \nabla v)\nabla v) \; = I_{app}, \tag{4.32}$$

with $Q(\mathbf{x}, \boldsymbol{\xi})$ defined in (4.17) and written explicitly in terms of the conductivity tensors as

$$Q(\mathbf{x}, \boldsymbol{\xi}) := \left(\frac{\boldsymbol{\xi}^T D_i(\mathbf{x})\boldsymbol{\xi}}{\boldsymbol{\xi}^T D(\mathbf{x})\boldsymbol{\xi}} \right)^2 D_e(\mathbf{x}) + \left(\frac{\boldsymbol{\xi}^T D_e(\mathbf{x})\boldsymbol{\xi}}{\boldsymbol{\xi}^T D(\mathbf{x})\boldsymbol{\xi}} \right)^2 D_i(\mathbf{x}), \qquad D := D_i + D_e. \tag{4.33}$$

The diffusion term is non-linear except when $D_e = \lambda D_i$, with a constant $\lambda \in \mathbb{R}$, i.e. for equal anisotropic ratio of the two media, $Q(\mathbf{x}, \boldsymbol{\xi}) = \frac{\lambda}{1+\lambda} D_i(\mathbf{x})$.

Proceeding by formal asymptotic expansions (see [39] Appendix A), the *relaxed Monodomain model* admits the same eikonal-curvature equation associated with the Bidomain model. The non-linear conductivity tensor of the medium $Q(\mathbf{x}, \nabla v)$, being homogeneous of degree zero in the second variable, is a function of the local direction of propagation of the front-like solution given by the unit vector $\nabla v/|\nabla v|$. In [39], we show that the eikonal-curvature equation as an approximate model for describing the evolution of the relaxed transmembrane potential v can be justified rigorously by estimating the distance between a suitable level set of the relaxed evolution v solution of (4.32) and the surface flowing under the geometric law (4.23). We observe here that a suitable convexity property of Φ is crucial for this rigorous result (see [39] for details). Such a property is true in a wide range of physiological choices but is not guaranteed for generic choices of matrices D_i, D_e. Pathological anisotropies, e.g., modeling ischemic tissue can lead to a nonconvex Φ, hence to a not well-posed relaxed model. This issue requires further study since it could be related to mechanisms of reentry phenomena associated with cardiac arrhythmias in presence of ischemic substrates (see [16]).

4.4   Dimensional Form of the Reduced Models

Recalling the definition of the function Φ in (4.18), the motion of the excitation wavefront is described by the following kinetic equation

$$\theta(\boldsymbol{v}) = \Phi(\mathbf{x}, \boldsymbol{v}) \left(\rho - \frac{1}{c_m}\, \text{div}\, \Phi_\xi(\mathbf{x}, \boldsymbol{v}) \right), \tag{4.34}$$

which is the dimensional form of Eq. (4.23). In terms of the activation time $\psi(\mathbf{x})$, since $\boldsymbol{v} = \frac{\nabla\psi}{|\nabla\psi|}$ and thanks to the homogeneity properties of Φ and Φ_ξ, we obtain the

Eikonal-Curvature equation (see (4.23) for the dimensionless form)

$$-\frac{1}{c_m}\Phi(\mathbf{x}, \nabla\psi(\mathbf{x})) \operatorname{div}\left(\Phi_\xi(\mathbf{x}, \nabla\psi(\mathbf{x}))\right) + \rho\Phi(\mathbf{x}, \nabla\psi(\mathbf{x})) = 1 \qquad \text{in } \Omega_H.$$

$$(4.35)$$

An equivalent formulation of (4.34) can be derived using the level set approach, in terms of the zero level set of a function $w(\mathbf{x}, t)$. Setting the depolarized cardiac region at time t by

$$H_d(t) = \{\mathbf{x} \in \Omega_H : \ t < \psi(\mathbf{x})\}$$

and considering a function $w(\mathbf{x}, t)$ positive inside $H_d(t)$ and negative outside, the excitation wavefront $S(t)$ at time t can be represented as

$$S(t) = \partial H_d(t) = \{\mathbf{x} \in \Omega_H : \ w(\mathbf{x}, t) = 0\}.$$

Denoting as previously by ν the normal to the excitation wavefront pointing toward the resting region, we have that

$$\nu = -\frac{\nabla w}{|\nabla w|}.$$

Since the normal velocity can be now written as

$$\theta(\nu) = -\frac{\partial_t w}{\nu^T \nabla w},$$

Eq. (4.34) becomes

$$\frac{\partial w}{\partial t} = \Phi(\mathbf{x}, \nabla w)\left(\rho + \frac{1}{c_m}\operatorname{div}\Phi_\xi(\mathbf{x}, \nabla w)\right).$$

$$(4.36)$$

Eikonal-Diffusion equation (see (4.25) for the dimensionless form)

$$-\frac{1}{c_m}\operatorname{div}\left(\Phi(\mathbf{x}, \nabla\psi(\mathbf{x}))\Phi_\xi(\mathbf{x}, \nabla\psi(\mathbf{x}))\right) + \rho\Phi(\mathbf{x}, \nabla\psi(\mathbf{x})) = 1 \qquad \text{in } \Omega_H.$$

$$(4.37)$$

We remark that, in isotropic homogeneous media ($D_i = \sigma_i I$ and $D_e = \sigma_e I$), the propagation velocity $\theta(\nu)$ along the normal ν of a plane activation wavefront is derived from (4.35) dropping the curvature term, i.e.

$$\rho\Phi(\nabla\psi) = \rho|\nabla\psi|\Phi(\nu) = 1,$$

thus

$$\theta(v) = \frac{1}{|\nabla \psi|} = \rho \Phi(v) = \rho \sqrt{\sigma}, \quad \text{with} \quad \sigma = \frac{\sigma_i \sigma_e}{\sigma_i + \sigma_e}.$$

The membrane constant ρ can be computed analytically in the case of Fitzhugh equation. In the case of complex membrane models, in order to estimate ρ, one considers the propagation of the action potential along a one dimensional fiber. For given membrane area per unit volume χ and conductivity coefficient σ, one solves numerically the cable equation

$$\chi \left(C_m \frac{\partial v}{\partial t} + I_{ion} \right) = \sigma \frac{\partial^2 v}{\partial x^2},$$

coupled with the membrane model considered. Then, estimating the steady velocity of the action potential θ along the cable and the conductivity coefficient σ, we derive $\rho = \frac{\theta}{\sqrt{\sigma}}$.

While we have focused so far on the use of reduced models for the excitation phase, we note that the linear anisotropic Monodomain model and the relaxed Monodomain model could also be used as reduced models in all phases of the heartbeat. These two models in dimensional form are

Linear Anisotropic Monodomain model

$$\begin{cases} c_m \dfrac{\partial v}{\partial t} - \text{div}(D_m \nabla v) + i_{ion}(v, w, c) = I_{app}^m & \text{in } \Omega_H \times (0, T) \\ \dfrac{\partial w}{\partial t} - R(v, w) = 0, \quad \dfrac{\partial c}{\partial t} - S(v, w, c) = 0 & \text{in } \Omega_H \times (0, T) \\ \mathbf{n}^T D_m \nabla v = 0 & \text{in } \Gamma_H \times (0, T) \\ v(\mathbf{x}, 0) = v_0(\mathbf{x}), \quad w(\mathbf{x}, 0) = w_0(\mathbf{x}), \quad c(\mathbf{x}, 0) = c_0(\mathbf{x}) & \text{in } \Omega_H, \end{cases}$$

$$(4.38)$$

with $D_m = D_e (D_i + D_e)^{-1} D_i$.

Relaxed Monodomain model (see (4.32) for the dimensionless form)

$$\begin{cases} c_m \dfrac{\partial v}{\partial t} - \text{div}(\Phi(\mathbf{x}, \nabla v) \Phi_\xi(\mathbf{x}, \nabla v)) + i_{ion}(v, w, c) = I_{app} & \text{in } \Omega_H \times (0, T) \\ \dfrac{\partial w}{\partial t} - R(v, w) = 0, \quad \dfrac{\partial c}{\partial t} - S(v, w, c) = 0 & \text{in } \Omega_H \times (0, T) \\ \mathbf{n}^T \Phi(\mathbf{x}, \nabla v) \Phi_\xi(\mathbf{x}, \nabla v) \nabla v = 0 & \text{in } \Gamma_H \times (0, T) \\ v(\mathbf{x}, 0) = v_0(\mathbf{x}), \quad w(\mathbf{x}, 0) = w_0(\mathbf{x}), \quad c(\mathbf{x}, 0) = c_0(\mathbf{x}) & \text{in } \Omega_H. \end{cases}$$

$$(4.39)$$

4.4.1   Well-Posedness Results for Reduced Models

From (3.45), it follows that there exist c_1^m, $c_2^m > 0$ such that

$$c_1^m |\mathbf{z}|^2 \leq \mathbf{z}^T D_m(\mathbf{x})\mathbf{z} \leq c_2^m |\mathbf{z}|^2 \quad \forall \mathbf{z} \in \mathbb{R}^3, \forall \mathbf{x} \in \Omega_H.$$

This property, coupled with the assumptions of Theorem 3.10, guarantees the well-posedness of the Linear Anisotropic Monodomain model (4.38).

Assuming that $\forall \mathbf{x} \in \Omega_H$ the map $\xi \to \Phi^2(\mathbf{x}, \xi)$ is uniformly strongly convex, i.e. there exists $c > 0$ independent of $\mathbf{x}$ such that $\Phi^2(\mathbf{x}, \xi) - \frac{c}{2}|\xi|^2$ is convex, then the mapping $\xi \to \Phi(\mathbf{x}, \xi)\Phi_\xi(\mathbf{x}, \xi)$ is uniformly strongly monotone, i.e.

$$(\Phi(\mathbf{x}, \xi)\Phi_\xi(\mathbf{x}, \xi) - \Phi(\mathbf{x}, \eta)\Phi_\xi(\mathbf{x}, \eta)) \cdot (\xi - \eta) \geq c|\xi - \eta|^2.$$

This monotonicity property, coupled with the assumptions of Theorem 3.10 on the non-linear reaction terms of FitzHugh-Nagumo type, ensures the well-posedness of the Relaxed Monodomain model (4.39).

Considering the Eikonal-Diffusion equation (4.37) with mixed Dirichlet-Neumann boundary conditions, the same monotonicity property should guarantee the well-posedness.

Regarding the level set formulation (4.36) of the Eikonal-Curvature model, we remark that the mapping associated to the right hand side of (4.36) is continuous, degenerate elliptic and geometric. Moreover, it is easy to verify that the map $\Phi(\mathbf{x}, \xi)$ satisfies the properties (6.1) and (6.2) of [37]. Thus, proceeding as in [37], one can prove that Eq. (4.36) admits a unique continuous viscosity solution by applying Theorem (4.9) of [204], see also [27, 202, 203].

We recall that differently from to the Relaxed Monodomain and Eikonal models, the convexity assumption on the map Φ^2 is not needed for the well-posedness of the Bidomain model, and the only assumption required on the tensors $D_{i,e}$ is the uniform ellipticity (3.45).

We refer to [3, 40] for works investigating a generalized multidomain system and eikonal models with non-convex indicatrix function Φ.

4.4.2   Frank and Wulff Diagrams

We have seen before that the solvability of both the eikonal *curvature* and *diffusion* equations, as well as of the *relaxed Monodomain* model, is guaranteed if the function $\xi \to \Phi^2(\mathbf{x}, \xi)$ is strictly convex. Such property depends on the conductivity tensors $D_i(\mathbf{x})$, $D_e(\mathbf{x})$. After some relatively easy computations, this strict convexity is equivalent to the following property:

$$1 - 4 \frac{\omega(\mathbf{x}, \mathbf{p})^T [Q(\mathbf{x}, \mathbf{p})]^{-1} \omega(\mathbf{x}, \mathbf{p})}{\mathbf{p}^T D(\mathbf{x}) \mathbf{p}} > 0, \quad \forall \mathbf{p} \in \mathbb{R}^n \ ||\mathbf{p}||_2 = 1 \ \forall \mathbf{x} \in \Omega_H, \qquad (4.40)$$

where

$$\omega(\mathbf{x}, \mathbf{p}) := \frac{\mathbf{p}^T D_i(\mathbf{x}) \mathbf{p}}{\mathbf{p}^T D(\mathbf{x}) \mathbf{p}} D_e(\mathbf{x}) \, \mathbf{p} - \frac{\mathbf{p}^T D_e(\mathbf{x}) \mathbf{p}}{\mathbf{p}^T D(\mathbf{x}) \mathbf{p}} D_i(\mathbf{x}) \, \mathbf{p}, \qquad D := D_i + D_e,$$

$$Q(\mathbf{x}, \mathbf{p}) := \left(\frac{\mathbf{p}^T D_i(\mathbf{x}) \mathbf{p}}{\mathbf{p}^T D(\mathbf{x}) \mathbf{p}} \right)^2 D_e(\mathbf{x}) + \left(\frac{\mathbf{p}^T D_e^*(\mathbf{x}) \mathbf{p}}{\mathbf{p}^T D(\mathbf{x}) \mathbf{p}} \right)^2 D_i(\mathbf{x}).$$

The conductivity tensors are defined as in (3.41) by

$$D_{i,e}(\mathbf{x}) = A(\mathbf{x}) D_{i,e}^* A(\mathbf{x})^T,$$

where

$$D_{i,e}^*(\mathbf{x}) = diag(\sigma_l^{i,e}(\mathbf{x}), \sigma_t^{i,e}(\mathbf{x}), \sigma_n^{i,e}(\mathbf{x})).$$

Since $A(\mathbf{x})$ is an orthogonal matrix, then it easy to verify that the previous property (4.40) is equivalent to

$$\min_{||\xi||_2 = 1} \xi^T D^*(\mathbf{x}) \xi - 4 \omega^*(\mathbf{x}, \xi)^T [Q^*(\mathbf{x}, \xi)]^{-1} \omega^*(\mathbf{x}, \xi) > 0 \quad \forall \mathbf{x} \in \Omega_H, \qquad (4.41)$$

where $D^* := D_i^* + D_e^*$, the diagonal matrix Q^* is defined by

$$Q^*(\mathbf{x}, \xi) := (\xi^T D_i^*(\mathbf{x}) \xi) \, D_e^*(\mathbf{x}) + (\xi^T D_e^*(\mathbf{x}) \xi) \, D_i^*(\mathbf{x}),$$

and

$$\omega(\mathbf{x}, \xi) := (\xi^T D_i^*(\mathbf{x}) \xi) \, D_e^*(\mathbf{x}) \xi - (\xi^T D_e^*(\mathbf{x}) \xi) \, D_i^*(\mathbf{x}) \xi.$$

After some computations, the property (4.41) reduces to the condition

$$0 < \mathscr{F}(\sigma_{l,t,n}^i(\mathbf{x}), \sigma_{l,t,n}^e(\mathbf{x})) =$$

$$\min_{||\xi||_2 = 1} \xi^T D_i^*(\mathbf{x}) \xi - 4 (\xi^T D_i^*(\mathbf{x}) \xi - \xi^T D_e^*(\mathbf{x}) \xi)^2 \, \xi^T \left[D_e^*(\mathbf{x}) Q^*(\mathbf{x}, \xi)^{-1} D_i^*(\mathbf{x}) \right] \xi.$$

$$(4.42)$$

Therefore the property (4.42) depends on the six parameters $\sigma_l^{i,e}(\mathbf{x}), \sigma_t^{i,e}(\mathbf{x}), \sigma_n^{i,e}(\mathbf{x})$. Assuming axially symmetric anisotropy, $\mathscr{F}$ depends on the anisotropy ratios defined by

$$\rho_i = \frac{\sigma_l^i}{\sigma_t^i}, \qquad \rho_e = \frac{\sigma_l^e}{\sigma_t^e}, \qquad r_t = \frac{\sigma_t^i}{\sigma_t^e}.$$

In order to visualize the convexity property, we introduce the unit sphere of the indicatrix function $\Phi(\mathbf{x}, \boldsymbol{\xi})$ at $\mathbf{x}$

$$B_\Phi(\mathbf{x}) = \{\boldsymbol{\xi} \in \mathbb{R}^n \ : \Phi(\mathbf{x}, \boldsymbol{\xi}) \leq 1\},$$

called *Frank diagram*, and the unit sphere associated with the dual function Φ^*

$$B_{\Phi^*}^*(\mathbf{x}) = \{\boldsymbol{\xi}^* \in \mathbb{R}^n \ : \Phi^*(\mathbf{x}, \boldsymbol{\xi}^*) \leq 1\}, \ \text{ with } \ \Phi^*(\mathbf{x}, \boldsymbol{\xi}^*) = \{\boldsymbol{\xi}^* \cdot \boldsymbol{\xi} \ : \boldsymbol{\xi} \in B_\Phi(\mathbf{x})\},$$

usually called the *Wulff form* of the anisotropy in cristal growth and multiphase problems.

Neglecting the dependence on $\mathbf{x}$, the boundary of B_Φ is given by the set

$$\partial B_\Phi = \left\{ \boldsymbol{\xi} \in \mathbb{R}^n : \ \boldsymbol{\xi} = \frac{\boldsymbol{\nu}}{\Phi(\boldsymbol{\nu})}, \ ||\boldsymbol{\nu}||_2 = 1 \right\}.$$

Thanks to [37, Lemma 2.1], the following identity holds

$$\Phi^*(\Phi(\boldsymbol{\xi})\Phi_\xi(\boldsymbol{\xi})) = \Phi(\boldsymbol{\xi}),$$

implying that

$$\boldsymbol{\xi}^* \in \partial B_{\Phi^*}^* \iff \boldsymbol{\xi}^* = \Phi_\xi(\boldsymbol{\xi}) \text{ with } \boldsymbol{\xi} \in \partial B_\Phi.$$

Thus

$$\partial B_{\Phi^*}^* = \left\{ \boldsymbol{\xi}^* \in \mathbb{R}^n : \ \boldsymbol{\xi}^* = \Phi_\xi\left(\frac{\boldsymbol{\nu}}{\Phi(\boldsymbol{\nu})}\right) = \frac{Q(\boldsymbol{\xi})\boldsymbol{\nu}}{\Phi(\boldsymbol{\nu})}, \ \boldsymbol{\xi} = \frac{\boldsymbol{\nu}}{\Phi(\boldsymbol{\nu})}, \ ||\boldsymbol{\nu}||_2 = 1 \right\}.$$

In Figs. 4.2–4.7, we display the Frank diagram and Wulff form using a nominal anisotropy and various estimates of the conductivity coefficients taken from [100, 123, 131, 420, 421] and related to a normal cardiac tissue. From the graphics, we see that all these estimates guarantee the convexity of Φ and Φ^*. In Fig. 4.8, we display the Frank and Wulff diagrams for the extreme case called reciprocal anisotropy ($\rho_i = 1/\rho_e$), where it is evident that convexity is lost. We remark that at the concave portion of the Frank diagram corresponds a caustic in the Wulff diagram. We recall that the conductivity coefficients are average values over a unit volume of tissue and in particular σ_t^i is related to the density of the gap-junctions in the across fiber direction. Particularly in a pathological tissue as in presence of myocardial ischemia, the decreasing number of across gap-junctions yields a reduction of σ_t^i. Considering the conductivity values in Fig. 4.6, but with σ_t^i reduced in order to have $\rho_i = 20$, the diagrams displayed in Fig. 4.9 show that the two sets are not convex, as clearly evidenced by the presence of caustics in the Wulff form, see Fig. 4.10.
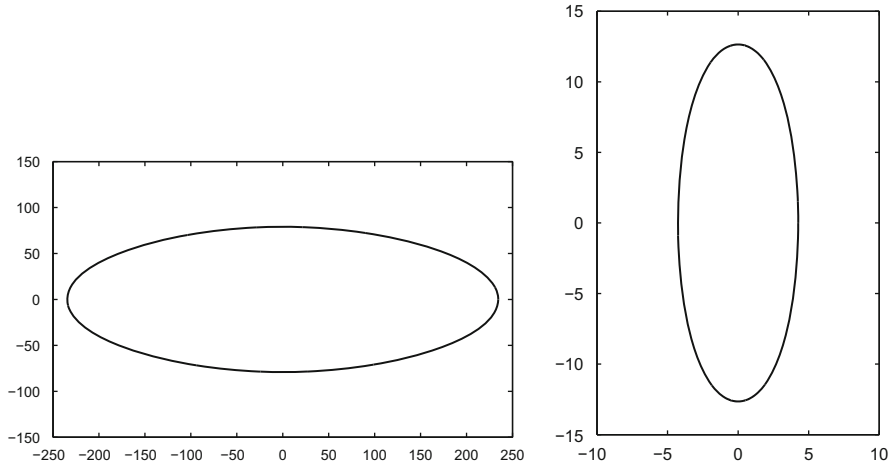
Fig. 4.2 Frank and Wulff diagrams for the conductivity values $\sigma_l^i = 0.2$, $\sigma_t^i = 0.02$, $\sigma_l^e = 0.8$, $\sigma_t^e = 0.2$ (all in mS cm^{-1})
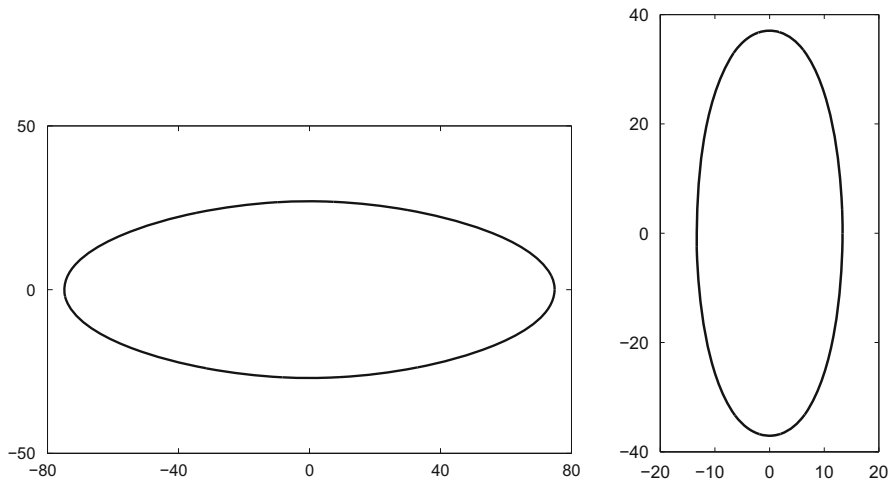
Fig. 4.3 Frank and Wulff diagrams for the conductivity values $\sigma_l^i = 1.74$, $\sigma_t^i = 0.193$, $\sigma_l^e = 6.52$, $\sigma_t^e = 2.36$ (all in mS cm^{-1}) (From [100])
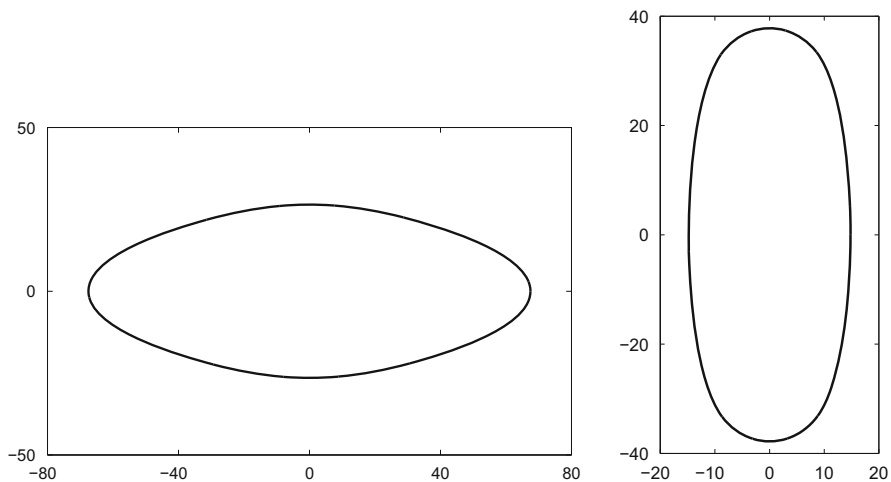
Fig. 4.4 Frank and Wulff diagrams for the conductivity values $\sigma_l^i = 2.78$, $\sigma_t^i = 0.263$, $\sigma_l^e = 2.94$, $\sigma_t^e = 1.33$ (all in mS cm^{-1}) (From [421])
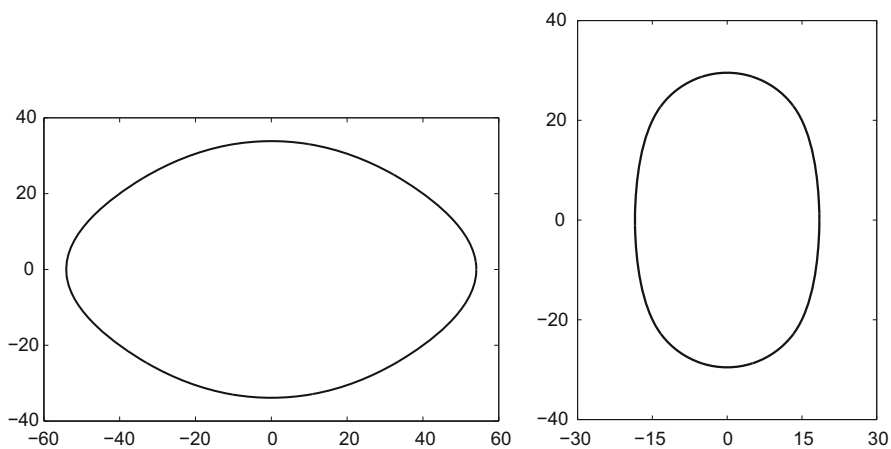
Fig. 4.5 Frank and Wulff diagrams for the conductivity values $\sigma_l^i = 3.43$, $\sigma_t^i = 0.596$, $\sigma_l^e = 1.17$, $\sigma_t^e = 0.802$ (all in mS cm^{-1}) (From [420])
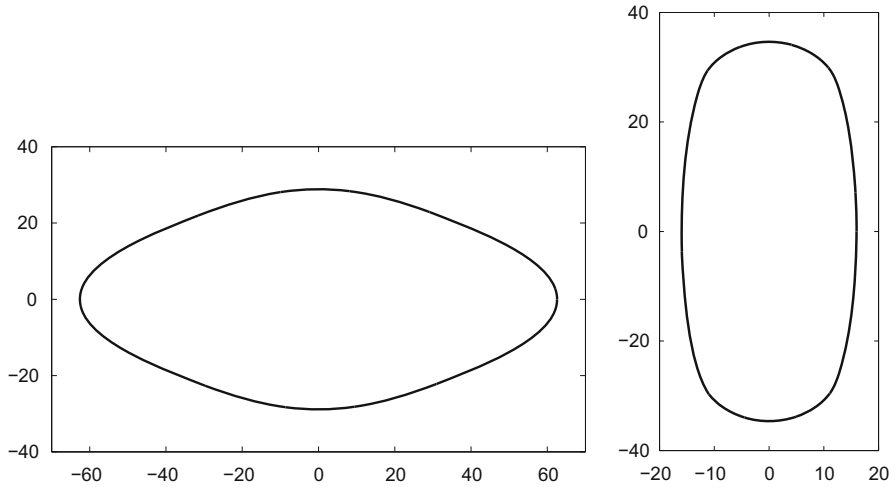
Fig. 4.6 Frank and Wulff diagrams for the conductivity values $\sigma_l^i = 3$, $\sigma_t^i = 0.315$, $\sigma_l^e = 2$, $\sigma_t^e = 1.35$ (all in mS cm^{-1}) (From [123])
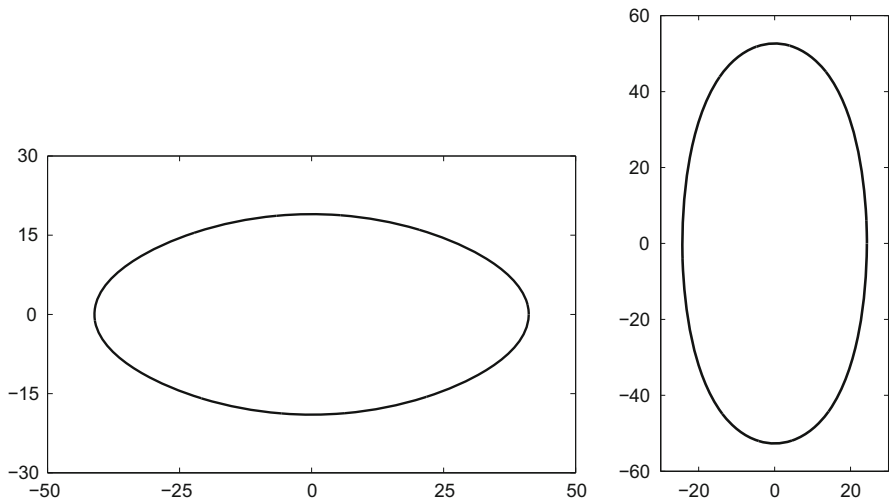
Fig. 4.7 Frank and Wulff diagrams for the conductivity values $\sigma_l^i = 1.55$, $\sigma_t^i = 0.243$, $\sigma_l^e = 2.32$, $\sigma_t^e = 1.04$ (all in mS cm^{-1}) (From [131])
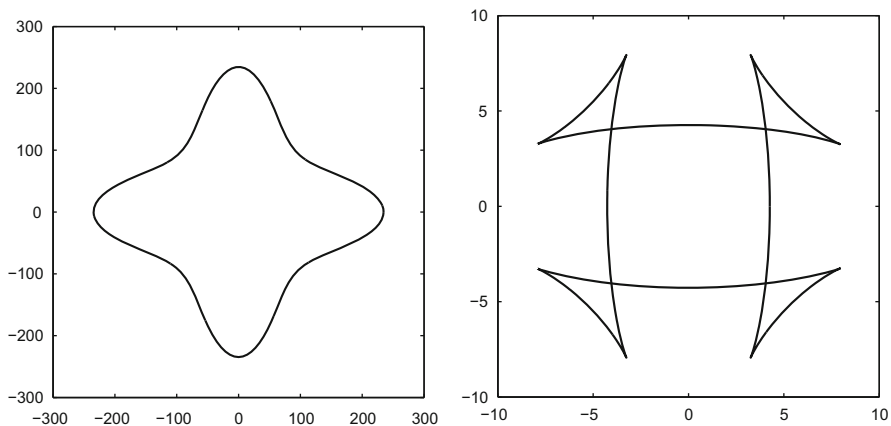
Fig. 4.8 Frank and Wulff diagrams for the conductivity values $\sigma_l^i = 0.2$, $\sigma_t^i = 0.02$, $\sigma_l^e = 0.02$, $\sigma_t^e = 0.2$ (all in mS cm^{-1})
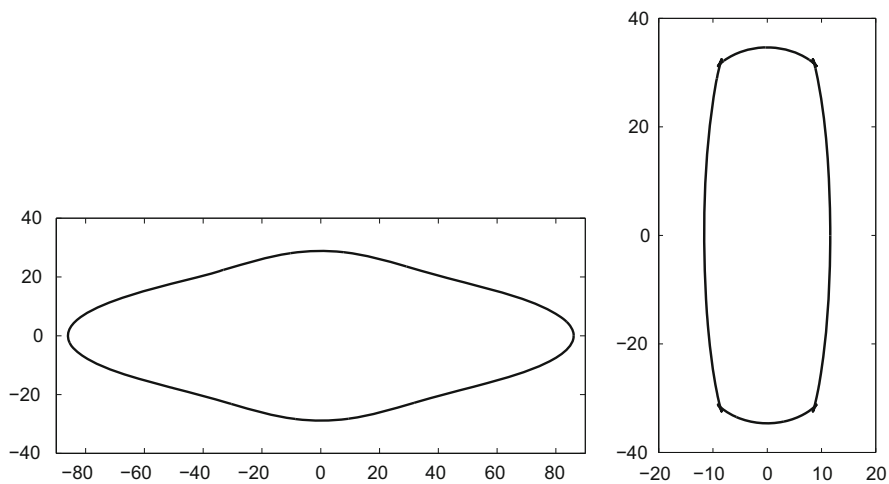
Fig. 4.9 Frank and Wulff diagrams for the conductivity values $\sigma_l^i = 3$, $\sigma_t^i = 0.15$, $\sigma_l^e = 2$, $\sigma_t^e = 1.35$ (all in mS cm^{-1})

Fig. 4.10 Zoom of the Wulff diagram displayed in Fig. 4.9 for the conductivity values $\sigma_l^i = 3$, $\sigma_t^i = 0.15$, $\sigma_l^e = 2$, $\sigma_t^e = 1.35$ (all in mS cm^{-1})
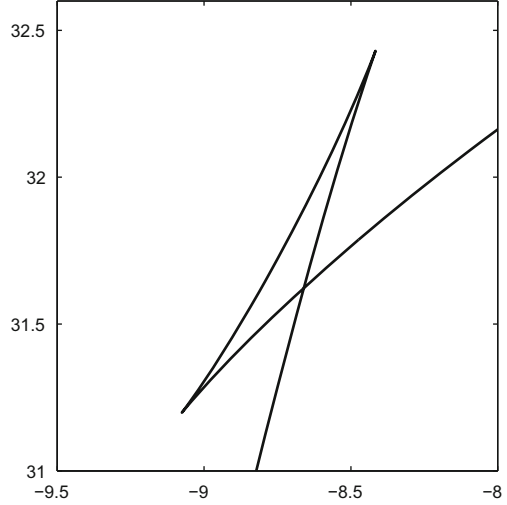
4.5 Numerical Comparison

The complex interactions between epi-to-endocardial counterclockwise fiber rotation and orthotropic anisotropy described in Sect. 1.3 determine a complex propagation of cardiac excitation. Many experimental works have studied the complex pattern of epicardial excitation generated by epicardial and intramural ventricular pacing in animals, see e.g. [12, 184, 506, 507, 516]. The first computer simulations of the spread of cardiac excitation were based on eikonal equations in order to understand possible mechanisms of the complex excitation patterns, see e.g. [102, 112–115, 226, 251, 268, 271, 272, 275, 470, 575].

In this section, we compare the activation time (AT) maps computed by solving the Eikonal-Diffusion (4.37), the linear Monodomain (4.38) and the Relaxed Monodomain (4.39) models with those computed by solving the reference Bidomain model (3.42).

The domain considered is a half truncated ellipsoid described by the parametric equations

$$\begin{cases} x = a(r)\cos\theta\cos\varphi & \varphi_{min} \leq \varphi \leq \varphi_{max}, \\ y = b(r)\cos\theta\sin\varphi & \theta_{min} \leq \theta \leq \theta_{max}, \\ z = c(r)\sin\theta & 0 \leq r \leq 1, \end{cases}$$

where $a_1 = b_1 = 0.2$, $a_2 = b_2 = 0.5$, $c_1 = 0.85$, $c_2 = 1$, all in cm, $\varphi_{min} = -\frac{\pi}{2}$, $\varphi_{max} = \frac{\pi}{2}$, $\theta_{min} = -\frac{3\pi}{8}$ and $\theta_{max} = \frac{\pi}{8}$. The fibers rotate counterclockwise from epicardium (r = 1) and endocardium (r = 0) for a total amount of 120°, see the schematic drawing of Figs. 1.4 and 9.28. The orthotropic conductivity coefficients of the 3D conductivity tensors (3.41) are

$$\sigma_l^i = 2.687 \cdot 10^{-3}, \qquad \sigma_t^i = 3.515 \cdot 10^{-4}, \qquad \sigma_n^i = 1.137 \cdot 10^{-4},$$
$$\sigma_l^e = 1.792 \cdot 10^{-3}, \qquad \sigma_t^e = 1.141 \cdot 10^{-3}, \qquad \sigma_n^e = 3.839 \cdot 10^{-4}.$$

All values are given in $\Omega^{-1}\text{cm}^{-1}$. The membrane model considered is the Luo-Rudy I model [308]. The external stimulus of $200\,\text{mA/cm}^3$ lasting $1\,\text{ms}$ is applied in a small volume of about $0.04 \times 0.04 \times 0.02\,\text{cm}^3$ at the center of the epicardial surface. The computed AT is defined at each point in space $\mathbf{x}$ as the unique instant t_a during the upstroke phase of the action potential when $v(\mathbf{x}, t_a) = -50\,\text{mV}$.

The space discretization of all the four models considered is performed by Q_1 finite elements in space and semi-implicit finite differences in time; for details see Chap. 7. The AT considered as a reference solution is computed by solving the Bidomain model on a mesh of $512 \times 512 \times 128$ finite elements, yielding a total amount of 67 897 602 degree of freedom (dof).

In Table 4.1, we report the l^2 relative errors of the AT computed by solving the Bidomain, Linear Monodomain and Relaxed Monodomain models on four increasing Q_1 finite element meshes with respect to the reference AT. At the finest level, the errors of the Linear Monodomain and Relaxed Monodomain models are about 4.5 and 1.5 %, respectively.

The Eikonal-Diffusion equation is solved on a very coarse mesh of $64 \times 64 \times 16$ elements, with a total amount of only 71 825 dof. The relative error in l^2 norm between the AT computed by the Eikonal-Diffusion equation and the reference AT is 0.0772. The AT maps reported in Figs. 4.11–4.14 confirm that, even on a such coarse mesh, the Eikonal-Diffusion equation is able to approximate very accurately the AT.

Table 4.1 Relative errors in l^2 norm of the activation time computed by solving the Bidomain, Linear Monodomain and Relaxed Monodomain models on four increasing Q_1 finite element meshes with respect to the reference activation time computed by solving the Bidomain model on a mesh of $512 \times 512 \times 128$ finite elements. The degrees of freedom (dof) are also reported. Note that in the case of the Bidomain model the dof are doubled because the unknowns are both the transmembrane potential v and extracellular potential u_e. The Bidomain dof for the computation of the reference solution are 67 897 602

Mesh	dof	Bidomain	Linear monodomain	Relaxed monodomain
$128 \times 128 \times 32$	549 153	0.0301	0.0649	0.0387
$192 \times 192 \times 48$	1 825 201	0.0198	0.0493	0.0239
$256 \times 256 \times 64$	4 293 185	0.0129	0.0463	0.0185
$384 \times 384 \times 96$	14 377 825	0.0047	0.0471	0.0158
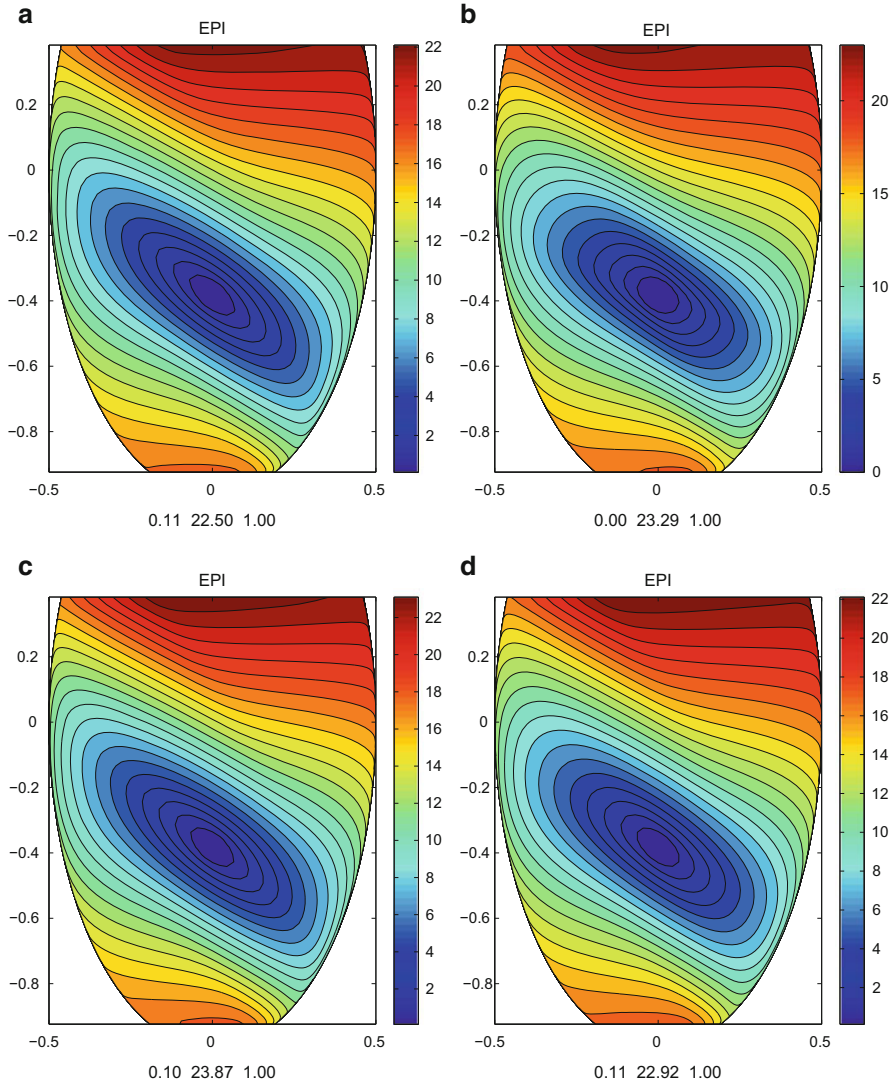
Fig. 4.11 Epicardial activation time isochrones computed by solving the Bidomain model (**a**), the Linear Monodomain model (**c**) and the Relaxed Monodomain model (**d**) with a mesh of 384 × 384 × 96 finite elements, and the Eikonal-Diffusion equation (**b**) with a mesh of 64 × 64 × 16 finite elements (**b**). Below each panel are reported the minimum, maximum and step in mV of the displayed map and the colorbar denotes the range of values of the displayed equipotential lines
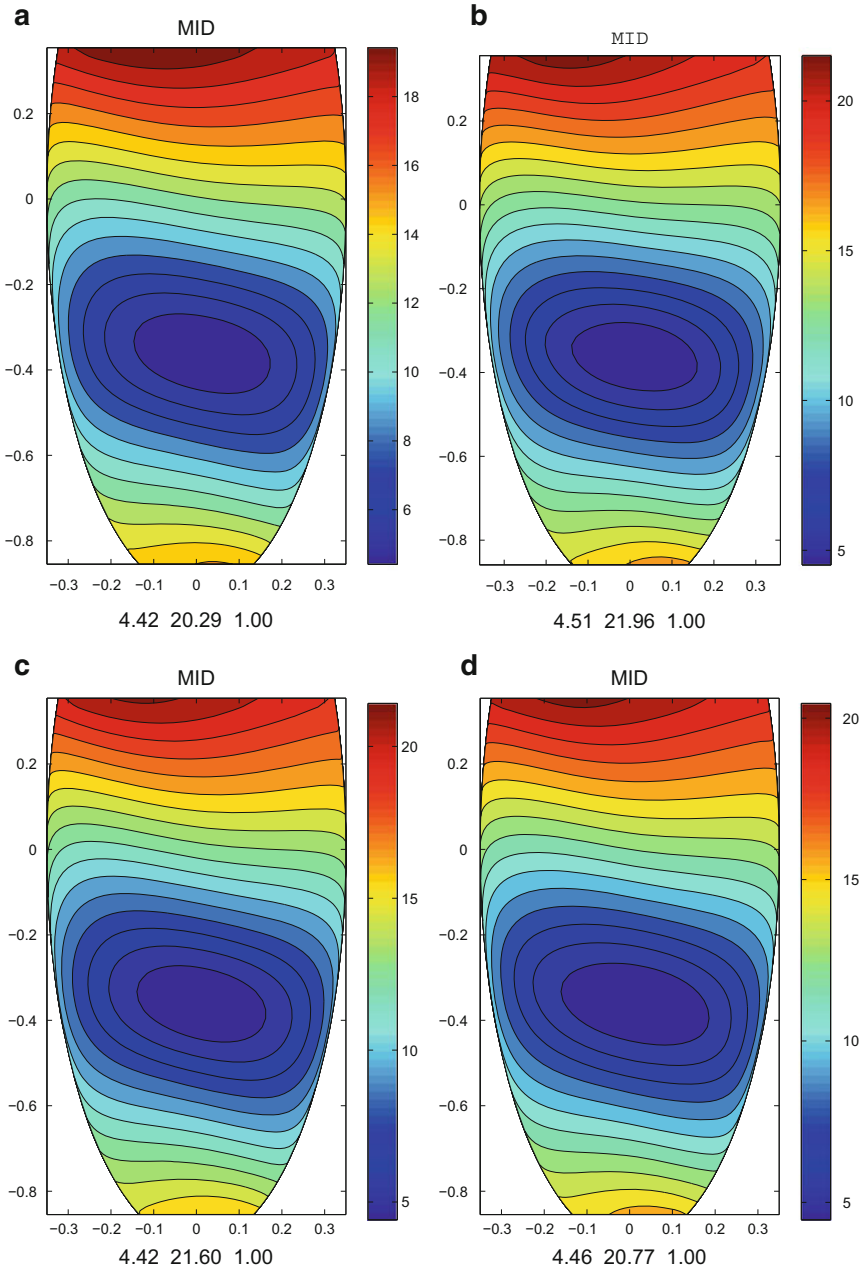
Fig. 4.12 Mid-myocardial activation time isochrones computed by solving the Bidomain model (**a**), the Linear Monodomain model (**c**) and the Relaxed Monodomain model (**d**) with a mesh of $384 \times 384 \times 96$ finite elements, and the Eikonal-Diffusion equation (**b**) with a mesh of $64 \times 64 \times 16$ finite elements (**b**). Below each panel are reported the minimum, maximum and step in mV of the displayed map and the colorbar denotes the range of values of the displayed equipotential lines
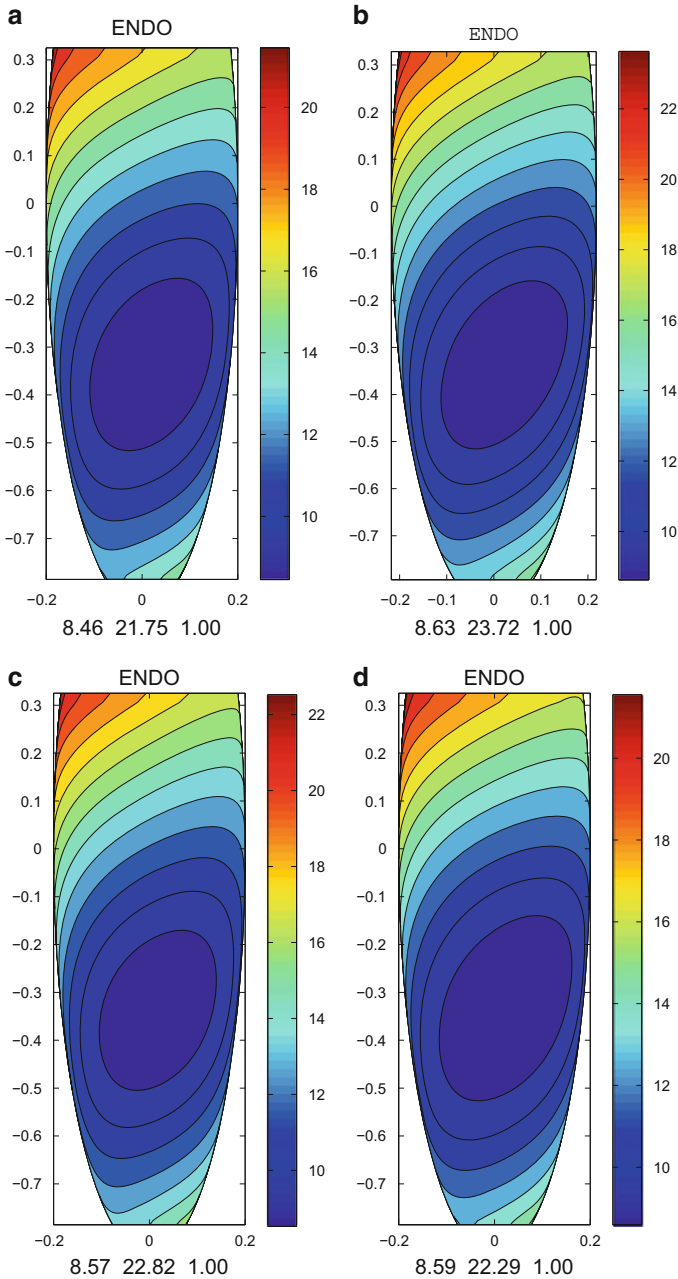
Fig. 4.13 Endocardial activation time isochrones computed by solving the Bidomain model (**a**), the Linear Monodomain model (**c**) and the Relaxed Monodomain model (**d**) with a mesh of 384 × 384 × 96 finite elements, and the Eikonal-Diffusion equation (**b**) with a mesh of 64 × 64 × 16 finite elements (**b**). Below each panel are reported the minimum, maximum and step in mV of the displayed map and the colorbar denotes the range of values of the displayed equipotential lines
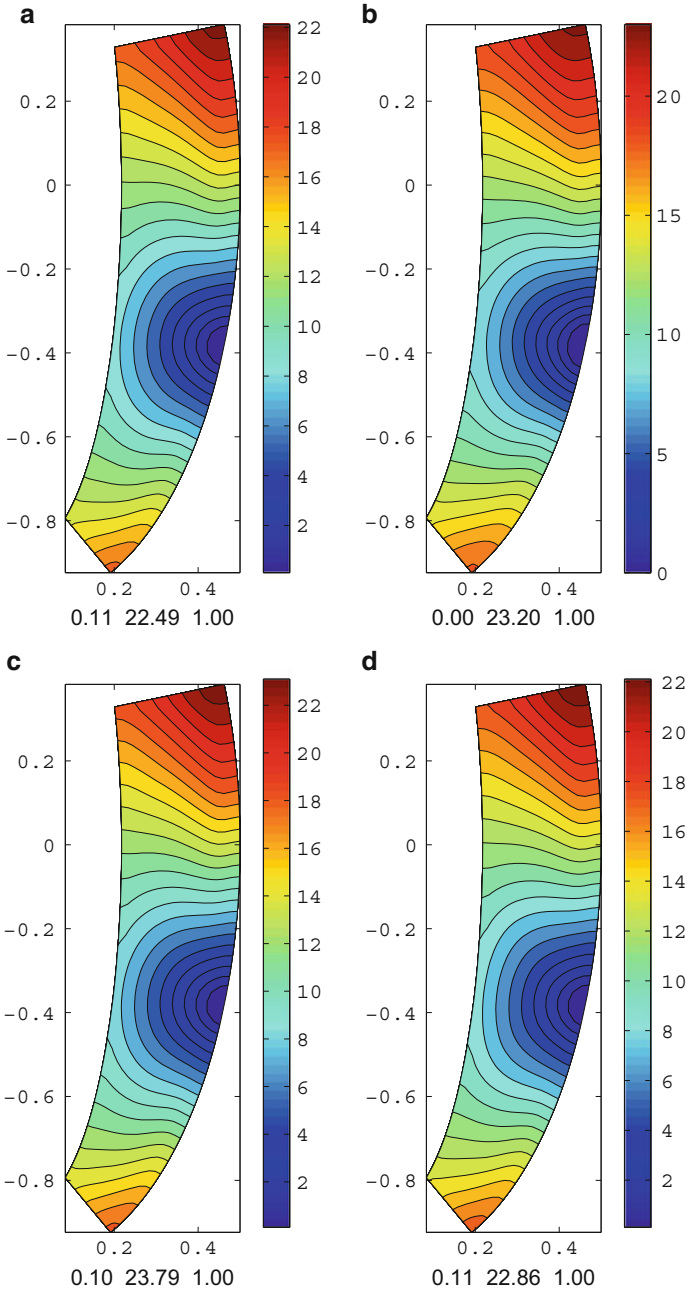
Fig. 4.14 Transmural activation time isochrones computed by solving the Bidomain model (**a**), the Linear Monodomain model (**c**) and the Relaxed Monodomain model (**d**) with a mesh of 384 × 384 × 96 finite elements, and the Eikonal-Diffusion equation (**b**) with a mesh of 64 × 64 × 16 finite elements (**b**). Below each panel are reported the minimum, maximum and step in mV of the displayed map and the colorbar denotes the range of values of the displayed equipotential lines

Chapter 5
Anisotropic Cardiac Sources

The electrical activity of the heart is revealed and usually detected by measuring the time–dependent extracellular or extracardiac potential $u(\mathbf{x}, t)$.

Definition 5.1. The electrogram (EG) at a point $\mathbf{x}$ inside or outside the myocardium is defined as the time course of the potential $u(\mathbf{x}, t)$, i.e. with $\mathbf{x}$ fixed and t variable.

In electrocardiography what is really measured is a difference between the potential at an observation point and a reference potential. In the usual practice body surface, epicardial, intramural and intracavitary EGs are recorded against the potential average on a given set of points or against the potential at a distant electrode. The classical reference potential is the average of the potentials at three different points on the torso (Wilson Central Terminal), see Sect. 1.5. More generally we can consider as reference potential the average potential on a given surface. In this study we choose the reference potential which yields zero average on the insulated boundary of the volume conductor where the heart is embedded (see [510]).

As described in Sect. 3.3, the representation at macroscopic level of the cardiac tissue is given by the anisotropic Bidomain [225], constituted by two interpenetrating anisotropic continua, intra- and extracellular, connected by the distributed cellular membrane. In the Bidomain model the following potentials are considered:

- $u_i(\mathbf{x}, t)$, $u_e(\mathbf{x}, t)$ intra- and extracellular potential;
- $v(\mathbf{x}, t) = u_i(\mathbf{x}, t) - u_e(\mathbf{x}, t)$ transmembrane potential;
- $u_0(\mathbf{x}, t)$ the extracardiac potential;

then the potential $u(\mathbf{x}, t)$ is given by $u_e(\mathbf{x}, t)$ inside the myocardium and by $u_0(\mathbf{x}, t)$ outside. The bioelectric sources generating the electric potential field in the heart (extracellular potential u_e) and outside (extracardiac potential u_0) are related to the gradient of the transmembrane potential distribution $v(\mathbf{x}, t)$, as detailed in the following of this chapter.

We shall present and compare two different equivalent formulations of the mathematical model related to the generation of electrograms; this model assumes that the transmembrane potential is known, which is equivalent to know the time dependent distribution of the electric sources.

In the following we shall denote by Ω_H the heart tissue, by Ω_0 an extracardiac medium in contact with Ω_H (cavitary blood and/or fluid adjacent to the epicardium), by D_i, D_e, D_0 the conductivity tensors in the intra- extracellular and extracardiac media.

5.1   Differential Formulation of the Potential Field

We recall that the current vector densities associated to the intra, extracellular and extracardiac potentials are given by $\mathbf{J}_i = -D_i \nabla u_i$, $\mathbf{J}_e = -D_e \nabla u_e$ and $\mathbf{J}_0 = -D_0 \nabla u_0$. Assuming that there are no externally applied sources, then the total field $\mathbf{J}_i + \mathbf{J}_e$ in the cardiac tissue Ω_H must be solenoidal, see Sect. 3.3; the same holds for $\mathbf{J}_0$ since there are no sources in Ω_0. Hence we have:

$$\text{div}\,(\mathbf{J}_i + \mathbf{J}_e) = 0 \ \text{ in } \Omega_H \tag{5.1}$$

$$\text{div}\,\mathbf{J}_0 = 0 \ \text{ in } \Omega_0. \tag{5.2}$$

If $\Sigma = \partial\Omega_H \cap \partial\Omega_0$ denotes the parts of the epi and/or endocardium in contact with Ω_0, then the flux continuity across Σ implies the transmission conditions:

$$u_e = u_0 \qquad\qquad (\mathbf{J}_i + \mathbf{J}_e) \cdot \mathbf{n} = \mathbf{J}_0 \cdot \mathbf{n} \qquad\qquad \text{on } \Sigma.$$

Setting $\overline{\Omega} = \overline{\Omega_0} \cup \overline{\Omega_H}$, $\Gamma_H = \partial\Omega_H \setminus \Sigma$, $\Gamma_0 = \partial\Omega_0 \setminus \Sigma$, $\Gamma = \partial\Omega = \Gamma_H \cup \Gamma_0$, and assuming that the total volume Ω is insulated, we have:

$$(\mathbf{J}_i + \mathbf{J}_e) \cdot \mathbf{n} = 0 \qquad \text{on } \Gamma_H \qquad\qquad \mathbf{J}_0 \cdot \mathbf{n} = 0 \qquad \text{on } \Gamma_0.$$

The unit normal $\mathbf{n}$ is outward to Ω_H or Ω according as we consider the boundary condition on Σ or on Γ; hence on Σ the normal $\mathbf{n}$ points outside Ω_H (see Fig. 5.1). In the following, we set $D = D_i + D_e$ ("bulk" conductivity tensor),

$$\hat{D} = \begin{cases} D & \text{in } \Omega_H \\ D_0 & \text{in } \Omega_0 \end{cases} \qquad \text{and} \qquad u(\mathbf{x}, t) = \begin{cases} u_e(\mathbf{x}, t) & \text{in } \mathbf{x} \in \Omega_H \\ u_0(\mathbf{x}, t) & \text{in } \mathbf{x} \in \Omega_0 \end{cases}$$

and we define the *equivalent* cardiac source for the extracardiac and extracellular potentials by

$$\mathbf{J}_v(\mathbf{x}, t) = -D_i \nabla v(\mathbf{x}, t), \tag{5.3}$$

Fig. 5.1 Schematic representation of the domain Ω
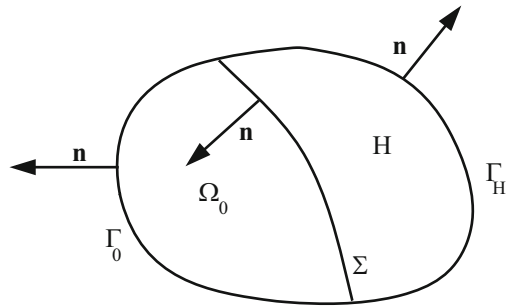
where $v(\mathbf{x}, t)$ is the transmembrane potential. Then problem (5.1)–(5.2) can be written as:

$$
\begin{cases}
\text{div } \hat{D}\nabla u(\mathbf{x}, t) = \begin{cases} \text{div } \mathbf{J}_v(\mathbf{x}, t) & \text{in } \Omega_H \\ 0 & \text{in } \Omega_0 \end{cases} \\
[\![u(\mathbf{x}, t)]\!]_\Sigma = 0 \qquad\qquad [\![(\hat{D}\nabla u(\mathbf{x}, t)) \cdot \mathbf{n}]\!]_\Sigma = \mathbf{J}_v(\mathbf{x}, t) \cdot \mathbf{n} \\
(D_0 \nabla u(\mathbf{x}, t)) \cdot \mathbf{n} = 0 \qquad\quad \text{on } \Gamma_0 \\
(D \nabla u(\mathbf{x}, t)) \cdot \mathbf{n} = \mathbf{J}_v(\mathbf{x}, t) \cdot \mathbf{n} \qquad \text{on } \Gamma_H
\end{cases}
\tag{5.4}
$$

where $[\![\varphi]\!]_\Sigma$ denotes the jump of φ through Σ, i.e. $[\![\varphi]\!]_\Sigma = \varphi_{|_{\Sigma^+}} - \varphi_{|_{\Sigma^-}}$ with $\varphi_{|_{\Sigma^\pm}}$ the traces taken on the positive and negative side of Σ with respect to the oriented normal. Therefore problem (5.4) provides the extracellular or extracardiac potential $u(\mathbf{x}, t)$ from the knowledge of $v(\mathbf{x}, t)$.

In the remaind of this Chapter we will assume:

- Ω and Ω_H bounded Lipschitz open set of $\mathbf{R}^3$;
- The conductivity tensors $D_i(\mathbf{x})$, $D_e(\mathbf{x}) \in C^1(\Omega_H)$;
- $\forall t \in [0, T]$ the transmembrane potential $v(\mathbf{x}, t) \in W^{2,p}(\Omega)$ with $p > 3$.

These regularity properties imply that $\mathbf{J}_v \in W^{1,p}(\Omega_H)$ and div $\mathbf{J}_v \in L^p(\Omega_H)$, hence $\mathbf{n} \cdot \mathbf{J}_{v_{|\partial\Omega_H}} \in W^{1/p,p}(\partial\Omega_H)$ and the first Green formula holds, see e.g. [305]. The conormal derivative, in the boundary value problem (5.4), exhibits a jump discontinuity on Σ. Defining the following bilinear form

$$
a(\varphi, \phi) = \int_\Omega (\hat{D}(\mathbf{x})\nabla\varphi) \cdot \nabla\phi \, d\mathbf{x}, \qquad \forall \varphi, \phi \in W^{1,2}(\Omega)
\tag{5.5}
$$

the variational formulation of (5.4) is:

$\forall t \in [0, T]$ *find* $u(\mathbf{x}, t) \in W^{1,2}(\Omega)$ *such that*

$$
a(u, \phi) = \int_{\Omega_H} \mathbf{J}_v(\mathbf{x}, t) \cdot \nabla\phi(\mathbf{x}) \, d\mathbf{x} \qquad \forall \phi \in W^{1,2}(\Omega).
\tag{5.6}
$$

We remark that $\forall t \in [0, T]$ problem (5.6) admits a solution $u(\mathbf{x}, t) \in W^{1,2}(\Omega)$ unique up to an additive constant. This constant depends on t and it is related to the reference potential chosen.

It is easy to verify, applying the Green formula, that the solution of (5.6) satisfies problem (5.4) in the sense of distributions and of the trace theorems (see e.g. [305]).

5.2   Integral Formulation of the Potential Field

Usually EGs are recorded at a limited number of points $\mathbf{x}$, from 12 to 24 derivations, see Sect. 1.5. Consequently the differential formulation (5.4) is not computationally convenient, since for any $t \in [0, T]$ the solution of the elliptic problem (5.4) is needed and yields $u(\mathbf{x}, t)$ for all nodes of the mesh (at the given time instant t), while we are interested only in the value of $u(\mathbf{x}, t)$ in few points $\mathbf{x}$ on $[0, T]$. An integral formulation [197, 198] of the potential $u(\mathbf{x}, t)$ turns out to be a more efficient tool, because this formulation requires the solution of only a number of problems given by the chosen set of points $\mathbf{x}$, i.e. $\mathbf{x}$ appears as a parameter. This integral representation is given by:

$$u(\mathbf{x}, t) - u_{ref} = \int_{\Omega_H} \mathbf{J}_v(\mathbf{x}, t) \cdot \nabla_\xi \psi \, d\xi = -\int_{\Omega_H} (D_i \nabla v) \cdot \nabla_\xi \psi \, d\xi. \qquad (5.7)$$

This formulation gives a potential difference with respect to a reference potential. In this study, we consider as reference potential the one given by the potential at a reference point $\mathbf{x}_0$ or by the average on the insulated boundary Γ. The representation (5.7) uses the function $\psi(\boldsymbol{\xi}; \mathbf{x})$ defined as the potential field in the medium Ω with conductivity tensor $\hat{D}$. This function is generated by a unit current source at lead $\mathbf{x}$ and a unit current sink at lead $\mathbf{x}_0$ or a current sink uniformly distributed on the surface Γ with density $1/|\Gamma|$ according to the first or the second choice of the reference potential, see [197, 214, 570]. More precisely, the potential field ψ, usually called *lead field* in electrocardiographic literature, is the Green function associated to the following boundary value problem of Neumann type:

$$\begin{cases} -\mathrm{div}_\xi \hat{D} \nabla_\xi \psi = \mu_\Omega & \text{in } \Omega \\ \hat{D} \nabla_\xi \psi \cdot \mathbf{n} = \mu_\Gamma & \text{on } \Gamma, \end{cases} \qquad (5.8)$$

where, for the first choice of *reference potential* with $\mathbf{x}_0 \in \Omega$, we define:

$$\begin{aligned} \mu_\Omega &= \delta(\boldsymbol{\xi} - \mathbf{x}) - \delta(\boldsymbol{\xi} - \mathbf{x}_0), \ \mu_\Gamma = 0, & \text{when } \mathbf{x} \in \Omega \\ \mu_\Omega &= -\delta(\boldsymbol{\xi} - \mathbf{x}_0), & \mu_\Gamma = \delta(\boldsymbol{\xi} - \mathbf{x}), & \text{when } \mathbf{x} \in \Gamma \end{aligned} \qquad (5.9)$$

and, for the second choice of *reference potential*, we have:

$$\mu_\Omega = \delta(\boldsymbol{\xi} - \mathbf{x}), \ \mu_\Gamma = -\frac{1}{|\Gamma|} \qquad\qquad \text{when } \mathbf{x} \in \Omega$$

$$\mu_\Omega = 0, \qquad \mu_\Gamma = \delta(\boldsymbol{\xi} - \mathbf{x}) - \frac{1}{|\Gamma|} \qquad \text{when } \mathbf{x} \in \Gamma, \tag{5.10}$$

with $\delta(\boldsymbol{\xi} - \mathbf{x})$ denoting, as usual, the Dirac δ-function at point $\mathbf{x}$.

Formal derivation of (5.7). Proceeding formally we apply the second Green formula to the couple (u, ψ) in Ω_0 and in Ω_H. Adding these two relations we obtain:

$$\int_{\Omega_0 \cup \Omega_H} \left[u \operatorname{div} \hat{D}\nabla\psi - \psi \operatorname{div} \hat{D}\nabla u \right] d\xi$$

$$= \int_\Gamma u \, (\hat{D}\nabla\psi) \cdot \mathbf{n} \, d\sigma_\xi - \int_\Gamma \psi \, (\hat{D}\nabla u) \cdot \mathbf{n} \, d\sigma_\xi$$

$$+ \int_\Sigma [\![\, (\hat{D}\nabla\psi) \cdot \mathbf{n} \,]\!]_\Sigma \, u \, d\sigma_\xi - \int_\Sigma [\![\, (\hat{D}\nabla u) \cdot \mathbf{n} \,]\!]_\Sigma \, \psi \, d\sigma_\xi. \tag{5.11}$$

Taking into account that, if $\mathbf{x}, \mathbf{x}_0 \notin \Sigma$, then $[\![\, (\hat{D}\nabla\psi) \cdot \mathbf{n} \,]\!]_\Sigma = 0$ otherwise, if $\mathbf{x} \in \Sigma$, $[\![\, (\hat{D}\nabla\psi) \cdot \mathbf{n} \,]\!]_\Sigma = \delta(\boldsymbol{\xi} - \mathbf{x})$, from (5.11) we have:

$$u(\mathbf{x}, t) + \int_{\Omega_0 \cup \Omega_H} \psi \operatorname{div} \hat{D}\nabla u \, d\xi - \int_\Gamma \psi \, (\hat{D}\nabla u) \cdot \mathbf{n} \, d\sigma_\xi$$

$$- \int_\Sigma [\![\, (\hat{D}\nabla u) \cdot \mathbf{n} \,]\!]_\Sigma \, \psi \, d\sigma_\xi - u_{ref} = 0,$$

where $u_{ref} = u(\mathbf{x}_0, t)$ or $u_{ref} = \dfrac{1}{|\Gamma|} \displaystyle\int_\Gamma u \, d\sigma_\xi$ according as $\psi(\boldsymbol{\xi}; \mathbf{x})$ satisfies (5.9) or (5.10). Hence taking into account (5.4) and denoting by $w(\mathbf{x}, t)$ the potential difference with respect to the chosen reference potential, i.e. $w(\mathbf{x}, t) = u(\mathbf{x}, t) - u_{ref}$, it follows:

$$w(\mathbf{x}, t) = -\int_{\Omega_H} \psi \operatorname{div} \mathbf{J}_v \, d\xi + \int_{\partial\Omega_H} \psi \, \mathbf{J}_v \cdot \mathbf{n} \, d\sigma_\xi$$

and applying the first Green formula we obtain the integral representation:

$$w(\mathbf{x}, t) = \int_{\Omega_H} \mathbf{J}_v \cdot \nabla_\xi \psi \, d\xi = -\int_{\Omega_H} (D_i \nabla v) \cdot \nabla_\xi \psi \, d\xi. \tag{5.12}$$

The previous derivation can be easily justified, in the framework of Sobolev spaces, when $\hat{D}$ is assumed *regular* in Ω. When $\hat{D}$ exhibits, as in real cases, a jump discontinuity on the interface Σ then the Green function ψ is solution of a boundary

value problem with discontinuous coefficients and cannot be uniquely defined in the sense of distributions.

Rigorous mathematical derivation of (5.7). To rigorously introduce Green functions associated to the previous Neumann problems we consider a notion of *weak solution* similar to the one proposed by Stampacchia for the Dirichlet problem (see [343, 495]).

We denote by $\mathscr{A} = -\mathrm{div}\,\hat{D}\nabla_\xi$ and by $\partial_{v_\mathscr{A}} = \hat{D}\nabla_\xi \cdot \mathbf{n}$ with $\mathscr{D}(\Omega)$ and $\mathscr{D}(\Gamma)$ the set of measures with bounded variation and support on Ω and on Γ respectively.

Problem (5.8) is a non homogeneous Neumann problem of the type:

$$\begin{cases} \mathscr{A}\omega = \mu_\Omega & \text{in } \Omega \\ \partial_{v_\mathscr{A}}\omega = \mu_\Gamma & \text{on } \Gamma \end{cases} \tag{5.13}$$

with data as measures given by (5.9) and (5.10). Extending the classical approach of Stampacchia [495], we introduce the following notion of weak formulation of (5.13):

Definition 5.2. Given μ_Ω, μ_Γ measures of bounded variation on Ω and Γ respectively, such that $\int_\Omega d\mu_\Omega + \int_\Gamma d\mu_\Gamma = 0$, a function $\omega \in L^1(\Omega)/\mathbf{R}$ is a weak solution of problem (5.13) if

$$\int_\Omega \omega \mathscr{A}\varphi = \int_\Omega \varphi \, d\mu_\Omega + \int_\Gamma \varphi \, d\mu_\Gamma \tag{5.14}$$

$$\forall \varphi \in C^0(\bar{\Omega}) \cap W^{1,2}(\Omega), \ \mathscr{A}\varphi \in C^0(\bar{\Omega}), \partial_{v_\mathscr{A}}\varphi_{|\partial\Omega_H} = 0.$$

We remark that the set of the test functions is not empty since, due to Corollary 7.8 in [343], the following regularity result holds:

Theorem 5.1. *Let Ω be a domain with Lipschitz continuous boundary, $f_0 \in L^p(\Omega)$ such that $\int_\Omega f_0 \, dx = 0$ and $\mathbf{F} \in (L^p(\Omega))^3$ with $p > 3$. If $z \in W^{1,2}(\Omega)/\mathbf{R}$ is the unique solution of*

$$a(z, \varphi) = \int_\Omega f_0\varphi \, dx + \int_\Omega \nabla\varphi \cdot \mathbf{F} \, dx \qquad \forall \varphi \in W^{1,2}(\Omega),$$

then

$$\max_{\bar{\Omega}} |z| \leq C \left(\|f_0\|_{L^p} + \|\mathbf{F}\|_{(L^p)^3} \right).$$

Taking into account that the operator $\mathscr{A}$ is self-adjoint, by duality of this regularity result we obtain the existence and uniqueness of the solution ω of problem (5.13) with $\omega \in W^{1,p'}(\Omega)$ and $p' < 3/2$ (p' conjugate number of p).

Therefore, defining the Green function $\psi(\xi; \mathbf{x})$ of problem (5.8) as the weak solution of (5.13) with μ_Ω and μ_Γ given by (5.9) and (5.10), we have $\forall \mathbf{x} \in \bar{\Omega}$:

$$\int_\Omega \psi(\boldsymbol{\xi};\mathbf{x})\, \mathscr{A}\varphi\, d\xi = \varphi(\mathbf{x}) - \varphi_{ref} \tag{5.15}$$

$$\forall \varphi \in C^0(\bar{\Omega}) \cap W^{1,2}(\Omega),\ \mathscr{A}\varphi \in C^0(\bar{\Omega}), \partial_{\nu_\mathscr{A}}\varphi_{|\partial\Omega_H} = 0,$$

where $\varphi_{ref} = \varphi(\mathbf{x}_0)$ or $\varphi_{ref} = \frac{1}{|\Gamma|}\int_\Gamma \varphi\, d\sigma_\xi$; moreover, since $\mathscr{A}$ is self-adjoint, $\psi(\boldsymbol{\xi};\mathbf{x}) = \psi(\mathbf{x};\boldsymbol{\xi})$.

For $g \in C^0(\bar{\Omega})$ with $\int_\Omega g\, dx = 0$, we consider $\varphi \in C^0(\bar{\Omega}) \cap W^{1,2}(\Omega)$ solution of

$$\begin{cases} \mathscr{A}\varphi = g & \text{in } \Omega \\ \partial_{\nu_\mathscr{A}}\varphi = 0 & \text{on } \Gamma. \end{cases} \tag{5.16}$$

From (5.15) we have the following integral representation for the solution of problem (5.16) $\forall \mathbf{x} \in \bar{\Omega}$:

$$\varphi(\mathbf{x}) - \varphi_{ref} = \int_\Omega \psi(\boldsymbol{\xi};\mathbf{x})\, g(\boldsymbol{\xi})\, d\xi. \tag{5.17}$$

Using Fubini's theorem and formula (5.17) with $\varphi_{ref} = 0$, it follows that:

$$\int_\Omega \varphi\, d\mu_\Omega + \int_\Gamma \varphi\, d\mu_\Gamma = \int_\Omega g(\mathbf{x})\left(\int_\Omega \psi(\mathbf{x};\boldsymbol{\xi})\, d\mu_\Omega + \int_\Gamma \psi(\mathbf{x};\boldsymbol{\xi})\, d\mu_\Gamma\right) dx$$

and, comparing with (5.14), we obtain that the solution $\omega(\mathbf{x})$ of problem (5.13), apart from an additive constant ω_{ref}, is given by:

$$\omega(\mathbf{x}) = \int_\Omega \psi(\mathbf{x};\boldsymbol{\xi})\, d\mu_\Omega + \int_\Gamma \psi(\mathbf{x};\boldsymbol{\xi})\, d\mu_\Gamma + \omega_{ref}. \tag{5.18}$$

Going back to the variational problem (5.6) and defining the potential $u(\mathbf{x},t)$, it is easy to verify that $u(\mathbf{x},t)$ is also a weak solution of problem (5.13) for the data μ_Ω, μ_Γ defined by the functional on $C^0(\bar{\Omega})$

$$\varphi \mapsto -\int_{\Omega_H} \varphi\, \text{div}\, \mathbf{J}_\nu + \int_\Sigma \varphi\, \mathbf{J}_\nu \cdot \mathbf{n} + \int_{\Gamma_H} \varphi\, \mathbf{J}_\nu \cdot \mathbf{n}.$$

From the representation formula (5.18), since $\psi \in W^{1,p'}(\Omega)$ with $p' < 3/2$, applying the Green formula, $u(\mathbf{x},t)$, apart from an additive constant, is given by

$$u(\mathbf{x},t) - u_{ref} = \int_{\Omega_H} \mathbf{J}_\nu \cdot \nabla_\xi \psi\, d\xi. \tag{5.19}$$

This formula coincides with (5.12), which represents the solution having zero reference potential and holds $\forall \mathbf{x} \in \bar{\Omega}$ since, from the regularity Theorem 5.1, we have that $u(\mathbf{x}, t) \in C^0(\bar{\Omega})$. In conclusion the following Proposition holds:

Proposition 5.1. *The solution of (5.6) with zero reference potential is given by:*

$$w(\mathbf{x}, t) = \int_{\Omega_H} \mathbf{J}_v \cdot \nabla_\xi \psi(\boldsymbol{\xi}; \mathbf{x}) \, d\xi \qquad \forall \mathbf{x} \in \bar{\Omega}, \ \forall t \in [0, T],$$

where, $\forall \mathbf{x} \in \bar{\Omega}$, $\psi(\boldsymbol{\xi}; \mathbf{x})$ *is solution of problem (5.15).*

In the following, we denote by

$$w_0(\mathbf{x}, t) = w(\mathbf{x}, t) \ \text{ for } \mathbf{x} \in \Omega \setminus \Omega_H$$
$$w_e(\mathbf{x}, t) = w(\mathbf{x}, t) \ \text{ for } \mathbf{x} \in \Omega_H.$$

Finally, we observe that in both the differential and integral formulations of the Bidomain representation of the multicellular cardiac tissue, the macroscopic cardiac bioelectric sources generating the extracellular and extracardiac potentials consist of the volume dipole density $\mathbf{J}_v$.

5.3 Approximate Representation of Cardiac Sources

During the excitation phase of the heartbeat, the transmembrane potential v exhibits a steep transition layer propagating throughout the myocardium with a thickness of about 1 mm. At every point of the cardiac domain, this upstroke phase lasts about 1 ms. Therefore, the accurate simulation of the excitation process requires discretization methods based on small space and time steps (of the order of 0.1 mm and 0.01 ms). This fact constrained 3–D simulations, see e.g. [102, 104, 226, 544] and the recent survey [545], and in order to reduce the computational costs for the simulations of potential maps and electrocardiograms, approximate models of the cardiac sources have been developed and used.

The evolving thin layer of cells undergoing the depolarization upstroke and sweeping the whole ventricle is called the excitation wavefront and the excitation wavefront surface is defined by means of the so called *excitation or activation time* of the cell. During the excitation phase of the heart beat, each cell undergoes a fast upstroke of the transmembrane potential, starting from the resting state v_r, increasing monotonically during the depolarization upstroke and reaching finally a depolarized state v_d.

Therefore, at any point $\mathbf{x} \in \Omega_H$ there exists a unique instant $\varphi(\mathbf{x})$, called the activation time, such that

$$v(\mathbf{x}, \varphi(\mathbf{x})) = \frac{v_r + v_d}{2}.$$

Hence, at time t, the set

$$H_d(t) = \{\mathbf{x} \in \Omega_H : \varphi(\mathbf{x}) \le t\}$$

denotes the depolarized volume and we call its boundary

$$\partial H_d(t) = S_t = \{\mathbf{x} \in \Omega_H : \varphi(\mathbf{x}) = t\}$$

the excitation wavefront.

5.3.1   Heart Surface Source Model

In this subsection, we assume that the observation point $\mathbf{x} \in \Omega \setminus \Omega_H$ and the two conducting media have *equal anisotropy ratios*, i.e. $\frac{\sigma^e_{l,t,n}}{\sigma^i_{l,t,n}} = \lambda$ constant, which implies $D_e = \lambda D_i$. By Green's formula

$$\int_{\Omega_H} (\nabla_\xi v)^T D_i \nabla_\xi \psi(\boldsymbol{\xi}; \mathbf{x})\, d\xi = \int_{\partial H} v\, \mathbf{n}^T D_i \nabla_\xi \psi(\boldsymbol{\xi}; \mathbf{x})\, d\sigma_\xi$$

$$- \int_{\Omega_H} v\, \mathrm{div}(D_i \nabla_\xi \psi(\boldsymbol{\xi}; \mathbf{x}))\, d\xi,$$

where ∂H is the surface (endocardial and epicardial) bounding the ventricular myocardium Ω_H. Due to (5.8), because $\mathbf{x} \in \Omega \setminus \Omega_H$, the second term above is zero, in fact in Ω_H we have

$$0 = \mathrm{div}((D_i + D_e)\nabla_\xi \psi) = \mathrm{div}((1+\lambda)D_i \nabla_\xi \psi) = (1+\lambda)\,\mathrm{div}(D_i \nabla_\xi \psi). \quad (5.20)$$

Therefore, from Proposition 5.1, we obtain for $\mathbf{x} \in \Omega \setminus \Omega_H$

$$w_0(\mathbf{x}, t) = -\int_{\partial H} v(\boldsymbol{\xi}, t)\, \mathbf{n}^T D_i \nabla_\xi \psi(\boldsymbol{\xi}; \mathbf{x})\, d\sigma_\xi. \quad (5.21)$$

Thus, under the assumption of *equal anisotropy ratio*, the cardiac sources are represented as a dipole layer distributed on the epi-endocardial heart surface. For this reason, this model is called *heart surface source model*, see [197–199, 329, 570]. The dipole distribution has dipolar moment proportional to the transmembrane potential $v(\boldsymbol{\xi}, t)$, with oblique direction parallel to $D_i \mathbf{n}$ and oriented outward the cardiac tissue since $\mathbf{n}^T D_i \mathbf{n} > 0$.

Remark 5.1. If the transmembrane potential v is constant on the heart surface, then (5.21) predicts a zero potential w_0 at any point $\mathbf{x}$ outside the cardiac tissue. Indeed, for $v = c$ constant, due to (5.20) we have

$$\int_{\partial H} v\,\mathbf{n}^T D_i \nabla_\xi \psi(\boldsymbol{\xi};\mathbf{x})\,d\sigma_\xi = c \int_{\partial H} \mathbf{n}^T D_i \nabla_\xi \psi(\boldsymbol{\xi};\mathbf{x})\,d\sigma_\xi$$

$$= c \int_{\Omega_H} \operatorname{div}(D_i \nabla_\xi \psi(\boldsymbol{\xi};\mathbf{x}))\,d\mathbf{x} = 0. \quad (5.22)$$

It is reasonable to assume that the cardiac fibers are tangential to the cardiac surface, i.e. $a_l, a_n \perp \mathbf{n}$ on ∂H. Then we have $D_i \mathbf{n} = \sigma_t^i \mathbf{n}$, hence

$$w_0(\mathbf{x}, t) = -\int_{\partial H} \sigma_t^i v(\xi, t)\mathbf{n}^T \nabla_\xi \psi(\boldsymbol{\xi};\mathbf{x})\,d\sigma_\xi.$$

This model describes the evolution of w_0 during the entire heartbeat. Given the time interval $[0\ T]$, the average of the extracardiac potential w_0 can be written as

$$\frac{1}{T}\int_0^T w_0(\mathbf{x}, t)dt = -\int_{\partial H} \frac{1}{T}\left(\int_0^T v(\xi, t)dt\right)\sigma_t^i \mathbf{n}^T \nabla_\xi \psi(\boldsymbol{\xi};\mathbf{x})\,d\sigma_\xi.$$

This formula can be used to obtain the following two interesting expressions for time averages of the extracardiac potential.

(a) **QRS – T average.** During the QRS – T interval, the average transmembrane potential, shifted with respect to the resting value v_r,

$$\bar{v}(\xi) = \frac{1}{T}\int_0^T (v(\xi, t) - v_r)dt,$$

where T is the time of the T-wave ending, is the normalized area below the action potential time course. Hence we can express the QRS – T average of the extracardiac potential

$$\overline{w}_0(\mathbf{x}) = \frac{1}{T}\int_0^T w_0(\mathbf{x}, t)dt$$

as a heart surface integral involving the normalized area $\bar{v}(\xi)$ below the transmembrane potential v,

$$\overline{w}_0(\mathbf{x}) = -\int_{\partial H} \bar{v}(\xi)\sigma_t^i \mathbf{n}^T \nabla_\xi \psi(\boldsymbol{\xi};\mathbf{x})\,d\sigma_\xi.$$

(b) **QRS average.** During the QRS interval, the action potential is in the depolarization phase and it can be approximated with an activation profile $v(\xi, t) = A(t - \varphi(\xi))$, where $\varphi(\xi)$ is the activation time at point ξ. Then the QRS average

$$\overline{\overline{w}}_0(\mathbf{x}) = \frac{1}{T_d}\int_0^{T_d} w_0(\mathbf{x}, t)dt,$$

where T_d is the ending time of the QRS interval, has the representation

$$\overline{\overline{w}}_0(\mathbf{x}) = -\frac{1}{T_d} \int_{\partial H} \left(\int_0^{T_d} A(t - \varphi(\xi)) dt \right) \sigma_t^i \mathbf{n}^T \nabla_\xi \psi(\boldsymbol{\xi};\mathbf{x}) \, d\sigma_\xi. \qquad (5.23)$$

If we further approximate the activation profile with a Heaviside step function $\mathscr{H}$ from the resting value of v_r to the depolarized value v_d of v

$$A(t - \varphi(\xi)) = \mathscr{H}(t - \varphi(\xi))(v_d - v_r) + v_r,$$

then $\int_0^{T_d} A(t - \varphi(\xi)) dt = v_d T_d - (v_d - v_r)\varphi(\xi)$ and the QRS average (5.23) becomes

$$\overline{\overline{w}}_0(\xi) = \frac{v_d - v_r}{T_d} \int_{\partial H} \varphi(\xi) \sigma_t^i \mathbf{n}^T \nabla_\xi \psi(\boldsymbol{\xi};\mathbf{x}) \, d\sigma_\xi,$$

since by (5.22) it holds $\int_{\partial H} c \sigma_t^i \mathbf{n}^T \nabla_\xi \psi(\boldsymbol{\xi};\mathbf{x}) \, d\sigma_\xi = 0$ for any constant c. Thus, we can express the QRS average of the extracardiac potential as the heart surface integral involving the activation time.

5.3.2 Oblique Dipole Source Model

In this subsection, we assume general anisotropy of the intra- and extracellular media, but we focus only on the depolarization phase. Then, if the heart tissue is initially at rest and all cells undergo the same action potential profile $A(\xi)$ during the upstroke, the transmembrane potential can be approximated as

$$v(\mathbf{x}, t) = A(t - \varphi(\mathbf{x})).$$

From the representation formula in Proposition 5.1, we then have

$$w(\mathbf{x}, t) = \int_{\Omega_H} A'(t - \varphi(\mathbf{x}))(\nabla_\xi \varphi(\xi))^T D_i \nabla_\xi \psi(\boldsymbol{\xi};\mathbf{x}) \, d\xi.$$

Applying the *co-area formula*, see [5, 167],

$$\int_{\Omega_H} g(\xi)|\nabla_\xi \varphi(\xi)| \, d\xi = \int_{\mathbb{R}} \left(\int_{\varphi^{-1}(\tau) = S_\tau} g(\xi) d\sigma_\xi \right) d\tau$$

for a non-negative measurable function g and a Lipschitz function φ, and setting $\mathbf{n}_\xi(\xi) = \dfrac{\nabla_\xi \varphi(\xi)}{|\nabla_\xi \varphi(\xi)|}$, we have

$$w(\mathbf{x}, t) = \int_{\mathbb{R}} \int_{\varphi^{-1}(\tau) = S_\tau} A'(t - \varphi(\mathbf{x})) \mathbf{n}_\xi(\xi)^T D_i \nabla_\xi \psi(\xi; \mathbf{x}) d\sigma_\xi d\tau$$

$$= \int_{\mathbb{R}} A'(t - \tau) \left(\int_{S_\tau} (D_i \mathbf{n}_\xi)^T \nabla_\xi \psi(\xi; \mathbf{x}) d\sigma_\xi \right) d\tau. \tag{5.24}$$

By approximating the action potential profile during the depolarization phase with the jump discontinuity described by

$$A(t - \tau) = \mathscr{H}(\tau - t)(v_d - v_r) + v_r,$$

where $\mathscr{H}$ is the Heaviside step function, then $A'(t - \tau) = (v_d - v_r)\delta(\tau - t)$. In the limit when τ tends to t, we then obtain from (5.24) the following representation formula for $\mathbf{x} \notin S_t$

$$w(\mathbf{x}, t) = (v_d - v_r) \int_{\mathbb{R}} \delta(\tau - t) \left(\int_{S_\tau} (D_i \mathbf{n}_\xi)^T \nabla_\xi \psi(\xi; \mathbf{x}) d\sigma_\xi \right) d\tau$$

$$= (v_d - v_r) \int_{S_t} (D_i \mathbf{n}_\xi)^T \nabla_\xi \psi(\xi; \mathbf{x}) d\sigma_\xi d\tau. \tag{5.25}$$

In this formula, the cardiac excitation sources are represented as a dipole distribution supported on the excitation wavefront S_t, having oblique directions parallel to $D_i \mathbf{n}_\xi$ and with dipolar moment per unit surface area given by $(v_d - v_r)\|D_i \mathbf{n}_\xi\|_2$.

Assuming an infinite extracardiac medium and the same constant conductivity for the extracardiac and bulk tissue, i.e. $D_0 = D_i + D_e = \sigma_0 I$, then the Green function becomes

$$\psi(\xi; \mathbf{x}) = \frac{1}{4\pi\sigma_0} \frac{1}{|\xi - \mathbf{x}|},$$

so the extracellular potential w in (5.25) can be written as

$$w(\mathbf{x}, t) = \frac{(v_d - v_r)}{4\pi\sigma_0} \int_{S_t} (D_i \mathbf{n}_\xi)^T \nabla_\xi \frac{1}{|\xi - \mathbf{x}|} d\sigma_\xi.$$

If we assume further that $D_i = \sigma_i I$, then

$$w(\mathbf{x}, t) = \frac{1}{4\pi\sigma_0} \int_{S_t} \sigma_i (v_d - v_r) \frac{\partial}{\partial \mathbf{n}_\xi} |\xi - \mathbf{x}|^{-1} d\sigma_\xi, \tag{5.26}$$

which coincides with the representation of the cardiac excitation source in terms of normal dipoles uniformly distributed over the excitation surface S_t, also known as *uniform double layer*, see [535, Ch. 6]. If we define the moment per unit surface

$$p = \sigma_i (v_d - v_r),$$

then (5.26) becomes

$$w(\mathbf{x}, t) = \frac{1}{4\pi\sigma_0} p \int_{S_t} \frac{\partial}{\partial \mathbf{n}_\xi} |\xi - \mathbf{x}|^{-1} d\sigma_\xi.$$

Setting

$$d\omega(\mathbf{x}, \xi) = \frac{\partial}{\partial \mathbf{n}_\xi} |\xi - \mathbf{x}|^{-1} d\sigma_\xi = \mathbf{n}_\xi^T \nabla_\xi |\xi - \mathbf{x}|^{-1} d\sigma_\xi,$$

and defining the so-called *solid angle*

$$\omega(\mathbf{x}) = \int_{S_t} d\omega(\mathbf{x}, \xi) = -\int_{S_t} \frac{\mathbf{n}_\xi^T (\mathbf{x} - \xi)}{|\mathbf{x} - \xi|^3} d\sigma_\xi, \tag{5.27}$$

we obtain the representation

$$w(\mathbf{x}, t) = \frac{1}{4\pi\sigma_0} p \omega(\mathbf{x}). \tag{5.28}$$

This formula shows that the magnitude of the potential at a point $\mathbf{x}$ is proportional to the solid angle $\omega(\mathbf{x})$ under which the activation wavefront is seen from $\mathbf{x}$. The solid angle formula (5.27) and the associated potential representation (5.28) yield immediately some important consequences:

(a) The potential field external to a closed surface S_t is zero;
(b) The potential field due to an open surface S_t is completely defined by its boundary (rim);
(c) The potential is positive at a point $\mathbf{x}$ located "in front" of the surface S_t, i.e. where $\mathbf{n}_\xi^T (\xi - \mathbf{x}) < 0$, since there the solid angle is negative; viceversa, the potential is negative at a point $\mathbf{x}$ located "behind" the surface S_t, i.e. where $\mathbf{n}_\xi^T (\xi - \mathbf{x}) > 0$, since there the solid angle is positive.

These properties can be applied to the simple case of a single depolarizing wavefront spreading through the myocardium to obtain an approximate explanation of the ECG inflections. Indeed, by (c) a depolarization front propagating toward a positive electrode located at point $\mathbf{x}$ produces a positive signal, while a depolarization front propagating away from a positive electrode located at point $\mathbf{x}$ produces a negative signal. Moreover, if an excitation wavefront S_{t_1} at time t_1 propagates to a larger wavefront S_{t_2} at time $t_2 > t_1$ toward a positive electrode, then the potential increases,

$w(\mathbf{x}, t_1) < w(\mathbf{x}, t_2)$, while if the propagation is away from the electrode then the potential decreases, $w(\mathbf{x}, t_1) > w(\mathbf{x}, t_2)$. The previous prediction takes not into account the role of the anisotropic structure of the myocardium, which is instead incorporated in the following Sects. 5.4 and 5.5.

5.4 Cardiac Source Splitting

We present now a useful split form of the potential field, previously introduced in [116–118, 121, 510] to investigate some features of the potential $u(\mathbf{x}, t)$. It is used also as a tool for a more accurate computation of $u(\mathbf{x}, t)$. We focus first on the case, frequently considered, of a cardiac tissue which is characterized by conductivity tensors that are axially symmetric with respect to the local fiber direction; the extension of the split form to tensors with no axial symmetry can be found at the end of this paragraph.

5.4.1 Axially Symmetric Media

If $\mathbf{a} = \mathbf{a}(\mathbf{x})$ is the unit vector defining locally the fiber direction and $\sigma_l^{i,e}$, $\sigma_t^{i,e}$ are the conductivity coefficients along and across fiber in the intra- and extracellular medium, then the assumption of axial symmetry implies that the conductivity tensors D_i, D_e can be defined as

$$D_{i,e} = \sigma_t^{i,e} I + (\sigma_l^{i,e} - \sigma_t^{i,e})\mathbf{a} \otimes \mathbf{a}.$$

We recall that the bulk conductivity tensor D is given by

$$D = D_i + D_e = \sigma_t I + (\sigma_l - \sigma_t)\mathbf{a} \otimes \mathbf{a},$$

where $\sigma_t = \sigma_t^i + \sigma_t^e$ and $\sigma_l = \sigma_l^i + \sigma_l^e$. The conductivity coefficients may depend on the position $\mathbf{x}$ according to the local state, normal or diseased, of the various part of the myocardial tissue. It is easy to verify the following identity:

$$D_i = \alpha\, D + \beta\, \mathbf{a} \otimes \mathbf{a} \qquad (5.29)$$

with $\alpha = \sigma_t^i/\sigma_t$, $\beta = \sigma_l^i - \sigma_t^i \dfrac{\sigma_l}{\sigma_t}$, $\sigma_l = \sigma_l^i + \sigma_l^e$, $\sigma_t = \sigma_t^i + \sigma_t^e$. In fact, from the definition of the bulk conductivity tensor D, we have that

$$\sigma_t I = D - (\sigma_l - \sigma_t)\mathbf{a} \otimes \mathbf{a}.$$

Substituting it into the definition of the intracellular conductivity tensor D_i, we get

$$
\begin{aligned}
D_i &= \frac{\sigma_t^i}{\sigma_t}\left(D - (\sigma_l - \sigma_t)\mathbf{a} \otimes \mathbf{a}\right) + (\sigma_l^i - \sigma_t^i)\mathbf{a} \otimes \mathbf{a} \\
&= \frac{\sigma_t^i}{\sigma_t}D + \left(\sigma_l^i - \sigma_t^i - \frac{\sigma_t^i}{\sigma_t}(\sigma_l - \sigma_t)\right)\mathbf{a} \otimes \mathbf{a} \\
&= \frac{\sigma_t^i}{\sigma_t}D + \left(\sigma_l^i - \sigma_t^i\frac{\sigma_l}{\sigma_t}\right)\mathbf{a} \otimes \mathbf{a},
\end{aligned}
$$

thus identity (5.29) holds true.

The split (5.29) of D_i leads to the corresponding split of the "impressed" or "source" current density $\mathbf{J}_v = -D_i \nabla v$ yielding

$$
\mathbf{J}_v = -D_i \nabla v = \mathbf{J}_a + \mathbf{J}_c \tag{5.30}
$$

where

$$
\mathbf{J}_a = -\beta\,(\mathbf{a} \otimes \mathbf{a})\,\nabla v \qquad \text{and} \qquad \mathbf{J}_c = -\alpha D \nabla v. \tag{5.31}
$$

We call $\mathbf{J}_a$, $\mathbf{J}_c$ *axial* and *conormal* current densities since they define two distributions of dipolar current sources in the heart with dipole axes parallel respectively to the fiber direction $\mathbf{a}$ and to the vector $D\nabla v$.

Setting

$$
w(\mathbf{x}, t) = u(\mathbf{x}, t) - \frac{1}{|\Gamma|}\int_\Gamma u(\mathbf{x}, t)\,d\sigma
$$

and using the split form (5.30) of $\mathbf{J}_v$, relation (5.12) can be written as:

$$
w(\mathbf{x}, t) = w_a(\mathbf{x}, t) + w_c(\mathbf{x}, t) \tag{5.32}
$$

with

$$
w_a(\mathbf{x}, t) = \int_{\Omega_H} \mathbf{J}_a \cdot \nabla_\xi \psi\,d\xi \qquad \text{and} \qquad w_c(\mathbf{x}, t) = \int_{\Omega_H} \mathbf{J}_c \cdot \nabla_\xi \psi\,d\xi \tag{5.33}
$$

axial and *conormal* potential components. We remark that w_c and w_a, similarly to w, have zero average on Γ.

We can perform a further split of the field component w_c; in fact since $\alpha \nabla v = \nabla(\alpha v) - v\nabla\alpha$ it follows that:

$$
\mathbf{J}_c = -\alpha D \nabla v = -D\nabla(\alpha v) + vD\nabla\alpha
$$

hence, if the observation point $\mathbf{x} \notin \Sigma$:

$$
\begin{aligned}
w_c(\mathbf{x}, t) &= \int_{\Omega_H} \mathbf{J}_c \cdot \nabla \psi \, d\xi = - \int_{\Omega_H} \alpha \, (D\nabla v) \cdot \nabla \psi \, d\xi \\
&= - \int_{\Omega_H} (D\nabla(\alpha v)) \cdot \nabla \psi \, d\xi + \int_{\Omega_H} v \, (D\nabla \alpha) \cdot \nabla \psi \, d\xi \\
&= - \int_{\partial H} \alpha v \, (D\nabla_\xi \psi) \cdot \mathbf{n} \, d\sigma_\xi + \int_{\Omega_H} \alpha v \, \mathrm{div} \, D\nabla \psi \, d\xi \\
&\quad + \int_{\Omega_H} v \, (D\nabla \alpha) \cdot \nabla \psi \, d\xi.
\end{aligned}
$$

Noting that ψ is solution of problem (5.8) with (5.10) if $\mathbf{x} \in \Gamma$, we obtain:

$$
w_c(\mathbf{x}, t) = u_{hs}(\mathbf{x}, t) + u_d(t) + u_j(\mathbf{x}, t) + u_{nh}(\mathbf{x}, t), \tag{5.34}
$$

where

$$
u_{hs}(\mathbf{x}, t) = - \int_\Sigma \alpha v \, (D\nabla_\xi \psi) \cdot \mathbf{n} \, d\sigma_\xi \quad \text{heart surface component} \tag{5.35}
$$

$$
u_d(t) = \frac{1}{|\Gamma|} \int_{\Gamma_H} \alpha v \, d\sigma_\xi \quad\quad\quad \text{drift component} \tag{5.36}
$$

$$
u_j(\mathbf{x}, t) = \begin{cases} -\alpha v(\mathbf{x}, t) & \mathbf{x} \in \Omega_H \\ 0 & \mathbf{x} \in \Omega_0 \end{cases} \quad \text{jump component} \tag{5.37}
$$

$$
u_{nh}(\mathbf{x}, t) = \int_{\Omega_H} v \, (D\nabla \alpha) \cdot \nabla_\xi \psi \, d\xi \quad \text{non-homogeneous component.} \tag{5.38}
$$

Note that $u_d(t)$ is independent of the observation point $\mathbf{x}$ hence it acts as a drift component; moreover the component $u_{nh}(\mathbf{x}, t)$ gives a contribution only for tissue with non homogeneous anisotropy, i.e. when α is not constant.

The above decomposition of the conormal component holds if the observation point $\mathbf{x}$ does not lie on the non insulated boundary Σ (e.g. the endocardium in contact with intracavitary blood). If $\mathbf{x} \in \Sigma$ then the splitting of the conormal component must account for the discontinuity of the two components u_{hs} and u_j on Σ. More precisely applying classical limit formulae for the generalized double-layer potentials on Σ (see formula 15.3 of Theorem 15.II in [332]) we obtain the following trace and jump relationships:

$$
u_{hs}^\pm = \mp \frac{1}{2}\alpha v_{|_\Sigma} - \int_\Sigma \alpha v \, (D\nabla \psi) \cdot \mathbf{n} \, d\sigma_\xi, \quad\quad [\![\, u_{hs} \,]\!]_\Sigma = -\alpha \, v_{|_\Sigma}
$$

where $u_{hs}^{\pm}$ denotes the trace of the function on the positive and negative side of Σ with respect to the oriented normal $\mathbf{n}$. We remark that $w_c(\mathbf{x}, t) = u_{hs}(\mathbf{x}, t) + u_d(t) + u_j(\mathbf{x}, t)$ is continuous across Σ and has the following expression:

$$\mathbf{x} \in \Sigma, \; w_c(\mathbf{x}, t) = -\frac{1}{2}\alpha v|_{\Sigma} - \int_{\Sigma} \alpha v \, (D\nabla\psi) \cdot \mathbf{n} \, d\sigma_{\xi} + u_d(t) + u_j(\mathbf{x}, t) + u_{nh}(\mathbf{x}, t).$$

In the special case of Ω_H fully insulated (i.e. $\Gamma_H = \partial H$ and $\Sigma = \emptyset$) and α constant (i.e. $\nabla\alpha = 0$) the conormal component reduces to:

$$w_c(\mathbf{x}, t) = -\alpha v(\mathbf{x}, t) + \frac{\alpha}{|\Gamma|} \int_{\Gamma} v \, d\sigma_{\xi} \tag{5.39}$$

5.4.2 Orthotropic Media

Recent findings suggest that the cardiac tissue anisotropy is not symmetric across fibers, but, due to the presence of myocardial sheets (or laminae) (see [352]), three material principal axes can be identified, thus it presents an orthotropic structure. Actually, the split form of the potential $w(\mathbf{x}, t)$ can be extended to the case of no axial symmetry for the conductivity tensors D_i, D_e. In fact we can assume that $D_{i,e}$ have three distinct eigenvalues $\sigma_l^{i,e}$, $\sigma_t^{i,e}$ and $\sigma_n^{i,e}$ with the same principal axes given by the set of orthonormal eigenvectors $\mathbf{a}_k$, $k = l, t, n$ with $\mathbf{a}_k \cdot \mathbf{a}_j = \delta_{jk}$ and $\mathbf{a}_l = \mathbf{a}$, i.e. tangent locally to the fiber. Setting $A = (\mathbf{a}_l, \mathbf{a}_t, \mathbf{a}_n)$, $D_{diag}^{i,e} = diag(\sigma_l^{i,e}, \sigma_t^{i,e}, \sigma_n^{i,e})$ and using the property that $AA^T = A^T A = I$, where A^T and I denote respectively the transpose of A and the identity matrix, we obtain:

$$D_{i,e} = AD_{diag}^{i,e} A^T.$$

The equivalent expression of $D_{i,e}$ is

$$D_{i,e} = \sigma_t^{i,e} I + (\sigma_l^{i,e} - \sigma_t^{i,e})\mathbf{a}_l \otimes \mathbf{a}_l + (\sigma_n^{i,e} - \sigma_t^{i,e})\mathbf{a}_n \otimes \mathbf{a}_n,$$

and as a by-product the bulk conductivity tensor is given by

$$D = \sigma_t I + (\sigma_l - \sigma_t)\mathbf{a}_l \otimes \mathbf{a}_l + (\sigma_n - \sigma_t)\mathbf{a}_n \otimes \mathbf{a}_n,$$

with $\sigma_{l,t,n} = \sigma_{l,t,n}^i + \sigma_{l,t,n}^e$. It is easy to verify that, if the axial symmetry is not assumed (i.e. distinct eigenvalues) then

$$D_i = \alpha D + \beta \mathbf{a}_l \otimes \mathbf{a}_l + \gamma(I - \mathbf{a}_l \otimes \mathbf{a}_l), \tag{5.40}$$

with $\alpha = (\sigma_n^i - \sigma_t^i)/(\sigma_n - \sigma_t)$, $\beta = \sigma_l^i - \alpha\sigma_l$, $\gamma = \sigma_t^i - \alpha\sigma_t$. In fact, given $\alpha \in \mathbb{R}$, we have

$$D_i - \alpha D = (\sigma_t^i - \alpha\sigma_t)I$$
$$+ (\sigma_l^i - \sigma_t^i - \alpha(\sigma_l - \sigma_t))\mathbf{a}_l \otimes \mathbf{a}_l$$
$$+ (\sigma_n^i - \sigma_t^i - \alpha(\sigma_n - \sigma_t))\mathbf{a}_n \otimes \mathbf{a}_n.$$

Choosing $\alpha = (\sigma_n^i - \sigma_t^i)/(\sigma_n - \sigma_t)$, the last term vanishes and we get the split form (5.40). We remark that $I - \mathbf{a}_l \otimes \mathbf{a}_l$ is the orthogonal projection matrix on a plane perpendicular to the fiber direction $\mathbf{a}_l$.

If $\sigma_n^{i,e} = \rho_{i,e}\sigma_t^{i,e}$, then the media (i) and (e) tend to become axially symmetric for $\rho_{i,e} \to 1$ with the limit values $\sigma_n^{i,e} = \sigma_t^{i,e}$. Setting $\tau_{i,e} = 1 - \rho_{i,e}$, if $\tau_i/\tau_e \to 1$ as $\rho_{i,e} \to 1$ then it is easy to verify that α, β, γ tend to σ_t^i/σ_t, $\sigma_l^i - \sigma_t^i \dfrac{\sigma_l}{\sigma_t}$, 0 respectively, which are the values obtained directly under the assumption of axial symmetry.

In the orthotropic case, the split of the conductivity tensor D_i leads to a corresponding split of the impressed current $\mathbf{J}_v$ yielding:

$$\mathbf{J}_v = \mathbf{J}_c + \mathbf{J}_a + \mathbf{J}_o$$

with $\mathbf{J}_a$ and $\mathbf{J}_c$ defined as before with different α and β whereas $\mathbf{J}_o = -\gamma(I - \mathbf{a}_l \otimes \mathbf{a}_l)\nabla v$ is a new current density of dipoles transverse to the fibers.

5.5 Interpretation of the Field Components

From the relation between the field components and their sources we establish some correlations between pattern features displayed by the full potential and some structure of the underlying cardiac sources. The potential components deduced from the potential split depend on $v(\mathbf{x}, t)$, which is a quantity of direct electrophysiological significance since it characterizes the electric state of the myocardial cells. The analysis of these components can shed light on the properties of the full potential field. In the following, we focus only on the axisymmetric components of the splitting.

Axial component (w_a): the potential w_a can be related to the source $\mathbf{J}_a$ by

$$w_a(\mathbf{x}, t) = \int_{\Omega_H} \mathbf{J}_a^T \nabla_\xi \psi \, d\xi = -\int_{\Omega_H} \beta(\mathbf{a}_l^T \nabla v)\mathbf{a}_l^T \nabla_\xi \psi \, d\xi.$$

This expression shows that the potential w_a is generated by volume sources represented by a current dipole density with dipole moment per unit volume proportional to the vector $(\mathbf{a}_l^T \nabla v)\mathbf{a}_l$. Therefore the dipole current sources are parallel to the local fiber direction $\mathbf{a}_l$ and we call w_a *axial* potential. Since the fiber architecture defines the direction of the current source flow, we expect that structural properties like epi–endocardial fiber rotation will be the major determinants affecting the axial potential pattern.

When the excitation wavefront propagates through the heart muscle, it occupies a thin layer of myocardium, 1 or 2 mm thick, that is passing from the resting to the excited state. Within this layer, the distribution of axial sources has greater dipole strength per unit volume in those regions in which the wavefront is spreading mainly along fibers, i.e. where ∇v is nearly parallel to $\mathbf{a}_l$.

Jump component (u_j): we recall that the resting value v_r has been set to zero so that in our model v measures the deviation of the transmembrane potential from the resting state. We remark that the potential component $u_j(\mathbf{x}, t) = -\alpha v(\mathbf{x}, t)$ is zero in Ω_0, whereas in Ω_H it is proportional to the spatial distribution of the transmembrane potential. Since v, in our model, displays an upstroke in a thin layer of tissue containing the wavefront and it is practically constant everywhere else, this field component does not generate an appreciable current flow at distance from the front. Moreover in the fully activated region the effect of u_j on the full potential u reduces only to a shift proportional to the jump of the transmembrane potential from the resting to the plateau value. For this reason we call u_j *jump* component.

Heart surface component (u_{hs}): the potential component u_{hs} is given by

$$u_{hs}(\mathbf{x}, t) = \int_\Sigma (\alpha v D\mathbf{n})^T \nabla_\xi \psi \, d\sigma_\xi. \tag{5.41}$$

We remark that u_{hs} contributes to the full potential u only when the heart surface is in contact with an extracardiac conducting medium (i.e. the non-insulated cardiac interface Σ is not empty) and depends on the trace on Σ of the transmembrane potential v. Since the sources lie on the non-insulated heart surface Σ, we refer to this field component, as usual in the literature (see e.g. [197, 198, 483]), as heart surface component.

The differential formulation shows that u_{hs} exhibits a jump through Σ equal to αv and the moment of the dipole layer source on Σ is proportional to this jump; on the unexcited parts of Σ, i.e. where v is practically zero, this jump vanishes.

In order to describe in a different and more meaningful way the relationship between the field component u_{hs} and its heart surface source, we make the following simplifying assumptions: uniform anisotropy on ∂H, homogeneity on $\partial \Omega_0$ (i.e. $\sigma_l^{i,e}$, $\sigma_t^{i,e}$, σ_0 constant on Σ) and the fibers tangent to the epi- and endocardial surfaces (i.e. $\mathbf{a}_l^T \mathbf{n} = 0$ on Σ). Hence in particular on Σ we have $D\mathbf{n} = \sigma_t I$, $D_0 \mathbf{n} = \sigma_0 I$ implying $D\mathbf{n} = \lambda D_0 \mathbf{n}$ with $\lambda = \sigma_t / \sigma_0$; consequently u_{hs} can be viewed as the potential generated by a source term $\mathbf{J}_{hs}$ satisfying in the sense of distribution (see [110, 305]) the equation

$$\text{div } D\nabla u_{hs} = \text{div } \mathbf{J}_{hs} \text{ in } \Omega, \qquad \text{with} \quad \mathbf{J}_{hs} = \sigma_t^i v \delta_\Sigma \mathbf{n}_\Sigma, \tag{5.42}$$

where $D = D$ in Ω_H and $D = \lambda D_0$ in Ω_0, $\mathbf{n}_\Sigma$ is the unit normal to Σ and δ_Σ the Dirac measure on Σ. Therefore u_{hs} can be viewed as the field generated by a normal dipole layer on Σ with moment $\sigma_t^i v$. If the excitation wavefront is far from Σ then v and consequently u_{hs} are practically zero. Otherwise, denoting by Σ_d the intersection on Σ of the activated region, since v, apart a thin strip near $\partial \Sigma_d$, is

very close to v_J on Σ_d and α is constant, it follows that the normal dipole layer is practically uniform on Σ_d. Thus, the most remarkable property of u_{hs} is that it can be well approximated by means of the *classical model*, i.e. the potential generated by a normal and uniform dipole layer on Σ_d in the conducting medium described by the tensor $\hat{D}$.

Non-homogeneous component (u_{nh}): the field component u_{nh} is given by

$$u_{nh}(\mathbf{x}, t) = \int_{\Omega_H} v(D\nabla\alpha)^T \nabla_\xi \psi \, d\xi.$$

Component u_{nh} makes no contribution to the potential distribution when α is constant, i.e. when the anisotropy ratio σ_t^e/σ_t^i is constant characterizing a cardiac tissue with a transverse 'uniform' anisotropy. Hence in normal cardiac tissue, this field component should not affect the potential distribution. This is due to the fact that the normal tissue can be modeled assuming a uniform anisotropy. This field component should significantly affect the full potential pattern only in presence of pathological myocardial tissue with inhomogeneous transverse conductivity, as occurs for instance in the surviving tissue near a chronic infarct. Due to this interpretation we call u_{nh} the *non-homogeneous* tissue component.

In the previous derivation of the split form we have implicitly assumed that $\alpha(\mathbf{x})$ is a smooth function; when $\alpha(\mathbf{x})$ presents a discontinuity interface Λ, a new surface integral term appears given by

$$\int_\Lambda v [\![\, \alpha \,]\!] \mathbf{n}^T D \nabla_\xi \psi \, d\sigma_\xi, \tag{5.43}$$

where $[\![\, \alpha \,]\!]$ measures the jump through the interface Λ, i.e. $[\![\, \alpha \,]\!] = \alpha^+ - \alpha^-$, where $\alpha^\pm$ are the traces taken on the positive and negative side of Λ with respect to the oriented normal. A sudden variation of α could model the transition from a region with normal conduction to a pathological one with depressed conduction. Moreover if α is piecewise constant in two contiguous tissue volumes, the u_{nh} component reduces to the surface integral (5.43), which is a potential generated by a secondary source distributed on the discontinuity interface Λ having a current dipole moment density $v [\![\, \alpha \,]\!] D\mathbf{n}$, hence with dipoles parallel to $D\mathbf{n}$.

This component should affect the electrocardiogram (ECG) waveform, recorded from the transition regions, in a manner similar to the one described in [45, 297].

5.6   The Limit Case: Oblique Dipole Layer Model

Let us denote by $H_d(t)$ the depolarized region, by $H_r(t)$ the resting region and by Σ_d and Σ_r their intersections with Σ (one of the two can be void). The two regions $H_d(t)$ and $H_r(t)$, are characterized by an activation time $\varphi(\mathbf{x})$ whose value is respectively smaller or greater than the fixed time instant t. Remembering that

the transmembrane potential v is approximated by $v(\mathbf{x}, t) = A(t - \varphi(\mathbf{x}))$, the upstroke phase is characterized by the steepest part of the profile of the action potential $\mathscr{A}$ and by a corresponding thin layer of tissue, containing the excitation wavefront, across which the fast variation of the transmembrane potential occurs. Focusing on the potential pattern at a distance from the excitation wavefront, the details of the upstroke phase can be neglected and it is natural to consider the limit case obtained when $\mathscr{A}(\tau)$ approaches the step function $v_J \mathscr{H}(\tau)$, where $\mathscr{H}$ is the Heaviside function. Remembering that v measures the deviation of the transmembrane potential from the resting state, then the jump component $u_j = -\alpha v$ in Ω_H approaches $-\alpha v_J \mathscr{H}(t - \varphi(\mathbf{x}))$, i.e. it is constant in the activated and resting regions and undergoes a jump through the wavefront surface $S_t = \{\mathbf{x} \in \Omega_H, \varphi(\mathbf{x}) = t\}$. Hence the jump component does not contribute to the extracellular current. At the same time $\nabla v(\mathbf{x}, t)$ tends to $-v_J \mathbf{n}_{S_t} \delta_{S_t}$ in the distributional sense, where δ_{S_t} is the Dirac measure on S_t and $\mathbf{n}_{S_t}$ is the unit normal to S_t directed toward the resting tissue. Thus using Eq. (5.19), in the limit case, we obtain

$$u(\mathbf{x}, t) = \int_{S_t} v_J \mathbf{n}_{S_t}^T D_i \nabla_\xi \psi d\sigma_\xi = \begin{cases} u_a(\mathbf{x}, t) + u_{hs}(\mathbf{x}, t) & t < \varphi(\mathbf{x}) \\ u_a(\mathbf{x}, t) + u_{hs}(\mathbf{x}, t) - \alpha v_J & t > \varphi(\mathbf{x}), \end{cases}$$
(5.44)

where the axial and the heart surface components, in the limit case, are given by the following surface integrals:

$$u_a(\mathbf{x}, t) = \beta \int_{S_t} v_J (\mathbf{a}_l^T \mathbf{n}_{S_t}) \mathbf{a}_l^T \nabla_\xi \psi d\sigma_\xi \quad \text{and} \quad u_{hs}(\mathbf{x}, t) = \alpha \int_{\Sigma_d} v_J \mathbf{n}_{S_t}^T D \nabla_\xi \psi d\sigma_\xi.$$
(5.45)

In Eq. (5.44), the current sources are concentrated on the wavefront surface S_t and are defined by a dipole layer with local dipole direction $D_i \mathbf{n}$. This model, also called *oblique dipole layer model*, was proposed in [108] and subsequently investigated in [110, 113].

   We remark that the u_{hs} component presents a jump equal to αv_J through Σ_d whereas it is continuous across Σ_r. This means that different depolarized regions H_d having the same Σ_d on Σ give rise to the same field component u_{hs}. This is reminiscent of a property of the potential field generated by a uniform normal dipole layer. Indeed, the potential generated by these sources, when they are imbedded in an infinite homogeneous isotropic medium (i.e. $\psi = (|\mathbf{x} - \xi|^{-1} - |\mathbf{x}_0 - \xi|^{-1})/(4\pi\sigma_0)$) is given by $u_{hs} = \alpha v_J \omega(\mathbf{x})$, where ω is the solid angle subtended in $\mathbf{x} \in H_r$ by the surface Σ_d. Thus for a given Σ the field component u_{hs} depends only on the rim of the wave front intersection on Σ.

   In summary, we have shown that when the anisotropic myocardial tissue is in contact with conducting media, the potential presents a component u_{hs}, having, in the anisotropic context, the same features as the classical solid angle formula.

In particular, this component has the peculiarity that it acts only when either the epicardial or endocardial surface or both are not completely insulated and is revealed, becoming measurable, only when activation reaches these non-insulated boundaries; moreover the magnitude of its contribution is practically independent of the wave front shape but depends only on the activated areas enclosed by the wave front rim lying on the noninsulated boundaries. The jump component u_j, related to activated region (see Eq. (5.44)), introduces a shift of the potential. The sum of these two components u_j and u_{hs} is the conormal component u_c, usually referred to as the heart surface source model, see [197, 198, 483].

From the split form it follows that for tissue having uniform anisotropy the full potential is derived by superimposing the axial potential to the previously mentioned potential components (due to the heart surface model and activating volume).

For tissue having uniform anisotropy, i.e. $\sigma_l^{i,e}$, $\sigma_t^{i,e}$ constant in Ω_H, as assumed in the numerical simulations, the full potential is derived by superimposing the axial potential to the conormal component which in turn is the sum of the heart surface component u_{hs} and the potential jump u_j across the wave front. The ability of expressing the field as the sum of the axial and conormal components enables us to underline the difference between the field produced by the classical conormal model and the actual cardiac field.

It is worth mentioning here that the estimates of the intra- and extracellular conductivities do not verify the condition of equal anisotropy ratio. Nevertheless many computational studies in electrocardiology have often used this assumption. Under this hypothesis $\beta = 0$ hence u_a drops out and consequently the cardiac fiber arrangement plays no role in determining the structure of the current source density. Cardiac anisotropy influences only the current conduction flow in the bulk medium, described by the tensor D but frequently handled as an isotropic conducting medium [108, 113, 198, 295, 483]. Therefore under the equal anisotropy ratio condition the model reduces to $u = u_c + u_{hs} + u_j$ and coincides with the heart surface source model used in [197, 198, 483]. As a consequence this model reduces to the conormal one.

The more realistic physiological situation of a Bidomain model with unequal anisotropy ratio, involves the heart surface model with the addition of the axial potential component; the latter introduces a strong dependence of the cardiac sources on the fiber anisotropy and architecture.

5.7 Experimental and Simulation Results

Figure 5.2 illustrates the connections between the epicardial potential patterns and the intramural currents produced by the various source components described in the previous section. Potential distributions are shown on the epicardial surface and on three intramural sections: vertical, horizontal and oblique. On the intramural
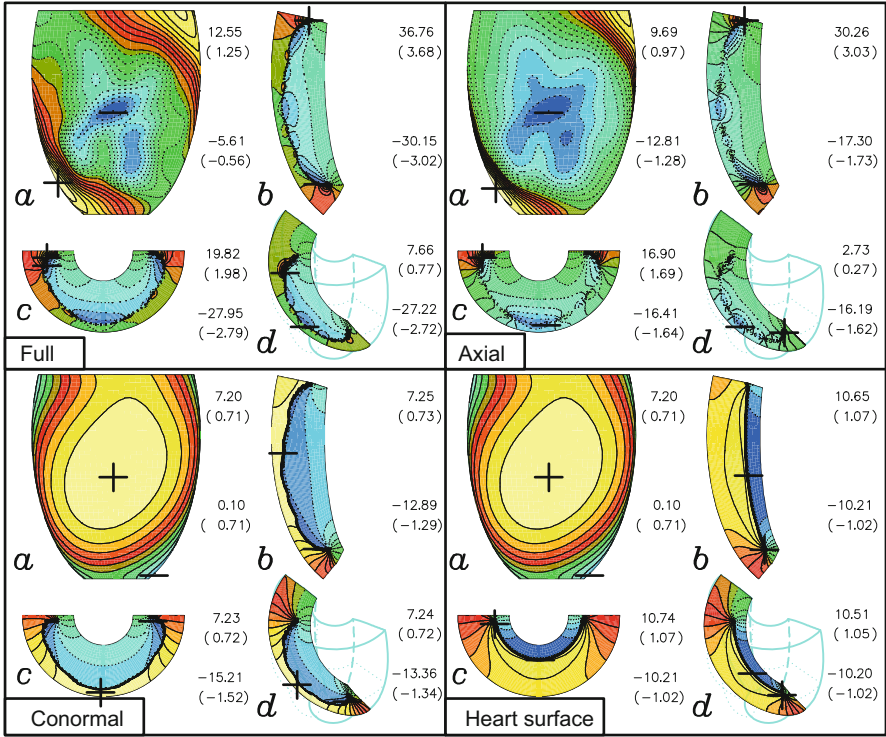
Fig. 5.2 Source splitting of the full extracellular potential into axial, conormal and heart surface components at 30 ms after endocardial pacing. In each panel, the potentials are shown on epicardial (*a*), meridian (*b*), horizontal (*c*), oblique (*d*) sections of a truncated ellipsoid in contact with intracavitary blood, with $\rho_i = 9.5$, $\sigma_b = 6\,\mathrm{mS\,cm^{-1}}$

sections (panels b, c, d) the axial and conormal components produce substantially different current fields. In fact, the inspection of the potential gradients shows that the currents generated by the conormal component flow from all portions of the wavefront toward the epicardial surface (outflowing currents), whereas the axial component produces currents that flow toward and into extensive portions of the advancing wavefront, propagating mainly across fibers (inflowing currents). The densely packed lines characterizing the intersection of the wavefront with the three sections b, c, d, indicate a strong gradient associated with the conormal component. Conversely, the potential gradients produced by the axial component where the currents flow toward the wavefront are comparatively weaker. The conormal and heart surface panels of Fig. 5.2 show that, at 30 ms, the two components coincide on the epicardium. This indicates an extremely weak effect of the jump component (the difference between the conormal and heart surface components) on the epicardial surface, in accordance with the lack of epicardial breakthrough. In addition, in the heart surface panel of Fig. 5.2, the narrow strip of level lines, located at the basis

of the wavefront in contact with the intracavitary blood, indicates that the heart surface component presents a jump through this basis. This jump characterizes a source, lying on this interface, generating a current that spreads through the wall thickness and reaches the insulated epicardial surface tangentially. If we disregard the medium anisotropy, the heart surface features are similar to those exhibited by the potential field generated in an isotropic medium by a classical source model, i.e. a normal dipole layer lying on the same wavefront basis and having dipole moment proportional to the jump component.

Figure 5.3 shows other simulation results on an oblique section in a test with intracavitary blood and extracardiac conducting medium (outside the red contour delimiting the cardiac tissue). The full (left panel) and conormal (right panel) components are shown on an oblique section of the domain. The full component shows that at 30 ms the epicardial breakthrough has not yet occurred, so in the potential map on the epicardium we observe a typical pattern characterized by the presence of two positive maxima separated by a negative area surrounding a central minimum. Most of the epicardial current lines, issuing from the area of maximum positivity, point toward the minimum site, either directly or after bending. Consequently this minimum acts as a sink for the current flow, whereas the conormal component predicts that any portion of the wavefront surface acts as a source for the current flow.

These simulated results are confirmed by the experimental results of Fig. 5.4, where the current lines are shown (in red) both inside the cardiac domain and in the torso, on the indicated diagonal section. As in the simulated results of Fig. 5.3,
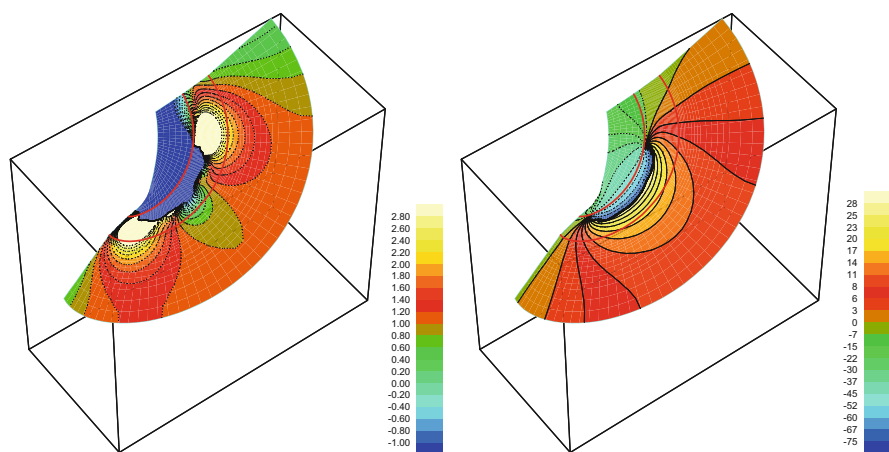
Fig. 5.3 Source splitting; full (*left*) and conormal (*right*) components of extracellular potentials at 30 ms on truncated ellipsoid, with $\rho_i = 9.5$, $\sigma_b = 6\,\mathrm{mS\,cm}^{-1}$
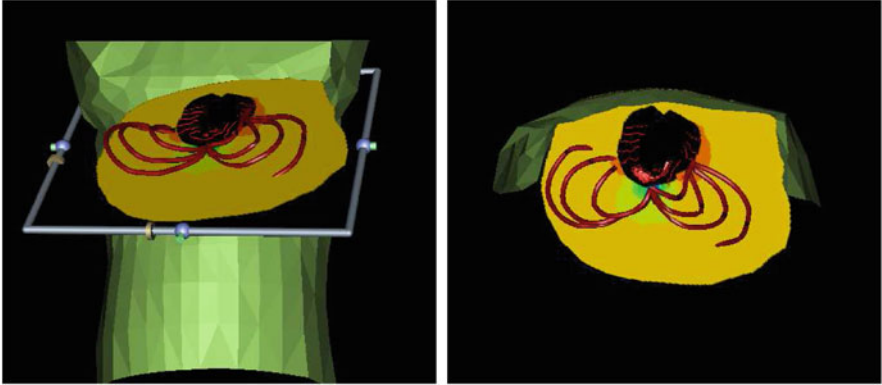
Fig. 5.4 Experimental results of extracellular potentials related to an isolated heart embedded in a torso tank (Courtesy of prof. B. Taccardi)

the current lines issue from two positive maxima and point toward the sink (marked in green in the right panel of Fig. 5.4). For more details, analysis and physiological interpretation of the potential and current pathways in the extracardiac medium, see [350, 513, 514, 516].

Chapter 6
The Inverse Problem of Electrocardiology

Since the end of the 1970s, automated instruments have been employed to record potential Body Surface Maps (BSM), see e.g. [144, 504, 505, 511]. The spreading of these techniques of potential recording is motivated by the fact that BSM provide diagnostic information which could not be obtained by conventional electrocardiograms in many heart diseases, such as Wolff-Parkinson-White and myocardial ischemia. In fact some features of the potential surface field, such as the number, location and time course of potential maxima and minima on the chest surface, are correlated to the shape of the depolarization wavefronts and to the spatial distribution of the repolarization processes in the heart, which are the phenomena generating bioelectrical currents.

BSM exhibit a highly changeable surface pattern as characterized by equipotential lines; moreover there is a high variability of the surface signal magnitude over the entire heartbeat. The diffusion of BSM technique has raised the problem of the interpretation of potential distribution on the thorax. The problem of the best use of the information content of the large amount of data provided by BSM may be attempted by solving the so-called Forward and Inverse problems of Electrocardiology. Two approaches are possible:

- (P) in terms of potential alone;
- (S) in terms of cardiac sources.

In the first approach (P), the *Forward problem* consists of:
  simulating the BSM from the epicardial extracellular potential distribution,
while the *Inverse problem* consists of:
  estimating the epicardial extracellular potential distribution from the BSM.
We remark that this approach is justified by experimental studies on animals both in vitro and in vivo, which show that epicardial maps contain a great amount of information more directly readable in terms of the underlying cardiac events than BSM; moreover in this approach it is possible to compare quantitatively computed epicardial maps with the measured ones collected in experiments on animals.

The second approach (S) consists of modeling the cardiac sources by means of the so-called *equivalent cardiac generators*, hence the *Forward problem* consists of:

simulating the BSM by means of an *adequate* Equivalent Generator Model,

while the *Inverse problem* consists of:

identifying an *adequate* Equivalent Generator of the heart from BSM.

Many groups have investigated methods for reconstructing the cardiac electric activity with both the approaches, see e.g. [29, 64, 89, 106, 107, 111, 143, 210, 215, 222, 325, 353, 407, 440–442, 534, 550].

6.1 Inverse Problem in Terms of Potential Alone

In relation to the feasibility of the inverse problem in terms of potential alone, the following question arises: *to what extent can the potential distribution on the heart surface be computed from BSM?* We discuss here the relevant features concerning this question.

The human body Ω can be considered as an isotropic linear resistive conducting medium excluding the cardiac region Ω_H. At any time instant of the heartbeat the electric field can be considered quasi-static (see [394]) and the volume conductor Ω is embedded into an insulating medium (the air), i.e. the normal derivative of the potential is zero on $\Gamma = \partial\Omega$. We set $\Omega_0 = \Omega \setminus \Omega_H$, i.e. the extracardiac medium, $k(\mathbf{x})$ the electrical conductivity and $\Gamma_H = \partial\Omega_H$ represents a fixed surface surrounding the heart and lying in proximity of the heart surface; in the following, Γ_H is referred to as epicardial surface. At any time t let $V(\mathbf{x})$ be the electric potential distribution in Ω_0. If $u(\mathbf{x}) = V(\mathbf{x})_{|\Gamma_H}$ is known, then $V(\mathbf{x})$ in Ω_0 is characterized by the following mixed boundary problem:

$$\begin{cases} \text{div } k(\mathbf{x})\nabla V(\mathbf{x}) = 0 & \text{in } \Omega_0 \\ V(\mathbf{x}) = u(\mathbf{x}) & \text{on } \Gamma_H \\ \dfrac{\partial V(\mathbf{x})}{\partial \mathbf{n}} = 0 & \text{on } \Gamma \end{cases}$$

and the forward problem consists of evaluating $V(\mathbf{x})$ on Γ. If no information is available about $V(\mathbf{x})$ on Γ_H, but it is possible to measure $V(\mathbf{x}) = z(\mathbf{x})$ on $\Sigma \subset \Gamma$, then we have:

$$\begin{cases} \text{div } k(\mathbf{x})\nabla V(\mathbf{x}) = 0 & \text{in } \Omega_0 \\ V(\mathbf{x}) = z(\mathbf{x}) & \text{on } \Sigma \\ \dfrac{\partial V(\mathbf{x})}{\partial \mathbf{n}} = 0 & \text{on } \Gamma \end{cases} \tag{6.1}$$

and the inverse problem consists of estimating $V(\mathbf{x})$ on Γ_H. If the observed potential z on Σ were measured error-free, the Cauchy problem for the elliptic operator (6.1) would define a unique solution $V(\mathbf{x})$, but in a highly unstable fashion, since, as it

is well known, the Cauchy problem for elliptic operators is an ill-posed problem in usual Sobolev spaces, see [236, 249, 374, 518]. Let $v \in L^2(\Gamma_H)$ define the state $y(\mathbf{x}; v) = y(v)$ as the unique solution in $H^{\frac{1}{2}}(\Omega_0)$ of

$$\begin{cases} \operatorname{div} k(\mathbf{x}) \nabla y(v) = 0 & \text{in } \Omega_0 \\ y(v) = v & \text{on } \Gamma_H \\ \dfrac{\partial y(v)}{\partial \mathbf{n}} = 0 & \text{on } \Gamma, \end{cases}$$

then we introduce the following operator

$$Av = y(v)_{|\Sigma}$$

and for $z \in L^2(\Sigma)$ the cost function

$$J(v) = \int_{\Sigma} |y(v) - z|^2 d\sigma = ||Av - z||_{0,\Sigma}^2.$$

We consider the minimization problem:

$$\text{find } u \in L^2(\Gamma_H) : \quad J(u) = \inf_{v \in L^2(\Gamma_H)} J(v). \tag{6.2}$$

If $z \in A(L^2(\Gamma_H))$, i.e. there exists a unique solution of the Cauchy problem, then $u = V(\mathbf{x})_{|\Gamma_H} \in L^2(\Gamma_H)$ satisfies $Au = z$, hence u is the unique minimizer of J. But the problem is still unstable, i.e. the operator A admits an unbounded inverse operator in the spaces H^s, $\forall s \in \mathbb{R}$. In order to solve the problem one must approximate it with a family of stable problems. Many methods are available to perform this stabilization. We first present *Tikhonov* regularization techniques, by imposing smoothing constraints justified by the physical problem. We consider the following Tikhonov zero-order, first-order and second-order regularizations:

Space of admissible Controls U		Regularization Operator B
$U = L^2(\Gamma_H)$	with	$B = I_{|\Gamma_H}$
$U = H^1(\Gamma_H) = \{v \in L^2(\Gamma_H) : Bv \in L^2(\Gamma_H)\}$	with	$B = \nabla_{|\Gamma_H}$
$U = H^2(\Gamma_H) = \{v \in L^2(\Gamma_H) : Bv \in L^2(\Gamma_H)\}$	with	$B = \Delta_{|\Gamma_H}.$

Defining the regularization cost function

$$J_\epsilon(v) = J(v) + \epsilon \int_{\Gamma_H} |Bv|^2 d\sigma, \quad v \in U, \quad \epsilon > 0 \text{ “small”}, \tag{6.3}$$

then the inverse problem (6.2) is approximated by the following family of stable problems dependent on ϵ:

$$\text{find } u_\epsilon \in U : \ J_\epsilon(u_\epsilon) = \min_{v \in U} J_\epsilon(v). \tag{6.4}$$

We refer to [304] for the existence, the uniqueness of the minimizer u of (6.4) and for the convergence of u_ϵ to u.

Some Authors have also recently considered $L1$-regularizations considering the total variation of v, i.e.

$$J_\epsilon(v) = J(v) + \epsilon \int_{\Gamma_H} |\nabla v| d\sigma, \quad v \in U, \quad \epsilon > 0 \text{ "small"},$$

yielding two non-linear minimization problems, see e.g. [200, 477].

For the numerical approximation of the regularized problem (6.4), it is necessary to introduce a finite dimension approximation U_h of the control space U and an approximate observation operator A_h of A. If we consider a parametrization of the control u (having n degrees of freedom):

$$u(\mathbf{x}) = \sum_{i=1}^{n} u_i w_i^0(\mathbf{x}) \quad \text{then} \quad y(\mathbf{x}; u) = \sum_{i=1}^{n} u_i y_i(\mathbf{x}),$$

where $y_i(\mathbf{x})$ is the solution of:

$$\begin{cases} \operatorname{div} K(\mathbf{x}) \nabla y_i(\mathbf{x}) = 0 \quad \text{in} \quad \Omega \\ y_i(\mathbf{x})_{|\Gamma_0} = w_i^0(\mathbf{x}), \quad \dfrac{\partial y_i(\mathbf{x})}{\partial \mathbf{n}}_{|\Gamma_1} = 0 \qquad i = 1, \ldots, n \\ Au = \sum_{i=1}^{n} u_i y_i(\mathbf{x})_{|\Sigma}. \end{cases} \tag{6.5}$$

Hence a way of building an approximate operator of A consists in the numerical solution of the previous n mixed boundary elliptic problems. The approximate solution $y_i^h(\mathbf{x})$ of $y_i(\mathbf{x})$, solution of (6.5), can be obtained by means of the finite element method applied to the three-dimensional variational formulation of problem (6.5). The numerical computation can be performed using finite elements of first order, see [111]. Denoting by Σ^h, Γ_0^h the discretized surfaces respectively of Σ and Γ_0 and by $\{\mathbf{x}_j^\Sigma\}_{j=1,m}$, $\{\mathbf{x}_k^{\Gamma_0}\}_{k=1,n}$ the mesh points of Σ^h and Γ_0^h, we define:

$$A_h u_h = y^h(\mathbf{x}; u_h)_{|\Sigma^h} = \sum_{k=1}^{n} u_k y_k^h(\mathbf{x})_{|\Sigma^h}, \tag{6.6}$$

where $u_h = \sum_{k=1}^{n} u_k w_k^0(\mathbf{x})$, $\{w_k^0\}_{k=1,n}$ is a basis of the finite element space used on Γ_0^h and $\underline{u} = (u_1, \ldots, u_n)^T$ is the vector of the nodal values of u_h on Γ_0^h. Setting

$\underline{z} = \{(A_h u_h)(\mathbf{x}_j^{\Sigma})\}_{j=1,m}$ the vector of nodal values of $A_h u_h$ on Σ^h then in terms of $\underline{z}$ and $\underline{u}$ the relation (6.6) implies

$$\underline{z} = T\underline{u},$$

where

$$T = \{T_{ji}\} \qquad \text{with} \qquad T_{ji} = y_i^h(\mathbf{x}_j^{\Sigma}) \quad i = 1, n \quad j = 1, m$$

is the so called transfer matrix between Γ_0^h and Σ^h. Moreover the matrix T depends only on the geometric data Ω. The first step of the numerical procedure consists in the computation of T; T is obtained solving the n mixed boundary value problems (6.5), which differ only for the Dirichlet data on Γ_0, by implementing a suitable version of the frontal method which performs a triangular factorization only once for all the n problems. The matrix T is a very ill-conditioned matrix reflecting the ill-posedness of the inverse problem (6.2). We remark that the transfer matrix can also be computed by means of methods based on boundary integral representations of the potential. Since the accuracy of the transfer matrix is not a relevant factor in the experimental inverse problem, all the following results will be related to the transfer matrix computed by the three dimensional method outlined above, which is convenient in order to reduce computational time and storage requirement. It is easy to verify that the discretized form of the regularized problem (6.4) can be restated in the following least square form:

$$\text{find } \underline{u}_\epsilon \in \mathbb{R}^n : \min_{v \in \mathbb{R}^n} ||\mathscr{T}\underline{v} - \underline{b}||_{\mathbb{R}^m}^2 + \epsilon ||\mathscr{R}\underline{v}||_{\mathbb{R}^n}^2, \tag{6.7}$$

where $\mathscr{T}$ is a suitable matrix related to the transfer matrix T, $\underline{b}$ is related to the observation $z(\mathbf{x})$ on Σ and $\mathscr{R}$ is obtained by discretizing the operator B (see [111] for details). For results about convergence and error estimates of the solution of the approximate regularized problem to the solution of the continuous one (6.4), we refer to [111]. We will limit the discussion about the numerical results obtained using $\mathscr{T} = T$, i.e. instead of the residual $\int_{\Sigma^h} |A_h u_h - z|^2 \, d\sigma$ we consider the discrete residual $||T\underline{u} - \underline{z}_m||$, where $\underline{z}_m$ is the vector of the measured potential values at the nodes of Σ^h. In the application no improvement in accuracy was achieved using a distributed observation $z(\mathbf{x})$ obtained by interpolating suitably $\underline{z}_m$. We remark that the problem (6.7) must be solved for a sequence of $\underline{z}_m$ data, i.e. the measured surface potential at different time instants of the heartbeat and several values of the smoothing parameter ϵ must be considered. Hence in order to reduce the computational load it is important to apply a very efficient procedure. This can be done by computing, only once, the generalized singular value decomposition of the matrix T and R, after that the solution $\underline{u}_\epsilon$ can be written explicitly as a function of ϵ. Further regularization techniques used in inverse electrocardiography are the *truncated singular value decomposition* and *truncated iterative Krylov methods*. For an improved spatio-temporal approach for estimating the epicardial potential on a whole heartbeat we refer to [211].

6.2   Macroscopic Equivalent Excitation Cardiac Sources

Let Ω be the body volume and Ω_H the heart muscle. We suppose that Ω and Ω_H are open connected sets of class C^2 and $\overline{\Omega_H} \subset \Omega$. We recall that at a macroscopic level the excitable cardiac tissue Ω_H is conceived as the superposition of two continuous media: the intra-(i) and extra-(e) cellular media. We denote by D_i and D_e the intra- and extracellular conductivity tensors of these media. The anisotropic conduction properties characterized by the tensors $D_{i,e}$ are related to the fiber structure of the heart muscle. We make the following assumptions regarding the anatomical fiber architecture:

  (i)   The fibers are mathematically described by regular curves;
 (ii)   Through any point of Ω_H passes a unique fiber;
(iii)   On those parts of $\partial\Omega_H$, which lie on the heart surface (epi- or endocardium), the fibers are tangent to $\partial\Omega_H$.

During the excitation phase of the myocardium, a layer of cardiac cells, changing in time, undergoes the so-called *depolarization process*, i.e. a rapid change occurs in the transmembrane electric potential $v(\mathbf{x}, t)$, with an approximately monotone variation from a resting value v_r to a plateau value v_a. The following assumption is usually made:

(iv)   The depolarization of a cell is instantaneous and is the same for all cells ($v_r < v_a$ constants).

For $\mathbf{x} \in \Omega_H$, let $\sigma_l^{i,e}(\mathbf{x})$ be the (i)-(e) conductivity coefficients along the fiber direction at point $\mathbf{x}$. Assuming *axial symmetry* around the fiber direction, let $\sigma_t^{i,e}(\mathbf{x})$ be the (i)-(e) conductivity coefficients in any direction perpendicular to the fiber direction at point $\mathbf{x}$. If $\{\mathbf{a}_l, \mathbf{a}_t, \mathbf{a}_n\}$ denotes a local basis of $\mathbb{R}^3$ with $\mathbf{a}_l$ parallel to the fiber direction, then the (i)-(e) conductivity tensors are defined by:

$$D_{i,e} = \sigma_t^{i,e} I + (\sigma_l^{i,e} - \sigma_t^{i,e})\mathbf{a}_l \mathbf{a}_l^T .$$

The axis $\mathbf{a}_t$, $\mathbf{a}_n$ are defined up to a rotation around $\mathbf{a}_l$. Moreover $D_{i,e}$ do not depend on the orientation of $\mathbf{a}_l$ parallel to the longitudinal fiber direction. If $\mathbf{n}$ is a unit vector at point $\mathbf{x}$, then:

$$D_i\mathbf{n} = \sigma_t^i \mathbf{n} + (\sigma_l^i - \sigma_t^i)(\mathbf{n} \cdot \mathbf{a}_l)\mathbf{a}_l;$$

moreover $D_i\mathbf{n}$ is independent of the orientation of $\mathbf{a}_l$. In the following, we will make the simplifying assumption that:

(v)   The *bulk* cardiac medium and the body volume are isotropic homo–geneous with constant conductivity σ_0 ($D_i + D_e = \sigma_0 I$).

Assuming an instantaneous depolarization process at any time instant t, we denote by

$$H^+(t) = \{\mathbf{x} \in \Omega_H : v(\mathbf{x}, t) = v_a\},$$
$$H^-(t) = \{\mathbf{x} \in \Omega_H : v(\mathbf{x}, t) = v_r\},$$

with $\overline{H^+} \cup \overline{H^-} = \overline{\Omega_H}$, $H^+ \cap H^- = \emptyset$ and $S = \partial H^+ \cap \partial H^-$, the excitation wavefront surface. We also assume that v_r, v_a are constant and S is an orientable regular surface. Denoting by $u(\mathbf{x})$ the potential in Ω and by $\mathbf{J} = \sigma_0 \nabla u$, $\mathbf{J}_i = -D_i \nabla v$ the current density in Ω and in the intracellular medium, the current conservation implies (see Sect. 3.3):

$$\begin{cases} \operatorname{div}(\mathbf{J} + \mathbf{J}_i) = 0 & \text{in } \Omega_H \\ \operatorname{div} \mathbf{J} = 0 & \text{in } \Omega \setminus \overline{\Omega_H} \text{ (no sources)} \\ \mathbf{n}^T \mathbf{J} = 0 & \text{on } \Gamma = \partial\Omega \text{ (insulating boundary).} \end{cases}$$

The boundary condition on $\Gamma = \partial\Omega$ describes the fact that the thorax is surrounded by air, which is an insulating medium. In terms of potential, we have:

$$\begin{cases} \sigma_0 \Delta u = \begin{cases} -\operatorname{div} D_i \nabla v & \text{in } \Omega_H \\ 0 & \text{in } \Omega \setminus \overline{\Omega_H} \end{cases} \\ \dfrac{\partial u}{\partial \mathbf{n}} = 0 & \text{on } \Gamma. \end{cases}$$

Denoting by δ_S the Dirac measure on S:

$$< \delta_S, \varphi > = \int_S \varphi \, dS \qquad \varphi \in \mathscr{D}(\Omega)$$

and observing that

$$-\nabla v = (v_a - v_r)\delta_S \mathbf{n}_S$$

where $\mathbf{n}_S$ is the normal to S directed toward $H^-(t)$, we obtain the following boundary value problem:

$$\begin{cases} \Delta u = \dfrac{v_a - v_r}{\sigma_0} \operatorname{div} D_i(\delta_S \mathbf{n}_S) & \text{in } \Omega \\ \dfrac{\partial u}{\partial \mathbf{n}} = 0 & \text{on } \Gamma. \end{cases} \tag{6.8}$$

Setting

$$M = \frac{v_a - v_r}{\sigma_0} D_i = A\mathrm{diag}(m_t, m_t, m_l)A^T, \quad m_t = \frac{v_a - v_r}{\sigma_0}\sigma_t^i, \quad m_l = \frac{v_a - v_r}{\sigma_0}\sigma_l^i,$$
(6.9)

where $A = (\mathbf{a}_l, \mathbf{a}_t, \mathbf{a}_n)$, and using the results of [305] (for the Sobolev space H^s see e.g. [305]), the following result holds:

Theorem 6.1. *Assuming that:*

- *The elements of M can be extended in the whole Ω as functions of $C^1(\Omega)$;*
- *S is a surface of class C^2 and if S is open there exists an open subset Ω' of Ω of class C^2 such that $\Omega' \subset \Omega$,*

then there exists a solution $u \in H^{\frac{1}{2}-\epsilon}(\Omega)$, $\forall \epsilon > 0$ of problem (6.8) defined up to an additive constant.

Using the Green's formula it is also possible to prove the following theorem, see [110]:

Theorem 6.2. *Under the assumptions of Theorem 6.1, the solution of (6.8) in $H^{\frac{1}{2}-\epsilon}(\Omega)$, $\forall \epsilon > 0$, satisfies the following boundary value problem:*

$$\begin{cases} \Delta u = 0 & \text{in } \Omega \setminus \overline{S} \\ \dfrac{\partial u}{\partial \mathbf{n}} = 0 & \text{on } \Gamma \quad (\text{in the sense of } H^{-1-\epsilon}(\Gamma)) \\ [u]_S = u_{|S+} - u_{|S-} = \mathbf{n}^T M \mathbf{n} & (\text{in the sense of } H^{-\epsilon}(S)) \\ \left[\dfrac{\partial u}{\partial \mathbf{n}}\right]_S = \dfrac{\partial u}{\partial \mathbf{n}_{|S+}} - \dfrac{\partial u}{\partial \mathbf{n}_{|S-}} = div_S \, \boldsymbol{\beta} & (\text{in the sense of } H^{-1-\epsilon}(S)), \end{cases}$$
(6.10)

where $\boldsymbol{\beta} = M\mathbf{n} - (\mathbf{n}^T M \mathbf{n})\mathbf{n}$ is a tangential field on S and div_S is the divergence operator on S.

In order to investigate the structure of the source model on the wavefront S generating the potential u and also for the numerical approximation of u we state the following useful theorem, see [109, 110]:

Theorem 6.3. *Under the assumptions of Theorem 6.1, the solution of (6.8) admits the following boundary integral representation:*

$$u(\mathbf{x}) = -\int_\Gamma v(\boldsymbol{\xi})\frac{\partial s(\mathbf{x}, \boldsymbol{\xi})}{\partial \mathbf{n}_{\boldsymbol{\xi}}}d\Gamma_{\boldsymbol{\xi}} + \int_S \mathbf{n}_{\boldsymbol{\xi}}^T M \nabla_{\boldsymbol{\xi}} s(\mathbf{x}, \boldsymbol{\xi})dS_{\boldsymbol{\xi}}, \quad \forall \mathbf{x} \in \Omega \setminus \overline{S}, \quad (6.11)$$

where v is the unique solution in $L^2(\Gamma)/\mathbb{R}$ of the following Integral Equation on Γ

$$\frac{1}{2}v(\mathbf{x}) + \int_\Gamma v(\boldsymbol{\xi})\frac{\partial s(\mathbf{x}, \boldsymbol{\xi})}{\partial \mathbf{n}_{\boldsymbol{\xi}}}d\Gamma_{\boldsymbol{\xi}} = \int_S \mathbf{n}_{\boldsymbol{\xi}}^T M \nabla_{\boldsymbol{\xi}} s(\mathbf{x}, \boldsymbol{\xi})dS_{\boldsymbol{\xi}} \qquad a.e. \text{ on } \Gamma, \quad (6.12)$$

*and $s(\mathbf{x}, \boldsymbol{\xi}) = \frac{1}{4\pi|\mathbf{x}-\boldsymbol{\xi}|}$ is the fundamental solution of the Laplace operator Δ in $\mathbb{R}^3$.
Moreover $u_{|\Gamma} = v$.*

In the integral representation given by Theorem 6.3, there appear two terms: the
first of them takes into account the presence of the insulating boundary Γ, while the
second is related to the source model on the wavefront S, see also [238]. Since we
have:

$$\int_S \mathbf{n}^T M \nabla s dS = \int_S ||M\mathbf{n}|| \frac{\partial s}{\partial \boldsymbol{v}} dS, \quad \boldsymbol{v} = \frac{M\mathbf{n}}{||M\mathbf{n}||},$$

we derive that, under the assumption (iv), the mathematical model of the excitation
wavefront S consists of:

   *an oblique dipole (double) layer on S having the same orientation of the vector
   M$\mathbf{n}$ and moment density on S given by $||M\mathbf{n}||$.*

Hence M can be viewed as a dipolar moment tensor. Introducing the unit vectors
$\mathbf{a}_l$, $\mathbf{a}_t$ such that $\mathbf{a}_l$ is parallel to the longitudinal fiber direction, $\mathbf{a}_t$ is perpendicular
to $\mathbf{a}_l$ and coplanar with $\mathbf{n}$, $\mathbf{a}_l$ and orienting $\mathbf{a}_t$, $\mathbf{a}_l$ toward the resting tissue so that
$\mathbf{a}_t \cdot \mathbf{n} \geq 0$ and $\mathbf{a}_l \cdot \mathbf{n} \geq 0$, it is easy to verify:

$$\int_S \mathbf{n}^T M \nabla s dS = \int_S m_t (\mathbf{n} \cdot \mathbf{a}_t) \frac{\partial s}{\partial \mathbf{a}_t} dS + \int_S m_l (\mathbf{n} \cdot \mathbf{a}_l) \frac{\partial s}{\partial \mathbf{a}_l} dS.$$

The source can be viewed as the superposition of a transverse dipole layer with
density $m_t (\mathbf{n} \cdot \mathbf{a}_t)$ and an axial dipole layer with density $m_l (\mathbf{n} \cdot \mathbf{a}_l)$, where, in this
context, transverse and axial means respectively perpendicular and parallel to the
local fiber direction.

   Moreover the following decomposition holds:

$$\int_S \mathbf{n}^T M \nabla s dS = \int_S m_t \frac{\partial s}{\partial \mathbf{n}} dS + \int_S (m_l - m_t)(\mathbf{n} \cdot \mathbf{a}_l) \frac{\partial s}{\partial \mathbf{a}_l} dS,$$

which shows that the oblique dipole layer potential can be thought of as the
superposition of a normal dipole layer with density m_t and of an axial dipole layer
with density $(m_l - m_t)(\mathbf{n} \cdot \mathbf{a}_l)$. If $m_t = m_l$ constant, we recover the classical model,
i.e. the source is represented by a normal dipole layer. We remark that $m_t = m_l$
implies $\sigma_t^i = \sigma_l^i$, i.e. the intracellular medium is isotropic; however experimental
measurements have shown that $\sigma_t^i \neq \sigma_l^i$ and the experimental data of [30, 134] did
not agree with the prediction of the normal dipole layer model, thus questioning
the general validity of the classical model. The model presented here generalizes
the *classical model* and also the *axial model* introduced in [134] for explaining the
discrepancy with the prediction of the classical model in dog heart experiments. Our
source model is an *anisotropic oblique dipole model* where the anisotropy derives
from the properties of the tensor M.

6.3   Boundedness of the Potential

If the wavefront S is a closed surface, the solution u of problem (6.8) belongs to $L^\infty(\Omega)$. We now discuss the condition for boundedness of the potential field u in the case of an open surface S.

From the integral representation (6.11), we have:

$$u(\mathbf{x}) = -\int_\Gamma v \frac{\partial s}{\partial \mathbf{n}} d\Gamma + P(\mathbf{x}), \qquad \text{with } P(\mathbf{x}) = \int_S \mathbf{n}^T M \nabla s dS.$$

If S is an open surface, the following decomposition holds:

$$P(\mathbf{x}) = \int_S \alpha \frac{\partial s}{\partial \mathbf{n}} dS - \int_S \operatorname{div}_S \boldsymbol{\beta} s dS + \int_{\partial S} \boldsymbol{\beta} \cdot \mathbf{n}_b s d\partial S,$$

where $\alpha = \mathbf{n}^T M \mathbf{n}$, $\boldsymbol{\beta} = M\mathbf{n} - \alpha\mathbf{n}$ and $\mathbf{n}_b$ is the normal to ∂S contained in the tangent plane to S. This decomposition shows that the presence of the simple layer on ∂S introduces a logarithmic singularity in the potential. Since the physical potential is bounded in Ω, we must impose that the line integral must be zero $\forall \mathbf{x} \in \Omega \setminus \overline{S}$, hence

$$\boldsymbol{\beta} \cdot \mathbf{n}_b = 0 \quad \text{on } \partial S. \tag{6.13}$$

On electrophysiological grounds, we assume that:

(vi) The fiber direction on $\partial\Omega_H$ (the epi-endo-cardial heart surface) is tangent to $\partial\Omega_H$, i.e. $\mathbf{a}_l \cdot \mathbf{n}_H = 0$ on $\partial\Omega_H$ (where $\mathbf{n}_H$ is the unit normal to $\partial\Omega_H$) and, if S is open, $\partial S \subset \partial\Omega_H$.

It is not difficult to verify that (see [109]):

Proposition 6.1. *Under the assumption (vi) and if $m_t(\mathbf{x}) \neq m_l(\mathbf{x})$ $\forall \mathbf{x} \in \partial S$, then*

$$\begin{cases} \boldsymbol{\beta} \cdot \mathbf{n}_b = 0 \text{ on } \partial S \text{ if } \mathbf{n}_S \text{ is parallel to } \mathbf{n}_H \text{ or} \\ \qquad\qquad \mathbf{n}_S \text{ is perpendicular to } \mathbf{n}_H \text{ or} \\ \qquad\qquad \mathbf{a}_l \text{ is tangent to } \partial S. \end{cases} \tag{6.14}$$

That is the wavefront surface S and the heart surface $\partial\Omega_H$ are, respectively, tangent or perpendicular or else intersect at an arbitrary angle in the point of ∂S in which $\mathbf{a}_l$ is tangent to ∂S.

6.4   Numerical Approximation of the Integral Representation of the Potential

The numerical approximation of the potential u in $\Omega \setminus \overline{S}$ was obtained considering the boundary integral representation of u given by Theorem 6.3, i.e.

$$u(\mathbf{x}) = -\int_\Gamma v \frac{\partial s}{\partial \mathbf{n}} d\Gamma + \int_S \mathbf{n}^T M \nabla s \, dS \quad \forall \mathbf{x} \in \Omega \setminus \overline{S},$$

where v is the solution of

$$\frac{1}{2} v(\mathbf{x}) + \int_\Gamma v \frac{\partial s}{\partial \mathbf{n}} d\Gamma = \int_S \mathbf{n}^T M \nabla s \, dS \quad \text{on } \Gamma.$$

The numerical approximation of the integral equation on Γ can be performed using:

 (i) The Galerkin boundary element method;
(ii) The collocation boundary element method.

We remark that for (i) an optimal error estimate was proved in [103] in the case of linear finite element approximation of the surface and function:

$$||v - v_h||_{L^2(\Gamma)/\mathbb{R}} = O(h^2).$$

For (ii) we do not know error estimate results. However in the following we will present this second strategy, that is the most used in practice due to the high computational costs required by the approximation of a double surface integral in the (i) procedure.

   The surfaces Γ, S are approximated by means of two polyhedral surfaces Γ^h, S^h with triangular elements. The potential v is approximated by a piecewise linear continuous function $v_h(\mathbf{x})$ on Γ^h, i.e.

$$v_h(\mathbf{x}) = \sum_{j=1}^N v_j \, p_j(\mathbf{x}), \quad \text{with } p_j(\mathbf{x}_k) = \delta_{jk}, \ v_k = v_h(\mathbf{x}_k),$$

where $\mathbf{x}_k$ denote the nodes on Γ^h. Applying the collocation method at the nodes of Γ^h, the integral equation is approximated by:

$$\omega(\mathbf{x}_k) v_k + \int_{\Gamma^h} v_h(\boldsymbol{\xi}) \frac{\partial s(\mathbf{x}_k, \boldsymbol{\xi})}{\partial \mathbf{n}_{h,\boldsymbol{\xi}}} d\Gamma_{\boldsymbol{\xi}}^h = \int_{S^h} \mathbf{n}_h^T M \nabla_{\boldsymbol{\xi}} s(\mathbf{x}_k, \boldsymbol{\xi}) dS_{\boldsymbol{\xi}}^h \quad \text{for } k = 1, \ldots, N,$$

$$(6.15)$$

where

$$\omega(\mathbf{x}_k) = \frac{\alpha(\mathbf{x}_k)}{4\pi} \quad \text{with } \alpha(\mathbf{x}) = -\int_{\Gamma^h} \frac{\partial s(\mathbf{x}, \boldsymbol{\xi})}{\partial \mathbf{n}_{h,\boldsymbol{\xi}}} d\Gamma_{\boldsymbol{\xi}}^h,$$

i.e. $\alpha(\mathbf{x})$ is the solid angle under which the surface Γ^h is seen from the point $\mathbf{x}$, $\mathbf{n}_h$ is the normal to the triangular elements belonging to Γ^h or S^h. Setting

$$K = \left\{ a_{kj} = \omega(\mathbf{x}_k)\delta_{kj} + \int_{\Gamma^h} p_j(\boldsymbol{\xi}) \frac{\partial s(\mathbf{x}_k, \boldsymbol{\xi})}{\partial \mathbf{n}_h} d\Gamma_{\boldsymbol{\xi}}^h \right\}$$

$$\mathbf{b} = \left\{ b_k = \int_{S^h} \mathbf{n}_h^T M \nabla_{\boldsymbol{\xi}} s(\mathbf{x}_k, \boldsymbol{\xi}) dS_{\boldsymbol{\xi}}^h \right\}, \quad \mathbf{v} = (v_1, \ldots, v_N)^T,$$

the solution of (6.15) is equivalent to the solution of the linear system

$$K\mathbf{v} = \mathbf{b}. \tag{6.16}$$

With $\omega(\mathbf{x})$ defined as above, matrix K admits the zero eigenvalue associated to the right eigenvector

$$\mathbf{e} = (1, \ldots, 1)^T.$$

We remark that the integral operator associated to the first side of Eq. (6.12) admits zero as a simple eigenvalue; in the following we assume that zero is a simple eigenvalue also for the approximate operator K. Hence the solution of the linear system is defined up to an additive constant; moreover system (6.16) admits a solution if $\boldsymbol{\ell}^T \mathbf{b} = 0$, where $\boldsymbol{\ell}^T K = \mathbf{0}^T$, i.e. $\boldsymbol{\ell}$ is the left eigenvector of K, associated to the zero eigenvalue. While in the continuous case the corresponding compatibility condition is exactly satisfied by the term $\int_S \mathbf{n}^T M \nabla s dS$, on the other hand due to approximation errors, the term $\mathbf{b}$ does not satisfy exactly the condition $\boldsymbol{\ell}^T \mathbf{b} = 0$. For solving the singular linear system by direct methods, the following deflation method is used. Let $\mathbf{q}$ be a vector such that $\mathbf{q}^T \mathbf{b} = 1$. It is easy to verify that:

if $\boldsymbol{\ell}^T \mathbf{b} = 0$ then the solution $\mathbf{w}$ of the system $B\mathbf{w} = (K + \mathbf{e}\mathbf{q}^T)\mathbf{w} = \mathbf{b}$,

where B is non-singular, satisfies the equations $K\mathbf{w} = \mathbf{b}$, $\mathbf{q}^T \mathbf{w} = 0$.

For $\boldsymbol{\ell}^T \mathbf{b} \simeq 0$, we solve the linear system

$$(K + \mathbf{e}\mathbf{q}^T)\mathbf{v} = \mathbf{b}$$

and we consider $\mathbf{v}$ as an approximation of $v_h(\mathbf{x})$.

In practice we choose $p_i = \delta_{ij}$. We remark that K is a full matrix. The determination of the coefficients requires the computation of the integrals

$$\int_T p(\boldsymbol{\xi}) \frac{\partial s(\mathbf{x}, \boldsymbol{\xi})}{\partial \mathbf{n}_{\boldsymbol{\xi}}} dT_{\boldsymbol{\xi}},$$

where T is a triangle of Γ^h. These integrals are computed by means of Gaussian quadrature rules if $\mathbf{x}$ is *not very near* to T, otherwise the computation is performed analytically.

6.5   Inverse Problem in Terms of Wavefront

In this section, we present the inverse problem in terms of wavefront, using the oblique dipole layer model as a representation of the depolarization wavefront.

The problem can be roughly formulated a s follows: *is it possible to determine the wavefront S from the knowledge of the potential on the thorax Γ?*

We recall that the knowledge of:

- The myocardial fibers direction ($\mathbf{a}_l$);
- The jump of the intracellular action potential ($u_a - u_r$);
- The coefficients of the longitudinal and transverse intracellular conductivity (σ_l^i, σ_t^i);
- The extracellular and extracardiac conductivity (σ_0)

characterizes the matrix M given in (6.9).

In the following, we assume that σ_l^i, σ_t^i are positive constants and $\sigma_l^i \neq \sigma_t^i$, i.e. we have homogeneous intracellular anisotropy, or equivalently we assume:

$$\begin{aligned} &\text{the eigenvalues of } M \text{ are independent of } x \text{ in } \Omega_H \text{ and} \\ &m_t \neq m_l \text{ with } m_t, \ m_l > 0, \ (m_t \text{ double eigenvalue}). \end{aligned} \tag{6.17}$$

We introduce the following family $\mathscr{W}$ of admissible wavefront S:

$$\mathscr{W} = \left\{ \begin{array}{l} \text{set of the open orientable connected surfaces } S \text{ of} \\ \text{class } C^2 \text{ contained in } \Omega_H \text{ with boundary } \partial S \subset \partial \Omega_H \text{ and } S \text{ can be} \\ \text{considered as a part of a } C^2 \text{ closed surface contained in } \Omega \\ \text{moreover } \partial S \text{ satisfies contition (6.14)} \end{array} \right\}$$

Then for $S \in \mathscr{W}$ we consider the following operator, defined up to an additive constant:

$$S \rightarrow U_S = u_{|\Gamma},$$

where u is the solution of problem (6.8) of Theorem 6.1 or equivalently

$$S \rightarrow U_S = v,$$

where v is the solution of the integral equation (6.12) of Theorem 6.3. That is, given S we consider the potential U_S on the insulating boundary Γ generated by the

oblique dipole layer on S. We remark that in the special case in which $\mathbf{a}_l$ is always perpendicular or tangent to a given surface S, i.e. $\mathbf{a}_l = \mathbf{n}_S$ or $\mathbf{a}_l \cdot \mathbf{n}_S = 0$ then the oblique dipole layer on S is a normal double layer; if S_1 and S_2 are two surfaces of W satisfying the preceding constraint, then it is well known that $U_{S_1} = U_{S_2}$ implies $\partial S_1 = \partial S_2$, i.e. the potential characterizes only the boundary ∂S of S. Assuming that the wavefront is generally oblique w.r.t the fiber direction, i.e. $\mathbf{a}_l$ is not always perpendicular or tangent to the wavefront, the following uniqueness result holds (see [110]):

Theorem 6.4. *If S_1, $S_2 \in W$ and on at least one of them, e.g. S_1, $\mathbf{a}_l$ is generally oblique to S_1, i.e. $\mathbf{a}_l \cdot \mathbf{n}_S \neq 0$ or $\mathbf{a}_l \cdot \mathbf{n}_S \neq 1$, but there exists at least one point where $\mathbf{a}_l \cdot \mathbf{n}_S = 1$ or $\mathbf{a}_l \cdot \mathbf{n}_S = 0$, then*

$$U_{S_1} = U_{S_2} \Rightarrow S_1 = S_2.$$

Under the same hypotheses of Theorem 6.4, the uniqueness result holds also for closed wavefronts, i.e. S_1 and S_2 are C^2 closed surfaces one inside the other. These first results and others suggest the conjecture that the uniqueness result should hold under the same hypotheses of Theorem 6.4 in a more general admissible wavefront class W and for $m_l \neq m_t$ variable in Ω_H. Finally we outline the following open problems:

- Extension of the results to an extracellular anisotropic medium and to a body volume with piecewise constant conductivity;
- Numerical approaches for solving the inverse problem.

We now describe the inverse problem presented in [142,143,241,534,536] for the reconstruction of the activation time on the endo- and epicardial surfaces, assuming homogeneous isotropic properties of the cardiac and extracardiac media. As we have seen in Chap. 5, in the general anisotropic case, the spatio-temporal transmembrane potential distribution over the whole heart muscle must be taken into account as primary cardiac electric source. Indeed, the integral representation of the electric potential u at a point $\mathbf{x}$ of the body surface is

$$u(\mathbf{x}, t) = -\int_{\Omega_H} D_i \nabla v(\mathbf{y}, t) \cdot \nabla \psi(\mathbf{y}, \mathbf{x}) d\mathbf{y},$$

where D_i is the intracellular conductivity tensor and ψ the Bidomain Green function, see Eq. (5.7). However, if we assume isotropy for the intra- and extracellular domains and accept the model error involved, only the transmembrane potential distribution over the heart's surface (epi- and endocardium) takes effect as primary source, because the volume integral is converted to a surface integral by means of Gauss divergence theorem. In fact, assuming all the media isotropic and the extracardiac medium unbounded, we obtain

$$u(\mathbf{x}, t) = -\frac{\sigma_i}{4\pi\sigma_0} \int_{\Omega_H} \nabla v(\mathbf{y}, t) \cdot \nabla \frac{1}{|\mathbf{y} - \mathbf{x}|} d\mathbf{y},$$

which, applying the Green formula, becomes

$$u(\mathbf{x}, t) = -\frac{\sigma_i}{4\pi\sigma_0} \int_{\partial\Omega_H} v(\mathbf{y}, t)\nabla\frac{1}{|\mathbf{y} - \mathbf{x}|} \cdot \mathbf{n(y)}d\mathbf{y}. \tag{6.18}$$

This simplification is necessary because the fiber orientation of the individual patient is unknown and cannot be assessed by current imaging methods.

The onset of the transmembrane potential v is described by the activation time τ. The non-linear relationship between the activation time τ and the transmembrane potential v makes the problem non-linear. This non-linear problem can be reduced to a linear problem in the unknown activation time τ by approximating the time evolution of the transmembrane potential by a Heaviside step function $\mathscr{H}$, i.e.

$$v(\mathbf{y}, t) = v_r + (v_a - v_r)\mathscr{H}(t - \tau(\mathbf{y})).$$

For depolarization, this assumption is reasonable, because the excitation wavefront has a thin spatial layer. Thus, Eq. (6.18) becomes

$$u(\mathbf{x}, t) = -\frac{\sigma_i(v_a - v_r)}{4\pi\sigma_0} \int_{\partial\Omega_H} \mathscr{H}(t - \tau(\mathbf{y}))\nabla\frac{1}{|\mathbf{y} - \mathbf{x}|} \cdot \mathbf{n(y)}d\mathbf{y},$$

and, integrating over the QRS interval $(0, T)$, we obtain finally the following linear problem in τ

$$\int_0^T u(\mathbf{x}, t)dt = \frac{\sigma_i(v_a - v_r)}{4\pi\sigma_0} \int_{\partial\Omega_H} \tau(\mathbf{y})\nabla\frac{1}{|\mathbf{y} - \mathbf{x}|} \cdot \mathbf{n(y)}d\mathbf{y},$$

which relates the measured body surface potential u with the unknown activation time τ on the heart surface. A minimum-norm least-square solution to this linear problem, however, contains unphysiological characteristics and additional regularization is inevitable. The additional regularization yields a non-linear inverse problem. For a comparison between the potential- and the activation-based inverse problems see [89].

An alternative strategy followed e.g. by [335] consists of representing the transmembrane potential v as an analytical function with a sigmoidal shape,

$$v(\mathbf{y}, t) = \frac{v_a}{2}\left(1 + \frac{2}{\pi}\arctan\left(\pi\frac{t - \tau(\mathbf{y})}{w}\right)\right) + v_r,$$

where the unknowns are

- The activation time $\tau(\mathbf{y})$;
- The resting and depolarized potential values v_r and v_a;
- The time constant of rise w.

The same type of approach can be extended to the entire heartbeat, representing the transmembrane potential waveform by an analytical function involving some parameters as v_r and v_a and markers of local depolarization and repolarization time, see [534, 537].

The inverse method described here attempt to reconstruct the electrical activity on the epi- and/or endocardial surfaces of the heart. In recent years, there have also been several attempts to reconstruct cardiac electrical activity inside the myocardial wall, see e.g. [217, 222, 325, 326, 468, 478, 549–551]; see also [353, 354] for inverse problems to locate transmural ischemia. This problem is even more difficult than that of reconstructing surface electrical activity, as it is less constrained and hence more likely to loose uniqueness of solutions.

Chapter 7
Numerical Methods for the Bidomain and Reduced Models

In this chapter, we review the main numerical techniques used in the literature for the space and time discretizations of the Monodomain and Bidomain cardiac models. Then we present a Bidomain discretization based on the finite element method in space and finite difference methods in time. The latter can be fully implicit or semi-implicit, and can employ decoupling techniques and operator splitting methods between the ordinary and partial differential equation components of the cardiac models. The chapter is concluded by a review of numerical methods for the eikonal-diffusion equation.

7.1 Space Discretization of Monodomain and Bidomain Models

Many different approaches have been developed for the space discretization of the Bidomain and Monodomain equations. Finite difference methods have been studied in [66, 223, 368, 399, 413, 449, 529, 568, 569, 591]. Finite element methods have been widely used, see e.g. [104, 124, 177, 302, 303, 318, 388, 455, 543, 544]. Finite volume methods, which have the advantage of conserving local flux, have been developed in [43, 139, 218, 220, 252, 375, 528]. Some researchers have also investigated spectral element methods [54] and high-order finite elements [13, 14]. Non-conforming finite element discretizations have been studied in [376, 377]. In order to reduce the computational load of the Bidomain system and of general parabolic reaction-diffusion systems, also adaptive remeshing techniques have been developed, see e.g. [35, 36, 90, 91, 124, 147, 290, 336, 524, 556, 577, 578]; these techniques have been proven successful for problems of moderate size and are currently under investigation. Numerical methods and simulations for different eikonal approaches can be found in [268, 271, 272, 365] and in [115, 116, 121, 522].

Variational formulation. Finite element discretizations of the Bidomain and Monodomain systems are based on the classical Galerkin procedure for the variational formulation of these systems.

Let V be the Sobolev space $H^1(\Omega_H)/\mathbb{R}$ and define by

$$(\varphi, \psi) = \int_{\Omega_H} \varphi\psi \, dx \quad \forall \varphi, \psi \in L^2(\Omega_H)$$

$$a_{i,e}(\varphi, \psi) = \int_{\Omega_H} (\nabla\varphi)^T D_{i,e}(\mathbf{x}) \nabla\psi \, dx \quad \forall \varphi, \psi \in H^1(\Omega_H)$$

$$a(\varphi, \psi) = \int_{\Omega_H} (\nabla\varphi)^T D(\mathbf{x}) \nabla\psi \, dx \quad \forall \varphi, \psi \in H^1(\Omega_H)$$

the usual L^2-inner product and elliptic bilinear forms. The variational formulation of the Monodomain model reads as follows. Given $v_0, w_0 \in L^2(\Omega_H)$, $I_{app} \in L^2(\Omega_H \times (0, T))$, find $v \in W^{1,1}(0, T; V)$ and $w \in W^{1,1}(0, T; L^2(\Omega_H)^M)$ such that $\forall t \in (0, T)$

$$\begin{cases} \chi C_m \dfrac{\partial}{\partial t}(v(t), \varphi) + a(v(t), \varphi) + \chi(I_{ion}(v, w), \varphi) = (I_{app}, \varphi) \; \forall \varphi \in V \\[2ex] \dfrac{\partial}{\partial t}(w(t), \psi) = (R(v(t), w(t)), \psi) \qquad\qquad\qquad \forall \psi \in L^2(\Omega_H)^M, \end{cases}$$
$$\tag{7.1}$$

with appropriate initial conditions on v, w.

Analogously, the variational formulation of the Bidomain model (3.42) reads as follows. Given $v_0, w_0 \in L^2(\Omega_H)$, $I_{app}^{i,e} \in L^2(\Omega_H \times (0, T))$, find $u_{i,e} \in L^2(0, T; V)$ and $w \in L^2(0, T; L^2(\Omega_H)^M)$ such that $\frac{\partial v}{\partial t} \in L^2(0, T; V), \frac{\partial w}{\partial t} \in L^2(0, T; L^2(\Omega_H)^M)$, and $\forall t \in (0, T)$

$$\begin{cases} \chi C_m \dfrac{\partial}{\partial t}(v(t), \hat{u}_i) + a_i(u_i(t), \hat{u}_i) + \chi(I_{ion}(v, w), \hat{u}_i) = (I_{app}^i, \hat{u}_i) \qquad \forall \hat{u}_i \in V \\[2ex] -\chi C_m \dfrac{\partial}{\partial t}(v(t), \hat{u}_e) + a_e(u_e(t), \hat{u}_e) - \chi(I_{ion}(v, w), \hat{u}_e) = (I_{app}^e, \hat{u}_e) \qquad \forall \hat{u}_e \in V \\[2ex] \dfrac{\partial}{\partial t}(w(t), \hat{w}) = (R(v(t), w(t)), \hat{w}), \qquad v(\mathbf{x}, t) = u_i(\mathbf{x}, t) - u_e(\mathbf{x}, t) \; \forall \hat{w} \in L^2(\Omega_H)^M, \end{cases}$$
$$\tag{7.2}$$

with the proper initial conditions on v, w and compatibility condition on $I_{app}^{i,e}$.

Finite element discretizations. Let $\mathscr{T}^h$ be a uniform hexahedral triangulation of Ω_H and V^h the associated finite element space, see [414]. Choosing a finite element basis $\{\phi_i\}$ for V^h and appropriate quadrature rule, we denote by

$$\mathrm{M} = \{m_{rs} = \int_{\Omega_H} \phi_r \phi_s dx\}, \qquad \mathrm{A}_{i,e} = \{a_{rs}^{i,e} = \int_{\Omega_H} (\nabla\phi_r)^T D_{i,e} \nabla\phi_s dx\},$$

the symmetric mass matrix and stiffness matrices, respectively, and by I_{ion}^h, I_{app}^h the finite element interpolants of I_{ion} and I_{app}, respectively. In the following, we will denote by the same letters finite element functions and the vectors of their nodal values. In the Monodomain model, the finite element approximation $\mathbf{v}_h$ of the transmembrane potential is the solution of

$$\chi C_m \mathrm{M} \frac{\partial \mathbf{v}_h}{\partial t} + \mathrm{A}\mathbf{v}_h + \chi \mathrm{MI}_{ion}^h(\mathbf{v}_h, \mathbf{w}_h) = \mathrm{MI}_{app}^h, \tag{7.3}$$

while in the Bidomain model, the finite element approximations $\mathbf{u}_{i,h}, \mathbf{u}_{e,h}$ of the intra ed extracellular potentials are the solutions of the system

$$\begin{cases} \chi C_m \mathrm{M} \dfrac{\partial \mathbf{v}_h}{\partial t} + \mathrm{A}_i \mathbf{u}_{i,h} + \chi \mathrm{MI}_{ion}^h(\mathbf{v}_h, \mathbf{w}_h) = \mathrm{MI}_{app}^{i,h} \\[2mm] -\chi C_m \mathrm{M} \dfrac{\partial \mathbf{v}_h}{\partial t} + \mathrm{A}_e \mathbf{u}_{e,h} - \chi \mathrm{MI}_{ion}^h(\mathbf{v}_h, \mathbf{w}_h) = \mathrm{MI}_{app}^{e,h}, \end{cases} \tag{7.4}$$

where $\mathbf{v}_h = \mathbf{u}_{i,h} - \mathbf{u}_{e,h}$. In both cases, these equations are coupled with the semidiscrete approximations of the gating and concentration system

$$\frac{\partial \mathbf{w}_h}{\partial t} = R(\mathbf{v}_h, \mathbf{w}_h).$$

The Bidomain system can be written in compact form as

$$\chi C_m \mathcal{M} \frac{\partial}{\partial t} \begin{pmatrix} \mathbf{u}_{i,h} \\ \mathbf{u}_{e,h} \end{pmatrix} + \mathcal{A} \begin{pmatrix} \mathbf{u}_{i,h} \\ \mathbf{u}_{e,h} \end{pmatrix} + \chi \begin{pmatrix} \mathrm{MI}_{ion}^h(\mathbf{v}_h, \mathbf{w}_h) \\ -\mathrm{MI}_{ion}^h(\mathbf{v}_h, \mathbf{w}_h) \end{pmatrix} = \begin{pmatrix} \mathrm{MI}_{app}^{i,h} \\ \mathrm{MI}_{app}^{e,h} \end{pmatrix}, \tag{7.5}$$

where

$$\mathcal{M} = \begin{bmatrix} \mathrm{M} & -\mathrm{M} \\ -\mathrm{M} & \mathrm{M} \end{bmatrix}, \quad \mathcal{A} = \begin{bmatrix} \mathrm{A}_i & 0 \\ 0 & \mathrm{A}_e \end{bmatrix}.$$

The Bidomain system (7.4) can alternatively be written in a parabolic-elliptic formulation in terms of $\mathbf{v}_h, \mathbf{u}_{e,h}$. By adding the two equations and substituting $\mathbf{u}_{i,h} = \mathbf{v}_h + \mathbf{u}_{e,h}$ into the first equation, we obtain:

$$\begin{cases} \chi C_m \mathrm{M} \dfrac{\partial \mathbf{v}_h}{\partial t} + \mathrm{A}_i \mathbf{v}_h + \mathrm{A}_i \mathbf{u}_{e,h} + \chi \mathrm{MI}_{ion}^h(\mathbf{v}_h, \mathbf{w}_h) = \mathrm{MI}_{app}^{i,h} \\[2mm] \mathrm{A}_i \mathbf{v}_h + (\mathrm{A}_e + \mathrm{A}_i)\mathbf{u}_{e,h} = \mathrm{M}(\mathrm{I}_{app}^{i,h} + \mathrm{I}_{app}^{e,h}). \end{cases} \tag{7.6}$$

In the language of Differential-Algebraic equations (DAE), this formulation separates the differential variable ($\mathbf{v}_h$) from the algebraic variable ($\mathbf{u}_{e,h}$). Since this parabolic-elliptic formulation lends itself to different operator splitting techniques, treated in the next chapter, it has been and still is used by many researchers in the field.

7.2   Time Discretization of Monodomain and Bidomain Models

The time discretization of the Bidomain and Monodomain equations can be performed by several techniques employing explicit, semi-implicit or implicit schemes, requiring accordingly vector updates or the solution of linear or non-linear systems at each time step. We refer, e.g., to Ethier and Bourgault [166] for a comparative study of the stability and accuracy of several semi-implicit Bidomain time discretizations.

Explicit methods. Explicit schemes, in particular the Forward Euler method, have been used e.g. in [97, 368, 409, 520].

Operator splitting and decoupling PDE/ODE techniques. One of the most popular technique is known as operator splitting, and is based on separating the diffusion operator, associated with the conduction in the media, from the reaction operator, associated with the ionic current, gating and ionic concentrations dynamics. The advantage of operator splitting methods is to allow different numerical schemes for the diffusion and the reaction terms in order to maximize computational efficiency and eliminate complex dependencies between variables. The disadvantage is a loss of accuracy, because the simultaneous dependencies between variables is neglected. For the parabolic-elliptic formulation of the Bidomain model, a further splitting method consists in solving sequentially the elliptic equation, followed by the parabolic one. For more details on Bidomain operator splitting techniques, we refer e.g. to the studies [319, 389, 399, 410, 501–503, 544, 545, 552]. Finally, we mention the approximation results related to semi-discrete approximation in time of the Bidomain model with the FHN membrane model. In [32] a priori and a posteriori error estimates have been developed for the implicit Euler scheme.

Linear implicit methods. Additional methods that show a good compromise between stability and efficiency are the linear implicit methods, which require at each time step the solution of a few (2–4) linear systems. Bidomain linear implicit methods have been studied e.g. in [124, 147, 340, 574].

We will now give some more details in case of implicit and semi-implicit discretizations of the Bidomain system in its parabolic–parabolic form. For simplicity of notation, we will now drop the mesh size index h from all finite element functions, writing e.g. $\mathbf{v}^n$ instead of $\mathbf{v}_h^n$.

7.2.1   Fully Implicit Methods

The advantage of implicit methods is that they do not require stability constraints on the choice of the time step, but they can be quite expensive, because at each time step one has to solve a non-linear system. Fully implicit methods in time have been considered in [233, 338–340, 342, 574].

Considering for simplicity the Backward Euler (BE) method with time step size $\tau = t_{n+1} - t_n$, the Bidomain system requires at each time step the solution of the non-linear system

$$F(\mathbf{u}) = 0,$$

defined as

$$F(\mathbf{u}) = \begin{bmatrix} (\gamma \mathcal{M} + \mathcal{A}) \begin{pmatrix} \mathbf{u}_i^{n+1} \\ \mathbf{u}_e^{n+1} \end{pmatrix} + \chi \begin{pmatrix} \mathrm{MI}_{ion}(\mathbf{v}^{n+1}, \mathbf{w}^{n+1}, \mathbf{c}^{n+1}) \\ -\mathrm{MI}_{ion}(\mathbf{v}^{n+1}, \mathbf{w}^{n+1}, \mathbf{c}^{n+1}) \end{pmatrix} - \\ -\gamma \mathcal{M} \begin{pmatrix} \mathbf{u}_i^n \\ \mathbf{u}_e^n \end{pmatrix} - \begin{pmatrix} \mathrm{MI}_{app}^i \\ \mathrm{MI}_{app}^e \end{pmatrix} \\ \mathbf{w}^{n+1} - \tau \mathrm{R}(\mathbf{v}^n, \mathbf{w}^{n+1}) = \mathbf{w}^n, \qquad \mathbf{c}^{n+1} = \mathbf{c}^n + \tau\, \mathrm{S}(\mathbf{v}^n, \mathbf{w}^{n+1}, \mathbf{c}^n) \end{bmatrix},$$

where

$$\gamma = \frac{\chi C_m}{\tau}, \quad \mathcal{M} = \begin{bmatrix} \mathrm{M} & -\mathrm{M} \\ -\mathrm{M} & \mathrm{M} \end{bmatrix}, \quad \mathcal{A} = \begin{bmatrix} \mathrm{A}_i & 0 \\ 0 & \mathrm{A}_e \end{bmatrix}.$$

7.2.2   Decoupled Implicit Methods

A first attempt to reduce the computational cost of fully implicit methods is based on decoupling the gating variables w from the potentials u_i, u_e (hence v). This strategy could be motivated by the nonzero pattern of the Jacobian of a fully-implicit discretization when this shows a weak coupling between the gating and the potential variables (for example using the LR1 ionic model the Jacobian is dominated by its diagonal entries). Another motivation is that these two groups of variables are associated to two very different submodels (the ionic model and the tissue model, respectively) that describe different scales and are expressed mathematically by different systems (an ODE and a PDE system, respectively).

We describe this decoupling technique here by employing for simplicity a backward Euler scheme for the parabolic reaction-diffusion system.

Decoupled backward Euler (BE) method. Each time step of a decoupled backward Euler (BE) time discretization of the Bidomain system (7.5) consists of the following two steps. Analogous decoupled techniques could be applied to high-order time discretizations, such as, e.g., third-order Rosenbrock methods (see [338]). For simplicity, we will consider a fixed time step size τ.

Step 1:   Updating gating and ionic concentration variables. Given $\mathbf{v}^n$, $\mathbf{w}^n$, $\mathbf{c}^n$, computed at the previous time step t_n, first update the gating and ion concentration variables at time t_{n+1} by solving

$$\mathbf{w}^{n+1} - \tau R(\mathbf{v}^n, \mathbf{w}^{n+1}) = \mathbf{w}^n, \qquad \mathbf{c}^{n+1} = \mathbf{c}^n + \tau\, S(\mathbf{v}^n, \mathbf{w}^{n+1}, \mathbf{c}^n),$$

where $\tau = t_{n+1} - t_n$ is the time step size.

Step 2: **Updating intra- and extracellular potentials.** Given the potentials $\mathbf{u}_i^n, \mathbf{u}_e^n, \mathbf{v}^n$ computed at the previous time step and the gating and ionic concentration variables $\mathbf{w}^{n+1}, \mathbf{c}^n$, computed at Step 1, find $\mathbf{u}_i^{n+1}, \mathbf{u}_e^{n+1}$ and hence $\mathbf{v}^{n+1} = \mathbf{u}_i^{n+1} - \mathbf{u}_e^{n+1}$, by solving the non-linear system

$$\mathbf{F}(\mathbf{u}_i^{n+1}, \mathbf{u}_e^{n+1}) = \mathbf{G}, \tag{7.7}$$

where

$$\mathbf{F}(\mathbf{u}_i^{n+1}, \mathbf{u}_e^{n+1}) = (\gamma \mathcal{M} + \mathcal{A}) \begin{bmatrix} \mathbf{u}_i^{n+1} \\ \mathbf{u}_e^{n+1} \end{bmatrix} + \chi \begin{bmatrix} \mathbf{MI}_{ion}(\mathbf{v}^{n+1}, \mathbf{w}^{n+1}, \mathbf{c}^{n+1}) \\ -\mathbf{MI}_{ion}(\mathbf{v}^{n+1}, \mathbf{w}^{n+1}, \mathbf{c}^{n+1}) \end{bmatrix},$$

$$\gamma = \frac{\chi C_m}{\tau},$$

and

$$\mathbf{G} = \gamma \mathcal{M} \begin{bmatrix} \mathbf{u}_i^n \\ \mathbf{u}_e^n \end{bmatrix} + \begin{bmatrix} \mathbf{MI}_{app}^{i,n+1} \\ \mathbf{MI}_{app}^{e,n+1} \end{bmatrix}.$$

7.2.3 Decoupled Semi-implicit Methods

Semi-implicit methods (also known as implicit-explicit methods) for the Bidomain system have been studied e.g. in [104, 125, 166, 270, 455, 487, 494, 555]. We here sketch a semi-implicit time discretization of the Bidomain system, using for the diffusion term the implicit Euler method, while the non-linear reaction term I_{ion} is treated explicitly. The implicit treatment of the diffusion terms appearing in the Monodomain or Bidomain models is essential in order to adaptively change the time step according to the stiffness of the various phases of the heartbeat. The ODE system for the gating variables is discretized by the semi-implicit Euler method and the explicit Euler method is applied for solving the ODE system for the ion concentrations. Given the potential $\mathbf{v}_M^n$ at the previous time-step, the Bidomain system is decoupled by first solving for the gating and ion concentrations and then by solving a linear system for the intra- and extracellular potentials.

Decoupled method for the parabolic–parabolic formulation.

Step 1: **Updating gating and ionic concentration variables.**

$$\mathbf{w}^{n+1} - \tau\, R(\mathbf{v}^n, \mathbf{w}^{n+1}) = \mathbf{w}^n, \qquad \mathbf{c}^{n+1} = \mathbf{c}^n + \tau\, S(\mathbf{v}^n, \mathbf{w}^{n+1}, \mathbf{c}^n).$$

Step 2: Updating intra- and extracellular potentials. Find $\mathbf{u}^{n+1} = (\mathbf{u}_i^{n+1}, \mathbf{u}_e^{n+1})$ by solving the linear system

$$A_{bid}\mathbf{u}^{n+1} = \mathscr{F} \tag{7.8}$$

where

$$A_{bid} = \gamma\mathscr{M} + \mathscr{A} = \gamma\begin{bmatrix} M & -M \\ -M & M \end{bmatrix} + \begin{bmatrix} A_i & 0 \\ 0 & A_e \end{bmatrix}, \quad \gamma = \frac{\chi C_m}{\tau}, \tag{7.9}$$

and

$$\mathscr{F} = \begin{pmatrix} M[-I_{ion}(\mathbf{v}^n, \mathbf{w}^{n+1}, \mathbf{c}^{n+1}) + I_{app}^{i,n+1}] \\ M[\ I_{ion}(\mathbf{v}^n, \mathbf{w}^{n+1}, \mathbf{c}^{n+1}) + I_{app}^{e,n+1}] \end{pmatrix}. \tag{7.10}$$

As in the continuous model, $\mathbf{v}^n$ is uniquely determined, while $\mathbf{u}_i^n$ and $\mathbf{u}_e^n$ are determined only up to the same additive time-dependent constant chosen by imposing the condition $\mathbf{1}^T M\mathbf{u}_e^n = 0$. Hence, at each time step we have to solve the large linear system (7.8), that, as shown in [104], is very ill-conditioned and increases considerably the computational costs of the simulations.

Following the techniques from [166], we now investigate the stability of this semi-implicit scheme. For sake of simplicity, we consider a membrane model with only one gating variable and without stimulus currents I_{app}^i, I_{app}^e. Since the reaction terms are taken explicitly, we suppose that I_{ion} and F satisfy the following Lipschitz condition:

$$\begin{aligned} ||I_{ion}(v, w)||_0 &\leq \lambda_{ion}(||v||_0 + ||w||_0) \\ ||F(v, w)||_0 &\leq \lambda_F(||v||_0 + ||w||_0). \end{aligned} \tag{7.11}$$

Using as test functions the solutions u_i^{n+1}, u_e^{n+1} and w^{n+1} in their respective variational equations, we obtain

$$\int_{\Omega_H} \frac{v^{n+1} - v^n}{\tau} u_i^{n+1} + a_i(u_i^{n+1}, u_i^{n+1}) + \int_{\Omega_H} I_{ion}(v^n, w^{n+1})u_i^{n+1} = 0$$

$$-\int_{\Omega_H} \frac{v^{n+1} - v^n}{\tau} u_e^{n+1} + a_e(u_e^{n+1}, u_e^{n+1}) - \int_{\Omega_H} I_{ion}(v^n, w^{n+1})u_e^{n+1} = 0$$

$$\int_{\Omega_H} \frac{w^{n+1} - w^n}{\tau} w^{n+1} - \int_{\Omega_H} F(v^n, w^{n+1})w^{n+1} = 0.$$

Adding these three equations and using the identity

$$2(a^{n+1} - a^n)a^{n+1} = (a^{n+1})^2 + (a^{n+1} - a^n)^2 - (a^n)^2,$$

we get

$$\begin{aligned}
||v^{n+1}||_0^2 + ||v^{n+1} - v^n||_0^2 - ||v^n||_0^2 + \\
2\tau a_i(u_i^{n+1}, u_i^{n+1}) + 2\tau a_e(u_e^{n+1}, u_e^{n+1}) + \\
||w^{n+1}||_0^2 + ||w^{n+1} - w^n||_0^2 - ||w^n||_0^2 \leq \\
-2\tau \int_{\Omega_H} I_{ion}(v^n, w^{n+1})v^{n+1} + 2\tau \int_{\Omega_H} F(v^n, w^{n+1})w^{n+1},
\end{aligned}$$

which, thanks to the uniform ellipticity of the conductivity tensors $D_{i,e}$ and to the Lipschitz condition (7.11), becomes

$$\begin{aligned}
||v^{n+1}||_0^2 + ||v^{n+1} - v^n||_0^2 - ||v^n||_0^2 + \\
2\tau m_i |u_i^{n+1}|_1^2 + 2\tau m_e |u_e^{n+1}|_1^2 + \\
||w^{n+1}||_0^2 + ||w^{n+1} - w^n||_0^2 - ||w^n||_0^2 \leq \\
\tau 2\lambda_{ion}||v^{n+1}||_0^2 + \tau(\lambda_{ion} + 3\lambda_F)||w^{n+1}||_0^2 + \tau(\lambda_{ion} + \lambda_F)||v^n||_0^2.
\end{aligned}$$

Denote now by M the index of the final time step (thus $T = M\tau$) and sum the previous inequality for n going from 0 to $m-1$ with $1 \leq m \leq M$, to obtain

$$||v^m||_0^2 + \sum_{n=0}^{m-1} ||v^{n+1} - v^n||_0^2 + 2\tau\overline{m} \sum_{n=0}^{m-1}(|u_i^{n+1}|_1^2 + |u_e^{n+1}|_1^2) + ||w^m||_0^2 + \sum_{n=0}^{m-1}||w^{n+1} - w^n||_0^2 \leq$$

$$||v^0||_0^2 + ||w^0||_0^2 + \tau C_1(||v^m||_0^2 + ||w^m||_0^2) + \tau C_2 \sum_{n=0}^{m-1}(||v^n||_0^2 + ||w^n||_0^2),$$

where $\overline{m} = \min(m_i, m_e)$, $C_1 = \max(2\lambda_{ion}, \lambda_{ion} + 3\lambda_F)$ and $C_2 = \max(3\lambda_{ion} + \lambda_F, \lambda_{ion} + 3\lambda_F)$. Hence it follows

$$(1 - \tau C_1)(||v^m||_0^2 + ||w^m||_0^2) + 2\tau\overline{m} \sum_{n=0}^{m-1}(|u_i^{n+1}|_1^2 + |u_e^{n+1}|_1^2) \leq$$

$$||v^0||_0^2 + ||w^0||_0^2 + \tau C_2 \sum_{n=0}^{m-1}(||v^n||_0^2 + ||w^n||_0^2).$$

Lemma 7.1 (Discrete Gronwall). *Let* $\{k_n\}$, $\{p_n\}$ *be two sequences of non-negative real numbers,* Φ^m *a discrete real-valued function and* g_0 *a non-negative real number such that* $\Phi^0 \leq g_0$. *Suppose also that* $\forall m \geq 1$,

$$\Phi^m \leq g_0 + \sum_{n=0}^{m-1} p_n + \sum_{n=0}^{m-1} k_n \Phi^n.$$

Then the following property holds true:

$$\Phi^m \leq \left(g_0 + \sum_{n=0}^{m-1} p_n\right) e^{\sum_{n=0}^{m-1} k_n}.$$

The lemma implies that, assuming $\tau < 1/C_1$,

$$\max_{n=1,\ldots,M}(||v^n||_0^2 + ||w^n||_0^2) \leq \left(\frac{1}{1-\tau C_1}(||v^0||_0^2 + ||w^0||_0^2)\right) e^{\frac{TC_2}{1-\tau C_1}}.$$

We can now use this inequality to bound the H^1 terms as

$$\sum_{n=0}^{m-1} \tau(|u_i^{n+1}|_1^2 + |u_e^{n+1}|_1^2) \leq \frac{1}{2m}(||v^0||_0^2 + ||w^0||_0^2) + \frac{TC_2}{2m}\max_n(||v^n||_0^2 + ||w^n||_0^2).$$

We shall now consider the stability of a semi-implicit second order BDF method (SBDF). Taking u_i^{n+1}, u_e^{n+1}, w^{n+1} as test functions, the associated variational equations read as follows

$$\int_{\Omega_H} \frac{3v^{n+1} - 4v^n + v^{n-1}}{2\tau} u_i^{n+1} \quad + a_i(u_i^{n+1}, u_i^{n+1}) +$$

$$\int_{\Omega_H} (2I_{ion}(v^n, w^n) - I_{ion}(v^{n-1}, w^{n-1}))u_i^{n+1} = 0$$

$$-\int_{\Omega_H} \frac{3v^{n+1} - 4v^n + v^{n-1}}{2\tau} u_e^{n+1} \quad + a_e(u_e^{n+1}, u_e^{n+1}) -$$

$$\int_{\Omega_H} (2I_{ion}(v^n, w^n) - I_{ion}(v^{n-1}, w^{n-1}))u_e^{n+1} = 0$$

$$\int_{\Omega_H} \frac{3w^{n+1} - 4w^n + w^{n-1}}{2\tau} w^{n+1} \quad - \int_{\Omega_H} (2F(v^n, w^n) - F(v^{n-1}, w^{n-1}))w^{n+1} = 0.$$

Adding these three equations, multiplying by 4 and applying to the time discretization terms the identity

$$(6a^{n+1} - 8a^n + 2a^{n-1})a^{n+1} = (a^{n+1})^2 + (2a^{n+1} - a^n)^2 + (\delta_{tt}a^{n+1})^2 -$$
$$(a^n)^2 - (2a^n - a^{n-1})^2,$$

where $\delta_{tt}a^{n+1} = a^{n+1} - 2a^n + a^{n-1}$, we obtain

$$||v^{n+1}||_0^2 + ||2v^{n+1} - v^n||_0^2 - ||v^n||_0^2 - ||2v^n - v^{n-1}||_0^2 +$$
$$4\tau(a_i(u_i^{n+1}, u_i^{n+1}) + a_e(u_e^{n+1}, u_e^{n+1})) +$$
$$||w^{n+1}||_0^2 + ||2w^{n+1} - w^n||_0^2 - ||w^n||_0^2 - ||2w^n - w^{n-1}||_0^2 \leq$$
$$-\tau 8 \int_{\Omega_H} (2I_{ion}(v^n, w^n) - I_{ion}(v^{n-1}, w^{n-1}))v^{n+1} +$$
$$8\tau \int_{\Omega_H} (2F(v^n, w^n) - F(v^{n-1}, w^{n-1}))w^{n+1}.$$

Thanks to the uniform ellipticity of the conductivity tensors $M_{i,e}$ and to the Lipschitz condition (7.11), we get

$$
\begin{aligned}
&||v^{n+1}||_0^2 - ||v^n||_0^2 + ||2v^{n+1} - v^n||_0^2 - ||2v^n - v^{n-1}||_0^2 + \\
&\quad 4\tau(m_i|u_i^{n+1}|_1^2 + m_e|u_e^{n+1}|_1^2) + \\
&||w^{n+1}||_0^2 - ||w^n||_0^2 + ||2w^{n+1} - w^n||_0^2 - ||2w^n - w^{n-1}||_0^2 \leq \\
&\quad \tau 12(\lambda_{ion}||v^{n+1}||_0^2 + \lambda_F||w^{n+1}||_0^2) + \\
&\tau 4(\lambda_{ion} + \lambda_F)(||v^n||_0^2 + ||w^n||_0^2 + ||v^{n-1}||_0^2 + ||w^{n-1}||_0^2).
\end{aligned}
$$

Denoting now by M the index of the final time step (thus $T = M\tau$) and summing the previous inequality for n going from 0 to $m - 1$ with $1 \leq m \leq M$, we will see the values v^{-1} and w^{-1} appear. They are used during the first time step of the SBDF scheme and we take them $v^{-1} = v^0$ and $w^{-1} = w^0$. Then we get

$$
\begin{aligned}
&||v^m||_0^2 + ||2v^m - v^{m-1}||_0^2 + 4\tau\overline{m}\sum_{n=0}^{m-1}(|u_i^{n+1}|_1^2 + |u_e^{n+1}|_1^2) + ||w^m||_0^2 + ||2w^m - w^{m-1}||_0^2 \leq \\
&2(||v^0||_0^2 + ||w^0||_0^2) + \tau C_1(||v^m||_0^2 + ||w^m||_0^2) + \tau C_2 \sum_{n=0}^{m-1}(||v^n||_0^2 + ||w^n||_0^2),
\end{aligned}
$$

with $C_1 = \max(12\lambda_{ion}, 12\lambda_F)$ and $C_2 = \max(24\lambda_{ion} + 12\lambda_F, 12\lambda_{ion} + 24\lambda_F)$. Hence it follows

$$
\begin{aligned}
&(1 - \tau C_1)(||v^m||_0^2 + ||w^m||_0^2) + 4\tau\overline{m}\sum_{n=0}^{m-1}(|u_i^{n+1}|_1^2 + |u_e^{n+1}|_1^2) \leq \\
&2(||v^0||_0^2 + ||w^0||_0^2) + \tau C_2 \sum_{n=0}^{m-1}(||v^n||_0^2 + ||w^n||_0^2).
\end{aligned}
$$

From the Gronwall lemma, it follows that, assuming $\tau < 1/C_1$,

$$
\max_{n=1,\dots,M}(||v^n||_0^2 + ||w^n||_0^2) \leq \left(\frac{2}{1 - \tau C_1}(||v^0||_0^2 + ||w^0||_0^2)\right)e^{\frac{TC_2}{1-\tau C_1}}.
$$

We can now use this inequality to bound the H^1 terms as

$$
\sum_{n=0}^{m-1}\tau(|u_i^{n+1}|_1^2 + |u_e^{n+1}|_1^2) \leq \frac{1}{4\overline{m}}(||v^0||_0^2 + ||w^0||_0^2) + \frac{TC_2}{4\overline{m}}\max_n(||v^n||_0^2 + ||w^n||_0^2).
$$

A further decoupling approach consists of splitting the parabolic PDE from the elliptic PDE in the parabolic-elliptic formulation of the Bidomain model (7.6). We will now present some stability estimates originally developed by Fernandez and Zemzemi [172] for this decoupled method. At each time step, the numerical scheme consists of the following steps.

Decoupled method for the parabolic–elliptic formulation.

Step 1:   given the initial conditions $\mathbf{v}^n$, $\mathbf{w}^n$, $\mathbf{c}^n$ computed at the previous time step, find $\mathbf{w}^{n+1}$, $\mathbf{c}^{n+1}$

$$\mathbf{w}^{n+1} - \tau\, R(\mathbf{v}^n, \mathbf{w}^{n+1}) = \mathbf{w}^n, \qquad \mathbf{c}^{n+1} = \mathbf{c}^n + \tau\, S(\mathbf{v}^n, \mathbf{w}^{n+1}, \mathbf{c}^n).$$

Step 2:   given $\mathbf{v}^n$, update the extracellular potential $\mathbf{u}^n_e$ by solving the elliptic PDE

$$(A_i + A_e)\mathbf{u}^n_e = -A_i \mathbf{v}^n + \mathbf{I}^{i,n}_{app} + \mathbf{I}^{e,n}_{app}.$$

Step 3:   given $\mathbf{u}^n_e$, $\mathbf{w}^{n+1}$, $\mathbf{c}^{n+1}$ update the transmembrane potential $\mathbf{v}^{n+1}$ by solving the parabolic PDE

$$\left(\frac{\chi C_m}{\tau}M + A_i\right)\mathbf{v}^{n+1} = \frac{\chi C_m}{\tau}M\mathbf{v}^n - A_i\mathbf{u}^n_e - \mathbf{I}_{ion}(\mathbf{v}^n, \mathbf{w}^{n+1}, \mathbf{c}^{n+1}) + \mathbf{I}^{i,n+1}_{app}.$$

Following [172], let us investigate the stability of this decoupled semi-implicit scheme in the case of a membrane model with only one gating variable, satisfying the Lipschitz condition (7.11). For simplicity, we now disregard the presence of the applied currents. Using as test functions the solutions v^{n+1}, u^n_e and w^{n+1} in their respective variational equations, we obtain

$$\int_{\Omega_H} \frac{v^{n+1} - v^n}{\tau}v^{n+1} + a_i(v^{n+1}, v^{n+1}) + a_i(u^n_e, v^{n+1}) + \int_{\Omega_H} I_{ion}(v^n, w^{n+1})u^{n+1}_i = 0$$
$$a_i(u^n_e, u^n_e) + a_e(u^n_e, u^n_e) + a_i(v^n, u^n_e) = 0$$
$$\int_{\Omega_H} \frac{w^{n+1} - w^n}{\tau}w^{n+1} - \int_{\Omega_H} F(v^n, w^{n+1})w^{n+1} = 0.$$

Adding these three equations and using the identity

$$2(a^{n+1} - a^n)a^{n+1} = (a^{n+1})^2 + (a^{n+1} - a^n)^2 - (a^n)^2,$$

we get

$$||v^{n+1}||^2_0 + ||v^{n+1} - v^n||^2_0 - ||v^n||^2_0 +$$
$$2\tau a_i(v^{n+1}, v^{n+1}) + 2\tau a_i(u^n_e, v^{n+1}) + 2\tau a_i(u^n_e, u^n_e) +$$
$$2\tau a_e(u^n_e, u^n_e) + 2\tau a_i(v^n, u^n_e) +$$
$$||w^{n+1}||^2_0 + ||w^{n+1} - w^n||^2_0 - ||w^n||^2_0 \leq$$
$$-2\tau \int_{\Omega_H} I_{ion}(v^n, w^{n+1})v^{n+1} + 2\tau \int_{\Omega_H} F(v^n, w^{n+1})w^{n+1}.$$

By summing and subtracting the term $2\tau a_i(v^{n+1}, u_e^n)$ at the left hand side, we get

$$||v^{n+1}||_0^2 + ||v^{n+1} - v^n||_0^2 - ||v^n||_0^2 +$$
$$2\tau a_i(v^{n+1} + u_e^n, v^{n+1} + u_e^n) + 2\tau a_e(u_e^n, u_e^n) + 2\tau a_i(v^n - v^{n+1}, u_e^n) +$$
$$||w^{n+1}||_0^2 + ||w^{n+1} - w^n||_0^2 - ||w^n||_0^2 \le$$
$$-2\tau \int_{\Omega_H} I_{ion}(v^n, w^{n+1})v^{n+1} + 2\tau \int_{\Omega_H} F(v^n, w^{n+1})w^{n+1}.$$

Let us now focus on the term $2\tau a_i(v^n - v^{n+1}, u_e^n)$ and perform the following computations

$$\begin{aligned}
2\tau a_i(v^n - v^{n+1}, u_e^n) &= 2\tau a_i(v^n - v^{n+1}, u_e^n - v^{n+1} + v^{n+1}) \\
&= 2\tau a_i(v^{n+1} - v^n, v^{n+1}) + 2\tau a_i(v^n - v^{n+1}, v^{n+1} + u_e^n) \\
&= \tau a_i(v^{n+1}, v^{n+1}) + \tau a_i(v^{n+1} - v^n, v^{n+1} - v^n) - \tau a_i(v^n, v^n) + \\
&\quad 2\tau a_i(v^n - v^{n+1}, v^{n+1} + u_e^n).
\end{aligned}$$

Moving the term $2\tau a_i(v^n - v^{n+1}, v^{n+1} + u_e^n)$ to the right hand side and using the Lipschitz condition (7.11), we finally get

$$||v^{n+1}||_0^2 + ||v^{n+1} - v^n||_0^2 - ||v^n||_0^2 +$$
$$\tau a_i(v^{n+1} + u_e^n, v^{n+1} + u_e^n) + 2\tau a_e(u_e^n, u_e^n) + \tau a_i(v^{n+1}, v^{n+1}) - \tau a_i(v^n, v^n)$$
$$||w^{n+1}||_0^2 + ||w^{n+1} - w^n||_0^2 - ||w^n||_0^2 \le$$
$$\tau 2\lambda_{ion}||v^{n+1}||_0^2 + \tau(\lambda_{ion} + 3\lambda_F)||w^{n+1}||_0^2 + \tau(\lambda_{ion} + \lambda_F)||v^n||_0^2.$$

Denoting now by M the index of the final time step (thus $T = M\tau$), summing the previous inequality for n going from 0 to $m - 1$ with $1 \le m \le M$ and using the uniform ellipticity of the conductivity tensors $M_{i,e}$, we obtain

$$||v^m||_0^2 + \sum_{n=0}^{m-1} ||v^{n+1} - v^n||_0^2 + \tau \sum_{n=0}^{m-1} (m_i |v^{n+1} + u_e^n|_1^2 + 2m_e |u_e^n|_1^2) +$$
$$\tau m_i |v^m|_1^2 + ||w^m||_0^2 + \sum_{n=0}^{m-1} ||w^{n+1} - w^n||_0^2 \le$$
$$||v^0||_0^2 + \tau C_i |v^0|_1^2 + ||w^0||_0^2 + \tau C_1(||v^m||_0^2 + ||w^m||_0^2) + \tau C_2 \sum_{n=0}^{m-1} (||v^n||_0^2 + ||w^n||_0^2),$$

where $C_1 = \max(2\lambda_{ion}, \lambda_{ion} + 3\lambda_F)$ and $C_2 = \max(3\lambda_{ion} + \lambda_F, \lambda_{ion} + 3\lambda_F)$. Hence it follows

$$(1 - \tau C_1)(||v^m||_0^2 + ||w^m||_0^2) + \tau \sum_{n=0}^{m-1} (m_i |v^{n+1} + u_e^n|_1^2 + 2m_e |u_e^n|_1^2) + \tau m_i |v^m|_1^2 \le$$
$$||v^0||_0^2 + \tau C_i |v^0|_1^2 + ||w^0||_0^2 + \tau C_2 \sum_{n=0}^{m-1} (||v^n||_0^2 + ||w^n||_0^2).$$

The Gronwall lemma implies that, assuming $\tau < 1/C_1$,

$$\max_{n=1,\dots,M} (||v^n||_0^2 + ||w^n||_0^2) \le \left(\frac{1}{1 - \tau C_1} (||v^0||_0^2 + \tau C_i |v^0|_1^2 + ||w^0||_0^2) \right) e^{\frac{TC_2}{1 - \tau C_1}}.$$

We can now use this inequality to bound the H^1 terms as

$$\sum_{n=0}^{m-1} \tau(m_i |v^{n+1} + u_e^n|_1^2 + 2m_e |u_e^n|_1^2) + \tau m_i \max_{n=1,\dots,M} |v^n|_1^2 \le$$
$$||v^0||_0^2 + \tau C_i |v^0|_1^2 + ||w^0||_0^2 + T C_2 \max_n (||v^n||_0^2 + ||w^n||_0^2).$$

7.2.4   Operator Splitting Methods: Splitting ODEs and PDEs

In this section, we will present two operator splitting techniques for the Bidomain model, based on splitting the ODEs of the membrane model from the PDEs. The first method, Godunov splitting, is first order accurate in time, while the second method, Strang splitting, is second order accurate in time. Both methods were first introduced for the Bidomain model by Sundnes et al. [501]. The Godunov splitting for the Monodomain model was developed by Qu and Garfinkel [410].

Godunov splitting.

Step 1:   given the initial conditions $\mathbf{v}^n$, $\mathbf{w}^n$, $\mathbf{c}^n$ computed at the previous time step, find $\tilde{\mathbf{v}}^{n+1}$, $\mathbf{w}^{n+1}$, $\mathbf{c}^{n+1}$ by solving the ODEs system

$$\begin{cases} \chi C_m \dfrac{d\mathbf{v}}{dt} = -\mathbf{I}_{ion}(\mathbf{v}, \mathbf{w}, \mathbf{c}) & t_n \le t \le t_n + \tau \\[2mm] \dfrac{d\mathbf{w}}{dt} = \mathbf{R}(\mathbf{v}, \mathbf{w}) & t_n \le t \le t_n + \tau \\[2mm] \dfrac{d\mathbf{c}}{dt} = \mathbf{S}(\mathbf{v}, \mathbf{w}, \mathbf{c}) & t_n \le t \le t_n + \tau. \end{cases}$$

Step 2:   given the initial condition $\tilde{\mathbf{v}}^{n+1}$ computed at Step 1, find $\mathbf{u}_i^{n+1}$ and $\mathbf{u}_e^{n+1}$ by solving the PDEs system

$$\begin{cases} \chi C_m \dfrac{d\mathbf{v}}{dt} + A_i \mathbf{u}_i = \mathbf{I}_{app}^i & t_n \le t \le t_n + \tau \\[2mm] -\chi C_m \dfrac{d\mathbf{v}}{dt} + A_e \mathbf{u}_e = \mathbf{I}_{app}^e & t_n \le t \le t_n + \tau. \end{cases}$$

Strang splitting.

Step 1:   given the initial conditions $\mathbf{v}^n$, $\mathbf{w}^n$, $\mathbf{c}^n$ computed at the previous time step, find $\mathbf{v}^{n+1/2}$, $\mathbf{w}^{n+1/2}$, $\mathbf{c}^{n+1/2}$ by solving the ODEs system

$$
\begin{cases}
\chi C_m \dfrac{d\mathbf{v}}{dt} = -\mathbf{I}_{ion}(\mathbf{v}, \mathbf{w}, \mathbf{c}) & t_n \le t \le t_n + \tau/2 \\[2mm]
\dfrac{d\mathbf{w}}{dt} = \mathbf{R}(\mathbf{v}, \mathbf{w}) & t_n \le t \le t_n + \tau/2 \\[2mm]
\dfrac{d\mathbf{c}}{dt} = \mathbf{S}(\mathbf{v}, \mathbf{w}, \mathbf{c}) & t_n \le t \le t_n + \tau/2.
\end{cases}
$$

Step 2:   given the initial condition $\mathbf{v}^{n+1/2}$ computed at Step 1, find $\tilde{\mathbf{u}}_i^{n+1}$ and $\tilde{\mathbf{u}}_e^{n+1}$ by solving the PDEs system

$$
\begin{cases}
\chi C_m \dfrac{d\mathbf{v}}{dt} + A_i \mathbf{u}_i = \mathbf{I}_{app}^i & t_n \le t \le t_n + \tau \\[2mm]
-\chi C_m \dfrac{d\mathbf{v}}{dt} + A_e \mathbf{u}_e = \mathbf{I}_{app}^e & t_n \le t \le t_n + \tau.
\end{cases}
$$

Step 3:   given the initial conditions $\tilde{\mathbf{v}}^{n+1} = \tilde{\mathbf{u}}_i^{n+1} - \tilde{\mathbf{u}}_e^{n+1}$, $\mathbf{w}^{n+1/2}$, $\mathbf{c}^{n+1/2}$ computed at Step 1 and 2, find $\mathbf{v}^{n+1}$, $\mathbf{w}^{n+1}$, $\mathbf{c}^{n+1}$ by solving the ODEs system

$$
\begin{cases}
\chi C_m \dfrac{d\mathbf{v}}{dt} = -\mathbf{I}_{ion}(\mathbf{v}, \mathbf{w}, \mathbf{c}) & t_n + \tau/2 \le t \le t_n + \tau \\[2mm]
\dfrac{d\mathbf{w}}{dt} = \mathbf{R}(\mathbf{v}, \mathbf{w}) & t_n + \tau/2 \le t \le t_n + \tau \\[2mm]
\dfrac{d\mathbf{c}}{dt} = \mathbf{S}(\mathbf{v}, \mathbf{w}, \mathbf{c}) & t_n + \tau/2 \le t \le t_n + \tau.
\end{cases}
$$

In order to achieve the second order convergence for the Strang splitting scheme, the sub-problems in each step must be solved to at least second-order accuracy.

7.3   Numerical Approximation of the Eikonal-Diffusion Equation

Numerical methods for finding the evolving surface $S(t)$ based on a direct discretization of (4.23) encounters many difficulties, e.g. front–tracking techniques, when high curvature and topological changes of the wavefronts occur. One way to overcome the singularities due to collisions, merging and extinction is the level set approach of (4.23) (see e.g. [365, 471]) which represents $S(t)$ as the zero level surface of a function $w(\mathbf{x}, t)$ formally solving

$$
\frac{\partial w}{\partial t} = \Phi(\mathbf{x}, \nabla w)(c + \varepsilon \operatorname{div} \Phi_\xi(\mathbf{x}, \nabla w)). \tag{7.12}
$$

As observed before, during the excitation sequence in a fully recovered tissue the wavefront surface $S_\varepsilon(t)$ admits a cartesian representation. Therefore $\theta_\varepsilon(\mathbf{v}) = 1/|\nabla\psi|$ hence, dropping $\mathcal{O}(\varepsilon^2)$, the eikonal-curvature equation (4.22) reduces to

$$
\Phi(\mathbf{x}, \nabla\psi)(c - \varepsilon \operatorname{div} \Phi_\xi(\mathbf{x}, \nabla\psi)) = 1, \tag{7.13}
$$

and the eikonal-diffusion equation (4.26) to

$$- \varepsilon \, \mathrm{div} \, (\Phi(\mathbf{x}, \nabla \psi) \Phi_{\xi}(\mathbf{x}, \nabla \psi)) + c \, \Phi(\mathbf{x}, \nabla \psi) = 1. \qquad (7.14)$$

In both equations, the term of order ε is related to the influence of the wavefront curvature on the propagation in an anisotropic medium.

In a fully recovered tissue the propagation front admits a cartesian representation and, from (4.17), (4.18), it is easy to verify that

$$\Phi(\mathbf{x}, \mathbf{p}) = \sqrt{\mathbf{p}^T Q(\mathbf{x}, \mathbf{p})\mathbf{p}} \quad \text{and} \quad \Phi_{\xi}(\mathbf{x}, \mathbf{p}) = \frac{Q(\mathbf{x}, \mathbf{p})\mathbf{p}}{\Phi(\mathbf{x}, \mathbf{p})},$$

with $\mathbf{p} = \nabla \psi$. At the collision points, where $\nabla \psi = 0$, only a discontinuity appears in the divergence term, thus the eikonal–diffusion equation (7.14) is more convenient than the level set approach [365, 471] for the eikonal-curvature model, which, under the same circumstances, exhibits singularities requiring a regularization of Φ. Introducing boundary conditions, we have to solve the non-linear elliptic problem

$$\begin{cases} -\varepsilon \, \mathrm{div} Q(\mathbf{x}, \mathbf{p})\mathbf{p} + c \, \sqrt{\mathbf{p}^T Q(\mathbf{x}, \mathbf{p})\mathbf{p}} = 1 & \text{in } \Omega_H \\ \mathbf{n}^T \, Q \, \mathbf{p} = 0 \quad \text{on } \Gamma, \qquad \psi(\mathbf{x}) = t_a(\mathbf{x}) \quad \text{on } S_a, \end{cases} \qquad (7.15)$$

where S_a is the boundary of the initial activated region and $t_a(\mathbf{x})$ the corresponding activation instants. The solution $\psi(\mathbf{x})$ of this non-linear problem can be viewed as the steady–state solution of the following parabolic problem associated with (7.15)

$$\begin{cases} \dfrac{\partial w}{\partial t} - \varepsilon \, \mathrm{div} Q(\mathbf{x}, \nabla w) \nabla w + c \, \sqrt{\nabla w^T Q(\mathbf{x}, \nabla w) \nabla w} = 1 & \text{in } \Omega_H \\ \mathbf{n}^T \, Q \, \nabla w = 0 \quad \text{on } \Gamma, \\ w(\mathbf{x}, t) = w_a(\mathbf{x}) \quad \text{on } S_a \qquad w(\mathbf{x}, 0) = w_0. \end{cases} \qquad (7.16)$$

Equation (7.16) belongs to a broad class of equations known as *Hamilton-Jacobi* equations, with the Hamiltonian term given by $c \, \Phi(\mathbf{x}, \nabla w)$ and a second order non-linear diffusion term $-\varepsilon \, \mathrm{div} Q(\mathbf{x}, \nabla w) \nabla w$. We considered the following discretization in time obtained by applying a semi–implicit approximation for the diffusive term and an explicit one for the transport term

$$\frac{w_{n+1} - w_n}{\tau_n} - \varepsilon \, \mathrm{div} Q(\mathbf{x}, \nabla w_n) \nabla w_{n+1} + c \, \sqrt{(\nabla w_n)^T Q(\mathbf{x}, \nabla w_n) \nabla w_n} = 1,$$

with w_n the approximate solution at the time t_n and $\tau_n = t_{n+1} - t_n$. The space discretization was carried out by the usual Galerkin finite element method. We remark that the solution of the discrete problem can exhibit spurious secondary fronts originating at the domain boundary, see [102]. This is due to the fact that

in Eq. (7.15) the transport term is dominant with respect to the non-linear diffusion term. To overcome this problem the term $\Phi(\mathbf{x}, \nabla w)$ required special treatment. A way to avoid these numerical artifacts is to use the upwind scheme proposed by Osher-Sethian for propagating fronts with curvature dependent speed. This upwind method proved to be quite efficient and allowed us to solve our equation in every case and using a mesh-size h of the order of 1 mm (see [102, 115] and also [522]). Interested readers can find many results of numerical simulations with the eikonal approach in [102, 114, 115, 117, 121] and [268, 271, 272, 369]. See [186] for recent developments of numerical techniques to solve the eikonal equations.

Finally, we remark that the non-linear parabolic equation shares the same non-linear diffusion term of the Relaxed Monodomain model. A similar implicit-explicit time discretization could be applied for the numerical solution of the Relaxed Monodomain model where the reaction term, modeling the ionic current membrane, is treated explicitly instead of the Hamiltonian term. Therefore the semi-discretization in time of the Relaxed Monodomain model reads:

$$\begin{cases} w^{n+1} - \tau_n R(v^n, w^{n+1}) = w^n \\ c^{n+1} = c^n + \tau_n S(v^n, w^{n+1}, c^n) \\ c_m \dfrac{v^{n+1} - v^n}{\tau_n} - \operatorname{div}(Q(\mathbf{x}, \nabla v^n)\nabla v^{n+1}) + i_{ion}(v^n, w^{n+1}, c^{n+1}) = I_{app}^{n+1}. \end{cases}$$

Chapter 8
Parallel Solvers for the Bidomain System

We have seen in Chap. 7 that most numerical approaches to solve the Bidomain system lead to the solution of linear systems of equations. Linear solvers can be classified as direct and iterative solvers. Direct solvers compute the solution of the linear system in a finite number of steps, for instance by Gaussian elimination or computing a factorization of the matrix, and in exact arithmetic would provide the exact solution of the system. LU factorization is one of the most common direct solvers, together with the Cholesky factorization for symmetric positive definite matrices. On the other hand, in finite precision arithmetic, rounding errors and the matrix ill-conditioning may spoil the approximate solution computed by direct methods. Moreover, these direct methods have a high computational cost (cubic in the number of unknowns of the linear system) and can suffer from fill-in, that is the sparsity pattern of the original sparse matrix can be filled during the factorization process, thus requiring large amounts of memory. One advantage of direct methods in the context of evolution problems is that, if the system matrix does not change during the time evolution, one needs to compute the factorization only once as a preprocessing step.

The most popular methods to solve the linear systems arising from the discretization of Bidomain and Monodomain systems are iterative methods. In these methods, approximate solutions of the linear system are computed iteratively until a stopping criterion, typically involving the residual norm, is reached. Most published approaches for the numerical discretisation of Monodomain and Bidomain models leads to symmetric positive definite or semi-definite matrices. In this case, the best choice of iterative method is the Conjugate Gradient method (CG). In some cases, due to the formulation chosen and numerical scheme implemented, non-symmetric matrices may arise, see e.g. [195,381,382], requiring alternative methods as Krylov subspace solvers, in particular the Generalized Minimal Residual Method (GMRES).

In order to accelerate the convergence of iterative methods, several types of preconditioners for the Bidomain system have been proposed in the literature: diagonal preconditioners [485], Symmetric Successive Over Relaxation [379], Block Jacobi (BJ) preconditioners with incomplete LU factorization (ILU) for each block [104, 371, 544], block triangular [195], optimized Schwarz [196], geometric multigrid [19, 499, 552], algebraic multigrid [381, 382, 389], and domain decomposition preconditioners such as Multilevel Schwarz [341, 372, 373], Neumann-Neumann and BDDC [581, 582]. We refer finally to [380] for substructuring preconditioners applied to mortar discretizations of the Bidomain model.

In this chapter, we introduce Multilevel Schwarz methods for the Bidomain system. Optimal convergence properties of the algorithms are established and supported by numerical simulations in two and three dimensions. The numerical tests were all performed on the Linux clusters described in Sect. 8.5. More details and a proof of the main convergence rate bound can be found in [372]. Extensions to hybrid and multiplicative Bidomain preconditioners can be found in [458, 459] and to block preconditioners in [373]. For a general introduction to Domain Decomposition methods and for Additive Schwarz preconditioners applied to parabolic problems, we refer the interested reader to the monograph by Toselli and Widlund [523] and to the papers by Cai [72, 73].

8.1 Bidomain Variational Setting

In this section, we briefly describe the variational formulation of the Bidomain model. Assume that:

(H1) The cardiac region Ω_H is a bounded Lipschitz connected open subset of $\mathbb{R}^3$;
(H2) The tensors $D_{i,e}(\mathbf{x})$ satisfy the following uniform ellipticity condition:

$$\exists \alpha_{i,e}, C_{i,e} > 0: \quad \alpha_{i,e}|\boldsymbol{\xi}|^2 \leq \boldsymbol{\xi}^T D_{i,e}(\mathbf{x})\boldsymbol{\xi} \leq C_{i,e}|\boldsymbol{\xi}|^2, \quad \forall \boldsymbol{\xi} \in R^3, \, \mathbf{x} \in \Omega_H;$$

$$(8.1)$$

(H3) The coefficients of $D_{i,e}(\mathbf{x})$ are Lipschitz continuous.

Let V be the Sobolev space $H^1(\Omega_H)$, define the spaces

$$\tilde{V} = \{v \in V : \int_{\Omega_H} v = 0\} \quad \text{and} \quad U = V \times \tilde{V} = \{u = (u_i, u_e) : u_i \in V, u_e \in \tilde{V}\},$$

define the usual L^2-inner product

$$(\varphi, \psi) = \int_{\Omega_H} \varphi \psi \, dx \quad \forall \varphi, \psi \in L^2(\Omega_H)$$

and the elliptic bilinear forms

$$a_{i,e}(\varphi, \psi) = \int_{\Omega_H} (\nabla \varphi)^T D_{i,e}(x) \nabla \psi \, dx$$

$$a(\varphi, \psi) = \int_{\Omega_H} (\nabla \varphi)^T D(x) \nabla \psi \, dx \quad \forall \varphi, \psi \in H^1(\Omega_H), \quad \text{with} \quad D = D_i + D_e.$$

The variational formulation of the Bidomain model reads as follows. Given $v_0, w_0 \in L^2(\Omega_H)$, $I_{app}^{i,e} \in L^2(\Omega_H \times (0, T))$, find $u_i \in L^2(0, T; V)$, $u_e \in L^2(0, T; \tilde{V})$, $w \in L^2(0, T; L^2(\Omega_H)^M)$ and $c \in L^2(0, T; L^2(\Omega_H)^M)$ such that $\frac{\partial v}{\partial t} \in L^2(0, T; V)$, $\frac{\partial w}{\partial t} \in L^2(0, T; L^2(\Omega_H)^M)$, $\frac{\partial c}{\partial t} \in L^2(0, T; L^2(\Omega_H)^S)$ and $\forall t \in (0, T)$ it holds

$$\begin{cases} c_m \dfrac{\partial}{\partial t}(v, \hat{u}_i) + a_i(u_i, \hat{u}_i) + (I_{ion}(v, w, c), \hat{u}_i) = (I_{app}^i, \hat{u}_i) & \forall \hat{u}_i \in V \\[2mm] -c_m \dfrac{\partial}{\partial t}(v, \hat{u}_e) + a_e(u_e, \hat{u}_e) - (I_{ion}(v, w, c), \hat{u}_e) = (I_{app}^e, \hat{u}_e) & \forall \hat{u}_e \in \tilde{V} \\[2mm] \dfrac{\partial}{\partial t}(w, \hat{w}) - (R(v, w), \hat{w}) = 0, \quad \dfrac{\partial}{\partial t}(c, \hat{c}) - (S(v, w, c), \hat{c}) = 0 & \forall \hat{w}, \hat{c} \in V \end{cases}$$

$$(8.2)$$

with the initial conditions (3.42).

We refer to [455] for a convergence analysis of finite element approximation of the Bidomain model.

The anisotropic Bidomain model (8.2) is discretized by the finite element method (see e.g. [61, 92]) in space and a semi-implicit method in time; see e.g. [414] for a general introduction to these numerical methods.

Time discretization. The time discretization is performed by a semi-implicit method using for the diffusion term the implicit Euler method, while the non-linear reaction term I_{ion} is treated explicitly. The implicit treatment of the diffusion terms appearing in the Bidomain model is essential in order to adaptively change the time step according to the stiffness of the various phases of the heart-beat. The ODE system for the gating variables is discretized by the semi-implicit Euler method and the explicit Euler method is applied for solving the ODE system for the ion concentrations. As a consequence, the full evolution system is decoupled by first solving the gating and ion concentrations system (given the transmembrane potential $v^n = u_i^n - u_e^n$ at the previous time-step)

$$(w^{n+1} - \Delta t \, R(v^n, w^{n+1}), \hat{w}) = (w^n, \hat{w}) \quad \forall \hat{w} \in V$$

$$(c^{n+1}, \hat{c}) = (c^n + \Delta t \, S(v^n, w^{n+1}, c^n), \hat{c}) \quad \forall \hat{c} \in V,$$

and then solving for $(u_i^{n+1}, u_e^{n+1}) \in U$ the variational problem

$$\begin{cases} \gamma(v^{n+1}, \hat{u}_i) + a_i(u_i^{n+1}, \hat{u}_i) = (\gamma \, v^n - I_{ion}(v^n, w^{n+1}, c^{n+1}) + I_{app}^i, \hat{u}_i) & \forall \hat{u}_i \in V \\ -\gamma(v^{n+1}, \hat{u}_e) + a_e(u_e^{n+1}, \hat{u}_e) = -(\gamma \, v^n - I_{ion}(v^n, w^{n+1}, c^{n+1}) - I_{app}^e, \hat{u}_e) & \forall \hat{u}_e \in \tilde{V} \end{cases}$$
(8.3)

where $v^{n+1} = u_i^{n+1} - u_e^{n+1}$ and $\gamma = c_m / \Delta t$.

Lemma 8.1. *The symmetric bilinear forms* $((\cdot, \cdot))$, $((\cdot, \cdot))_0 : U \times U \to R$ *defined by*

$$((u, v)) := \int_{\Omega_H} \nabla u_i \cdot \nabla v_i + \int_{\Omega_H} \nabla u_e \cdot \nabla v_e + \int_{\Omega_H} (u_i - u_e)(v_i - v_e)$$

and

$$((u, v))_0 := \int_{\Omega_H} u_i \, v_i + \int_{\Omega_H} u_e \, v_e$$

are inner products.

Proof. Clearly $((u, u)) \geq 0$, $\forall u \in U$. If $((u, u)) = 0$ for some $u \in U$, then its extracellular component would satisfy $\int_{\Omega_H} |\nabla u_e|^2 = 0$. But $\int_{\Omega_H} u_e = 0$, hence, since (H1) holds, $u_e \equiv 0$. This in turn implies that $u_i \equiv 0$, since $((u, u)) = 0$ also implies $\int_{\Omega_H} u_i^2 = 0$, hence in conclusion $u \equiv 0$. The proof for $((\cdot, \cdot))_0$ is trivial.

We denote by $||| \cdot ||| : U \to R$ the norm induced by the $((\cdot, \cdot))$ inner product, i.e.

$$|||u|||^2 = \int_{\Omega_H} |\nabla u_i|^2 + \int_{\Omega_H} |\nabla u_e|^2 + \int_{\Omega_H} (u_i - u_e)^2.$$

Lemma 8.2. *The bilinear form* $a_{bid}(\cdot, \cdot) : U \times U \to R$ *defined by*

$$a_{bid}(u, v) := \int_{\Omega_H} D_i \nabla u_i \cdot \nabla v_i + \int_{\Omega_H} D_e \nabla u_e \cdot \nabla v_e + \gamma \int_{\Omega_H} (u_i - u_e)(v_i - v_e)$$

is continuous and elliptic with respect to the $||| \cdot |||$-*norm.*

Proof. The lemma follows from the uniform ellipticity condition (8.1) and the definition of $||| \cdot |||$-norm. (a) Continuity:

$$a_{bid}(u, v) = \int_{\Omega_H} D_i \nabla u_i \cdot \nabla v_i + \int_{\Omega_H} D_e \nabla u_e \cdot \nabla v_e + \gamma \int_{\Omega_H} (u_i - u_e)(v_i - v_e)$$

$$\leq C_i \int_{\Omega_H} \nabla u_i \cdot \nabla v_i + C_e \int_{\Omega_H} \nabla u_e \cdot \nabla v_e + \gamma \int_{\Omega_H} (u_i - u_e)(v_i - v_e)$$

$$\leq max(C_i, C_e, \gamma)((u, v)) \leq C_{bid} |||u||| \, |||v|||.$$

(b) Ellipticity:

$$
a_{bid}(u, u) = \int_{\Omega_H} D_i \nabla u_i \cdot \nabla u_i + \int_{\Omega_H} D_e \nabla u_e \cdot \nabla u_e + \gamma \int_{\Omega_H} (u_i - u_e)^2
$$

$$
\geq \alpha_i \int_{\Omega_H} (\nabla u_i)^2 + \alpha_e \int_{\Omega_H} (\nabla u_e)^2 + \gamma \int_{\Omega_H} (u_i - u_e)^2
$$

$$
\geq min(\alpha_i, \alpha_e, \gamma) |||u|||^2 \geq \alpha_{bid} |||u|||^2.
$$

Given the previous notations, the stationary Bidomain system (8.3) can be rewritten in the compact form:

Given v^n, w^{n+1}, c^{n+1}, find $u^{n+1} \in U$ such that

$$
a_{bid}(u^{n+1}, \hat{u}) = (\gamma \, v^n - I_{ion}(v^n, w^{n+1}, c^{n+1}), \hat{u}_i - \hat{u}_e) + (I^i_{app}, \hat{u}_i) + (I^e_{app}, \hat{u}_e) \quad \forall \hat{u} \in U,
$$
(8.4)

which in a more general setting reads:

Given $F = (F_i, F_e) \in L^2(\Omega_H) \times L^2(\Omega_H)$, find $u \in U$ such that

$$
a_{bid}(u, v) = \; <F, v> \quad \forall v \in U,
$$
(8.5)

where

$$
<F, v> = (F_i, v_i) + (F_e, v_e).
$$

To ensure the solvability of (8.5), F must satisfy the compatibility condition

$$
<F, \mathbf{1}> = 0, \text{ i.e.}
$$

$$
\int_{\Omega_H} F_i + \int_{\Omega_H} F_e = 0,
$$

which in case (8.4) implies

$$
\int_{\Omega_H} (I^i_{app} + I^e_{app}) = 0,
$$

that is satisfied e.g. for

$$
I^i_{app} = -I^e_{app}
$$
(8.6)

or for

$$
I^i_{app} = 0, \quad \text{and} \quad \int_{\Omega_H} I^e_{app} = 0.
$$
(8.7)

In the following, we assume (8.6), and setting $f = I_{app}^i = -I_{app}^e$ problem (8.5) reduces to: find $u \in U$ such that

$$a_{bid}(u, v) = (f, v_i - v_e) \quad \forall v \in U. \tag{8.8}$$

Theorem 8.1. *Given $f \in L^2(\Omega_H)$, problem (8.8) is equivalent to: find $u \in U$ such that*

$$a_{bid}(u, v) = (f, v_i - v_e) \quad \forall v \in V \times V. \tag{8.9}$$

Proof. (8.9) $\Rightarrow$ (8.8) is trivial.
In order to prove (8.8) $\Rightarrow$ (8.9), it is sufficient to verify that (8.9) holds true taking $v = (0, 1)$. Substituting $v = (0, 1)$ in (8.9), we obtain

$$\gamma \int_{\Omega_H} u_i = \int_{\Omega_H} f,$$

but this follows from (8.8) with $v = (1, 0)$, hence (8.8) and (8.9) are equivalent.

Remark 8.1. We note that, if (H1)–(H2)–(H3) hold, problem (8.8) is H^2-regular, i.e.

$$|u_i|_{H^2(\Omega_H)} + |u_e|_{H^2(\Omega_H)} \leq C ||f||_{L^2(\Omega_H)}. \tag{8.10}$$

Space discretization. The domain Ω_H is discretized by introducing a quasi-uniform finite element grid $\mathcal{T}_h$. Le V^h be an associated conforming finite element space. Define also the spaces

$$\tilde{V}^h = \{v^h \in V^h : \int_{\Omega_H} v^h = 0\} \quad \text{and} \quad U^h = V^h \times \tilde{V}^h.$$

The discrete Bidomain system is obtained by applying a standard Galerkin procedure. Given $v^{h,n} \in V^h$, $w^{h,n} \in V^h$, $c^{h,n} \in V^h$ we first find $w^{h,n+1}$ and $c^{h,n+1}$ solving

$$(w^{h,n+1} - \Delta t \, R(v^{h,n}, w^{h,n+1}), \hat{w}^h) = (w^{h,n}, \hat{w}^h) \quad \forall \hat{w}^h \in V^h$$

$$(c^{h,n+1}, \hat{c}^h) = (c^{h,n} + \Delta t \, S(v^{h,n}, w^{h,n+1}, c^{h,n}), \hat{c}^h) \quad \forall \hat{c}^h \in V^h,$$

and then $(u_i^{h,n+1}, u_e^{h,n+1}) \in U^h$ solving

$$\begin{cases} \gamma(v^{h,n+1}, \hat{u}_i^h) + a_i(u_i^{h,n+1}, \hat{u}_i^h) \\ \quad = (\gamma \, v^{h,n} - I_{ion}^h(v^{h,n}, w^{h,n+1}, c^{h,n+1}) + I_{app}^i, \hat{u}_i^h) \quad \forall \hat{u}_i^h \in V^h \\ -\gamma(v^{h,n+1}, \hat{u}_e^h) + a_e(u_e^{h,n+1}, \hat{u}_e^h) \\ \quad = (-\gamma \, v^{h,n} + I_{ion}^h(v^{h,n}, w^{h,n+1}, c^{h,n+1}) + I_{app}^e, \hat{u}_e^h) \, \forall \hat{u}_e^h \in V^h \end{cases} \tag{8.11}$$

where I_{ion}^h is the finite elements interpolants of I_{ion}.

Choose a finite element basis $\{\varphi_i\}$ for V_h and let $M = (m_{rs})$ and $A_{i,e} = (a_{rs}^{i,e})$ be the symmetric mass and stiffness matrices defined by

$$m_{rs} = \sum_E \int_E \varphi_r\,\varphi_s\mathrm{d}x, \quad a_{rs}^{i,e} = \sum_E \int_E (\nabla\varphi_r)^T D_{i,e}(\mathbf{x})\,\nabla\varphi_s\mathrm{d}x.$$

Numerical quadrature with a simple trapezoidal rule in three dimensions is used in order to compute these integrals. We can now enunciate the matrix formulation of (8.11). Given $\mathbf{v}^n, \mathbf{w}^n, \mathbf{c}^n$, we first find $\mathbf{w}^{n+1}, \mathbf{c}^{n+1}$ solving

$$\mathbf{w}^{n+1} - \Delta t\ R(\mathbf{v}^n, \mathbf{w}^{n+1}) = \mathbf{w}^n$$

$$\mathbf{c}^{n+1} = \mathbf{c}^n + \Delta t\ S(\mathbf{v}^n, \mathbf{w}^{n+1}, \mathbf{c}^n),$$

and then $\mathbf{u}_i^{n+1}, \mathbf{u}_e^{n+1}$ solving

$$A_{bid}\begin{pmatrix} \mathbf{u}_i^{n+1} \\ \mathbf{u}_e^{n+1} \end{pmatrix} = \frac{c_m}{\Delta t}\begin{pmatrix} M[\ \mathbf{u}_i^n - \mathbf{u}_e^n] \\ M[-\mathbf{u}_i^n + \mathbf{u}_e^n] \end{pmatrix} + \begin{pmatrix} M[-\mathbf{I}_{ion}^h(\mathbf{v}^n, \mathbf{w}^{n+1}, \mathbf{c}^{n+1}) + \mathbf{I}_{app}^i] \\ M[\ \mathbf{I}_{ion}^h(\mathbf{v}^n, \mathbf{w}^{n+1}, \mathbf{c}^{n+1}) + \mathbf{I}_{app}^e] \end{pmatrix},$$
(8.12)

where

$$A_{bid} = \gamma \begin{bmatrix} M & -M \\ -M & M \end{bmatrix} + \begin{bmatrix} A_i & 0 \\ 0 & A_e \end{bmatrix}$$

and $\mathbf{u}_i^n, \mathbf{u}_e^n, \mathbf{w}^n, \mathbf{c}^n, \mathbf{u}_i^{n+1}, \mathbf{u}_e^{n+1}, \mathbf{w}^{n+1}, \mathbf{c}^{n+1}, \mathbf{I}_{ion}^h, \mathbf{I}_{app}^{i,e}$ are the vectors of nodal values of $u_i^{h,n}, u_e^{h,n}, w^{h,n}, c^{h,n}, u_i^{h,n+1}, u_e^{h,n+1}, w^{h,n+1}, c^{h,n+1}, I_{ion}^h, I_{app}^{i,e}$ respectively. As in the continuous model, $\mathbf{v}^{n+1}$ is uniquely determined, while $\mathbf{u}_i^{n+1}$ and $\mathbf{u}_e^{n+1}$ are determined only up to the same additive time-dependent constant chosen by imposing the condition $\mathbf{1}^T M\mathbf{u}_e^{n+1} = 0$. Hence, at each time step we have to solve the large linear system (8.12), that, as shown in [104], is very ill-conditioned and increases considerably the computational costs of the simulations.

In order to introduce in the next chapter multilevel Schwarz preconditioners for the discrete Bidomain system, as we did in (8.4), we need to rewrite (8.11) in the compact form:

Given $v^{h,n}, w^{h,n+1}, c^{h,n+1}$, find $u^{h,n+1} \in U^h$ such that $\forall \hat{u}^h \in V^h \times V^h$

$$a_{bid}(u^{h,n+1}, \hat{u}^h) = (\gamma\,v^{h,n} - I_{ion}^h(v^{h,n}, w^{h,n+1}, c^{h,n+1}), \hat{u}_i^h - \hat{u}_e^h) + (I_{app}^i, \hat{u}_i^h) + (I_{app}^e, \hat{u}_e^h),$$
(8.13)

which, assuming as before $I_{app}^i = -I_{app}^e = f$, we reformulate the problem as:

Given $f \in L^2(\Omega_H)$, find $u^h \in U^h$ such that

$$a_{bid}(u^h, v^h) = (f, v_i^h - v_e^h) \quad \forall v^h \in V^h \times V^h.$$
(8.14)

Remark 8.2. Clearly, (8.14) arises from the finite element discretization of (8.8).

By defining the linear operator $\mathscr{A}_{bid} : U^h \to U^h$ as

$$((\mathscr{A}_{bid}u^h, v^h))_0 = a_{bid}(u^h, v^h) \quad \forall v^h \in V^h \times V^h,$$

we have that (8.14) is equivalent to the linear operator equation

$$\mathscr{A}_{bid}u^h = f^h, \tag{8.15}$$

with right-hand side $f^h \in U^h$ defined as

$$((f^h, v^h))_0 = (f, v_i^h) - (f, v_e^h) \quad \forall v^h \in V^h \times V^h.$$

We will construct in the next chapter multilevel Schwarz preconditioners for problem (8.15) and, following the standard abstract Schwarz theory described e.g. in [489, 523], we will prove their convergence.

In the proof of our main result on the optimality of the multilevel preconditioner, we need an L^2-error estimate for the solutions of (8.8) and (8.14).

Theorem 8.2. *Let u and u^h be the solutions of (8.8) and (8.14), respectively. Then the following error estimate holds*

$$||u_i - u_i^h||_{L^2(\Omega_H)} + ||u_e - u_e^h||_{L^2(\Omega_H)} \leq C\, h\, |||u - u^h|||. \tag{8.16}$$

Proof. Consider the following dual problems:

D1. Given $f \in L^2(\Omega_H)$, find $\varphi(f) \in U$:

$$a_{bid}(v, \varphi(f)) = (f, v_i - v_e) \quad \forall v \in U. \tag{8.17}$$

D2. Given $f \in L^2(\Omega_H) : \int_{\Omega_H} f = 0$, find $\varphi(f) \in U$:

$$a_{bid}(v, \varphi(f)) = (f, v_i + v_e) \quad \forall v \in U. \tag{8.18}$$

Let us define $e^h = (e_i^h, e_e^h) := u - u^h = (u_i - u_i^h, u_e - u_e^h)$. Taking $f = e_i^h$ and $v = e^h$ in (8.17), one has

$$||e_i^h||_{L^2(\Omega_H)}^2 - (e_i^h, e_e^h) = (e_i^h, e_i^h - e_e^h) = a_{bid}(e^h, \varphi(e_i^h)).$$

Thanks to the Galerkin orthogonality, for all $v^h \in U^h$ it holds

$$||e_i^h||_{L^2(\Omega_H)}^2 - (e_i^h, e_e^h) = a_{bid}(e^h, \varphi(e_i^h) - v^h) \leq C\, |||e^h|||\, |||\varphi(e_i^h) - v^h|||.$$

Choosing $v^h = (P_i\varphi(e_i^h), P_e\varphi(e_i^h))$, where $P_i : V \to V^h$ and $P_e : \tilde{V} \to \tilde{V}^h$ are standard finite element interpolation operators, and using (8.10), we get

$$||e_i^h||_{L^2(\Omega_H)}^2 - (e_i^h, e_e^h) \leq C\,h\,|||e^h|||\,||e_i^h||_{L^2(\Omega_H)}. \tag{8.19}$$

Taking now $f = e_e^h$ and $v = e^h$ in (8.18), and following the same arguments, we have

$$||e_e^h||_{L^2(\Omega_H)}^2 + (e_i^h, e_e^h) \leq C\,h\,|||e^h|||\,||e_e^h||_{L^2(\Omega_H)}. \tag{8.20}$$

Summing (8.19) and (8.20), we obtain

$$||e_i^h||_{L^2(\Omega_H)}^2 + ||e_e^h||_{L^2(\Omega_H)}^2 \leq C\,h\,|||e^h|||\,(||e_i^h||_{L^2(\Omega_H)} + ||e_e^h||_{L^2(\Omega_H)})$$

and hence the thesis.

8.2 Abstract Convergence Theory for Schwarz Methods

In this section we recall the main results of the abstract Schwarz theory for Domain Decomposition methods; for a more complete treatment, see the monographs [489, 523].

Let U be a finite dimensional Hilbert space with inner product $(\cdot, \cdot)$, $a(\cdot, \cdot)$ a symmetric elliptic bilinear form on $U \times U$ and $f \in U$. Consider the following problem:

Find $u \in U$ such that

$$a(u, v) = (f, v) \quad \forall v \in U. \tag{8.21}$$

Define the linear operator $\mathbf{A} : U \to U$ by

$$(\mathbf{A}u, v) = a(u, v) \quad \forall v \in U.$$

Then (8.21) is equivalent to the linear operator equation

$$\mathbf{A}u = f. \tag{8.22}$$

Let $U_m, m = 0, \ldots, N$, be a set of $N+1$ auxiliary spaces. In most application, these subspaces are related to a decomposition of the domain Ω_H into subdomains Ω_m. The subspace U_0 plays a special role: it corresponds to a coarse mesh and provides a global transportation of information. In addition, assume that there exists a set of interpolation operators

$$\mathbf{I}_m : U_m \to U.$$

We will refer to the case when $U_m \subset U$ as the nested case. In this case $\mathbf{I}_m$ are simply imbedding operators. Assume also that on each subspace U_m there is a symmetric positive definite bilinear form

$$a_m(\cdot, \cdot) : U_m \times U_m \to \mathbb{R}$$

and define the projections $\tilde{\mathbf{T}}_m : U \to U_m$ by

$$a_m(\tilde{\mathbf{T}}_m u, v) = a(u, \mathbf{I}_m v) \quad \forall v \in U_m.$$

This formalism allows us to consider inexact solvers for the subproblems. If we use exact solvers, then $a_m(\cdot, \cdot) = a(\cdot, \cdot)$. Now define the operators

$$\mathbf{T}_m = \mathbf{I}_m \tilde{\mathbf{T}}_m : U \to U.$$

We can now introduce the Additive Schwarz operator $\mathbf{T}_{AS}$ given by

$$\mathbf{T}_{AS} = \mathbf{B}_{AS} \mathbf{A} := \mathbf{T}_0 + \mathbf{T}_1 + \ldots + \mathbf{T}_N, \tag{8.23}$$

where $\mathbf{B}_{AS}$ is the Additive Schwarz preconditioner. The Additive Schwarz method replaces problem (8.22) by:
Find $u \in U$ such that

$$\mathbf{T}_{AS} u = \mathbf{B}_{AS} f, \tag{8.24}$$

which can be solved by a Krylov subspace method, with $\mathbf{B}_{AS}$ as preconditioner.

We will now describe the tools used in the convergence analysis of the Schwarz methods, beginning with the following lemma.

Lemma 8.3. *Let $\mathbf{T}_{AS}$ be the Additive Schwarz operator defined in (8.23). Then holds*

$$a(\mathbf{T}_{AS}^{-1} u, u) = \min_{u_m \in U_m, u = \sum_m \mathbf{I}_m u_m} \sum_m a_m(u_m, u_m). \tag{8.25}$$

Proof. We first construct a particular decomposition of u which satisfies (8.25) exactly, and then prove

$$a(\mathbf{T}_{AS}^{-1} u, u) \leq \sum_m a_m(u_m, u_m) \quad \forall u_m \in U_m, \sum_m \mathbf{I}_m u_m = u. \tag{8.26}$$

Let $u_m = \tilde{\mathbf{T}}_m \mathbf{T}_{AS}^{-1} u$, then $\sum_m \mathbf{I}_m u_m = (\sum_m \mathbf{T}_m) \mathbf{T}_{AS}^{-1} u$ and

$$
\sum_m a_m(u_m, u_m) = \sum_m a_m(\tilde{\mathbf{T}}_m \mathbf{T}_{AS}^{-1} u, \tilde{\mathbf{T}}_m \mathbf{T}_{AS}^{-1} u)
$$

$$
= \sum_m a(\mathbf{T}_{AS}^{-1} u, \mathbf{T}_m \mathbf{T}_{AS}^{-1} u)
$$

$$
= a(\mathbf{T}_{AS}^{-1} u, u).
$$

We now prove (8.26),

$$
a(\mathbf{T}_{AS}^{-1} u, u) = a(\mathbf{T}_{AS}^{-1} u, \sum_m \mathbf{I}_m u_m)
$$

$$
= \sum_m a(\mathbf{T}_{AS}^{-1} u, \mathbf{I}_m u_m)
$$

$$
= \sum_m a_m(\tilde{\mathbf{T}}_m \mathbf{T}_{AS}^{-1} u, u_m)
$$

$$
\leq \left[\sum_m a_m(\tilde{\mathbf{T}}_m \mathbf{T}_{AS}^{-1} u, \tilde{\mathbf{T}}_m \mathbf{T}_{AS}^{-1} u) \right]^{1/2} \left[\sum_m a_m(u_m, u_m) \right]^{1/2}
$$

$$
= \left[\sum_m a(\mathbf{T}_{AS}^{-1} u, \mathbf{T}_m \mathbf{T}_{AS}^{-1} u) \right]^{1/2} \left[\sum_m a_m(u_m, u_m) \right]^{1/2}
$$

$$
= a(\mathbf{T}_{AS}^{-1} u, u)^{1/2} \left[\sum_m a_m(u_m, u_m) \right]^{1/2}.
$$

Therefore it follows (8.26).

The abstract Schwarz convergence theory centers around three assumptions.

Assumption 8.1 (Stable decomposition). $\exists\, C_0 > 0$ *such that* $\forall u \in U$ *there exists a representation* $u = \sum_m \mathbf{I}_m u_m$, $u_m \in U_m$, *with*

$$
\sum_m a_m(u_m, u_m) \leq C_0^2 a(u, u).
$$

Assumption 8.2 (Strengthened Cauchy-Schwarz inequality). $\exists\, 0 \leq \mathscr{E}_{ml} \leq 1$ *such that*

$$
|a(\mathbf{I}_m u_m, \mathbf{I}_l u_l)| \leq \mathscr{E}_{ml} a(\mathbf{I}_m u_m, \mathbf{I}_m u_m)^{1/2} a(\mathbf{I}_l u_l, \mathbf{I}_l u_l)^{1/2}
$$

$$
\forall u_m \in U_m, u_l \in U_l\, m, l = 1, \ldots, N.
$$

Define $\rho(\mathscr{E})$ *to be the spectral radius of* $\mathscr{E} = \{\mathscr{E}_{ml}\}$.

Assumption 8.3 (Local stability). $\exists\, \omega > 0$ *such that*

$$a(\mathbf{I}_m u, \mathbf{I}_m u) \le \omega a_m(u, u) \quad \forall u \in U_m, \quad m = 0, \dots, N.$$

We recall for a linear operator $\mathbf{L}$ self-adjoint with respect to $a(\cdot, \cdot)$ the Rayleigh quotient characterization of the extreme eigenvalues,

$$\lambda_{min}(\mathbf{L}) = \min_{u \ne 0} \frac{a(\mathbf{L}u, u)}{a(u, u)}, \quad \lambda_{max}(\mathbf{L}) = \max_{u \ne 0} \frac{a(\mathbf{L}u, u)}{a(u, u)}.$$

We recall that for the condition number of $\mathbf{L}$ ($\kappa(\mathbf{L})$) in the norm induced by a, it holds

$$\kappa(\mathbf{L}) = \frac{\lambda_{max}(\mathbf{L})}{\lambda_{min}(\mathbf{L})}.$$

Note that by definition

$$\lambda_{min}(\mathbf{L})a(u, u) \le a(\mathbf{L}u, u) \le \lambda_{max}(\mathbf{L})a(u, u) \quad \forall u \in U.$$

Lemma 8.4. *The operators* $\mathbf{T}_m$, *and hence* $\mathbf{T}_{AS}$, *are self-adjoint with respect to* $a(\cdot, \cdot)$; *that is*

$$a(\mathbf{T}_m u, v) = a(u, \mathbf{T}_m v).$$

Proof. See [489]. $\qquad\qquad\qquad\qquad\qquad\qquad\qquad\qquad\qquad\qquad\qquad\square$

We can now provide a bound on the condition number for the abstract Additive Schwarz method.

Theorem 8.3. *If Assumptions 8.1–8.3 are satisfied, then the condition number of the abstract Additive Schwarz method is bounded by*

$$\kappa(\mathbf{T}_{AS}) \le \omega[1 + \rho(\mathscr{E})]C_0^2.$$

Proof. The bound on the smallest eigenvalue follows immediately from Lemma 8.3 and Assumption 8.1.

We now bound the largest eigenvalue. We first treat the subspaces U_m, for $m = 1, \dots, N$. The special subspace U_0 is treated separately. Observe that

$$a\Big(\sum_{m=1}^{N} \mathbf{T}_m v, \sum_{m=1}^{N} \mathbf{T}_m v\Big) = \sum_{m,l=1}^{N} a(\mathbf{T}_m v, \mathbf{T}_l v),$$

$$\le \sum_{m,l=1}^{N} \mathscr{E}_{ml} a(\mathbf{T}_m v, \mathbf{T}_m v)^{1/2} a(\mathbf{T}_l v, \mathbf{T}_l v)^{1/2},$$

$$\leq \rho(\mathcal{E}) \sum_{m=1}^{N} a(\mathbf{T}_m v, \mathbf{T}_m v),$$

$$\leq \omega \rho(\mathcal{E}) \sum_{m=1}^{N} a_m(\tilde{\mathbf{T}}_m v, \tilde{\mathbf{T}}_m v),$$

$$\leq \omega \rho(\mathcal{E}) \sum_{m=1}^{N} a(v, \mathbf{T}_m v),$$

$$\leq \omega \rho(\mathcal{E}) a(v, \sum_{m=1}^{N} \mathbf{T}_m v),$$

$$\leq \omega \rho(\mathcal{E}) a(v, v)^{1/2} a(\sum_{m=1}^{N} \mathbf{T}_m v, \sum_{l=1}^{N} \mathbf{T}_l v)^{1/2}.$$

It follows

$$a([\sum_{m=1}^{N} \mathbf{T}_m]^2 v, v) = a(\sum_{m=1}^{N} \mathbf{T}_m v, \sum_{l=1}^{N} \mathbf{T}_l v),$$

$$\leq \omega^2 \rho^2(\mathcal{E}) a(v, v).$$

Thus the largest eigenvalue of $(\sum_{m=1}^{N} \mathbf{T}_m)^2$ is bounded by $\omega^2 \rho^2(\mathcal{E})$. Hence the largest eigenvalue of $\sum_{m=1}^{N} \mathbf{T}_m$ is bounded by $\omega \rho(\mathcal{E})$ and

$$a(\sum_{m=1}^{N} \mathbf{T}_m v, v) \leq \omega \rho(\mathcal{E}) a(v, v). \tag{8.27}$$

To estimate the largest eigenvalue of $\mathbf{T}_0$ we use

$$a(\mathbf{T}_0 v, \mathbf{T}_0 v) \leq \omega a_0(\tilde{\mathbf{T}}_0 v, \tilde{\mathbf{T}}_0 v),$$

$$= \omega a(v, \mathbf{T}_0 v),$$

$$\leq \omega a(v, v)^{1/2} a(\mathbf{T}_0 v, \mathbf{T}_0 v)^{1/2}.$$

Thus

$$a(\mathbf{T}_0 v, \mathbf{T}_0 v) \leq \omega^2 a(v, v),$$

which implies

$$a(\mathbf{T}_0 v, v) \leq \omega a(v, v).$$

Combine this with (8.27) and the proof is completed.

8.3   Two-Level Additive Schwarz Methods for the Bidomain System

In this section, we construct and analyze a two-level overlapping Additive Schwarz method for problem (8.14). Let $\mathcal{T}_0 = \mathcal{T}_H$ be a coarse shape-regular triangulation of Ω_H consisting of N non-overlapping hexahedral subdomains Ω_m, $m = 1, \ldots, N$ of diameter H_m and let $H = \max_m H_m$. Let $\mathcal{T}_1 = \mathcal{T}_h$ be a fine shape-regular triangulation nested in $\mathcal{T}_0$, consisting of hexahedral elements τ_j, $j = 1, \ldots, N_e$ of diameter h_j and let $h = \max_j h_j$. An overlapping partition of Ω_H is then constructed using the standard technique of adding to each subdomain Ω_m all the fine elements $\tau_j \in \mathcal{T}_1$ within a distance δ from its boundary $\partial \Omega_m$. We denote by Ω'_m the overlapping subdomain obtained by such extensions of Ω_m. With each subdomain Ω'_m, we associate the following finite element spaces

$$V_m := \{v \in V^h : v(x) = 0 \ x \in \Omega_H \backslash \Omega'_m\} \quad \text{and} \quad U_m := V_m \times V_m.$$

Let V^H be the space of trilinear finite elements associated to the coarse triangulation $\mathcal{T}_0$ and define

$$\tilde{V}^H := \{v \in V^H : \int_{\Omega_H} v = 0\}, \quad U_0 = U^H := V^H \times \tilde{V}^H.$$

We remark that $U_0 \subset U^h$ instead U_m is not a subset of U^h, $m = 1, \ldots, N$. Define the interpolation operators $\mathbf{I}_m : U_m \to U^h$, $m = 1, \ldots, N$, as

$$\text{given } u = (u_i, u_e) \in U_m, \quad \mathbf{I}_m u = (\mathbf{I}_{m,i} u, \mathbf{I}_{m,e} u) := \left(u_i - \int_{\Omega_H} u_e, u_e - \int_{\Omega_H} u_e \right).$$

$\mathbf{I}_0 : U_0 \to U^h$ is simply the imbedding operator. Defining the projection operators

$$\tilde{\mathbf{T}}_m : U^h \to U_m$$

by

$$a_{bid}(\tilde{\mathbf{T}}_m u, v) = a_{bid}(u, \mathbf{I}_m v) \quad \forall v \in U_m,$$

and $\mathbf{T}_m = \mathbf{I}_m \tilde{\mathbf{T}}_m$, we can define the Additive Schwarz operator as

$$\mathbf{T}_{AS} = \mathbf{B}_{AS} \mathscr{A}_{bid} := \mathbf{T}_0 + \mathbf{T}_1 + \ldots + \mathbf{T}_N. \tag{8.28}$$

where $\mathbf{B}_{AS}$ is the two-level Additive Schwarz preconditioner. As in the scalar elliptic case, it is easy to see that the matrix form B_{AS} of $\mathbf{B}_{AS}$ is

$$B_{AS} = \sum_{m=0}^{N} B_m = \sum_{m=0}^{N} R_m^T A_m^{-1} R_m. \tag{8.29}$$

Here, for $m = 1, \ldots, N$, R_m are boolean restriction matrices and A_m the local stiffness matrices for the Bidomain problems restricted to the subdomain Ω'_m, while for $m = 0$ R_0 is the fine-to-coarse restriction matrix and A_0 is the coarse Bidomain stiffness matrix associated with the coarse space $U_0 = U^H$. More general projection-like operators $\tilde{\mathbf{T}}_m$ associated with approximate bilinear forms and inexact local solvers could be used as well, see [489, 523]. The use of the $\mathbf{B}_{AS}$ preconditioner (8.29) for the iterative solution of the Bidomain discrete system (8.15) can also be regarded as replacing (8.15) with the preconditioned system

$$\mathbf{T}_{AS} u = g,$$

where $g = \mathbf{B}_{AS} f$, which can be accelerated by a Krylov subspace method.

The following result extends the classical overlapping Schwarz analysis to the condition number of $\mathbf{T}_{AS}$.

Theorem 8.4. *The condition number of the 2-level additive Schwarz operator $\mathbf{T}_{AS}$ defined in (8.28) is bounded by*

$$\kappa(\mathbf{T}_{AS}) \leq C \left(1 + \frac{H}{\delta} \right),$$

with C independent of h, H, δ.

Proof. We apply the general abstract Schwarz theory of the previous section based on verifying the three assumptions stable decomposition, strengthened Cauchy-Schwarz inequality and local stability, that provide an upper and lower bound on $\kappa(\mathbf{T}_{AS})$, see also [523, p. 40].

(a) Since we use exact local solvers, the local stability assumption holds true with a unit constant.
(b) Using a standard coloring argument, see [523, Ch. 2], we obtain that the spectral radius $\rho(\mathscr{E})$ of the matrix in the strengthened Cauchy-Schwarz inequality is bounded from above by the number of colors, hence we have a constant upper bound.
(c) It only remains to prove a stable decomposition for our subspace decomposition.

We will prove that this assumption is satisfied with a constant $C_0^2 = C(1 + \frac{H}{\delta})$, with C independent of h, H and δ.

Let

- $Q^H : V^h \to V_0$ be the L^2-projection onto V_0,
- I^h the linear interpolation operator onto V^h and
- θ_m a partition of unity such that $\theta_m \in C_0^\infty(\Omega'_m)$, $0 \leq \theta_m \leq 1$, $\sum_{m=1}^N \theta_m = 1$,

$$|\nabla \theta_m|_{L^\infty}^2 \leq \frac{C}{\delta^2}, \tag{8.30}$$

and

$$\|\theta_m - \bar{\theta}_m\|_{L^\infty(K)}^2 \le C \left(\frac{h}{\delta}\right)^2, \tag{8.31}$$

where $\bar{\theta}_m$ is the average of θ_m on the element $K \in \mathcal{T}_h$.

Given $u \in U^h$, we define:

$$u_0 \in U_0 \text{ by } u_{0,i} := Q^H u_i \text{ and } u_{0,e} := Q^H u_e;$$

$$w \in U^h \text{ by } w_i := u_i - u_{0,i} \text{ and } w_e := u_e - u_{0,e};$$

$$u_m \in U_m \text{ by } u_{m,i} := I^h(\theta_m w_i) \text{ and } u_{m,e} := I^h(\theta_m w_e).$$

Thanks to the definition of $\mathbf{I}_m$ and because I^h is a linear operator, it follows that

$$u = \sum_{m=0}^N \mathbf{I}_m u_m.$$

We can bound each scalar component as in the standard proof for scalar elliptic problems (see e.g. [489, 523])

$$\sum_{m=0}^N |u_{m,i}|_{H^1(\Omega_H)}^2 \le C \left(1 + \frac{H}{\delta}\right) |u_i|_{H^1(\Omega_H)}^2 \text{ and } \sum_{m=0}^N |u_{m,e}|_{H^1(\Omega_H)}^2$$

$$\le C \left(1 + \frac{H}{\delta}\right) |u_e|_{H^1(\Omega_H)}^2. \tag{8.32}$$

Moreover, for all $m = 1, \dots, N$ and $K \in \mathcal{T}_h$, we have

$$\|u_{m,i} - u_{m,e}\|_{L^2(K)}^2 = \|I^h(\theta_m w_i) - I^h(\theta_m w_e)\|_{L^2(K)}^2 =$$

$$= \|I^h(\theta_m(w_i - w_e))\|_{L^2(K)}^2 \le \|w_i - w_e\|_{L^2(K)}^2.$$

Since a finite bounded number (independent of h, H and δ) of $u_{m,i}$ and $u_{m,e}$ are nonzero for any element K, summing over m we obtain

$$\sum_{m=1}^N \|u_{m,i} - u_{m,e}\|_{L^2(K)}^2 \le C \|w_i - w_e\|_{L^2(K)}^2,$$

and summing over all the elements K

$$\sum_{m=1}^N \|u_{m,i} - u_{m,e}\|_{L^2(\Omega_H)}^2 \le C \|w_i - w_e\|_{L^2(\Omega_H)}^2.$$

Since

$$\|w_i - w_e\|^2_{L^2(\Omega_H)} = \|u_i - u_e + Q^H(u_e - u_i)\|^2_{L^2(\Omega_H)} \leq 4\|u_i - u_e\|^2_{L^2(\Omega_H)},$$

$$\|u_{0,i} - u_{0,e}\|^2_{L^2(\Omega_H)} = \|Q^H(u_i - u_e)\|^2_{L^2(\Omega_H)} \leq \|u_i - u_e\|^2_{L^2(\Omega_H)},$$

we obtain

$$\sum_{m=0}^{N} \|u_{m,i} - u_{m,e}\|^2_{L^2(\Omega_H)} \leq C\|u_i - u_e\|^2_{L^2(\Omega_H)}.$$

Adding this and the bounds (8.32), we have

$$\sum_{m=0}^{N} (|u_{m,i}|^2_{H^1} + |u_{m,e}|^2_{H^1} + \|u_{m,i} - u_{m,e}\|^2_{L^2}) \leq C\left(1 + \frac{H}{\delta}\right)(|u_i|^2_{H^1} + |u_e|^2_{H^1} + \|u_i - u_e\|^2_{L^2}),$$

hence

$$\sum_{m=0}^{N} |||u_m|||^2 \leq C\left(1 + \frac{H}{\delta}\right)|||u|||^2.$$

From the continuity and coercivity of $a_{bid}(\cdot, \cdot)$, it follows the stable decomposition

$$\sum_{m=0}^{N} a_{bid}(u_m, u_m) \leq C\left(1 + \frac{H}{\delta}\right)a_{bid}(u, u).$$

8.4   Multilevel Additive Schwarz Methods for the Bidomain System

The method described in the previous section uses two levels with a coarse and a fine mesh. The smaller is H, the smaller are the local problems, but the algebraic linear system corresponding to the problem in U_0 becomes larger. We can then apply recursively this two-level technique to the coarse problem and obtain an additive multilevel method for the Bidomain system. We refer to the original works by Dryja and Widlund [151], Zhang [584] and later Dryja, Sarkis and Widlund [153] for an overview of these methods for scalar elliptic problems, including multilevel diagonal scaling variants and different choices of coarse spaces.

Let us consider $L \geq 2$ rather than just two mesh levels: on each level $k = 0, 1, \ldots, L - 1$, Ω_H is discretized with a shape-regular mesh $\mathcal{T}_k$ with elements of characteristic size h_k. $\mathcal{T}_k$ is a refinement of $\mathcal{T}_{k-1}$, with level $L - 1$ being the finest, hence $h_{L-1} = h$ and $h_0 = H$. On each level $k = 0, \ldots, L - 1$, we define a finite

element space V^{h_k}, with $V^{h_{L-1}} = V^h$ and $V^{h_0} = V^H$, and the spaces $\tilde{V}^{h_k}, U^{h_k}$ as in the previous section. We introduce $L-1$ sets of overlapping subdomains $\{\Omega'_{km}\}_{m=1}^{N_k}$ for $k = 1, \ldots, L-1$, such that on each level there is an overlapping decomposition $\Omega_H = \bigcup_{m=1}^{N_k} \Omega'_{km}$ and we denote with δ_k the overlap at level k. As in [584], we make the following assumption about the sets $\{\Omega'_{km}\}$.

Assumption 8.4. *On each level the decomposition $\Omega_H = \bigcup_{m=1}^{N_k} \Omega'_{km}$ satisfies:*

(a) *$\partial\Omega'_{km}$ aligns with the boundaries of level k elements, i.e. Ω'_{km} is the union of level k elements. The diameter$(\Omega'_{km}) = O(h_{k-1})$.*
(b) *The subdomains $\{\Omega'_{km}\}_{m=1}^{N_k}$ form a finite covering of Ω_H, with a covering constant N_c, i.e. we can color $\{\Omega'_{km}\}_{m=1}^{N_k}$ using at most N_c colors in such a way that subdomains of the same color are disjoint.*
(c) *There exists a partition of unity $\{\theta_{km}\}$, associated with $\{\Omega'_{km}\}_{m=1}^{N_k}$, which satisfies*

$$\sum_m \theta_{km} = 1, \quad \text{with} \ \ \theta_{km} \in H_0^1(\Omega_{km}) \cap C^0(\Omega_{km}), \ \ 0 \leq \theta_{km} \leq 1,$$

$$|\nabla\theta_{km}|_{L^\infty} \leq C/\delta_k \qquad \text{and} \qquad ||\theta_{km} - \bar{\theta}_{km}||_{L^\infty(K)} \leq C(h_k/\delta_k), \qquad (8.33)$$

where $K \in \mathscr{T}_k$ and $\bar{\theta}_{km}$ is the average of θ_{km} on K.

For $k = 1, \ldots, L-1$ and $m = 1, \ldots, N_k$, we define the spaces

$$V_{km} := V^{h_k} \cap H^1(\Omega'_{km}), \quad U_{km} = V_{km} \times V_{km}.$$

Define the interpolation operators $\mathbf{I}_{km}$ as in the two-level case. Defining the projections $\tilde{\mathbf{T}}_{km} : U^h \to U_{km}$ by

$$a_{bid}(\tilde{\mathbf{T}}_{km}u, v) = a_{bid}(u, \mathbf{I}_{km}v) \quad \forall v \in U_{km},$$

and $\mathbf{T}_{km} = \mathbf{I}_{km}\tilde{\mathbf{T}}_{km}$, we can introduce the Multilevel Additive Schwarz (MAS) operator

$$\mathbf{T}_{MAS} = \mathbf{B}_{MAS}\mathscr{A}_{bid} := \mathbf{T}_0 + \sum_{k=1}^{L-1} \sum_{m=1}^{N_k} \mathbf{T}_{km}. \qquad (8.34)$$

As mentioned before, approximate local solvers could be used as well. The matrix form B_{MAS} of the preconditioner $\mathbf{B}_{MAS}$ is given by

$$B_{MAS} = R_0^T A_0^{-1} R_0 + \sum_{k=1}^{L-1} \sum_{m=1}^{N_k} R_{km}^T A_{km}^{-1} R_{km},$$

where A_{km} is the local stiffness matrix of subdomain Ω'_{km} at level k and R_{km} is the restriction matrix from the finest level to subdomain Ω'_{km}, see [489] for more details. We can then prove our main result for the multilevel case.

Theorem 8.5. *The condition number of the multilevel additive Schwarz operator* $\mathbf{T}_{MAS}$ *defined in (8.34) is bounded by*

$$\kappa(\mathbf{T}_{MAS}) \le C \max_{k=1,\dots,L-1} \left(1 + \frac{h_{k-1}}{\delta_k}\right),$$

where C is a constant independent of the mesh sizes h_k and the number of levels L.

Proof. Upper bound. The proof of the optimal upper bound follows from the steps of the original proof by Zhang [584], from Lemma 3.2 to Lemma 3.5. These results can be applied to our case since they hold also for general conforming finite elements (Remark 3.2 in [584]) and uniform elliptic operators (Remark 3.3 in [584]).

Lower bound. In order to prove the left inequality, we need a *stable decomposition* of $u \in U^h$. For each level $k = 0,\dots,L-2$, we introduce the projections $Q^k : U^h \to U^{h_k}$ induced by the $a_{bid}(\cdot,\cdot)$ bilinear form, i.e.

$$a_{bid}(Q^k u, \varphi) = a_{bid}(u, \varphi) \quad \forall \varphi \in U^{h_k}.$$

We denote by Q_i^k and Q_e^k the two components of Q^k, i.e. $Q^k u = (Q_i^k u, Q_e^k u)$. It follows from Theorem 8.2 that, given $u \in U^h$

$$||u_i - Q_i^k u||_{L^2} + ||u_e - Q_e^k u||_{L^2} \le C\, h_k\, |||u - Q^k u|||. \tag{8.35}$$

Let $u_0 = Q^0 u$, $u_k = (Q^k - Q^{k-1})u$ for $k = 1,\dots,L-2$ and $u_{L-1} = (I - Q^{L-2})u$. $\forall k$ let $u_{k,i}$ and $u_{k,e}$ be the two components of u_k. It follows from (8.35) that

$$||u_{k,i}||_{L^2} + ||u_{k,e}||_{L^2} \le C\, h_{k-1}\, |||u_k|||. \tag{8.36}$$

$\forall u \in U^h$ we use the $a_{bid}(\cdot,\cdot)$-orthogonal decomposition

$$u = u_0 + u_1 + \dots + u_{L-1}.$$

Consider then for each $k = 1,\dots,L-1$ a partition of unity $\{\theta_{km}\}$ as in Assumption 8.4. Let I_{h_k} be the linear interpolation operator onto V^{h_k} and u_{km} the function in U_{km} such that

$$u_{km,i} = I_{h_k}(\theta_{km} u_{k,i}) \quad \text{and} \quad u_{km,e} = I_{h_k}(\theta_{km} u_{k,e}),$$

hence $u_k = \sum_{m=1}^{N_k-1} \mathbf{I}_{km} u_{km}$. We prove first that for each k

$$\sum_{m=1}^{N_k} |||u_{km}|||^2 \le C\, |||u_k|||^2.$$

Thanks to a well-known inverse inequality, it holds that

$$|u_{km,i}|^2_{H^1(K)} = |I_{h_k}(\theta_{km}u_{k,i})|^2_{H^1(K)} = |I_{h_k}(\bar\theta_{km}u_{k,i}) - I_{h_k}((\theta_{km} - \bar\theta_{km})u_{k,i})|^2_{H^1(K)} \le$$

$$\le 2|\bar\theta_{km}u_{k,i}|^2_{H^1(K)} + Ch_k^{-2}||I_{h_k}((\theta_{km} - \bar\theta_{km})u_{k,i})||^2_{L^2(K)}.$$

The last term above is zero for all elements K in the interior of an Ω_{km}, since $\theta_{km} = \bar\theta_{km} = 1$ on the non overlapping regions. Therefore, summing over all the elements, the last term only includes the elements in the overlapping regions $\Gamma_{\delta_k,m}$. Hence

$$\sum_{m=1}^{N_k}|u_{km,i}|^2_{H^1(\Omega_H)} \le C(|u_{k,i}|^2_{H^1(\Omega_H)} + \sum_{m=1}^{N_k}\sum_{K\in\Gamma_{\delta_k,m}} h_k^{-2}||I_{h_k}((\theta_{km} - \bar\theta_{km})u_{k,i})||^2_{L^2(K)})$$

$$\le C(|u_{k,i}|^2_{H^1(\Omega_H)} + \sum_{m=1}^{N_k}\delta_k^{-2}||u_{k,i}||^2_{L^2(\Gamma_{\delta_k,m})}). \tag{8.37}$$

We can bound the last terms using the following result by Dryja and Widlund [152]:

Lemma 8.5. *Let Ω_H be a shape regular region, in R^2 or R^3, of diameter H and let Γ_δ be a strip along its boundary of width $\delta > 0$. Then*

$$||u||^2_{L^2(\Gamma_\delta)} \le C\delta^2[(1 + \frac{H}{\delta})|u|^2_{H^1(\Omega_H)} + \frac{1}{H\delta}||u||^2_{L^2(\Omega_H)}].$$

Applying this lemma to (8.37), we obtain

$$\sum_{m=1}^{N_k}|u_{km,i}|^2_{H^1(\Omega_H)} \le C(|u_{k,i}|^2_{H^1(\Omega_H)} + (1 + \frac{h_{k-1}}{\delta_k})|u_{k,i}|^2_{H^1(\Omega_H)} + \frac{1}{h_{k-1}\delta_k}||u_{k,i}||^2_{L^2(\Omega_H)}),$$

and using (8.36)

$$\sum_{m=1}^{N_k}|u_{km,i}|^2_{H^1(\Omega_H)} \le C(1 + \frac{h_{k-1}}{\delta_k})|||u_k|||^2, \quad \sum_{m=1}^{N_k}|u_{km,e}|^2_{H^1(\Omega_H)} \le C(1 + \frac{h_{k-1}}{\delta_k})|||u_k|||^2.$$

Following the same arguments as in the two-level case, we get

$$\sum_{m=1}^{N_k}||u_{km,i} - u_{km,e}||^2_{L^2(\Omega_H)} \le C||u_{k,i} - u_{k,e}||^2_{L^2(\Omega_H)} \le C|||u_k|||^2,$$

$$\sum_{m=1}^{N_k}|||u_{km}|||^2 \le C(1 + \frac{h_{k-1}}{\delta_k})|||u_k|||^2.$$

Using the coercivity and the continuity of the Bidomain bilinear form $a_{bid}(\cdot, \cdot)$ and summing over the levels, we finally obtain the stable decomposition

$$a_{bid}(u_0, u_0) + \sum_{k=1}^{L-1} \sum_{m=1}^{N_k} a_{bid}(u_{km}, u_{km}) \leq C \max_{k=1,...,L-1} (1 + \frac{h_{k-1}}{\delta_k}) a_{bid}(u, u).$$

8.5   Numerical Results for Multilevel Schwarz Preconditioners

The numerical experiments were performed on the Linux Cluster IBM CLX/1024 of the Cineca Consortium (www.cineca.it), with 1024 processors (Intel Xeon Pentium IV 3 GHz, 512 KB cache), grouped into 512 biprocessor nodes. The total RAM is 1 TB and the peak performance is declared to 6.1 Tflops. We were allowed to use up to 240 processors in each run. Our FORTRAN code is based on the parallel library PETSc from the Argonne National Laboratory [24, 25]. We solve the Bidomain system on a domain Ω_H that is either a cartesian slab (see Fig. 8.2, left) or the image of a cartesian slab using ellipsoidal coordinates, yielding a portion of a truncated ellipsoid (see Fig. 8.1). This second choice can be used in simulations with idealized ventricular geometries, see e.g. [104, 125] These two choices allow us to also test the performance of our multilevel preconditioner in presence of severe domain deformations.

The values of the conductivity coefficients used in the numerical tests are reported in Table 8.1 and the capacitance per unit volume is set to $c_m = 1\,\mathrm{mF\,cm^{-3}}$. The values of the coefficients and parameters in the LR1 model are given in the original paper [308].

For both types of domains, we denote a level mesh by the triplet $\mathscr{T} = \mathscr{T}_i \cdot \mathscr{T}_j \cdot \mathscr{T}_k$ indicating the number of subdivisions in each coordinate direction. When we scale up the mesh, for brevity we define $c\mathscr{T} = c\mathscr{T}_i \cdot c\mathscr{T}_j \cdot c\mathscr{T}_k$. In all tests, the the finest mesh size is $h = 0.1\,\mathrm{mm}$, which has been shown to accurately resolve the steep excitation fronts in the Bidomain–LR1 model without numerical artifacts, see [104, 125].

We perform 5 time steps of 0.05 ms each with the semi-implicit Euler scheme described in Chap. 7 and at each time step we solve iteratively the discrete Bidomain system (8.12) by the Preconditioned Conjugate Gradient (PCG, see [445]) method with the L-level MAS preconditioner (8.34). The PCG initial guess is the discrete solution of the previous time step and the stopping criterion is a 10^{-4} residual reduction. The problem on the coarsest level is solved by PCG with 10^{-8} residual reduction as stopping criterion. In all runs, we report the PCG condition number, extreme eigenvalues, iteration counts and cpu timings relative to the 5th time step, in order to avoid special right-hand side configurations associated with the first few time steps.
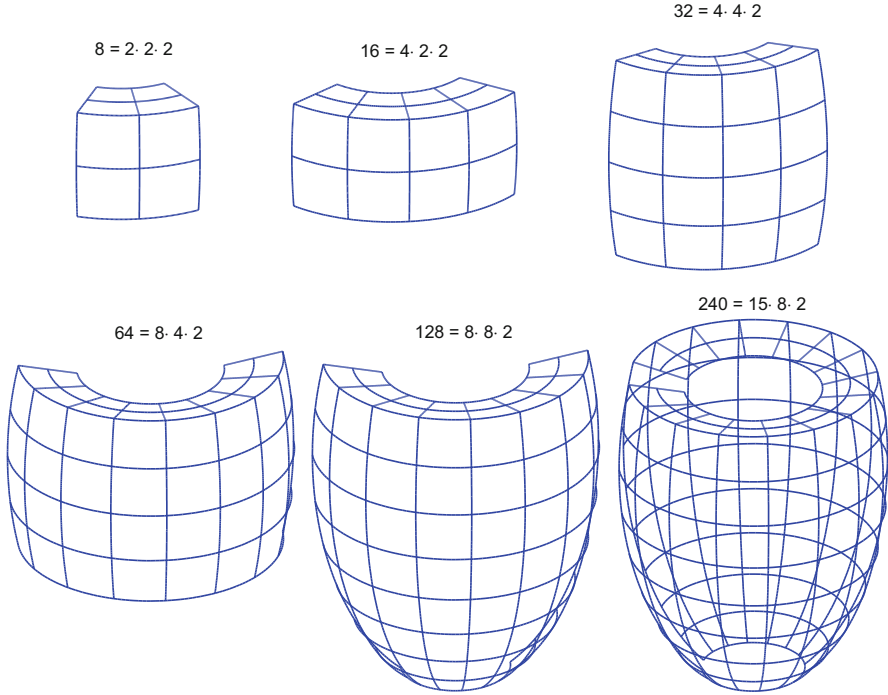
Fig. 8.1 Portions of ellipsoidal domain decomposed in 8, 16, 32, 64, 128, 240 subdomains for scaled speedup test

Table 8.1 Conductivity coefficients used in the numerical tests

Conductivity coefficients	
Normal tissue	
$\sigma_l^i = 3 \cdot 10^{-3}\,\Omega^{-1}\,\mathrm{cm}^{-1}$	$\sigma_l^e = 2 \cdot 10^{-3}\,\Omega^{-1}\,\mathrm{cm}^{-1}$
$\sigma_t^i = 3.1525 \cdot 10^{-4}\,\Omega^{-1}\,\mathrm{cm}^{-1}$	$\sigma_t^e = 1.3514 \cdot 10^{-3}\,\Omega^{-1}\,\mathrm{cm}^{-1}$
$\sigma_n^i = 3.1525 \cdot 10^{-5}\,\Omega^{-1}\,\mathrm{cm}^{-1}$	$\sigma_n^e = 6.757 \cdot 10^{-4}\,\Omega^{-1}\,\mathrm{cm}^{-1}$
Ischemic tissue	
$\sigma_l^i = 3 \cdot 10^{-4}\,\Omega^{-1}\,\mathrm{cm}^{-1}$	$\sigma_l^e = 1 \cdot 10^{-3}\,\Omega^{-1}\,\mathrm{cm}^{-1}$
$\sigma_t^i = 6.305 \cdot 10^{-6}\,\Omega^{-1}\,\mathrm{cm}^{-1}$	$\sigma_t^e = 3.3785 \cdot 10^{-4}\,\Omega^{-1}\,\mathrm{cm}^{-1}$
$\sigma_n^i = 6.305 \cdot 10^{-7}\,\Omega^{-1}\,\mathrm{cm}^{-1}$	$\sigma_n^e = 1.6892 \cdot 10^{-4}\,\Omega^{-1}\,\mathrm{cm}^{-1}$

8.5.1 Additive Preconditioner

Test MAS-3D-1. Increasing levels and increasing global size, cartesian slab. We first consider in Table 8.2 a cartesian slab, see Fig. 8.2, left panel, and increase the number of levels L in our MAS preconditioner from 3 to 6, while increasing the fine meshes as $\mathcal{T}_{i+1} = 2\mathcal{T}_i$, starting with a fixed coarse mesh $\mathcal{T}_0 = 8 \cdot 8 \cdot 2$. The number of processors and subdomains is fixed at 128, but the global problem size increases

Table 8.2 Test MAS-3D-1. Increasing number of levels L for cartesian slabs on Fig. 8.2 with increasing fine meshes $\mathscr{T}_{i+1} = 2\mathscr{T}_i$ starting with a fixed coarse mesh $\mathscr{T}_0 = 8 \cdot 8 \cdot 2$; fixed number of processors $= 128$

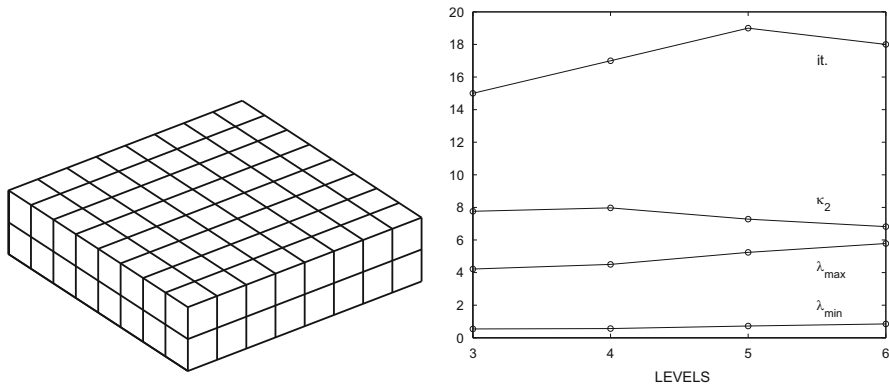| L	Meshes	d.o.f.	$\kappa = \lambda_{max}/\lambda_{min}$	it.	Time
3	$\mathscr{T}_0, 2\mathscr{T}_0, 4\mathscr{T}_0$	19 602	$7.76 = 4.217/0.543$	15	1.05
4	$\mathscr{T}_0, 2\mathscr{T}_0, 4\mathscr{T}_0, 8\mathscr{T}_0$	143 650	$7.97 = 4.501/0.564$	17	2.74
5	$\mathscr{T}_0, 2\mathscr{T}_0, 4\mathscr{T}_0, 8\mathscr{T}_0, 16\mathscr{T}_0$	1.1 M	$7.28 = 5.241/0.720$	19	5.20
6	$\mathscr{T}_0, 2\mathscr{T}_0, 4\mathscr{T}_0, 8\mathscr{T}_0, 16\mathscr{T}_0, 32\mathscr{T}_0$	8.6 M	$6.82 = 5.783/0.847$	18	11.29

Fig. 8.2 *Left*: Cartesian slab subdivided into $128 = 8 \cdot 8 \cdot 2$ subdomains. *Right*: plot of $\lambda_{min}, \lambda_{max}, \kappa, it$. Reported in Table 8.2

from 19 602 d.o.f. (for L $=$ 3, fine mesh $\mathscr{T}_2 = 4\mathscr{T}_0$) to 8.6 millions d.o.f. (for L $=$ 6, fine mesh $\mathscr{T}_5 = 32\mathscr{T}_0$). The MAS preconditioner has overlap size $\delta_k = h_k$ and ILU(0) local solvers for the subdomains of each level. The main results of this table are also plotted in Fig. 8.2, right panel. The condition numbers and iteration counts do not grow with increasing L (actually they even decrease for higher values of L), in spite of the strong growth of the problem size. Of course, the cpu timings reported in the last column grow because the global problem size grow, due to the growth of the subdomain size on the finest mesh from 4^3 ($L = 3$) to 32^3 ($L = 6$). These results confirm the optimality result of Theorem 8.5, with constant bounds independent of L and depending only on $\max\limits_{k=1,...,L-1} \left(1 + \dfrac{h_{k-1}}{\delta_k}\right)$.

Test MAS-3D-2. Scaled speedup on ellipsoidal domains. In Table 8.3, we then consider a scaled speedup test for our MAS operator with 2, 3, 4 levels. Again, we fix the overlap size $\delta_k = h_k$ and ILU(0) local solvers on the subdomains of each level. The local size of each subdomain on the finest mesh is kept fixed at the value 48^3 and each subdomain is assigned to one processor. The number of subdomains (hence number of processors) is increased from $8 = 2 \cdot 2 \cdot 2$ to $240 = 15 \cdot 8 \cdot 2$ (first and second columns), forming increasing domains Ω_H that are portions of a truncated ellipsoidal domain as shown in Fig. 8.1. These subdomains

Table 8.3 Test MAS-3D-2. Condition numbers, extreme eigenvalues, iteration counts, cpu timings for 2, 3, 4 level MAS, $\delta_k = h_k$, ILU(0) local solvers: scaled speedup with fixed subdomain size $48 \cdot 48 \cdot 48$ on the ellipsoidal domains of Fig. 8.1

2 levels: $\mathcal{T}_0$, $\mathcal{T}_1 = 48\mathcal{T}_0$

Procs.	$\mathcal{T}_0$	$\mathcal{T}_1 = 48\mathcal{T}_0$	d.o.f. (M)	$\kappa = \lambda_{max}/\lambda_{min}$	it.	Time
8	$2 \cdot 2 \cdot 2$	$96 \cdot 96 \cdot 96$	1.8	$183.50 = 2.268/0.012$	45	53.1
16	$4 \cdot 2 \cdot 2$	$192 \cdot 96 \cdot 96$	3.6	$172.44 = 2.265/0.013$	45	65.0
32	$4 \cdot 4 \cdot 2$	$192 \cdot 192 \cdot 96$	7.2	$228.63 = 2.455/0.011$	50	65.8
64	$8 \cdot 4 \cdot 2$	$384 \cdot 192 \cdot 96$	14.4	$226.95 = 2.479/0.011$	50	74.7
128	$8 \cdot 8 \cdot 2$	$384 \cdot 384 \cdot 96$	28.7	$150.31 = 2.413/0.016$	43	66.2
240	$15 \cdot 8 \cdot 2$	$720 \cdot 384 \cdot 96$	53.8	$149.98 = 2.415/0.016$	43	68.1

3 levels: $\mathcal{T}_0$, $\mathcal{T}_1 = 4\mathcal{T}_0$, $\mathcal{T}_3 = 48\mathcal{T}_0$

Procs.	$\mathcal{T}_0$	$\mathcal{T}_2 = 48\mathcal{T}_0$	d.o.f. (M)	$\kappa = \lambda_{max}/\lambda_{min}$	it.	Time
8	$2 \cdot 2 \cdot 2$	$96 \cdot 96 \cdot 96$	1.8	$21.70 = 2.903/0.134$	23	23.9
16	$4 \cdot 2 \cdot 2$	$192 \cdot 96 \cdot 96$	3.6	$23.33 = 3.092/0.132$	24	30.4
32	$4 \cdot 4 \cdot 2$	$192 \cdot 192 \cdot 96$	7.2	$25.07 = 3.263/0.130$	24	34.2
64	$8 \cdot 4 \cdot 2$	$384 \cdot 192 \cdot 96$	14.4	$25.56 = 3.269/0.128$	25	32.0
128	$8 \cdot 8 \cdot 2$	$384 \cdot 384 \cdot 96$	28.7	$30.70 = 3.347/0.109$	26	40.2
240	$15 \cdot 8 \cdot 2$	$720 \cdot 384 \cdot 96$	53.8	$30.99 = 3.381/0.109$	26	40.8

4 levels: $\mathcal{T}_0$, $\mathcal{T}_1 = 4\mathcal{T}_0$, $\mathcal{T}_2 = 16\mathcal{T}_0$, $\mathcal{T}_3 = 48\mathcal{T}_0$

Procs.	$\mathcal{T}_0$	$\mathcal{T}_3 = 48\mathcal{T}_0$	d.o.f. (M)	$\kappa = \lambda_{max}/\lambda_{min}$	it.	Time
8	$2 \cdot 2 \cdot 2$	$96 \cdot 96 \cdot 96$	1.8	$10.81 = 3.815/0.348$	20	27.2
16	$4 \cdot 2 \cdot 2$	$192 \cdot 96 \cdot 96$	3.6	$11.65 = 4.141/0.355$	20	29.6
32	$4 \cdot 4 \cdot 2$	$192 \cdot 192 \cdot 96$	7.2	$10.18 = 4.137/0.406$	19	31.0
64	$8 \cdot 4 \cdot 2$	$384 \cdot 192 \cdot 96$	14.4	$9.95 = 4.117/0.414$	19	33.1
128	$8 \cdot 8 \cdot 2$	$384 \cdot 384 \cdot 96$	28.7	$9.96 = 4.089/0.411$	19	34.8
240	$15 \cdot 8 \cdot 2$	$720 \cdot 384 \cdot 96$	53.8	$9.95 = 4.083/0.410$	19	36.0

are the elements of the coarse mesh $\mathcal{T}_0$. The finest mesh is then $48\mathcal{T}_0$, since the local mesh size is kept fixed at 48^3. The intermediate level meshes in case of 3 and 4 levels are $\mathcal{T}_1 = 4\mathcal{T}_0$ and $\mathcal{T}_2 = 16\mathcal{T}_0$. With these data, the global size of the discrete Bidomain system increases then from 1.8 million d.o.f. for the smallest domain with 8 subdomains to 53.8 million d.o.f. for the largest domain with 240 subdomains. In each of these cases, the last columns of Table 8.3 report the condition number κ, extreme eigenvalues λ_{max}, λ_{min}, iteration counts it. and cpu timings of the PCG solver with MAS preconditioner. The same data are plotted in Fig. 8.3 vs. the processor count. The results clearly show the scalability of the MAS operator, since all the reported quantities seem to approach constant values as the number of subdomains (hence processors) increases. As expected, these asymptotic values improve with the number of levels, since for increasing L the MAS preconditioner becomes more powerful.

Table 8.4 reports the results of a scaled speedup test run recently on the BlueGene Q cluster of the CINECA consortium (www.cineca.it). The preconditioner considered is the MAS(4), the domains are portions of a truncated ellipsoid, the number
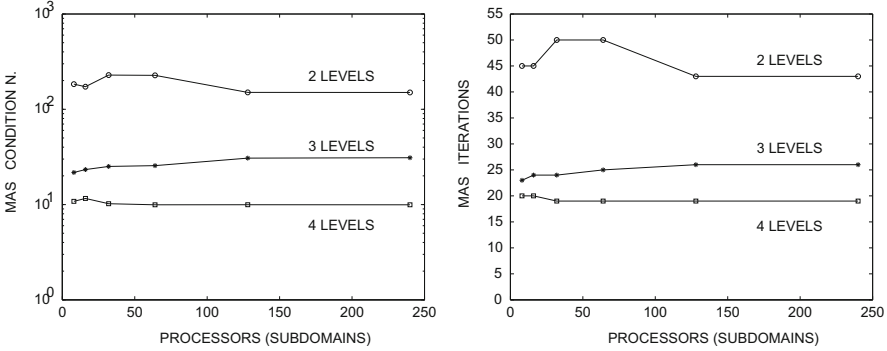
Fig. 8.3 Test MAS-3D-2. Scalability of 2, 3, 4 level MAS: condition numbers and iteration counts reported in Table 8.3

Table 8.4 Test MAS-3D-2. Weak scaling for MAS(4) solvers on ellipsoidal structured meshes, run on the BlueGene Cluster

Procs	d.o.f.	MAS(4)		
		$\kappa = \lambda_M / \lambda_m$	it.	Time
64	4 319 890	41.85 = 8.70/2.08e-1	43	5.65
128	8 553 474	33.41 = 6.79/2.03e-1	39	5.57
256	17 040 642	36.37 = 6.81/1.87e-1	40	5.70
512	33 949 186	27.37 = 5.16/1.88e-1	36	5.48
1 024	67 766 274	29.53 = 5.16/1.75e-1	36	5.69
2 048	135 268 866	27.56 = 5.08/1.84e-1	34	8.50
4 096	270 274 050	28.91 = 5.09/1.76e-1	34	16.39
8 192	540 021 250	25.03 = 5.10/2.04e-1	32	16.51
16 384	1 079 515 650	26.55 = 5.11/1.92e-1	32	17.39

Average condition number (κ), extreme eigenvalues (λ_M, λ_m), PCG iteration count (*it*) and CPU time in seconds (*time*) per time step

Table 8.5 Test MAS-3D-3. Increasing number of levels L for fixed coarse mesh $\mathcal{T}_0 = 8 \cdot 8 \cdot 2$ (486 d.o.f.) and fine mesh $\mathcal{T}_{L-1} = 48\mathcal{T}_0 = 384 \cdot 384 \cdot 96$ (28.7M d.o.f.), intermediate meshes $\mathcal{T}_{i+1} = 2\mathcal{T}_i$; ellipsoidal domain of Fig. 8.1, fixed number of processors = 128

L	Meshes	$\kappa = \lambda_{max} / \lambda_{min}$	it.	Time
2	$\mathcal{T}_0, 48\mathcal{T}_0$	150.31 = 2.413/0.016	43	66.2
3	$\mathcal{T}_0, 2\mathcal{T}_0, 48\mathcal{T}_0$	86.55 = 3.375/0.039	38	158.5
4	$\mathcal{T}_0, 2\mathcal{T}_0, 4\mathcal{T}_0, 48\mathcal{T}_0$	43.31 = 4.374/0.101	33	124.9
5	$\mathcal{T}_0, 2\mathcal{T}_0, 4\mathcal{T}_0, 8\mathcal{T}_0, 48\mathcal{T}_0$	17.82 = 5.118/0.287	24	139.1
6	$\mathcal{T}_0, 2\mathcal{T}_0, 4\mathcal{T}_0, 8\mathcal{T}_0, 16\mathcal{T}_0, 48\mathcal{T}_0$	10.94 = 5.892/0.539	20	32.7

of processors varies from 64 to 16 384, while the number of d.o.f. increases from 4 million to about 1 billion.

Test MAS-3D-3. Increasing levels and fixed global size, ellipsoidal domain. In Table 8.5, we fix the coarse mesh $\mathcal{T}_0 = 8 \cdot 8 \cdot 2$ (486 d.o.f.) and fine mesh $\mathcal{T}_{L-1} = 48\mathcal{T}_0 = 384 \cdot 384 \cdot 96$ (28.7M d.o.f.), hence the number of subdomains

and processors are fixed to 128 (the number of coarse elements). We then vary the number of levels L from 2 to 6, with intermediate meshes defined by $\mathcal{T}_{i+1} = 2\mathcal{T}_i$. The ellipsoidal domain is the one of Fig. 8.1 decomposed into 128 subdomains. Both the condition numbers and iteration counts improve considerably when the number of levels increases, because the improvement of the minimum eigenvalues more than compensate a slight increase of the maximum eigenvalue.

Test MAS-3D-4. Scaled speedup with variable overlap and ILU/LU local solvers, cartesian slab. We now focus on the effect of two variables that we have kept fixed so far: the overlap size δ_k and the use of inexact/exact local solvers. Therefore, we repeat a scaled speedup test as in Table 8.1 but on slab domains and with smaller subdomain size 16^3 in order to be able to run our MAS preconditioner with exact LU local solvers. The finest mesh is then always $\mathcal{T}_{L-1} = 16\mathcal{T}_0$, while the intermediate meshes for $L = 3, 4$ are $2\mathcal{T}_0$ and $4\mathcal{T}_0$. Table 8.6 reports the

Table 8.6 Test MAS-3D-4. Iteration counts and condition numbers of 2, 3, 4 level MAS: scaled speedup with fixed subdomain size $16 \cdot 16 \cdot 16$ and varying overlap size $\delta_k = 1, 2, 4 \cdot h_k$, with inexact ILU(0) local solvers (in brackets exact LU local solvers)

| 2 levels: $\mathcal{T}_0$, $\mathcal{T}_1 = 16\mathcal{T}_0$							
		$\delta_k = h_k$		$\delta_k = 2 \cdot h_k$		$\delta_k = 4 \cdot h_k$	
Procs.	$\mathcal{T}_0$	it.	κ	it.	κ	it.	κ
8	$2 \cdot 2 \cdot 2$	38 (23)	104.5 (36.1)	39 (17)	85.3 (14.6)	34 (14)	58.7 (10.2)
18	$3 \cdot 3 \cdot 2$	47 (24)	143.4 (51.5)	49 (18)	129.1 (19.6)	37 (16)	72.0 (12.3)
32	$4 \cdot 4 \cdot 2$	45 (21)	123.3 (33.1)	41 (17)	96.9 (17.2)	39 (17)	80.3 (12.6)
50	$5 \cdot 5 \cdot 2$	45 (21)	148.1 (30.1)	41 (17)	96.8 (16.7)	43 (18)	95.9 (13.9)
72	$6 \cdot 6 \cdot 2$	41 (20)	117.2 (27.5)	42 (18)	97.9 (19.1)	43 (18)	97.3 (13.9)
128	$8 \cdot 8 \cdot 2$	39 (20)	92.0 (24.5)	42 (18)	100.8 (17.5)	44 (17)	95.4 (11.5)
3 levels: $\mathcal{T}_0$, $\mathcal{T}_1 = 2\mathcal{T}_0$, $\mathcal{T}_2 = 16\mathcal{T}_0$							
		$\delta_k = h_k$		$\delta_k = 2 \cdot h_k$		$\delta_k = 4 \cdot h_k$	
Procs.	$\mathcal{T}_0$	it.	κ	it.	κ	it.	κ
8	$2 \cdot 2 \cdot 2$	18 (14)	11.6 (6.5)	18 (12)	10.5 (4.6)	17 (12)	9.7 (3.7)
18	$3 \cdot 3 \cdot 2$	19 (14)	13.3 (6.6)	18 (13)	12.0 (4.8)	18 (13)	11.6 (5.1)
32	$4 \cdot 4 \cdot 2$	19 (14)	13.6 (6.4)	19 (13)	12.9 (5.0)	19 (13)	12.2 (4.4)
50	$5 \cdot 5 \cdot 2$	19 (14)	13.6 (6.1)	19 (14)	12.9 (4.9)	19 (13)	12.3 (4.9)
72	$6 \cdot 6 \cdot 2$	19 (14)	13.4 (6.1)	19 (14)	12.8 (4.8)	19 (13)	12.1 (5.2)
128	$8 \cdot 8 \cdot 2$	19 (14)	13.5 (6.0)	19 (13)	12.8 (4.7)	19 (14)	12.0 (4.6)
4 levels: $\mathcal{T}_0$, $\mathcal{T}_1 = 2\mathcal{T}_0$, $\mathcal{T}_2 = 4\mathcal{T}_0$, $\mathcal{T}_3 = 16\mathcal{T}_0$							
		$\delta_k = h_k$		$\delta_k = 2 \cdot h_k$		$\delta_k = 4 \cdot h_k$	
Procs.	$\mathcal{T}_0$	it.	κ	it.	κ	it.	κ
8	$2 \cdot 2 \cdot 2$	18 (16)	8.9 (8.1)	18 (16)	8.9 (7.3)	18 (16)	8.3 (6.7)
18	$3 \cdot 3 \cdot 2$	20 (18)	14.6 (12.3)	20 (18)	14.4 (10.9)	19 (17)	13.9 (8.2)
32	$4 \cdot 4 \cdot 2$	17 (17)	7.5 (7.9)	17 (16)	7.2 (7.8)	17 (16)	7.0 (7.8)
50	$5 \cdot 5 \cdot 2$	17 (17)	7.4 (7.5)	17 (16)	7.1 (7.3)	17 (16)	6.8 (7.2)
72	$6 \cdot 6 \cdot 2$	17 (17)	7.3 (7.1)	16 (16)	7.0 (6.9)	16 (16)	6.7 (6.8)
128	$8 \cdot 8 \cdot 2$	16 (16)	7.3 (6.6)	16 (16)	7.0 (6.3)	16 (16)	6.7 (6.1)
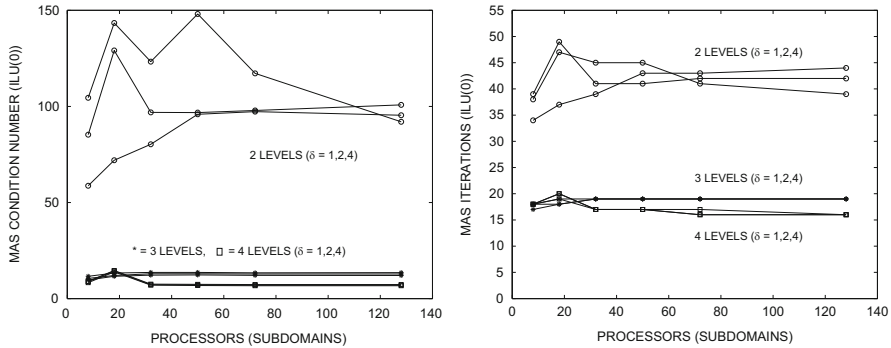
Fig. 8.4 Test MAS-3D-4. Scalability of 2, 3, 4 level MAS with ILU(0) local solvers and variable overlap $\delta_k = 1, 2, 4 \cdot h_k$: condition numbers (*left*) and iteration counts (*right*) reported in Table 8.6
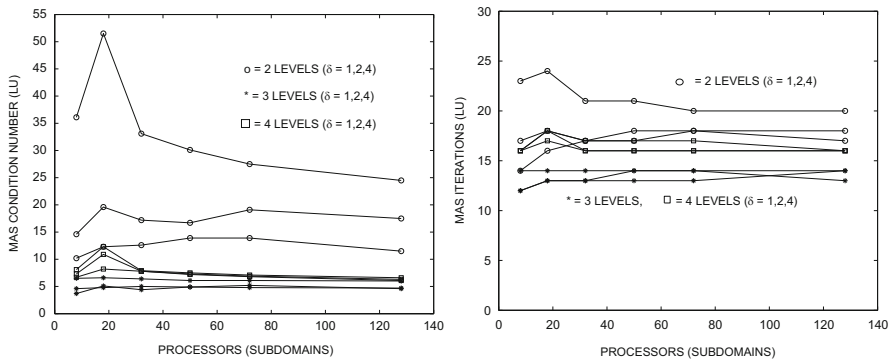

Fig. 8.5 Test MAS-3D-4. Scalability of 2, 3, 4 level MAS with LU local solvers and variable overlap $\delta_k = 1, 2, 4 \cdot h_k$: condition numbers (*left*) and iteration counts (*right*) reported in Table 8.6

iteration counts and condition numbers of 2, 3, 4 level MAS with inexact ILU(0) local solvers; in brackets are the same quantities for MAS with exact LU local solvers. We consider three cases of increasing overlap size $\delta_k = 1, 2, 4 \cdot h_k$. The ILU(0) results are then plotted in Fig. 8.4, and the LU results in Fig. 8.5, where the 2, 3, 4 level data are denoted by $\circ, \star, \ldots$, respectively. The scalability of the MAS preconditioner is evident in all cases; as expected, the LU results are better than the ILU(0) results and increasing the overlap size improves the conditioning of the preconditioned operator but only by a marginal amount when $L > 2$ (in fact the iteration counts are basically independent of δ for $L > 2$), except in the 2-level ILU(0) case, where the results are a bit erratic. Increasing the levels improve the results in the ILU(0) case, but in the LU case the 3-level MAS seems to be slightly better conditioned than the 4-level MAS for this choice of meshes and parameters.

8.5.2   Multiplicative and Hybrid Preconditioners

In this section, we study numerically the behavior of a hybrid variant $\mathbf{B}_{MHS}$ of the multilevel additive Schwarz preconditioner $\mathbf{B}_{MAS}$. This variant is multiplicative among the levels and additive in the levels (see [489]). We recall the same notations used in Sect. 8.4. Let $\mathcal{T}_k$, $k = 0, \ldots, L - 1$ be a family of nested triangulations of Ω_H, coarsening from $L - 1$ to 0, and A_k the matrix obtained discretizing (8.2) on $\mathcal{T}_k$: so $A_{L-1} = \mathscr{A}_{bid}$. R_k are the restriction operators from $\mathcal{T}_{k+1}$ to $\mathcal{T}_k$. We decompose each grid $\mathcal{T}_k$ into N_k overlapping subdomains Ω'_{km} for $m = 1, \ldots, N_k$, such that the overlap δ_k at level $k = 1, \ldots, L - 1$ is equal to the mesh size h_k of the grid $\mathcal{T}_k$. Let R_{km} be the restriction operator from $\mathcal{T}_k$ to Ω'_{km} and A_{km} the local stiffness matrix of subdomain Ω'_{km}. The action of this Multilevel Hybrid Schwarz (MHS) preconditioner on a given residual $\mathbf{r} = \mathbf{r}_{L-1}$ is given by:

$$\mathbf{u}_{L-1} \leftarrow \sum_{m=1}^{N_{L-1}} R_{L-1m}^T A_{L-1m}^{-1} R_{L-1m} \mathbf{r}_{L-1}$$

$$\mathbf{r}_{L-2} \leftarrow R_{L-2}(\mathbf{r}_{L-1} - A_{L-1}\mathbf{u}_{L-1})$$

$$\mathbf{u}_{L-2} \leftarrow \sum_{m=1}^{N_{L-2}} R_{L-2m}^T A_{L-2m}^{-1} R_{L-2m} \mathbf{r}_{L-2}$$

$$\cdots$$

$$\mathbf{u}_0 \leftarrow A_0^{-1} \mathbf{r}_0$$

$$\mathbf{u}_1 \leftarrow \mathbf{u}_1 + R_0^T \mathbf{u}_0$$

$$\mathbf{u}_1 \leftarrow \mathbf{u}_1 + \sum_{m=1}^{N_1} R_{1m}^T A_{1m}^{-1} R_{1m}(\mathbf{r}_1 - A_1\mathbf{u}_1)$$

$$\cdots$$

$$\mathbf{u}_{L-1} \leftarrow \mathbf{u}_{L-1} + R_{L-2}^T \mathbf{u}_{L-2}$$

$$\mathbf{u}_{L-1} \leftarrow \mathbf{u}_{L-1} + \sum_{m=1}^{N_{L-1}} R_{L-1m}^T A_{L-1m}^{-1} R_{L-1m}(\mathbf{r}^{L-1} - A_{L-1}\mathbf{u}_{L-1})$$

$$\mathbf{u} \leftarrow \mathbf{u}_{L-1}$$

In the following, we will denote the MHS preconditioner with L levels MHS(L).
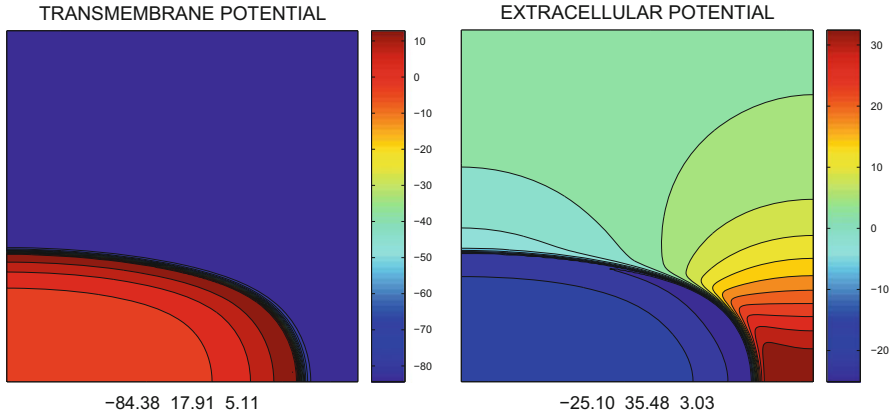
Fig. 8.6 Test MHS-2D-1. Patterns of level lines of the transmembrane and extracellular potentials during the excitation phase (t = 25 ms after the stimulus). Reported below each panel are the minimum, maximum and step in mV of the displayed map

8.5.2.1   MHS: Two-Dimensional Domains

Test MHS-2D-1. Fixed global size, increasing number of subdomains, square domain. We simulate the initial depolarization of a square section of cardiac tissue, having dimensions of 2.56×2.56 cm^2, applying a stimulus of 200 mA/cm^3 for 1 ms on a small area of 2×2 elements at a vertex of the domain, see Fig. 8.6. The two-dimensional conductivity tensors are given by

$$D_{i,e} = \begin{bmatrix} \sigma_l^{i,e} & 0 \\ 0 & \sigma_n^{i,e} \end{bmatrix}.$$

The global mesh is fixed to be of 256×256 elements ($132\,098$ unknowns), 512×512 elements ($526\,338$ unknowns) and $1\,024 \times 1\,024$ elements ($2\,101\,250$ unknowns). The cases of 4, 16, 64 subdomains (processors) and 2–7 levels are considered. The model is run for 200 time steps of 0.05 ms, i.e. for a time interval of 10 ms on the CLX Linux cluster. In Tables 8.7 and 8.8, we report the average number of PCG iterations per time step, the average condition number and the average time needed to solve the linear system. The results show the scalability of the MHS preconditioner, since both the condition numbers and the iteration counts remain almost constant when the number of subdomains and levels increase.

Test MHS-2D-2. Increasing levels and increasing global size, square domain. The aim of this test is to study the behavior of the preconditioner increasing the number of levels from 2 to 9. The size of the fine mesh varies form 4×4 elements (50 unknowns) with 2 levels to 512×512 elements ($526\,338$ unknowns) with 9 levels, hence the dimensions of the square domain increase from 0.04×0.04 to 5.12×5.12 cm^2. The number of subdomains (and processors) is kept fixed to 4. As

Table 8.7 Test MHS-2D-1. Condition numbers, iteration counts, cpu timings for 2, 3, 4 level MHS. Fixed global size, increasing the number of subdomains, square domain

Procs.	Mesh	2 levels			3 levels			4 levels		
		κ	it.	Time	κ	it.	Time	κ	it.	Time
4	256^2	1.05	4	2.93	1.05	4	1.17	1.05	4	0.98
16	256^2	1.04	4	0.84	1.05	4	0.43	1.05	4	0.35
64	256^2	1.04	4	0.68	1.05	4	0.43	1.05	4	0.35
4	512^2	1.04	2	15.04	1.05	3	3.60	1.05	3	3.14
16	512^2	1.04	2	4.02	1.05	3	1.25	1.05	3	1.15
64	512^2	1.04	2	1.44	1.05	3	0.61	1.05	3	0.50
4	$1\,024^2$	1.06	2	81.89	1.07	2	21.96	1.07	2	14.20
16	$1\,024^2$	1.06	2	20.71	1.07	2	6.08	1.07	2	3.91
64	$1\,024^2$	1.06	2	6.91	1.07	2	1.98	1.07	2	1.29

Table 8.8 Test MHS-2D-1. Same format as in Table 8.7 for 5, 6, 7 level MHS

Procs.	Mesh	5 levels			6 levels			7 levels		
		κ	it.	Time	κ	it.	Time	κ	it.	Time
4	256^2	1.05	4	0.98	1.06	4	0.98	1.06	4	0.98
16	256^2	1.05	4	0.38	1.05	4	0.33	1.05	4	0.36
64	256^2	1.05	4	0.37	1.12	5	0.36	–	–	–
4	512^2	1.05	3	3.10	1.05	3	3.08	1.05	3	3.09
16	512^2	1.05	3	0.84	1.05	3	0.95	1.05	3	0.95
64	512^2	1.05	3	0.47	1.05	3	0.43	1.05	3	0.57
4	$1\,024^2$	1.07	3	14.55	1.07	3	13.20	1.07	3	13.26
16	$1\,024^2$	1.07	3	3.44	1.07	3	3.23	1.07	3	3.28
64	$1\,024^2$	1.07	3	1.19	1.07	3	1.30	1.07	3	1.28

in the previous tests, we run the model for 10 ms after the stimulus. Table 8.9 reports the average minimum and maximum eigenvalues, the average condition number, the average number of PCG iterations and the average solving time per time step. The condition numbers and iteration counts do not grow with increasing L, in spite of the strong growth of the problem size. Of course, the cpu timings reported in the last column grow because the global problem size grow, due to the growth of the subdomain size on the finest mesh.

Test MHS-2D-3. Scaled speedup on square domains. In this test, we vary the number of subdomains from 4 to 64, keeping fixed the local mesh in each subdomain to 64×64 elements (8 450 unknowns), hence varying the global number of degrees of freedom (d.o.f.) from 33 800 in the smallest case with 4 subdomains to 540 800 in the largest with 64 subdomains. The number of levels varies from 2 to 7. As in test MHS-2D-1, we simulate the initial depolarization of a myocardial section, running the model for 200 time steps on the CLX cluster of CINECA. Tables 8.10 and 8.11 report the average number of PCG iterations and the average solving time per time

Table 8.9 Test MHS-2D-2. Increasing number of levels L for square domains with increasing fine meshes $\mathcal{T}_{i+1} = 2\mathcal{T}_i$ starting with a fixed coarse mesh $\mathcal{T}_0 = 2 \cdot 2$; fixed number of processors = 4

L	Meshes	d.o.f.	$\kappa = \lambda_{max}/\lambda_{min}$	it.	Time
2	$\mathcal{T}_0, 2\mathcal{T}_0$	50	1.16 = 1.05/0.90	4	0.01
3	$\mathcal{T}_0, 2\mathcal{T}_0, 4\mathcal{T}_0$	162	1.05 = 1.01/0.97	3	0.01
4	$\mathcal{T}_0, 2\mathcal{T}_0, 4\mathcal{T}_0, 8\mathcal{T}_0$	578	1.04 = 1.00/0.97	3	0.02
5	$\mathcal{T}_0, 2\mathcal{T}_0, 4\mathcal{T}_0, 8\mathcal{T}_0, 16\mathcal{T}_0$	2 178	1.04 = 1.00/0.97	3	0.03
6	$\mathcal{T}_0, 2\mathcal{T}_0, 4\mathcal{T}_0, 8\mathcal{T}_0, 16\mathcal{T}_0, 32\mathcal{T}_0$	8 450	1.05 = 1.01/0.96	4	0.08
7	$\mathcal{T}_0, 2\mathcal{T}_0, 4\mathcal{T}_0, \ldots, 32\mathcal{T}_0, 64\mathcal{T}_0$	33 282	1.05 = 1.01/0.96	4	0.25
8	$\mathcal{T}_0, 2\mathcal{T}_0, 4\mathcal{T}_0, \ldots, 64\mathcal{T}_0, 128\mathcal{T}_0$	132 098	1.05 = 1.01/0.96	4	0.99
9	$\mathcal{T}_0, 2\mathcal{T}_0, 4\mathcal{T}_0, \ldots, 128\mathcal{T}_0, 256\mathcal{T}_0$	526 338	1.01 = 1.00/0.99	3	3.12

Table 8.10 Test MHS-2D-3. Condition numbers, iteration counts, cpu timings for 2, 3, 4 level MHS. Scaled speedup with fixed subdomain size $64 \cdot 64$ on square domains

Procs.	d.o.f.	2 levels			3 levels			4 levels		
		κ	it.	Time	κ	it.	Time	κ	it.	Time
4	33 800	1.04	4	0.46	1.05	4	0.25	1.05	4	0.25
9	76 050	1.04	4	0.63	1.04	4	0.33	1.05	4	0.32
16	135 200	1.05	4	0.87	1.05	4	0.43	1.05	4	0.45
25	211 250	1.05	4	1.07	1.05	4	0.51	1.05	4	0.45
36	304 200	1.05	4	1.43	1.05	4	0.53	1.05	4	0.55
49	414 050	1.05	4	1.57	1.05	4	0.66	1.05	4	0.66
64	540 800	1.05	4	1.94	1.05	4	0.86	1.05	4	0.75

Table 8.11 Test MHS-2D-3. Same format as in Table 8.10 for 5, 6, 7 level MHS

Procs.	d.o.f.	5 levels			6 levels			7 levels		
		κ	it.	Time	κ	it.	Time	κ	it.	Time
4	33 800	1.05	4	0.23	1.05	4	0.25	1.05	4	0.26
9	76 050	1.04	3	0.29	1.05	4	0.28	1.05	4	0.30
16	135 200	1.05	4	0.37	1.05	4	0.33	1.05	4	0.36
25	211 250	1.05	4	0.40	1.05	4	0.41	1.05	4	0.43
36	304 200	1.05	4	0.44	1.05	4	0.44	1.07	4	0.43
49	414 050	1.05	4	0.53	1.05	4	0.48	1.08	4	0.50
64	540 800	1.05	4	0.66	1.05	4	0.55	1.09	5	0.58

step. We observe that, in this case too, both condition numbers and iteration counts remain constant when increasing the number of subdomains and levels.

8.5.2.2   MHS: Three-Dimensional Domains

Test MHS-3D-1. Increasing levels and increasing global size, cartesian slab. As in test MAS-3D-1 of the previous section, the behavior of the MHS preconditioner

Table 8.12 Test MHS-3D-1. Increasing number of levels L for cartesian slabs with increasing fine meshes $\mathcal{T}_{i+1} = 2\mathcal{T}_i$ starting with a fixed coarse mesh $\mathcal{T}_0 = 4 \cdot 4 \cdot 2$; fixed number of processors = 32

L	Meshes	d.o.f.	$\kappa = \lambda_{max}/\lambda_{min}$	it.	Time
3	$\mathcal{T}_0, 2\mathcal{T}_0, 4\mathcal{T}_0$	5 202	1.97=1.18/0.60	7	0.13
4	$\mathcal{T}_0, 2\mathcal{T}_0, 4\mathcal{T}_0, 8\mathcal{T}_0$	37 026	1.53=1.03/0.67	5	0.27
5	$\mathcal{T}_0, 2\mathcal{T}_0, 4\mathcal{T}_0, 8\mathcal{T}_0, 16\mathcal{T}_0$	278 850	1.46=1.01/0.68	5	0.94
6	$\mathcal{T}_0, 2\mathcal{T}_0, 4\mathcal{T}_0, 8\mathcal{T}_0, 16\mathcal{T}_0, 32\mathcal{T}_0$	2.1M	1.34=1.01/0.74	5	5.9

Table 8.13 Test MHS-3D-2. Condition numbers, iteration counts, cpu timings for 3, 4 level MHS. Scaled speedup with fixed subdomain size $48 \cdot 48 \cdot 48$ on the ellipsoidal domains of Fig. 8.1

Procs.	d.o.f. (M)	3 levels			4 levels		
		κ	it.	Time	κ	it.	Time
8	1.8	1.17	4	19.11	1.18	4	16.67
16	3.6	1.17	4	21.21	1.18	4	19.82
32	7.2	1.18	4	21.86	1.20	5	20.57
64	14.4	1.18	4	23.8	1.20	5	21.32
128	28.7	1.30	5	25.83	1.30	5	22.02
240	53.8	1.30	5	28.27	1.30	5	23.13

is studied here increasing the number of levels from 3 to 6. We consider again a slab domain. The size of the fine mesh varies form $16 \times 16 \times 8$ elements (5 202 d.o.f.) with 3 levels to $128 \times 128 \times 64$ elements (2 163 330 unknowns) with 6 levels, hence the dimensions of the slab domain increase from $0.16 \times 0.16 \times 0.08$ to $1.28 \times 1.28 \times 0.64 \, \text{cm}^3$. The number of subdomains (and processors) is kept fixed to $32 = 4 \times 4 \times 2$. We run the model for 0.5 ms after the stimulus. Table 8.12 reports the average minimum and maximum eigenvalues, the average condition number, the average number of PCG iterations and the average solving time per time step. As in the two-dimensional case, the condition number and the iteration counts are independent of the number of levels, result that confirms the optimality of the MHS(L) preconditioner.

Test MHS-3D-2. Scaled speedup on ellipsoidal domains. We consider in this case an ellipsoidal geometry (See Fig. 8.1). We vary the number of subdomains from 8 to 240, keeping fixed the local mesh in each subdomain to $48 \times 48 \times 48$ nodes (221 184 unknowns), hence varying the global number of degrees of freedom (d.o.f.) from 1.7×10^6 in the smallest case with 8 subdomains to 5.3×10^7 in the largest with 240 subdomains. We simulate the initial depolarization phase for 0.5 ms, i.e. 10 time steps. The number of levels varies from 3 to 6. Tables 8.13 and 8.14 report the average condition number, the average number of PCG iterations and the average solving time per time step. These results show the scalability of the MHS preconditioner also in a three-dimensional deformed domain. The condition numbers and iteration counts are essentially the same for MHS with 3,4,5 levels and only marginally larger with 6 levels. The best performance in term of CPU time

Table 8.14 Test MHS-3D-2. Same format as in Table 8.13 for 5, 6 level MHS

		5 levels			6 levels		
Procs.	d.o.f. (M)	κ	it.	Time	κ	it.	Time
8	1.8	1.18	4	15.98	1.38	5	16.86
16	3.6	1.18	4	16.97	1.38	5	17.07
32	7.2	1.21	5	21.71	1.43	6	21.32
64	14.4	1.21	5	21.62	1.39	5	20.96
128	28.7	1.30	5	21.36	1.56	6	22.81
240	53.8	1.30	5	22.82	1.56	6	24.65

Table 8.15 Test MHS-3D-3. Presence of transmural ischemia: comparison of the three preconditioners BJ, MG(5) and MHS(5) in presence of discontinuous conductivity coefficients due to ischemia

	BJ			MG(5)			MHS(5)		
Procs.	κ	it.	time	κ	it.	Time	κ	it.	Time
8	3 060	156	33.61	2.86	9	16.58	2.33	8	16.73
16	3 384	163	17.48	2.96	10	10.64	2.39	8	8.58
32	3 500	167	10.16	2.95	10	5.14	2.41	8	5.47
64	4 268	183	5.68	3.35	11	3.47	2.83	9	3.44

seems to be attained with 5 levels, hence in the following tests we focus on the MHS(5).

Test MHS-3D-3. Presence of transmural ischemia. The domain considered in this case is an anisotropic slab of dimensions $1.28 \times 1.28 \times 0.32\,\mathrm{cm}^3$, with a transmural ischemic region of dimensions $0.32 \times 0.32 \times 0.32\,\mathrm{cm}^3$ located at the center of the slab. The portion of tissue is discretized by a cartesian grid of $128 \times 128 \times 32$ elements (1 098 306 unknowns). The excitation process is started by applying a stimulus of $200\,\mu\mathrm{A/cm}^3$ for 1 ms on a small area of $2 \times 2 \times 2$ elements at a vertex of the endocardium. The ischemic condition is modeled by increasing the extracellular concentration of potassium in the LR1 model from 5.4 mV (control) to 20 mV (ischemia) (see [569]) and reducing the conductivity coefficients in the ischemia region as indicated in Table 8.1 (see [235]), hence the conductivity coefficients present discontinuities on the boundaries of the ischemic region and this makes the resolution more difficult. See also Chap. 3 for more details on modeling ischemic conditions.

We compare MHS(5) with the standard one-level Block Jacobi preconditioner (BJ) and the multigrid preconditioner with 5 levels (MG(5)) proposed in [552]. We observe that the hybrid method is also in this case scalable and comparable to (sometimes better than) the multigrid preconditioner MG(5) (Table 8.15).

MHS-3D-4. Complete cardiac cycle. In this last test, we simulate a complete heartbeat (400 ms, about 3 000 time steps) in a portion of ventricle having dimension $1.92 \times 1.92 \times 0.48\,\mathrm{cm}^3$, discretized by a cartesian grid of $192 \times 193 \times 49$ nodes (3.6×10^6 d.o.f.). We run the simulation on 36 processors of the Linux cluster of Milan (cluster.mat.unimi.it). Table 8.16 reports the average PCG iterations per time

Table 8.16 Test MHS-3D-4.
Complete cardiac cycle

Prec.	it.	Time (s)	Total time
BJ	205	46.02	29 h 49 min
MG(5)	8	11.11	7 h 21 min
MHS(5)	6	9.67	6 h 26 min

it average PCG iterations per time step,
time average execution time per time step
in seconds, *total time* total simulation time
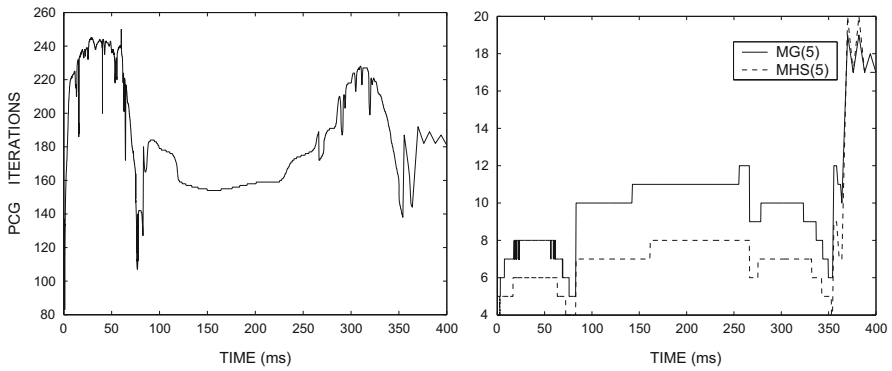
Fig. 8.7 Test MHS-3D-4. Time evolution of the PCG iterations with BJ preconditioners (*left*) and multilevel preconditioners MG(5), MHS(5) (*right*)
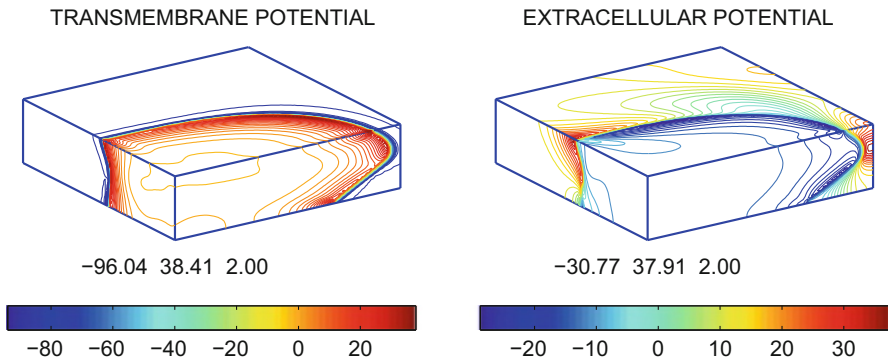
Fig. 8.8 Test MHS-3D-4. Patterns of level lines of the transmembrane and extracellular potentials during the excitation phase (t = 40 ms). Reported below each panel are the minimum, maximum and step in mV of the displayed map

step, the average execution time per time step and the total simulation time. The detailed iteration counts as function of time during the complete heartbeat are shown in Fig. 8.7 (left panel for BJ and right panel for MG(5) and MHS(5)). Figure 8.8 shows the spatial maps of the transmembrane and extracellular potentials computed 40 ms after the stimulus was given at a vertex of the domain, i.e. during the excitation phase. Figure 8.9 shows the transmembrane and extracellular potentials
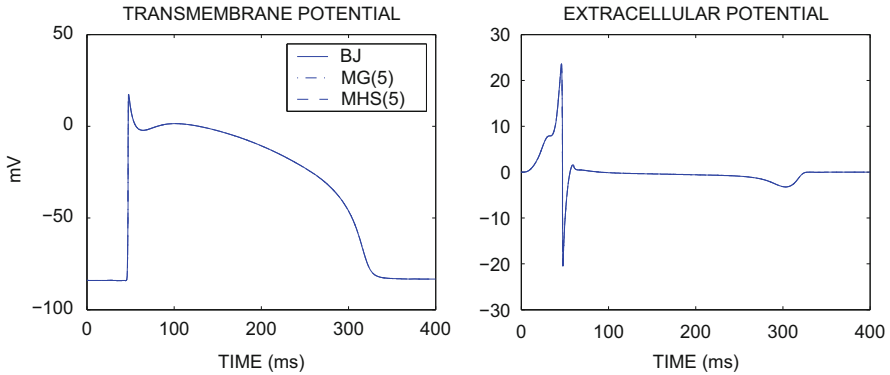
Fig. 8.9 Test MHS-3D-4. Time evolution at a fixed point of the transmembrane and extracellular potentials, computed with the three methods

computed in a fixed point of the domain by the three methods (the three plots are indistinguishable because superimposed). MHS(5) reduces the computational time of about 78 and 12 %, compared to BJ and MG(5) respectively.

8.6 Block Preconditioners for the Bidomain System

Block preconditioners can be used, and combined with Schwarz preconditioners, for both the parabolic-parabolic (PP, see 3.42) and parabolic-elliptic (PE, see 3.43) formulations of the Bidomain system. Such block preconditioners for the Bidomain system have been studied e.g. in [373, 379, 381, 382].

We recall that after the time and space discretization described in Chap. 7, the Bidomain discrete systems in both PP (7.5) and PE (7.6) formulations involve matrices with a 2×2 block structure

$$A_{PP} = \begin{bmatrix} \gamma M + A_i & -\gamma M \\ -\gamma M & \gamma M + A_e \end{bmatrix}, \qquad A_{PE} = \begin{bmatrix} \gamma M + A_i & A_i \\ A_i & A \end{bmatrix},$$

where $\gamma = \frac{\chi C_m}{\tau}$ is proportional to the inverse time step size, see (7.9).

8.6.1 Block-Diagonal and Block-Factorized Bidomain Preconditioners

Denoting by

$$A = \begin{bmatrix} A_{11} & A_{12} \\ A_{12} & A_{22} \end{bmatrix}$$

either one of A_{PP}, A_{PE}, we will consider the following classical block preconditioners for A (see Axelsson [20]):

- The block-diagonal preconditioner

$$B_D = \begin{bmatrix} B_1 & 0 \\ 0 & B_2 \end{bmatrix}; \tag{8.38}$$

- The block-factorized preconditioner

$$B_F = \begin{bmatrix} I & 0 \\ A_{12}B_1^{-1} & I \end{bmatrix} \begin{bmatrix} B_1 & A_{12} \\ 0 & B_2 \end{bmatrix}. \tag{8.39}$$

The main abstract results for these preconditioners are given in the following two propositions, see Axelsson [20] for a proof. For both propositions, we define the constant

$$\gamma^2 = \sup_{\mathbf{v} \in \mathbb{R}^n \backslash Ker(A_{22})} \frac{\mathbf{v}^T A_{12} A_{11}^{-1} A_{12} \mathbf{v}}{\mathbf{v}^T A_{22} \mathbf{v}} \tag{8.40}$$

and the function $\phi(x) = \frac{1}{2}(1 + x) + \sqrt{\frac{1}{4}(1 - x^2) + x\gamma^2}$.

Proposition 8.1 (Axelsson [20, Th. 9.3]). *If $\alpha_1 A_{11} \leq B_1 \leq \alpha_2 A_{11}$, $\beta_1 A_{22} \leq B_2 \leq \beta_2 A_{22}$, with $\alpha_2 \geq \beta_2$, then*

$$\kappa(B_D^{-1}A) \leq \frac{\alpha_2}{\alpha_1(1 - \gamma^2)} \phi\left(\frac{\alpha_1}{\beta_1}\right) \phi\left(\frac{\beta_2}{\alpha_2}\right).$$

Proposition 8.2 (Axelsson [20, Th. 9.5]). *If $\alpha_1 A_{11} \leq B_1 \leq \alpha_2 A_{11}$, $\delta_1 A_{22} \leq S_2 \leq \delta_2 A_{22}$, where $S = B_2 + A_{12}B_1^{-1}A_{12}$, with $\alpha_2 \geq 1 \geq \alpha_1 > \gamma^2$, $\delta_2 \geq 1 \geq \delta_1 > \gamma^2$, then*

$$\lambda_{min}(B_F^{-1}A) \geq \left(1 + \frac{\max\{\alpha_2, \delta_2\} - 1}{1 - \gamma^2} \phi(r_2)\right)^{-1},$$

where $r_2 = \min\{\frac{\alpha_2 - 1}{\delta_2 - 1}, \frac{\delta_2 - 1}{\alpha_2 - 1}\}$, and $\alpha_2 > 1$ and/or $\delta_2 > 1$,

$$\lambda_{max}(B_F^{-1}A) \leq \left(1 - \frac{1 - \min\{\alpha_1, \delta_1\}}{1 - \gamma^2} \phi(r_1)\right)^{-1},$$

where $r_1 = \min\{\frac{1 - \alpha_1}{1 - \delta_1}, \frac{1 - \delta_1}{1 - \alpha_1}\}$, and $\alpha_1 < 1$ and/or $\delta_1 < 1$.

We now define the diagonal blocks B_1, B_2 of our block preconditioners (8.38), (8.39) as scalar overlapping Schwarz preconditioners for each scalar component. Therefore, for the PP formulation, we define:

$$
\begin{aligned}
B_1^{-1} &= \text{ scalar } B_{MAS}^{-1} \text{ preconditioner for } c_t M + A_i, \\
B_2^{-1} &= \text{ scalar } B_{MAS}^{-1} \text{ preconditioner for } c_t M + A_e,
\end{aligned} \tag{8.41}
$$

while for the *PE*-formulation, we define

$$
\begin{aligned}
B_1^{-1} &= \text{ scalar } B_{MAS}^{-1} \text{ preconditioner for } c_t M + A_i, \\
B_2^{-1} &= \text{ scalar } B_{MAS}^{-1} \text{ preconditioner for } A_i + A_e.
\end{aligned} \tag{8.42}
$$

We could also build our scalar blocks using the hybrid multilevel preconditioner B_{MHS}^{-1} instead of B_{MAS}^{-1}.

The following convergence rate bound for the block-diagonal preconditioner can be found in [373].

Lemma 8.6. *For both Bidomain PP and PE formulations ($A = A_{PP}$ or $A = A_{PE}$), the condition number of the block-diagonal preconditioned operator with MAS scalar blocks (8.41), (8.42) is bounded by*

$$
\kappa(B_D^{-1} A) \leq c \max_{1 \leq k \leq L-1} \left(1 + \frac{h_{k-1}}{\delta_k} \right) \frac{1+\gamma}{1-\gamma}.
$$

This result shows that in addition to the standard domain decomposition parameters, convergence with the block-diagonal preconditioner B_D depends on the parameter γ, which in turn depends only on the original Bidomain blocks. The following estimates on γ^2 can be found in [381]:

(a) For the PP formulation, $\gamma^2 \leq (1 + \lambda_{min}(A_e, M))^{-1}$, where $\lambda_{min}(A_e, M)$ is the minimum eigenvalue of $A_e M^{-1}$ (see [381, Lemma 4.3]) and numerical experiments show that γ is very close to 1, so the bound of Lemma 8.6 might be large and convergence slow;

(b) For the PE formulation, $\gamma^2 \leq (1 + \lambda_{min}(A_e, A_i))^{-1}$, where $\lambda_{min}(A_e, A_i)$ is the minimum eigenvalue of $A_e A_i^{-1}$ (see [381, Lemma 4.1]) and numerical experiments seem to indicate that γ is close to $1/2$, so the bound of Lemma 8.6 is satisfactory.

The following convergence rate bound for the block-factorized preconditioner can be found in [373].

Lemma 8.7. *For both Bidomain PP and PE formulations ($A = A_{PP}$ or $A = A_{PE}$), the extreme eigenvalues of the block-factorized preconditioned operator with MAS*

scalar blocks ([8.41](#)), ([8.42](#)) are bounded by

$$
\lambda_{min}(B_F^{-1}A) \geq \left(1 + 2\frac{c \max\limits_{1 \leq k \leq L-1} \left(1 + \dfrac{h_{k-1}}{\delta_k} \right) + N_c}{1 - \gamma^2} \right)^{-1},
$$

$$
\lambda_{max}(B_F^{-1}A) \leq \left(1 - \frac{1 - (N_c + 1)^{-1}}{1 - \gamma} \right)^{-1}.
$$

These bounds are pessimistic because, due to Prop. [8.2](#), they require that $\gamma^2 < \delta_1$ and predict a large condition number when γ^2 approaches δ_1, while our numerical results seem to indicate that the same considerations on γ for the block-diagonal case also hold for the block-factorized case.

8.6.2 Numerical Results with Block Preconditioners

In this section, we present the results of parallel numerical experiments performed on Linux Clusters using the parallel library PETSc [24, 25], from the Argonne National Laboratory.

The Parabolic-Parabolic (PP) and Parabolic-Elliptic (PE) formulations of the Bidomain system coupled to the LR1 model are integrated by the Implicit-Explicit Method described in the previous sections. The values of the coefficients and parameters in the LR1 model are given in the original paper [308]. The linear system at each time step is solved by the preconditioned conjugate gradient (PCG) method, using as stopping criterion a 10^{-4} reduction of the residual l^2-norm. We precondition the PCG iteration by the multilevel Schwarz preconditioner in either its additive version MAS(L) with L levels defined in ([8.34](#)) or its hybrid version MHS(L), studied in [458, 459]. These preconditioners are employed both as coupled preconditioners for the whole PP and PE Bidomain systems and as block preconditioners in the block-diagonal and block-factorized preconditioners. Inexact ILU(0) local solvers are used for the local problems on the subdomains.

Domain geometry and fiber structure. The domain Ω is the image of a cartesian slab using ellipsoidal coordinates, yielding a portion of truncated ellipsoid (see Fig. [8.10](#)). The family of truncated ellipsoids is described by the parametric equations

$$
\begin{cases}
x = a(r) \cos \theta \cos \phi & \phi_{min} \leq \phi \leq \phi_{max}, \\
y = b(r) \cos \theta \sin \phi & \theta_{min} \leq \theta \leq \theta_{max}, \\
z = c(r) \sin \theta & 0 \leq r \leq 1,
\end{cases}
$$
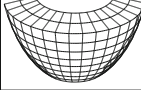
procs.	8	16	32	64	128	256
$\mathscr{T}_0$	$2 \cdot 2 \cdot 2$	$4 \cdot 2 \cdot 2$	$4 \cdot 4 \cdot 2$	$8 \cdot 4 \cdot 2$	$8 \cdot 8 \cdot 2$	$16 \cdot 8 \cdot 2$
$\mathscr{T}_{L-1}$	$96 \cdot 96 \cdot 96$	$192 \cdot 96 \cdot 96$	$192 \cdot 192 \cdot 96$	$384 \cdot 192 \cdot 96$	$384 \cdot 384 \cdot 96$	$768 \cdot 384 \cdot 96$
d.o.f.	1.8M	3.6M	7.2M	14.4M	28.7M	57.4M

Fig. 8.10   Mesh parameters for weak scaling Tests 1 and 2

where $a(r) = a_1 + r(a_2 - a_1)$, $b(r) = b_1 + r(b_2 - b_1)$, $c(r) = c_1 + r(c_2 - c_1)$, and $a_i, b_i, c_i, i = 1, 2$ are given coefficients determining the main axes of the ellipsoid. The fibers rotate intramurally linearly with the depth for a total amount of $120°$ proceeding counterclockwise from epicardium to endocardium. More precisely, in a local ellipsoidal reference system $(u_{e\phi}, u_{e\theta}, u_{er})$, the fiber direction $\mathbf{a}_l(\mathbf{x})$ at a point $\mathbf{x}$ is given by

$$\mathbf{a}_l(\mathbf{x}) = u_{e\phi} \cos\alpha(r) + u_{e\theta} \sin\alpha(r), \quad \text{with} \ \ \alpha(r) = \frac{2}{3}\pi(1-r) - \frac{\pi}{4}, \qquad 0 \le r \le 1.$$

Conductivity coefficients. The values of the conductivity coefficients used in all the numerical tests are the following:

$$\begin{aligned} \sigma_l^i &= 3 \cdot 10^{-3} \, \Omega^{-1} \, \text{cm}^{-1} & \sigma_l^e &= 2 \cdot 10^{-3} \, \Omega^{-1} \, \text{cm}^{-1} \\ \sigma_t^i &= 3.1525 \cdot 10^{-4} \, \Omega^{-1} \, \text{cm}^{-1} & \sigma_t^e &= 1.3514 \cdot 10^{-3} \, \Omega^{-1} \, \text{cm}^{-1} \\ \sigma_n^i &= 3.1525 \cdot 10^{-5} \, \Omega^{-1} \, \text{cm}^{-1} & \sigma_n^e &= 6.757 \cdot 10^{-4} \, \Omega^{-1} \, \text{cm}^{-1}. \end{aligned}$$

Mesh hierarchy. We denote the cartesian mesh used to discretize our domains by $\mathscr{T} = \mathscr{T}_i \cdot \mathscr{T}_j \cdot \mathscr{T}_k$, indicating the number of elements in each coordinate direction. This notation applies to both fine and coarse meshes. When we scale up the mesh by a factor c, for brevity we define $c\mathscr{T} = c\mathscr{T}_i \cdot c\mathscr{T}_j \cdot c\mathscr{T}_k$, i.e. the number of elements in $c\mathscr{T}$ is c^3 times the number of elements in $\mathscr{T}$. Figure 8.10 shows the domains used in our parallel tests described below, reporting for each test the number of processors (procs.), the coarse mesh ($\mathscr{T}_0$), the fine mesh ($\mathscr{T}_{L-1}$), and the number of degrees of freedom (d.o.f). Our tests will range from 1.8 million d.o.f. on 8 procs. to 57.4 million d.o.f. on 256 procs.

Stimulation site, initial and boundary conditions. The depolarization process is started by applying a stimulus of $I_{app} = 200 \, \text{mA/cm}^3$ lasting 1 ms on the face of the domain modeling the endocardial surface. The initial conditions are at resting values for all the potentials and LR1 gating variables, while the boundary conditions are for insulated tissue. In all simulations, the fine mesh size is $h = 0.01 \, \text{cm}$. The time step size is $\Delta t = 0.05 \, \text{ms}$.
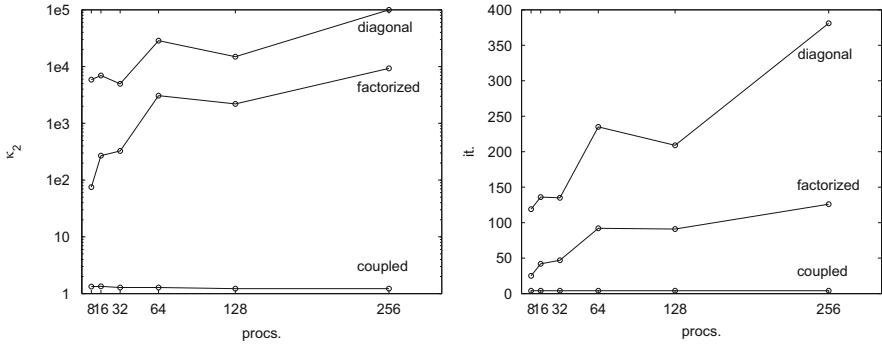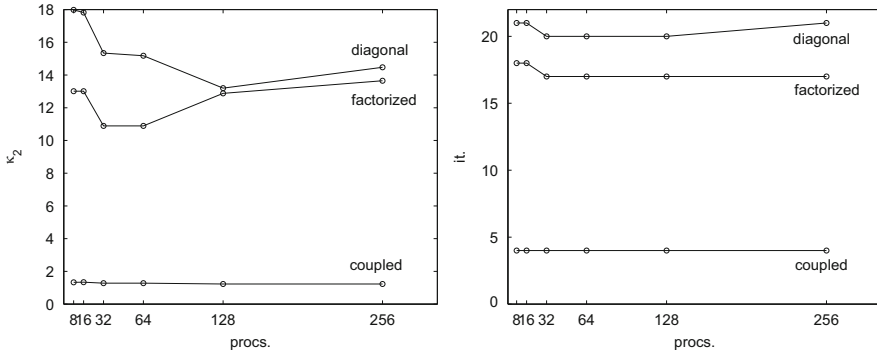
Fig. 8.11 Test 1, weak scaling on ellipsoidal domains of Fig. 8.10 for PP formulation with coupled, diagonal and factorized MHS(4) preconditioners. *Top*: table with condition numbers (κ), extreme eigenvalues (λ_{max}, λ_{min}), iteration counts (*it.*) for each preconditioner as a function of the number of processors/subdomains (*procs*). *Bottom*: plots of condition numbers (*left*) and iteration counts (*right*) from the table above

8.6.2.1   Test 1: Weak Scaling for Coupled, Diagonal, Factorized MHS Preconditioners Applied to the PP Formulation

In this test, we compare the performance of coupled, diagonal, factorized MHS preconditioners applied to the PP formulation. In the table of Fig. 8.11, a weak scaling test on increasing ellipsoidal domains is considered. The number of levels is kept fixed to 4. The results show that the MHS-coupled preconditioner is completely scalable, with the PCG iterations which remain constant when increasing the number of processors. On the other hand, both diagonal and factorized MHS preconditioners are not scalable, because condition numbers and PCG iterations increase considerably when the number of processors grows.

8.6.2.2   Test 2: Weak Scaling for Coupled, Diagonal, Factorized MHS Preconditioners Applied to the PE Formulation

As in Test 1, we compare here the performance of coupled, diagonal, factorized MHS preconditioners, but applied to the PE formulation. The same weak scaling test on increasing ellipsoidal domains is considered, as in the previous Test 1. The number of levels is kept fixed to 4. The results in the table of Fig. 8.12 show that now the coupled, diagonal and factorized MHS preconditioners are all completely scalable, with the PCG iterations which remain bounded when increasing the number of processors. The best convergence is achieved by the MHS-coupled preconditioner (4 PCG iterations), the worst by the MHS-diagonal (21 PCG iterations).

Fig. 8.12 Test 2, weak scaling on ellipsoidal domains of Fig. 8.10 for PE formulation with coupled, diagonal and factorized MHS(4) preconditioners. *Top*: table with condition numbers (κ), extreme eigenvalues (λ_{max}, λ_{min}), iteration counts (*it.*) for each preconditioner as a function of the number of processors/subdomains (*procs*). *Bottom*: plots of condition numbers (*left*) and iteration counts (*right*) from table above

8.6.2.3   Test 3: Strong Scaling for Coupled, Diagonal, Factorized MHS Preconditioners Applied to the PP and PE Formulations

In this strong scaling (standard speedup) test, we compare again the performance of coupled, diagonal, factorized MHS preconditioners applied to both PP and PE formulations. The number of levels is kept fixed to 4. The cardiac domain Ω is the portion of ellipsoid in Fig. 8.10, discretized by a fine mesh of $128 \cdot 128 \cdot 64$ finite elements, for a total amount of $2\,163\,330$ dof. Since this is a strong scaling test, the fine mesh is fixed, while the number of subdomains ($=$ number of processors) increases from 8 to 512. In this way, the subdomain size is reduced when the number of subdomains is increased. The simulation is run for 0.5 ms during the excitation phase, i.e. for 10 time steps.

Table 8.17 reports the average condition number, PCG iterations count and CPU time per time step. The results show that the coupled preconditioners for both PP and PE formulations have comparable performances and they are better than the block preconditioners, especially for the PP formulation. The speedups, defined with respect to the base 8 processors run, are good for the coupled preconditioners up to 128 processors (up to 64 processors they are even superlinear for the PP formulation), while they degenerate with 256 and 512 processors, because the local problems become too small and the increasing communication costs deteriorate the parallel performance. The block preconditioners have a much worse performance in the PP formulation (as already seen in Test 1), showing reasonable speedups up to 64 processors but degenerating rapidly afterward, with even negative return (decreasing speedups) for 512 processors. For the PE formulation the block preconditioners show better timings, initially even better than the coupled preconditioner since each iteration of the latter is more expensive, but such timings worsen rapidly after 128 processors and become triple the coupled preconditioner timings for 512

Table 8.17 Test 3, strong scaling test on ellipsoidal domain for PP and PE formulations with coupled, diagonal and factorized MHS(4) preconditioners

Procs.	MHS(4)-coupled			MHS(4)-diagonal			MHS(4)-factorized		
	κ	it.	Time	κ	it.	Time	κ	it.	Time
PP formulation									
8	2.56	7	8.4	1.1e + 5	239	88.6	3.6e + 3	90	49.2
16	2.63	7	3.6	1.3e + 5	255	51.0	3.4e + 3	89	26.5
32	2.63	7	1.9	1.3e + 5	254	24.8	3.4e + 3	89	13.0
64	2.63	7	1.0	1.3e + 5	254	16.5	3.4e + 3	89	6.8
128	3.20	8	0.6	2.1e + 5	319	10.9	4.4e + 3	96	4.8
256	3.21	8	0.5	2.1e + 5	317	10.1	4.5e + 3	96	4.7
512	3.21	8	0.5	2.1e + 5	316	12.8	4.5e + 3	96	7.9
PE formulation									
8	2.61	7	8.2	27.62	25	5.9	21.82	21	6.1
16	2.68	7	4.0	27.60	25	3.3	21.62	22	3.3
32	2.68	7	2.0	27.60	25	1.7	21.62	22	1.6
64	2.68	7	1.4	27.60	25	1.0	21.62	22	0.9
128	3.27	8	0.8	27.16	25	0.9	19.67	23	0.8
256	3.29	8	0.6	27.16	25	1.1	19.70	23	0.9
512	3.29	8	0.5	27.16	25	1.5	19.70	23	1.4

Condition numbers (κ), iteration counts (*it.*) for each preconditioner, CPU times (*time*) in seconds as a function of the number of processors/subdomains (*procs*)

processors. This is also confirmed by the low speedups that degenerate rapidly and start decreasing already at 256 processors.

In conclusions, these results show that block preconditioners for the Bidomain PP formulation are not scalable, while they are scalable for the PE formulation, but with higher iteration counts and computational costs than the coupled preconditioner. Therefore, in our parallel tests (with idealized ventricular geometries and structured finite elements) multilevel Schwarz preconditioners seem to be more efficient when applied as coupled rather than block Bidomain preconditioners.

Chapter 9
Simulation Studies of Cardiac Bioelectrical Activity

Anisotropic Bidomain computer simulations have been used to study cardiac conduction since the beginning of the 1980s. At that time, computational power limited investigations to simple geometries corresponding to two-dimensional sheets [28, 392] and idealized three-dimensional cylindrical domains, which for symmetry reduce to two-dimensional domains [426, 434]. With the evolution of computer technology and in particular the development of parallel computer platforms, Bidomain numerical simulations of the cardiac bioelectrical activity have become three-dimensional [101, 102, 226, 295, 397] and increasingly more realistic [399, 452, 526, 530], allowing a wider range of investigations to elucidate the mechanisms underlying the propagation of electrical impulse in cardiac tissue under normal and pathological conditions.

In this chapter, we illustrate how the orthotropic Bidomain system described in the previous chapters can be used to simulate and study the space-time evolution of the most important phenomena in cardiac electrophysiology. We consider three-dimensional blocks modeling a portion of ventricular wall. Three-dimensional models have been developed also for atrial tissue, accounting for both spatial heterogeneity and anisotropy and they have been coupled with a human torso to simulate body surface maps and electrocardiograms; for studies focusing on the propagation in normal and fibrillating atria, we refer to e.g. [17, 219, 253, 466].

In the following, we will focus on:

- The genesis of cardiac excitation and virtual electrode polarization;
- The anisotropic propagation of excitation and recovery fronts;
- The effects of cardiac heterogeneities on fronts propagation and APD distribution;
- The morphology of electrograms;
- The computation of excitation and repolarization time markers;
- The effects of ischemic regions;
- The simulation of cardiac reentry phenomena.

9.1 Cardiac Excitation and Virtual Electrode Phenomena

It is well known that the macroscopic electrical properties of the cardiac muscle are markedly anisotropic. Experimental studies have confirmed that the Bidomain representation of the cardiac tissue as superimposition of two continuous conductive media, the intracellular and extracellular spaces, exhibits different anisotropy ratios on the order of 2 and 10, with the intracellular domain the most anisotropic one; see e.g. [100,277,420,421]. The development of optical mappings of cardiac transmembrane action potential, starting in the mid 1990s, has led to experimental studies by several groups that have investigated the effects of unipolar extracellular cathodal or anodal stimulations of cardiac tissue, see e.g. [156, 157, 281, 349, 480, 559]. These studies have established that the stimulation by a unipolar electrode produces a characteristic transmembrane pattern called *virtual electrodes response*.

After an anodal stimulus, the transmembrane potential distribution exhibits a virtual anode (VA), i.e. negatively polarized (hyperpolarized) volume around the stimulating electrode having a dog-bone shape, and by two virtual cathodes (VCs), i.e. positively polarized (depolarized) regions adjacent to the concave part of the hyperpolarized anodal dog-bone boundary, see e.g. Fig. 9.4. The central dog-bone VA is aligned across the fiber direction, while the two adjacent VCs are aligned along the fiber direction. Conversely, after a cathodal stimulus, the polarity is reversed, i.e. the transmembrane potential pattern exhibits a central dog-bone shaped VC aligned across fiber and two adjacent VAs aligned along fiber. It is well known that only Bidomain models with unequal anisotropy ratios of the intra- and extracellular media are able to generate the observed *virtual electrode polarization* regions, see e.g. [469,557]. Therefore, the experimental detection of virtual electrode responses by [281,349,559] strongly supports the evidence for the unequal anisotropy ratios assumption in Bidomain models; see the recent survey of the Bidomain theory of pacing in [256].

The heart can be stimulated electrically in four different ways, see e.g. [146,207, 300, 301]:

- By turning on a negative current (cathode make, CM);
- By turning on a positive current (anode make, AM);
- By turning off of negative current (cathode break, CB);
- By turning off of positive current, (anode break, AB).

See Fig. 9.1 for a schematic illustration of these four cardiac stimulations.

In [427, 435], the Bidomain model with unequal anisotropic ratio was first proposed and used to establish a theoretical framework able to explain the *make* and *break* mechanisms of excitability in terms of the underlying virtual electrodes polarization. The effects and features of make and break excitation mechanisms, generated by unipolar extracellular cathodal or anodal stimulations, have been subsequently investigated by simulation studies in [164,390,416,428–430,432,436, 450,451,486] and by experimental studies in [156,157,480,559]; see also the recent surveys [256,558] and the book [158].
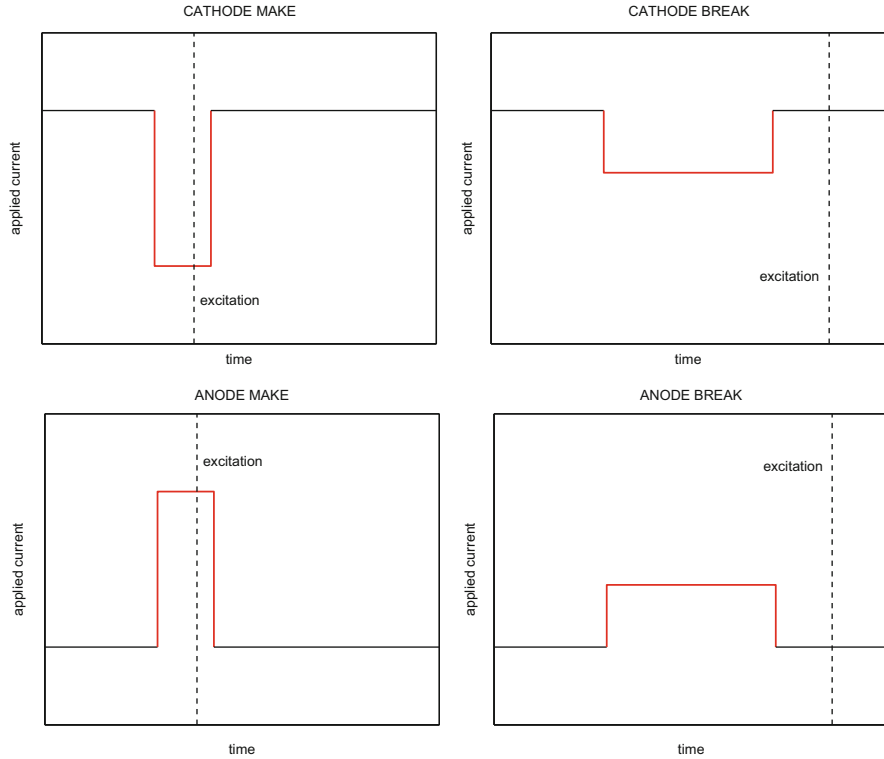
Fig. 9.1 Schematic illustration of the cathode make (*CM*), cathode break (*CB*), anode make (*AM*), anode break (*AB*) excitation mechanisms

We briefly recall the main activation features of these mechanisms. With the make stimulation, activation occurs with the stimulus onset either at the central VC during cathodal stimulation (cathode make CM) or at the two VCs along the fiber direction during anodal stimulation (anode make AM). With the break stimulation, activation occurs after the stimulus termination at the two VAs during cathodal stimulation (cathode break CB) or at the central VA during anodal stimulation (anode break AB).

The break modes CB and AB generated by local electrode stimulation have been confirmed by optical recordings and Bidomain simulations when a short stimulation is delivered during the relative refractory period (systolic phase), whereas the make modes CM and AM have been observed experimentally and simulated during the diastolic phase. Many studies have underlined the important role played by the anode break excitation in reentry induction mechanisms [429] and defibrillation [11, 156, 157, 486, 525].

Here we focus on the 3D investigation of the excitation mechanisms associated with an anodal stimulation, which can be generated only in tissues with unequal anisotropy ratio. Additional simulations and results can be found in [131, 132].

9.1.1   Methods and Parameter Calibration

The anisotropic Bidomain model. Let us consider a three-dimensional domain Ω_H modeling the cardiac tissue, in contact with a conducting medium Ω_0, representing either the intracavitary blood or an extracardiac bath. We define $\overline{\Omega} = \overline{\Omega_H} \cup \overline{\Omega_0}$ and $S = \partial \cap \partial \Omega_0$ the common not insulated interface. The remaining interface $\partial \Omega$ is assumed insulated. The evolution of the transmembrane potential $v(\mathbf{x}, t)$, extracellular potential $u_e(\mathbf{x}, t)$, extracardiac potential $u_b(\mathbf{x}, t)$, gating variables $w(\mathbf{x}, t)$ and ionic concentrations $c(\mathbf{x}, t)$ is described by the macroscopic Bidomain model:

$$\begin{cases} c_m \partial_t v - \text{div}(D_i \nabla v) - \text{div}(D_i \nabla u_e) + i_{ion}(v, w, c) = 0 & \text{in } \Omega_H \\ \partial_t w - R(v, w) = 0, \quad \partial_t c - S(v, w, c) = 0 & \text{in } \Omega_H \\ -\text{div}(D_i + D_e)\nabla u_e = \text{div } D_i \nabla v + i_{app}^e & \text{in } \Omega_H \\ \mathbf{n}^T D_i \nabla(v + u_e) = 0 & \text{on } \partial \Omega_H \\ -\text{div } \sigma_b \nabla u_b = i_{app}^e & \text{in } \Omega \setminus \Omega_H \\ u_e = u_b & \text{on } \partial \Omega_H \\ \mathbf{n}^T D_e \nabla u_e = \mathbf{n}^T \sigma_b \nabla u_b & \text{on } \partial \Omega_H \\ \mathbf{n}^T \sigma_b \nabla u_b = 0 & \text{on } \partial \Omega \end{cases} \qquad (9.1)$$

with appropriate initial conditions on $v(\mathbf{x}, 0)$, $w(\mathbf{x}, 0)$ and $c(\mathbf{x}, 0)$. Here c_m and i_{ion} denote the capacitance and the ionic current of the membrane per unit volume, i_{app} represents the applied current per unit volume with the compatibility condition $\int_\Omega i_{app}^e = 0$, and σ_b is the conductivity coefficient of the extracardiac medium.

Choice of reference potential. The extracellular potential u_e is defined up to an independent constant $R(t)$ determined by the choice of the reference potential. In this paper, we consider as a reference potential the average of the extracellular potential over the cardiac volume, i.e. we impose $\int_{\Omega_H} u_e(\mathbf{x}, t)dx = 0$.

Membrane model. In our implementation of the Bidomain model for cardiac tissue with normal bioelectric properties, the Luo-Rudy phase I (LR1) action potential model is used to represent the nonlinear kinetics of the ventricular membrane current according to the original parameters of [308], with the addition of

(i)   The funny current I_f, modeled as in [31, 81, 82, 149, 579];
(ii) The electroporation current I_e, modeled as in [145];
(iii) The outward current I_a activated upon induced depolarization, modeled as in [88].

We remark that the incorporation of (i) and (ii) have also been carried out in [16] in order to investigate by means of 2D Bidomain simulations the cardiac tissue response to electric shocks. The augmented LR1 model with the incorporation of I_f, I_e and I_a currents in the following is called *full membrane model*.

Myocardial conductivity tensors and fiber architecture. We recall that the macroscopic fiber structure of the cardiac tissue induces anisotropic conductivity properties along and across the fiber directions. Assuming axial-symmetric anisotropy, the macroscopic conductivity tensors $D_i(\mathbf{x})$ and $D_e(\mathbf{x})$ at any point $\mathbf{x} \in \Omega_H$ are defined as

$$D_{i,e}(\mathbf{x}) = \sigma_l^{i,e}\, \mathbf{a}_l(\mathbf{x})\mathbf{a}_l^T(\mathbf{x}) + \sigma_t^{i,e}\, (I - \mathbf{a}_l(\mathbf{x})\mathbf{a}_l^T(\mathbf{x})), \tag{9.2}$$

where $\mathbf{a}_l(\mathbf{x})$ is a unit vector parallel to the local fiber direction and $\sigma_{l,t}^{i,e}$ are the effective intra and extracellular conductivity coefficients measured along (l) and across (t) the fiber direction.

Computational domain. The cardiac domain Ω_H considered in this study is a cartesian slab of dimensions $0.96 \times 0.96 \times 0.32\,\mathrm{cm}^3$, modeling a portion of the left ventricular wall. The endocardial surface is in contact with a smaller slab of dimensions $0.96 \times 0.96 \times 0.16\,\mathrm{cm}^3$, modeling the extracardiac bath, where $\sigma_b = 6e^{-3}\,\Omega^{-1}\,\mathrm{cm}^{-1}$ similar to the blood conductivity.

Stimulation site. Diastolic cathodal or anodal stimuli are delivered at the center of the epicardial surface in a small region of dimensions $0.06 \times 0.06 \times 0.03\,\mathrm{cm}^3$ of a tissue at rest. In order to ensure the compatibility condition, we inject a total stimulation current in a strip of dimensions $0.96\times0.96\times0.08\,\mathrm{cm}^3$ in the extracardiac bath with equal strength and opposite polarity of that used at the subepicardial level. Moreover, in order to reduce the effects of the delivered bath current on the potential field in the subepicardial layer, we have lowered the excitability of the subendocardial layer by strongly decreasing the maximal sodium conductance during the stimulation interval. In order to simulate the break excitation mechanisms during systole, we perform an S1-S2 stimulation protocol. We first apply an initial S1 cathodal stimulus to the resting tissue and simulate the resulting action potential propagation, that sweeps the cardiac domain until a suitable time during the relative refractory period (RRP). At this instant, a subsequent S2 cathodal or anodal stimulus is delivered and we simulate the resulting action potential propagation where the surrounding tissue has recovered its excitability properties.

Activation time isochrones. During the Bidomain simulations, we process the distribution of the transmembrane potential $v(\mathbf{x}, t)$ in order to define the activation time $at(\mathbf{x})$ as the first time instant for which $v(\mathbf{x}, at(\mathbf{x})) = v_{up}$; we choose $v_{up} = -50\,\mathrm{mV}$, a value above the threshold value of v capable of initiating the upstroke of the action potential. Then the excitation wavefronts are displayed by drawing the isochrone surfaces of the activation time.

Numerical methods. In all computations, a structured grid of $96 \cdot 96 \cdot 48$ hexahedral isoparametric Q_1 finite elements of size $h = 0.1\,\mathrm{mm}$ is used in space, while the time discretization is based on the following double operator splitting procedure, based on splitting both the ODEs from the PDEs and the elliptic PDEs from the parabolic one, similar to the second decoupled semi-implicit method

described in Sect. 7.2.3, with the addition of the blood volume. Thus, at the general time step t^{n+1}, given the transmembrane potential v^n at the previous time step, we find:

1. The gating variables w^{n+1}, by solving the related ODEs with the Backward Euler method;
2. The ionic concentration variables c^{n+1}, by solving the related ODEs with the Forward Euler method;
3. The extracellular and extracardiac potentials u_e^{n+1} and u_b^{n+1}, by solving the algebraic linear system resulting from the finite element discretization of the elliptic PDEs in (9.1);
4. The transmembrane potential v^{n+1}, by solving the algebraic linear system resulting from the finite element discretization of the parabolic PDE in (9.1).

This operator splitting strategy yields two large linear systems of algebraic equations that must be solved at each time step. In order to ensure parallelization and portability of our Fortran code, we use the PETSc parallel library [24, 25], a suite of data structures and functions for building large-scale parallel scientific applications, based on the MPI communication library. The parallel strategy employed assigns each subdomain to one processor and the information associated with the interior of the subdomain is uniquely owned by that processor. The processor stores all subvectors and a block of the matrices (mass, stiffness) associated to each overlapping subdomain. Our parallel code employs different DA (Distributed Arrays) PETSc objects for representing v on the domain Ω_H (tissue) and for u_e^{n+1}, u_b^{n+1} on the domain Ω (tissue and bath). The two large linear systems at each time step are solved by a parallel conjugate gradient method, preconditioned by the Multilevel Hybrid Schwarz preconditioner, described in Chap. 8, for the ill-conditioned elliptic system (461 041 d.o.f.) and the Block Jacobi preconditioner for the well conditioned parabolic system (310 497 d.o.f.). These preconditioners are based on the multilevel PETSc objects PCMG (MultiGrid) with ILU(0) local solvers.

9.1.2 Anode and Cathode Make Mechanisms

Figures 9.2 and 9.3 show the epicardial distribution of the intracellular potential (top), extracellular potential (middle) and transmembrane potentials (bottom) 2 ms after the anodal stimulus elicited in a slab without and with transmural fiber rotation, respectively. In each figure, the panels on the right column refer to a tissue with the unequal anisotropy ratios of Table 9.1, while the panels on the left column refer to a tissue slab with equal anisotropy ratio. In the left panel of Fig. 9.2, the intra- and extracellular potential elliptical patterns have the same major to minor semi-axis ratio, yielding a transmembrane potential pattern (bottom left panel) with more rounded elliptical lines around the anodal electrode. Conversely, in a slab with unequal anisotropy ratio, the intra- and extracellular equipotential contour lines, displayed in top and middle right panels of Fig. 9.2, have elliptical shapes

intracellular potential

−157.37 270.81 10.00

intracellular potential

−123.88 215.32 10.00

extracellular potential

−71.49 503.33 5.00

extracellular potential

−37.84 491.53 5.00

transmembrane potential

−232.52 −85.07 10.00
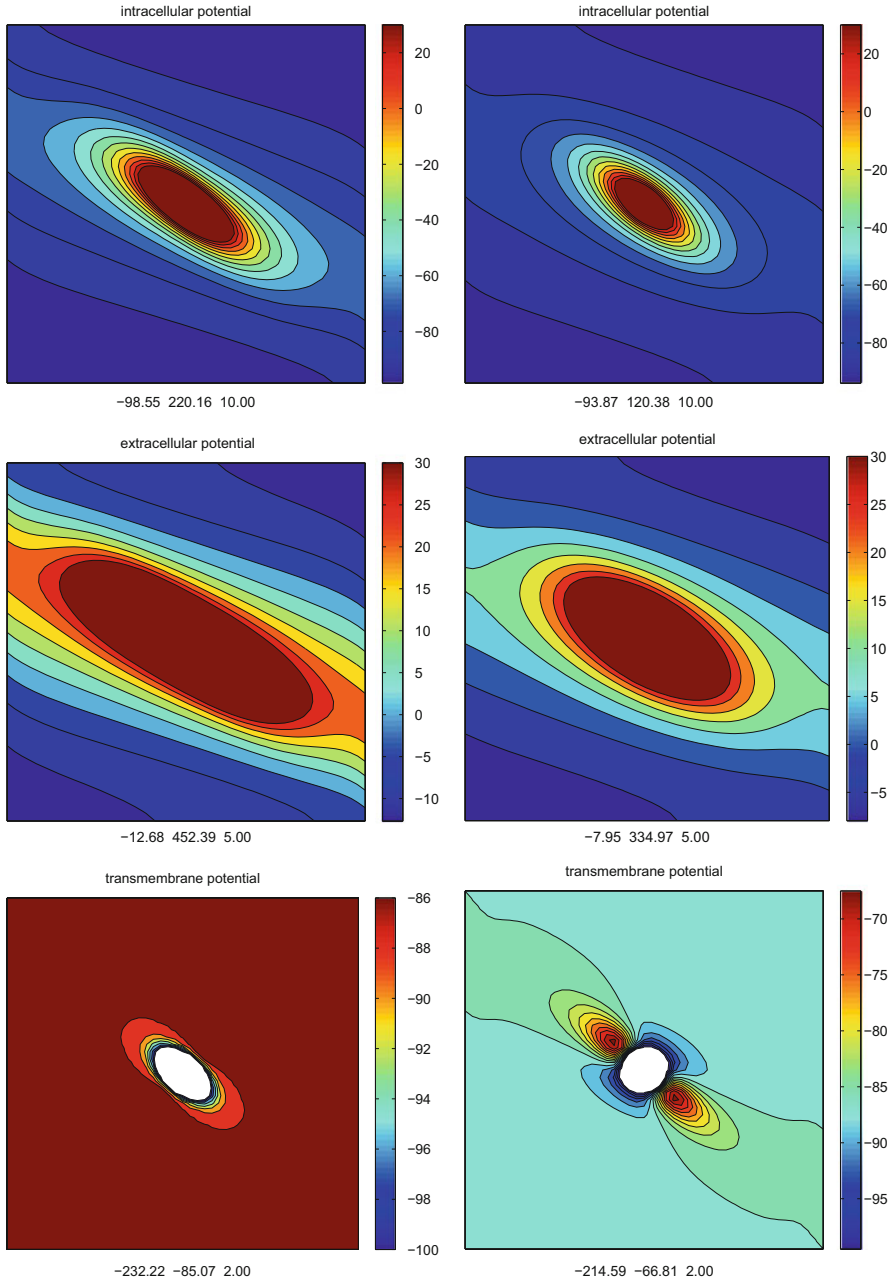
transmembrane potential

−276.21 −54.83 5.00
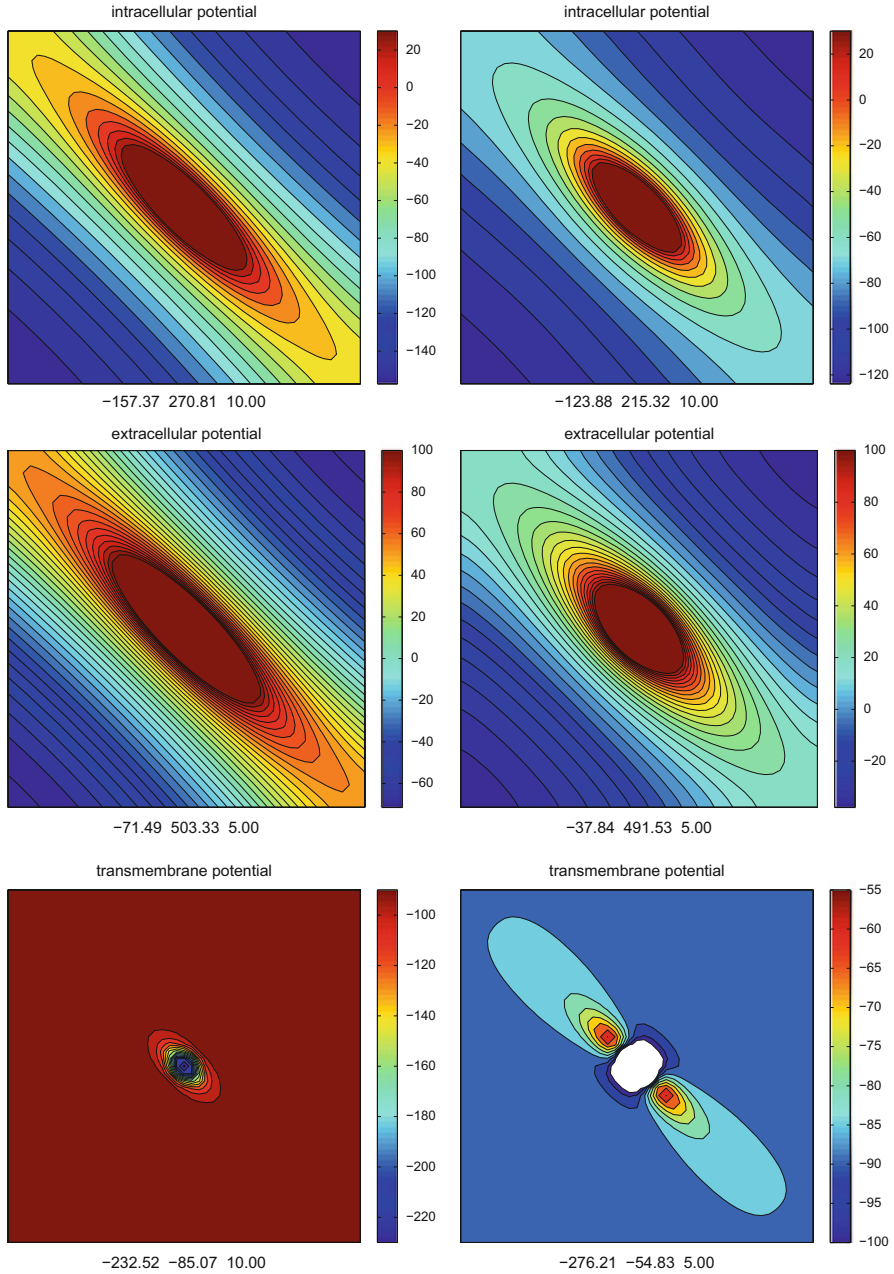
Fig. 9.2 Slab without transmural fiber rotation. Epicardial distribution of the intracellular potential (*top*), extracellular potential (*middle*) and transmembrane potentials (*bottom*) 2 ms after an anodal stimulus. *Right panels*: tissue with the unequal anisotropy ratios of Table 9.1. *Left panels*: tissue with equal anisotropy ratio. Below each panel are reported the minimum, maximum and step of the displayed map and the colorbar denotes the range of values of the displayed equipotential lines

Fig. 9.3 Slab with transmural fiber rotation. Epicardial distribution of the intracellular potential (*top*), extracellular potential (*middle*) and transmembrane potentials (*bottom*) 2 ms after an anodal stimulus. *Right panels*: tissue with the unequal anisotropy ratios of Table 9.1. *Left panels*: tissue with equal anisotropy ratio. Below each panel are reported the minimum, maximum and step of the displayed map and the colorbar denotes the range of values of the displayed equipotential lines

with different ratio of the two semiaxis. The difference of these two epicardial patterns yields a transmembrane potential distribution with the typical virtual electrode response (Fig. 9.2, bottom right panel). In fact, the tissue within and around the anodal electrode is negatively polarized (hyperpolarized) and it exhibits an epicardial *dog-bone* shape, developing perpendicularly to the epicardial fiber direction of $-45°$. Two regions of positive polarization (depolarization), i.e. two virtual cathodes, develop along the fiber direction adjacent to the concave parts of the epicardial virtual anode boundary.

The same anodal stimulation was applied to a tissue slab with transmural fiber rotation. In case of unequal anisotropy ratio, see right panels of Fig. 9.3, the epicardial transmembrane potential pattern exhibits a *virtual electrode response* with a twisted hyperpolarized *dog-bone* shaped region, which is not symmetric with respect to the epicardial fiber direction because of the counterclockwise fiber rotation from epicardium to endocardium. In fact, the equipotential surfaces inside the virtual cathode volumes, shown in Fig. 9.4, are shaped as two horns pointing counterclockwise when proceeding from the upper (epicardial) face to the lower (endocardial) face. On intramural sections parallel to the epicardial face, the equipotential lines inside the virtual anode preserve the same *dog-bone* shape as on the epicardium but with a counterclockwise rotation, thus reducing

Table 9.1 Conductivity coefficients of the intra and extracellular media in $S\,cm^{-1}$ and anisotropy ratios $\rho_{lt}^{i,e} = \sigma_l^{i,e}/\sigma_t^{i,e}$, $\rho_{tn}^{i,e} = \sigma_t^{i,e}/\sigma_n^{i,e}$

Unequal anisotropy					
Medium	σ_l^i	σ_t^i	σ_n^i	ρ_{lt}^i	ρ_{tn}^i
Intra	2.31724e−3	2.43504e−4	5.69083e−5	9.51622	4.27889
Medium	σ_l^e	σ_t^e	σ_n^e	ρ_{lt}^e	ρ_{tn}^e
Extra	1.54483e−3	1.04385e−3	3.7221e−4	1.47993	2.80447
Equal anisotropy					
Medium	σ_l^i	σ_t^i	σ_n^i	ρ_{lt}^i	ρ_{tn}^i
Intra	1.34511e−3	3.36278e−4	8.40695e−5	4	4
Medium	σ_l^e	σ_t^e	σ_n^e	ρ_{lt}^e	ρ_{tn}^e
extra	5.35282e−3	1.3382e−3	3.34551e−4	4	4
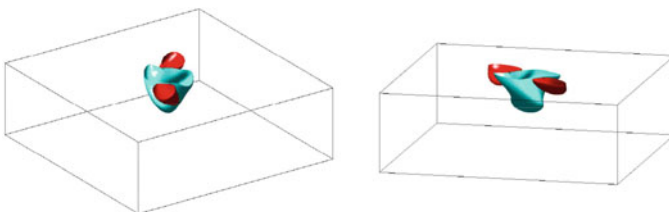
Fig. 9.4 Slab with transmural fiber rotation. Anodal stimulation applied to a slab with unequal anisotropy ratio. Two different views of the isopotential surfaces of the transmembrane potential distribution of values −88 and −75 mV, 2 ms after the beginning of the stimulation

their area and yielding a twisted tote bag; see Fig. 9.4. On the contrary, the same anodal stimulus applied to a slab with equal anisotropy ratios and transmural fiber rotation does not yield virtual cathodal regions but only an slightly twisted elliptical hyperpolarized region centered at the stimulation site; see Fig. 9.3, bottom left panel. This confirms that *virtual electrodes* can only be generated by bidomain models with unequal anisotropy ratios of the intra- and extracellular media. The formation of the two virtual cathodes elicited by the anodal stimulation explains why an anodal stimulation is able to excite the myocardium, as shown by the excitation sequence shown in Figs. 9.5 and 9.6 described below.

Anode make mechanism of excitability. We apply an anodal stimulus, lasting 10 ms and with an amplitude of 0.1112 mA, to the center of the epicardial face of a tissue slab at rest with unequal anisotropy and with the full membrane model. Figure 9.5 shows the snapshots of the simulated transmembrane po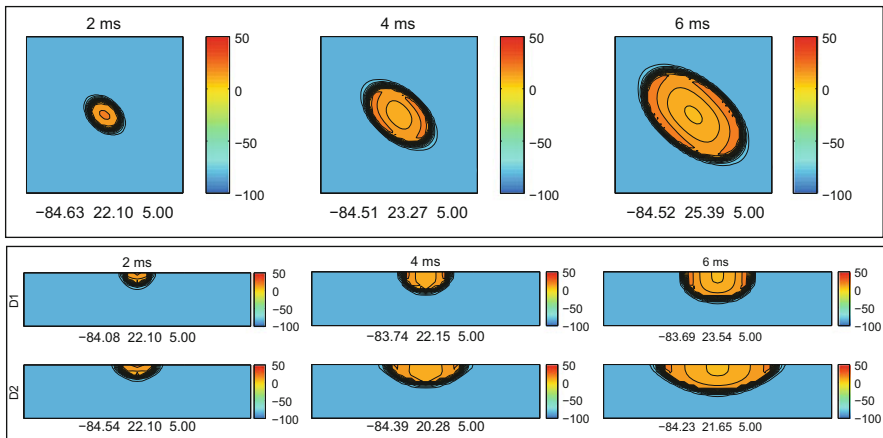tential distributions on the epicardial surface and on the transmural diagonal sections. The densely packed equipotential transmembrane lines indicate the location of the excitation layers, propagating on the epicardial face and transmurally. The snapshots in Fig. 9.5 reveal two distinct wavefronts propagating on the epicardial face and transmurally, which subsequently merge at epicardial and intramural levels. In fact, distinct activation wavefronts arise from two epicardial locations inside the virtual cathodes and first propagate in all directions on the epicardial face. In particular, they propagate outward and inward along the diagonal parallel to the fiber direction,
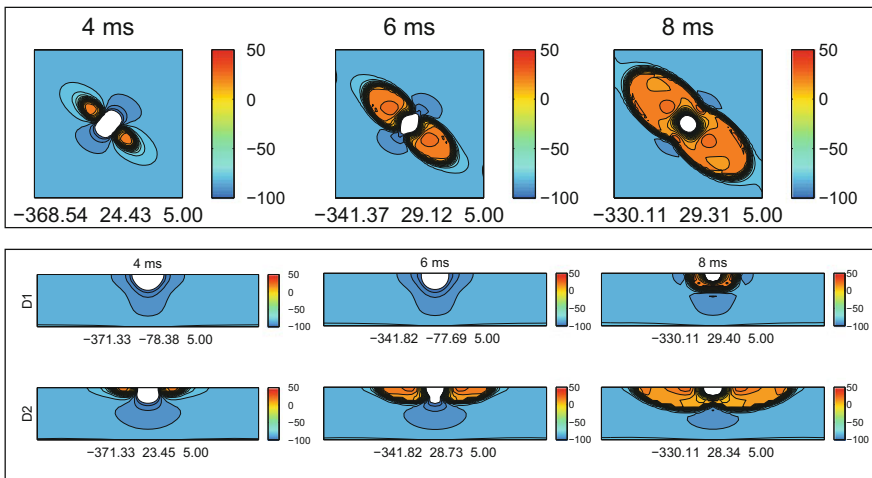
Fig. 9.5 Diastolic anode make excitation. Anodal stimulation during the diastolic interval with total current $I_{app} = 0.1177$ mA and 10 ms duration, applied to a slab with unequal anisotropic calibration and funny current. *Top panel*. Transmembrane potential distributions on the epicardial section at 3 time instants during the diastolic interval for cathode make stimulation. *Bottom panel*. Transmembrane potential distributions on the two diagonal transmural sections of the slab d1 (*top*) and d2 (*bottom*) at 3 time instants during the diastolic interval. Same conditions as in the *top panel* (Reproduced with permission from [131])
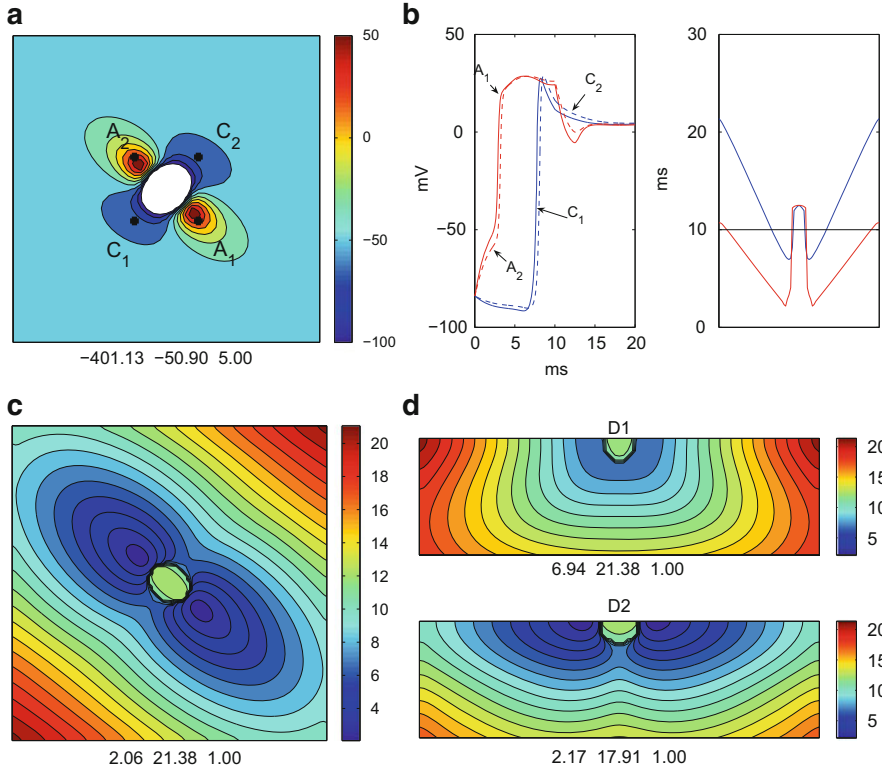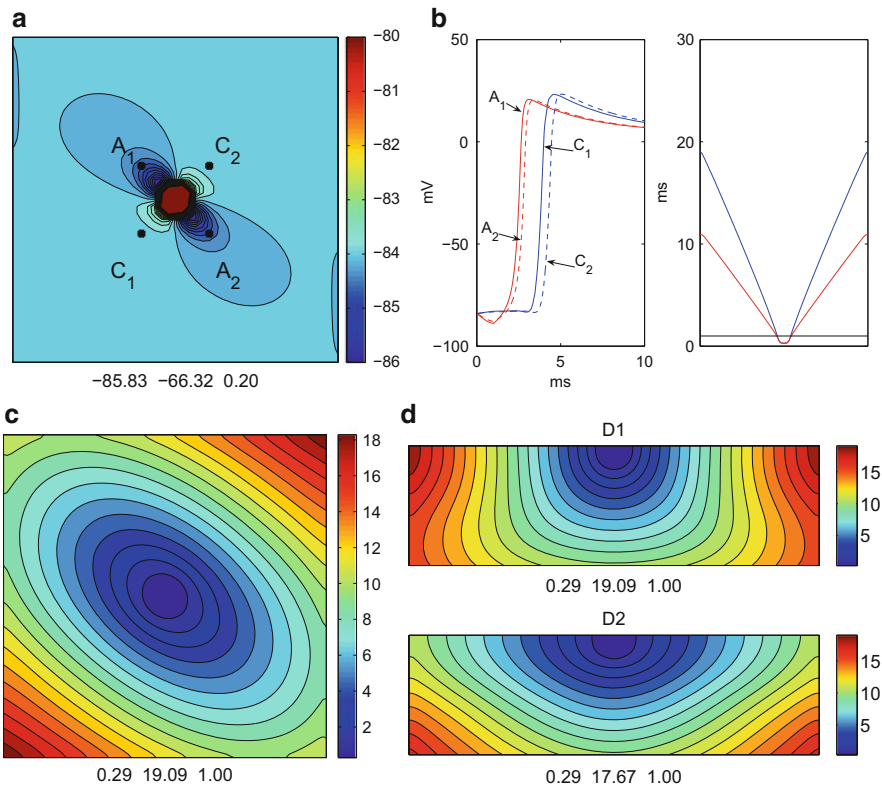
Fig. 9.6   Diastolic anode make excitation. Anodal stimulation during the diastolic interval with total current $I_{app} = 0.1177$ mA and 10 ms duration, applied to a slab with unequal anisotropic calibration and funny current. (**a**) Transmembrane potential distribution on the epicardial surface 0.5 ms after the beginning of the stimulation. (**b**)-left. Transmembrane potential waveforms in points C_1 (*blue continuous*), A_1 (*red continuous*), A_2 (*red dashed*) and C_2 (*blue dashed*), indicated in figure (**a**). (**b**)-right. Activation time profiles on the diagonal across (*blue*) and along (*red*) fibers. The *black line* indicates the instant (10 ms), when the stimulus ends. (**c**). Epicardial isochrones of activation time. (**d**). Isochrones of activation time on the two transmural diagonals. Same format as in Fig. 9.6 (Reproduced with permission from [131])

but, when the excitation isochrones reach points lying on a boundary of the virtual anode, a block of the inward propagation takes place during the stimulation interval, as also shown by the large slope of the activation time of Fig. 9.6b inside the anodal area. Therefore, from about 2 to 6 ms, two distinct activation wavefronts propagate outward, moving faster along fibers. At about 12 ms, the central epicardial area of the virtual anode is suddenly activated (0.5 ms), since it becomes excitable only after the stimulus turn off. Subsequently, all fronts finally merge in a unique large wavefront.

Excitation starts at about 2 ms, as shown by the activation time plot along the diagonal parallel to the epicardial fiber direction, displayed in Fig. 9.6b, thus inducing an anode make excitation. The isochrones of activation time on the epicardial surface and transmural diagonal sections (Fig. 9.6c, d) show clearly that the first triggered areas are the two epicardial sites located at the center of the virtual cathodes, generating two distinct excitation wavefronts propagating intramurally and separated by a central region within the virtual anode volume, which is inexcitable until the stimulus is turned off. These two wavefronts are open surfaces, each having a closed curve as rim lying on the epicardial surface. There are epicardial and intramural excitation pathways that, starting from the virtual cathodes, proceed turning around the boundary of the virtual anode volume and point toward its epicardial center. These pairs of pathways, coming from the virtual cathodes, cause the merging of the two wavefronts forming an activated tissue volume bounded by two intramural surfaces, one consisting of a wavefront moving toward the epicardial boundary and intramurally toward the endocardial face, and the other being the conduction block surface surrounding the inexcitable region, which is suddenly activated after the stimulus is turned off. From the inspection of the transmural isochrones pattern displayed in Fig. 9.6d, we observe that the major transmural effect of the virtual electrode polarization is the propagation of two wavefronts, separated by the transmural part of the virtual anode region, that merge 5 ms after the beginning of epicardial excitation at 1 mm depth.

Cathode make mechanism of excitability. We now consider the application of a cathodal stimulus, lasting 1 ms and with an amplitude of -0.0378 mA, to a slab with unequal anisotropy and full membrane model. Figure 9.7 shows the snapshots of the transmembrane potential distribution on the epicardial surface and on the two

Fig. 9.7 Diastolic cathode make excitation. Cathodal stimulation with total current $I_{app} = -0.0378$ mA and 1 ms duration, applied to a slab with unequal anisotropic calibration and funny current. Same format as in Fig. 9.5 (Reproduced with permission from [131])

diagonal transmural sections (bottom panel) at instants subsequent to the end of the stimulus pulse. The densely packed equipotential transmembrane lines indicates the location of the excitation layer, propagating on the epicardial face and transmurally. This excitation wavefront has an approximate ellipsoidal shape with the major axis and one of the two minor axes parallel and perpendicular, respectively, to the epicardial fiber direction of $-45°$; the remaining minor axis develops intramurally through the wall thickness and transversally to fiber layers.

Figure 9.8a illustrates the characteristic pattern of the epicardial transmembrane potential at 0.5 ms (at the beginning of the stimulation interval), with a *dog-bone* shaped virtual cathode, located around the site of the stimulation electrode, and two adjacent virtual anode areas. A cathode make excitation mechanism occurs, because activation arises before the end of stimulation as confirmed by the activation time plots at points A_1, A_2, C_1, C_2 along the two epicardial diagonals, displayed in Fig. 9.8b.

Fig. 9.8 Diastolic cathode make excitation. Cathodal stimulation during the diastolic interval with total current $I_{app} = -0.0378$ mA and 1 ms duration, applied to a slab with unequal anisotropic calibration and funny current. Same format as in Fig. 9.6 (Reproduced with permission from [131])

In order to describe in detail the origin, development and shape of the excitation wavefronts, we plot in Fig. 9.8c, d the activation time isochrones on the epicardial face and on two transmural diagonal sections. Excitation originates at locations surrounding the physical cathode and propagates outward in all epicardial and intramural directions, moving faster along fibers and assuming an approximate semi-ellipsoidal shape. The epicardial velocities of propagation along and across fibers are about 0.060 and 0.035 cm/ms, respectively, for unequal anisotropy, as also confirmed by the activation time slope in Fig. 9.8b.

9.1.3 Anode and Cathode Break Mechanisms

In order to study the anodal and cathodal virtual electrode phenomena during systole, an $S1 - S2$ stimulation protocol has been considered. The cathodal $S1$ stimulus is applied at the center of the epicardial surface and the entire activation-repolarization process is simulated. At 380 ms after the $S1$ stimulus, during the relative refractory period (RRP) of the repolarization phase, a cathodal or anodal $S2$ stimulus is applied at the same site of the $S1$ stimulus pulse. In the following, we denote by $T1$ anisotropy the anisotropic calibration of Table 9.1, and by $T2$ anisotropy a calibration with a 20 % reduction of intracellular anisotropy ratios, see also [131].

Anode break mechanism of excitability. We consider an $S2$ anodal stimulus of amplitude 0.2916 mA and duration 10 ms, in a slab with $T1$ anisotropy with the full membrane model. Figure 9.9 shows the snapshots of the transmembrane potential
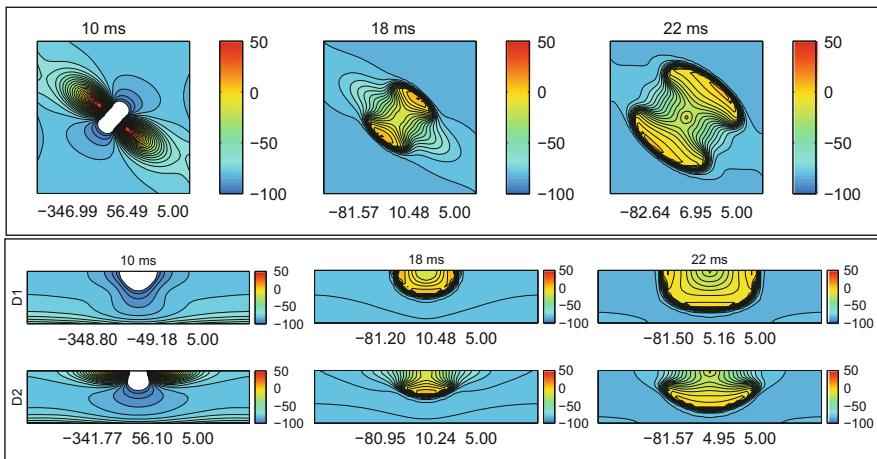
Fig. 9.9 Systolic anode break excitation. Anodal stimulation during the systolic interval (S1-S2 protocol, S2 at 380 ms) with total current $I_{app} = 0.2916$ mA and 10 ms duration applied to a slab with unequal anisotropy and membrane model with the addition of I_f, I_e, I_a. Same format as in Fig. 9.5 (Reproduced with permission from [131])

distribution at 10, 18, 22 ms after the end of the $S2$ anodal pulse. During the 10 ms of stimulation, a large *dog-bone* shaped region of strongly hyperpolarized tissue (virtual anode) is generated, while two virtual cathodes develop along the fiber direction near the concave portion of the anodal region, see Fig. 9.10. Although the virtual cathode volumes are depolarized above threshold (above -20 mV in Fig. 9.10a), anode make stimulation does not occur, because the surrounding regions are in the refractory period and still inexcitable, since the sodium inactivation gates are closed. When the stimulus is turned off, the combined effects of the membrane funny current I_f, of the electroporation current I_e and of the outward current I_a, depolarize the tissue inside the virtual anode, inducing anode break excitation with a delay of about 2 ms. The densely packed equipotential lines in the snapshots of Fig. 9.9 reveal the development of two epicardial excitation wavefronts propagating mainly in the direction across the epicardial fibers. The intramural diagonal sections exhibit a strongly different shape of the excitation layers, that originate from
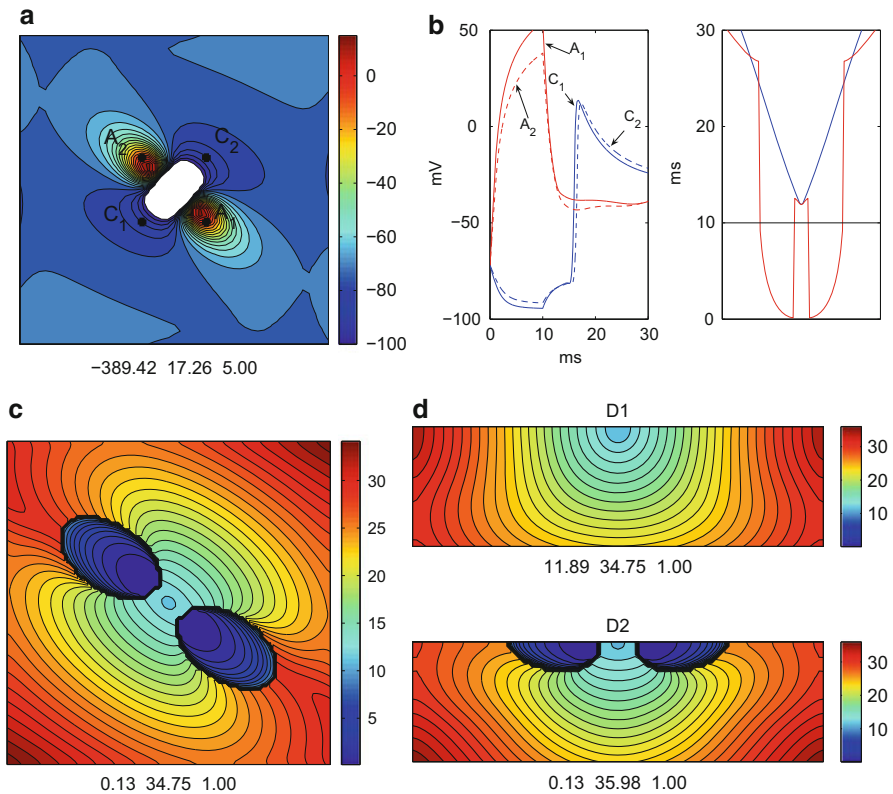
Fig. 9.10 Systolic anode break excitation. Anodal stimulation during the systolic interval (S1-S2 protocol, S2 at 380 ms) with total current $I_{app} = 0.2916$ mA and 10 ms duration applied to a slab with unequal anisotropy and membrane model with the addition of I_f, I_e, I_a. Same format as in Fig. 9.6 (Reproduced with permission from [131])

the center of the virtual anode and then reach and collide on the epicardial and intramural boundary of the virtual cathode volumes, which are inexcitable. Then the wavefront rims move around these obstacles until the activated tissue fully surrounds them.

In order to describe in detail the origin, development and shape of the excitation wavefronts, the isochrone lines drawn in Fig. 9.10c, d show clearly that the first activated point is the epicardial central site of the anodal region. Moreover, there are intramural excitation pathways that, starting from the epicardial anodal areas, first point toward the endocardium, progressively bend and proceed around the intramural boundary of the virtual cathodes, and finally point toward the epicardial face where a wavefront collision happens.

The initial phase of this anode break mechanism is due to the interplay between the I_f, I_e currents, yielding a transmembrane potential above the threshold excitability inside the virtual anode region, and the sodium channels dynamics. Therefore, we have a membrane-based trigger excitation mechanism. Apart from the different triggering process, the excitation wavefront pattern is strongly similar to the activation sequence generated by a cathodal pulse applied at the center of the epicardial surface in the presence of two obstacles (i.e. non conducting volumes), located inside the virtual cathode regions, which are inexcitable.

Figure 9.11e reports the transmembrane potential distributions after the end of an $S2$ anodal stimulus of 0.1512 mA amplitude, lower than in the previous case, and 10 ms duration. After the pulse turns off, the transmembrane potential in the virtual cathode regions decays toward the resting value, while that in the virtual anode area, due to the effect of the membrane funny current, depolarizes with a delay of about 9 ms from the end of the stimulus pulse. The propagating wavefront assumes an approximate semi-elliptical shape, as in the diastolic anode break excitation, because the virtual cathodes at the end of the stimulation interval are excitable again and do not behave like obstacles. The transition between the two systolic break excitation patterns happens smoothly when decreasing the strength of the anodal impulse. This is confirmed by the patterns displayed in Fig. 9.11, showing that decreasing the pulse amplitude the cathodal volumes become re-excitable and a dimple like inflection appears in the epicardial isochrones associated with slow propagation along the fiber direction (panel c). Decreasing further the intensity of the anodal stimulus allows an almost full re-excitability of the virtual cathodes after the stimulus end, yielding approximate semi-ellipsoidal propagating wavefronts with flat isochrone lines in the direction along fibers (panel e). Below the threshold of 0.1512 mA, anode break excitation does not occur.

The systolic anode break mechanism of excitation has been also simulated for a slab with $T2$ anisotropy and a strongly similar excitation sequences, depending on the amplitude of the stimulus pulse, was observed (not shown). The velocities of propagation along (across) fibers are 0.042 cm/ms (0.031) for $T1$ anisotropy and 0.040 (0.030) for $T2$. The degree of anisotropy influences weakly the stimulus threshold of the anode break excitation, which is slightly higher for $T2$ anisotropy (0.1809 mA) than for $T1$ anisotropy (0.1512 mA).
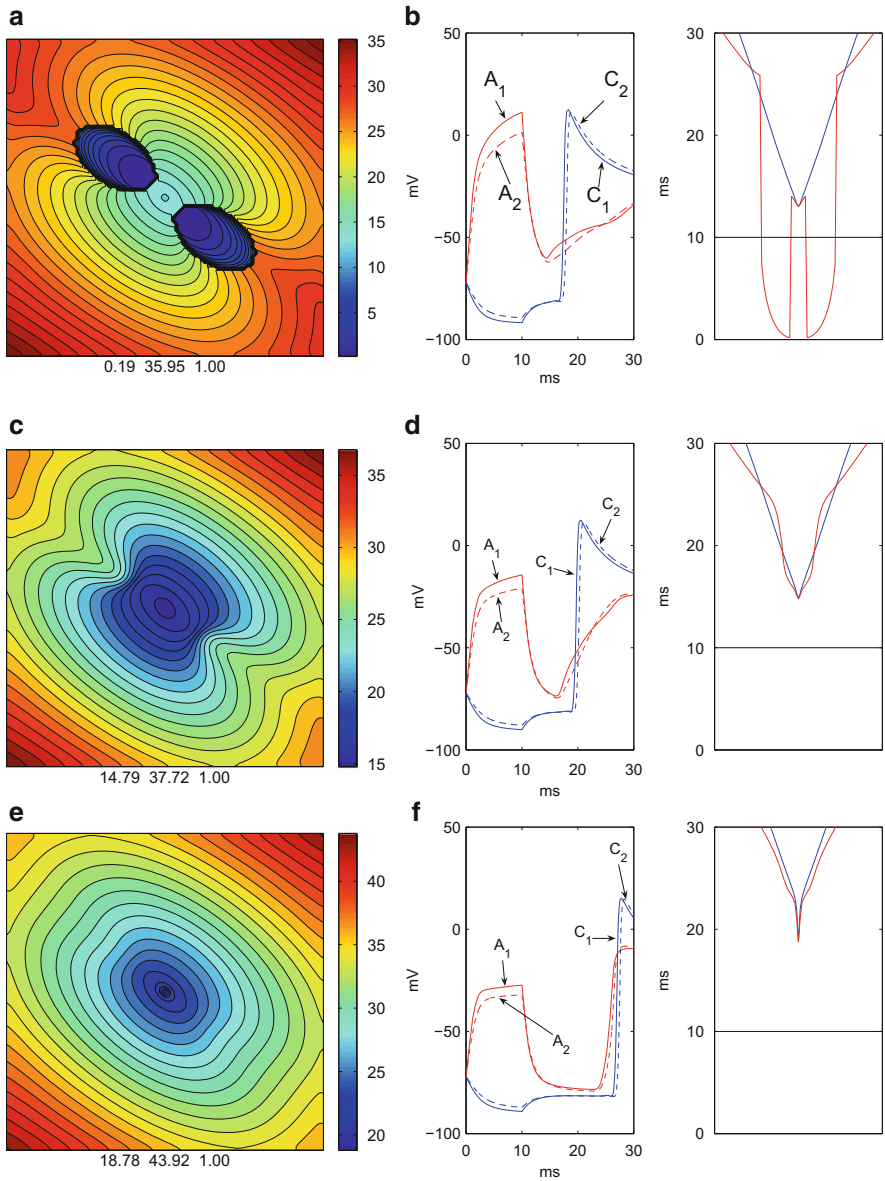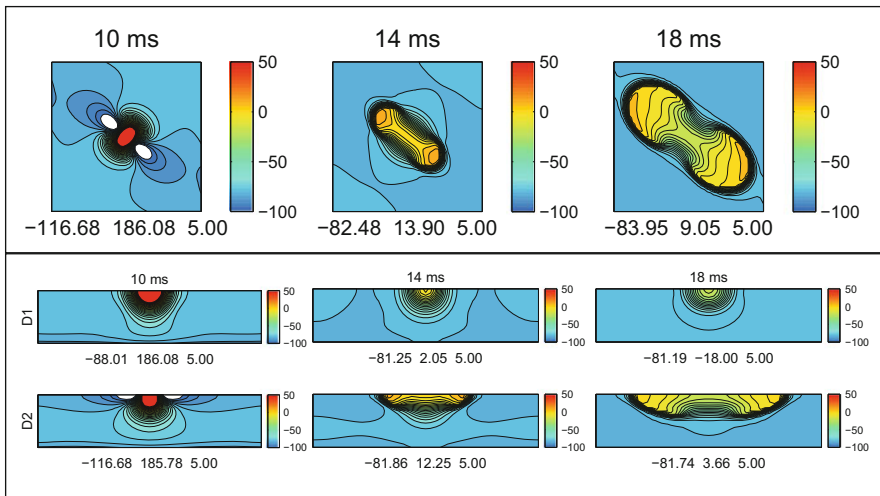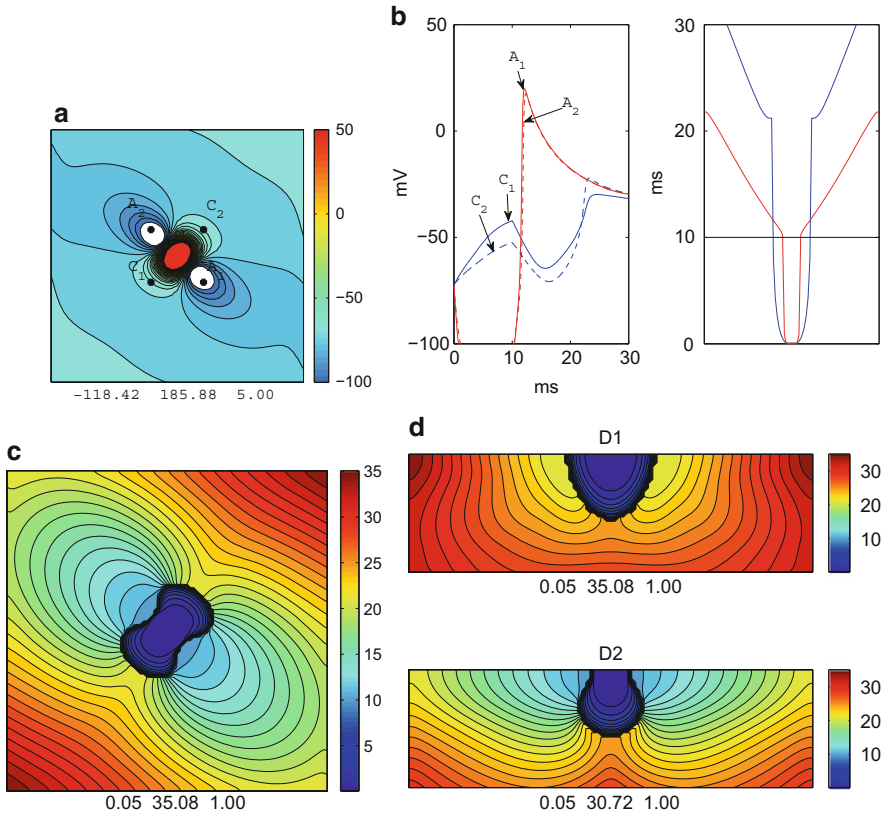
Fig. 9.11 Systolic anode break excitation. Anodal stimulations during the systolic interval (S1-S2 protocol, S2 at 380 ms) with total current $I_{app} = 0.2160$ mA (*first row*), $I_{app} = 0.1728$ mA (*second row*), $I_{app} = 0.1512$ mA (*third row*), and 10 ms duration applied to a slab with unequal anisotropy and membrane model with the addition of I_f, I_e, I_a. Panels (**a-c-e**): Epicardial isochrones of activation time. Panels (**b-d-f**)-left: Transmembrane potential waveforms in points C_1 (*blue continuous*), A_1 (*red continuous*), A_2 (*red dashed*) and C_2 (*blue dashed*), indicated in Fig. 9.8a. Panel (**b-d-f**)-right: Activation time profiles on the diagonal across (*blue*) and along (*red*) fibers. The *black line* indicates the instant (10 ms) when the stimulus ends (Reproduced with permission from [131])

Cathode break mechanism of excitability. An $S2$ cathodal stimulus of -0.2160 mA in amplitude and lasting 10 ms is applied to a slab with $T1$ anisotropy and full membrane current model. The tissue under the cathode is strongly depolarized and at the end of the $S2$ stimulus pulse, i.e. at $380 + 10 = 390$ ms, the transmembrane potential reaches a maximum value of about 185 mV, see Fig. 9.12. The epicardial transmembrane potential pattern exhibits a cathodal region around the site of stimulation with a pair of hyperpolarized regions (virtual anodes) developing along fiber near the concave parts of the cathodal region. Because the $S2$ stimulus is still applied during the relative refractory period, the depolarized tissue under the cathode is not excitable, thus cathode make excitation does not occur. After the termination of the stimulus, the hyperpolarized tissue around the virtual anode areas removes the inactivation of the sodium channels, rendering the tissue excitable. The electrotonic currents (charge diffusion), coming from strong depolarization under the cathodal area and directed toward the virtual anode, are able to originate simultaneously two activation wavefronts arising from the concave portions of the epicardial boundary of the virtual cathode. Thus, a cathode break excitation mechanism is induced immediately after the end of the stimulus pulse with a delay of 0.05 ms, as also confirmed by the inspection of the activation time plot of Fig. 9.13b.

Figure 9.12 displays the transmembrane potential distribution on the epicardial surface and on transmural sections at three instants after the start of the $S2$ cathodal stimulus, showing that two almost symmetrical wavefronts propagate on the epicardial face and at subepicardial levels, mainly along the fiber direction, assuming a semi-dumbbell shape.

Fig. 9.12 Systolic cathode break excitation. Cathodal stimulation during the systolic interval (S1-S2 protocol, S2 at 380 ms) with total current $I_{app} = -0.2160$ mA and 10 ms duration, applied to a slab with unequal anisotropy and membrane model with the addition of I_f, I_e, I_a. Same format as in Fig. 9.5 (Reproduced with permission from [131])

Fig. 9.13 Systolic cathode break excitation. Cathodal stimulation during the systolic interval (S1-S2 protocol, S2 at 380 ms) with total current $I_{app} = -0.2160$ mA and 10 ms duration, applied to a slab with unequal anisotropy and membrane model with the addition of I_f, I_e, I_a. Same format as in Fig. 9.6 (Reproduced with permission from [131])

From the isochrone lines displayed in Fig. 9.13c, we clearly see that the excitation sequence between 10 and 21 ms consists of two separated epicardial isochrones, being the rims of two distinct wavefronts, which collide at 12 ms. As a major transmural effect of the virtual electrode polarization, Fig. 9.13d shows that each of the two propagating open wavefront surfaces has a rim partly coinciding with a curve lying on the transmural boundary surrounding the virtual cathode volume. The transmural wavefronts merge at about 25 ms in the midwall, then, after collision, we have a unique wavefront propagating around the virtual cathode volume. Apart from the virtual cathode volume, the activation patterns associated to the diastolic anode make and to the systolic cathode break excitation mechanisms are similar, especially after the merging of the separated wavefronts, as shown by comparing the isochrones displayed in Figs. 9.13 and 9.6. Despite this qualitative similarity, Fig. 9.13 shows that, for cathode break excitation, the first activated sites are not

located in the epicardial central sites in the virtual anodes, but at the two concave portions of the boundary surrounding the virtual cathode volume. The trigger of the systolic cathode break mechanism is due to the interplay between the outward electrotonic current from the cathodal region and the membrane current dynamics at the locations around the virtual anode. The wavefront propagation coincides with an activation sequence moving around an obstacle (i.e. unexcitable volume) associated with the depolarized region under the cathode.

Cathode break excitability mechanism is simulated also for a slab with $T2$ anisotropy and exhibits a strongly similar excitation sequence (not shown). The epicardial velocities of propagation along (across) fibers are 0.049 cm/ms (0.030) for $T1$ anisotropy and 0.040 (0.030) for $T2$. These values are lower than the corresponding diastolic velocities, because the tissue during the RRP is less excitable than at rest. The degree of anisotropy influences the stimulus threshold of the cathode break excitation, which is higher for the weaker $T2$ anisotropy (-0.1075 mA) than for the stronger $T1$ anisotropy (-0.0578 mA). Finally, the cathode break mechanism occurs, as expected, independently of the membrane funny current incorporation (not shown).

9.1.4 Cathodal and Anodal Strength-Interval S-I Curves

In order to investigate the influence of the electroporation current I_e on the shape of the S-I curves, we have computed the S-I curves with both strong and weak I_e electroporation currents, associated to the electroporation characteristic voltages of $V_{ep} = 126$ mV and $V_{ep} = 258$ mV, respectively. Figure 9.14 reports the cathodal and anodal S-I curves for an orthotropic three-dimensional slabs using the augmented LRd model with the strong and weak electroporation currents.

S1-S2 stimulation protocol and S-I curves. We first apply at a small volume centered on the epicardial surface of the resting tissue an initial S1 cathodal ($i_{app}^e < 0$) stimulus of 0.0324 mA amplitude and 1 ms duration super-threshold initiating a propagating excitation wavefronts that sweeps the cardiac domain. At a suitable time (coupling interval) during the relative refractory period (RRP) a subsequent premature S2 cathodal ($i_{app}^e < 0$) or anodal ($i_{app}^e > 0$) stimulus (with duration 10 ms and amplitude specified case by case in the Results) is delivered at the same subepicardial thin volume and we simulate the resulting action potential propagation where the surrounding tissue has recovered its excitability properties. We compute, for the augmented LRd model and the orthotropic anisotropic slab, the cathodal and the anodal strength-interval (S-I) curve evaluating the minimal amplitude S2 cathodal or anodal pulse able to elicit an excitation propagating response thus, under which the tissue failed to respond. The values I_{stim} of S2 stimulation amplitudes reported are given in mA, obtained multiplying i_{app}^e times the volume of the stimulation site. We first determine the S-I curve for S1-S2 coupling interval increasing with 5 ms steps. Since propagating excitation can be elicited before and after the end of an S2 pulse, as usual, we call *make and break*
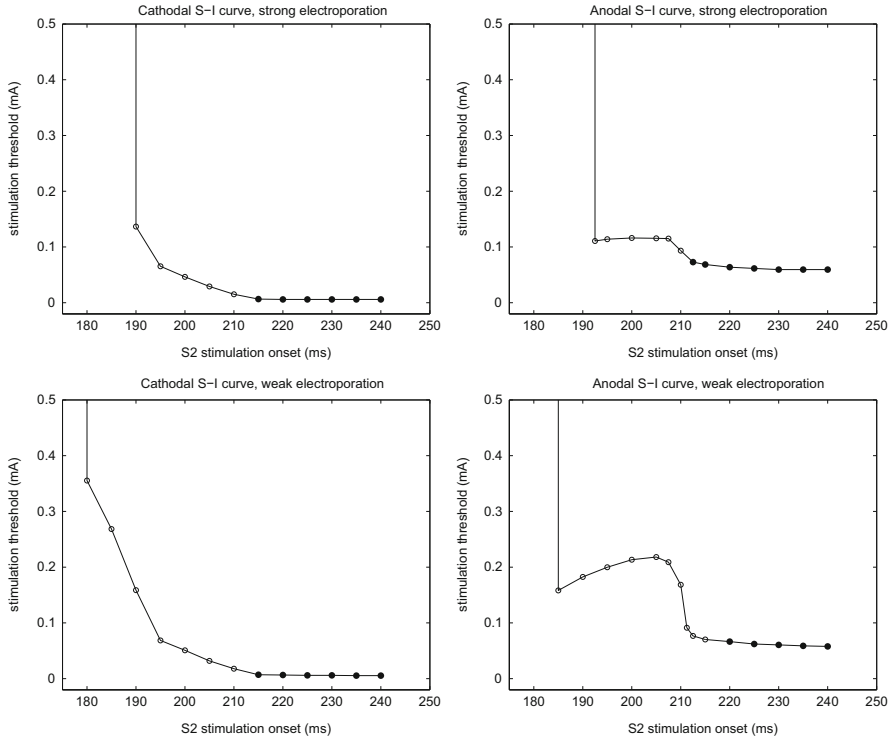
Fig. 9.14 Cathodal (*left*) and anodal (*right*) strength-interval curves for strong (*top*) and weak (*bottom*) electroporation. *Bold points* and *empty circles* denote make and break stimulation responses, respectively (Reproduced with permission from [132])

stimulation responses the two type of responses. When computing the anodal S-I curves described above, we refine the step from 5 to 1.25 ms around the break/make transition in order to better resolve the S-I curve in this interval.

S-I curves. Both cathodal S-I curves display a monotonically decreasing behavior in the portions corresponding to the *cathode break stimulation response* and the subsequent phase corresponding to the *cathode make stimulation response*, with an almost constant threshold stimulus strength. The use of strong electroporation has a weak effect on the make portion of the S-I curve, while on the break portions it induces a slight decrease of the threshold stimulus strength with a shift of the effective refractory period which is increased from 180 to about 190 ms.

The anodal S-I curves displayed in Fig. 9.14 exhibit the following main features: a dip close to the effective refractory period, a subsequent plateau or dome phase corresponding to the *anode break stimulation response* and a sudden decrease close to the end of the relative refractory period, separating the anode break and make mechanisms. By relative refractory period, we mean the time interval, between the effective refractory period and the resting phase, where another action potential can

be elicited only by a sufficiently strong stimulus. The comparison of the strong and weak electroporation S-I curves shows no significant threshold variation in the make portion of the S-I curve, while the presence of weak electroporation increases the threshold values in the break phase, with a more sudden and large jump in the transition from *break* to *make stimulation responses*. Weak electroporation also produces a slight increase of the relative refractory period, (from 20 to 27 ms). The break portion of the anodal S-I curves exhibits a typical dip followed by a dome and a subsequent sudden fall sharing the same features of the S-I curves observed experimentally in [146, 324, 480] and computed in [255, 256, 428]; we refer to [428] for an explanation of these features.

In the cathodal S-I curve, the transition from break to make stimulation responses occurs during the coupling interval between 210 and 215 ms. In the anodal S-I curve, the same transition occurs between 215 and 220 ms with weak electroporation and between 210 and 212.5 ms with strong electroporation. We remark that any pulse amplitude above threshold yields the same type of response (make or break) as the threshold response, except during a short interval around the transition between *break* and *make stimulation responses.*

9.2 Anisotropic Propagation of Excitation and Recovery Fronts

In this section, we present some simulations of excitation and repolarization sequences on myocardial slabs of different sizes, showing how the distribution of the action potential durations (APD) is influenced by both the anisotropic electrical conduction and the fiber rotation. This influence occurs in spite of the homogeneous intrinsic properties of the cell membrane. The APD dispersion patterns are closely correlated to the anisotropic curvature of the excitation wavefront. More detailed results can be found in [123].

Parameter calibration. In the following, we shall assume that both the intra-cellular coupling and the extracellular matrix are uniform, i.e. the intra- and extra-cellular conductivity coefficients along and across fibers $\sigma_{l,t,nu}^{i,e}$ are independent of position. The conductivity coefficients given in Table 9.2 have been calibrated so that the associated propagation velocities $(\theta_l, \theta_t, \theta_v)$ of ideal plane wavefronts can be conservatively estimated by $(60, 25, 10)$ cm s^{-1}, respectively. These estimates have been obtained by simulating the activation sequence elicited by a vertex stimulation of a 2D rectangular sheet of dimensions 3×3 cm^2 with fibers parallel to a side. The excitation wave front propagated along fiber with a velocity of 58.7 cm s^{-1}, while the velocity across fiber was 24.6 cm s^{-1} if the conductivity coefficient was $\sigma_t^{i,e}$ or 9.3 cm s^{-1} if the conductivity coefficient was $\sigma_v^{i,e}$. Due to the convexity of the fronts, i.e with a negative curvature sign, the wave front velocities were lower than those of plane fronts propagating parallel or perpendicular to fiber direction, as expected. In the following, we will consider 3D parallelepipedal slabs and we

Table 9.2 Parameters calibration for numerical tests

$\chi = 10^3\,\mathrm{cm}^{-1}$, $C_m = 1\,\mu\mathrm{F/cm}^2$
$\sigma_l^e = 2 \cdot 10^{-3}\,\mathrm{S\,cm}^{-1}$, $\sigma_l^i = 3 \cdot 10^{-3}\,\mathrm{S\,cm}^{-1}$
$\sigma_t^e = 1.3514 \cdot 10^{-3}\,\mathrm{S\,cm}^{-1}$, $\sigma_t^i = 3.1525 \cdot 10^{-4}\,\mathrm{S\,cm}^{-1}$
$\sigma_v^e = \sigma_t^e/\mu_1$, $\sigma_n^i = \sigma_t^i/\mu_2$
$\mu_1 = \mu_2 = 1$ axisymmetric case, $\mu_1 = 2, \mu_2 = 10$ orthotropic case

will identify the upper and lower face planes with the epicardial and endocardial surfaces, respectively. The minimal velocity $\theta_v = 10\,\mathrm{cm\,s}^{-1}$ corresponds to a propagation across fibers on intramural planes parallel to the epicardial surface, while the velocity $\theta_t = 25\,\mathrm{cm\,s}^{-1}$ corresponds to a propagation across fibers in directions perpendicular to the epicardial plane. The initial conditions are $(\mathbf{u}_i^0, \mathbf{u}_e^0) = (-84, 0)\,\mathrm{mV}$, so that $\mathbf{v}^0 = -84\,\mathrm{mV}$ and we apply a large stimulus of $200\,\mu\mathrm{A}$ for 1 ms on a small volume (3 or 5 mesh points in each direction). The slow inward current I_{si} in the LR1 model is scaled by a factor 2/3. This yields an action potential duration (APD) of about 265 ms.

The fibers rotate intramurally linearly with depth for a total amount of 90°, i.e. $\mathbf{a}_l(\mathbf{x}) = u_{ex} \cos\alpha(r) + u_{ey} \sin\alpha(r), \alpha(r) = \pi(1 - 2r)/4, \; r \in [0, 1]$. The fiber direction on the epicardium is $-45°$ with respect to the horizontal side of the panels displayed in Figs. 9.15–9.17, while on the endocardium is 45°. In the orthotropic anisotropy case, we choose $\mathbf{a}_v = u_{ex} \sin\alpha(r) - u_{ey} \cos\alpha(r)$ and $\mathbf{a}_t = u_{ez}$. In order to strengthen the role played by the rotational anisotropy, the counter-clockwise (CCW) intramural fiber rotation amounts to 90° on a slab thickness of 0.5 cm, with direction varying linearly from epicardium to endocardium. The stimulus was applied at an appropriate epicardial vertex or at the center of the slab. In all cases, the finite element mesh size is $h = 0.1\,\mathrm{mm}$.

9.2.1   Excitation and Repolarization Sequences

In order to study the influence of fiber rotational anisotropy on the activation and repolarization sequences and on the APD distribution, we simulate the electrical activity in a slab of cardiac tissue, from the onset of excitation to the end of repolarization. We consider the following test problems:

- Bidomain-LR1 model on a $2 \times 2 \times 0.5\,\mathrm{cm}^3$ slab, vertex stimulation (orthotropic (left Panel) and axisymmetric (right Panel) in Fig. 9.15 top);
- Monodomain-LR1 model on a $2 \times 2 \times 0.5\,\mathrm{cm}^3$ slab, vertex stimulation (orthotropic (left Panel) and axisymmetric (right Panel) in Fig. 9.15 bottom);
- Monodomain-LR1 model on a $4 \times 4 \times 0.5\,\mathrm{cm}^3$ slab (central stimulation, axisymmetric in Fig. 9.16, orthotropic in Fig. 9.17).
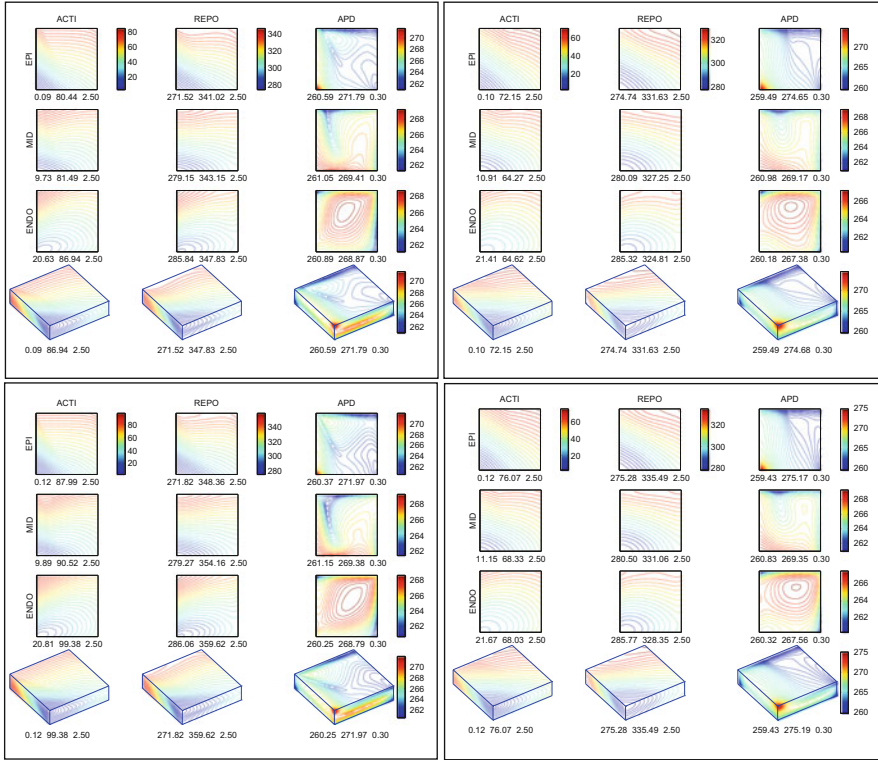
Fig. 9.15 Orthotropic (*left Panels*) and axisymmetric (*right Panels*) Bidomain Models (*top row*) and Monodomain Models (*bottom row*) on a slab $2 \times 2 \times 0.5\,\text{cm}^3$ with vertex stimulation and homogeneous cellular membrane properties. Patterns of level lines of the depolarization time (*first column ACTI*), repolarization time (*second column REPO*) and action potential duration (*third column APD*) on epi, midwall and endocardial planes and at the bottom 3D view. Reported below each panel are the maximum, minimum and step in ms of the displayed map (Reproduced with permission from [123])

9.2.1.1 Bidomain Model: Orthotropic Versus Axisymmetric Anisotropy

In order to contain the computational cost required by the simulation of an entire QT interval (excitation plus recovery) using the Bidomain model, we consider a slab of dimensions $2 \times 2 \times 0.5\,\text{cm}^3$.

Previous experimental studies (see e.g. Burgess et al. [67], Osaka et al. [364], Gotoh et al. [208], Taccardi et al. [512]) indicate that the main effects of anisotropy on the APD occur in regions where the wave fronts move across fibers. To best illustrate cross-fiber propagation, we oriented the epicardial fibers along a diagonal and we stimulated a vertex situated at one end of the other diagonal, so that the elicited wave fronts move mainly across fiber on the epicardium (see Fig. 9.15 top).
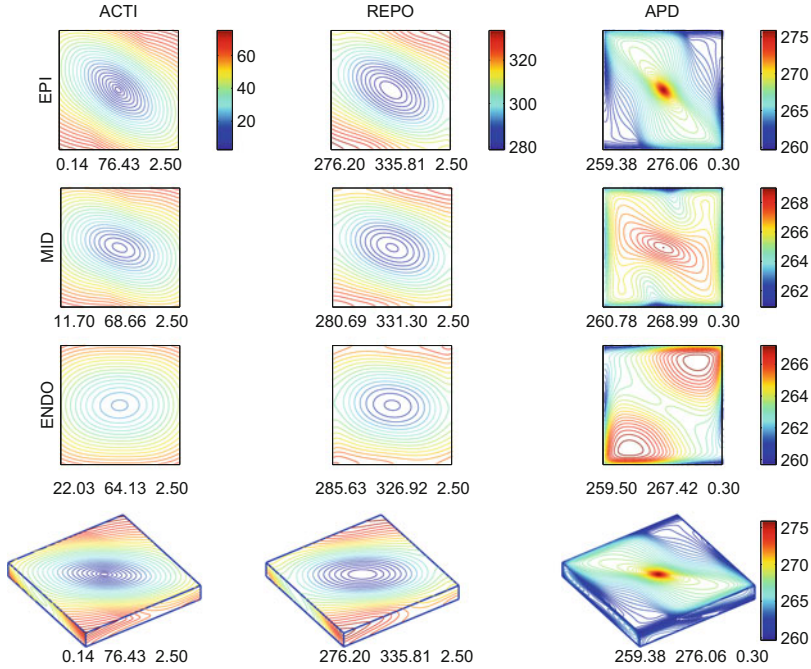
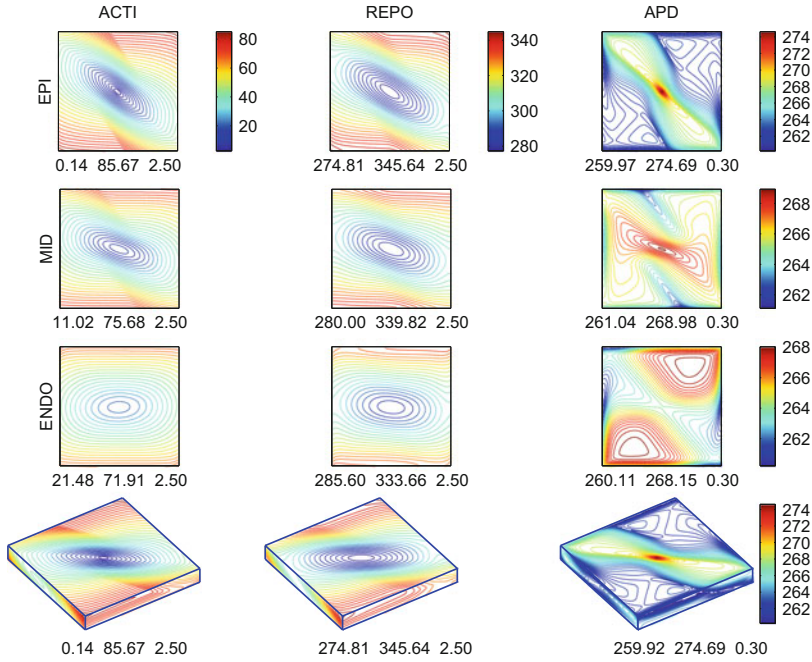**Fig. 9.16** Axisymmetric monodomain model with intramural fiber rotation on a slab $4 \times 4 \times 0.5 \, \text{cm}^3$ with central epicardial stimulation. Same format as in Fig. 9.15 (Reproduced with permission from [123])

The macroscopic sequences of excitation and recovery and the spatial distribution of the APDs are illustrated in Fig. 9.15 top, that relates to a Bidomain model implemented in a slab with orthotropic and axisymmetric anisotropy, respectively. Both anisotropic slabs exhibit similar qualitative features of the patterns of excitation, recovery and APD distribution.

Activation sequence. It is well known that in the presence of rotational anisotropy, intramural excitation, starting from an epicardial stimulation site, first proceeds toward the endocardium but subsequently, due to fiber rotation, comes back pointing toward the epicardial plane (see e.g. [67, 102, 116, 184, 506, 508, 509]). Due to these intramural return pathways, propagation undergoes an acceleration, in particular in epicardial areas where the excitation moves mainly across fibers. In the orthotropic slab, the lower epicardial velocity across fiber (as compared to axisymmetric model) causes the appearance of more pronounced dimple-like inflections.

Repolarization sequence. Repolarization wave fronts exhibit a somewhat smoother shape and faster propagation compared with the excitation sequence, as shown by the isochronal lines on the epi, midwall and endocardial planes. Indeed, the epicardial plane is fully activated in about 80.35 ms and repolarizes in 69.50 ms,

Fig. 9.17 Orthotropic monodomain model with intramural fiber rotation on a slab $4 \times 4 \times 0.5\,\mathrm{cm}^3$ with central epicardial stimulation. Same format as in Fig. 9.15 (Reproduced with permission from [123])

giving rise to a total amount of APD dispersion of 11.2 ms in the orthotropic case. In the axisymmetric case, the same section is fully activated and repolarized in about 72 and 57 ms, respectively, with an APD dispersion of 15 ms.

APD distribution. The main common features, displayed by the APD on the epicardial, intramural and endocardial planes, in both the anisotropic slabs are: a maximum located at the epicardial stimulation site, higher APD values in regions where propagation is mainly along fibers, an intramural valley configuration of APD reduction, a relative minimum in areas of front-boundary collision, and a maximum located on the endocardial plane. A detailed comparison between orthotropic and axisymmetric cases shows that the former emphasizes some anisotropic features displayed by the APD distribution pattern. In particular, the presence of a dimple-like inflection exhibited by the excitation isochronal lines on intramural horizontal planes ranging from the epicardium to the midwall, and of a corresponding finger-shaped valley of low APD are more pronounced in the orthotropic slab, as shown e.g. by comparing the midwall panels of Fig. 9.15 top.

We remark that the axisymmetric and the orthotropic slabs are fully excited in about 72 and 87 ms, respectively. The extinction area of excitation is located at a vertex on the endocardium in the orthotropic slab, whereas it appears at the

epicardium in the axisymmetric slab. This is the result of the reduced velocity θ_t across fibers on planes parallel to epicardium being lower than the transmural velocity θ_v across the slab thickness, combined with the effects of the intramural return pathways of the excitation toward the epicardium. The main quantitative discrepancy between the two slabs lies at the epicardium, where different activation and repolarization isochrone shapes in the front-boundary collisions are present; they are associated with the appearance, in the APD pattern of the orthotropic slab, of an epicardial relative maximum located at a side of the finger-shaped valley of APD reduction which started from a relative minimum located at the boundary.

The APD distributions show several common features in our different simulations, namely: APDs are longest near the pacing site and tend to be shorter near the front-boundary collisions. Moreover, the spatial distribution of APDs are influenced by the anisotropic motion of the wave front. Thus, in a slab with homogeneous cellular membrane properties, i.e. where all individual cells have the same intrinsic transmembrane action potential, the rotational anisotropy produces an APD variability displaying an anisotropic pattern. The orthotropic anisotropy further increases the distortion of the propagating wavefront, emphasizing the corresponding anisotropic features of the APD dispersion of the axisymmetric case.

9.2.1.2   Vertex Stimulation of Anisotropic Models: Bidomain Versus Monodomain Models

Due to the high computational cost of the Bidomain model on a slab with dimensions $2 \times 2 \times 0.5\,\text{cm}^3$, we performed simulations including both excitation and recovery using the Monodomain model on the same slab with orthotropic and axisymmetric anisotropy. We focus the comparison on the shape and propagation of the excitation and recovery isochrones, as well as the spatial distribution of the APD.

Activation and repolarization sequences. The comparison of Fig. 9.15 top and bottom for both orthotropic and axisymmetric slabs evidences a strong qualitative similarity between the simulated isochrones of the Bidomain and Monodomain models. This fairly good match is confirmed by the values of the correlation coefficient $\text{CC}(x, y) = \frac{1}{n}(\sum(x_i - \overline{x})(y_i - \overline{y}))/(\sigma_x \sigma_y)$, where $\overline{x} = \frac{1}{n}\sum x_i$ is the arithmetic mean of x, $\sigma_x = \sqrt{\frac{1}{n}\sum(x_i - \overline{x})^2}$ is the standard deviation of x and analogously for $\overline{y}$ and σ_y. The correlation coefficient CC for the activation times of the two models in the entire slab amounts to 0.9971 in the orthotropic case and to 0.9997 in the axisymmetric case. Similarly, the CC for the repolarization times on the entire slab amounts to 0.99976 and to 0.9998 in the orthotropic and axisymmetric cases, respectively. The wave front velocity depends on the propagating direction and the Bidomain and Monodomain models exhibit a different anisotropic dependence. In spite of this difference, we found not only a strong

qualitative agreement but also a small quantitative difference in the activation and repolarization sequences between the Monodomain and the Bidomain model. The relative error RE $= \|T_B - T_M\|_2/\|T_B\|_2$ (with $\|\cdot\|_2$ the Euclidean norm) between the activation times T_B, T_M of the Bidomain and Monodomain models is 0.115 in the orthotropic case and 0.063 in the axisymmetric case. The relative error between the repolarization times of the two models is 0.018 in the orthotropic case and 0.009 in the axisymmetric case. We remark that the repolarization isochrones simulated by both models, especially on the epicardial plane, exhibit a smoother dimple-like inflection than that appearing in the excitation sequence.

APD distribution. Both orthotropic model simulations exhibit a common narrow valley of low APD values (see Fig. 9.15 top and bottom), corresponding to the pathway joining the dimple-like inflections appearing in the epicardial and intramural excitation isochrones. These dimple-like inflections are a reflection of the intramural pathways of excitation that, starting from the stimulation site, first proceed toward the endocardium but subsequently, due to fiber rotation, return toward the epicardial plane. Therefore, the narrow valley configuration in the APD distribution is an effect of the rotational anisotropy. We found a good qualitative and quantitative agreement between the APD related to the Bidomain and Monodomain models, since CC and RE on the entire slab are 0.9534 and 1.882 $\times 10^{-3}$ in the orthotropic case, while they are 0.987 and 8.9 $\times 10^{-4}$ in the axisymmetric case.

The previous comparison validates the use of the Monodomain model as a tool for investigating the *qualitative macroscopic features* of the activation and repolarization sequences, as well as the APD distribution. Therefore, the high costs required, at present, by the Bidomain simulations can be avoided by implementing the Monodomain model, which qualitatively preserves the anisotropic features of the APD distribution.

9.2.1.3 Central Stimulation in Anisotropic Monodomain Models

To further analyze the factors that modulate the APD in a model with homogeneous membrane properties, we simulate the excitation and recovery sequences elicited by a central epicardial stimulation, in case of axisymmetric and orthotropic Monodomain slabs with intramural fiber rotation (Figs. 9.16 and 9.17).
The comparison between the APD dispersion patterns should allow us to detect the role played by:

- The different phases of the wave front sequence of excitation and recovery (i.e. the initial and extinction wave fronts, the occurrence of front-boundary collisions) and the wave front shape;
- The anisotropic electrical conductivity (i.e. the different electrotonic currents flowing along and across the fiber direction);
- The intramural fiber rotation, which causes the occurrence of return pathways of excitation and recovery toward the stimulated plane.

Since similar observations apply to both cases, in the results description we refer, preferentially, to the orthotropic case in which some features are more pronounced.

Activation and recovery sequences. Stimulation at the center of the epicardial face produces approximately elliptical excitation and repolarization isochrone lines, a clear sign of their anisotropic propagation. Actually, activation and repolarization spread symmetrically with respect to the center of the epicardial face. The major axes of the oblong excitation isochrones are nearly parallel to the epicardial fiber direction ($-45°$ with respect to the horizontal sides of the panels in Figs. 9.16 and 9.17) while those associated to repolarization isochrones are rotated CCW with respect to epicardial fiber direction. The oblong epicardial isochrones are slightly rotated and bulging CCW with respect to the fiber direction, see Figs. 9.16 and 9.17 Panels ACTI, REPO. The spread of excitation and the sequence of recovery show an acceleration in the cross-fiber direction. Also, the excitation isochrones show an inflection corresponding to a dimple-like inflection of the wave front. These findings, i.e. the accelerating propagation across fibers, the bulging and the dimple-like inflection of the isochrones, are attributed to the influence on the epicardium of the activation and recovery processes through the deeper layers, where the fiber direction rotates CCW relative to epicardial fibers.

Proceeding from epi- to endo-cardium, on the intramural planes parallel to the epicardium the spacing between excitation (recovery) isochrones increases, the wave front shapes become rounder and we observe a transmural twisting of the isochrones, i.e. the major axis of the oblong isochrones progressively rotates CCW with increasing depth. However, their rotation lags behind the rotation of the fiber direction at corresponding depths (see e.g. the Panels MID of Fig. 9.17, where the fiber direction is horizontal). It is worth mentioning that the total transmural rotation of the recovery isochrones is slightly less than the rotation of the excitation isochrones. The spacing between the recovery isochrones, in the sections parallel to the epicardial face, is greater than the corresponding excitation spacing, denoting a faster motion of the recovery fronts.

On the endocardial plane, both the excitation and recovery front-boundary collision first occur at the center of the face. This happens because our current model does not incorporate the epi- endocardial obliqueness of the fibers (Streeter [498], Taccardi et al. [507]), that was included in some of our previous simulations (Colli Franzone et al. [116, 116]). Subsequent excitation and recovery isochrones have a well rounded, elliptical shape centered at the point of endocardial BKT of the excitation and repolarization wave front with the endocardial plane. On the endocardium, the large spacing between successive isochrones indicates a fast excitation and repolarization progression with a maximum apparent speed at the BKT point where a sudden change of the wave front curvature occurs and the high curvature values bring about high speeds of propagation around the BKT site, see e.g. Colli Franzone et al. [102], Keener [268], Fast et al. [169]. The results for the excitation sequence confirm earlier findings of Colli Franzone et al. [102, 116] obtained with an eikonal approach, and are in agreement with previous experimental data (Taccardi et al.

[507]). The results relating the repolarization sequence are the main novelty of this work.

APD distribution. Adding the intramural fiber rotation to the axisymmetric or orthotropic anisotropic tissue, the epicardial and intramural APD distribution exhibit a pattern displaying elongated level lines, (see Figs. 9.16 and 9.17), surrounding the central point of the epicardial or intramural plane, corresponding to the stimulation site and to first point reached by the excitation wave front. At first, the pattern exhibits a quasi-elliptical shape with the major axis correlated with that of the excitation isochrones. This indicates that APD decreases more rapidly when moving away from the center of the face in the cross-fiber direction than along fibers. Subsequently, the isochrones lose the quasi-elliptical shape but are still stretched along a preferential direction, which does not coincide with the local fiber direction, except at the epicardial level, see Panel MID in Figs. 9.16 and 9.17. The APD decrease shows that the velocity of the repolarization front exceeds the one of the activation front, both along and across the preferential directions, and moreover the difference between the repolarization and the activation velocities is greater across this direction, as confirmed by the more rapid APD decrease.

At some distance from the center of the face, the stretched portion of the level lines of the APD, due to boundary effects, becomes straight while the presence of valleys of APD reduction induces hollow, dog-bone profiles, more pronounced in the orthotropic slab (see Fig. 9.17). The total dispersion in the axisymmetric and in the orthotropic slabs amount to 16.7 and 14.8 ms, respectively.

On the intramural sections (from subepicardial (not shown) to midwall ones), two valleys of decreasing APD values occur. Each valley exhibits a minimum located at the boundary of the slab. These narrow valleys of low APD values are located in the regions where excitation isochrones exhibit a dimple-like inflections. These depression valleys are not related to boundary collisions but are strictly correlated with the anisotropic influence of the intramural fiber rotation.

In the endocardial plane, the APD distribution displays a saddle point at the endocardial BKT; the APD increases reaching a maximum when moving away from the BKT point in a direction parallel to the endocardial fibers of 45° CW, while in the cross-fiber direction the APD decreases toward two minima located at the boundary and corresponding to front-boundary collision points; the axis joining the two maxima is roughly parallel to the endocardial fiber direction of 45° CW and the two maxima are separated by a valley of APD reduction.

We remark that the anisotropic features appearing in the APD pattern are more pronounced in the orthotropic case; because these emphasized effects are likely to help in the investigation of their origin and due to the recent interest about the influence of orthotropic myocardial structure on the cardiac electric activity (see LeGrice et al. [292,293], Costa et al. [137] for anatomical studies and Colli Franzone et al. [121] for simulation studies), in the following the simulations have been performed only for an orthotropic Monodomain model with orthotropic anisotropy.

Intramural excitation and repolarization sequences in the wall thickness. Excitation and recovery isochronal profiles on the epicardial, subepicardial (not shown) and midwall intramural planes exhibit a dimple-like inflection, which is smoothed in the repolarization sequence, in a region where excitation wave fronts propagate mainly across fibers, see Fig. 9.17, Panels EPI, MID. These dimple-like inflections are an effect of the presence of excitation and recovery pathways that start from the stimulation site, proceed first toward the endocardium and subsequently, due to fiber rotation, return toward the epicardium; this results in accelerated propagation in some portions of the epicardial fronts that move mainly across fibers.

9.2.2   Discussion on APD Distribution and Dispersion

Previous simulation studies considered simulations of the entire excitation and repolarization sequences on 1D cables (Joyner [264], Steinhaus [497], Shaw and Rudy [474], Wang and Rudy [548], Viswanathan et al. [546]), 2D sheets (Burgess et al. [67], Cates and Pollard [80]) and 3D slabs (Efimov et al.[155], Pollard et al. [398], Garfinkel et al. [191]). A limited number of simulations studies used the full Bidomain Model in three dimensions. Some histological findings (see LeGrice [292, 293]) have supported the idea that the cardiac tissue anisotropy could be orthotropic, but most simulations have been performed for axisymmetric anisotropy, with the exception of Colli et al. [121], Hooks et al [234] for the excitation phase and Colli Franzone et al. [120] for both the excitation and recovery phases.

The results presented in the previous Section describe the features of the excitation and recovery sequence, using both the Bidomain and the Monodomain models, and show that APD patterns present a definite spatial dispersion in spite of the assigned homogeneity of the individual cellular membrane properties. These patterns, are qualitatively similar in the Bidomain and the Monodomain models. The anisotropic features of the excitation and recovery times, briefly mentioned in describing the vertex simulations, are easier to detect and to interpret when we inspect the patterns elicited by central epicardial stimulations (Figs. 9.16 and 9.17). We considered both axisymmetric and orthotropic anisotropy and our simulations show that several features are more pronounced in the orthotropic case.

Now we briefly review these main anisotropic features appearing in both the excitation and repolarization processes, elicited by an epicardial central stimulation in an orthotropic slab. A main anisotropic feature is the presence of return excitation pathways, i.e. pathways that, starting from the epicardial stimulation site, proceed toward the endocardium but about midway of the wall thickness return pointing toward the epicardial side. Signs of these returning pathways are the dimple-like inflections appearing in the excitation wave front profiles in the epi and midwall planes parallel to the epicardial face (see Fig. 9.17), and, in planar sections

perpendicular to the epicardium, V-shaped intramural profiles with the epi- and endo-cardial foot of the profiles overcoming the peak of the Vs. The simulated anisotropic behavior of the excitation sequence is in agreement with previous experimental and simulated observations, e.g. Burgess et al. [67], Taccardi et al. [506–508], Colli Franzone et al. [102, 114, 116, 121], Keener [268] and Henriquez et al. [226, 344].

With regard to repolarization, the recovery isochrones on the epi, midwall and endocardial planes elicited by an epicardial pacing exhibit a somewhat smoother shape and faster propagation compared with the excitation sequence. In particular, the epicardial repolarization isochrones propagate across fibers faster than the excitation wave, yielding a progressive APD shortening in the cross-fiber direction of propagation as shown by Figs. 9.16 and 9.17. This prediction is in agreement with the data of Gotoh et al. [208] related to cardiac laminae. The recovery isochrones through the thickness of the wall show the presence of repolarization return pathways as in the excitation sequence. These pathways accelerate the repolarization process in epicardial areas where the recovery proceeds mainly across fibers. Unlike the excitation propagation, experimental studies of intramural repolarization is less complete and their interpretation is still the subject of intense research.

The finger-shape valleys of APD reduction associated to the dimple-like inflections appearing in the excitation and recovery fronts are the result of the interaction between excitation and repolarization return pathways. Since these valleys are not present in APD distribution in a slab with parallel fibers, they can be attributed to the rotational anisotropic structure of the ventricular wall. Moreover, these valley are narrower in the orthotropic case. These results relating the repolarization sequence and APD dispersion are the main novelty of this work.

Anisotropic spatial variations of the APD along and across fibers were observed experimentally in 2D cardiac laminae by Osaka et al. [364] and Gotoh et al. [208] and on the epicardium of dog hearts by Burgess et al. [67] and Taccardi et al. [512]. More precisely, Taccardi et al. [512] observed a typical tripolar epicardial APD pattern, with one central maximum and two minima along a cross-fiber direction, on the left ventricle of exposed dog hearts during left ventricular pacing. Results were recently confirmed by optical mapping. On the other hand, Bertran et al. [48], working with pig hearts, did not observe anisotropic APD differences only in 2D laminae.

We remark that simulation studies and experimental data have shown that excitation return pathways, proceedings toward the pacing level, have been observed for pacing sites located at any intramural level, from epi- to endo-cardium. On this ground, we expect that repolarization return pathways, here reproduced only for epicardial pacing, will be present also for intramural pacing.

Rules for APD modulation. Even if the plane sections reported cannot completely capture the complex evolution of the excitation and repolarization surfaces in a three-dimensional domain, the results suggest the following rules for APD modulation on plane sections:

(i) Relatively long APDs occur at points where the excitation and recovery fronts diverge, with maxima attained at the stimulation site and at each breakthrough point on intramural planes parallel to the epicardium with the exception of the endocardial plane;

(ii) A relative APD shortening occurs at points where the excitation and recovery fronts converge, with minima attained at points of front-boundary collision and front extinction;

(iii) Moving away from the stimulation site, the APD shortening is greater in the directions across fibers than along fibers;

(iv) Valleys of relative APD shortening are associated with areas containing dimple-like inflection in the excitation isochrones and the level lines of the APD display dog-bone shaped profiles.

Anisotropic curvature as a parameter affecting the APD modulation. The motion of the excitation wave front first depends on the characteristics of the anisotropic media, on the other hand it is well known that the shape of the wave front is a factor which contributes to the wave propagation, see e.g. [102, 114, 116, 169, 268, 273].

In the following, we consider an excitation (or repolarization) wave front locally convex, relative to the propagating direction, according to whether the front bulges into the resting (excited) volume; concave when it bulges into the excited (resting) volumes from which it is coming.

With regard to the electrotonic load, we observe that currents flowing from the excitation layers of a locally concave front are focusing toward points ahead of the front, whereas for locally convex front they are scattering; the former case, producing a more rapid membrane depolarization, yields a speed up of the excitation propagation, compared to the velocity of a local plane front, whereas a slower spreading results in the latter case. The opposite electrotonic process takes place when considering points ahead of repolarization fronts i.e. for locally concave (convex) fronts we have a depletion (convergence) of repolarizing currents. In spite of this opposite behavior, we have similar effects on the recovery propagation, i.e. in the concave case a faster recovery while in the convex case a slowing down repolarization.

The dependence of the conduction velocity on the wave front shape is quantitatively described by means of the *curvature* of the wave front. It is well known that in isotropic homogeneous media with conductivity σ, the velocity, along the Euclidean normal $\mathbf{n}$ of the front at a point $\mathbf{x}$, oriented in the direction of motion, can be approximated by $\theta(\mathbf{x}, \mathbf{n}) = \theta_p (1 + K/c_m)$, with $K = \sqrt{\sigma} \, k$, where $k = -\operatorname{div} \mathbf{n}$ is twice the mean curvature of the front, see e.g [268, 273]. The velocity of a local plane front θ_p also depends on the conductivity of the excitable medium, i.e. we have $\theta_p = \rho\sqrt{\sigma}$, with the constant ρ only dependent on the membrane model. Then a locally convex front, such as an expanding circle, has negative curvature, while a locally concave front, such as a contracting circle, has positive curvature. Hence, a locally convex (concave) front propagates with velocity smaller (greater) than that of a plane wave.

For an anisotropic Monodomain slab the velocity of the excitation wave front is described by a similar law of motion $\theta(\mathbf{x}, \mathbf{n}) = \theta_p(\mathbf{x}, \mathbf{n})(1 + K/c_m)$. The principal term $\theta_p(\mathbf{x}, \mathbf{n})$ predicts the velocity of an ideal locally plane wave propagating along the normal direction, given by $\theta_p(\mathbf{x}, \mathbf{n}) = \rho\sqrt{\sigma(\mathbf{x}, \mathbf{n})}$, with $\sigma(\mathbf{x}, \mathbf{n}) = \mathbf{n}^T D_m(\mathbf{x})\mathbf{n}$ and $D_m(\mathbf{x}) = D_i(D_i + D_e)^{-1}D_e$. The additional term is related to the *anisotropic curvature* (see Bellettini et al. [37]), whose expression for the Monodomain model is given by $K = -\operatorname{div} v$, where differently from the usual Euclidean normal, $v(\mathbf{x}) = D(\mathbf{x})\mathbf{n}/\sqrt{\mathbf{n}^T D\mathbf{n}}$; see Bellettini et al. [39, 102, 268].

Burgess et al. [67] observed in experiments on pulmonary cone preparations that the repolarization pattern can be affected by the direction of the excitation wave front and that anisotropic differences in conduction velocity induce electrotonic effects on the cell repolarization. Their findings show that the APD is relatively long at sites where the activation front decelerates and is relatively short at sites where the activation front accelerates, suggesting that acceleration and deceleration of the excitation wave front are associated with a relative APD reduction and prolongation, respectively. They established a significant correlation between the APD distribution
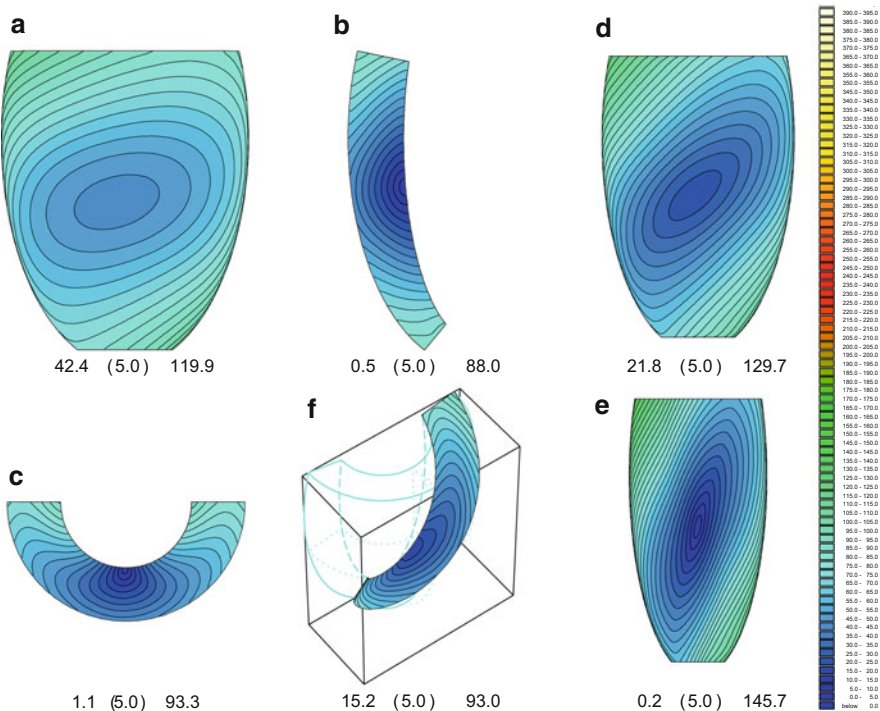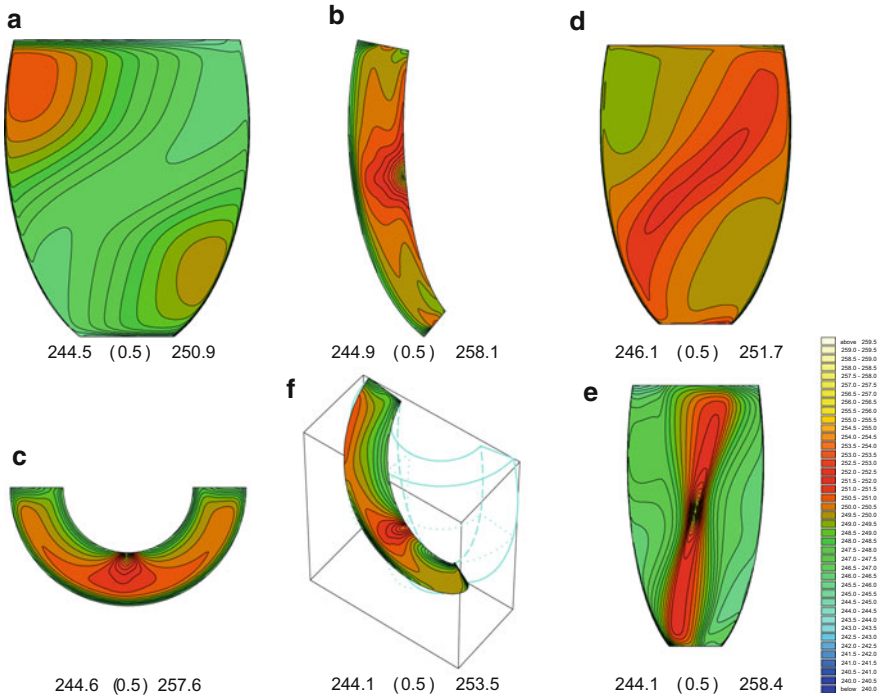

Fig. 9.18 Axisymmetric monodomain model with intramural fiber rotation on a truncated ellipsoidal domain with central endocardial stimulation. Activation time isochrones on endocardial (**e**), mid-myocardial (**d**), epicardial (**a**) and different transmural sections (**b-c-f**). All values are expressed in ms
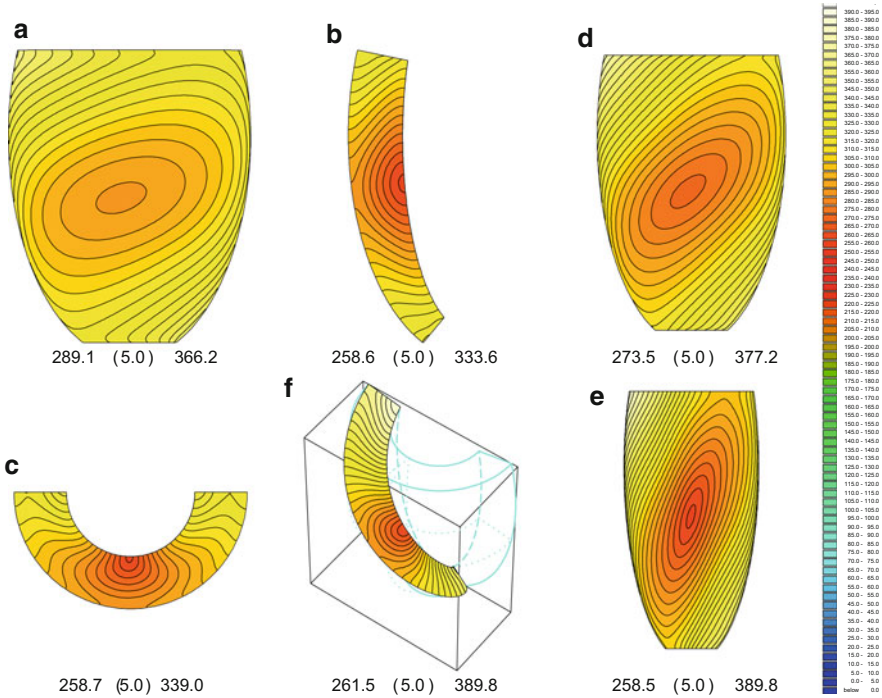
Fig. 9.19 Axisymmetric Monodomain model with intramural fiber rotation on a truncated ellipsoidal domain with central endocardial stimulation. Repolarization time isochrones on endocardial (**e**), mid-myocardial (**d**), epicardial (**a**) and different transmural sections (**b-c-f**). All values are expressed in ms

and an index related to $\Delta\phi(\mathbf{x})$, where ϕ is the activation time at point $\mathbf{x}$. We remark that, for isotropic homogeneous media, the anisotropic curvature reduces to $K = \sqrt{\sigma}k$, with $k = -\mathrm{div}(\nabla\phi/\|\nabla\phi\|) = \Delta\phi(\mathbf{x}) - \nabla\|\nabla\phi\|^T\nabla\phi$, hence the index used in Burgess et al. [67] is only a part of the front curvature in isotropic media. Therefore Burgess et al. [67] implicitly established a correlation between the shape of the wave front and the APD distribution, which is here confirmed using the more appropriate *anisotropic curvature* index.

Similar considerations hold for the activation, repolarization and APD isochrones elicited by an endocardial stimulation on a truncated ellipsoidal domain, see Figs. 9.18–9.20.

Fig. 9.20 Axisymmetric monodomain model with intramural fiber rotation on a truncated ellipsoidal domain with central endocardial stimulation. Action potential duration isochrones on endocardial (**e**), mid-myocardial (**d**), epicardial (**a**) and different transmural sections (**b-c-f**). All values are expressed in ms

9.3 Heterogeneous Cardiac Tissue

In this section, we extend the simulations of excitation and repolarization sequences of the previous section to cardiac slabs with heterogeneous intrinsic properties of the cell membrane. More complete results can be found in [122, 126].

The cardiac domain considered is a cartesian slab of dimensions $\{L_1 \times L_2 \times L_3\} = \{5 \times 5 \times 1\}$ cm^3 modeling a portion of the left ventricle. A structured grid of $500 \times 500 \times 100$ hexahedral isoparametric Q_1 elements with size $h = 0.1$ mm was used in all computations.

Parameter calibration. In a parallelepipedal geometry, modeling a portion of the ventricular wall, we consider the following simple fiber-sheet model sharing the previous qualitative rules. In our slab geometry using the cartesian coordinate system $\{\mathbf{x}_1, \mathbf{x}_2, \mathbf{x}_3\}$ and associated axis unit vectors $\{u_{e1}, u_{e2}, u_{e3}\}$, the $\mathbf{x}_3$ coordinate represents the transmural thickness from the endo to epicardial planes. Proceeding

from endocardium to epicardium, we consider a linear transmural fiber rotation (clockwise) for a total amount of 120°, i.e.

$$\left\{ \mathbf{a}_l(\mathbf{x}) = u_{e1} \cos\alpha(x_3) + u_{e2} \sin\alpha(x_3), \qquad \alpha(r) = \tfrac{2}{3}\pi(1-r) - \tfrac{\pi}{4}, \qquad 0 \le r \le 1. \right.$$

The myocardial tissue is represented as a set of surfaces, called radial laminae or sheets, that connect the epicardial with the endocardial surface having tangent plane defined by $\mathbf{a}_l$ and by the transmural transverse fiber direction $\mathbf{a}_t = u_{e3}$; therefore, the sheet normal is given by $\mathbf{a}_n(\mathbf{x}) = -u_{e1} \sin\alpha(x_3) + u_{e2} \cos\alpha(x_3)$, i.e. laminae develops intramurally with zero sheet angle and intersects perpendicularly the epi- and endocardial surfaces.

For our slab geometry, the conductivity tensors are $D_{i,e} = \sigma_t^{i,e} I + (\sigma_l^{i,e} - \sigma_t^{i,e})\mathbf{a}_l \, \mathbf{a}_l^T + (\sigma_n^{i,e} - \sigma_t^{i,e})\mathbf{a}_n \, \mathbf{a}_n^T$. In any model of the cardiac tissue, the calibration of the parameter values is not an easy task, because the data available in the literature refer to diverse experimental setups. The macroscopic conductivities of the media are here based on conservative values and are determined by requiring that the simulated excitation wavefront motion has physiologically reasonable velocities of propagations, see [102, 123]. The conductivity coefficients, in mS cm^{-1}, used in the orthotropic anisotropic simulations are:

$$\sigma_l^e = 2 \qquad \sigma_t^e = 1.35 \qquad \sigma_l^i = 3 \qquad \sigma_t^i = 0.465 \qquad \sigma_n^e = 0.5\sigma_t^e, \quad \sigma_n^i = 0.1\sigma_t^i.$$

In the numerical tests, we have used the parameters $C_m = 10^{-3}$ mF/cm^2, $\chi = 10^3$ cm^{-1}. The previous calibration parameters and the LR1 model, in case of ideal plane wavefronts moving along the directions $\mathbf{a}_l, \mathbf{a}_t, \mathbf{a}_n$, respectively, produce conservative estimates of the propagation velocities equal to (60, 35, 10) cm s^{-1}, respectively. More precisely, one dimensional simulations using as a conductivity coefficient $\sigma_{l,t,n} = \sigma_{l,t,n}^i \sigma_{l,t,n}^e / (\sigma_{l,t,n}^i \sigma_{l,t,n}^e)$, yield propagation velocities equal to (60.6, 32.01, 9.59), respectively, using a space resolution of 0.05 mm. These velocities agree with those measured in canine experiments along fiber and across fiber in the transmural direction, see [401, Table 16-1, p. 148]. Since the coupling between adjacent laminae occurs through thin, sparse, muscle bundles bridging the clefts that separate adjacent laminae (see [293]), it is expected that the intrinsic cross-fiber velocity should be 2 or 3 times greater in the plane of a muscle lamina than perpendicular to it. The conductivity coefficients $\sigma_n^{1,e}$ have been calibrated so that the propagation velocities (θ_n) of an ideal planar wavefronts moving across the fiber sheet is reduced by a factor 3.5 with respect to θ_t. This epicardial cross-fiber velocity is difficult to evaluate experimentally since the underlying fiber rotation accelerates the excitation epicardial motion, as shown in our work [121], for epicardial cross-fiber velocities in the range 14–25 cm/s.

The initial conditions for the Monodomain model with the phase I Luo-Rudy model (LR1) [308] are chosen at the steady state, so that the rest potential is $\mathbf{v}^0 = -83.84\,\text{mV}$. In order to elicit the excitation front, we apply a stimulus of $250\,\mu\text{A}$ for 1 ms on a small volume (containing 5 mesh points in each $x-$ and $y-$direction and 3 mesh points in the $z-$direction) at the center of the epi- or endocardial face. Other than potentials and gating variables, at each time-step, we compute also the activation (ACTI) and the repolarization (REPO) times, defined as the times when the action potential crosses $-60\,\text{mV}$ during the upstroke and when it reaches -75.46 in the downstroke phase (i.e. $-90\,\%$ of the resting value), respectively.

Intrinsic transmural heterogeneity. We consider three different types of transmural distribution of the intrinsic APDs of the cells, the first homogeneous (denoted by H-slab) and the other two heterogeneous, (denoted by 3-slab and W-slab). We assume that the transmural intrinsic heterogeneity is the same along any transmural epi-endocardial straight line, i.e. in any plane parallel to the epicardium all cells have the same APD.

- **H-slab**: the cardiac slab has homogeneous *intrinsic* properties of the cellular membrane; the I_K current of the LR1 model is multiplied by 2.325, yielding an APD of 250 ms.
- **3-slab**: the cardiac slab is subdivided transmurally into three layers of $1/3$ cm thickness. More precisely, proceeding from the endocardial to the epicardial surfaces, the values of *intrinsic* cellular APD amount to 235, 272, 225 ms on the intervals $[0, 0.33], [0.33, 0.66], [0.66, 1]$, respectively. The transmural heterogeneity is simulated by multiplying the current I_K of the LR1 model by (2.62, 1.952, 2.88), corresponding to intrinsic APDs of (235, 272, 225) ms, respectively. See Fig. 9.21, left panel and the dashed plots in Fig. 9.23. Figure 9.21 left panel, displays the three different action potential waveforms related to the three different intrinsic properties of transmural cells, i.e. they are
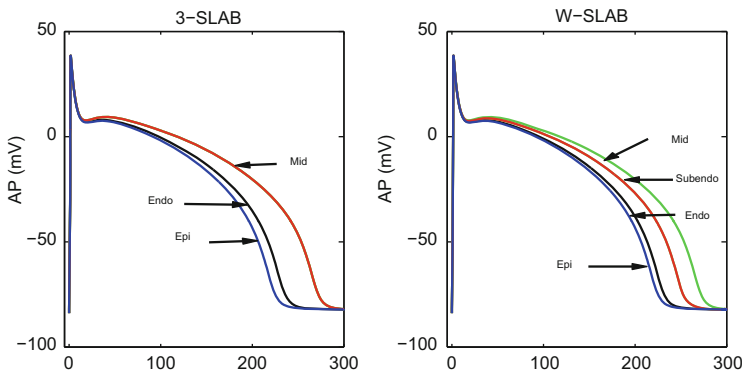
Fig. 9.21 Intrinsic action potential waveforms assigned to the intramural heterogeneity of type 3-slab (*left*) and W-slab (*right*). Each panel shows subendocardial, midwall and subepicardial intrinsic action potentials obtained with 0D simulations and assigned to each transmural layer

obtained by 0D simulations modeling the intrinsic response of the isolated cell. We have considered this kind of transmural heterogeneity composed of three layers of cellular types, (i.e. epi-subepicardial, mid-myocardial and subendo-endocardial cells), since this simplified heterogeneity model was previously used in simulations with 1D models in [546] and in [96].

- **W-slab**: the cardiac slab is subdivided transmurally into four layers with different *intrinsic* membrane properties in order to reproduce qualitatively the APD transmural behavior measured in wedge preparations, see e.g. [572], Fig. 4 and [395] Fig. 5. More precisely, proceeding from the endocardial to the epicardial surfaces, we subdivided the slab into four layers of thickness (0.12, 0.2, 0.55, 0.15) cm, respectively, and multiplied the current I_K of the LR1 model by (2.715, 1.952, 2.47, 2.88), corresponding to intrinsic APDs of (232, 272, 242, 225) ms, respectively, right panel. Hence, we assume that sub-endocardial and mid-myocardial layers display a longer APD than the epi- and endocardial cells. See Fig. 9.21 and the dashed plots in Fig. 9.23.

We remark that the two transmural heterogeneity assignments are not symmetric in the slab thickness, therefore they could yield a different APD dispersion for an epicardial and an endocardial pacing. In this study, we consider both epi- and endocardial stimulations for both types of transmural heterogeneities, 3-slab and W-slab.

9.3.1 Transmural Heterogeneity in 3-D Cardiac Slabs

We now consider 3-D simulations of the excitation and repolarization processes, elicited by an epicardial or an endocardial stimulation, in an orthotropic slab with homogeneous (H-slab) or heterogeneous (3-slab, W-slab) intrinsic cellular membrane properties. Our main goal is to determine how intramural heterogeneity affects the repolarization sequence and the spatial distribution of action potential durations.

Because the complete set of results of these 3-D simulations are too large to report for all sections, slab types and stimulation sites, we show first the results along simple 1-D and 2-D transmural sections of the domain and then show the results on the whole 3-D slab for endocardial stimulation. In particular, we present the results on:
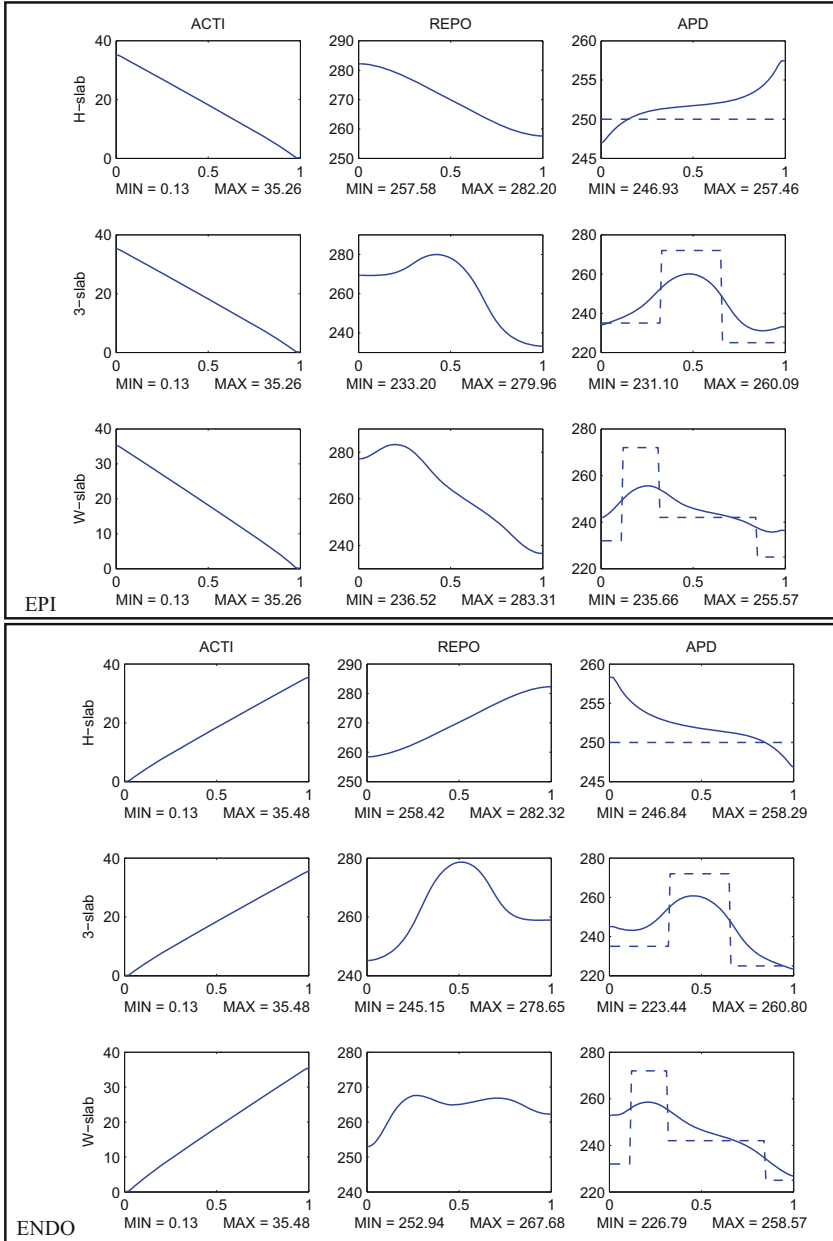
- A 1-D transmural line passing through the stimulation site and orthogonal to both epicardial and endocardial surfaces, for both stimulations;
- 2-D transmural planar sections passing through the center of the slab and orthogonal to both epicardial and endocardial surfaces (see Fig. 9.22):
  - for *endocardial* stimulation, we focus on section C for all slabs, on sections A, B and D for the W-slab;
- The whole 3-D slab and its planar intramural sections, parallel to the epicardium, for endocardial stimulation.
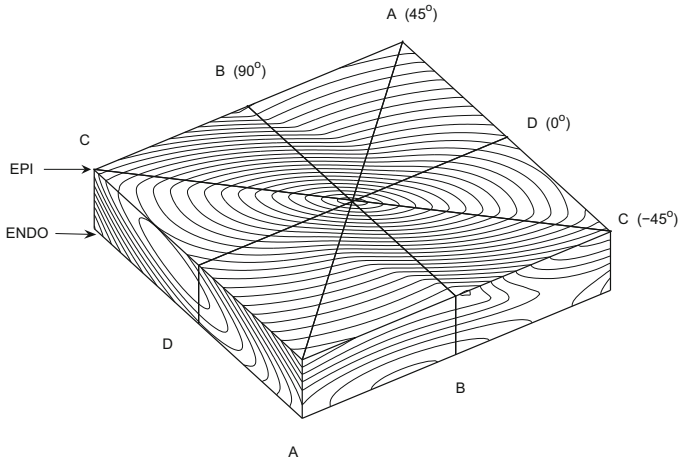
Fig. 9.22 Intramural sections *A, B, C,* and *D* of the orthotropic Monodomain slab of size $5 \times 5 \times 1\,\text{cm}^3$, with isochrone contours elicited by epicardial central stimulation

We will then show some results on homogeneous and heterogeneous 3-D curved walls.

In each case, we will examine the distributions of activation times (ACTI($\mathbf{x}$)), repolarization times (REPO($\mathbf{x}$)) and action potential durations (APD($\mathbf{x}$) = REPO($\mathbf{x}$)–ACTI($\mathbf{x}$)), generated by a stimulus at the center of the epicardial or endocardial surface of each slab.

We remark that fiber direction at a depth of 0 cm from the epicardium is parallel to section C; at 0.375, to section D; at 0.75 cm, to section A, while the fiber direction is never parallel to section B.

9.3.1.1   1-D Transmural Line

(a) Epicardial stimulation. In the homogeneous case (H-slab), the profiles of the activation time, displayed in Fig. 9.23 (top panel, top row left), are almost linear. The intramural excitation wavefront reaches a quasi-stationary speed across fibers, apart from the short acceleration in the initial phase of propagation and the subsequent collision with the endocardial plane. On the other hand, the profile of the repolarization time shows a less linear behavior and the recovery wavefront does not reach a steady intramural speed, due to the interaction between the wave length of the fast component of the repolarization process, i.e. the downstroke phase of the action potential around the inflection point; we remark that, for an across fiber velocity of 0.3 mm/ms, see Fig. 4 and a conservative duration of the fast repolarization phase of the AP of 60 ms, it follows an estimate of 18 mm for the wave length, which is greater than the wall thickness of the slab.

Fig. 9.23 Profiles along the 1-D transmural line (passing through the stimulation site and orthogonal to both epicardial and endocardial surfaces) of the activation time (*ACTI*, *first column*), of the repolarization time (*REPO*, *second column*), of the action potential duration (*APD*, *third column*) for H-slab (*first row*), 3-slab (*second row*), W-slab (*third row*). Central stimulation: epicardial (*top panel*), endocardial (*lower panel*). The piecewise constant *dashed lines* in the APD column are the intrinsic (0D) APD of the cells. Vertical axis reports times in ms and the horizontal axis reports distances in cm from the endocardial site

Therefore, the intramural repolarization sequence is faster than the depolarization sequence. This brings about a progressive intramural reduction of the APD away from the stimulation site, see Fig 9.23. The time required for activation and recovery to reach the endocardial side is about 35.26 and 24.62 ms, respectively. Thus, transmural repolarization moves slightly faster than activation in the homogeneous model, see Gotoh et al. [208] and Taccardi et al. [512]. The APD dispersion amounts to about 10.53 ms, mostly concentrated around the stimulation site.

In the heterogeneous cases 3-slab, W-slab (middle and last rows of top panel of Fig. 9.23), as expected, the activation time profiles are essentially unchanged with respect to the H-slab, while the repolarization times have a higher dispersion of about 47 ms. The APD dispersion amounts to 29 and 20 ms in the 3-slab and W-slab, respectively, i.e., it is three or two times larger than in the homogeneous case. Due to APD modulation induced by electrotonic currents, the intrinsic APD differences between the three or four different cell layers are strongly smoothed, as shown by comparing the profiles with the piecewise constant dashed lines in Fig. 9.23 right column, which displays the assigned intrinsic transmural APD distribution in the three slab types. Moreover, both the 3-slab and W-slab cases exhibit a strongly reduced transmural APD dispersion with respect to the intrinsic dispersion, which amounts to 47 ms. In both heterogeneous slabs, the transmural profiles of the repolarization time exhibit a maximum located in the cell layer with the greatest intrinsic APD; this site is also associated with the collision of the primary recovery front, which starts at the epicardial stimulation site, with a secondary recovery wave, which starts from the endocardium. Also, the APDs reach a maximum in the layer with highest intrinsic APD, but the magnitude is strongly reduced, compared with the intrinsic value. As expected, longest APD is observed near the collision of the recovery waves.

(b) Endocardial stimulation. We now examine the results described in the lower panel of Fig. 9.23, obtained with an endocardial stimulation at the center of the endocardial face of the slab. In the H- slab case, apart from the change of the epi and endocardial sides, the activation, recovery and APD profiles practically coincide with those elicited by the epicardial stimulation. The propagation of the excitation, following epicardial and the endocardial pacing, along the transmural vertical line, is strictly across fibers for symmetry reasons. Note that we did not incorporate fiber imbrication in our model. For the endocardial stimulation, the total activation and recovery times are 35.48 and 23.90, respectively, while in the epicardial stimulation they are 35.26 and 24.62, respectively. These small differences in the total activation and recovery times are expected and are mainly due to differences in the initial direction and shape of the propagating excitation wavefront, since in all our slabs, the endocardial fiber direction is 75°, while on the epicardial surface it is −45°.

In 3-slab and W-slab, transmural excitation profiles coincide with those of H-slab. The repolarization processes are completed in 33.5 and 14.74 ms, respectively. This large difference in the dispersion of the repolarization times is associated with the different morphology of the transmural profiles, i.e. the presence of one maximum in 3-slab, located at the midwall level, and of two relative maxima of comparable values in W-slab, located one at subendocardial and the other at subepicardial level.

The midwall maximum in 3-slab is related to the collision of the primary recovery front, originated at the endocardial stimulation site, with a secondary phase front, originating at the epicardial side at a later instant. In W-slab, two collisions of the recovery fronts are present because an additional recovery wave, starting from the intramural site corresponding to a minimum of the repolarization time profile, spreads toward the endocardium and the other toward the epicardium. This dynamic behavior is confirmed by the repolarization speed profile in which, the intramural maxima correspond to points of collision.

The APD dispersions, amounting to 37.36 (3-slab) and to 31.78 ms (W-slab), are about four and three times greater than in the H-slab.

In comparison with the H-slab case, the endocardial stimulus yields a reduction or increase of the recovery dispersion depending on the type of heterogeneity. Conversely, the epicardial stimulus produces recovery dispersions, in both 3-slab and W-slab, that are roughly twice the H-slab dispersion. For both stimulations, the APD dispersions are higher than the H-slab APD dispersion, with greater values in case of endocardial stimulation and 3-slab heterogeneity. Thus, the type of intrinsic transmural heterogeneities could be inferred by comparing repolarization profiles and APD dispersions along the 1-D transmural line, where epicardial and endocardial stimulations produce very different values of repolarization and APD dispersions.

Comparing the results of the two stimulations, we observe that the repolarization profiles display greater morphological changes than the APD profiles, suggesting a major sensitivity of the former to the distribution of transmural heterogeneity.

9.3.1.2 Transmural Sections: Endocardial Stimulation

We first describe the transmural patterns elicited by a central endocardial stimulation, displayed in Fig. 9.24, on section C of the three cases H-slab, 3-slab, W-slab.

(a) **Transmural excitation sequence on section C**. As occurred with epicardial stimulation, the excitation sequence is unaffected by the transmural heterogeneity. We note that the epicardial side of section C is parallel to the fiber direction, while its endocardial side forms an acute angle of $60°$ with fiber direction. After epicardial breakthrough, the foot of the wavefront on the upper side of the section propagates along fibers, while the endocardial foot propagates slowly, mainly across fibers and is overtaken by the subepicardial portions of the front. This generates excitation pathways that return toward the endocardium. The latest depolarized areas are near the vertices of section C on the endocardial side.

(b) **Transmural repolarization sequence on section C**. In the H-slab case, the repolarization isochrones follow the activation sequence: return pathways toward the endocardial plane of stimulation are present and the areas that repolarize last coincide with those that depolarize last.
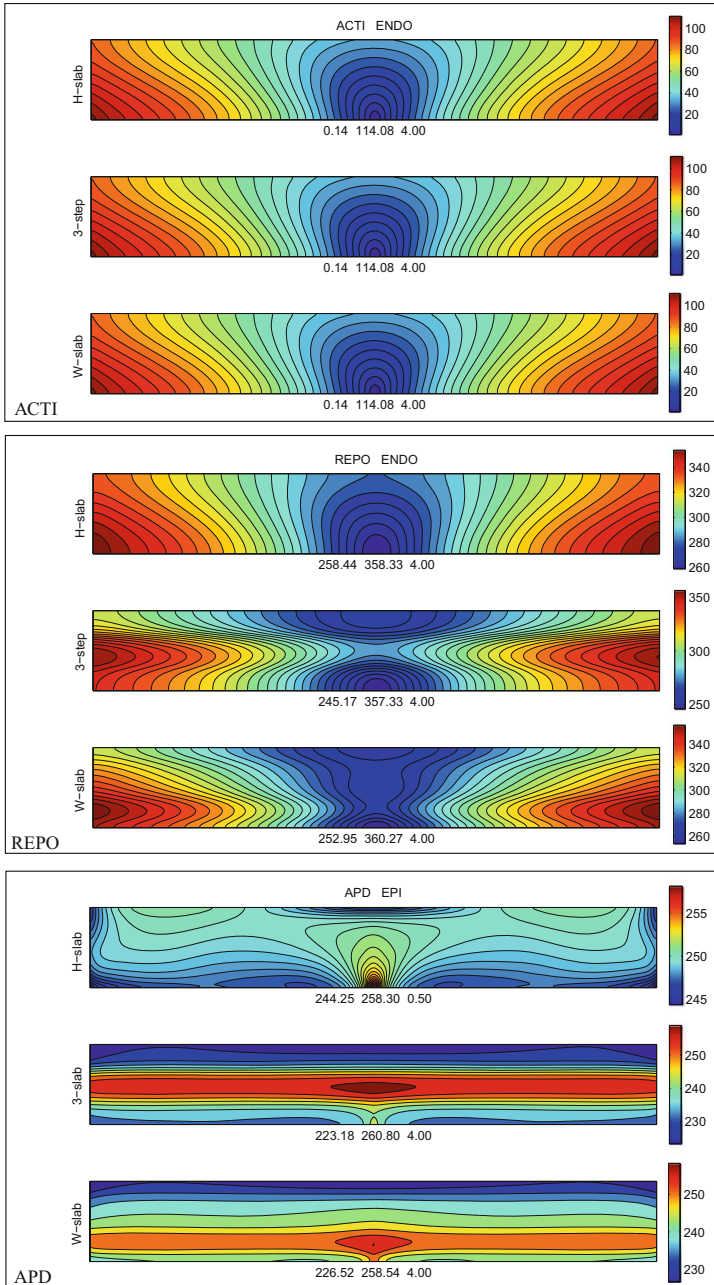
Fig. 9.24 Isochrone lines of the activation time (*ACTI*, *top*), repolarization time (*REPO*, *middle*) and action potential duration (*APD*, *bottom*) on the transmural section C for models H-slab, 3-slab, W-slab, with endocardial stimulation. Reported below each panel are the maximum, minimum and step in ms of the displayed map (Reproduced with permission from [126])

In the 3-slab case, recovery starts at the stimulation site. After about 13 ms, a secondary recovery wave starts from the opposite point on the epicardial side. After collision at midwall level, the merged repolarization front spreads laterally with a smooth V-shaped profile. In the W-slab case, as discussed in Sect. 9.3.1.1, the recovery process arises from three different sites and at different times: at 253 ms at the endocardial stimulation site, at 262 ms from the opposite point on the epicardial side. Finally, at 265 ms, a new repolarization front arises at about midwall point. After the merging of these three different recovery fronts, the transmural isochrones exhibit V-shape profiles with some initial undulation associated with the four different transmural layers of intrinsic heterogeneity.

The repolarization dispersion on section C amounts to (99.89, 110.84, 108.32) ms for H-slab, 3-slab, W-slab, respectively. These values are lower then those for activation dispersion, which amount to about 114.08 ms. This confirms that recovery is slightly faster than excitation, especially in the homogeneous case (Table 9.3).

(c) Transmural APD distribution on section C. The APD dispersion on section C amounts to (14.05, 37.62, 32.02) ms for H-slab, 3-slab, W-slab, respectively, These values are comparable to the values of APD dispersion observed along the 1-D transmural line described in Sect. 9.3.1.1. In the H-slab, the APD distribution, displayed in Fig. 9.24 (bottom panel), exhibits the absolute maximum at the stimulation site and two symmetric subepicardial minima. Shortening of the APD and associated relative minima are present at points of front-boundary collision of the excitation wavefront. Two maxima on the epicardial side appear symmetrically with respect to the minimum located at the excitation breakthrough point on the epicardium.

In both heterogeneous slabs, the APD distribution displays a striped pattern; the stripe having the highest APD has the same location as the intramural layer with the highest intrinsic APD.

9.3.1.3   3-D Slab: Epicardial, Endocardial and Planar Intramural Sections Parallel to the Epicardium

We now consider the excitation, repolarization and APD values on the whole 3-D slabs and their planar intramural sections parallel to the epicardial face, with both endocardial and epicardial pacing.

Table 9.3 Dispersion (MAX–MIN value) of activation time (ACTI), repolarization time (REPO), APD 90 on the transmural sections A and C

	Epicardial stimulation, section A			Endocardial stimulation, section C		
	ACTI	REPO	APD 90	ACTI	REPO	APD 90
H-slab	100.53	88.00	12.39	114.08	99.89	14.05
3-slab	100.53	107.81	38.42	114.08	110.84	37.62
W-slab	100.53	95.21	30.54	114.08	108.32	32.02

(a) H-slab. In the homogeneous case, displayed in Fig. 9.25, the spread of excitation and the sequence of recovery, displayed on five planar sections parallel to the epicardial face (located at z = 0, 0.25, 5, 0.75, 1 cm, respectively), undergo an acceleration in endocardial areas where the fronts proceed mainly across fibers, due to the presence of underlying intramural returning pathways of excitation and recovery, as shown by the isochrones displayed on the transmural section C with endocardial stimulation (Fig. 9.24). Dimple-like inflections appear in the isochrone profiles, due to the faster propagation of the fronts in higher layers where the fiber direction rotates CW relatively to the lower planes. The recovery isochrones on the endo, intramural and epicardial planes exhibit a somewhat smoother shape and faster propagation compared with the excitation sequence.

The rotational anisotropy of the media yields APD patterns strongly correlated with the excitation wavefront motion and the front-boundary collisions. The APD spatial distribution shows finger-shape valleys of APD shortening associated to the dimple-like inflections appearing in the excitation and recovery fronts. The APD level lines display also dog-bone shaped profiles. These features can be attributed to the rotational anisotropic structure of the ventricular wall and to the interaction between excitation and repolarization return pathways. Moreover, APD maxima occur near the stimulation site and at breakthrough points on each plane section parallel to the epicardium (except on the epicardial plane), see [123, Fig. 7] for more detailed analysis of the APD pattern.

Similar features occur in case of epicardial stimulation (not shown), if we exchange in the description the role of endocardial and epicardial planes.

(b) 3-slab and W-slab. We now compare the H-slab patterns with those of the heterogeneous 3-slab and W-slab, see Figs. 9.26 and 9.27. Unexpectedly, the repolarization sequence and the APD patterns on the intramural planar sections parallel to the epicardium exhibit the same main anisotropic spatial features as in the homogeneous case. Therefore, the transmural heterogeneity remains mostly confined in the transmural direction and does not diffuse to the orthogonal planes, in spite of the combined effects of electrotonic modulation, orthotropic conduction velocity and fiber rotation. We have computed the correlation coefficients of the repolarization time and APD between H-slab and 3-slab and between H-slab and W-slab on each of the 101 intramural planar sections parallel to the epicardial face (the first being the endocardium and the last the epicardium). These coefficients show a remarkably strong correlation between homogeneous and heterogeneous repolarization times (the coefficients differ from 1 by less than $2 \cdot 10^{-4}$) and APD (the coefficients differ from 1 by at most $5.2 \cdot 10^{-2}$ with epicardial stimulation and at most $7.1 \cdot 10^{-2}$ with endocardial stimulation), despite the different magnitude of the repolarization times and APDs.
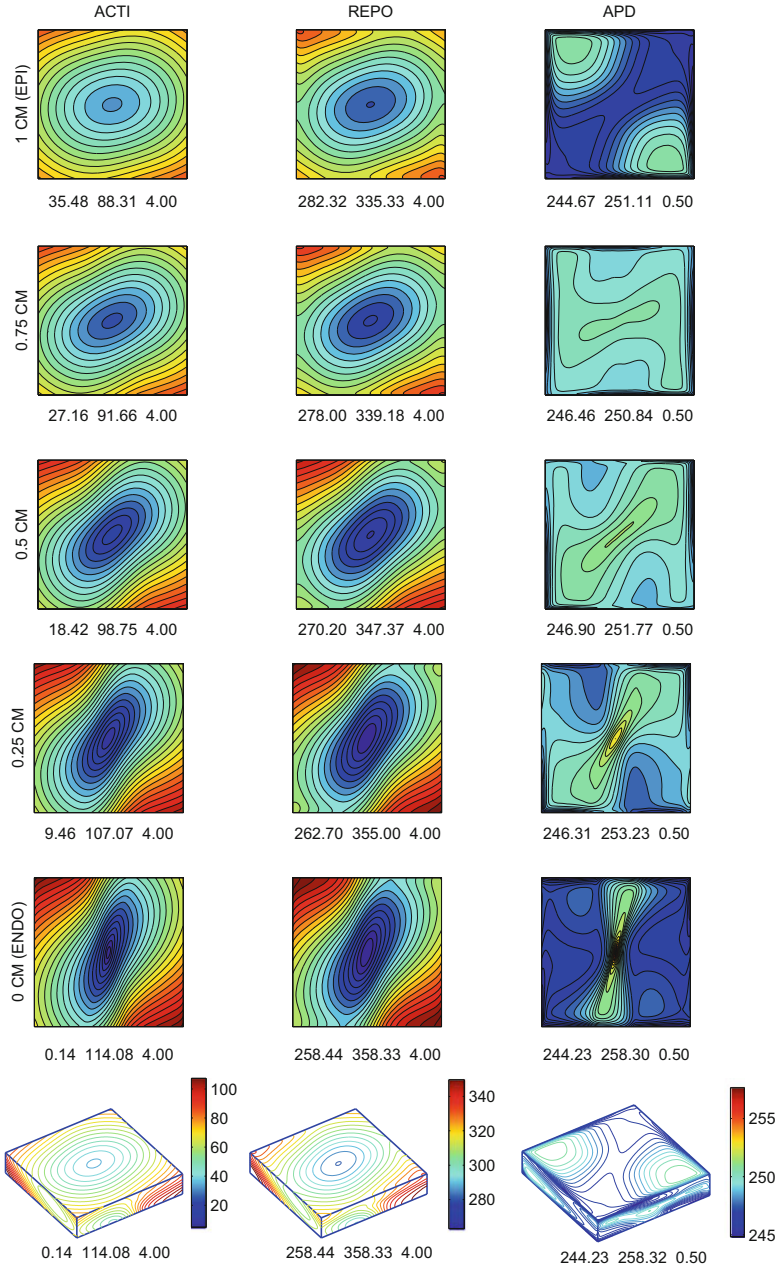
Fig. 9.25 Orthotropic Monodomain–LR1 model, homogeneous H-slab of size $5 \times 5 \times 1\,\mathrm{cm}^3$. Endocardial central stimulation. Isochrone lines of the depolarization time (*first column ACTI*), repolarization time (*second column REPO*) and action potential duration (*third column APD*) on five horizontal sections (z = 0, 0.25, 0.5, 0.75, 1 cm) and the whole slab. Reported below each panel are the maximum, minimum and step in ms of the displayed map (Reproduced with permission from [126])
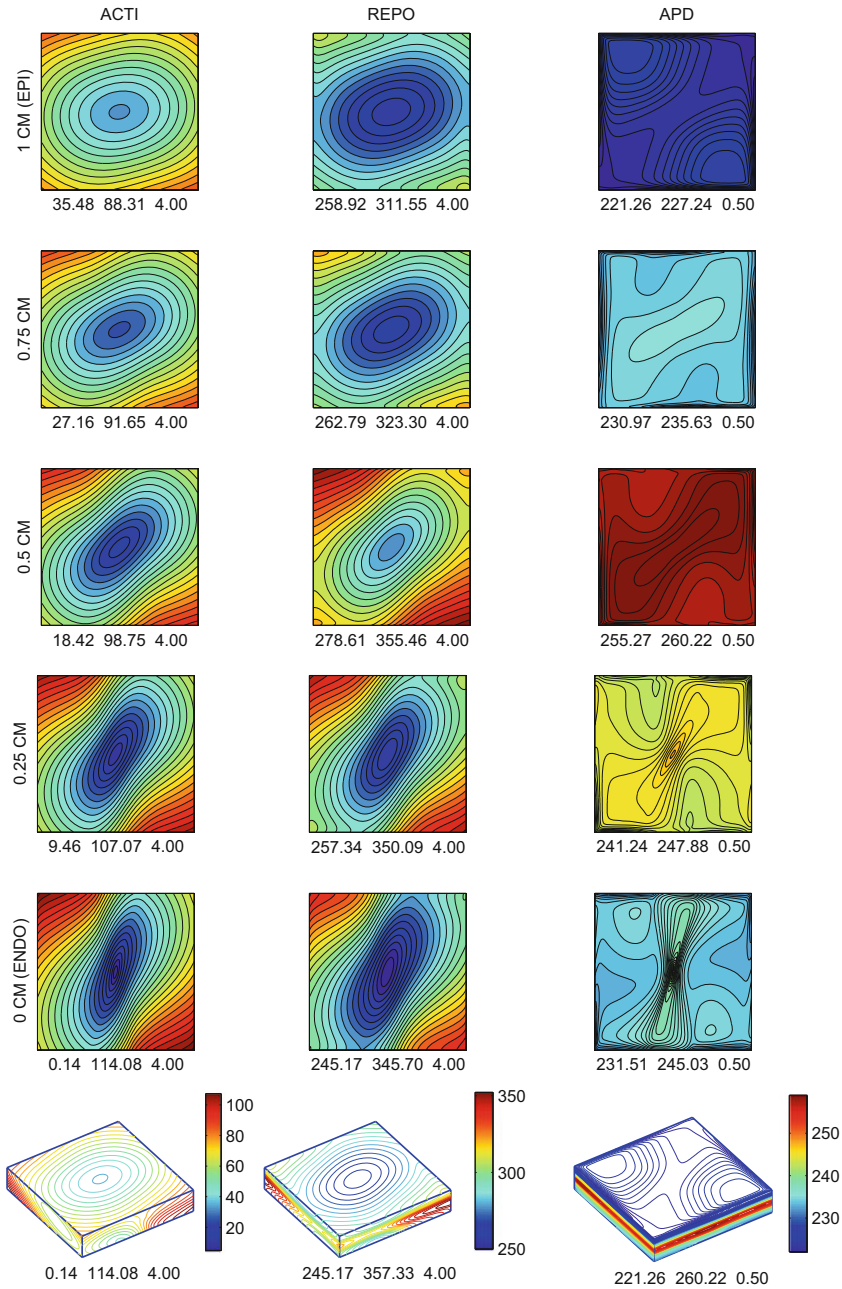
Fig. 9.26 Orthotropic Monodomain–LR1 model, heterogeneous 3-slab of size $5 \times 5 \times 1 \, cm^3$. Same format as in Fig. 9.25 (Reproduced with permission from [126])
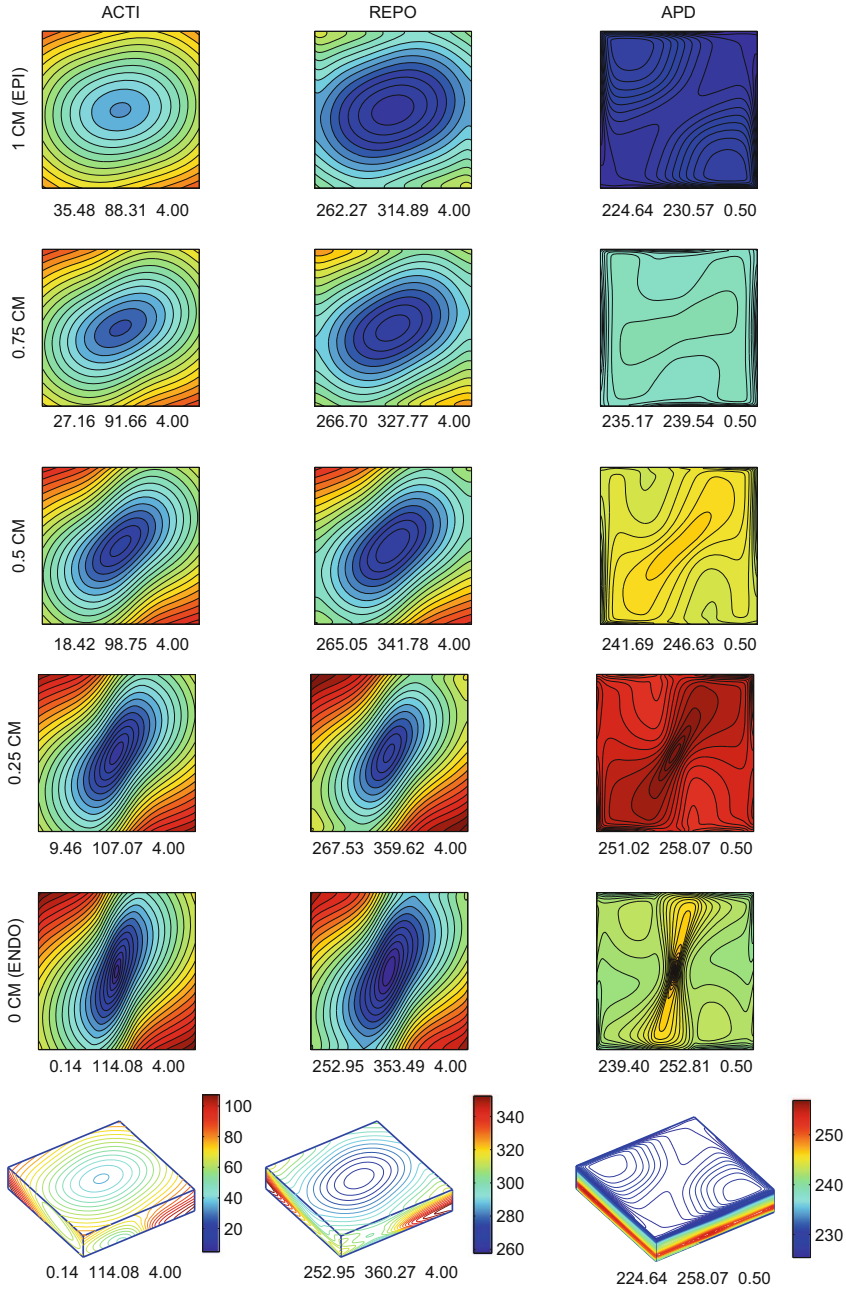
Fig. 9.27 Orthotropic Monodomain–LR1 model, heterogeneous W-slab of size $5 \times 5 \times 1 \, cm^3$. Same format as in Fig. 9.25 (Reproduced with permission from [126])

In the intramural sections parallel to the epicardium, the APD patterns elicited by an endocardial (epicardial) central stimulation in the homogeneous or heterogeneous slabs are characterized by the following features:

(i) The APD distributions on the endocardial (epicardial) and intramural planes exhibit a maximum located at the endocardial (epicardial) stimulation site or at the intramural points first reached by the excitation front, respectively; see Figs. 9.25–9.27. These maxima are surrounded by level lines elongated along the local fiber direction. This indicates that APD decreases more rapidly when moving away from the center of the face in the cross-fiber direction than along fibers. This finding confirms and extends to a three-dimensional myocardial slab the experimental findings by Gotoh et al. [208], Osaka et al. [364], Taccardi et al. [512].

(ii) On the intramural sections (from subendocardial (subepicardial) to midwall), two valleys of decreasing APD values occur. Each valley exhibits a minimum located at the boundary of the slab. These narrow valleys of low APD values are located in the regions where excitation isochrones exhibit a dimple-like inflections.

(iii) In the epicardial (endocardial) plane, the APD distribution displays a saddle point at the epicardial (endocardial) BKT point. The APD increases reaching a maximum when moving away from the BKT point in a direction parallel to the epicardial (endocardial) fibers of $-45°$ ($75°$), while in the cross-fiber direction the APD decreases toward two minima located at the boundary and corresponding to front-boundary collision points. The axis joining the two maxima is roughly parallel to the epicardial (endocardial) fiber direction of $-45°$ ($75°$) and the two maxima are separated by the valley of APD reduction.

We remark that the heterogeneity we consider is only transmural, i.e. the intrinsic membrane properties are constant in each intramural plane parallel to the epicardium. Our results show that the presence of transmural heterogeneities cannot be detected from the epicardial pattern of the APD distribution.

After the endocardial or epicardial breakthrough, the repolarization fronts spread laterally in the slab (Fig. 9.24) and display similar shapes associated with the 1-D transmural profiles of Fig. 9.23, independently of the pacing location.

9.3.2   Transmural Heterogeneity in 3-D Ellipsoids

We have extended the previous simulations to the case of a truncated ellipsoidal domain with transmural homogeneous and heterogeneous membrane properties.

The numerical simulations are performed on a simplified left ventricular wall shaped as an ellipsoidal volume, axisymmetric with respect to the vertical z–axis, truncated at the base and at the apex, described by the parametric equations

$$x = a(r)\cos\theta\cos\phi, \qquad y = a(r)\cos\theta\sin\phi, \qquad z = c(r)\sin\theta.$$

Here $r \in [0, 1]$, $\phi \in [\phi_{min}, \phi_{max}]$, $\theta \in [\theta_{min}, \theta_{max}]$, $a(r) = a_1 + r(a_2 - a_1)$, $c(r) = c_1 + r(c_2 - c_1)$ and $a_i, c_i, i = 1, 2$ are given coefficients determining the main axes of the ellipsoid. We denote by r-layers the ellipsoidal surfaces described by varying ϕ, θ for a fixed value of r; analogously, we denote by ϕ-layers the plane surfaces described by varying r, θ for a fixed value of ϕ and by θ-layers the surfaces described by varying r, ϕ for a fixed value of θ (see Fig. 9.28 and Table 9.4).

We consider transmural 3-wall and W-wall heterogeneous distribution of intrinsic APD. More precisely:

W-wall. The cardiac tissue is subdivided transmurally into four layers: endocardial ($r \in [0, 0.12)$), sub-endocardial ($r \in [0.12, 0.32)$), midmyocardial ($r \in [0.32, 0.85)$) and epicardial ($r \in [0.85, 1]$). The I_K factor assumes the following values

$$fact_{I_K}^W = \begin{cases} 2.715 & r \in [0, 0.12) \text{ (endo)} \\ 1.952 & r \in [0.12, 0.32) \text{ (sub-endo)} \\ 2.47 & r \in [0.32, 0.85) \text{ (mid)} \\ 2.88 & r \in [0.85, 1] \text{ (epi)}, \end{cases}$$
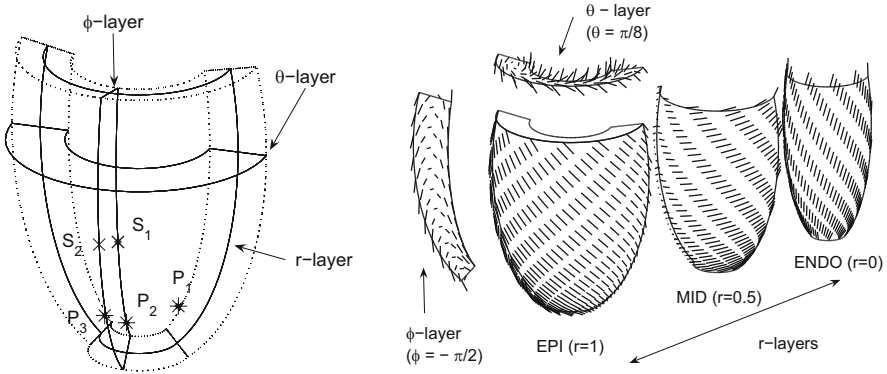
Fig. 9.28 *Left*: ellipsoidal domain and r, ϕ, θ-layers, S_1, S_2 = endocardial and epicardial stimulation sites, P_1, P_2, P_3 = Purkinje ventricular junctions. *Right*: fiber direction on r, ϕ, θ-layers

Table 9.4 Parameter calibration for the monodomain and bidomain models

$\chi = 10^3 \text{ cm}^{-1}$	$C_m = 10^{-3} \text{ mF/cm}^2$
$\sigma_l^e = 2 \times 10^{-3} \, \Omega^{-1} \text{ cm}^{-1}$	$\sigma_l^i = 3 \times 10^{-3} \, \Omega^{-1} \text{ cm}^{-1}$
$\sigma_t^e = 1.3514 \times 10^{-3} \, \Omega^{-1} \text{ cm}^{-1}$	$\sigma_t^i = 3.1525 \times 10^{-4} \, \Omega^{-1} \text{ cm}^{-1}$
$\sigma_n^e = \sigma_t^e/2$	$\sigma_n^i = \sigma_t^i/10$
$\phi_{min} = -\pi/2, \ \phi_{max} = \pi/2$	$\theta_{min} = -3\pi/8, \ \theta_{max} = \pi/8$
$a_1 = 1.5, \ a_2 = 2.7$	$c_1 = 4.4, \ c_2 = 5$
$n_\phi = 500, \ n_\theta = 500, \ n_r = 100$	

which yield APDs of 232 ms (endocardial), 272 ms (sub-endocardial), 242 ms (midmyocardial) and 225 ms (epicardial). This type of transmural heterogeneity composed of four cell layers reproduces qualitatively the APD heterogeneity measured in wedge preparations, see e.g. [572].

3-wall. The cardiac tissue is subdivided transmurally into three layers: endocardial ($r \in [0.0.33)$), midmyocardial ($r \in [0.33, 0.66)$) and epicardial ($r \in [0.66, 1]$). The factor for the I_K current assumes the following values

$$
fact^3_{I_K} = \begin{cases} 2.62 & r \in [0, 0.33) \text{ (endo)} \\ 1.952 & r \in [0.33, 0.66) \text{ (mid)} \\ 2.88 & r \in [0.66, 1] \text{ (epi)}, \end{cases}
$$

which yield APDs of 235 ms (endocardial), 272 ms (midmyocardial) and 225 ms (epicardial). The three resulting action potentials waveforms are shown in Fig. 9.29.
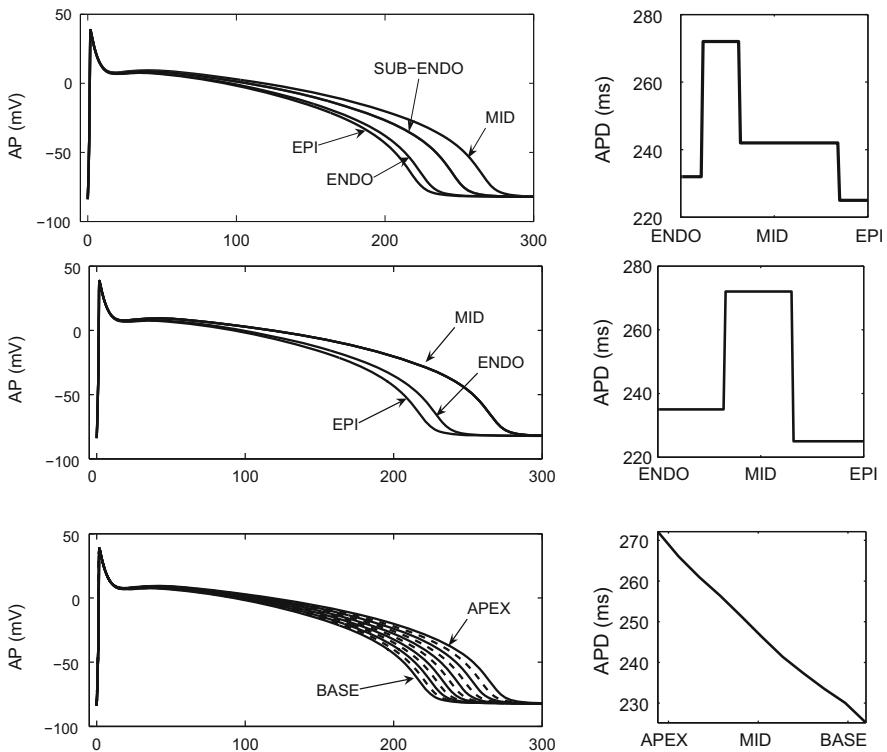
Fig. 9.29 *Top*: W-wall transmural intrinsic action potential profiles (*left*) and transmural intrinsic APD distribution (*right*). *Middle*: 3-wall transmural intrinsic action potential profiles (*left*) and transmural intrinsic APD distribution (*right*). *Bottom*: apex-to-base intrinsic action potential profiles (*left*) and apex-to-base intrinsic APD distribution (*right*)

This type of transmural heterogeneity composed of three cell layers has been previously used in [546] for 1D simulations.

Figures 9.30–9.33 display the patterns of excitation, repolarization and APD isochrones for the three ellipsoidal walls with endocardial stimulation. The same qualitative features of the excitation, repolarization and APD patterns previously described for the slab domains are also detected in these ellipsoidal walls. The visual inspection of the repolarization patterns on r-layers of the H-wall, 3-wall and W-wall shows that they are very similar, as confirmed by the high CC ($\geq$ 0.991) reported in Table 9.6. On the other hand, the APD correlation is lost on some r-layers. This correlation loss of the intramural APD patterns could be attributed to the interaction between the wall tapering and the associated curvature variation. This conclusion differs from the one obtained for cartesian slabs, where both repolarization and APD patters on intramural r-layers were found to be independent of the transmural variation of the intrinsic cellular APD.

9.3.2.1 Discussion

In the present investigation we studied the combined influence of (a) the transmural rotational anisotropy and (b) the transmural intrinsic APDs heterogeneity on the sequence of repolarization and APD distribution. We have used the Anisotropic Monodomain model coupled with the Luo-Rudy phase I membrane model, which has a lower computational cost than more advanced models incorporating additional ionic currents and a more complete intracellular calcium dynamics, see e.g. [243, 356]. We applied a single stimulus, either epicardial or endocardial, and compared the results obtained with homogeneous membrane properties (H-slab/wall) with the results obtained with two types of transmural heterogeneity (3-slab/wall and W-slab/wall). By considering action potentials elicited by a single stimulus (as opposed to a sequence of stimuli), our simulations are expected to enhance the disparity between excitation and recovery sequences and the dispersion of APDs, since it is well known that periodic stimulations, with relatively short cycle lengths, produce relatively short APDs with a reduced dispersion, see [479, Fig. 3].

In case of *homogeneous membrane* (H-slab/wall), the repolarization wave elicited by epi- or endocardial stimulation spreads anisotropically, like the corresponding activation pattern. Repolarization exhibits a somewhat faster motion, with intramural anisotropic patterns of APD distribution in sections parallel to the epicardial face and on transmural sections A, B, C, and D. Although the tissue is composed of cells with the same intrinsic properties, the electrotonic effects generate anisotropic spatial variations (epicardial and transmural) of the APD. The maximum of APD over the entire volume is consistently located at the stimulation site. Anisotropic spatial variations of the APD along and across fibers were observed experimentally in 2-D myocardial laminae by Osaka et al. [364], Gotoh et al. [208] and on the epicardium of dog hearts by Burgess et al. [67] and Taccardi et al. [512]. On the other hand, Bertran et al. [48], working with pig hearts, did not observe anisotropic APD differences in 2-D laminae from the
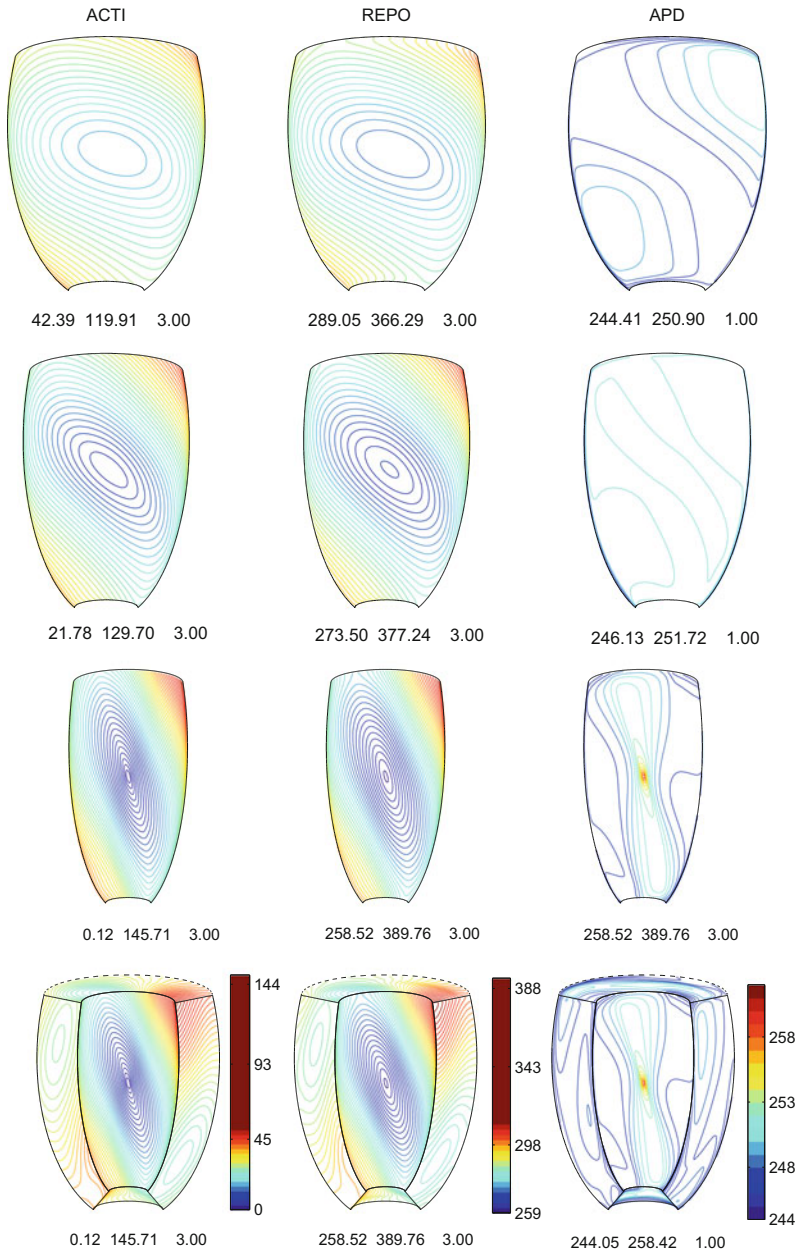
Fig. 9.30 Orthotropic Monodomain–LR1 model, homogeneous truncated ellipsoidal domain, endocardial central stimulation. Isochrone lines of the depolarization time (*first column ACTI*), repolarization time (*second column REPO*) and action potential duration (*third column APD*) on epicardial (*first row*), mid-myocardial (*second row*) and endocardial (*third row*) sections and on the whole domain (*fourth row*). Reported below each panel are the maximum, minimum and step in ms of the displayed map
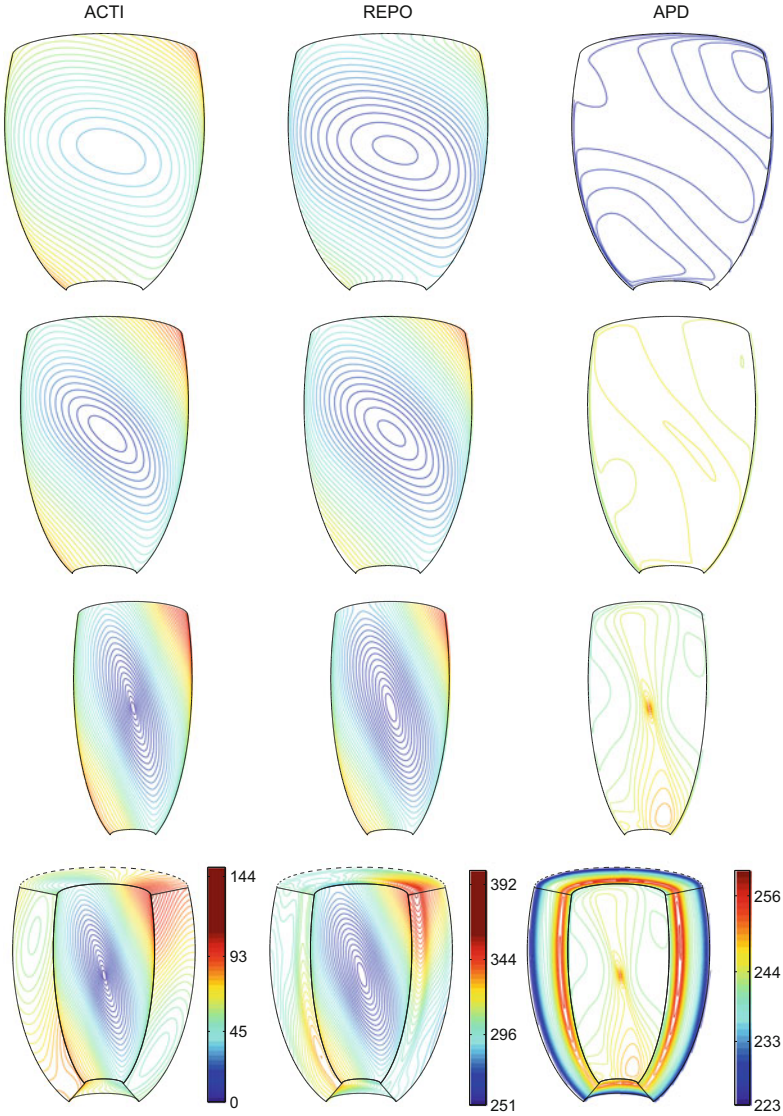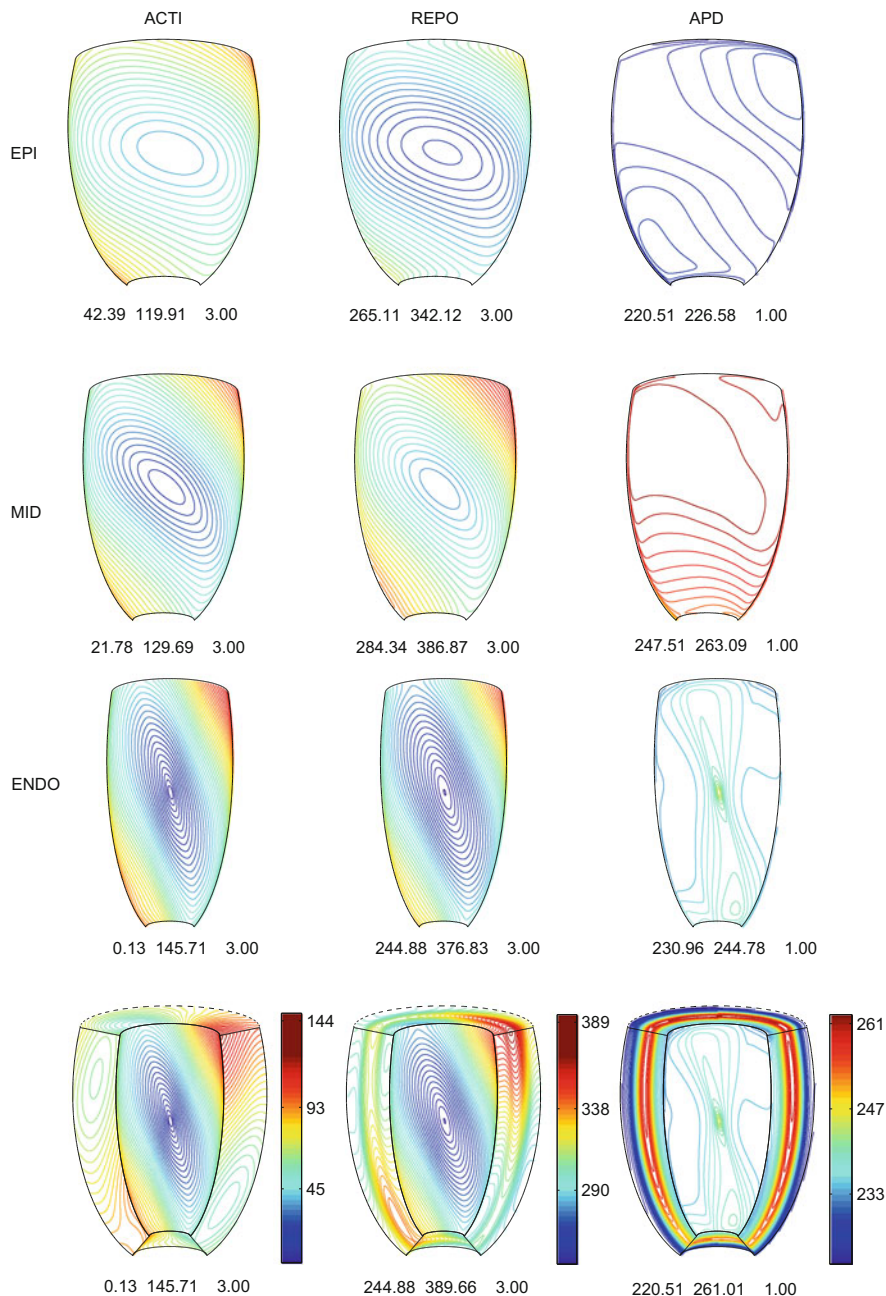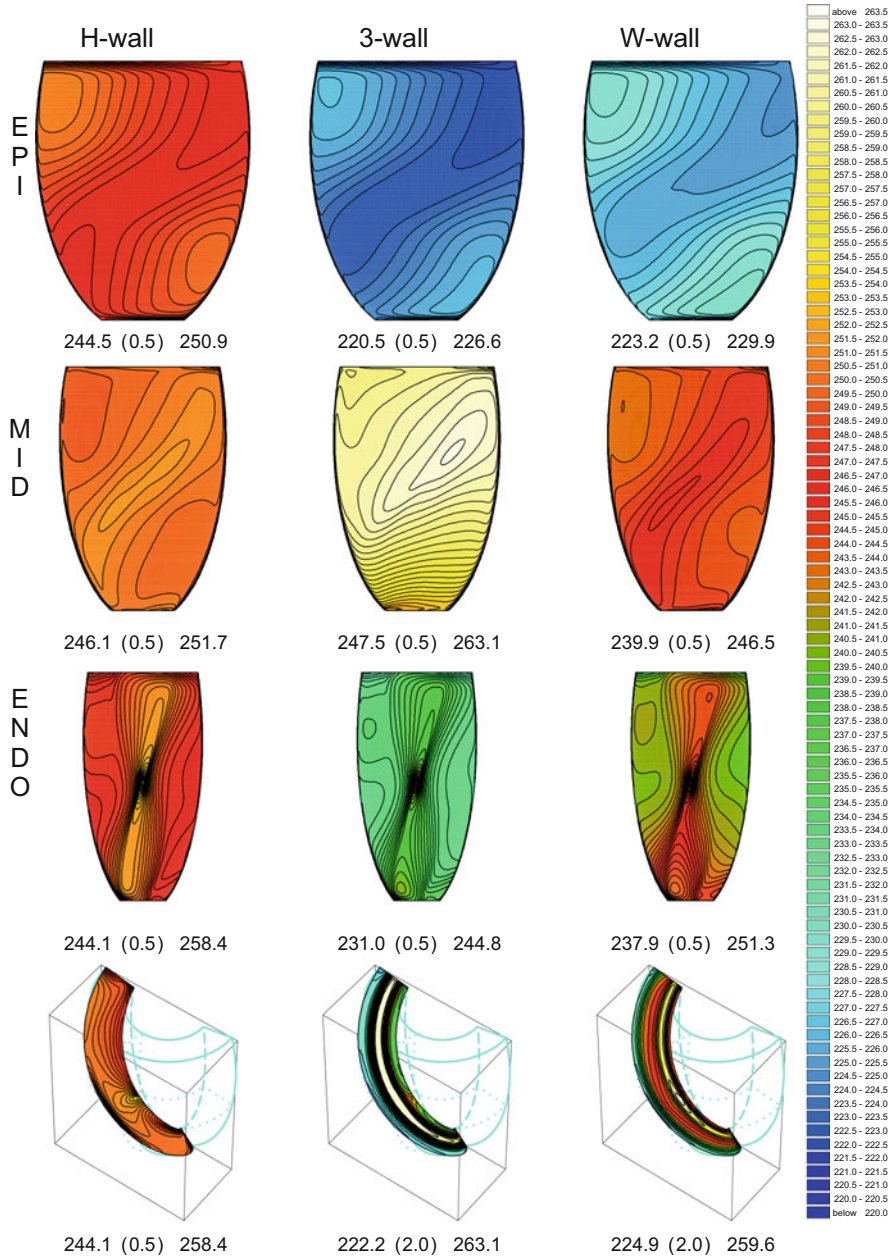
Fig. 9.31 Orthotropic Monodomain–LR1 model, W-wall with endocardial central stimulation. Isochrone lines of the depolarization time (*first column ACTI*), repolarization time (*second column REPO*) and action potential duration (*third column APD*) on epicardial (*first row*), mid-myocardial (*second row*) and endocardial (*third row*) sections and on the whole domain (*fourth row*). Reported below each panel are the maximum, minimum and step in ms of the displayed map

Fig. 9.32 Orthotropic Monodomain–LR1 model, 3-wall with endocardial central stimulation. Isochrone lines of the depolarization time (*first column ACTI*), repolarization time (*second column REPO*) and action potential duration (*third column APD*) on epicardial (*first row*), mid-myocardial (*second row*) and endocardial (*third row*) sections and on the whole domain (*fourth row*). Reported below each panel are the maximum, minimum and step in ms of the displayed map

Fig. 9.33 Orthotropic Monodomain–LR1 model, homogeneous and heterogeneous truncated ellipsoidal domains, endocardial central stimulation. Isochrone lines of the action potential duration on epicardial (*first row*), mid-myocardial (*second row*) and endocardial (*third row*) sections and on a transmural section (*fourth row*). Reported below each panel are the maximum, minimum and step in ms of the displayed map

left ventricle. In vitro experimental studies have demonstrated the heterogeneity of the action potential morphology and duration within the ventricular wall, see e.g. [7, 572] and the survey [8]. The intrinsic APD heterogeneity in the ventricular wall is not uniform, depending on the part of the ventricular wall where the myocytes or the transmural wedges are isolated [7] and also on the artificial environment of the preparation [533]. Therefore, in our simulations we have considered, in addition to homogeneous intrinsic membrane properties, also two different types of transmural heterogeneity, labeled 3-slab/wall and W-slab/wall in the previous sections, obtained by subdividing the cardiac domain into layers parallel to the epicardium, and assigning different cellular APD to each layer. In the 3-slab/wall, we considered three cell layers (subendo-, mid- and subepi-cardial), as used before in 1D simulation studies [96, 467, 546]. In the W-slab/wall, we incorporated four cell layers, in order to approximate the APD transmural distributions detected in experiments with wedge preparations (see [395, 396, 572]).

We have examined the effects of reversing the transmural activation from epicardial to endocardial central stimulation. In the heterogeneous cases, the distributions of both the transmural intrinsic APD and the transmural rotation of the fiber direction are not symmetric with respect to the intramural midwall plane, since the fiber direction rotates CCW from $-45°$ at the epicardium to $75°$ at the endocardium. Thus, the repolarization sequence and the APD distribution obtained with an endocardial stimulation display some differences with respect to the same features produced by an epicardial stimulation, and cannot be obtained from the latter by simply exchanging epicardium with endocardium.

Firstly, we have extracted from our 3D simulations the 1D profiles of the activation and repolarization times and of the APD elicited by a local epicardial or endocardial stimulation. These simulated profiles are qualitatively similar to those obtained by using homogeneous and heterogeneous 1D models of the ventricular wall, see [96, 452, 467, 496, 546], but they do not coincide due to the presence of anisotropic curvature effects. Only the case of a plane front obtained by stimulating the whole epicardial or endocardial face of our cardiac slab could be reduced to a 1D propagation, but this is not our case.

In our simulations on *heterogeneous slabs*, when we switched the pacing site from epicardium to endocardium, the dispersion of repolarization times along the vertical line passing through the pacing site decreased from 46 to 33 ms for the 3-slab and from 47 to 14 ms for the W-slab (Table 9.5); this is consistent with the simulations and measurement in Fish et al. [176]. Also, the profile of the repolarization time displayed very different shapes in the two pacing protocols (see Figs. 3 and 5). On the other hand, unlike Fish et al. [176] findings, the APD dispersion in the two pacing protocols increased, when we moved from epi to endo pacing while the APD profiles showed very similar shapes. These large differences between the epicardial and endocardial stimulations are not present in the full domain of the slab: for example, epicardial pacing for the W-slab yields a total dispersion of 103 ms for the repolarization time and 31 ms for the APD, while endocardial pacing for the same slab yields dispersions of 108 ms for the repolarization time and 34 ms for the APD.

Table 9.5 Dispersion (MAX–MIN value) of activation time (ACTI), repolarization time (REPO), APD 90 on the 1-D transmural line passing through the stimulation site and orthogonal to both epicardial and endocardial surfaces

	Epicardial stimulation			Endocardial stimulation		
	ACTI	REPO	APD 90	ACTI	REPO	APD 90
H-slab	35.26	24.62	10.53	35.48	23.90	11.45
3-slab	35.26	46.76	28.99	35.48	33.50	37.36
W-slab	35.26	46.79	19.91	35.48	14.74	31.78

In our heterogeneous models, the amount of assigned transmural intrinsic heterogeneity yields a dispersion of APDs which is lower than that observed in experimental wedge preparations, but is sufficient to produce a transmural change of the repolarization sequence, compared with the homogeneous model. This sequence is partially independent of the activation process and the lateral spread of repolarization is driven by the transmural intrinsic heterogeneity of APDs. The APD distribution on transmural sections exhibits a striped structure with elongated equilevel lines, which are mostly flat and parallel to the epi- and endocardial surfaces.

In sections parallel to the epi- and endocardial faces the repolarization sequences and APD patterns are not affected by the transmural APD heterogeneity, except for the absolute values of the two variables. More precisely, the distributions of the repolarization times and APDs on sections parallel to the epicardium are strongly correlated in the three different slabs/walls.

On intramural sections parallel to the epicardial surface, in the 3-slab and W-slab, the quasi-elliptical pattern of repolarization isochrones is qualitatively similar to that observed in the homogeneous slab, showing that the spread of repolarization in these sections is primarily determined by the activation sequence and the rotational anisotropy. This confirms that the repolarization sequence is not associated with a propagating wavefront, but it is a phase wave.

Thus, in spite of the coupling effects due to diffusion, reaction and modulation, the transmural heterogeneity does not influence the patterns on intramural sections parallel to the epicardial face, but produces effects that remain confined in the transmural direction. The finding that the effects of the heterogeneity and the rotational anisotropy are so clearly decoupled in the heterogeneous slabs was unexpected. Clearly, the former effects prevail in the transmural direction and the latter in the sections parallel to the epicardial surface. This complex interactions between orthotropic anisotropy, fiber rotation and cell heterogeneities determine complex excitation and repolarization wavefronts that cannot be understood by using simple 1D simulations.

We remark that in vivo experimental studies, see e.g. in intact canine [9,161,515] or human [517] hearts, the observed APD dispersions are lower than the dispersions observed in isolated cells and in wedge preparations. We refer also to [9,70] for a discussion about the difference between in vivo and in vitro measurements. Recent experimental studies [515] in exposed and isolated dog hearts have shown that the

transmural dispersion of APD in the left ventricular wall is on the order of 15–20 ms during ventricular pacing with cycle length of 350 or 400 ms. In these preparations, the repolarization sequence is often qualitatively similar to the activation sequence. When the pacing site was epicardial, both the excitation and the repolarization fronts returned toward the epicardium in a transmural plane perpendicular to the epicardial fiber direction near the pacing site. However, confirmatory studies are needed in order to determine whether these findings occur consistently in varying experimental conditions. Moreover, Taccardi et al. [512] observed a typical tripolar epicardial APD pattern, with one central maximum and two minima in the cross-fiber direction, on the left ventricular epicardium of exposed dog hearts during left ventricular pacing. Poelzing et al. [395, 396] found that in a narrow subepicardial layer the intercellular conductance is lower than in deeper layers, due to a local shortage of gap junctions. This factor contributes to the transmural inhomogeneity of excitation velocity and recovery durations.

As mentioned before, the data on transmural dispersion of APD currently available in the literature are not consistent, since there is a disparity between the transmural dispersion of the APD observed in in vivo hearts, see e.g. [9, 258], and in vitro experiments in wedge preparations, see e.g. [8, 572]. The transmural APD dispersion reported by the former authors is less than the one reported by the latter.

In this simulation study on the electrotonic modulation in a three dimensional structure, we assumed that: (i) the heterogeneity of the intrinsic APDs is transmural, i.e. the APDs values are constant in each section parallel to the epicardial face; (ii) the fibers have a constant orientation in each section parallel to the epicardial face; (iii) an idealized sheet-fiber model (iv) a normal cell coupling (i.e. normal conductivity coefficients). The simulations show that the electrotonic modulation is not strong enough to level the intrinsic transmural APD differences, but these strong differences are not revealed at the epicardial level. Hence, our results do not explain why in *intact* hearts several investigators, see e.g. [9, 258], have observed a strongly reduced dispersion of APD across the ventricular wall as compared with the dispersion observed in wedge preparations.

In conclusion, the complex 3-D paths of electrotonic currents during the repolarization phase in our orthotropic medium do not seem to extend the effects of transmural inhomogeneity to the sections parallel to the epicardium. These results suggest the presence of two separate and competing mechanisms that modulate the repolarization sequence and APD patterns, one due to the rotational anisotropy and the other to the transmural heterogeneity of intrinsic APD. While the first seems to prevail in the sections parallel to the epicardium, the second is the major determinant of the transmural shape of repolarization fronts and APD patterns outside a volume surrounding the transmural line issuing from the stimulation site.

9.3.3   Transmural and Apex-Base Heterogeneity in 3-D Ellipsoids

We now extend the previous simulations in ellipsoidal cardiac domains to the case of apex-to-base and mixed transmural APD heterogeneities; for more results and details we refer to [130]. In particular, we consider the following heterogeneous ellipsoidal domains:

Apex-base-wall. The intrinsic APDs of cells vary in this case with respect to the θ-direction. We define the intrinsic APD along the apex-to-base direction decreasing monotonically from apex to base, by introducing a scaling factor $fact_{I_K}$ of the I_K current depending linearly on θ according to the following rule

$$fact_{I_K}^{AB}(\theta) = \frac{2.88 - 1.952}{\theta_{max} - \theta_{min}}(\theta - \theta_{min}) + 1.952,$$

for $\theta \in [\theta_{min}, \theta_{max}]$. The resulting dependence of APD on θ is reported in Fig. 9.29, showing an almost linear variation from 272 ms at the apex to 225 ms at the base, with an intrinsic APD dispersion of 47 ms.

Mixed-wall. Both transmural 3-wall and apex-to-base-wall heterogeneities are introduced in the cardiac tissue by setting $fact_{I_K} = fact_{I_K}^3 + fact_{I_K}^{AB}(\theta)$, i.e.

$$fact_{I_K} = \begin{cases} 2.62 + fact_{AB}(\theta) & \theta \in [\theta_{min}, \theta_{max}], \ r \in [0, 0.33) \text{ (endo)} \\ 1.952 + fact_{AB}(\theta) & \theta \in [\theta_{min}, \theta_{max}], \ r \in [0.33, 0.66) \text{ (mid)} \\ 2.88 + fact_{AB}(\theta) & \theta \in [\theta_{min}, \theta_{max}], \ r \in [0.66, 1] \text{ (epi)}. \end{cases}$$

We investigate the interaction between the two intrinsic APD heterogeneities considered, one in the transmural direction (3-wall) and the other in the intramural apex-to-base direction (apex-base-wall). Unexpectedly, the repolarization and APD patterns on r-layers of the apex-base-wall (Fig. 9.34) and the mixed-wall (Fig. 9.35) are very similar apart from their numerical values. On the other hand, the patterns displayed on the transmural diagonal section are very dissimilar due to the transmural heterogeneity in the mixed-wall. As in the case without apex-to-base heterogeneity (Fig. 9.36), the transmural heterogeneity has only a weak influence on the repolarization patterns on the r-layers, apart from a shift toward the ventricular base of the site that repolarize first and an increase of the spatial dispersion.

In order to quantitatively study the influence of the two heterogeneities, we computed the correlation coefficient (CC) on the intramural r-layers and transmural ϕ- and θ-layers, for the pair 3-wall and mixed-wall, and for the pair apex-base-wall and mixed-wall. The average CCs on each layer are reported in Table 9.6. The results confirm that the two heterogeneities are somewhat decoupled, i.e. (a) the high CC values on θ-layers show that the repolarization and APD patterns are independent of the apex-to-base heterogeneity and mostly determined by the transmural heterogeneity; (b) the high CC values on r-layers show that the repolarization and APD patterns are independent of the transmural heterogeneity
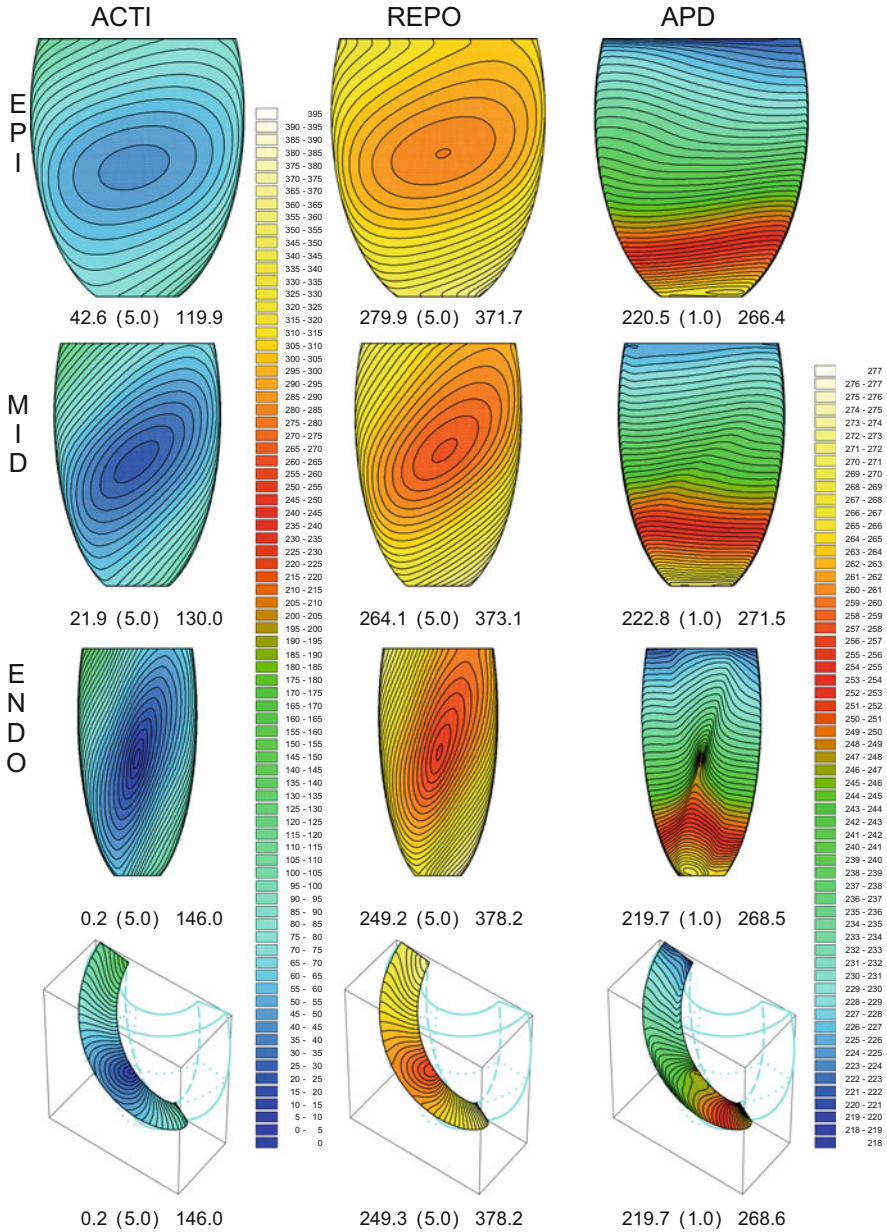
Fig. 9.34 Apex-base-wall with central endocardial stimulation. Same format as Fig. 9.36 (Reproduced with permission from [130])
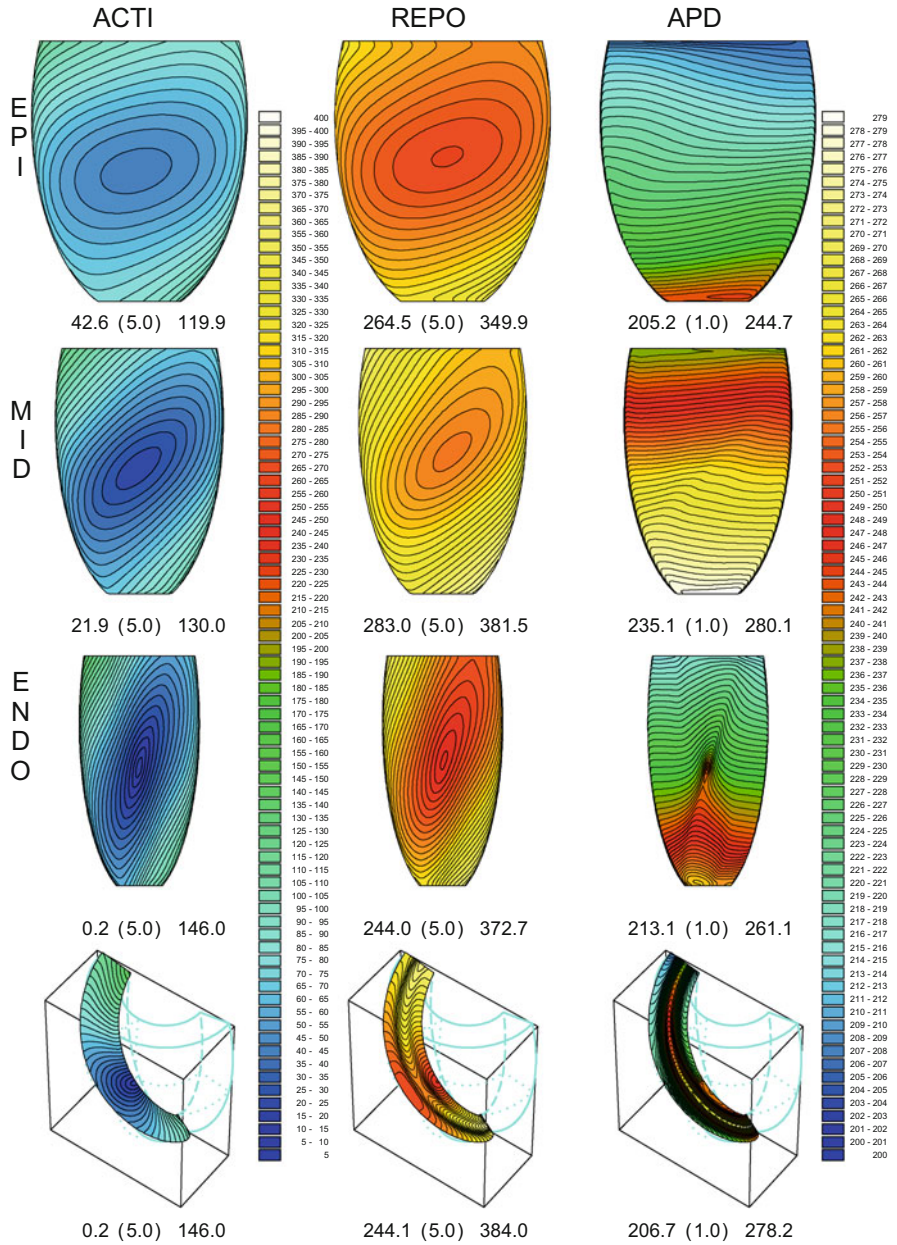
Fig. 9.35 Mixed-wall with central endocardial stimulation. Same format as Fig. 9.36 (Reproduced with permission from [130])
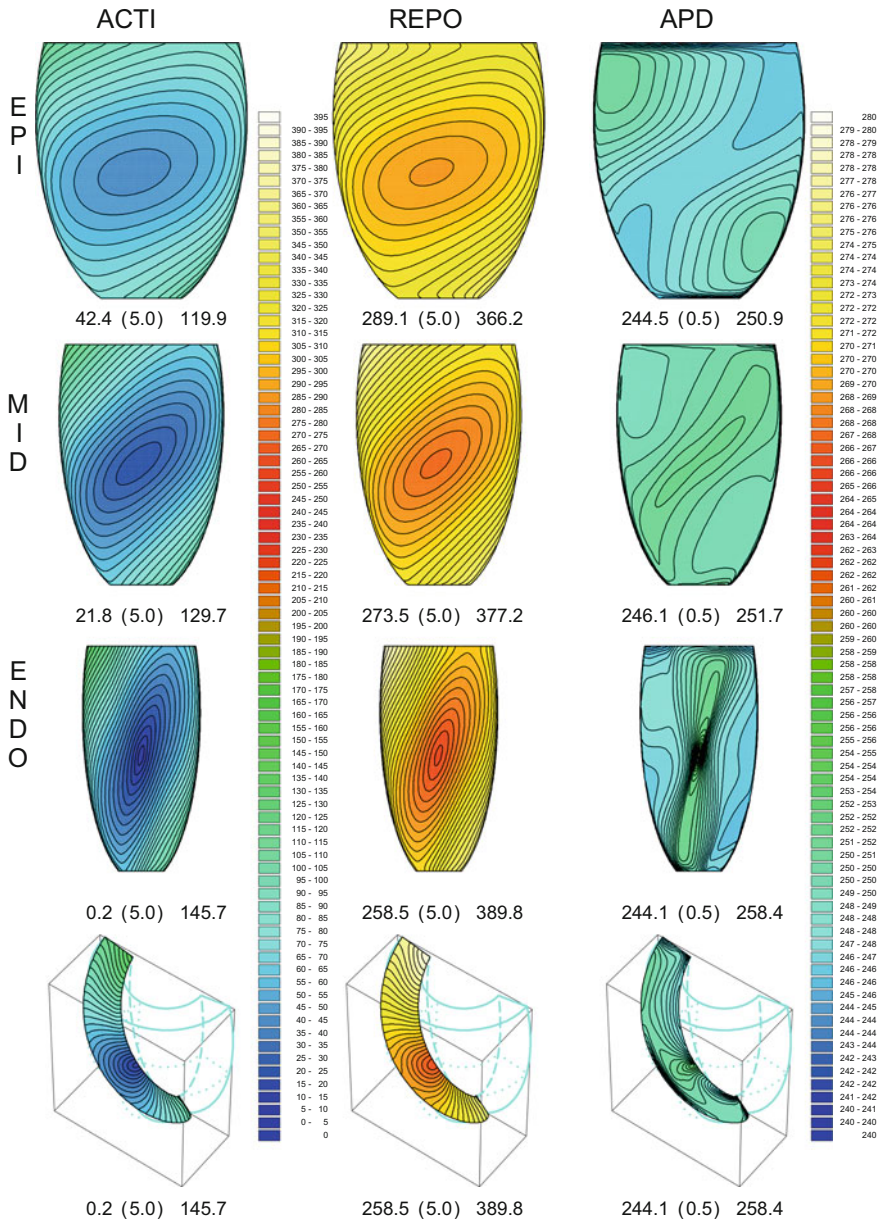
Fig. 9.36 H-wall with central endocardial stimulation. Activation (*ACTI*, *first column*), repolarization (*REPO*, *second column*), APD (*third column*) patterns on the epicardium (*EPI*, *first row*), midwall (*MID*, *second row*), endocardium (*ENDO*, *third row*), diagonal section (*fourth row*). Below each panel are reported the minimum, stepsize (*in brackets*), and maximum value of the displayed map (Reproduced with permission from [130])

Table 9.6 Average correlation coefficients of repolarization times and APD on r,ϕ, θ-layers

		Endo stim.			Epi stim.		
		Average CC on			Average CC on		
		r-layer	ϕ-layer	θ-layer	r-layer	ϕ-layer	θ-layer
H-wall,3-wall	REPO	0.997	0.838	0.841	0.998	0.842	0.565
	APD	0.590	0.460	0.442	0.699	0.386	0.366
H-wall,W-wall	REPO	0.999	0.913	0.911	0.999	0.914	0.657
	APD	0.830	0.273	0.275	0.873	0.373	0.376
3-wall,mixed-wall	REPO	0.853	0.890	0.997	0.882	0.887	0.997
	APD	0.146	0.673	0.999	0.150	0.668	0.999
Apex-base-wall, mixed-wall	REPO	0.998	0.854	0.829	0.999	0.904	0.562
	APD	0.993	0.745	0.455	0.992	0.739	0.375

and mostly determined by the apex-to-base heterogeneity. We remark that due to the transmural fiber rotation and the presence of the fiber imbrication angle, the complex three-dimensional anisotropic current density vectors cross each $r-$ and $\theta-$layers transversally. Nevertheless, the repolarization and APD patterns on $\theta-$layers unmask the transmural heterogeneity and musk the apex-to-base heterogeneity and opposite holds for the patterns on the r-layers.

We also consider a case with multiple stimulations in order to mimic the presence of a few Purkinje ventricular junctions. More precisely, we consider on the endocardium three stimulation sites near the apex, with stimuli delivered at 0, 4, 8 ms, see e.g. Fig. 9.37 for the apex-base-wall results. Similar results and observations described above apply to this strongly different case with multiple activation and repolarization wavefronts.

Our simulations have shown that in cardiac walls with constant curvature, such as a slab or a spherical wall geometry, the repolarization sequence and APD patterns on the wall surfaces parallel to the epicardium (r-layers) do not reveal the type of underlying transmural APD heterogeneity.

In walls with variable curvature and tapering, the repolarization sequences on all intramural r-layers (apart from their numerical values) again appear to be independent of the underlying transmural heterogeneity, while only the epicardial and endocardial APD patterns appear to be independent of the APD transmural heterogeneity.

As a corollary, the epicardial repolarization and APD patterns are dominated by the influence of the apex-to-base heterogeneity, whereas the same patterns on the transmural layers are dominated by the transmural heterogeneity. Hence, the epicardial features of the repolarization and APD patterns do not allow us to make inferences about the variation of the underlying transmural heterogeneities, while they allow us to detect the presence of apex-to-base heterogeneity. These findings are independent of the stimulus location (epicardial, endocardial) and of Purkinje involvement.
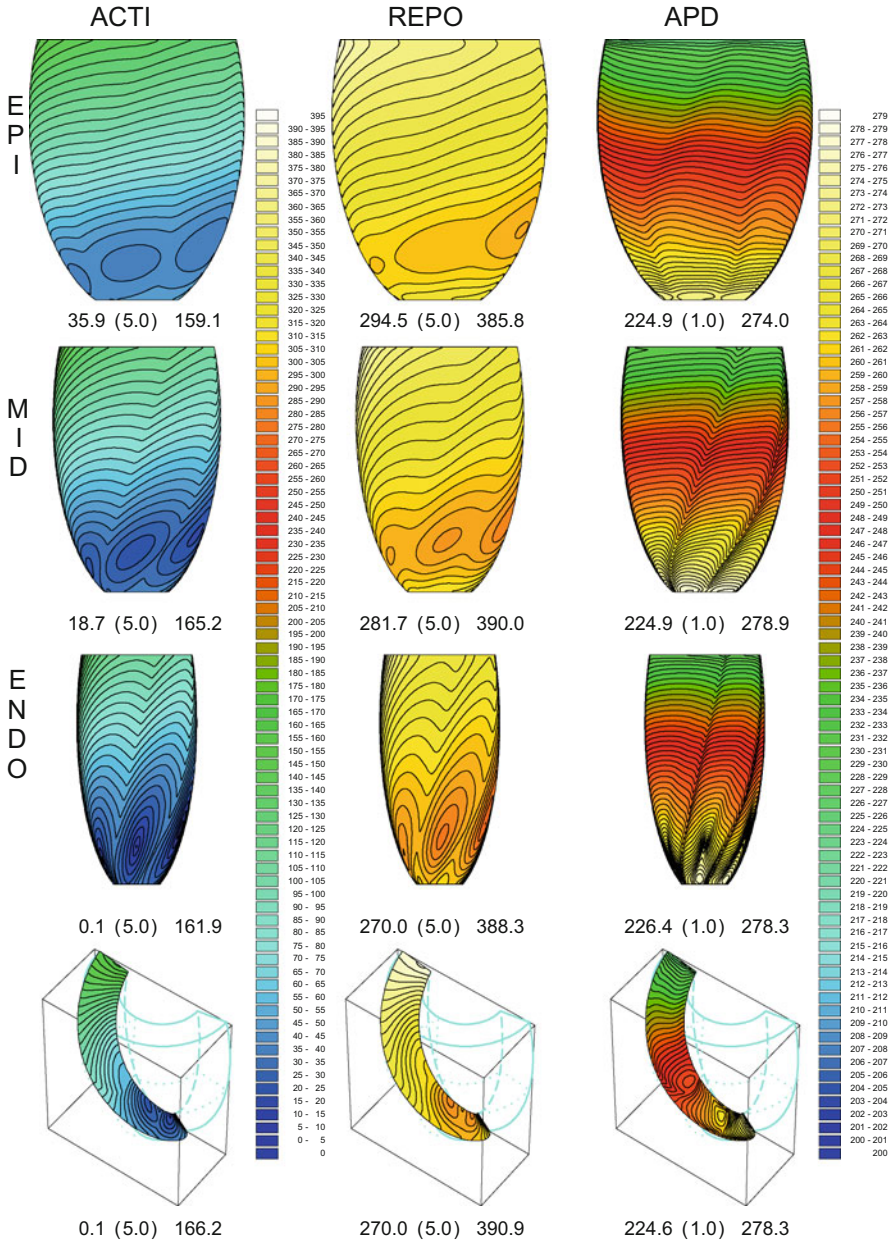
Fig. 9.37 Apex-base-wall, Purkinje stimulation. Same format as Fig. 9.36 (Reproduced with permission from [130])

Our main finding is that for cardiac tissue with normal cell coupling the anisotropic diffusion current (electrotonic modulation) is not sufficient to mask the intrinsic repolarization differences (both transmural and apex-to-base) between each myocyte and its neighboring cells. Thus, in our orthotropic ellipsoidal wall, the complex 3D electrotonic modulation of APDs does not fully mix the effects of the transmural and apex-to-base heterogeneity. The intrinsic spatial heterogeneity of the APDs is unmasked in the modulated APD patterns only in the appropriate transmural or intramural sections.

9.4   QRS Complex and T Wave Morphology in Electrograms

The factors determining the shape and polarity of the T wave in electrocardiograms (ECGs) are still a matter of debate. According to the classical theory based on the double layer source model (see e.g. [538] and the classical references therein), an activation sequence starting from the endocardium and proceeding towards the epicardium generates ECG waveforms at leads facing the epicardium with an R wave. By applying the heart surface model (see e.g. [483, 538]), it is generally believed that if the repolarization sequence follows the activation one, then a negative T wave is expected, due to opposite direction of the transmembrane potential gradients during the downstroke phase of the action potential. On the contrary, measured human Einthoven leads II exhibit QRS complex and T wave with the same positive polarity. In order to explain this discrepancy, a different transmural repolarization sequence within the ventricular wall has been proposed, where the epicardium recovers before the endocardium based on the assumption that the action potential duration (APD) of epicardial cells is considerably shorter than the APD of endocardial cells. Experimental evidence of transmural APD heterogeneity and of transmural repolarization gradients has been established in [571] for isolated cells and in vitro wedge preparations of canine left ventricles. Computational studies on isotropic [95, 148, 176, 205] or anisotropic cardiac tissue [58], with transmural APD cell heterogeneity, have been able to reproduce concordant R and T waves. Nevertheless, a repolarization sequence directed from epicardium to endocardium has never been observed in in vivo animal models; see [133, 183, 258, 517]. In alternative to transmural repolarization gradients, apico-basal APD heterogeneities have been proposed as a determinant of the T wave polarity. The aim of this section is to provide some insight on how the tissue anisotropy, cellular APD heterogeneities and shape of excitation wavefronts influence the polarity of the T wave in unipolar and bipolar ECGs. The study is based on three-dimensional simulations of the entire depolarization and repolarization phases of the propagating action potential, using the insulated anisotropic Monodomain model in a slab of cardiac tissue. Then the primary source is used to compute the extracardiac potential in an unbounded homogeneous conducting medium.

9.4.1   Methods and Parameter Calibration

The anisotropic Monodomain model. The evolution of the transmembrane potential $v(\mathbf{x}, t)$, extracellular/extracardiac potential $u(\mathbf{x}, t)$, gating variables $w(\mathbf{x}, t)$ and ionic concentrations $c(\mathbf{x}, t)$, is described by the reaction-diffusion system

$$
\begin{cases}
c_m \partial_t v - \operatorname{div}(D_m \nabla v) + i_{ion}(v, w, c) = i_{app} & \text{in } \Omega_H, \quad \mathbf{n}^T D_m \nabla v = 0 \text{ on } \partial\Omega_H \\
\partial_t w - R(v, w) = 0, \quad \partial_t c - S(v, w, c) = 0 & \text{in } \Omega_H \\
-\operatorname{div} D \nabla u = \begin{cases} \operatorname{div} D_i \nabla v & \text{in } \Omega_H \\ 0 & \text{in } \mathbb{R}^3 \setminus \Omega_H \end{cases} \quad \text{where } D = \begin{cases} D_i + D_e & \text{in } \Omega_H \\ \sigma_0 I & \text{in } \mathbb{R}^3 \setminus \Omega_H \end{cases}
\end{cases}
$$

$$(9.3)$$

with appropriate initial conditions. Here Ω_H is the cardiac volume, c_m and i_{ion} denote the capacitance and the ionic current of the membrane per unit volume, i_{app} represents the applied current per unit volume, and σ_0 is the conductivity coefficient of the extracardiac medium.

The conductivity tensors $D_i(\mathbf{x})$ and $D_e(\mathbf{x})$ at any point $\mathbf{x} \in \Omega_H$ are defined as in (3.41). The Monodomain conductivity tensor D_m is given by $D_m = D_e(D_i + D_e)^{-1} D_i$, see Chap. 4.

The fibers rotate intramurally linearly with the depth for a total amount of $120°$ and when the point of view is from the epicardial side, the rotation is counterclockwise proceeding from the epicardium to endocardium. More precisely, in the canonic reference system $(\mathbf{e}_1, \mathbf{e}_2, \mathbf{e}_3)$, the fiber direction $\mathbf{a}_l(\mathbf{x})$ and the other two principal axes at a point $\mathbf{x}$ are given by

$$
\mathbf{a}_l(\mathbf{x}) = u_{e1} \cos\alpha(r) + u_{e2} \sin\alpha(r), \quad \mathbf{a}_t(\mathbf{x}) = u_{e3}, \quad \mathbf{a}_n(\mathbf{x}) = u_{e1} \sin\alpha(r) - u_{e2} \cos\alpha(r)
$$
$$
\alpha(r) = \tfrac{2}{3}\pi(1 - r) - \tfrac{\pi}{4}, \quad \text{with } r \in [0, 1].
$$

The conductivity tensors are assumed orthotropic with conductivity coefficients along the principal axis given in the Table 9.7 (right) below.

Table 9.7 Parameter calibration for modeling the transmural heterogeneities (*left*) and conductivity coefficients in mS cm^{-1} (*right*)

Slab type	H-slab	3-slab				Conductivity coefficients		
Number of layers	1	3					Intra	Extra
Layer thickness (cm)		Endo	Mid	Epi		σ_l	3	2
	1	0.33	0.34	0.33		σ_t	0.3152	1.3514
fact_I_K	1	2.62	1.95	2.88		σ_n	0.0315	0.6757
APD (ms)	266	235	272	225		$\sigma_0 = 6$		

Transmural heterogeneity. The membrane model employed is the Luo-Rudy phase I (LR1) ionic membrane model (see [308]), requiring six gating variables and one calcium concentration variable. We consider two different types of transmural distribution of the intrinsic APDs of the cells, one homogeneous (**H-slab**) and one heterogeneous (**3-slab**). The transmural intrinsic APD heterogeneity is assumed to be the same along any transmural epi-endocardial straight line, i.e. in any plane parallel to the epicardium all cells have the same intrinsic APD. In the heterogeneous slab, the intrinsic APD of the cells is obtained by multiplying the potassium current I_K in the LR1 model by a factor fact_{I_K}. This modulation factor is chosen in order to introduce a transmural APD profile with M-cell layers; see Table 9.7, Fig. 9.38-right and [126, 205] for more details.

Computation of unipolar and bipolar electrograms. Unipolar ECGs u are computed at an array of 3×3 points on planes located 2 cm (1 cm, not shown) above the epicardium (plane L_1) and 2 cm (1 cm, not shown) below the endocardium (plane L_2), see Fig. 9.38-left. In order to investigate the qualitative behavior of the T wave of ECGs for sites at some distance from the active tissue, we disregard the anisotropic conduction effects of the bulk tissue, but we take into account the anisotropic cardiac source structure. Thus, the ECGs far away from the tissue slab are computed by assuming $D_i + D_e \approx \sigma_0 I$, hence according to the formula (see e.g. [117, 119, 295, 483])

$$u(\mathbf{x}, t) = -\frac{1}{4\pi\sigma_0} \int_{\Omega_H} D_i(\mathbf{y})\nabla v(\mathbf{y}, t) \cdot \nabla \left(\frac{1}{|\mathbf{y} - \mathbf{x}|}\right) d\mathbf{y}, \tag{9.4}$$

where $D_i(\mathbf{y})\nabla v(\mathbf{y}, t)$ represents the anisotropic cardiac electric sources generating the extracardiac potential field.
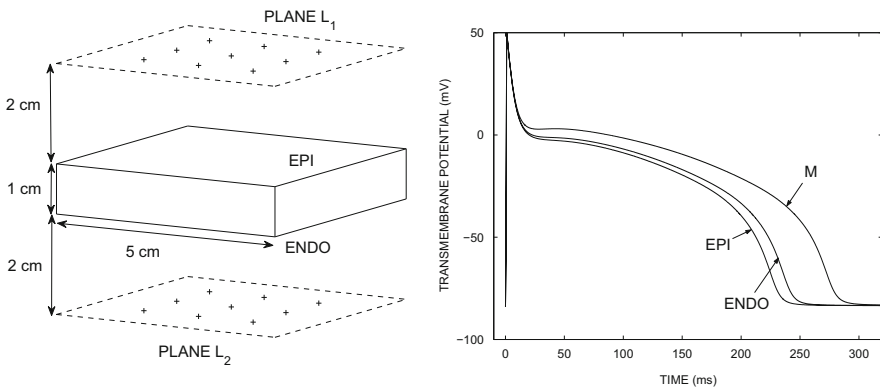
Fig. 9.38 *Left*: cardiac slab and location of the 3×3 transmural ECG electrode array 2 cm above the epicardial surface (plane L_1) and 2 cm below the endocardial surface (plane L_2). *Right*: Epicardial, Midmyocardial and Endocardial action potentials in the transmural heterogeneous **3-slab** calibration

Decomposition of the ECG waveform. In order to study the contribution of the anisotropic cardiac sources to the T wave morphology, we introduce an additive splitting of the intracellular conductivity tensor $D_i = D_{HS} + D_{AS}$ given by

$$D_{HS} = \sigma_t^i \mathbf{I} \quad \text{and} \quad D_{AS} = (\sigma_l^i - \sigma_t^i)\mathbf{a}_l(\mathbf{x})\mathbf{a}_l^T(\mathbf{x}) + (\sigma_n^i - \sigma_t^i)\mathbf{a}_n(\mathbf{x})\mathbf{a}_n^T(\mathbf{x}).$$

This splitting of D_i induces an analogous splitting of the cardiac sources into the so called double layer or heart surface (HS) source model (see [483, 538]) and into a residual anisotropic source (AS). Consequently, the source term is decomposed as $D_i \nabla v = D_{HS} \nabla v + D_{AS} \nabla v$ and since u depends linearly on $D_i \nabla v$ in Eq. (9.4), the full unipolar ECG is decomposed as the sum of an isotropic (heart surface) and anisotropic components $u = u_{HS} + u_{AS}$. Given two points $\mathbf{x}_{epi}$ 2 cm above the epicardium (plane L_1) and $\mathbf{x}_{endo}$ 2 cm below the endocardium (plane L_2), we introduce also the transmural bipolar ECG ψ given by $\psi(\mathbf{x}_{epi}, \mathbf{x}_{endo}, t) = u(\mathbf{x}_{epi}, t) - u(\mathbf{x}_{endo}, t)$. Using the same splitting as before, we also decompose the full bipolar ECG ψ into the HS component $\psi_{HS}(\mathbf{x}_{epi}, \mathbf{x}_{endo}, t)$ and the anisotropic component $\psi_{AS}(\mathbf{x}_{epi}, \mathbf{x}_{endo}, t)$.

Numerical methods. The cardiac domain Ω_H considered is a cartesian slab of dimensions $5 \times 5 \times 1 \, \text{cm}^3$ modeling a portion of the left ventricle; see Fig. 9.38-left. In all computations, a structured grid of $500 \cdot 500 \cdot 100$ hexahedral isoparametric Q_1 elements of size $h = 0.1 \, \text{mm}$ is used in space. The time discretization is based on an Euler Imex method.

9.4.2 Unipolar and Bipolar ECG Simulations

We consider two endocardial stimulation protocols: a single (ectopic) site stimulation (S_1), eliciting a twisted semi-ellipsoidal excitation front, or multiple (12) sites stimulation (S_2), modeling a simplified Purkinje network, eliciting a large excitation front spreading transmurally mainly across fiber. These two protocols are applied to both **H-slab** and **3-slab**, for a total of four simulations.

S_1**: unipolar ECGs.** The activation (ACTI) and repolarization (REPO90) isochrones on a transmural section of the tissue are reported in Fig. 9.39a. The HS components of all unipolar ECGs on plane L_2 (2 cm below the endocardium) for **H-slab** (see Fig. 9.40a) display a Q wave and a positive T wave, as expected. The same behavior is also observed in 3-slab case (not shown), where the intramural repolarization sequence displays a primary and a secondary fronts coming from the endocardial and epicardial surfaces, respectively. Instead, the HS components on plane L_1 (2 cm above the epicardium) display a QRS complex with R and S waves and, unexpectedly for a tissue without transmural heterogeneities, a positive T wave, see Fig. 9.41a, c. The AS components of unipolar ECGs on both planes L_1 and L_2 display a Q wave and a positive T wave. The same morphology is shared by the full unipolar ECGs on both planes L_1 and L_2 (Figs. 9.40a and 9.41a, c).
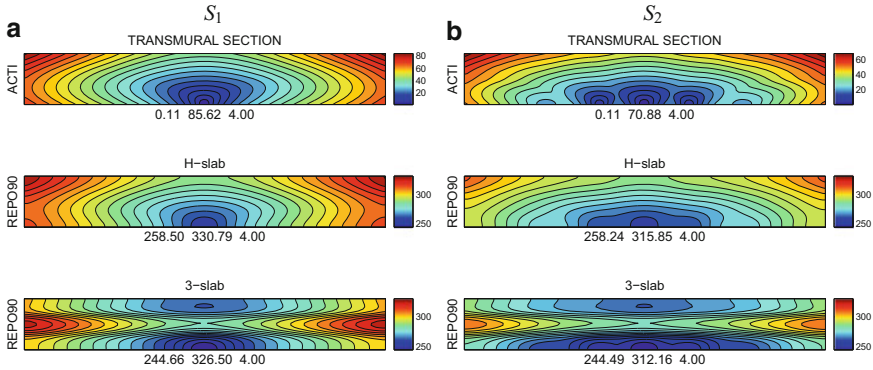
Fig. 9.39 (**a**): Single site stimulation (S_1), isochrones of activation time ACTI (*first row*) and repolarization time REPO90 (*second* and *third row*) on a transmural diagonal section of **H-slab**, **3-slab**. (**b**): Multiple sites stimulation (S_2), same format as in (**a**)
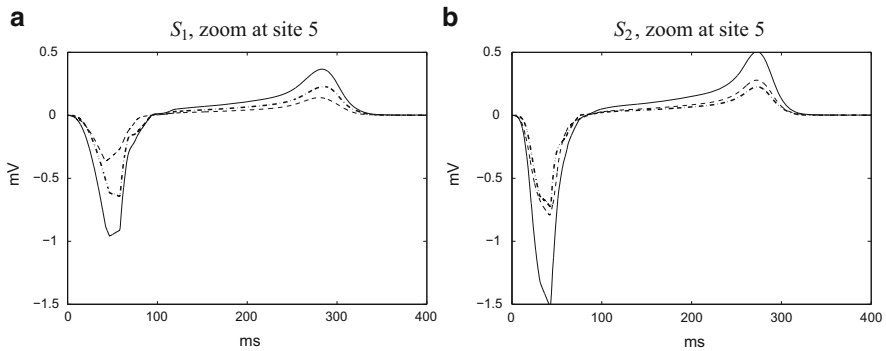

Fig. 9.40 H-slab: Unipolar ECGs at site 5 on plane L_2 (site 5 is the central one in the 3×3 array, see Fig. 9.41). (**a**): Single site stimulation (S_1). (**b**): Multiple sites stimulation (S_2). *Continuous line*: full unipolar ECG. *Dashed line*: HS component. *Dashed-Dotted line*: AS component

This fact indicates that the full unipolar ECGs are dominated by their anisotropic AS components. The HS components have little influence on the full ECGs, since their positive T waves reinforce those of the full ECGs but their R waves at almost all sites on plane L_1 are absent in the QRS complex of the full ECGs. Analogous morphological considerations hold for the **3-slab** (Fig. 9.42), although with slight differences in magnitude.

S_2**: unipolar ECGs.** The isochrones of ACTI and REPO90 on a transmural section of the tissue are reported in Fig. 9.39b. The excitation wavefronts are larger than those elicited by the ectopic stimulation. On plane L_2, the morphology of the unipolar ECGs is the same as in the ectopic case described before; see Fig. 9.40b. On plane L_1, all the AS components have Q waves and positive T waves, while the HS
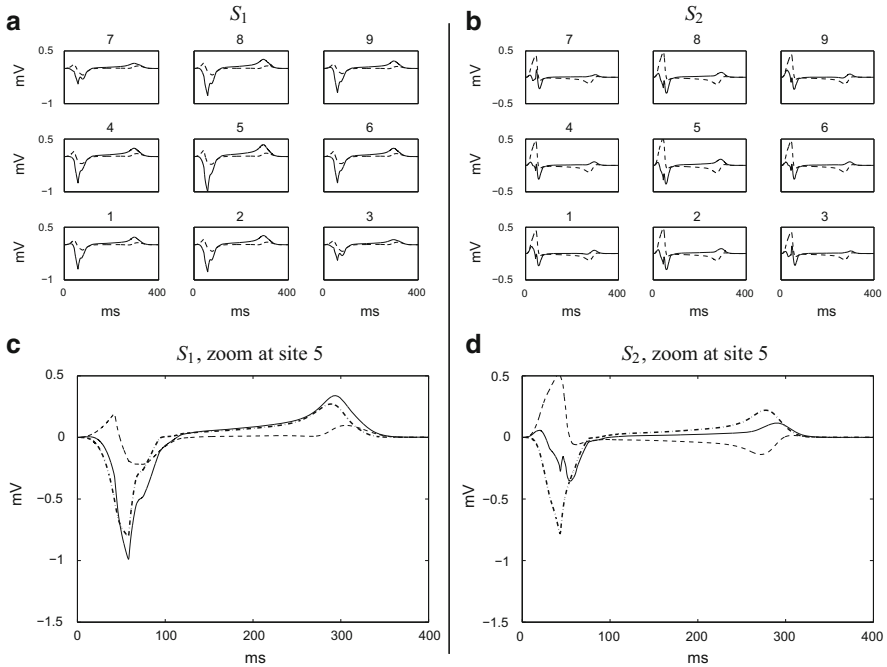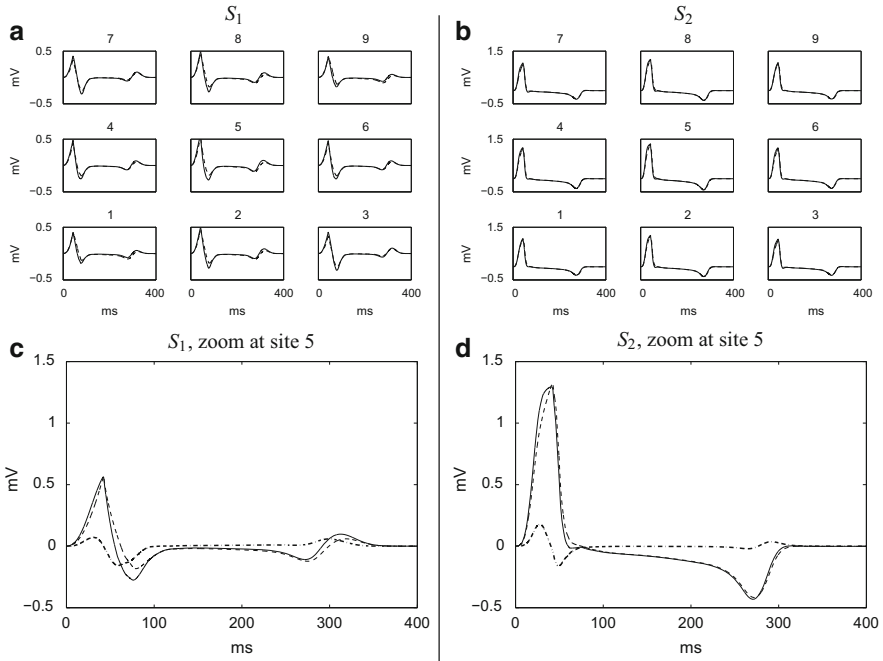
Fig. 9.41   H-slab: Unipolar ECGs on plane L_1. *Continuous line*: full unipolar ECG. *Dashed line*: HS component. *Dashed-Dotted line*: AS component (only in zoom). (**a**): Single site stimulation (S_1). (**b**): Multiple sites stimulation (S_2). (**c, d**): zoom at site 5

components exhibit R waves and negative (**H-slab**, Fig. 9.41b, d) or positive (**3-slab**, Fig. 9.42b, d) T waves. Nevertheless, the larger magnitude of the AS components prevail in the full unipolar ECGs and they still exhibit a positive T wave and QRS complex entirely negative or with RS configuration (small R and large S wave) and positive T wave. Therefore, the full unipolar ECGs are still dominated by their AS components.

S_1**: bipolar ECGs.** Unlike unipolar waveforms, the bipolar ECGs (Figs. 9.43 and 9.44a, c) appear to be dominated by their HS components, all with R and S waves and biphasic (for **H-slab**) or positive (for **3-slab**) T waves. Since the AS components of the unipolar ECGs on planes L_1 and L_2 are almost identical, the bipolar AS component has a very small magnitude in comparison with the bipolar HS component, hence they have a negligible influence on the full bipolar ECGs. The negative minimum of the biphasic T wave appearing in the bipolar ECGs in the **H-slab** case is due to the T peak of the unipolar HS components at sites on plane L_2 preceding the T peak of the symmetric sites on plane L_1.
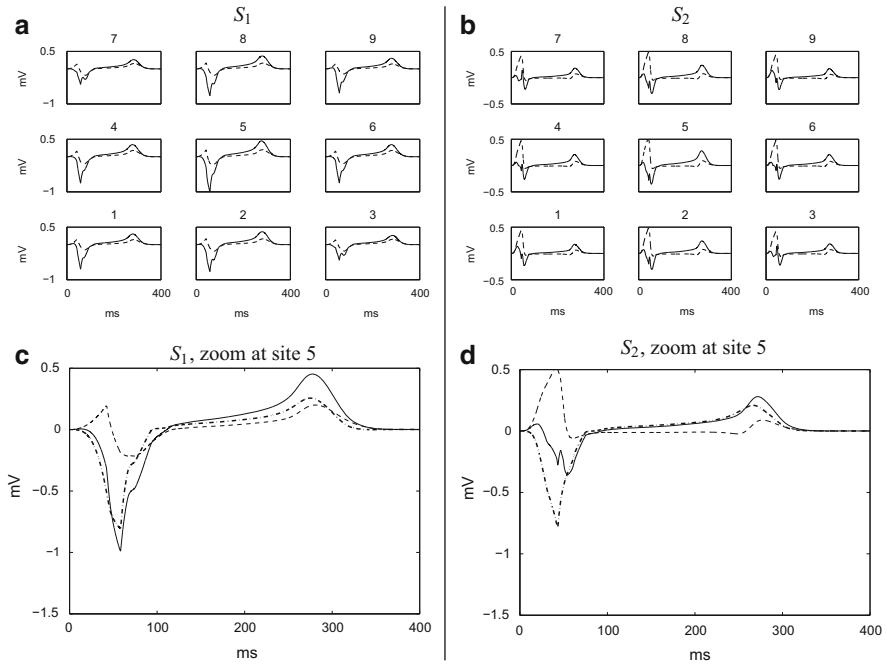
Fig. 9.42 3-slab: Unipolar ECGs on plane L_1. Same format as Fig. 9.41. (**a**) S_1. (**b**) S_2. (**c**) S_1, zoom at site 5. (**d**) S_2, zoom at site 5

S_2**: bipolar ECGs.** Bipolar ECGs now display a QRS complex with a large R wave and negative T wave (Figs. 9.43 and 9.44b, d), similarly to their HS components. The bipolar AS components have little influence because of their much smaller magnitude and therefore, as in the ectopic case, the full bipolar ECGs are dominated by their HS components.

Discussion of the results. By means of three-dimensional simulations based on the anisotropic Monodomain model, we have studied the influence of tissue anisotropy, cellular APD heterogeneities and the shape of the excitation wavefront on the T wave polarity. The simulation results have shown that: (i) unipolar ECGs exhibit a positive T wave mainly determined by the anisotropy of the cardiac tissue, irrespective of cellular APD heterogeneities and the shape of the excitation wavefront; (ii) on the other hand, bipolar ECGs are mainly determined by their isotropic component and their T wave turns out to be positive only for a single stimulation in presence of transmural APD heterogeneity, while it becomes always negative in case of multiple stimulation generating large activation wavefronts, regardless of the considered cellular APD heterogeneities. We remark that in our ECG computation, we have used an idealized cardiac geometry taking into account

Fig. 9.43 H-slab: Bipolar ECGs on plane L_1. *Continuous line*: full unipolar ECG. *Dashed line*: HS component. *Dashed-Dotted line*: AS component (only in zoom). (**a**): Single site stimulation (S_1). (**b**): Multiple sites stimulation (S_2). (**c, d**): zoom at site 5

anisotropic cardiac sources but considering the widely used assumptions of the same isotropic properties for bulk tissue and for the surrounding infinite extracardiac medium. Previous studies [117, 119] have shown that including anisotropic bulk tissue affects the ECGs magnitude far away from the cardiac surface but it does not alter their QRS morphology. The extension of our conclusions on T wave polarity to real 12-lead ECGs will require considering realistic geometries for both cardiac tissue and torso, as well as the anisotropy of the bulk tissue. Nevertheless, the real 12-lead ECGs are far-field signals and we expect that the full ECG and the isotropic/anisotropic ECG components will be smoothed out due to the greater distance from the active tissue.
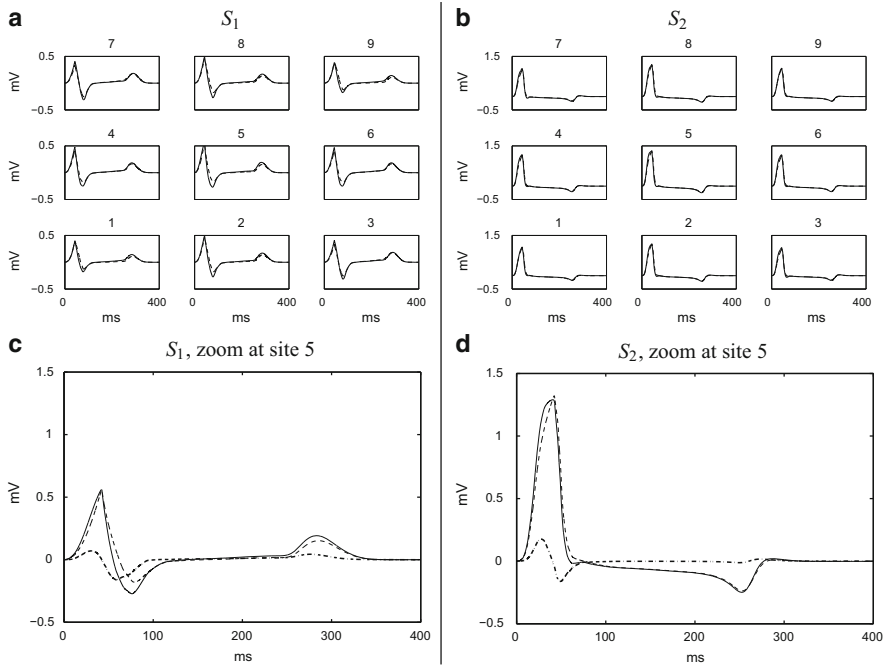
Fig. 9.44 3-slab: Bipolar ECGs. Same format as Fig. 9.43

9.5 Extracellular Markers of Excitation and Repolarization Times

The time evolution of the cardiac bioelectric activity is described by the time and spatial distribution of the intracellular and extracellular potential fields $u_i(\mathbf{x}, t), u_e(\mathbf{x}, t)$, both dependent on a chosen reference potential. By taking the difference between the intra- and extracellular potentials, we obtain the distribution of the transmembrane potential $v(\mathbf{x}, t) = u_i(\mathbf{x}, t) - u_e(\mathbf{x}, t)$, that is independent of the reference potential. During a heart beat, the transmembrane potential of each myocardial cell undergoes a time variation called *transmembrane action potential* (TAP), characterized by a fast upstroke of about 1 ms and a subsequent slower downstroke of about 50 ms, associated with the activation and recovery phases, respectively, also called depolarization and repolarization phases.

Maps of the activation and recovery sequences provide important information for identifying normal heart activity and cardiac arrhythmias that are often associated with abnormal recovery times and action potential durations. Methods for determining activation and recovery times on the epicardial and endocardial surfaces, as well as transmurally (i.e. in the thickness of the ventricular wall), are essential tools for understanding the recovery process in normal and pathological conditions at both experimental and clinical levels.

While methods for determining activation sequences from direct leads (recorded directly from the heart) are well established, the assessment of local recovery times is more difficult, due to the larger time and space scales involved in the recovery process. The activation time is generally defined as the time instant when the TAP exhibits the fastest upstroke and the *unipolar electrogram* (EG) shows the fastest downstroke (i.e. the intrinsic deflection) during the QRS complex; see e.g. [408] for a recent update. The assessment of local recovery times is based on indexes associated with the TAP downstroke phase and with the upstroke of the T wave in the EG, see Fig. 9.45.

Widely used TAP recovery markers are the time of fastest repolarization RT_{tap}, defined as the instant of TAP fastest downstroke during the recovery phase, and the late recovery time $RT90_{tap}$, defined as the instant when the TAP reaches 90 % of its resting value during the downstroke phase.

The potential drop across the membrane can be measured only from a few sites in a given preparation by microelectrodes (micropipette). Therefore, transmembrane potentials cannot be simultaneously recorded from hundreds of sites in vivo. Optical
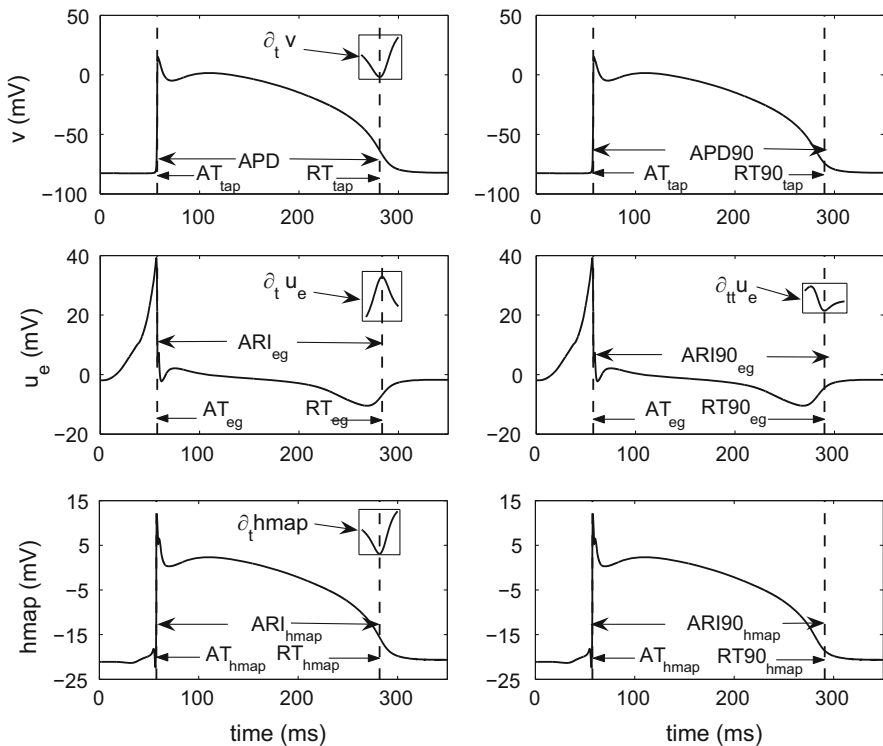
Fig. 9.45 Transmembrane action potential (v), unipolar electrogram (u_e) and hybrid monophasic action potential (*hmap*) waveforms and the associated activation and recovery time markers (Reproduced with permission from [461])

techniques can be used to detect the transmembrane potential on exposed tissue surface, such as the epicardial surface, but cannot be used for intramural recordings. Transmural and intramural explorations across the ventricular wall can only be afforded with extracellular multi-electrode arrays. These recording techniques are applicable especially when exploring large regions of a beating heart. Therefore, it is very important to derive from the analysis of the extracellular potential time course some recovery time markers that accurately estimate the recovery TAP markers.

The most widely accepted EG recovery time marker for the fastest recovery time RT_{tap} is the time RT_{eg} of maximum upslope during the T wave, see e.g. [221, 566]. The RT_{eg} marker has been widely employed in many experimental studies on animals [9, 135, 160, 194, 363, 512, 515] and humans [84, 87, 194, 517, 567, 580]; see also the survey paper [133]. Nevertheless, its reliability in estimating the RT_{tap} has been assessed experimentally in only a few papers, i.e. [160, 221], by evaluating the correlation between the *activation-recovery interval* (ARI, defined as the difference between RT_{eg} and the activation time) and the *action potential duration* (APD, defined as the difference between RT_{tap} and the activation time), under a variety of physiological conditions. A simulation study of the reliability of RT_{eg} versus RT_{tap} has been carried out in [496], using a one-dimensional model of a cardiac strand. Recently in [127], an EG marker for late recovery time based on the time $RT90_{eg}$ of minimum second derivative of the EG waveform during the T wave has been proposed.

Another extracellular technique for determining recovery times is based on bipolar signals recorded by taking the potential difference between a site inside a permanently depolarized area (obtained e.g. by pressure, suction or KCl injection) and an exploring site. When the exploring and permanently depolarized sites are very close to each other, we obtain the classical *monophasic action potential* (MAP), see e.g. [181]. Instead, when we record the potential difference between a fixed extracellular recording site inside a permanently depolarized region, and a generic exploring site, we obtain the *hybrid monophasic action potentials* (HMAP), see [553]. The TAP and MAP techniques cannot be implemented extensively in vivo. Conversely, the EG and HMAP extracellular recording techniques are applicable in studying the activation and recovery sequences in large regions of a beating heart in vivo. Since both TAP and HMAP waveforms exhibit monophasic downstroke phases, we can define the HMAP recovery markers RT_{hmap} and $RT90_{hmap}$ in the same way as the TAP markers RT_{tap} and $RT90_{tap}$, respectively. Due to the close resemblance of TAP and MAP waveforms at the same exploring site, there is a general agreement on the reliability of MAP recovery times. On the other hand, the use of a fixed extracellular recording site inside a permanently depolarized region and the more varied morphology of the HMAP signal has made controversial the information content of the HMAP, see e.g. [128, 135].

It is important to validate the previously described methods for assessing the local recovery time from unipolar or bipolar recordings by comparing these markers with the TAP markers, which are widely considered to be the best standard. The extension of the pioneering one-dimensional investigation of [496] to three dimensions is a demanding computational task, since it requires efficient numerical solvers for

the Bidomain model describing the cardiac bioelectric activity at a macroscopic tissue level. In the last years, the development of powerful computing platforms and efficient numerical parallel solvers have made possible large scale three-dimensional Bidomain simulations, see e.g. [104, 458, 545], allowing the investigators to plan and accomplish reliability studies of EG recovery time markers in 3D cardiac tissue models.

Recently, using parallel Bidomain solvers [399, 458], the reliability of RT_{eg} versus RT_{tap} markers has been investigated in normal [400, 460] and pathological [461] cardiac tissue. In the following sections, we will review some of the results obtained in [460, 461].

9.5.1 Waveform Postprocessing and Repolarization Time Markers

In addition to the intracellular, extracellular and transmembrane potential fields $u_i(\mathbf{x}, t), u_e(\mathbf{x}, t), v(\mathbf{x}, t) = u_i(\mathbf{x}, t) - u_e(\mathbf{x}, t)$ defined before, we will also consider the hybrid monophasic action potential (HMAP)

$$hmap(\mathbf{x}, t) = u_e(\mathbf{x}_{PD}, t) - u_e(\mathbf{x}, t),$$

where $\mathbf{x}_{PD}$ is a point in a permanently depolarized region of Ω_H, i.e. $v(\mathbf{x}_{PD}, t) = v_{PD}$ is constant in time. We now define some markers of activation time (AT) and repolarization time (RT) derived from these potentials.

Transmembrane action potential (TAP) waveforms and markers. We recall that the ventricular transmembrane action potential (TAP) given by the time course of $v(\mathbf{x}, t)$ at a given point $\mathbf{x} \in \Omega_H$ (see e.g. Fig. 9.45 top left panel) displays mainly five phases, having different time scales. The first (phase 0) is related to the excitation process, also called depolarization, where the TAP undergoes an abrupt temporal change lasting about 2 ms, followed by a fast initial repolarization (phase 1) characterized by a fast exponential decay toward a plateau value. The plateau phase (phase 2) lasts about 250–300 ms during normal heartbeats (depending on the heart rate) or about 50–100 ms during tachyarrhythmias. In this phase, the potential varies very slowly in comparison with the other phases. The plateau phase is followed by the faster terminal repolarization (phase 3), where the TAP returns to the resting value and after which the tissue becomes normally excitable again (phase 4).

The excitation phase of the TAP is characterized by a fast upstroke with a well-defined activation time, given by the instant AT_{tap} of the TAP maximum derivative. On the other hand, local repolarization time can be assessed by different markers associated with the TAP downstroke phase. Widely used repolarization markers are the time RT_{tap} of the TAP minimum derivative and the time $RT90_{tap}$ when the TAP reaches 90 % of the resting value during the downstroke phase (phase 3). The former

is related to the moment of fastest repolarization, while the latter indicates the ending phase of repolarization. The TAP activation and repolarization time markers (sketched graphically in Fig. 9.45) are defined as follows:

- $AT_{tap}(\mathbf{x}) = \text{argmax}\{\partial_t v(\mathbf{x}, t),\ t \in upstroke\}$,
  i.e. the instant of maximum time derivative of $v(\mathbf{x}, t)$ during the upstroke;
- $RT_{tap}(\mathbf{x}) = \arg\min\{\partial_t v(\mathbf{x}, t),\ t \in downstroke\}$,
  i.e. the instant of minimum time derivative of $v(\mathbf{x}, t)$ during the downstroke;
- $RT90_{tap}(\mathbf{x}) = \{\bar{t} : v(\mathbf{x}, \bar{t}) = 0.9 v_r\ during\ downstroke\}$,
  i.e. the instant when $v(\mathbf{x}, t)$ reaches 90 % of its resting value v_r during downstroke.

The TAP activation and repolarization markers AT_{tap}, RT_{tap} and $RT90_{tap}$ are the gold standards for determining cardiac activation and repolarization times.

Unipolar electrograms (EG) waveforms and markers. A typical morphology of an electrogram (EG), given by the time course of $u_e(\mathbf{x}, t)$ at a given point $\mathbf{x} \in \Omega_H$, is displayed in the mid panel of Fig. 9.45. The excitation phase is related to the QRS complex, while the faster terminal repolarization occurs during the T wave. This wave has positive and negative polarity for sites that repolarize early and late, respectively, while it has a biphasic waveform for intermediate repolarization states. A firmly established marker for the activation time from the EGs is the instant AT_{eg} of minimum derivative during the QRS complex; see e.g. [408, 493]. The most widely accepted EG repolarization marker is the time RT_{eg} of maximum upslope during the T wave, see e.g. [221, 566]. Recently, we have proposed an EG marker for late repolarization based on the time $RT90_{eg}$ of minimum second derivative of the EG waveform during the T wave, see [460]. Note that the second time derivative of electrograms has been used in [187, 188, 311] in order to define the end of the T wave. The EG activation and repolarization time markers (sketched graphically in Fig. 9.45) are defined as follows:

- $AT_{eg}(\mathbf{x}) = \arg\min\{\partial_t u_e(\mathbf{x}, t),\ t \in QRS\ complex\}$,
  i.e. the instant of minimum time derivative of $u_e(\mathbf{x}, t)$ during the QRS complex;
- $RT_{eg}(\mathbf{x}) = \text{argmax}\{\partial_t u_e(\mathbf{x}, t),\ t \in T\ wave\}$,
  i.e. the instant of maximum time derivative of $u_e(\mathbf{x}, t)$ during the T wave;
- $RT90_{eg}(\mathbf{x}) = \arg\min\{\partial_{tt} u_e(\mathbf{x}, t),\ t \in T\ wave\}$,
  i.e. the instant of minimum second time derivative of $u_e(\mathbf{x}, t)$ during the T wave.

Hybrid monophasic action potential (HMAP) waveforms and markers. The extracellular waveforms, recorded by Weissenburger et al. [553], are the potential difference between a fixed extracellular recording within a permanently depolarized region and a generic exploring site. These signals can be obtained directly from the heart or computed as the difference between the unipolar EG from a fixed permanently depolarized site and the unipolar EG from a generic exploring site. These computed signals are obviously independent of the (identical) reference potential used for the two unipolar EGs. We call these extracellular signals, hybrid monophasic action potentials (HMAPs) to distinguish them from the classical close bipolar monophasic action potentials (MAP) of Franz [181], where the exploring

and permanently depolarized sites are always very close to each other. HMAPs are contaminated by far-field effects, while MAPs, being close bipolar signals, are relatively insensitive to far-field effects. A typical morphology of an HMAP waveform is displayed in the bottom panel of Fig. 9.45. The HMAP signal exhibits multiple upstroke phases followed by the appearance of a monophasic component. The fastest upstroke is associated with the activation of the exploring site and the others with the depolarization of sites around the boundary of the PD volume. The HMAP activation and recovery time markers are defined in the same way as the TAP markers:

- $\text{AT}_{hmap}(\mathbf{x}) = \text{argmax}\{\partial_t hmap(\mathbf{x}, t), \ t \in upstroke\}$,
  i.e. the instant of maximum time derivative of hmap($\mathbf{x}, t$) during the upstroke;
- $\text{RT}_{hmap}(\mathbf{x}) = \arg\min\{\partial_t hmap(\mathbf{x}, t), \ t \in downstroke\}$,
  i.e. the instant of minimum time derivative of hmap($\mathbf{x}, t$) during the downstroke;
- $\text{RT90}_{hmap}(\mathbf{x} = \{\bar{t} : hmap(\mathbf{x}, \bar{t}) = 0.9v_r \ during \ downstroke\}$,
  i.e. the instant when hmap($\mathbf{x}, t$) reaches 90 % of its resting value during the downstroke.

We recall that the information content of the HMAP waveform is controversial, see e.g. [182, 265, 285, 347, 542, 553]. In particular, the reliability of recovery time markers derived from HMAP signals has been questioned, see [128, 135, 560].

As a byproduct of the AT and RT markers defined above, the following action potential duration (APD) and Activation–Recovery Interval (ARI) markers are defined.

APD markers from TAP waveforms.

- $\text{APD}(\mathbf{x}) = \text{RT}_{tap}(\mathbf{x}) - \text{AT}_{tap}(\mathbf{x})$,   • $\text{APD90}(\mathbf{x}) = \text{RT90}_{tap}(\mathbf{x}) - \text{AT}_{tap}(\mathbf{x})$.

ARI markers from EG waveforms.

- $\text{ARI}_{eg}(\mathbf{x}) = \text{RT}_{eg}(\mathbf{x}) - \text{AT}_{eg}(\mathbf{x})$,   • $\text{ARI}_{hmap}(\mathbf{x}) = \text{RT}_{hmap}(\mathbf{x}) - \text{AT}_{hmap}(\mathbf{x})$;

- $\text{ARI90}_{eg}(\mathbf{x}) = \text{RT90}_{eg}(\mathbf{x}) - \text{AT}_{eg}(\mathbf{x})$,   • $\text{ARI90}_{hmap}(\mathbf{x}) = \text{RT90}_{hmap}(\mathbf{x}) - \text{AT}_{hmap}(\mathbf{x})$.

ARI_{eg} has been widely used in estimating the APD in experiments on animals and humans, see e.g. [135, 221, 328] and [84, 194, 517], respectively.

We recall that the excitation process is a self-sustained propagating phenomenon and the isochrones of the activation time define a propagating excitation front. Conversely, the repolarization process is not a matter of conduction but it is a synchronization phenomenon, see e.g. [133]. Nevertheless, the isochrones of successive repolarization times define a sequence of repolarization fronts and even if these fronts are not propagating in a classical sense, for convenience of notation we will use in the following the terms acceleration, deceleration, collision regarding the sequence of repolarization fronts sweeping the myocardial volume.

9.5.2   Parameter Calibrations for the Model Simulations

In all computations, a structured grid of $192 \cdot 192 \cdot 48$ hexahedral isoparametric Q_1 finite elements of size $h = 0.1$ mm is used in space. All simulations have been run on a Linux Cluster with 56 Opteron AMD processors and Infiniband network. Each simulation required about 8 h on 36 processors.

Multi-electrode array. The cardiac domain Ω_H considered in this study is a cartesian slab of dimensions $1.92 \times 1.92 \times 0.48$ cm^3, modeling a portion of the left ventricular wall. In this slab, we consider a matrix of 12×12 exploring multielectrode needles spaced 1.6 mm from each other and 0.8 mm from the slab boundary, as shown in Fig. 9.46. Each needle carries 13 recording sites, spaced 0.4 mm along the shank. We then have 12×12 sites on each of the 13 intramural planes, for a total of $12 \times 12 \times 13 = 1\,872$ recording sites in the slab, each recording the intra and extracellular potentials. We will indicate each needle location by its column and row indexes, shown in the left panel of Fig. 9.46. This multi-electrode array mimics the experimental setup used in intramural mapping of the extracellular potential, see e.g. [162, 184].

Transmural heterogeneity. Three different types of transmural distribution of the intrinsic APDs of the cells are considered, one homogeneous (H-slab) and the other two heterogeneous (3-slab and W-slab). The transmural intrinsic APD heterogeneity is assumed to be the same along any transmural epi-endocardial straight line, i.e. in any plane parallel to the epicardium all cells have the same intrinsic APD. In the heterogeneous slabs, the intrinsic APD of the cells is obtained by multiplying the potassium current I_K in the LR1 model [308] by a factor fact$_{I_K}$, as detailed in Table 9.8. This modulation factor is chosen in order to introduce a transmural APD profile with M-cell layers as in [546] (3-slab) or as in [572, Fig. 4], [395, Fig. 5] (W-slab), to mimic their experimental transmural APD profile; see [126, 460] for more details.
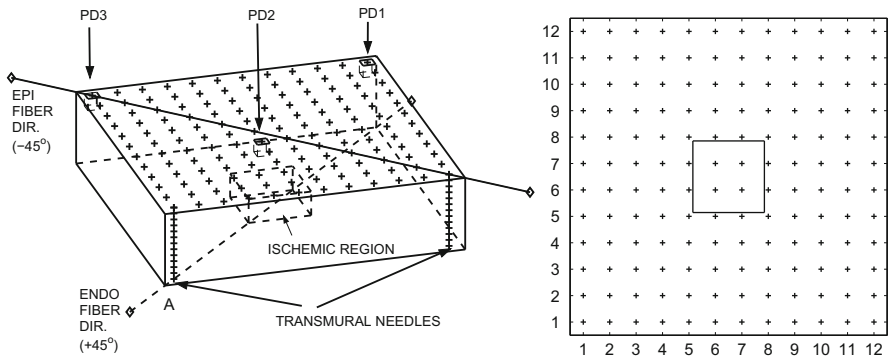

Fig. 9.46 *Left*: cardiac slab Ω_H, PD sites, ischemic region, transmural needles. *Right*: needle locations on the epicardial plane and their row and column indexes (Reproduced with permission from [461])

Table 9.8 Parameter calibration for modeling the transmural heterogeneities in the three cardiac slabs H-slab, 3-slab, W-slab

	H-slab	3-slab			W-slab			
# of layers	1	3			4			
		Endo	Mid	Epi	Endo	Sub-endo	Mid	Epi
Thickness (cm)	0.48	0.16	0.16	0.16	0.058	0.096	0.254	0.072
fact_I_K	1	2.62	1.95	2.88	2.71	1.95	2.47	2.88
APD (ms)	266	235	272	225	232	272	242	225

Subendocardial ischemia. Two simulations with subendocardial moderate (MI-slab) and severe (SI-slab) ischemic regions (defined below) are performed. The ischemic region has dimensions $0.4 \times 0.4 \times 0.16 \, \text{cm}^3$ and is located as shown in Fig. 9.46. In the LR1 model, the current I_K is scaled by a factor 2.325, yielding TAPs with APD90 $= 250$ ms. Inside the ischemic region, the extracellular potassium concentration $[K]_o$ is increased from 5.4 mM (control) to 10.5 mM (MI-slab) or 18 mM (SI-slab); for more details see [129].

Permanently depolarized (PD) volume. A permanently depolarized (PD) site is obtained experimentally by contact pressure or by a KCl injection in a region H_D, holding the TAP in such a region to some fixed depolarized value v_D, i.e. for $\mathbf{x} \in H_D$, $\quad v(\mathbf{x}, t) = v_D$. In our simulation study, such a PD site is obtained by assigning the extracellular potassium concentration equal to the intracellular one, i.e. I_{K1} is zero in the small PD volume. The PD site is labeled PD in Fig. 9.46 and it has dimensions $0.8 \times 0.8 \times 0.8 \, \text{mm}^3$.

Stimulation site. Inside the PD volume the transmembrane potential values are above threshold thus generating a first excitation-recovery TAP that sweeps the cardiac slab Ω_H. We wait for 500 ms and take the steady state reached by the Bidomain system as the initial condition for our simulations. An extracellular stimulus ($i^e_{app} = -250 \, \text{mA/cm}^3$ for 1 ms) is then applied in a small volume (3 mesh points in each direction) at the locations A in Fig. 9.46 and an intracellular stimulus $i^i_{app} = i^e_{app}$ is also applied in order to satisfy the compatibility condition for the solvability of the Bidomain system (3.42).

Figure 9.47 displays the isochrones of AT_{tap}, RT90_{tap} and APD90 on epicardial, midmyocardial and endocardial intramural sections and on a transmural diagonal section perpendicular to the epicardium in the PD3 case. The excitation wave front starts at the stimulated endocardial corner A and proceeds faster along the fiber direction than in the orthogonal direction. In fact, in Fig. 9.47 the endocardial and transmural activation isochrones present a quasi-elliptical shape with major axis parallel to the fibers. Excitation reaches the epicardial breakthrough about 20 ms after the stimulus, and then in about 40 more ms the whole epicardium is depolarized. Two distinct repolarization sequences start, almost simultaneously, on the endocardial and epicardial surfaces, and subsequently collide and merge transmurally in the middle region of the cardiac wall. This produces an APD90
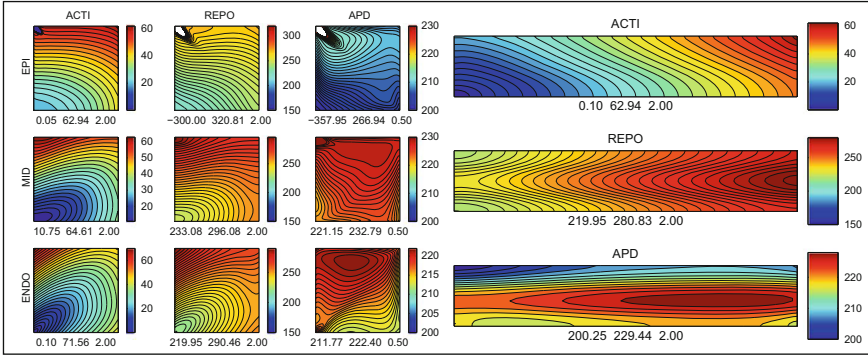
Fig. 9.47 3-slab, PD3. Activation (*ACTI*), repolarization (*REPO*) and action potential duration (*APD*) isochrone lines, computed with space resolution $h = 0.1$ mm, related to the transmembrane markers $AT_{tap}(x)$, $RT90_{tap}(x)$, $APD90(x)$. *Left panel*: intramural sections (epicardium, midwall, endocardium). *Right panel*: transmural diagonal section A perpendicular to the epicardium (see Fig. 9.46). Maximum, minimum and step of the displayed map are reported below each panel (Reproduced with permission from [461])

transmural pattern with a maximum in the midmyocardial regions, where cells with a longer intrinsic APD are located.

Postprocessing. We saved the extracellular and the intracellular potential waveforms $u_e(x, t)$ and $u_i(x, t)$ at the $12 \times 12 \times 13$ locations of the multi-electrode array described above. These waveforms for u_e and for the byproduct $v = u_i - u_e$ are then post-processed by computing the additional activation and repolarization markers defined previously. The TAP markers are assumed to be the *reference* markers.
The EG and HMAP markers are compared with the reference TAP markers, i.e.:
AT_{eg} and AT_{hmap} vs AT_{tap}; RT_{eg} and RT_{hmap} vs RT_{tap}; $RT90_{eg}$ and $RT90_{hmap}$ vs $RT90_{tap}$; ARI_{eg} and ARI_{hmap} vs APD; $ARI90_{eg}$ and $ARI90_{hmap}$ vs APD90.

In order to compare these large data sets, we then compute, for vectors X, Y of length $n = 1\,872$, the following quantities, reported in the Tables of the Results:

- $\text{mean}(X) = \frac{1}{n}\sum_1^n X_i =$ the average of X;
- $\text{std}(X) = \|X_0\|/\sqrt{n} =$ the standard deviation of X, where $X_0 = X - \text{mean}(X)\underline{1}$;
- $\text{corr}(X, Y) = (X_0/\|X_0\|, Y_0/\|Y_0\|) =$ the correlation coefficient between X and Y;
- $\text{mrd} = \text{mean}(|X - Y|)/\text{mean}(|Y|) =$ relative mean error of X with respect to Y,

where $\|\cdot\|, (\cdot, \cdot)$ denote the Euclidean norm and scalar product.

9.5.3   Global Quantitative Analysis of RT Markers

Effects of the PD location on the extracellular potential field. Table 9.9 reports the comparison between the EG and HMAP repolarization markers and the reference TAP markers (RT_{eg} vs RT_{tap}, RT_{hmap} vs RT_{tap}, $RT90_{eg}$ vs $RT90_{tap}$, $RT90_{hmap}$ vs $RT90_{tap}$). The sites with discrepancies larger than 30 ms are excluded but, in each case, the points excluded are less than 3. All the extracellular estimates show a high reliability as confirmed by a correlation coefficient always greater than 0.95. The $RT90_{eg}$ marker exhibits the best performance, followed by RT_{eg} and then by RT_{hmap}, with average absolute discrepancies ranging between 1.5 and 3.2 ms. Despite the high correlation coefficient, the $RT90_{hmap}$ estimate exhibits a larger average discrepancy ranging between 3.1 and 11.3 ms depending on the location of the PD volume. The relevant increase of both average discrepancies and standard deviations for all markers with respect to the case involving only isotropic waveforms (see [461]) indicates that the anisotropic component of the extracellular potential u_e is the major determinant of the discrepancies between EG and TAP repolarization markers.

The EG markers are weakly influenced by the location of the PD volume. The global performance of the RT_{hmap} marker exhibits a weak dependence on the position of the PD volume. Conversely, the performance of the $RT90_{hmap}$ marker, in terms of average discrepancy not of correlation, is strongly dependent on the PD volume location. This strong performance dependence on the location of the PD volumes may be related to the different morphology of the EGs in the PD

Table 9.9 RT markers discrepancies, 3-slab, PD volume in PD1, PD2 and PD3. EG and HMAP markers computed from extracellular waveforms (u_e and $hmap$) versus TAP markers. mean$|X - Y|$ = average of $|X - Y|$; mean$|Y|$ = average of $|Y|$; mrd = mean$|X - Y|$/mean$|Y|$ = relative mean discrepancy; std = standard deviation of $|X - Y|$; corr(X, Y) = correlation coefficient between X and Y

	X	Y	mrd	Mean $|X - Y|$	Mean $|Y|$	Std	Corr (X, Y)
PD1	RT_{eg}	RT_{tap}	0.76e−2	1.86	244.41	1.72	0.99
	RT_{hmap}	RT_{tap}	1.30e−2	3.17	244.43	3.50	0.96
	$RT90_{eg}$	$RT90_{tap}$	0.63e−2	1.59	252.94	1.79	0.99
	$RT90_{hmap}$	$RT90_{tap}$	4.46e−2	11.29	252.92	6.28	0.97
PD2	RT_{eg}	RT_{tap}	0.77e−2	1.91	246.87	1.63	0.98
	RT_{hmap}	RT_{tap}	1.23e−2	3.04	246.78	3.54	0.95
	$RT90_{eg}$	$RT90_{tap}$	0.64e−2	1.64	255.58	1.95	0.99
	$RT90_{hmap}$	$RT90_{tap}$	1.21e−2	3.08	255.26	2.51	0.96
PD3	RT_{eg}	RT_{tap}	0.78e−2	1.92	245.40	1.65	0.99
	RT_{hmap}	RT_{tap}	0.97e−2	2.39	245.42	2.23	0.98
	$RT90_{eg}$	$RT90_{tap}$	0.64e−2	1.63	254.01	1.75	0.99
	$RT90_{hmap}$	$RT90_{tap}$	2.07e−2	5.26	254.02	2.45	0.98

volumes. The EGs in the PD volumes exhibit an upstroke phase contaminated by some spikes followed by a downstroke phase. The EGs in PD1 and PD3 present also an undershooting behavior at the end of the downstroke phase, which is absent in the EGs morphology for sites inside the PD2 volume, see Fig. 9.48. In the following simulations, we fix the location of the PD volume in the PD3 region.

Transmural heterogeneity and subendocardial ischemia. We now simulate the excitation and repolarization processes in tissue slabs with different heterogeneous cellular membrane properties, i.e. in H-slab, 3-slab, W-slab, MI-slab, SI-slab with PD volume located in PD3, by applying a local stimulus at the endocardial vertex A in Fig. 9.46. We evaluate the global performance of the extracellular markers for each slab type and for the entire collection of the five simulations, by considering marker values with discrepancies less than 30 ms. In the multielectrode array of 1 872, the discarded marker values are at most 6 and mostly related to sites within the inexcitable regions, i.e. the PD volume and the ischemic region in the SI-slab type.

The comparison of the activation markers shows that both the extracellular markers AT_{eg} and AT_{hmap} are very accurate estimates of the reference marker AT_{tap}, with absolute discrepancies of the order of 0.05 ms. This shows that the instant of maximum time derivative of the HMAP matches very well the instant AT_{tap} in spite of the possible presence of multiple upstrokes in the HMAP signal.

The results reported in Table 9.10 show that all the extracellular recovery markers provide very reliable estimates of the reference transmembrane markers, with correlation coefficients always greater than 0.98. This good match between the EG repolarization markers and the reference TAP markers is also confirmed by
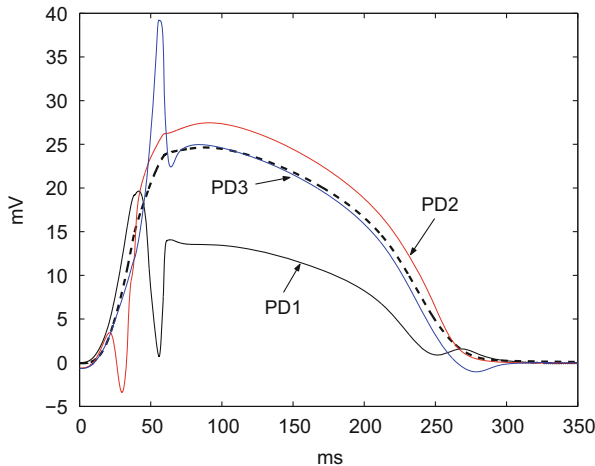
Fig. 9.48 Shifted extracellular waveforms $u_e(x_{PD}, t)$ in the PD volume for $x_{PD} \in$ $PD1$, $PD2$, $PD3$ (see Fig. 9.46) and $CR(t) = \frac{1}{|\Omega_H|} \int_{\Omega_H} v(x, t)\, dx$ (*dashed line*) for the 3-slab (Reproduced with permission from [461])

Table 9.10 Recovery time (RT) markers discrepancies for H-slab, 3-slab, W-slab, MI-slab and SI-slab with PD volume in PD3. Comparison between the RT markers (RT_{eg} vs RT_{tap}, RT_{hmap} vs RT_{tap}, $RT90_{eg}$ vs $RT90_{tap}$, $RT90_{hmap}$ vs $RT90_{tap}$): $\text{mean}|X - Y|$ = average of $|X - Y|$; $\text{mean}|Y|$ = average of $|Y|$; $\text{mrd} = \text{mean}|X - Y|/\text{mean}|Y|$ = relative mean discrepancy; std = standard deviation of $|X - Y|$; $\text{corr}(X, Y)$ = correlation coefficient between X and Y

	X	Y	mrd	Mean $|X - Y|$	Mean $|Y|$	Std	Corr (X, Y)
H-slab	RT_{eg}	RT_{tap}	0.84e−2	2.14	253.22	1.98	0.99
	RT_{hmap}	RT_{tap}	0.72e−2	1.83	253.15	1.60	0.99
	$RT90_{eg}$	$RT90_{tap}$	0.36e−2	0.95	260.32	0.86	0.99
	$RT90_{hmap}$	$RT90_{tap}$	1.17e−2	3.04	260.38	2.15	0.98
3-slab	RT_{eg}	RT_{tap}	0.78e−2	1.92	245.40	1.65	0.99
	RT_{hmap}	RT_{tap}	0.97e−2	2.39	245.42	2.23	0.98
	$RT90_{eg}$	$RT90_{tap}$	0.64e−2	1.63	254.01	1.75	0.99
	$RT90_{hmap}$	$RT90_{tap}$	2.07e−2	5.26	254.02	2.45	0.98
W-slab	RT_{eg}	RT_{tap}	0.56e−2	1.39	248.25	1.19	0.99
	RT_{hmap}	RT_{tap}	0.84e−2	2.09	247.52	2.18	0.98
	$RT90_{eg}$	$RT90_{tap}$	0.41e−2	1.04	255.66	1.09	0.99
	$RT90_{hmap}$	$RT90_{tap}$	2.00e−2	5.10	255.79	1.99	0.99
MI-slab	RT_{eg}	RT_{tap}	0.86e−2	2.16	250.76	2.23	0.99
	RT_{hmap}	RT_{tap}	0.77e−2	1.94	250.63	2.22	0.99
	$RT90_{eg}$	$RT90_{tap}$	0.51e−2	1.31	258.92	1.91	0.99
	$RT90_{hmap}$	$RT90_{tap}$	1.19e−2	3.07	258.95	2.24	0.98
SI-slab	RT_{eg}	RT_{tap}	0.79e−2	2.01	252.75	1.67	0.99
	RT_{hmap}	RT_{tap}	0.75e−2	1.90	252.24	1.80	0.99
	$RT90_{eg}$	$RT90_{tap}$	0.52e−2	1.34	258.86	2.19	0.99
	$RT90_{hmap}$	$RT90_{tap}$	1.14e−2	2.95	258.94	2.13	0.98

Fig. 9.49, reporting the regression plots of RT_{eg} vs RT_{tap}, RT_{hmap} vs RT_{tap}, $RT90_{eg}$ vs $RT90_{tap}$ and $RT90_{hmap}$ vs $RT90_{tap}$ on all five simulations. In terms of accuracy, the $RT90_{eg}$ marker gives the best performance, with a relative average discrepancy of at most 0.64e−2 and an average absolute discrepancy of at most 1.63 ms. The RT_{eg} and RT_{hmap}, as estimates of RT_{tap}, show comparable global performance, because both the absolute and relative averages of $|RT_{eg}-RT_{tap}|$ and $|RT_{hmap}-RT_{tap}|$ are about 2 ms and 0.8e−2 with a range 0.56e−2 $\div$ 0.97e−2. As previously observed only for the 3-slab, despite a global correlation coefficient of 0.98, the $RT90_{hmap}$ marker exhibits larger absolute (relative) average discrepancies, ranging between 3.04 (1.17e−2) and 5.3 ms (2.1e−2), than the other EG markers.

These global performance findings are also confirmed by the distributions of the discrepancies $RT_{eg}-RT_{tap}$, $RT_{hmap}-RT90_{tap}$, $RT90_{eg}-RT90_{tap}$ and $RT90_{hmap}-RT90_{tap}$, reported in Fig. 9.50. These distributions clearly show that almost all discrepancies range between −10 and 10 ms and most of them are confined within −5 and 5. Figure 9.51 reports the discrepancies with respect to the transmural
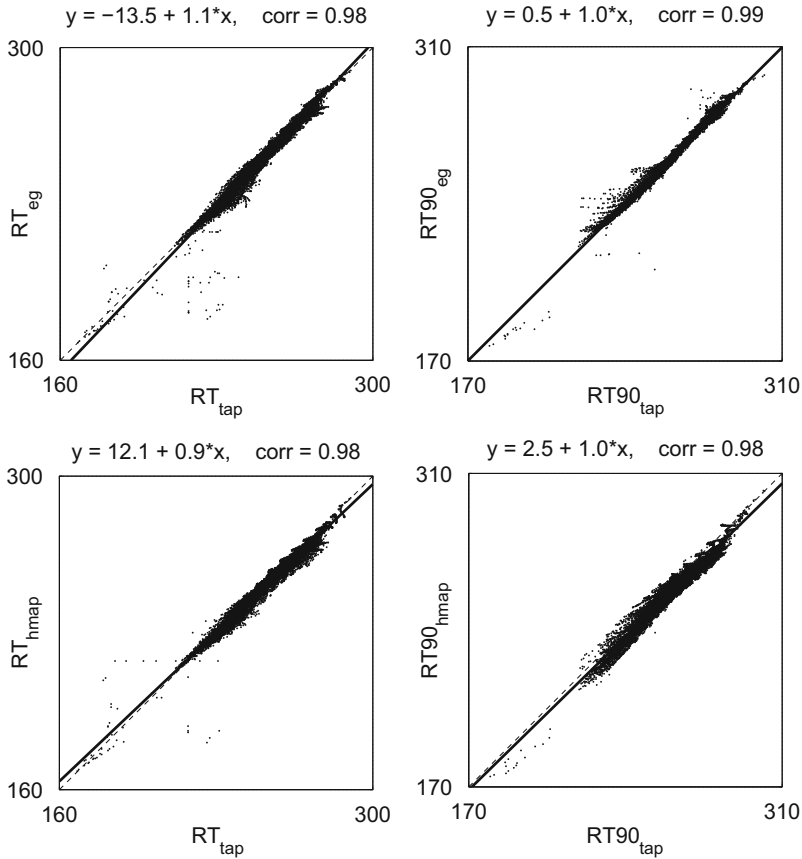
Fig. 9.49 Regression lines of RT_{eg} vs RT_{tap} (*first column*), $RT90_{eg}$ vs $RT90_{tap}$ (*second column*), RT_{hmap} vs RT_{tap} (*third column*) and $RT90_{hmap}$ vs $RT90_{tap}$ (*fourth column*) for all the five slab types H-slab, 3-slab, W-slab, MI-slab and SI-slab (Reproduced with permission from [461])

position of the electrodes for the 3-slab, i.e. the discrepancy variation over an intramural plane.

For 3-slab, we found that the largest discrepancies are located in the midmyocardial regions, where the two repolarization fronts, that started from the endocardium and the epicardium, merge. An analogous consideration apply to the subendocardial regions in W-slab. We refer to our recent paper [460] for a discussion of the locations and origin of the RT_{eg} and $RT90_{eg}$ markers largest discrepancies, as well as for a study of the associated artifacts appearing in the repolarization sequences. Signs of the presence of these discrepancies are the correlation coefficients of the APD markers, reported in Table 9.11, which are always lower than those of the associated RT markers, indicating a loss of precision of the extracellular RT markers. We remark that in all simulations the global performance indexes (mrd, mean, std)
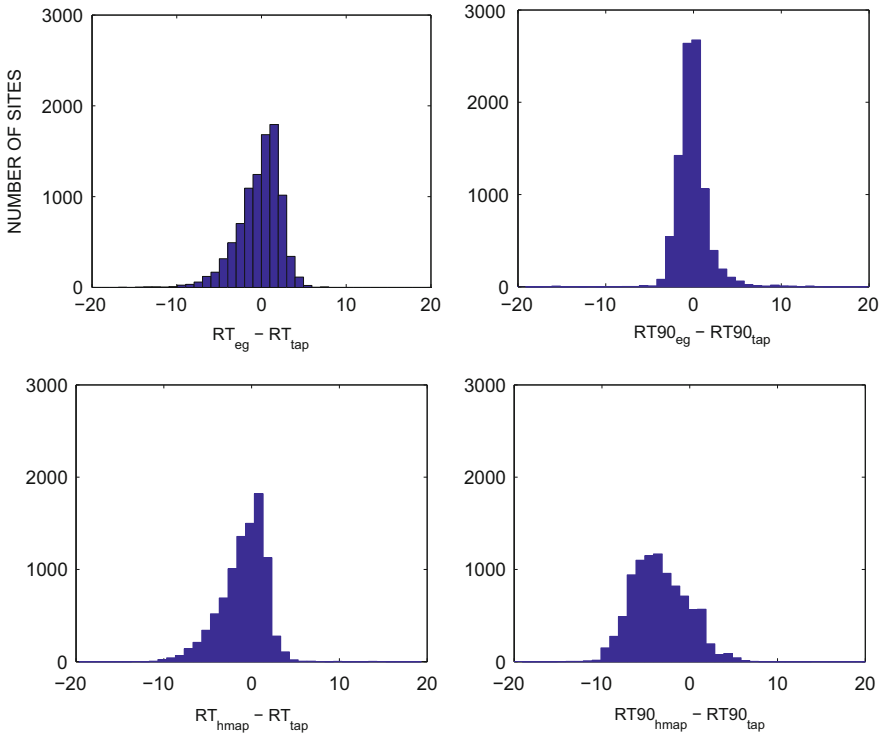
Fig. 9.50 Histograms of discrepancies $RT_{eg}-RT_{tap}$ (*first column*), $RT90_{eg}-RT90_{tap}$ (*second column*), $RT_{hmap}-RT_{tap}$ (*third column*) and $RT90_{hmap}-RT90_{tap}$ (*fourth column*) with 1 ms bins, for all the five slab types H-slab, 3-slab, W-slab, MI-slab and SI-slab (Reproduced with permission from [461])

reported in Table 9.10, except the correlation coefficients (corr), are the same for the pairs ARI_{eg} (ARI_{hmap}) vs APD and RT_{eg} (RT_{hmap}) vs RT_{tap}, as well as for the pairs $ARI90_{eg}$ ($ARI90_{hmap}$) vs APD90 and $RT90_{eg}$ ($RT90_{hmap}$) vs $RT90_{tap}$, because the relative and absolute discrepancies of $|AT_{eg}-AT_{tap}|$ and $|AT_{hmap}-AT_{tap}|$ are of the order of 1.e−4 and of 0.05 ms, respectively.

When considering exploring sites located a few mm from the PD volume, the bipolar signal HMAP simulates the condition of the classical monophasic action potential (MAP), see Franz [181], because the exploring and the PD reference electrode are very close. In order to evaluate the markers performance at these particular sites, we now consider in each simulation the six electrodes close to the PD volume (within 2 mm distance), yielding a total amount of 30 electrodes, and we compare the RT markers at these sites. The average indexes (mean, std, corr) are (1.06, 0.60, 0.99) for $|RT_{hmap}-RT_{tap}|$ and (1.99, 0.56, 0.96) for $|RT90_{hmap}-RT90_{tap}|$, to be compared with (3.84, 1.24, 0.99) for $|RT_{eg}-RT_{tap}|$ and with (2.04, 1.70, 0.95) for $|RT90_{eg}-RT90_{tap}|$, respectively.
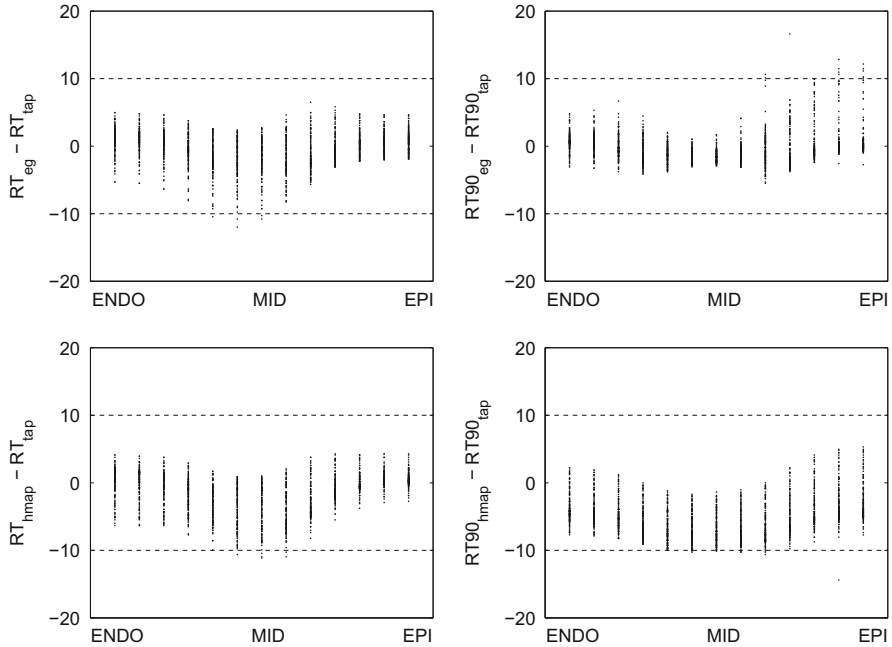
Fig. 9.51   3-slab, PD3. Discrepancies $RT_{eg}-RT_{tap}$ (*first column*), $RT90_{eg}-RT90_{tap}$ (*second column*), $RT_{hmap}-RT_{tap}$ (*third column*) and $RT90_{hmap}-RT90_{tap}$ (*fourth column*) (Reproduced with permission from [461])

Table 9.11 Correlations between action potential duration markers. ARI_{eg} vs APD, ARI_{hmap} vs APD, $ARI90_{eg}$ vs APD90, $ARI90_{hmap}$ vs APD90

	ARI_{eg} vs APD	ARI_{hmap} vs APD	$ARI90_{eg}$ vs APD90	$ARI90_{hmap}$ vs APD90
H-slab	0.84	0.77	0.91	0.72
3-slab	0.95	0.94	0.94	0.92
W-slab	0.96	0.92	0.98	0.95
MI-slab	0.91	0.93	0.95	0.90
SI-slab	0.90	0.84	0.90	0.63

These results show that near the PD volume RT_{hmap} ($RT90_{hmap}$) is a better estimate of RT_{tap} ($RT90_{tap}$) than RT_{eg} ($RT90_{eg}$) and consequently confirms that the downstroke phase of the HMAP yields a more accurate approximation of the TAP downstroke phase. This fact is also confirmed by the comparison of a suitable scaled and shifted TAP waveform with the HMAP waveform displayed in Fig. 9.52-top for a site close to the PD volume. Figure 9.52-bottom shows the plots of TAP, EG and HMAP waveforms at three endocardial sites, for the 3-slab in the PD3 case. The EGs exhibit T waves with different polarity, i.e. positive, biphasic and negative. We have
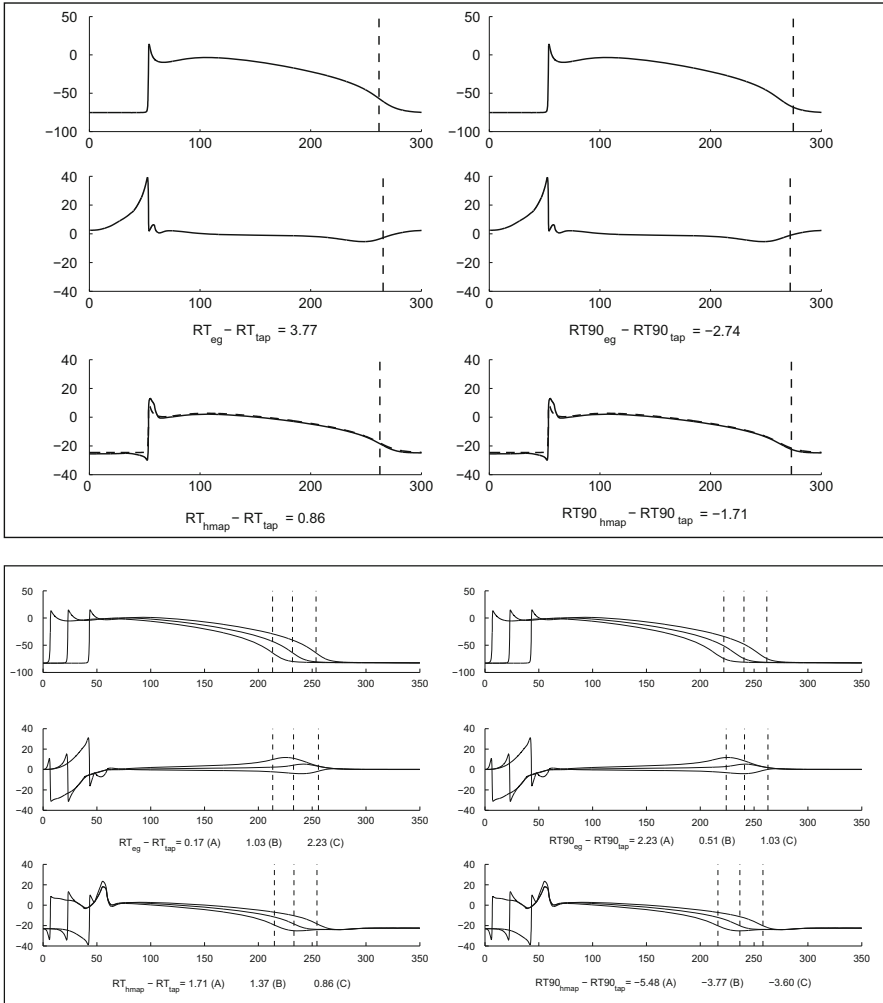
Fig. 9.52 *Top panel*. 3-slab, PD3: TAP (*first row*), EG (*second row*) and HMAP (*third row*) waveforms in the epicardial site located in the needle (2,12), see Fig. 9.46. The TAP waveform, plotted in *dashed line* in the *third row* superimposed to the HMAP, is shifted in order to have the same resting value of the HMAP waveform and it is scaled by a factor α. The *vertical lines* indicate RT_{tap} (*first row, left*), RT_{eg} (*second row, left*) and RT_{hmap} (*third row*), $RT90_{tap}$ (*first row, right*), $RT90_{eg}$ (*second row, right*) and $RT90_{hmap}$ (*third row, right*). *Bottom panel*. 3-slab, PD3: same format as in the *top panel* for the waveforms on the three endocardial sites located in the needles (2,2) (*A*), (6,6) (*B*) and (11,11) (*C*), see Fig. 9.46 (Reproduced with permission from [461])

not observed a significant dependence of the performance of the EG markers on the T wave polarity, in agreement with [127, 135] and in contrast with the controversial experimental findings of [87].

9.6 Subendocardial Ischemia, ST Depression and Elevation

Myocardial ischemia is a reduction of blood supply to a region of the myocardium, normally due to the occlusion of one or more coronary arteries. The ischemic region is classified either as subendocardial if it begins at the endocardial surface and extends partially through the heart wall, or as transmural, if it reaches the epicardium. Understanding the consequences of subendocardial ischemia on the epicardial surface has an important clinical interest. One way to locate ischemia in clinical electrocardiography is the so-called ST segment elevation in the electrocardiogram (ECG), but both the choice of this criterion and the mechanism underlying ST shifts are still controversial.

Several experimental works have studied these phenomena: Samson et al.[453], Prinzmetal et al.[403], Kjekshus et al.[286], and Kleber et al.[279], suggested that subendocardial ischemia produces ST elevation at the epicardial level, while Wolferth et al.[565] and Li et al.[298] found ST depression. MacLeod et al.[314] observed depression only under conditions of combined coronary occlusion and elevated heart rate. Many simulation studies (e.g. [235, 262, 263, 313]) investigated the mechanisms behind the ST segment shifts found in experiments as a marker for predicting and locating the myocardial injury within the first 15–20 min of an acute ischemic episode. These studies are mainly based on a time independent Bidomain model assuming a stationary transmembrane potential distribution with a sharp variation across the ischemic boundary during the diastolic or systolic phases of the heartbeat. It is shown in [235, 313] that for a subendocardial ischemic region the epicardial ST elevation is associated with the transmural ischemic boundary, while ST depression is associated with the lateral ischemic boundaries.

In this section, we simulate the entire QRST complex of the heartbeat by integrating the Bidomain model, a degenerate system of two parabolic reaction-diffusion equations, coupled with Luo-Rudy type models for the ionic currents, described by a stiff systems of ordinary differential equations. We study the influence of an ischemic subendocardial region on the excitation and the recovery sequences, the distribution of the action potential duration (APD) and the extracellular potential patterns at intramural and epicardial levels. In order to better understand the mechanism of ischemic ST segment shifts, we decompose the cardiac current sources into conormal, axial and orthogonal components and investigate which component is dominant during the ST interval. Other recent simulation studies of ischemic regions can be found in [353, 354, 456].

9.6.1 Mechanisms for the ST Segment Potential Patterns

We briefly recall the well-established mechanism at a cellular level (see [564] Ch. II Fig. 2.13) of the potential changes during ST interval, evidenced first by Samson and Sher[453], Prinzmetal et al.[403] and later confirmed by Kleber et al.[279]; see

also the updated surveys[257, 276] and the references therein. Due to the reduction of APD, the transmembrane potential in the ischemic cells during the ST interval is lower than in non-ischemic cells. This transmembrane potential difference produces a local intracellular current of injury flowing from non-ischemic to ischemic cells, associated with a local extracellular current flowing in opposite direction. This latter current is the cause of an elevation of the extracellular potential (ST elevation) recorded from the ischemic zone and a depression detected in the healthy part.

Thus, during the ST interval, at the tissue level we have a distribution of local injury currents sources around the ischemic boundary. According to Holland and Brooks[231], one way to extend the cellular mechanism to the ventricular wall is based on assuming that the elementary injury sources can be model as: (i) a dipole layer on the ischemic boundary, with dipole direction normal to this boundary and with moment proportional to the transmembrane potential jump; (ii) the dipole layer is embedded into an isotropic homogeneous and infinite conducting medium. This modeling of the injury sources, known as *solid angle theory*, predicts at the epicardial side an ST depression associated with the subendocardial ischemic volume. This extension of the cellular mechanisms to a tissue level is questionable, since the cardiac tissue exhibits a strong anisotropic structure and the injury currents sources are embedded in rotational anisotropic intra and extracellular media.

We apply now the source split of the extracellular potential field described in Chap. 5 to the particular case of the ST segment in the presence of an ischemic subendocardial region. Denoting by Ω_i the ischemic tissue, define $\Gamma_i = \partial\Omega_i$, $\Sigma_i = \Gamma_i \cap \Sigma$, and $\Gamma_l = \Gamma_i \setminus \Sigma_i$, where Σ is the non-insulated boundary of Ω_H, see Fig. 5.1. In the ST segment, the distribution of the transmembrane results can be practically approximated by a piecewise constant distribution. Denoting by v_r^I, v_r^N the values of the transmembrane potential in the ischemic and normal tissue, respectively, then $v(\mathbf{x}, t) = v_r^N + (v_r^I - v_r^N)\chi_{\Omega_i}(\mathbf{x})$, where χ_{Ω_i} denotes the characteristic function of the set Ω_i (i.e. $\chi_{\Omega_i}(\mathbf{x}) = 1$ if $\mathbf{x} \in \Omega_i$ or 0 if $\mathbf{x} \notin \Omega_i$).
The injury current sources are concentrated on the ischemic boundary Γ_i, hence $\nabla v(\mathbf{x}, t) = (v_r^I - v_r^N)\nabla\chi_{\Omega_i}(\mathbf{x}) = (v_r^I - v_r^N)\mathbf{n}_{\Gamma_i}\delta_{\Gamma_i}(\mathbf{x})$, where $\mathbf{n}$ denotes the normal vector to Γ_i pointing inside the ischemic domain Ω_i and $\delta_{\Gamma_i}(\mathbf{x})$ is a Dirac measure on Γ_i. Therefore, the injury current can be represented as an oblique dipolar layer with moment given by

$$\mathbf{J}_v = (v_r^I - v_r^N)\, D_i(\mathbf{x})\mathbf{n}(\mathbf{x})\, \delta_{\Gamma_i}(\mathbf{x}).$$

Applying the split of the tensor D_i given in (5.40), the oblique dipole layer $\mathbf{J}_v(\mathbf{x})$ can be viewed as the superposition of a conormal dipole with direction $D\mathbf{n}$, of a axial dipole layer having the same direction of the fiber $\mathbf{a}_l$, and of a cross-axial dipole layer, since the matrix $I - \mathbf{a}_l\mathbf{a}_l^T$ is the projection matrix on the plane orthogonal to $\mathbf{a}_l$, i.e.

$$\mathbf{J}_v = \mathbf{J}_c + \mathbf{J}_a + \mathbf{J}_o.$$

Here

$$\mathbf{J}_c = -\hat{\alpha}\, D\mathbf{n}\, \delta_{\Gamma_i} \qquad \mathbf{J}_a = -\hat{\beta}\left(\mathbf{a}_l^T \mathbf{n}\right)\mathbf{a}_l\, \delta_{\Gamma_i}, \qquad \mathbf{J}_o = -\hat{\gamma}\left(I - \mathbf{a}_l \mathbf{a}_l^T\right)\mathbf{n}\, \delta_{\Gamma_i},$$

with $\hat{\alpha} = (v_r^I - v_r^N)(\sigma_t^i - \sigma_n^i)/(\sigma_t - \sigma_n)$, $\hat{\beta} = (v_r^I - v_r^N)(\sigma_t^i - \alpha\sigma_t)$ and $\hat{\gamma} = (v_r^I - v_r^N)(\sigma_t^i - \alpha\sigma_t) = (v_r^I - v_r^N)(\sigma_n^i - \alpha\sigma_n)$. We remark that since $v_r^I > v_r^N$, $\sigma_t^i > \sigma_n^i$ and $\sigma_t^e > \sigma_n^e$, it follows that $\hat{\alpha} > 0$, $\hat{\beta} > 0$ and $\hat{\gamma} < 0$.

The *conormal*, *axial* and *orthogonal* current densities $\mathbf{J}_c$, $\mathbf{J}_a$, $\mathbf{J}_o$ define three distributions of dipolar current sources lying on the ischemic boundary with dipole axes parallel to the conormal direction $D\mathbf{n}$, to the fiber direction $\mathbf{a}_l$ and orthogonal to the fiber direction, respectively. Since only ∇v appears in the current density, we shift the distribution v by introducing the discrepancy with respect to the normal resting value v_r^N, i.e. $\hat{v} = v - v_r^N = (v_r^I - v_r^N)\chi_{\Omega_i}(\mathbf{x})$.

The transmembrane component $u_{\hat{v}}$ is given by

$$u_{\hat{v}}(\mathbf{x}) = -\hat{\alpha}(v_r^I - v_r^N)\left(\chi_{\Omega_i}(\mathbf{x}) - \frac{|\Omega_i|}{|\Omega_H|}\right).$$

In the case of the endocardial surface in contact with the cavitary blood, we have

$$u_c(\mathbf{x}, t) = u_{\hat{v}} + u_{hs}(\mathbf{x}, t),$$

where u_{hs} is the heart surface component, see (5.41) and (5.42).

The full potential distribution u is the superposition of its field components

$$u(\mathbf{x}, t) = u_{\hat{v}}(\mathbf{x}, t) + u_{hs}(\mathbf{x}, t) + u_a(\mathbf{x}, t) + u_o(\mathbf{x}, t).$$

This expression leads to the following remarks.

(a) The transmembrane component $u_{\hat{v}}$ is a *jump* component, because its effect on the full potential u reduces to a shift proportional to the jump $v_r^I - v_r^N$ of the transmembrane potential from the ischemic to the normal resting values through the ischemic boundary. Therefore, $u_{\hat{v}}$ does not contribute to extracellular currents and potential pattern.

(b) Since $\hat{v}(\mathbf{x}, t) = 0$, when $\mathbf{x} \in \Sigma_i = \Sigma \cap \Gamma_i$, we have $[\![\, u(\mathbf{x}, t)\,]\!]_{\Sigma_i} = \alpha\hat{v}(\mathbf{x}, t)$ on Σ_i and $[\![\, u(\mathbf{x}, t)\,]\!]_{\Sigma_i} = 0$ on $\Sigma \setminus \Sigma_i$. Therefore, the *heart surface* component u_{hs} depends on the ischemic resting value and on the area of boundary of the ischemic region in contact with the cavitary blood. This field is the potential generated by a dipole layer on Σ_i with moment αv_r^I and direction orthogonal to Σ_i and pointing toward the blood cavity. Thus it is similar to the *classical*

uniform dipole layer source on Σ_i, but embedded in the anisotropic bulk medium. We remark that for a fully insulated slab, the heart surface contribution disappears.

(c) The axial and orthogonal potentials u_a, u_o are generated by surface sources on Γ_i represented by a current dipole density parallel and orthogonal to the local fiber direction $\mathbf{a}_l$ on the ischemic boundary, respectively; since the fiber architecture defines the direction of the current source flow we expect that structural properties like epi-endocardial fiber rotation on the ischemic boundary will be the major determinants affecting the axial and orthogonal potential patterns.

An alternative and equivalent way to relate the potential field to its current source density is to use an integral representation that turns out to be more efficient than the previous differential representation for e.g. the computation of electrograms at a limited number of sites (see e.g[118, 483]).

Using as a reference potential the average potential on the cardiac volume Ω_H,

$$w(\mathbf{x}, t) = u(\mathbf{x}, t) - \frac{1}{|\Omega_H|} \int_{\Omega_H} u(\boldsymbol{\xi}, t) \, d\boldsymbol{\xi}.$$

For $\mathbf{x} \in \Omega_H \cup \Omega_b$, i.e. within the cardiac wall or in the extracardiac medium, the full potential can be expressed by means of the following integral over the cardiac domain

$$w(\mathbf{x}, t) = \int_{\Omega_H} \mathbf{J}_v^T \, \nabla_{\xi} \Psi(\boldsymbol{\xi}, \mathbf{x}) \, d\xi = - \int_{\Omega_H} (\nabla v(\boldsymbol{\xi}, t))^T \, D_i(\boldsymbol{\xi}) \nabla_{\xi} \Psi(\boldsymbol{\xi}, \mathbf{x}) \, d\xi,$$

$$(9.5)$$

where $\Psi(\boldsymbol{\xi}, \mathbf{x})$ is the solution of the following *lead field* problem

$$\begin{cases} -\mathrm{div}_{\xi} \hat{D} \nabla_{\xi} \Psi = -\dfrac{1}{|\Omega_H|} \, \chi_{\Omega_H}(\boldsymbol{\xi}) + \delta(\boldsymbol{\xi} - \mathbf{x}) \, \boldsymbol{\xi} \in \Omega_H \cup \Omega_b \\[2mm] [\![\, \Psi \,]\!]_{\Sigma} = 0, \quad [\![\, \mathbf{n}^T \hat{D} \nabla_{\xi} \Psi \,]\!]_{\Sigma} = 0 \qquad \boldsymbol{\xi} \in \Sigma \\[2mm] \mathbf{n}^T \hat{D} \nabla_{\xi} \Psi = 0 \qquad\qquad\qquad\qquad \text{on } \Gamma, \end{cases}$$

with $\chi_{\Omega_H}(\boldsymbol{\xi})$ the characteristic function of Ω_H, and $\delta(\boldsymbol{\xi} - \mathbf{x})$ denotes the Dirac delta function at point $\mathbf{x}$. Note that the boundary condition imposed on the "lead field" Ψ actually reflects the property that $w(\mathbf{x}, t)$, defined by (9.5), has zero average in the heart domain.

Using again as a reference the average potential on Ω_H, the split field components w_a, w_o, w_c, associate with the sources $\mathbf{J}_c$, $\mathbf{J}_a$ and $\mathbf{J}_o$, respectively, can be represented by means of the following surface integral on the ischemic boundary

$$w_c(\mathbf{x}, t) = \hat{\alpha} \int_{\Gamma_i} D(\boldsymbol{\xi}) \mathbf{n}(\boldsymbol{\xi}) \cdot \nabla_{\boldsymbol{\xi}} \Psi(\boldsymbol{\xi}, \mathbf{x}) \, d\sigma_{\boldsymbol{\xi}},$$

$$w_a(\mathbf{x}, t) = \hat{\beta} \int_{\Gamma_i} (\mathbf{a}_l^T(\boldsymbol{\xi}) \mathbf{n}(\boldsymbol{\xi})) \mathbf{a}_l(\boldsymbol{\xi}) \cdot \nabla_{\boldsymbol{\xi}} \Psi(\boldsymbol{\xi}, \mathbf{x}) \, d\sigma_{\boldsymbol{\xi}},$$

$$w_o(\mathbf{x}, t) = \hat{\gamma} \int_{\Gamma_i} \left(I - \mathbf{a}_l(\boldsymbol{\xi}) \mathbf{a}_l^T(\boldsymbol{\xi}) \right) \mathbf{n}(\boldsymbol{\xi}) \cdot \nabla_{\boldsymbol{\xi}} \Psi(\boldsymbol{\xi}, \mathbf{x}) \, d\sigma_{\boldsymbol{\xi}}.$$

In the following, we will denote by *full* extracellular waveform w, by *isotropic (IS)* extracellular waveform $w_{IS} = w_c$ and by *anisotropic (AS)* extracellular waveform the sum $w_{AS} = w_a + w_o$, and we will refer to the splitting

$$w = w_{IS} + w_{AS}$$

as the *decomposition* of the full extracellular waveform into its isotropic and anisotropic components.

9.6.2   Ischemic Simulations

We investigate the effects induced by the presence of an ischemic subendocardial region on the extracellular potential distributions, the activation-repolarization sequences and the action potential duration (APD).

A simplified left ventricular geometry is considered, defined as a set of packed ellipsoidal surfaces truncated at the base and the apex, according to the parametric equations

$$x = a(r) \cos \theta \cos \phi, \qquad y = a(r) \cos \theta \sin \phi, \qquad z = c(r) \sin \theta.$$

Here $r \in [0, 1]$, $\phi \in [\phi_{min}, \phi_{max}]$, $\theta \in [\theta_{min}, \theta_{max}]$, $a(r) = a_1 + r(a_2 - a_1)$, $c(r) = c_1 + r(c_2 - c_1)$ and $a_i, c_i, i = 1, 2$ are given coefficients determining the main axes of the ellipsoid. The intracavitary blood and the extracardiac bath are also modeled as a set of packed ellipsoidal surfaces in contact with the endocardial and the epicardial surface, respectively.

We have assumed homogeneous cellular membrane properties, i.e. all individual cells have the same intrinsic transmembrane action potential, except in the ischemic region. The three main pathophysiological conditions of myocardial ischemia are

elevated extracellular potassium, acidosis and anoxia, whose effects on transmembrane potential are elevation of resting potential and reduction of upstroke velocity and APD. After the occlusion of a coronary artery, we can distinguish three stages of ischemia: moderate, corresponding to the first 5–7 min, with an elevation of extracellular potassium $[K^+]_o$ to about 10 mM; early severe, after 10–12 min, with a second increase of $[K^+]_o$; and severe, characterized by the occurrence of gap junction uncoupling and irreversible cell damage. In our study, we consider the first and the second stages, and therefore we do not alter the conductance coefficients. In the remainder of the section, we will refer to early severe ischemia as severe (or acute) ischemia. In the LR1 model, we increase the value of extracellular potassium $[K^+]_o$ from 5.4 mM (control) to 10.5 (moderate) and 18 mM (severe); see [569]. The resting transmembrane potentials are −84 mV (control), −70 mV (moderate) and −55 mV (severe), while the APDs are 260 ms (control), 170 ms (moderate) and 70 ms (severe), see Fig. 9.53. For economy of space, we will report the details and figures for the case of acute ischemia and only comment on the differences in the case of moderate ischemia.

The fibers rotate intramurally linearly with the depth for a total amount of 120° and when the point of view is from the epicardial side, the rotation is counterclockwise (CCW) proceeding from the epicardium to endocardium. More precisely, in the canonic reference system (u_{e1}, u_{e2}, u_{e3}), the fiber direction $\mathbf{a}_l(\mathbf{x})$ and the other two principal axes at a point $\mathbf{x}$ are given by

$$\mathbf{a}_l(\mathbf{x}) = u_{e1} \cos \alpha(r) + u_{e2} \sin \alpha(r), \ \mathbf{a}_t(\mathbf{x}) = u_{e3}, \ \mathbf{a}_n(\mathbf{x}) = u_{e1} \sin \alpha(r) - u_{e2} \cos \alpha(r)$$
$$\alpha(r) = \frac{2}{3}\pi(1 - r) - \frac{\pi}{4}, \ \text{with } r = x_3/c. \tag{9.6}$$
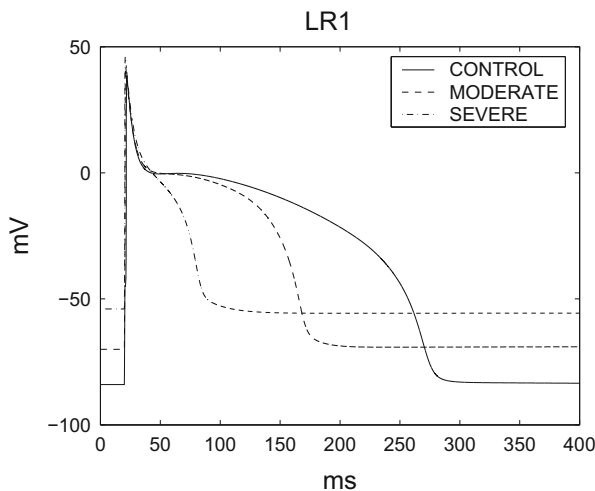
Fig. 9.53 Control, moderate and severe ischemic action potentials generated by 0-dimensional LR1 model

The conductivity tensors are assumed orthotropic with values

$$\sigma_l^i = 3 \cdot 10^{-3}, \; \sigma_t^i = 3.1525 \cdot 10^{-4}, \; \sigma_n^i = 3.1525 \cdot 10^{-5},$$
$$\sigma_l^e = 2 \cdot 10^{-3}, \; \sigma_t^e = 1.3514 \cdot 10^{-3}, \; \sigma_n^e = 6.757 \cdot 10^{-4} \, (\Omega^{-1} \, cm^{-1}).$$

We will also consider an isotropic conducting media modeling the cavitary blood with conductivity coefficient $\sigma_b = 6 \cdot 10^{-3} \, \Omega^{-1} \, cm^{-1}$.

The macroscopic features of the excitation and subsequent repolarization process are described by extracting from the spatio-temporal transmembrane potential the sequence of the propagating excitation and repolarization wave fronts. In particular, we define the excitation time $t_e(\mathbf{x})$ at a given point $\mathbf{x}$ as the unique time when $v(\mathbf{x}, t_e(\mathbf{x})) = -40 \, mV$ during the excitation phase. Analogously, during the repolarization phase we define the recovery time as the unique time instant $t_r(\mathbf{x})$ when $v(\mathbf{x}, t_r(\mathbf{x})) = -50 \, mV$. In Figs. 9.54 and 9.55, we report the isochrone lines
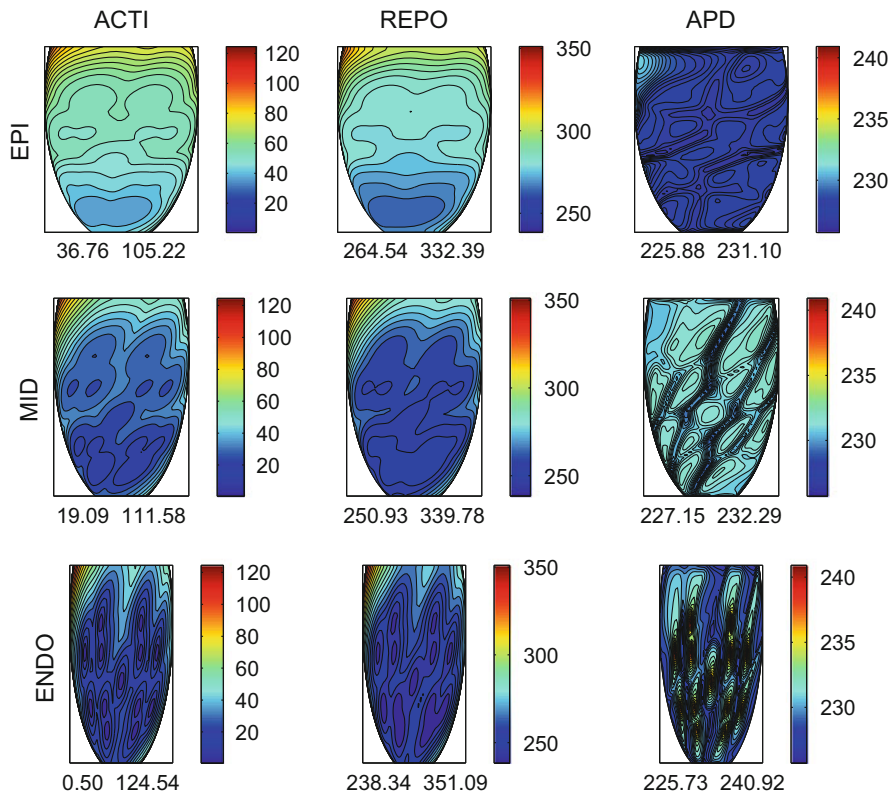
Fig. 9.54 Contour plots of depolarization time (*first column ACTI*), repolarization time (*second column REPO*) and action potential duration (*third column APD*) on epi, midwall and endocardial surfaces in case of healthy tissue with multiple endocardial stimulation. Reported below each panel are the maximum, minimum and step in ms of the displayed map
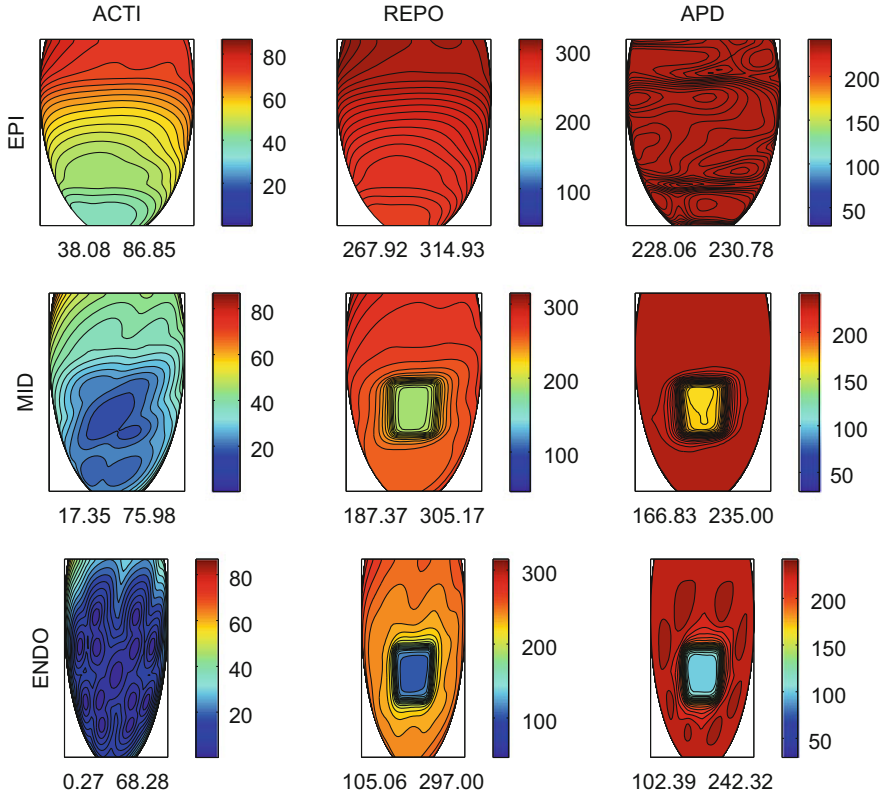
Fig. 9.55 Contour plots of depolarization time (*first column ACTI*), repolarization time (*second column REPO*) and action potential duration (*third column APD*) on epi, midwall and endocardial surfaces in case of an acute subendocardial ischemic region. Reported below each panel are the maximum, minimum and step in ms of the displayed map

of the activation time $t_e(\mathbf{x})$ (first column, ACTI), repolarization time $t_r(\mathbf{x})$ (second column, REPO) and APD $= t_r(\mathbf{x}) - t_e(\mathbf{x})$ (third column) on the epicardium (first row), midwall (second row) and endocardium (third row), for a healthy tissue with multiple endocardial stimulation and for a tissue with a subendordial ischemic region and central endocardial stimulation, respectively.

Extracellular potential distributions and electrograms: healthy tissue. We report in Fig. 9.56 the decomposition of four epicardial electrograms and in Fig. 9.57 the decomposition of 16 electrocardiograms recorded 2 *cm* far away from the epicardium, in case of normal tissue. We observe that all the isotropic components (in blue) present a mainly positive QRS complex, while the anisotropic components (in red) present a negative QRS complex. Due to the larger magnitude of the anisotropic components, the resulting full extracellular/extracardiac waveforms (in black) have a mainly negative biphasic QRS complex.
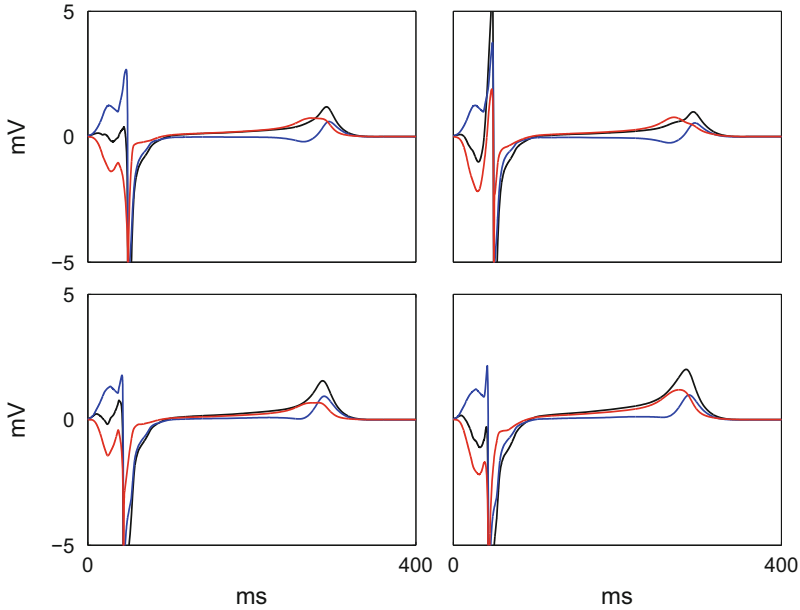
Fig. 9.56 Decomposition of four epicardial electrograms in case of normal tissue. Full extracellular waveform (*black*), isotropic component (*blue*) and anisotropic component (*red*)

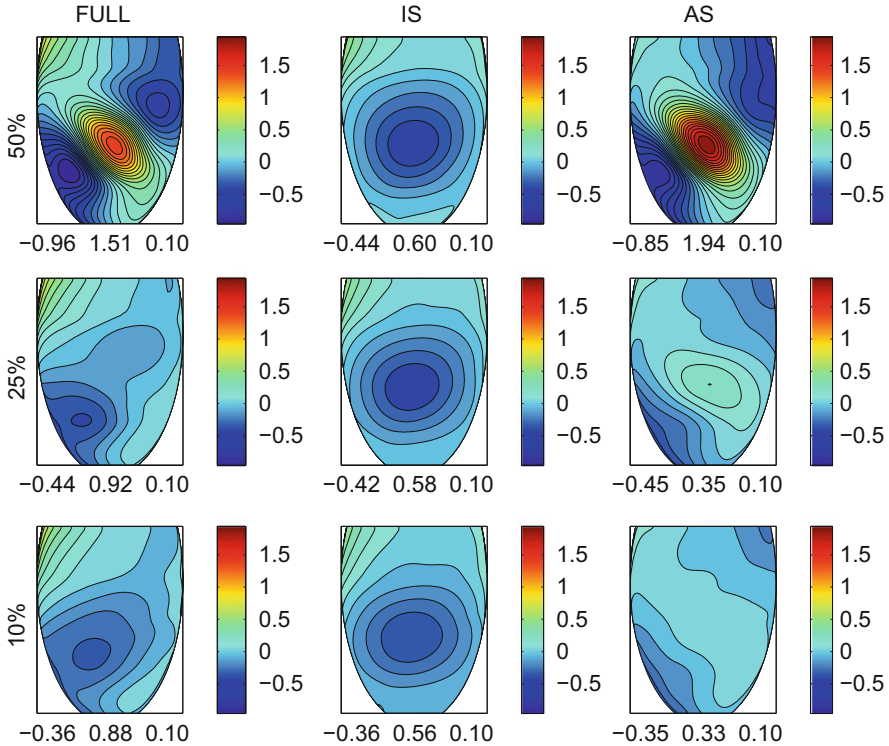**Extracellular potential distributions and electrograms: ischemic tissue**. Figure 9.58 reports the decomposition of the epicardial extracellular potential during the ST interval (140 ms) for different percentages (10, 25, 50 %) of the ischemic region thickness with respect to the total transmural wall thickness. For thin ischemic regions (10 and 25 % of the whole transmural thickness), the isotropic component is dominant and the full extracellular potential field presents a minimum (ST depression) on the epicardial projection of the subendocardial ischemic region. Instead, in the case of thick ischemia (50 % and more), the anisotropic component is dominant, because the lateral boundaries of the ischemic region are large, thus the full extracellular potential presents a maximum (ST elevation) on the epicardial projection of the ischemic region.

Figure 9.59 displays the epicardial electrograms calculated from a grid of 4×4 electrodes. Figure 9.60 shows the decomposition of the epicardial electrogram above the subendocardial ischemic region for different percentages of the ischemic region thickness. Again, if the subendocardial ischemic region is thicker, then the anisotropic component is more dominant, yielding the ST elevation in the full extracellular waveform.
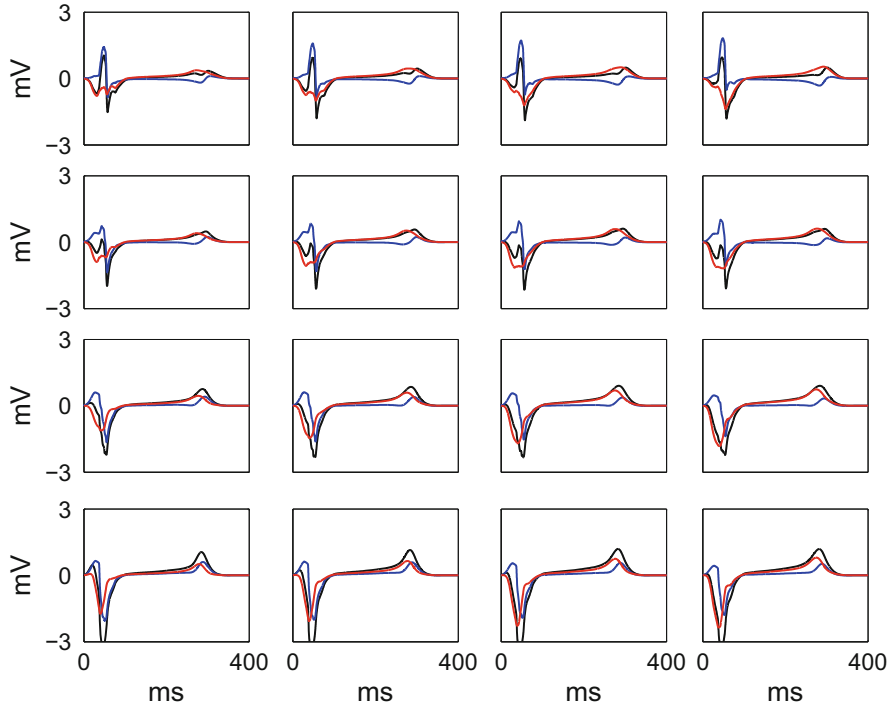
Fig. 9.57 Decomposition of 16 electrocardiograms recorded 2 cm far away from the epicardium in case of normal tissue. Full extracardiac waveform (*black*), isotropic component (*blue*) and anisotropic component (*red*)

9.7 Reentry Phenomena

Atrial or ventricular reentry is a type of arrhythmia where the electric signal is not completing the normal circuit, but it rather follows an alternative circuit looping back upon itself and developing a self-perpetuating rapid and abnormal activation, also called *circus movement*. Necessary conditions for the onset of reentry include a combination of unidirectional block and slowed conduction. Reentry is divided into two major types: *anatomical* and *functional reentry*. The circus movement can occur around an anatomical (e.g. an infarct region) or functional core. Either of two types may occur alone, or together. In the following, we will focus on functional reentry, and in particular on the causes of its induction.

A widely accepted theory for the induction of functional reentry in cardiac tissue is based on a hypothesis proposed by Winfree in [561], known as the *critical point hypothesis*, see also the review [431]. This hypothesis can be illustrated by considering the so-called *pinwheel experiment*. Suppose that an action potential wavefront, elicited by a brief electrical stimulus (S1), propagates from left to right in a two-dimensional sheet of cardiac tissue, as shown in Fig. 9.61, Panels a–c.

Fig. 9.58 Contour plots of the epicardial extracellular potential decomposition during the ST interval (140 ms) for different percentages (10, 25, 50 %) of the subendocardial ischemic region thickness with respect to the total transmural wall thickness. Reported below each panel are the maximum, minimum and step in mV of the displayed map

During the plateau and repolarization phases of the action potential, the tissue is refractory. The *critical phase* of the action potential is the time when the application of a stimulus of appropriate strength induces reentry and it occurs during the so-called *vulnerable window*, near the end of the refractory period.

Suppose now that a second brief point stimulus (S2) is applied at the center of the sheet. If the S2 stimulus is applied early (see Fig. 9.61, Panel d), the tissue under the stimulation electrode is still refractory and the stimulus does not elicit a wavefront (see Fig. 9.61, Panel g). On the other hand, if the S2 stimulus is applied late (see Fig. 9.61, Panel f), the tissue under the electrode has already recovered from refractoriness and a closed wavefront propagating outward is initiated (see Fig. 9.61, Panel i). However, if the S2 stimulus is applied at an intermediate time (see Fig. 9.61, Panel e), when the critical phase is occurring in the tissue under the electrode, the portion of tissue on the left of the electrode is excited, while that on the right is still too refractory to be excited. As a result, a wavefront is propagating outward, but it is not closed (see Fig. 9.61, Panel h). It ends at two points where the contours of critical
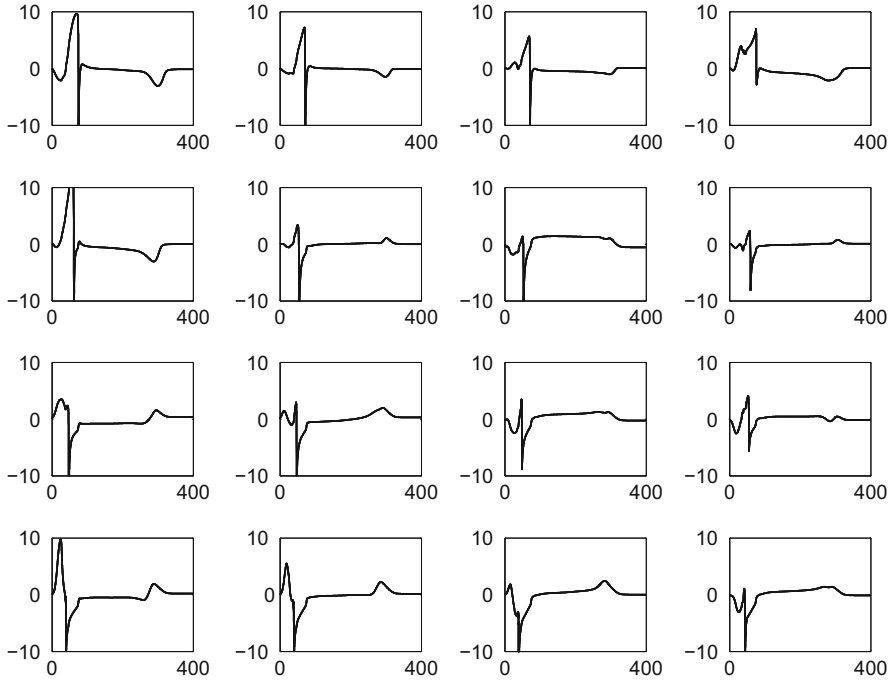
Fig. 9.59 Epicardial electrograms calculated from a grid of 4×4 electrodes in the case of an acute subendocardial ischemic region 50 % thick
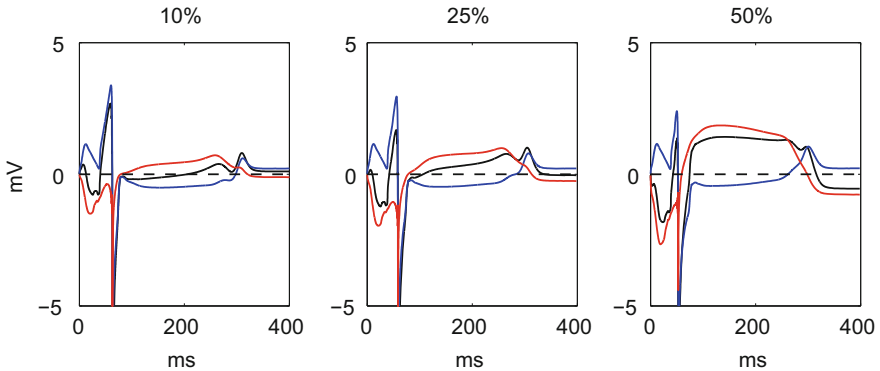
Fig. 9.60 Decomposition of the epicardial electrogram above the subendocardial ischemic region for different percentages (10, 25, 50 %) of the ischemic region thickness with respect to the total transmural wall thickness. Full extracellular waveform (*black*), isotropic component (*blue*) and anisotropic component (*red*)
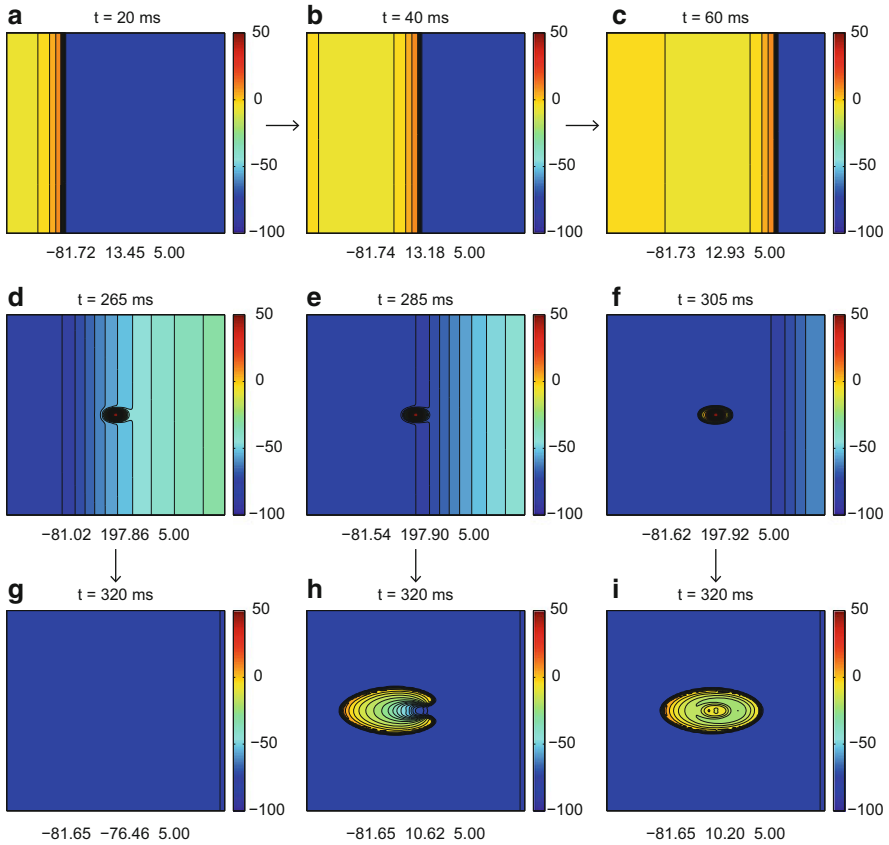
Fig. 9.61 The pinwheel experiment on a two-dimensional sheet of cardiac tissue. Panels **a-b-c**: transmembrane potential patterns at three instants during the propagation of the planar excitation wavefront elicited by the S1 stimulation. Panels **d-e-f**: transmembrane potential patterns during an early (**d**), intermediate (**e**) and late (**f**) S2 central point stimulation. Panels **g-h-i**: transmembrane potential patterns some instants after the onset of the early (**g**), intermediate (**h**) and late (**i**) S2 stimulations. Below each panel are reported the minimum, maximum and step in mV of the displayed map and the colorbar denotes the range of values of the displayed equipotential lines

phase and critical depolarization intersect. Frazier et al. in [185] refer to these points as *critical points*. As time proceeds further, the two critical points become the pivots of two spiral excitation waves. In the cardiac electrophysiology literature, spiral waves are also called *rotors* and the particular type of reentry described above is called *figure of eight* reentry.

The critical point hypothesis has been verified experimentally by Shibata et al. [476], who performed the pinwheel experiment in a dog heart. The critical point hypothesis also inspired an experimental method for the induction of a single rotor in the heart, known as cross-field stimulation. In this method, two electric stimulations, S1 and S2, are delivered with an appropriate delay through two lines of electrodes

aligned perpendicular to each other, see e.g. [185], where cross-field stimulation was used to initiate rotors in a dog heart.

The pinwheel experiments [476] and the cross-field stimulation experiments [185] validated strongly the critical point hypothesis, which now, thanks to this experimental evidence, is usually referred to as *critical point theory*.

In the pinwheel experiment, a pair of rotors is induced by applying two successive stimuli, S1 and S2, at different locations. Suppose now that both S1 and S2 are applied at the same site, so that the S1 critical phase contour and the S2 stimulus contour are both circles centered at the same point. Because two concentric circles never intersect, the critical point theory predicts that reentry cannot occur. However, Matta et al. in [322] performed this experiment and initiated reentry.

A possible explanation of this paradox is based on the anisotropic Bidomain model, and in particular on the *virtual electrode polarization* pattern due to the unequal anisotropy rations of the intra- and extracellular media. In [429], Roth showed by Bidomain numerical simulations that an S1-S2 stimulation protocol through the same unipolar electrode might induce reentry.

Three-dimensional reentry simulations. We now turn to the simulation of reentry phenomena in three dimensions, where the possible configurations of reentrant fronts are much more complex and less understood than in two dimensions (three-dimensional rotors are often called scroll waves). There is a vast literature on cardiac reentry simulations and experiments; among the several simulation works, we refer the interested reader to e.g. [49, 98, 170, 171, 191, 287, 345, 368, 411, 412, 431, 450, 488, 519, 562, 569], Part VII of [587, 588], and the references therein. Due to the high computational complexity of large scale simulations, virtually all works in the vast existing literature on cardiac reentry simulations employ some model simplifications in order to obtain a tractable discrete problem see e.g. [278], [589, Part V and VII], [369]. The most used simplifications are in the cardiac tissue model (Monodomain instead of Bidomain, fiber structure without intramural rotation or full anisotropy), in the ionic model (FHN or intermediate variations instead of LR models), in the domain (two instead of three dimensions), in the numerical methods (operator splitting instead of the fully coupled Bidomain system, coarse time and/or space mesh sizes compared to the length scale of the problem), etc. On the contrary, we retain here the full complexity of the coupled Bidomain–LR1 model with intramural fiber rotation and orthotropic anisotropy in three dimensions and we compare the resulting scroll waves with the one obtained with the Monodomain–LR1 model. With the latter, we then simulate scroll wave breakups on larger domains and counterrotating scroll waves on half ventricle.

9.7.1   Stable Scroll Waves

We start with the simulation of a stable scroll wave using both the anisotropic Bidomain–LR1 and the Monodomain–LR1 models. The conductivity tensors are assumed axisymmetric with values

$\sigma_l^i = 3 \cdot 10^{-3}$, $\sigma_t^i = 3.1525 \cdot 10^{-4}$, $\sigma_l^e = 2 \cdot 10^{-3}$, $\sigma_t^e = 1.3514 \cdot 10^{-3}$ $(\Omega^{-1}\,cm^{-1})$

in the Bidomain case and

$$\sigma_l = 1.2 \cdot 10^{-3}, \ \sigma_t = 2.5 \cdot 10^{-4} \ (\Omega^{-1}\,cm^{-1})$$

in the Monodomain case.

The original LR1 model is modified in order to shorten the APD according to Garfinkel et al. [191], setting $G_{Na} = 16$, $G_K = 0.432$, $G_{si} = 0$. We have assumed throughout the slab homogeneous intrinsic cellular membrane properties. Due to the high computational costs of the Bidomain model, we limit our simulation to a cartesian slab of dimensions $2 \times 2 \times 0.5\,cm^3$, discretized with $200 \times 200 \times 50$ finite elements.

The intramural fibers rotate linearly with depth for a total amount of 90°, i.e. 18°/mm, starting from −90° (0°) on the lower-endocardial (upper-epicardial) surface of the slab with respect to a side on the slab.

Reentry is initiated with a cross gradient procedure, applying at first an impulse of $200\,\mu A/cm^3$ for 1 ms along one of the main intramural sides of the slab, generating initially a plane wave, and then eliciting an orthogonal front by applying a second impulse at a proper time (in this case $t = 68.4$ ms) in the bottom-left quarter volume of the domain. This cross gradient stimulation elicites a vortex-like pattern, usually called scroll wave, rotating around a tube-like filament which is a 3D analog of the core of a spiral wave . The simulation was run for 200 ms at a fixed time step size of 0.05 ms.

The time evolution at a given point of the transmembrane potential v and of the LR1 variables during a reentry elicited by a stable scroll wave is shown in Fig. 9.62.

The contour plots of the resulting scroll waves are shown in Fig. 9.63 in the Bidomain case and in Fig. 9.64 in the Monodomain case, from $t = 90$ to $t = 200$ ms, every 10 ms. The colormap of the transmembrane potential distribution ranges from blue (resting values around −84 mV) to red (excitation front around 10 mV). The effect of the anisotropy appears stronger in the Bidomain model, as shown by the more elongated spirals on the epicardium and by the more twisted scroll waves in the intramural sections. Moreover, the meandering of the epicardial spiral tip follows a more regular trajectory in the Monodomain case than in the Bidomain case. Nevertheless, the plots in Fig. 9.65 of the transmembrane potential v in the two models, at a given point as a function of time, show very similar propagation speed and frequency, as the curves appear to be just shifted in time.

9.7.2   Scroll Waves Breakup

The breakup of spiral and scroll waves has been intensely studied in recent years because it could underlie ventricular fibrillation according to some authors
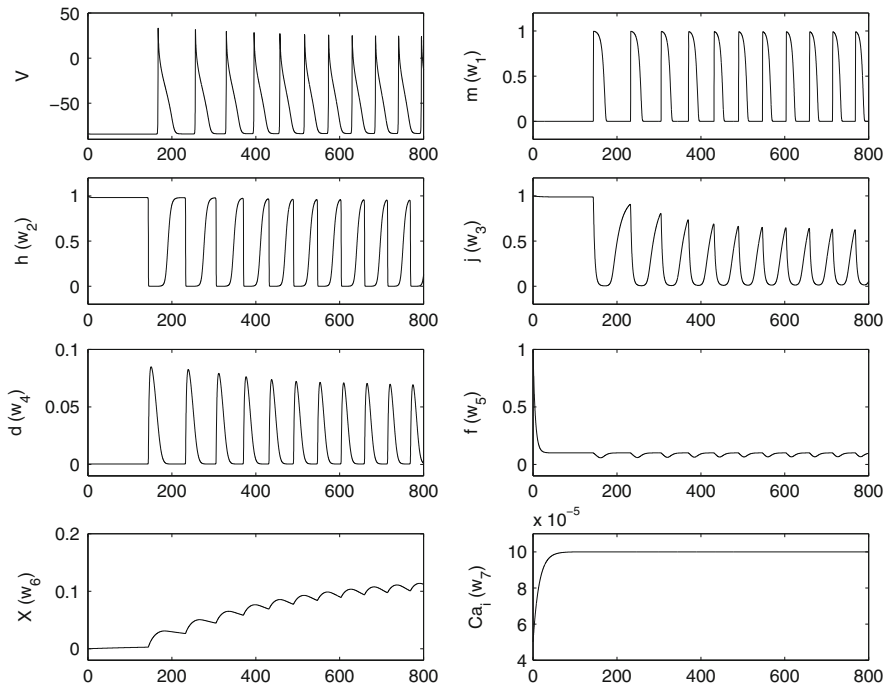
Fig. 9.62 Time course of the transmembrane potential v, of the LR1 gating variables m, h, j, d, f, X and of the C_a^{2+} concentration during reentry determined by a stable scroll wave (800 ms)

and it still remains a complex phenomenon with multiple causes not yet fully understood, see e.g. Fenton et al. [171], Garfinkel et al. [191]. Among the possible factors contributing to the breakup of the excitation front and to the instability of reentry circuits, many researchers indicated steep APD restitution curve, intramural rotational anisotropy, tissue thickness, filament twist, etc.

We simulated a spiral and scroll wave breakup using the axisymmetric anisotropic Monodomain with the conductivity coefficients

$$\sigma_l = 1.2 \cdot 10^{-3}, \ \sigma_t = 2.5 \cdot 10^{-4} \ (\Omega^{-1} \, cm^{-1}),$$

and the LR1 model with $G_{Na} = 16$, $G_K = 0.432$, as before, but setting the conductance of the slow-inward current $G_{si} = 0.056$. It has been shown that increasing this parameter increases the meandering of the scroll filament and eventually leads to a breakup regime if the cardiac tissue is thick enough; see Garfinkel et al. [191].
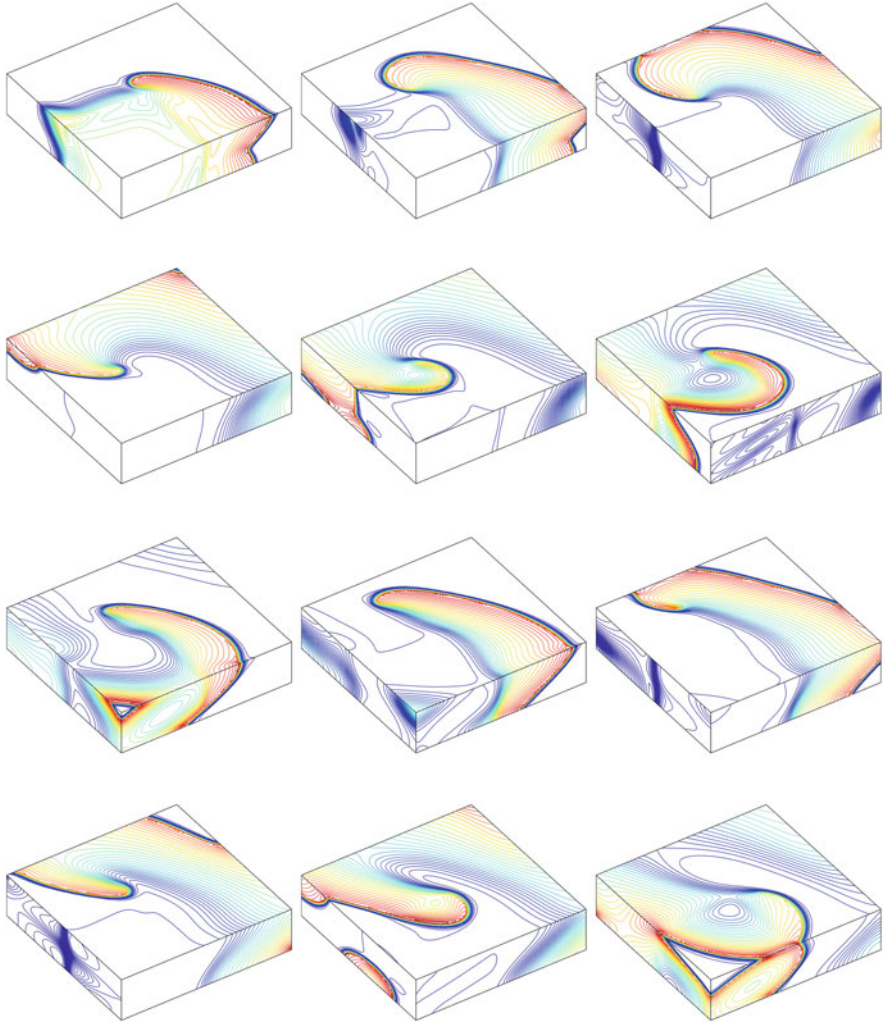
Fig. 9.63 Stable scroll wave with Bidomain–LR1 model. Domain: $2 \times 2 \times 0.5\,\text{cm}^3$, $\Delta x = 0.01$, $G_{si} = 0$, t $= 90, 100, 110, 120, 130, 140, 150, 160, 170, 180, 190, 200$ ms. The colormap ranges from *blue* (resting values around -84 mV) to *red* (excitation front around 10 mV)

Next, we consider scroll waves breakup in three dimensions. In order to contain the increased meandering of the filament inside the computational domain, we consider a three-dimensional domain of size $6 \times 6 \times 0.6\,\text{cm}^3$ and consider a high degree of intramural fiber rotation, for a total amount of $120°$. The spatial mesh consists of $400 \times 400 \times 40$ finite elements and the simulation is run up to $1\,300$ ms ($26\,000$ time steps with $\Delta t = 0.05$ ms), starting with the same cross gradient stimulation as before. The results displayed in Fig. 9.66 focus on three moments
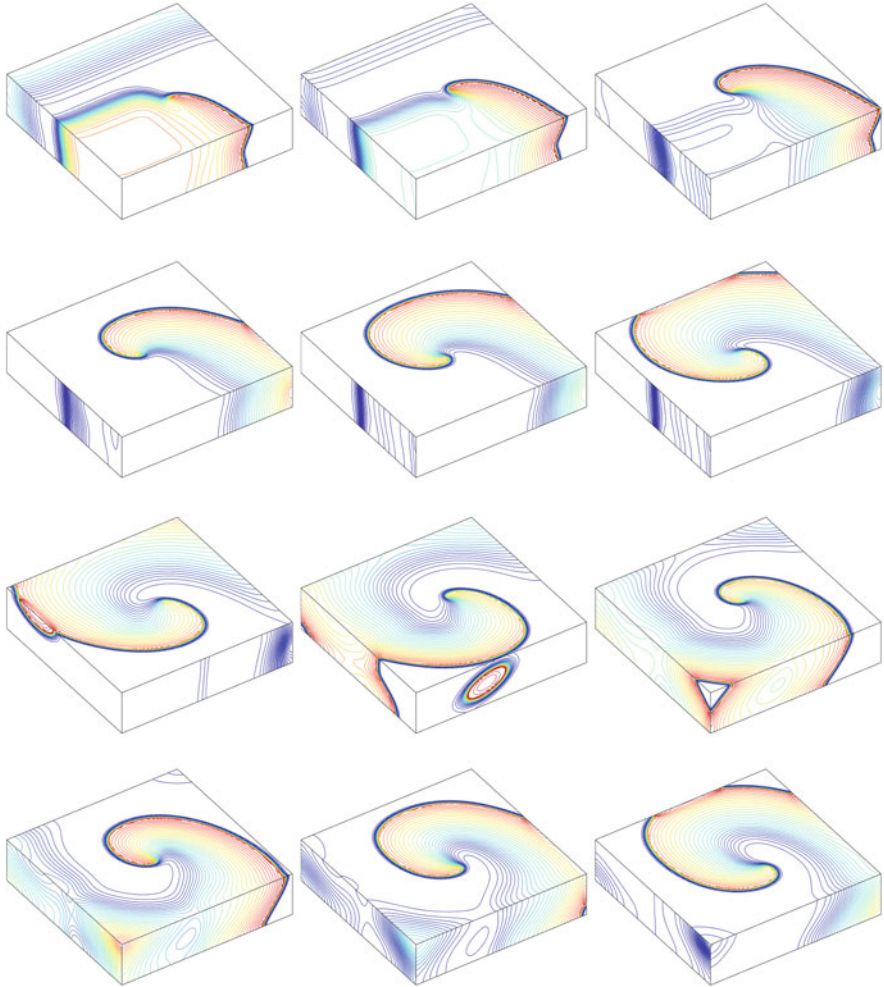
Fig. 9.64 Stable scroll wave with Monodomain–LR1 model. Domain: $2 \times 2 \times 0.5\,\text{cm}^3$, $\triangle x = 0.01$, $G_{si} = 0$, t = 90, 100, 110, 120, 130, 140, 150, 160, 170, 180, 190, 200 ms. The colormap ranges from *blue* (resting values around $-84\,\text{mV}$) to *red* (excitation front around $10\,\text{mV}$)

of the front evolution at differently spaced time intervals: (a) just after the first breakup (first rows, $t = 500, 505, 510\,\text{ms}$, second row, $t = 520, 530, 540\,\text{ms}$) due to a head-to-tail collision and generating two new spiral tips, one drifting outside the domain and the other, near the center of the slab, generating a new scroll wave; (b) a subsequent breakup (third row, $t = 705, 715, 725\,\text{ms}$) generating additional scroll waves and spiral tips; (c) a later time with many broken fronts (last row, $t = 1\,250, 1\,275, 1\,300\,\text{ms}$) displaying a spatio-temporal chaotic configuration of multiple wave reentry. Figure 9.67 shows the approximated scroll filaments at an early time after reentry initiation ($t = 265\,\text{ms}$, left panel) when only one filament
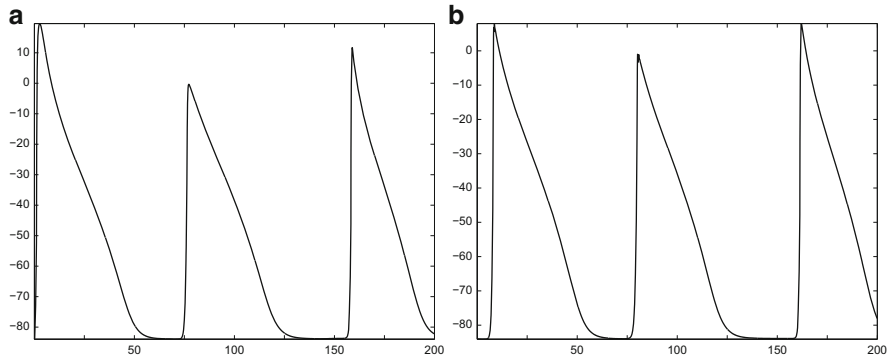
Fig. 9.65 Transmembrane potential at a given point as a function of time for the two tests of Fig. 9.63 ((**a**), Bidomain model) and Fig. 9.64 ((**b**), Monodomain model).

is present and almost at the end of our simulation ($t = 1\,207\,\text{ms}$) when many filaments have appeared (for clarity, the slab height has been magnified). Figure 9.68 compares the time course of the transmembrane potential v of the Monodomain–LR1 model for the stable scroll wave of Fig. 9.64 (left) and for the unstable scroll wave with breakups of Fig. 9.66 (right).

9.7.3 Scroll Waves in Ellipsoidal Geometry

We now extend our Monodomain–LR1 simulations to the more realistic geometry for half a ventricle modeled by a truncated half ellipsoid (with parameters described at the beginning of this section), discretized with $500 \times 500 \times 80$ isoparametric finite elements. The original LR1 model is modified as described before in order to shorten the APD ($G_{Na} = 16$, $G_K = 0.432$, $G_{si} = 0$); in addition, we set $G_{K1} = 0.6047$ and scale the time constants τ_d and τ_f by a factor 10. In order to see more clearly the effect of the curved geometry, we considered in this case parallel fibers (i.e. no fiber rotation). Reentry is initiated with a broken wave procedure, where at time $t = 0$ we set $v = 10\,\text{mV}$ on a vertical intramural section running from epi to endocardium and from the bottom to about $3/4$ of the ventricle height (see the first panel of Fig. 9.69); moreover, on another vertical section on the right side of the previous one, we set at $t = 0$ the gating variables w to their steady state corresponding to the fixed value $v = -10\,\text{mV}$, which is in the refractory phase of the action potential. In this way, an excitation front starts from the vertical section where $v = 10\,\text{mV}$, but on the right side the front is blocked by the other section where the gating variables are inhibiting propagation because they are in their refractory phase. Therefore, the front curls around the upper end of the sections and originates a scroll wave. Unexpectedly, the front also curls around the bottom end of the sections, possibly because of the high curvature of the domain geometry there, resulting in
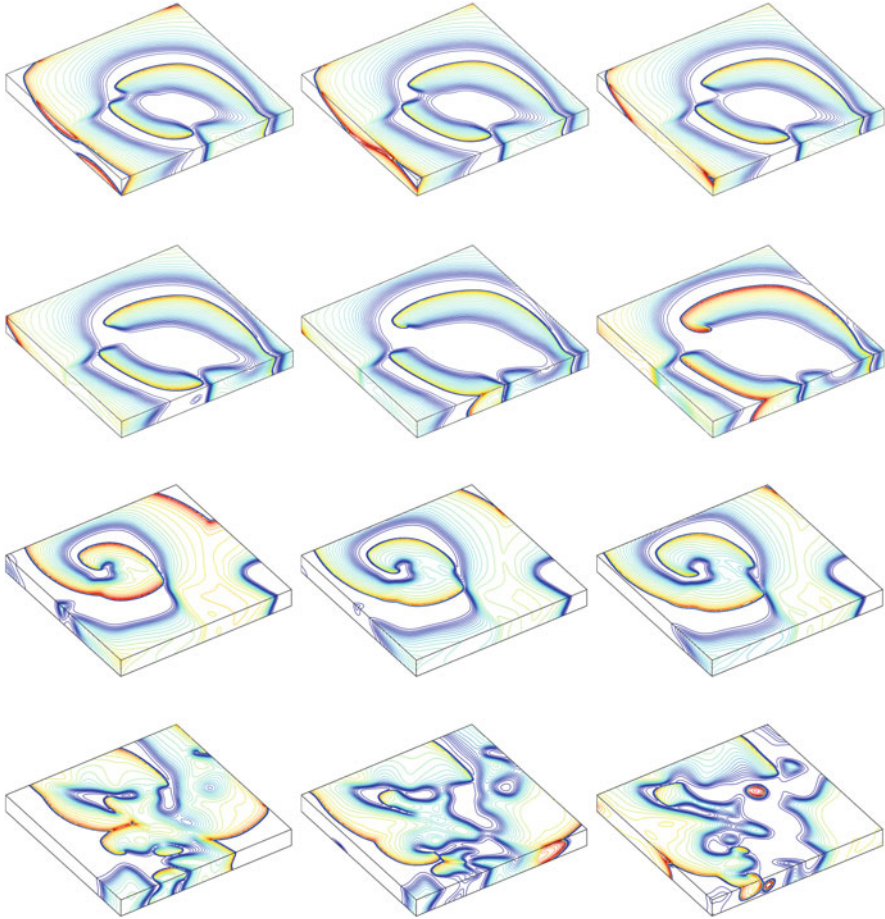
Fig. 9.66 Scroll wave breakup with Monodomain–LR1 model, $G_{si} = 0.056$, domain: $6 \times 6 \times 0.6\,\mathrm{cm}^3$. *First row*: t = 500, 505, 510; *second row*: t = 520, 530, 540; *third row*: t = 705, 715, 725; *fourth row*: t = 1 250, 1 275, 1 300 ms. The colormap ranges from *blue* (resting values around $-84\,\mathrm{mV}$) to *red* (excitation front around $10\,\mathrm{mV}$)

a second counterrotating scroll wave. The evolution of these two scroll waves is displayed in Fig. 9.69, where after an initial adjustment, the two scroll waves seem to reach a stable counterrotating configuration (last panel, $t = 500\,\mathrm{ms}$), also known as *figure-8* or *double loop* reentry, see e.g. Wit and Janse [564].
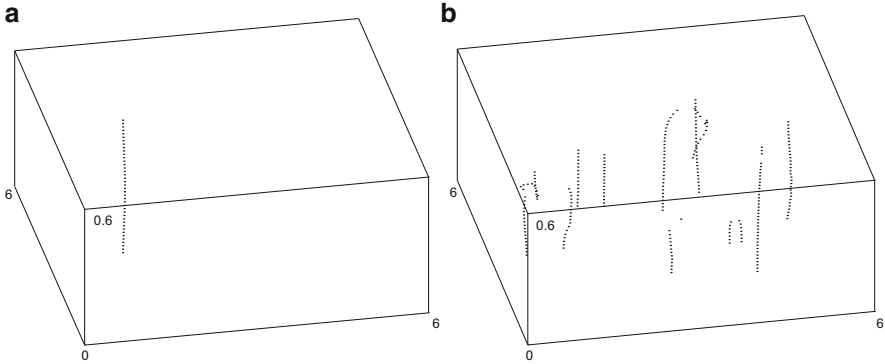
Fig. 9.67 Scroll wave filaments for the breakup test of Fig. 9.66 near reentry initiation ((**a**), t = 265 ms) and during breakup regime ((**b**), t = 1 297 ms). Monodomain–LR1 model with G_{si} = 0.056. Domain: $6 \times 6 \times 0.6 \, \text{cm}^3$ (height of the slab has been magnified)
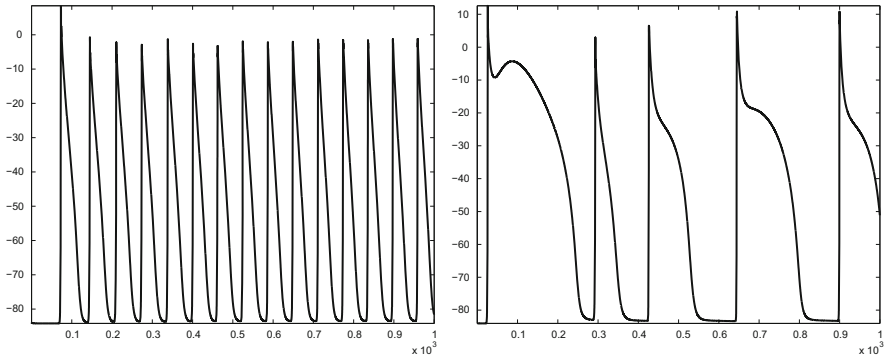
Fig. 9.68 Comparison of the transmembrane potential v at a point as a function of time ($0 \leq t \leq$ 1 000 ms) for the Monodomain–LR1 model. *Left*: stable scroll wave on a domain $2 \times 2 \times 0.5 \, \text{cm}^3$. *Right*: scroll wave breakup on a domain $6 \times 6 \times 0.6 \, \text{cm}^3$
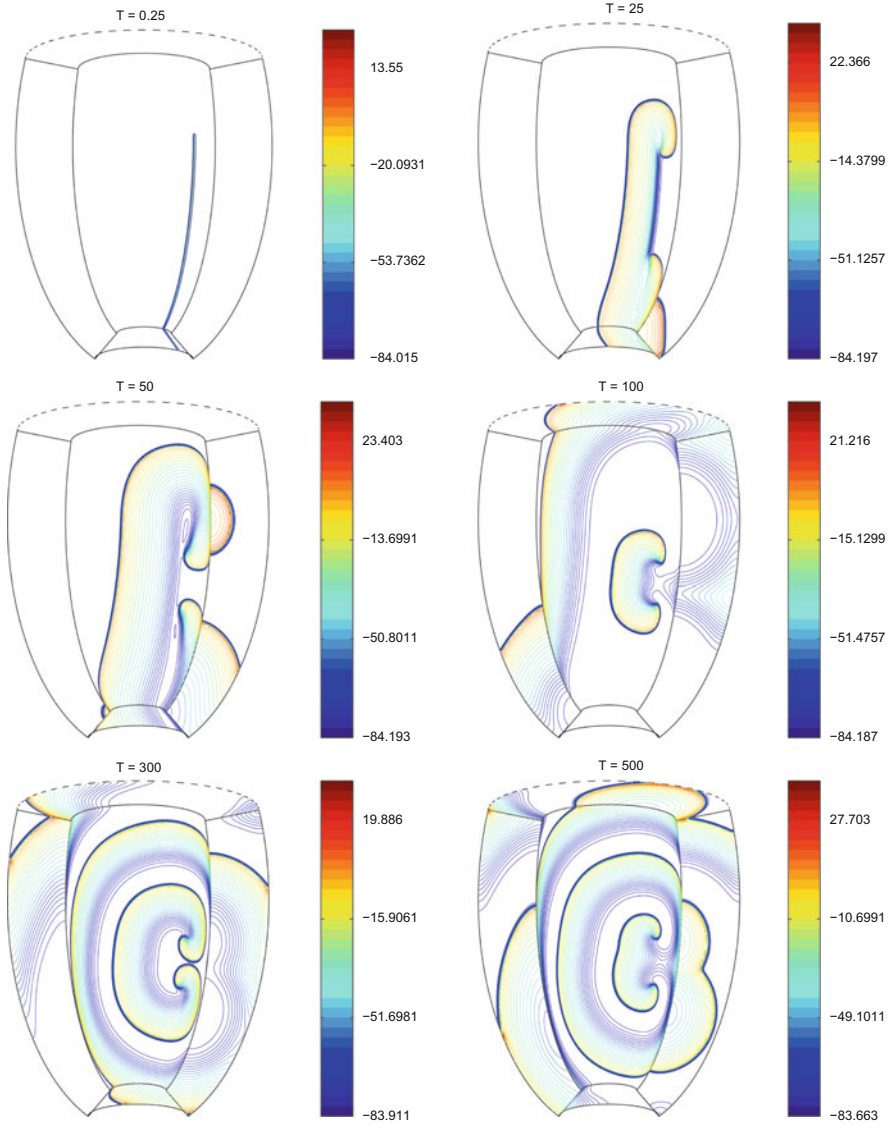
Fig. 9.69 Counterrotating double scroll wave with the Monodomain–LR1 model on half ventricle (500 × 500 × 80 elements). Distribution of v on the endocardium and intramural sections at times t = 0.25, 25, 50, 100, 300, 500 ms. Viewpoint is inside the ventricle

Appendix A
Cardiac Simulation Projects, Software, Libraries

We collect in this Appendix some of the available cardiac simulation projects, software, and libraries that we encountered while writing this book. This is only a partial list, due to both our involuntary omissions and to the vast and rapidly changing field we tried to survey. We apologize for the fact that some links, sites and references provided might change with time and become outdated.

A.1   IUPS Physiome Project

The Physiome Project (http://www.physiome.org.nz/) is a worldwide public domain effort to provide a computational framework for understanding human and other eukaryotic physiology. It aims to develop integrative models at all levels of biological organization, from genes to the whole organism via gene regulatory networks, protein pathways, integrative cell function, and tissue and whole organ structure/function relations. Current projects include the development of:

- Ontologies to organize biological knowledge and access to databases;
- Markup languages to encode models of biological structure and function in a standard format for sharing between different application programs and for re-use as components of more comprehensive models;
- Databases of structure at the cell, tissue and organ levels;
- Software to render computational models of cell function such as ion channel electrophysiology, cell signalling and metabolic pathways, transport, motility, the cell cycle, etc. in 2 and 3D graphical form;
- Software for displaying and interacting with the organ models which will allow the user to move across all spatial scales.

Under the wider umbrella program of the Physiome Project, there is also *The Wellcome Trust Heart Physiome Project* (http://www.physiome.ox.ac.uk/), a 5-year

international collaborative effort between the universities of Auckland and Oxford to develop a multi-scale modelling framework for the heart that can be used for addressing a wide range of scientific and clinical questions.

A.2   Virtual Physiological Human (VPH)

The VPH Initiative (VPH-I), http://www.vph-noe.eu/, was a project funded by the European Framework 7 (FP7) in 2008, aimed to support and foster European research in biomedical modeling and simulation of the human body. It has lead to the creation of the VPH Network of Excellence (VPH NoE), three integrated projects (IPs), nine specific targeted research projects (STREPs) and two cooperative actions (CAs). The VPH Network of Excellence (VPH NoE) was designed to foster, harmonise and integrate pan-European research in the field of (i) patient-specific computer models for personalised and predictive healthcare and (ii) ICT-based tools for modeling and simulation of human physiology and disease-related processes.

In 2011, the Virtual Physiological Human Institute for Integrative Biomedical Research, in short VPH Institute (http://www.vph-institute.org/what-is-vph-institute.html) was funded and started operating. The VPH Institute is an international non-profit organisation, whose mission is to ensure that the Virtual Physiological Human is fully realised, universally adopted, and effectively used both in research and clinic. VPH activities also include support for integrative research (in particular development of the VPH ToolKit http://toolkit.vph-noe.eu/), training and dissemination activities, networking activities (in particular the VPH Conferences); see also the review papers by Hunter et al. [247, 248].

A.3   NSR Physiome

NSR, the National Simulation Resource (http://www.physiome.org/) at the University of Washington, Department of Bioengineering, provides the following tools in support of the Physiome Project:

- The JSim Modeling System and Related Tools (http://www.physiome.org/jsim/). This is a Java-based simulation system for building quantitative numeric models and analyzing them with respect to experimental reference data. With primary focus in physiology and biomedicine, JSim computational engine may intermix ODEs, PDEs, implicit equations, integrals, summations, discrete events and procedural code.
- The NSR Physiome Model Repository (http://www.physiome.org/Models/), with Tutorials, Standards and a Consolidated Model Database.
- The Virtual Physiological Rat Project (http://virtualrat.org/).
- The Systems Biology Workbench (SBW) (http://sbw.sourceforge.net/).

A.4   Other Simulation Software and Modeling Environments

- Berkeley Madonna (www.berkeleymadonna.com/), developed at the University of California, Berkeley, CA, USA.
- Biomed Town (www.biomedtown.org) is an on-line community open and free to anyone has a professional or educational interest in biomedical research and practice. Started in 2006 as support of the coordination action STEP, it slowly became the de facto home for various biomedical research initiatives, in particular those related to the so-called integrative research, an umbrella concept that includes physiome, system biology, and multiscale modeling. etc.
- BIONT: Modeling Program for the Complex Biochemical Systems (members.tripod.com/mitoart/permtran/biont.htm).
- BioSpice – Arkin Lab (biospice.lbl.gov/), developed at the Lawrence Berkeley National Laboratory, University of California, Berkeley, USA.
- BISEN: The Biochemical Simulation Environment (june.phys.mcw.edu/BioWiki/index.php/BISEN), developed at the BioTech Center, Medical College of Wisconsin, Milwaukee, WI, USA.
- Chaste: Cancer, Heart and Soft Tissue Environment (www.cs.ox.ac.uk/chaste/) (see also [331]), is a general purpose simulation package aimed at multi-scale, computationally demanding problems arising in biology and physiology. Current functionality includes tissue and cell level electrophysiology, discrete tissue modeling, and soft tissue modeling. The package is being developed by a team mainly based in the Computational Biology Group at the Department of Computer Science, University of Oxford, and development draws on expertise from software engineering, high performance computing, mathematical modeling and scientific computing.
- CMISS (www.cmiss.org/), developed at the University of Auckland, Auckland, NZ.
- Continuity 6 (cmrg.ucsd.edu/Continuity), developed at the University of California, San Diego, CA, USA.
- E-Cell System (www.e-cell.org/software/), developed at the Keio University, Tokyo, Japan.
- GENESIS: GEneral NEural SImulation System (genesis-sim.org/), is a general purpose simulation platform that was developed to support the simulation of neural systems ranging from subcellular components and biochemical reactions to complex models of single neurons, simulations of large networks, and systems-level models.
- Gepasi: computer simulation of biochemistry (www.gepasi.org/).
- LifeV (http://www.lifev.org/) is a finite element (FE) library providing implementations of state of the art mathematical and numerical methods for biomedical research and production simulations, such as fluid structure interaction and mass transport. LifeV is the joint collaboration between EPFL (CMCS), Politecnico di Milano (MOX), INRIA (REO, ESTIME) and Emory University.

- SCIRun: Problem solving environment for modeling, simulation and visualization of scientific problems (www.sci.utah.edu/cibc/software/index.html), developed at the NCRR Center for Integrative Biomedical Computing, University of Utah, USA.
- SimTK simulation and modeling resources (simtk.org/xml/index.xml) is a software framework initiated and developed by Simbios, the National NIH Center for Biomedical Computing focusing on Physics-based Simulation of Biological Structures.
- Simbiome simulation resources (simbiome.org/): Resources for physics-based simulation of biomedical structures.
- The Virtual Heart (thevirtualheart.org/), with many interactive java applets and movies, mantained and developed by Flavio Fenton and Elizabeth Cherry.
- VHM: Penn Virtual Heart Model (www.seas.upenn.edu/~zhihaoj/VHM.html).
- Virtual Cell Modeling and Analysis Software (vcell.org/index.html), developed by the National Resource for Cell Analysis and Modeling (NRCAM) University of Connecticut Health Center.
- XPPAUT (www.math.pitt.edu/~bard/xpp/xpp.html): a software tool for simulating, animating, and analyzing dynamical systems based on differential equations, as well as difference, delay, functional, and stochastic equations.

A.5   Some Related Monographs

[47] Bers, D.M.: Excitation-Contraction Coupling and Cardiac Contractile Force, 2nd edn. Kluwer, Dordrecht (2001)

[56] Beuter, A., Glass, L., Mackey, M.C., Titcombe, M.S.: Nonlinear Dynamics in Physiology and Medicine. Springer, New York (2003)

[63] Britton, N.F.: Reaction – Diffusion Equations and Their Applications to Biology. Academic, London (1986)

[71] Cabo, C., Rosenbaum, D.: Quantitative Cardiac Electrophysiology. Marcel Dekker, New York (2002)

[78] Carmeliet, E., Vereecke, J.: Cardiac Cellular Electrophysiology. Kluwer, Dordrecht (2002)

[150] Doi, S., Inoue, J., Pan, Z., Tsumoto, K.: Computational Electrophysiology. Springer, Tokyo (2010)

[158] Efimov, I.E., Kroll, M.W., Tcho, P.J. (eds.): Cardiac Bioelectric Therapy. Springer, New York (2009)

[168] Fall, C.P., Marland, E.S., Wagner, J.M., Tyson, J.J.: Computational Cell Biology, 3rd edn. Springer, New York (2005)

[215] Gulrajani, R.M.: Bioelectricity and Biomagnetism. Wiley, New York (1998)

[250] Jack, J.J.B., Noble, D., Tsien, R.W.: Electric Current Flow in Excitable Cells. Oxford University Press, Oxford (1975)

[261] Johnston, P.: Computational Inverse Problems in Electrocardiography. WIT, Southampton (2001)

[273] Keener, J.P., Sneyd, J.: Mathematical Physiology, 2nd edn. Springer, New York (2008)

[274] Kerckhoffs, R.C.P. (ed.): Patient-Specific Modeling of the Cardiovascular System: Technology-Driven Personalized Medicine. Springer, New York (2010)

[283] Kogan, B.Y.: Introduction to Computational Cardiology. Springer, New York (2010)

[284] Kohl, P., Sachs, F., Franz, M.R.: Cardiac Mechano-Electric Coupling and Arrhythmias. Oxford University Press, Oxford (2011)

[312] Macfarlane, P.W., van Oosterom, A., Janse, M., Kligfield, P., Camm, J., Pahlm, O. (eds.): Basic Electrocardiology. Cardiac Electrophysiology, ECG Systems and Mathematical Modeling. Springer, New York (2012)

[317] Malmivuo, J., Plonsey, R.: Bioelectromagnetism. Oxford University Press, Oxford (1995)

[369] Panfilov, A.V., Holden, A.V.: Computational Biology of the Heart. Wiley, New York (1997)

[383] Peskin, C.S.: Mathematical Aspects of Heart Physiology. Lecture Notes of the Courant Institute of Mathematical Sciences, New York University, New York (1975)

[393] Plonsey, R., Barr, R.C.: Bioelectricity: A Quantitative Approach. Springer, New York (2007)

[406] Pullan, A.J., Buist, M.L., Cheng, L.K.: Mathematically Modelling the Electrical Activity of the Heart. World Scientific, Singapore (2005)

[446] Sachse, F.B.: Computational Cardiology. Modeling of Anatomy, Electrophysiology, and Mechanics. LNCS, vol. 2966. Springer, Berlin (2004)

[481] Sigg, D.C., Iaizzo, P.A., Xiao, Y.-F., He, B.: Cardiac Electrophysiology Methods and Models. Springer, New York (2010)

[500] Sundnes, J., Lines, G.T., Cai, X., Nielsen, B.F., Mardal, K.-A., Tveito, A.: Computing the Electrical Activity of the Heart. Springer, Berlin (2006)

[562] Winfree, A.T.: The Geometry of Biological Time, 2nd edn. Springer, New York (2001)

[586] Zipes, D., Jalife, J.: Cardiac Electrophysiology, 2nd edn. W. B. Saunders, Philadelphia (1995)

[587] Zipes, D., Jalife, J.: Cardiac Electrophysiology, 3rd edn. W. B. Saunders, Philadelphia (2000)

[588] Zipes, D., Jalife, J.: Cardiac Electrophysiology: From Cell to Bedside, 4th edn. W. B. Saunders, Philadelphia (2004)

[589] Zipes, D., Jalife, J.: Cardiac Electrophysiology, 5th edn. W. B. Saunders, Philadelphia (2009)

[590] Zipes, D., Jalife, J.: Cardiac Electrophysiology: From Cell to Bedside, 6th edn. W. B. Saunders, Philadelphia (2013)

A.6   Physical Units and Constants

Table A.1 Physical quantities and related unit measures

Quantity	Unit measure	SI unit symbol	Equivalent unit measure
Length	Meter	m	
Mass	Kilogram	kg	
Time	Second	s	
Electric current	Ampere	A	
Temperature	Kelvin	K	
Amount of substance	Mole	mol	
Frequency	Hertz	Hz	s^{-1}
Force	Newton	N	$kg\,m\,s^{-2}$
Pressure	Pascal	Pa	$N\,m^{-2}$
Electric charge	Coulomb	C	$A\,s$
Energy	Joule	J	$N\,m$
Electric potential	Volt	V	$J\,C^{-1}$
Electric resistance	Ohm	Ω	$V\,A^{-1}$
Electric conductance	Siemens	S	Ω^{-1}
Electric capacitance	Farad	F	$C\,V^{-1}$
Electric resistivity			$\Omega\,m$
Electric conductivity			$(\Omega\,m)^{-1}$
Electric current density			$A\,m^{-2}$
Electric charge density			$C\,m^{-3}$
Concentration of substance	Molar	M	$10^3\,mol\,m^{-3}$

Table A.2 Physical constants

Name	Symbol	Value	Dimension
Avogadro's number	N_A	$6.022 \cdot 10^{23}$	mol^{-1}
Faraday's constant	F	$9.64853 \cdot 10^4$	$C\,mol^{-1}$
Gas constant	R	8.31446	$J\,K^{-1}\,mol^{-1}$
Boltzmann's constant	k_B	$1.3806488 \cdot 10^{-23}$	$J\,K^{-1}$
Elementary charge	e	$1.602176 \cdot 10^{-19}$	C
Permittivity in vacuum	ϵ_0	$8.8542 \cdot 10^{-12}$	$A\,s\,V^{-1}\,m^{-1}$

References

1. Aliev, R.R., Panfilov, A.V.: A simple two-variable model of cardiac excitation. Chaos Solitons Fract. **7**, 293–301 (1996)
2. Alistair, Y., Frangi, A.: Computational cardiac atlases: from patient to population and back. Exp. Physiol. **94**(5), 578–596 (2009)
3. Amato, S., Bellettini, G., Paolini, M.: The nonlinear multidomain model: a new formal asymptotic analysis. In: Chambolle, A., Novaga, M., Valdinoci, E. (eds.) Proceedings of Geometric Partial Differential Equations, pp. 33–74. Edizioni della Normale, Pisa (2013)
4. Ambrosio, L., Colli Franzone, P., Savaré, G.: On the asymptotic behaviour of anisotropic energies arising in the cardiac bidomain model. Interfaces Free Bound. **2**(3), 213–266 (2000)
5. Ambrosio, L., Fusco, N., Pallara, D.: Functions of Bounded Variation and Free Discontinuity Problems. Oxford University Press, Oxford (2000)
6. Ambrosio, L., Gigli, N., Savaré, G.: Gradient flows in metric spaces and in the space of probability measures. Lectures in Mathematicsi, ETH Zuerich, 2nd edn. Birkhäuser, Basel (2008)
7. Antzelevitch, C., Fish, J.: Electrical heterogeneity within the ventricular wall. Basic Res. Cardiol. **96**, 517–527 (2001)
8. Antzelevitch, C., Sicouri, S., Lukas, A., Nesterenko, V.V., Lu, D.-W., Di Diego, J.M.: Regional differences in the electrophysiology of ventricular cells: physiological and clinical implications. In: Zipes, D., Jalife, J. (eds.) Cardiac Electrophysiology, chap. 23, pp. 228–245. W. B. Sauders, Philadelphia (1995)
9. Anyukhovsky, E.P., Sosunov, E.A., Rosen, M.R.: Regional differences in electrophysiological properties of epicardium, midmyocardium and endocardium. Circulation **94**, 1981–1988 (1996)
10. Anyukhovsky, E.P., Sosunov, E.A., Gainullin, R.Z., Rosen, M.R.: The controversial M cell. J. Cardiovasc. Electrophysiol. **10**, 244–260 (1999)
11. Arevalo, H., Rodriguez, B., Trayanova, N.A.: Arrhythmogenesis in the heart: multiscale modeling of the effects of defibrillation shocks and the role of electrophysiological heterogeneity. Chaos **17**(1), 015103 (2007)
12. Arisi, G., Macchi, E., Corradi, C., Lux, R.L., Taccardi, B.: Epicardial excitation during ventricular pacing. Relative independence of breakthrough sites from excitation sequence in canine right ventricle. Circ. Res. **71**, 840–849 (1992)
13. Arthurs, C.J., Bishop, M.J., Kay, D.: Efficient simulation of cardiac electrical propagation using high order finite elements. J. Comput. Phys. **231**(10), 3946–3962 (2012)
14. Arthurs, C.J., Bishop, M.J., Kay, D.: Efficient simulation of cardiac electrical propagation using high order finite elements. II: adaptive p-version. J. Comput. Phys. **253**, 443–470 (2013)

15. Asanov, G.S.: Finsler Geometry, Relativity and Gauge Theories. D. Reidel, Dordrecht (1985)
16. Ashihara, T., Trayanova, N.A.: Cell and tissue responses to electric shocks. Europace **7**(s2), S155–S165 (2005)
17. Aslanidi, O.V., Colman, M.A., Stott, J., Dobrzynski, H., Boyett, M.R., Holden, A.V., Zhang, H.: 3D virtual human atria: a computational platform for studying clinical atrial fibrillation. Prog. Biophys. Mol. Biol. **107**, 156–168 (2011)
18. Attin, M., Clusin, W.T.: Basic concepts of optical mapping techniques in cardiac electrophysiology. Biol. Res. Nurs. **11**(2), 195–207 (2009)
19. Austin, T.M., Trew, M.L., Pullan, A.J.: Solving the cardiac Bidomain equations for discontinuous conductivities. IEEE Trans. Biomed. Eng. **53**(7), 1265–1272 (2006)
20. Axelsson, O.: Iterative Solution Methods. Cambridge University Press, Cambridge (1994)
21. Ayache, N., Delingette, H., Sermesant, M. (eds.): Proceedings of the 5th International Conference on Functional Imaging and Modeling of the Heart, FIMH'09, Nice, 3–5 June 2009. LNCS, vol. 5528. Springer, Berlin (2009)
22. Azzouzi, A., Coudiere, Y., Turpault, R., Zemzemi, N.: A mathematical model of the Purkinje-muscle junctions. Math. Biosci. Eng. **8**(4), 915–930 (2011)
23. Backhvalov, N., Panasenko, G.: Homogenization: Averaging Processes in Periodic Media. Kluwer Academic, Dordrecht (1990)
24. Balay, S., Buschelman, K., Gropp, W.D., Kaushik, D., Knepley, M., Curfman McInnes, L., Smith, B.F., Zhang, H.: PETSc home page. http://www.mcs.anl.gov/petsc (2001)
25. Balay, S., Buschelman, K., Gropp, W.D., Kaushik, D., Knepley, M., Curfman McInnes, L., Smith, B.F., Zhang, H.: PETSc users manual. Tech. Rep. ANL-95/11 – Revision 2.1.5, Argonne National Laboratory (2002)
26. Barcilon, V., Chen, D.-P., Eisenberg, R.S., Jerome, J.W.: Qualitative properties of steady-state Poisson-Nernst-Planck systems: perturbation and simulation study. SIAM J. Appl. Math. **57**(3), 631–648 (1997)
27. Barles, G.: Fully non-linear Neumann type boundary conditions for second-order elliptic and parabolic equations. J. Differ. Equ. **106**, 90–106 (1993)
28. Barr, R.C., Plonsey, R.: Propagation of excitation in idealized two-dimensional tissue. Biophys. J. **45**, 1191–1202 (1984)
29. Barr, R.C., Spach, M.S.: Inverse calculation of QRS-T epicardial potentials from body surface potential distributions for normal and ectopic beats in the intact dog. Circ. Res. **42**, 661–675 (1978)
30. Baruffi, S., Spaggiari, S., Stilli, D., Musso, E., Taccardi, B.: The importance of fiber orientation in determining the features of cardiac electric field. In: Antaloczy, Z. (ed.) Modern Electrocardiology, pp. 89–92. Excerpta Medica, Amsterdam (1978)
31. Baruscotti, M., Barbuti, A., Bucchi, A.: The cardiac pacemaker current. J. Mol. Cell. Cardiol. **48**, 55–64 (2008)
32. Bassetti, F.: Variable time-step discretization of degenerate evolution equations in Banach space. Numer. Funct. Anal. Optim. **24**(3–4), 391–426 (2003)
33. Beeler, G.W., Reuter, H.T.: Reconstruction of the action potential of ventricular myocardial fibers. J. Physiol. **268**, 177–210 (1977)
34. Beg, M.F., Helm, P.A., McVeigh, E., Miller, M.I., Winslow, R.L.: Computational cardiac anatomy using MRI. Magn. Reson. Med. **52**,1167–1174 (2004)
35. Belhamadia, Y.: A time-dependent adaptive remeshing for electrical waves of the heart. IEEE Trans. Biomed. Eng. **55**(2), 443–452 (2008)
36. Belhamadia, Y., Fortin, A., Bourgault, Y.: Towards accurate numerical method for monodomain models using a realistic heart geometry. Math. Biosci. **220**(2), 89–101 (2009)
37. Bellettini, G., Paolini, M.: Anisotropic motion by mean curvature in the context of Finsler geometry. Hokkaido Math. J. **25**, 537–566 (1996)
38. Bellettini, G., Paolini, M., Venturini, S.: Some results on surface measures in calculus of variations. Ann. Math. Pura Appl. **170**, 329–359 (1996)
39. Bellettini, G., Colli Franzone, P., Paolini, M.: Convergence of front propagation for anisotropic bistable reaction-diffusion equations. Asymptot. Anal. **15**, 325–358 (1997)

40. Bellettini, G., Paolini, M., Pasquarelli, F.: Nonconvex mean curvature flow as a formal singular limit of the nonlinear bidomain model. Adv. Differ. Equ. **18**(9–10), 895–934 (2013)
41. Beltrami, A.P., et al.: Adult cardiac stem cells are multipotent and support myocardial regeneration. Cell **114**, 763–776 (2003)
42. Bendahmane, M., Karlsen, K.H.: Analysis of a class of degenerate reaction-diffusion systems and the bidomain model of cardiac tissue. Netw. Heterog. Media **1**, 185–218 (2006)
43. Bendahmane, M., Karlsen, K.H.: Convergence of a finite volume scheme for the bidomain model of cardiac tissue. Appl. Numer. Math. **59**(9), 2266–2284 (2009)
44. Bensoussan, A., Lions, J.-L., Papanicolaou, G.: Asymptotic Analysis for Periodic Structures. North-Holland, Amsterdam (1978)
45. Berbari, E.J., Lander, P., Scherlag, B.J., Lazzara, R., Geselowitz, D.B.: Ambiguities of epicardial mapping. J. Electrocardiol. **24**(Suppl), 16–20 (1992)
46. Bergmann, O., et al.: Evidence for cardiomyocyte renewal in humans. Science **324**, 98–102 (2009)
47. Bers, D.M.: Excitation-Contraction Coupling and Cardiac Contractile Force, 2nd edn. Kluwer, Dordrecht (2001)
48. Bertran, G., Biagetti, M.O., Valverde, E., Arini, P.D., Quinteiro, R.A., Lack of effect of conduction direction on action potential durations in anisotropic ventricular strips of pig heart. J. Cardiovasc. Electrophysiol. **13**(4), 380–387 (2002)
49. Biktashev, V.N., Holden, A.V., Mironov, S.F., Pertsov, A.M., Zaitsev, A.V.: Three-dimensional organisation of re-entrant propagation during experimental ventricular fibrillation. Chaos Solitons Fract. **13**(8), 1713–1733 (2002)
50. Bishop, M.J., Gavahan, D.J., Trayanova, N.A., Rodriguez, B.: Photon scattering effects in optical mapping of propagation and arrhythmogenesis in the heart. J. Electrocardiol. **40**, S75–S80 (2007)
51. Bishop, M.J., Boyle, P.M., Plank, G., Welsh, D.G., Vigmond, E.J.: Modeling the role of the coronary vasculature during external field stimulation. IEEE Trans. Biomed. Eng. **57**(10), 2335–2345 (2010)
52. Bishop, M.J., Plank, G., Burton, R., Schneider, J., Gavaghan, D., Grau, V., Kohl, P.: Development of an anatomically-detailed MRI-derived rabbit ventricular model and assessment of its impact on simulation of electrophysiological function. Am. J. Physiol. Heart Circ. Physiol. **298**, H699–H718 (2010)
53. Bondarenko, V.E., Szigeti, G.P., Bett, G.C., Kim, S.: A computer model for the action potential of mouse ventricular myocytes. Am. J. Physiol. Heart Circ. Physiol. **278**, H1378–H1403 (2004)
54. Bordas, R., Carpentieri, B., Fotia, G., Maggio, F., Nobes, R., Pitt-Francis, J., Southern, J.: Simulation of cardiac electrophysiology on next-generation high-performance computers. Philos. Trans. R. Soc. A **367**(1895), 1951–1969 (2009)
55. Bordas, R.M., Gillow, K., Gavaghan, D., Rodriguez, B., Kay, D.: A Bidomain model of the ventricular specialized conduction system of the heart. SIAM J. Appl. Math. **72**(5), 1618–1643 (2012)
56. Beuter, A., Glass, L., Mackey, M.C., Titcombe, M.S.: Nonlinear Dynamics in Physiology and Medicine. Springer, New York (2003)
57. Bouchard, S., Jacquemet, V., Vinet, A.: Automaticity in acute ischemia: bifurcation analysis of a human ventricular model. Phys. Rev. E **83**, 011911-1-10 (2011)
58. Boulakia, M., Fernandez, M.A., Gerbeau, J.-F., Zemzemi, N.: Towards the Numerical Simulation of Electrocardiograms. In: FIMH07, Salt Lake City, 7–9 June 2007. LNCS, vol. 4466, pp. 240–249. Springer, Berlin (2007)
59. Boulakia, M., Fernandez, M.A., Gerbeau, J.-F., Zemzemi, N.: A coupled system of PDEs and ODEs arising in electrocardiograms modelling. Appl. Math. Res. Exp. **2**, 1–28 (2008). doi:10.1093/amrx/abn002
60. Bourgault, Y., Coudiere, Y., Pierre, C.: Existence and uniqueness of the solution for the bidomain model used in cardiac electrophysiology. Nonlinear Anal. Real World Appl. **10**, 458–482 (2009)

61. Brenner, S.C., Scott, L.R.: The Mathematical Theory of Finite Element Methods. Texts in Applied Mathematics, vol. 15, 2nd edn. Springer, New York (2002)
62. Brezis, H.: Analyse Fonctionnelle, Theory and Applications. Masson, Paris (1983)
63. Britton, N.F.: Reaction – Diffusion Equations and Their Applications to Biology. Academic, London (1986)
64. Brooks, D.H., Ahmad, G.F., MacLeod, R.S., Maratos, G.M.: Inverse electrocardiography by simultaneous imposition of multiple constraints. IEEE Trans. Biomed. Eng. **46**(1), 3–18 (1999)
65. Bueno-Orovio, A., Cherry, E., Fenton, F.: Minimal model for human ventricular action potentials in tissue. J. Theor. Biol. **253**, 544–560 (2008)
66. Buist, M., Sands, G., Hunter, P., Pullan, A.: A deformable finite element derived finite difference method for cardiac activation problems. Ann. Biomed. Eng. **31**, 577–588 (2003)
67. Burgess, M.J., Steinhaus, B.M., Spitzer, K.W., Ershler, P.R.: Nonuniform epicardial activation and repolarization properties of in vivo canine pulmonary conus. Circ. Res. **62**(2), 233–246 (1988)
68. Burnes, J.E., Taccardi, B., Rudy, Y.: Noninvasive imaging modality for cardiac arrhythmias. Circulation **102**, 2152–2158 (2000)
69. Burnes, J.E., Taccardi, B., Ershler, P.R., Rudy, Y.: Noninvasive electrocardiographic imaging of substrate and intramural ventricular tachycardia in infarcted hearts. J. Am. Coll. Cardiol. **38**, 2071–2078 (2001)
70. Burton, F.L., Cobbe, S.M.: Dispersion of ventricular repolarization and refractory period. Cardiovasc. Res. **50**, 10–23 (2001)
71. Cabo, C., Rosenbaum, D.: Quantitative Cardiac Electrophysiology. Marcel Dekker, New York (2002)
72. Cai, X.-C.: Additive Schwarz algorithms for parabolic convection-diffusion equations. Numer. Math. **60**(1), 41–61 (1991)
73. Cai, X.-C.: Multiplicative Schwarz methods for parabolic problems. SIAM J. Sci. Comput. **15**(3), 587–603 (1994)
74. Camara, O., Pop, M., Rhode, K., Sermesant, M., Smith, N., Young, A. (eds.): Proceedings of Statistical Atlases and Computational Models of the Heart, STACOM'10, Beijing, 20 Sept 2010. LNCS, vol. 6364. Springer, Berlin (2010)
75. Camara, O., Konukoglu, E., Pop, M., Rhode, K., Sermesant, M., Young, A. (eds.): Proceedings of Statistical Atlases and Computational Models of the Heart, STACOM'11, Toronto, 22 Sept 2011. LNCS, vol. 7085. Springer, Berlin (2012)
76. Camara, O., Mansi, T., Pop, M., Rhode, K., Sermesant, M., Young, A. (eds.): Proceedings of Statistical Atlases and Computational Models of the Heart, STACOM'12, Nice, 5 Oct 2012. LNCS, vol. 7746. Springer, Berlin (2013)
77. Camelliti, P., Borg, T.K., Kohl, P.: Structural and functional characterization of cardiac fibroblasts. Cardiovasc. Res. **65**, 40–51 (2005)
78. Carmeliet, E., Vereecke, J.: Cardiac Cellular Electrophysiology. Kluwer, Dordrecht (2002)
79. Casten, R.G., Cohen, H., Lagerstrom, P.A.: Perturbation analysis of an approximation to the Hodgkin-Huxley theory. Q. Appl. Math. **32**(4), 365–402 (1975)
80. Cates, A.W., Pollard, A.E.: A model study of intramural dispersion of action potential duration in the canine pulmonary conus. Ann. Biomed. Eng. **26**, 567–576 (1998)
81. Cerbai, E., Barbieri, M., Mugelli, A.: Characterization of the hyperpolarization-activated current, I_f in ventricular myocytes isolated from hypertensive rats. J. Physiol. **481**(3), 585–591 (1994)
82. Cerbai, E., Barbieri, M., Mugelli, A.: Occurrence and properties of the hyperpolarization-activated current I_f in ventricular myocytes from normotensive and hypertensive rats during aging. Circulation **94**, 1674–1681 (1996)
83. Cerqueira, M.D., Weissman, N.J., Dilsizian, V., et al.: Standardized myocardial segmentation and nomenclature for tomographic imaging of the heart – a statement for healthcare professionals from the Cardiac Imaging Committee of the Council on Clinical Cardiology of the American Heart Association. Circulation **105**(4), 539–542 (2002)

84. Chauhan, V.S., Downar, E., Nanthakumar, K., Parker, J.D., Ross, H.J., Chan, W., Picton, P.: Increased ventricular repolarization heterogeneity in patients with ventricular arrhythmia vulnerability and cardiomyopathy: a human in vivo study. Am. J. Physiol. Heart Circ. Physiol. **290**(1), H79–H86 (2006)

85. Chen, X.-Y.: Dynamics of interfaces in reaction diffusion systems. Hiroshima Math. J. **21**, 47–83 (1991)

86. Chen, X.-Y.: Generation and propagation of interfaces in reaction-diffusion systems. Trans. Am. Math. Soc. **334**(2), 877–913 (1992)

87. Chen, P.-S., Moser, K.M., Dembitsky, W.P., Auger, W.R., Daily, P.O., Calisi, C.M., Jamieson, S.W., Feld, G.K.: Epicardial activation and repolarization patterns in patients with right ventricular hypertrophy. Circulation **83**, 104–118 (1991)

88. Cheng, D.K., Tung, L., Sobie, E.A.: Nonuniform responses of transmembrane potential during electric field stimulation of single cardiac cells. Am. J. Physiol. Heart Circ. Physiol. **277**, H351–H362 (1999)

89. Cheng, L.K., Bodley, J.M., Pullan, A.: Comparison of potential- and activation-based formulations for the inverse problem of electrocardiology. IEEE Trans. Biomed. Eng. **50**(1), 11–22 (2003)

90. Cherry, E.M., Greenside, H.S., Henriquez, C.S.: A space-time adaptive method for simulating complex cardiac dynamics. Phys. Rev. Lett. **84**(6), 1343–1346 (2000)

91. Cherry, E.M., Greenside, H.S., Henriquez, C.S.: Efficient simulation of three-dimensional anisotropic cardiac tissue using an adaptive mesh refinement method. Chaos **13**, 853–865 (2003)

92. Ciarlet, P.G.: The finite element method for elliptic problems. Classics in Applied Mathematics, vol. 40. SIAM, Philadelphia (2002)

93. Clancy, C.E., Rudy, Y.: Linking a genetic defect to its cellular phenotype in a cardiac arrhythmia. Nature **400** 566–569 (1999)

94. Clancy, C.E., Rudy, Y.: Na^+ channel mutation that causes both Brugada and Long-QT syndrome phenotypes: a simulation study of mechanism. Circulation **105**, 1208–1213 (2002)

95. Clayton, R.H., Holden, A.V.: Propagation of normal beats and re-entry in a computational model of ventricular cardiac tissue with regional differences in action potential shape and duration. Prog. Biophys. Mol. Biol. **85**(2–3), 473–499 (2004)

96. Clayton, R.H., Holden, A.V.: Dispersion of cardiac action potential duration and the initiation of re-entry: a computational study. Biomed. Eng. **4**, 11 (2005). Online: http://www.biomedical-engineering-oline.com/content/4/1/11

97. Clayton, R.H., Panfilov, A.V.: A guide to modelling cardiac electrical activity in anatomically detailed ventricles. Prog. Biophys. Mol. Biol. **96**, 19–43 (2008)

98. Clayton, R.H., Zhuchkova, E.A., Panfilov, A.V.: Phase singularities and filaments: simplifying complexity in computational models of ventricular fibrillation. Prog. Biophys. Mol. Biol. **90**, 378–398 (2006)

99. Clements, J.C., Nenonen, J., Li, P.K.J., Horacek, B.M.: Activation dynamics in anisotropic cardiac tissue via decoupling. Ann. Biomed. Eng. **32**(7), 984–990 (2004)

100. Clerc, L.: Directional differences of impulse spread in trabecular muscle from mammalian heart. J. Physiol. **255**, 335–346 (1976)

101. Colli Franzone, P., Guerri, L.: Models of the spreading of excitation in myocardial tissue. CRC Crit. Rev. Biomed. Eng. **20**, 211–253 (1992); Pilkington, T.C., Loftis, B., Palmer, T., Budinger, T.F. (eds.) High-Performance Computing in Biomedical Research, pp. 359–401. CRC, Boca Raton (1993)

102. Colli Franzone, P., Guerri, L.: Spread of excitation in 3-D models of the anisotropic cardiac tissue I: validation of the eikonal approach. Math. Biosci. **113**, 145–209 (1993)

103. Colli Franzone, P., Magenes, E.: On the inverse potential problem of electrocardiology. Calcolo **16**(4), 459–538 (1979)

104. Colli Franzone, P., Pavarino, L.F.: A parallel solver for reaction-diffusion systems in computational electrocardiology. Math. Model Methods Appl. Sci. **14**(6), 883–911 (2004)

105. Colli Franzone, P., Savaré, G.: Degenerate evolution systems modeling the cardiac electric field at micro and macroscopic level. In: Lorenzi, A., Ruf, B. (eds.) Evolution Equations, Semigroups and Functional Analysis, pp. 49–78. Birkhauser, Basel/Boston (2002)

106. Colli Franzone, P., Taccardi, B., Viganotti, C.: An approach to inverse calculation of epicardial potentials from body surface maps. Adv. Cardiol. **21**, 50–54 (1978)

107. Colli Franzone, P., Guerri, L., Taccardi, B., Viganotti, C.: The direct and inverse potential problem in electrocardiology. Numerical aspects of some regularization methods and application to data collected in isolated dog heart experiments. Tech. Rep. No. 222, IAN-CNR (1979)

108. Colli Franzone, P., Guerri, L., Viganotti, C., Macchi, E., Baruffi, S., Spaggiari, S., Taccardi, B.: Potential fields generated by oblique dipole layer modeling excitation wavefronts in the anisotropic myocardium. Comparison with potential fields elicited by paced dog hearts in a volume conductor. Circ. Res. **51**(3), 330–346 (1982)

109. Colli Franzone, P., Guerri, L., Viganotti, C.: Oblique dipole layer potentials applied to electrocardiology. J. Math. Biol. **17**(1), 93–124 (1983)

110. Colli Franzone, P., Guerri, L., Magenes, E.: Oblique dipole layer potential for the direct and inverse problems of electrocardiology. Math. Biosci. **68**, 23–55 (1984)

111. Colli Franzone, P., Guerri, L., Viganotti, C., Taccardi, B.: Finite element approximation of regularized solution of the inverse potential problem of electrocardiography and applications to experimental data. Calcolo **12**(1), 91–186 (1985)

112. Colli Franzone, P., Guerri, L., Rovida, S.: Wavefront propagation in an activation model of the anisotropic cardiac tissue: asymptotic analysis and numerical simulations. J. Math. Biol. **28**, 121–176 (1990)

113. Colli Franzone, P., Guerri, L., Tentoni, S.: Mathematical modeling of the excitation process in myocardial tissue: influence of fiber rotation on wavefront propagation and potential field. Math. Biosci. **101**, 155–235 (1990)

114. Colli Franzone, P., Guerri, L., Taccardi, B.: Spread of excitation in a myocardial volume. Simulation studies in a model of anisotropic ventricular muscle activated by point stimulation. J. Cardiovasc. Electrophysiol. **4**, 144–160 (1993)

115. Colli Franzone, P., Guerri, L., Pennacchio, M., Taccardi, B.: Spread of excitation in 3-D models of the anisotropic cardiac tissue II: effects of fiber architecture and ventricular geometry. Math. Biosci. **147**, 131–171 (1998)

116. Colli Franzone, P., Guerri, L., Pennacchio, M., Taccardi, B.: Spread of excitation in 3-D models of the anisotropic cardiac tissue III: effects of ventricular geometry and fiber structure on the potential distribution. Math. Biosci. **151**, 51–98 (1998)

117. Colli Franzone, P., Guerri, L., Pennacchio, M., Taccardi, B.: Anisotropic mechanisms for multiphasic unipolar electrograms. Simulation studies and experimental recordings. Ann. Biomed. Eng. **28**, 1–17 (2000)

118. Colli Franzone, P., Pennacchio, M., Guerri, L.: Accurate computation of electrograms in the left ventricular wall. Math. Model Methods Appl. Sci. **10**(4), 507–538 (2000)

119. Colli Franzone, P., Guerri, L., Taccardi, B.: On the polyphasic character of simulated and experimental electrograms. Biomed. Tech. **46**(2), 16–19 (2001)

120. Colli Franzone, P., Pavarino, L.F., Taccardi, B.: A parallel solver for anisotropic cardiac models. In: Proceedings of the IEEE Computers in Cardiology, Thessaloniki Chalkidiki, 21–24 Sept 2003. vol. 30, pp. 781–784 (2003)

121. Colli Franzone, P., Guerri, L., Taccardi, B.: Modeling ventricular excitation: axial and orthotropic effects on wavefronts and potentials. Math. Biosci. **188**, 191–205 (2004)

122. Colli Franzone, P., Pavarino, L.F., Taccardi, B.: Monodomain simulations of excitation and recovery in cardiac blocks with intramural heterogeneity. In: Frangi, A.F., et al. (eds.): FIMH05: Functional Imaging and Modeling of the Heart. LNCS, vol. 3504, pp. 267–277. Springer, Berlin (2005)

123. Colli Franzone, P., Pavarino, L.F., Taccardi, B.: Simulating patterns of excitation, repolarization and action potential duration with cardiac Bidomain and Monodomain models. Math. Biosci. **197**, 35–66 (2005)

124. Colli Franzone, P., Deuflhard, P., Erdmann, B., Lang, J., Pavarino, L.F.: Adaptivity in space and time for reaction-diffusion systems in electrocardiology. SIAM J. Sci. Comput. **28**(3), 942–962 (2006)

125. Colli Franzone, P., Pavarino, L.F., Savarè, G.: Computational electrocardiology: mathematical and numerical modeling. In: Quarteroni, A., et al. (eds.) Complex Systems in Biomedicine, pp. 187–241. Springer, New York (2006)

126. Colli Franzone, P., Pavarino, L.F., Taccardi, B.: Effects of transmural electrical heterogeneities and electrotonic interactions on the dispersion of cardiac repolarization and action potential duration: a simulation study. Math. Biosci. **204**(1), 132–165 (2006)

127. Colli Franzone, P., Pavarino, L.F., Scacchi, S., Taccardi, B.: Determining recovery times from transmembrane action potentials and unipolar electrograms in normal heart tissue. In: Sachse, F.B., Seemann, G. (eds.) FIMH'07, Salt Lake City, 7–9 June 2007. LNCS, vol. 4466, pp. 139–149. Springer, Berlin (2007)

128. Colli Franzone, P., Pavarino, L.F., Scacchi, S., Taccardi, B.: Monophasic action potentials generated by bidomain modeling as a tool for detecting cardiac repolarization times. Am. J. Physiol. Heart Circ. Physiol. **293**, H2771–H2785 (2007)

129. Colli Franzone, P., Pavarino, L.F., Scacchi, S.: Dynamical effects of myocardial ischemia in anisotropic cardiac models in three dimensions. Math. Model Methods Appl. Sci. **17**(12), 1965–2008 (2007)

130. Colli Franzone, P., Pavarino, L.F., Scacchi, S., Taccardi, B.: Modeling ventricular repolarization: effects of transmural and apex-to-base heterogeneities in action potential durations. Math. Biosci. **214**, 140–152 (2008)

131. Colli Franzone, P., Pavarino, L.F., Scacchi, S.: Exploring anodal and cathodal make and break cardiac excitation mechanisms in a 3D anisotropic bidomain model. Math. Biosci. **230**(2), 96–114 (2011)

132. Colli Franzone, P., Pavarino, L.F., Scacchi, S.: Cardiac excitation mechanisms, wavefront dynamics and strength – interval curves predicted by 3D orthotropic bidomain simulations. Math. Biosci. **235**(1), 66–84 (2012)

133. Conrath, C.E., Opthof, T.: Ventricular repolarization: an overview of (patho)physiology, sympathetic effects and genetic aspects. Prog. Biophys. Mol. Biol. **92**(3), 269–307 (2006)

134. Corbin II, L.V., Scher, A.M.: The canine heart as an electrocardiographic generator: dependence on cardiac cell orientation. Circ. Res. **41**, 58–67 (1977)

135. Coronel, R., de Bakker, J.M.T., Wilms-Schopman, F.J.G., Opthof, T., Linnenbank, A.C., Belterman, C.N., Janse, M.J.: Monophasic action potentials and activation recovery intervals as measures of ventricular action potential duration: experimental evidence to resolve some controversies. Heart Rhythm **3**(9), 1043–1050 (2006)

136. Cortassa, S., Aon, M., B. O'Rourke, Jacques, R., Tseng, H., Marban, E., et al.: A computational model integrating electrophysiology, contraction, and mitochondrial bioenergetics in the ventricular myocytes. Biophys. J. **91**, 1564–1598 (2006)

137. Costa, K.D., K. May-Newman, Farr, D., O'Dell, W.G., McCulloch, A.D., Omens, J.H.: Three-dimensional residual strain in midanterior canine left ventricle. Am. J. Physiol. Heart Circ. Physiol. **42**, H1968–H1976 (1997)

138. Costa, K.D., Holmes, J.W., McCulloch, A.D.: Modelling cardiac mechanical properties in three dimensions. Philos. Trans. R. Soc. Lond. A **359**(1783), 1233–1250 (2001)

139. Coudiere, Y., Pierre, C.: Stability, convergence of a finite volume method for two systems of reaction-diffusion equations in electro-cardiology. Nonlinear Anal. Real World Appl. **7**(4), 916–935 (2006)

140. Coveney, P., Diaz, V., Hunter, P., Viceconti, M.: Computational Biomedicine. Oxford University Press, Oxford (2014)

141. Cronin, J.: Mathematical Aspects of Hodgkin-Huxley Neural Theory. Cambridge University Press, Cambridge (1987)

142. Cuppen, J.J.M.: Calculating the isochrones of ventricular depolarization. SIAM J. Sci. Stat. Comput. **5**, 105–120 (1984)

143. Cuppen, J.J.M., van Oosterom, A.: Model studies with the inversely calculated isochrones of ventricular depolarization. IEEE Trans. Biomed. Eng. **31**(10), 652–659 (1984)

144. De Ambroggi, L., Musso, E., Taccardi, B.: Body-surface mapping. In: Macfarlane, P.W., Lawrie, T.D.V. (eds.) Comprehensive Electrocardiology, pp. 1015–1049. Pergamon, Oxford (1989)

145. DeBruin, K.A., Krassowska, W.: Electroporation and shock-induced transmembrane potential in a cardiac fiber during defibrillation strength shocks. Ann. Biomed. Eng. **26**, 584–596 (1998)

146. Dekker, E.: Direct current make and break thresholds for pacemaker electrodes on the canine ventricle. Circ. Res. **27**, 811–823 (1970)

147. Deuflhard, P., Erdmann, B., Roitzsch, R., Lines, G.T.: Adaptive finite element simulation of ventricular fibrillation dynamics. Comput. Vis. Sci. **12**(5), 201–205 (2009)

148. di Bernardo, D., Murray, A.: Computer model for study of cardiac repolarization. J. Cardiovasc. Electrophys. **11**(8), 895–899 (2000)

149. Di Francesco, D., Noble, D.: A model of cardiac electrical activity incorporating ionic pumps and concentration changes. Philos. Trans. R. Soc. Lond. B **307**(1133), 353–398 (1985)

150. Doi, S., Inoue, J., Pan, Z., Tsumoto, K.: Computational Electrophysiology. Springer, Tokyo (2010)

151. Dryja, M., Widlund, O.B.: Multilevel additive methods for elliptic finite element problems. In: Hackbusch, W. (ed.) Parallel Algorithms for Partial Differential Equations – Proceedings of the Sixth GAMM-Seminar, Kiel, 19–21 Jan 1990. Notes on Numerical Fluid Mechanics, vol. 31, pp. 58–69. Vieweg, Braunschweig (1991). 3-528-07631-3

152. Dryja, M., Widlund, O.B.: Domain decomposition algorithms with small overlap. SIAM J. Sci. Comput. **15**(3), 604–620 (1994)

153. Dryja, M., Sarkis, M.V., Widlund, O.B.: Multilevel Schwarz methods for elliptic problems with discontinuous coefficients in three dimensions. Numer. Math. **72**(3), 313–348 (1996)

154. Ebihara, L., Johnson, E.A.: Fast sodium current in cardiac muscle: a quantitative description. Biophys. J. **32** 779–790 (1980)

155. Efimov, I.R., Ermentrout, B., Huang, D.T., Salama, G.: Activation and repolarization patterns are governed by different structural characteristics of ventricular myocardium: experimental study with voltage-sensitive dyes and numerical simulations. J. Cardiovasc. Electrophysiol. **7**, 512–530 (1996)

156. Efimov, I.R., Gheng, Y., Van Eagoner, D.R., Mazgalev, T., Tchou, P.J.: Virtual electrode-induced phase singularity: a basic mechanism of defibrillation failure. Circ. Res. **82**, 918–925 (1998)

157. Efimov, I.R., Gray, R.A., Roth, B.J.: Virtual electrodes and deexcitation: new insights into fibrillation induction and defibrillation. J. Cardiovasc Electrophysiol. **11**, 339–353 (2000)

158. Efimov, I.E., Kroll, M.W., Tcho, P.J. (eds.): Cardiac Bioelectric Therapy. Springer, New York (2009)

159. Einstein, A.: Eine neue Bestimmung der Moleküldimensionen. Ann. Phys. **324**, 289–306 (1906)

160. Ejima, J., Martin, D., Engle, C., Sherman, Z., Kunimoto, S., Gettes, L.: Ability of activation recovery intervals to assess action potential duration during acute no-flow ischemia in the in situ porcine heart. J. Cardiovasc. Electrophysiol. **99**, 832–844 (1998)

161. El-Sherif, N., Caref, E.B., Yin, H., Estivo, M.: The electrophysiological mechanism of ventricular arrhythmias in the long QT syndrome. Tridimensional mapping of activation and recovery patterns. Circ. Res. **79**, 474–492 (1996)

162. El-Sherif, N., Chinushi, M., Caref, E.B., Restivo, M.: Electrophysiological mechanism of the characteristic electrocardiographic morphology of torsade de points tachyarrhythmias in the long-QT syndrome: detailed analysis of ventricular tridimensional activation patterns. Circulation **96**, 4392–4399 (1997)

163. Endresen, L.P., Hall, K., Hoye, J.S., Myrheim, J.: A theory for the membrane potential of living cells. Eur. Biophys. J. **29**, 90–103 (2000)

164. Entcheva, E., Eason, J., Efimov, I.R., Cheng, Y., Malkin, R., Clayton, F.: Virtual electrode effects in transvenous defibrillation-modulation by structure and interface: evidence from bidomain simulations an optical mapping. J. Cardiovasc. Electrophysiol. **9**, 949–961 (1998)

165. Ermentrout, B.: Simulating, analyzing, and animating dynamical systems: a guide to XPPAUT for researchers and students. SIAM, Philadelphia (2002)

166. Ethier, M., Bourgault, Y.: Semi-implicit time-discretization schemes for the Bidomain model. SIAM J. Numer. Anal. **46**(5), 2443–2468 (2008)

167. Evans, L.C., Gariepy, R.F.: Measure Theory and Fine Properties of Functions. Studies in Advanced Mathematics. CRC, New York (1997)

168. Fall, C.P., Marland, E.S., Wagner, J.M., Tyson, J.J.: Computational Cell Biology, 3rd edn. Springer, New York (2005)

169. Fast, V.G., Kléber, A.G.: Role of wavefront curvature in propagation of cardiac impulse. Cardiovasc. Res. **33**, 258–271 (1997)

170. Fenton, F.H., Karma, A.: Vortex dynamics in three-dimensional continuous myocardium with fiber rotation: filament instability and fibrillation. Chaos **8**, 20–47 (1998)

171. Fenton, F.H., Cherry, E.M., Hastings, H.M., Evans, S.J.: Multiple mechanisms of spiral wave breakup in a model of cardiac electrical activity. Chaos **12**(3), 852–892 (2002)

172. Fernandez, M.A., Zemzemi, N.: Decoupled time-marching schemes in computational cardiac electrophysiology and ECG numerical simulation. Math. Biosci. **226**, 58–75 (2010)

173. Fife, P.C.: Mathematical Aspect of Reacting and Diffusing Systems. Springer, Berlin (1979)

174. Fife, P.C.: Dynamics of Internal Layers and Diffusive Interfaces. CBMS-NSF Regional Conference Series in Applied Mathematics, vol. 53. SIAM, Philadelphia (1988)

175. Fife, P.C., McLeod, J.B.: The approach of solutions of nonlinear diffusion equations to travelling front solutions. Arch. Ration. Mech. Anal. **65**, 335–361 (1977)

176. Fish, J.M., Di Diego, J.M., Nesterenko, V., Antzelevich, C.: Epicardial activation of left ventricular wall prolongs QT interval and transmural dispersion of repolarization. Implications for biventricular pacing. Circulation **109**, 2136–2142 (2004)

177. Fischer, G., Tilg, B., Modre, R., Huiskamp, G.J.M., Fetzer, J., Rucker, W., Wach, P.: A bidomain model based BEM-FEM coupling formulation for anisotropic cardiac tissue. Ann. Biomed. Eng. **28**(10), 1229–1243 (2000)

178. FitzHugh, R.: Impulses and physiological states in theoretical models of nerve membrane. Biophys. J. **1**, 445–466 (1961)

179. FitzHugh, R.: Mathematical models of excitation and propagation in nerve. In: Schwan, H.P. (ed.) Biological Engineering, pp. 1–85. MacGraw-Hill, New York (1969)

180. Frangi, A.F., Radeva, P.I., Santos, A., Hernandez, M. (eds.): Proceedings of the Third International Workshop on Functional Imaging and Modeling of the Heart, FIMH'05, Barcelona, 2–4 June 2005. LNCS, vol. 3504. Springer, Berlin (2005)

181. Franz, M.R.: Monophasic Action Potentials: Bridging Cells to Bedside, pp. 19–45. Futura Publishing Company, Armonk (2000)

182. Franz, M.R.: What is a monophasic action potential recorded by Franz contact electrode? Cardiovasc. Res. **65**, 940–941 (2005)

183. Franz, M.R., et al.: Monophasic action potential mapping in human subjects with normal electrocardiograms: direct evidence for the genesis of the T wave. Circulation **75**, 379–386 (1987)

184. Frazier, D.W., Krassowska, W., Chen, P.-S., Wolf, P.D., Danieley, N.D., Smith, W.M., Ideker, R.E.: Transmural activation and stimulus potentials in three-dimensional anisotropic canine myocardium. Circ. Res. **63**, 135–146 (1988)

185. Frazier, D.W., Wolf, P.D., Wharton, J.M., Tang, A.S.L., Smith, W.M., Ideker, R.E.: Stimulus-induced critical point: mechanism for electrical initiation of reentry in normal canine myocardium. J. Clin. Invest. **83**, 1039–1052 (1989)

186. Fu, Z., Kirby, R.M., Whitaker, R.T.: A fast iterative method for solving the eikonal equation on tetrahedral domains. SIAM J. Sci. Comput. **35**(5), C473–C494 (2013)

187. Fuller, M.S., Sandor, G., Punske, B., Taccardi, B., MacLeod, R.S., Ershler, P.R., Green, L.S., Lux, R.L.: Estimates of repolarization dispersion from electrocardiographic measurements. Circulation **102**(6), 685–691 (2000)

188. Fuller, M.S., Sandor, G., Punske, B., Taccardi, B., MacLeod, R.S., Ershler, P.R., Green, L.S., Lux, R.L.: Estimates of repolarization and its dispersion from electrocardiographic

measurements: direct epicardial assessment in the canine heart. J. Electrocardiol. **33**(2), 171–180 (2000)

189. Fuster, V., Walsh, R.A., Harrington, R.A.: Hurst's the Heart, 13th edn. MacGraw-Hill, New York (2011)

190. Garbern, J.C., Lee, R.T.: Cardiac stem cell therapy and the promise of heart regeneration. Cell Stem Cell **12**(6), 689–698 (2013)

191. Garfinkel, A., Kim, Y.-H., Voroshilovsky, O., Qu, Z., Kil, J.R., Lee, M.-H., Karagueuzian, H.S., Weiss, J.N., Chen, P.-S.: Preventing ventricular fibrillation by flattening cardiac restitution. Proc. Natl. Acad. Sci. U S A **97**(11), 6061–6066 (2000)

192. Gaudesius, G., Miragoli, M., Thomas, S.P., Rohr, S.: Coupling of cardiac electrical activity over extended distances by fibroblasts of cardiac origin. Circ. Res. **93**, 421–428 (2003)

193. Gauthier, L.D., Greenstein, J.L., Winslow, R.L.: Toward an integrative computational model of the guinea pig cardiac myocyte. Front. Physiol. **3**, 244 (2012)

194. Gepstein, L., Hayam, G., Ben-Haim, S.A.: Activation-recovery coupling in the normal swine endocardium. Circulation **96**(11), 4036–4043 (1997)

195. Gerardo Giorda, L., Mirabella, L., Nobile, F., Perego, M., Veneziani, A.: A model-based block-triangular preconditioner for the Bidomain system in electrocardiology. J. Comput. Phys. **228**(10), 3625–3639 (2009)

196. Gerardo Giorda, L., Perego, M., Veneziani, A.: Optimized Schwarz coupling of Bidomain and Monodomain models in electrocardiology. Math. Model. Numer. Anal. **45**, 309–334 (2011)

197. Geselowitz, D.B.: On the theory of the electrocardiogram. Proc. IEEE **77**, 857–876 (1989)

198. Geselowitz, D.B.: Description of cardiac sources in anisotropic cardiac muscle. Application of bidomain model. J. Electrocardiol. **25**, 65–67 (1992)

199. Geselowitz, D.B., Miller, W.T.: A bidomain model for anisotropic cardiac muscle. Ann. Biomed. Eng. **11**, 191–206 (1983)

200. Ghosh, S., Rudy, Y.: Application of L1-norm regularization to epicardial potential solutions of the inverse electrocardiography problem. Ann. Biomed. Eng. **37**(5), 902–912 (2009)

201. Giaquinta, M., Hildebrandt, S.: Calculus of Variations I. Volume 310 of Grundlehren der mathematischen Wissenschaften. Springer, Berlin (1996)

202. Giga, Y., Goto, S.: Motion of hypersurfaces and geometric equations. J. Math. Soc. Jpn. **44**(1), 99–111 (1992)

203. Giga, Y., Sato, M.-H.: Neumann problem for singular degenerate parabolic equations. Differ. Integral Equ. **6**(6), 1217–1230 (1993)

204. Giga, Y., Goto, S., Ishii, H., Sato, M.-H.: Comparison principle and convexity preserving properties for singular degenerate parabolic equations on unbounded domains. Ind. Univ. Math. J. **40**(2), 443–469 (1991)

205. Gima, K., Rudy, Y.: Ionic current basis of electrocardiographic waveforms. A model study. Circ. Res. **90**, 889–896 (2002)

206. Goldsmith, E.C., et al.: Organization of fibroblasts in the heart. Dev. Dyn. **230**(4), 787–794 (2004)

207. Goto, M., Brooks, C.: Membrane excitability of the frog ventricle examined by long pulses. Am. J. Physiol. Heart Circ. Physiol. **217**, H1236–H1245 (1969)

208. Gotoh, M., Uchida, T., Fan, W., Fishbein, M.C., Karagueuzian, H.S., Chen, P.-S.: Anisotropic repolarization in ventricular tissue. Am. J. Physiol. (Heart Circ. Physiol.) **41**, 107–113 (1997)

209. Grandi, E., Pasqualini, F.S., Bers, D.M.: A novel computational model of the human ventricular action potential and Ca transient. J. Mol. Cell. Cardiol. **48**, 112–121 (2010)

210. Greensite, F.: The mathematical basis for imaging cardiac electrical function. CRC Crit. Rev. Biomed. Eng. **22**, 347–399 (1994)

211. Greensite, F., Huiskamp, G.: An improved method for estimating epicardial potentials from the body surface. IEEE Trans. Biomed. Eng. **45**, 98–104 (1998)

212. Griffith, B.E., Peskin, C.S.: Electrophysiology. Commun. Pure. Appl. Math. **66**, 1837–1913 (2013)

213. Guan, S., Lu, Q., Huang, K.: A discussion about the Di Francesco-Noble model. J. Theor. Biol. **189**, 27–32 (1997)

214. Gulrajani, R.M.: Models of the electrical activity of the heart and computer simulation of the electrocardiogram. CRC Crit. Rev. Biomed. Eng. **16**, 1–66 (1988)
215. Gulrajani, R.M.: Bioelectricity and Biomagnetism. Wiley, New York (1998)
216. Gulrajani, R.M., Roberge, F.A., Savard, P.: The inverse problem of electrocardiography. In: Macfarlane, P.W., Lawrie, T.T.V. (eds.) Comprehensive Electrocardiology, I: chap. 9, pp. 237–288. Pergamon, Oxford (1989)
217. Han, C., Pogwizd, S.M., Killingsworth, C.R., He, B.: Noninvasive reconstruction of the three-dimensional ventricular activation sequence during pacing and ventricular tachycardia in the canice heart. Am. J. Physiol. Heart Circ. Physiol. **302**, H244–H252 (2012)
218. Harrild, D.M., Henriquez, C.S.: A finite volume model of cardiac propagation. Ann. Biomed. Eng. **28**(2), 315–334 (1997)
219. Harrild, D.M., Henriquez, C.S.: A computer model of normal conduction in the human atria. Circ. Res. **87**, e25–e36 (2000)
220. Harrild, D.M., Penland, R., Henriquez, C.: A flexible method for simulating cardiac conduction in three-dimensional complex geometries. J. Electrocardiol. **33**(3), 241–251 (2000)
221. Haws, C.W., Lux, R.L.: Correlation between in vivo transmembrane action potential durations and activation–recovery intervals from electrograms. Circulation **81**, 281–288 (1990)
222. He, B., Li, G., Zhang, X.: Noninvasive imaging of cardiac transmembrane potentials within three-dimensional myocardium by means of a realistic geometry anisotropic heart model. IEEE Trans. Biomed. Eng. **50**(10), 1190–1202 (2003)
223. Heidenreich, E.A., Rodriguez, J.F., Gaspar, F.J., Doblaré, M.: Fourth-order compact schemes with adaptive time step for monodomain reaction–diffusion equations. J. Comput. Appl. Math. **216**(1), 39–55 (2008)
224. Heijman, J., Volders, P.G.A., Westra, R.L., Rudy, Y.: Local control of β-adrenergic stimulation: effects on ventricular myocyte electrophysiology and Ca^{2+}-transient. J. Mol. Cell. Cardiol. **50**(5), 863–871 (2011)
225. Henriquez, C.S.: Simulating the electrical behavior of cardiac tissue using the bidomain model. CRC Crit. Rev. Biomed. Eng. **21**, 1–77 (1993)
226. Henriquez, C.S., Muzikant, A.L., Smoak, C.K.: Anisotropy, fiber curvature, and bath loading effects on activation in thin and thick cardiac tissue preparations: simulations in a three-dimensional bidomain model. J. Cardiovasc. Electrophysiol. **7**(5), 424–444 (1996)
227. Herron, T.J., Lee, P., Jalife, J.: Optical imaging of voltage and calcium in cardiac cells and tissues. Circ. Res. **110**, 609–623 (2012)
228. Hille, B.: Ionic Channels of Excitable Membranes, 2nd edn. Sinauer Associates Inc., Sunderland (1982)
229. Hodgkin, A., Huxley, A.: A quantitative description of membrane current and its application to conduction and excitation in nerve. J. Physiol. (Lond.) **117**, 500–544 (1952)
230. Hoff, D.: Stability and convergence of finite difference methods for systems of nonlinear reaction-diffusion equations. SIAM J. Numer. Anal. **15**, 1161–1177 (1978)
231. Holland, R.P., Brooks, H.: Precordial end epicardial surface potentials during Myocardial ischemia in the pig. A theoretical and experimental analysis of the TQ and ST segments. Circ. Res. **37**, 471–480 (1975)
232. Holzapfel, G.A., Ogden, R.W.: Constitutive modelling of passive myocardium: a structurally based framework for material characterization. Philos. Trans. R. Soc. A **13**(367), 3445–3475 (2009)
233. Hooke, N.: Efficient simulation of action potential propagation in a bidomain. Ph.D. thesis, Department of Computer Science, Duke University (1992)
234. Hooks, D.A., Tomlinson, K.A., Mardsen, S.G., LeGrice, I.J., Smaill, B.H., Pullan, A.J., Hunter, P.J.: Cardiac microstructure. Implications for electrical propagation and defibrillation in the heart. Circ. Res. **91**, 331–338 (2002)
235. Hopenfeld, B., Stinstra, J.G., MacLeod, R.S.: Mechanism for ST depression associated with contiguous subendocardial ischemia. J. Cardiovasc. Electrophysiol. **29**, 1200–1206 (2004)
236. Hormander, L.: The Analysis of Linear Partial Differential Operators. Springer, Berlin (1983)

237. Hoyt, R.H., Cohen, M.L., Saffitz, J.E.: Distribution and three-dimensional structure of intercellular junctions in canine myocardium. Circ. Res. **64**, 563–574 (1989)

238. Hsiao, G.C., Wendland, W.L.: Boundary Integral Equations. Springer, Berlin (2008)

239. http://commons.wikimedia.org/wiki/File:Wiggers_Diagram.png

240. http://www.texasheartinstitute.org/HIC/Anatomy/images/fig1_crosslg.jpg

241. Huiskamp, G., Greensite, F.: A new method for myocardial activation imaging. IEEE Trans. Biomed. Eng. **44**, 433–446 (1997)

242. Humphrey, J.D.: Cardiovascular Solid Mechanics. Cells, Tissues, and Organs. Springer, New York (2002)

243. Hund, T.J., Rudy, Y.: Rate transient and regulation of action potential and calcium transient in a canine cardiac ventricular cell model. Circulation **110**, 3168–3174 (2004)

244. Hund, T.J., Kucera, J.P., Otani, N.F., Rudy, Y.: Ionic charge conservation and long-term steady state in hte Luo–Rudy dynamic cell model. Biophys. J. **81**, 3324–3331 (2001)

245. Hunter, P.J., Nash, M.P., Sands, G.B.: Computational electromechanics of the heart. In: Panfilov, A.V., Holden, A.V. (eds.) Computational Biology of the Heart. Wiley, New York (1997)

246. Hunter, P.J., McCulloch, A.D., ter Keurs, H.: Modelling the mechanical properties of cardiac muscle. Prog. Biophys. Mol. Biol. **69**(2–3), 289–331 (1998)

247. Hunter, P.J., et al.: A vision and strategy for the virtual physiological human in 2010 and beyond. Philos. Trans. R. Soc. A **368**, 2595–2614 (2010)

248. Hunter, P.J., et al.: A vision and strategy for the virtual physiological human: 2012 update. Interface Focus **3**, 1–9 (2013)

249. Isakov, V.: Inverse Problems for Partial Differential Equations, 2nd edn. Springer, Berlin (2006)

250. Jack, J.J.B., Noble, D., Tsien, R.W.: Electric Current Flow in Excitable Cells. Clarendon, Oxford (1983)

251. Jacquemet, V.: An eikonal approach for the initiation of reentrant cardiac propagation in reaction-diffusion models. IEEE Trans. Biomed. Eng. **57**(9), 2090–2098 (2010)

252. Jacquemet, V., Henriquez, C.: Finite volume stiffness matrix for solving anisotropic cardiac propagation in 2-D and 3-D unstructured meshes. IEEE Trans. Biomed. Eng. **52**(8), 1490–1492 (2005)

253. Jacquemet, V., Kappenberger, L., Henriquez, C.S.: Modeling atrial arrhythmias: impact on clinical diagnosis and therapies. IEEE Rev. Biomed. Eng. **1**, 94–114 (2008)

254. Jafri, S., Rice, J.J., Winslow, R.L.: Cardiac Ca^{2+} dynamics: the role of ryanodine receptor adaptation and sarcoplasmic reticulum load. Biophys. J. **74**, 1149–1168 (1998)

255. Janks D.L., Roth B.J.: Quaterfoil reentry caused by bursting pacing. J. Cardiovasc. Electrophysiol. **17**, 1362–1368 (2006)

256. Janks, D.L., Roth, B.J.: The bidomain theory of pacing. In: Efimov I.R., Kroll M.W., Tchou, J. (eds.) Cardiac Bioelectric Therapy, chap. 2.1, pp. 63–83. Springer, New York (2009)

257. Janse, M.J.: ST segment mapping and infarct size. Cardiovasc. Res. **45**, 190–193 (2000)

258. Janse, M., Sosunov, E.A., Corornel, R., Opthof, T., Anyukhovsky, E.P., de Bakker J.M.T., Plotnikov, A.N., Shlapakova, I.N., Danilo, P., J.Tijssen, G.P., Rosen, M.R.: Repolarization gradients in the canine left ventricle before and after induction of short-term cardiac memory. Circulation **112**, 1711–1718 (2005)

259. Jerome, J.W.: Convergence of successive iterative semidiscretizations for FitzHugh-Nagumo reaction systems. SIAM J. Numer. Anal. **27**, 2054–1065 (1984)

260. Jikov, V.V., Kozlov, S.M., Oleinik, O.A.: Homogenization of Differential Operators and Integral Functionals. Springer, Berlin (1994)

261. Johnston, P.: Computational Inverse Problems in Electrocardiography. WIT, Southampton (2001)

262. Johnston, P.R., Kilpatrick, D.: The effect of conductivity values on ST segment shift in subendocardial ischaemia. IEEE Trans. Biomed. Eng. **50**, 150–158 (2003)

263. Johnston, P.R., Kilpatrick, D., Li, C.Y.: The importance of anisotropy in modeling ST segment shift in subendocardial ischaemia. IEEE Trans. Biomed. Eng. **48**, 1366–1376 (2001)

264. Joyner, R.W.: Modulation of repolarization by electrotonic interactions. Jpn. Heart J. **27**, 167–183 (1986)
265. Jungschleger, J.G., Vos, M.A.: Hybrid action potential etiology. J. Cardiovasc. Electrophysiol. **11**(8), 946–948 (2000). (Letter to the Editor)
266. Katila, T., Magnin, I.E., Clarysse, P., Montagnat, J., Nenonen, J. (eds.): Proceedings of the First International Workshop on Functional Imaging and Modeling of the Heart, FIMH'01, Helsinki, 15–16 Nov 2001. LNCS, vol. 2230. Springer, Berlin (2001)
267. Katz, A.M.: Physiology of the Heart. Wolters Kluwer, Philadelphia (2011)
268. Keener, J.P.: An eikonal-curvature equation for action potential propagation in myocardium. J. Math. Biol. **29**, 629–651 (1991)
269. Keener, J.P.: Direct activation and defibrillation of cardiac tissue. J. Theor. Biol. **178**, 313–324 (1996)
270. Keener, J.P., Bogar, K.: A numerical method for the solution of the bidomain equations in cardiac tissue. Chaos **8**(1), 234–241 (1998)
271. Keener, J.P., Panfilov, A.V.: Three–Dimensional propagation in the heart: the effects of geometry and fiber orientation on propagation in myocardium. In: Zipes, D.P., Jalife, J. (eds.) Cardiac Electrophysiology: From Cell to Bedside, pp. 335–347. W. B. Sounders, Philadelphia (1995)
272. Keener, J.P., Panfilov, A.V.: The effects of geometry and fibre orientation on propagation and extracellular potentials in myocardium. In: Panfilov, A.V., Holden, A.V. (eds.) Computational Biology of the Heart, chap. 8, pp. 235–258. Wiley, New York (1997)
273. Keener, J.P., Sneyd, J.: Mathematical Physiology, 2nd edn. Springer, New York (2008)
274. Kerckhoffs, R.C.P. (ed.): Patient-Specific Modeling of the Cardiovascular System: Technology-Driven Personalized Medicine. Springer, New York (2010)
275. Kerckhoffs, R.C.P., Bovendeerd, B.H.M., Kotte, J.C.S., Prinzen, F.W., Smits, K., Arts, T.: Homogeneity of cardiac contraction despite physiological asynchrony of depolarization: a model study. Ann. Biomed. Eng. **31**, 536–547 (2003)
276. Kleber, A.G.: ST-segment elevation in the electrocardiogram: a sign of myocardial ischemia. Cardiovasc. Res. **45**, 111–118 (2000)
277. Kleber, A.G., Riegger, C.B.: Electrical constants of arterially perfused rabbit papillar muscle. J. Physiol. **385**, 307–324 (1987)
278. Kleber, A.G., Rudy, Y.: Basic mechanisms of cardiac impulse propagation and associated arrhythmias. Physiol. Rev. **84**(2), 431–488 (2004)
279. Kleber, A.G., Janse, M.J., van Capelle, F.J.L., Durrer, D.: Mechanism and time course of S-T and T-Q segment changes during acute regional myocardial ischemia in the pig heart determined by extracellular and intracellular recordings. Circ. Res. **42**(5), 603–613 (1978)
280. Kneller, J., Ramirez, R.J., Chartier, D., M.Courtemanche, Nattel, S.: Time-dependent transients in an ionically based mathematical model of the canine atrial action potential. Am. J. Physiol. Heart. Circ. Physiol. **282**, H1437–H1451 (2002)
281. Knisley, S.B.: Transmembrane voltage changes during unipolar stimulation of rabbit ventricle. Circ. Res. **77**(6), 1229–1239 (1995)
282. Koch, C.: Biophysics of Computation. Oxford University Press, New York (1999)
283. Kogan, B.Y.: Introduction to Computational Cardiology. Springer, New York (2010)
284. Kohl, P., Sachs, F., Franz, M.R.: Cardiac Mechano-Electric Coupling and Arrhythmias. Oxford University Press, Oxford (2011)
285. Kondo, M., Nesterenko, V., Antzelevitch, C.: Cellular basis for the monophasic action potential. Which electrode is the recording electrode? Cardiovasc. Res. **63**, 635–644 (2004)
286. Kjekshus, J.K., Maroko, P.R., Sobel, B.E.: Distribution of myocardial injury and its relation to epicardial ST-segment changes after coronary artery occlusion in the dog. Cardiovasc. Res. **6**, 490–499 (1972)
287. Krogh-Masden, T., Cristini, D.J.: Nonlinear dynamics in cardiology. Ann. Rev. Biomed. Eng. **14**, 179–203 (2012)
288. Kuznetsov, Y.: Elements of Applied Bifurcation Theory. Springer, New York (2000)
289. Laflamme, M.A., Murry, C.E.: Heart regeneration. Nature **473** 326–335 (2011)

290. Lang, J.: Adaptive Multilevel Solution of Nonlinear Parabolic PDE Systems. Theory, Algorithms, and Applications. LNCSE, vol. 16. Springer, Berlin (2000)

291. Leeson, P.: Cardiovascular Imaging. Oxford University Press, Oxford (2011)

292. LeGrice, I.J., Smaill, B.H., Chai, L.Z., Edgar, S.G., Gavin, J.B., Hunter, P.J.: Laminar structure of the heart: ventricular myocyte arrangement and connective tissue architecture in the dog. Am. J. Physiol. Heart Circ. Physiol. **269**(38), H571–H582 (1995)

293. LeGrice, I.J., Smaill, B.H., Hunter, P.J.: Laminar structure of the heart: a mathematical model. Am. J. Physiol. Heart Circ. Physiol. **272**(41), H2466–H2476 (1997)

294. LeGrice, I.J., Hunter, P.J., Young, A., Smaill, B.H.: The architecture of the heart: a data-based model. Philos. Trans. R. Soc. Lond. A **359**, 1217–1232 (2001)

295. Leon, L.J., Horacek, B.M.: Computer model of excitation and recovery in the anisotropic myocardium, I: rectangular and cubic arrays of excitable elements. II: excitation in the simplified left ventricle III: arrhythmogenic conditions in the simplified left ventricle. J. Electrocardiol. **14**, 1–15, 17–31, 33–41 (1991)

296. Leri, A., Kajstura, J., Anversa, P.: Role of cardiac stem cells in cardiac phatophysiology: a paradigm shift in human myocardial biology. Circ. Res. **109**, 941–961 (2011)

297. Lesh, M.D., Spear, J.F., Simson, M.B.: A computer model of the electrogram: what causes fractionation? J. Electrocardiol. **21**(Suppl), S69–S73 (1988)

298. Li, D., Li, C.Y., Yong, A.C., Johnston, P.R., Kilpatrick, D.: Epicardial ST depression in acute myocardial ischemia. Circ. Res. **85**, 959–964 (1999)

299. Li, L., Niederer, S., et al.: A mathematical model of the murine ventricular myocyte: a data-driven biophysically based approach applied to mice overexpressing the canine NCX isoform. Am. J. Physiol. HC **299**, H1045–H1063 (2010)

300. Lindemans, F.W., van der Gon, J.J.D.: Current threshold and liminal size in excitation of heart muscle. Cardiovasc. Res. **12**(8), 477–485 (1978)

301. Lindemans, F.W., Heethaar, R.M., van der Gon, J.J.D., Zimmerman, A.N.E.: Site of initial excitation and current threshold as a function of electrode radius in heart muscle. Cardiovasc. Res. **9**, 95–104 (1975)

302. Lines, G.T., Grottum, P., Tweito, A.: Modeling the electric activity of the heart: a bidomain model of the ventricles embedded in a torso. Comput. Vis. Sci. **5**, 195–213 (2003)

303. Linge, S., Sundnes, J., Hanslien, M., Lines, G.T., Tveito, A.: Numerical solution of the bidomain equations. Philos. Trans. R. Soc. A **367**(1895), 1931–1950 (2009)

304. Lions, J.L.: Optimal Control of Systems Governed by Partial Differential Equations. Springer, Berlin (1971)

305. Lions, J.L., Magenes, E.: Nonhomogeneous boundary value problems and applications. I. Springer, Berlin (1972)

306. Livshitz, L.M., Rudy, Y.: Regulation of Ca^{2+} and electrical alternans in cardiac myocytes: role of CAMKII and repolarizing currents. Am. J. Physiol. Heart Circ. Physiol. **292**, H2854–H2866 (2007)

307. Livshitz, L., Rudy, Y.: Uniqueness and stability of action potential models during rest, pacing, and conduction using problem-solving environment. Biophys. J. **97**, 1265–1276 (2009)

308. Luo, C., Rudy, Y.: A model of the ventricular cardiac action potential: depolarization, repolarization, and their interaction. Circ. Res. **68**(6), 1501–1526 (1991)

309. Luo, C., Rudy, Y.: A dynamic model of the cardiac ventricular action potential. I. Simulations of ionic currents and concentration changes. Circ. Res. **74**(6), 1071–1096 (1994)

310. Luo, C., Rudy, Y.: A dynamic model of the cardiac ventricular action potential. II. Afterdepolarizations, triggered activity, and potentiation. Circ. Res. **74**(6), 1097–1113 (1994)

311. Lux, R.L., Gettes, L., Mason, J.W.: Understanding proarrhythmic potential in therapeutic drug development: alternate strategies for measuring and tracking repolarization. J. Electrocardiol. **39**, S161–S164 (2006)

312. Macfarlane, P.W., van Oosterom, A., Janse, M., Kligfield, P., Camm, J., Pahlm, O. (eds.): Basic Electrocardiology. Cardiac Electrophysiology, ECG Systems and Mathematical Modeling. Springer, New York (2012)

313. MacLachlan, M.C., Sundnes, J., Lines, G.T.: Simulation of ST segment changes during subendocardial ischemia using a realistic 3-D cardiac geometry. IEEE Trans. Biomed. Eng. **52**, 799–807 (2005)

314. MacLeod, R.S., Punske, B., Yilmaz, B., Shome, S., Taccardi, B.: The role of heart rate in myocardial ischemia from restricted coronary perfusion. J. Electrocardiol. **34**, 43–51 (2001)

315. Mahajan, A., Shiferaw, Y., Sato, D., Baher, A., Olcese, R., Xie, L.H., Yang, M.J., Chen, P.S., Restrepo, J.G., Karma, A., Garfinkel, A., Qu, Z., Weiss, J.N.: A rabbit ventricular action potential model replicating cardiac dynamics at rapid heart rates. Biophys. J. **94**(2), 392–410 (2008)

316. Magnin, I.E., Montagnat, J., Clarysse, P., Nenonen, J., Katila, T. (eds.): Proceedings of the Second International Workshop on Functional Imaging and Modeling of the Heart, FIMH'03, Lyon, 5–6 June 2003. LNCS, vol. 2674. Springer, Berlin (2003)

317. Malmivuo, J., Plonsey, R.: Bioelectromagnetism. Oxford University Press, Oxford (1995)

318. Mardal, K.A., Sundnes, J., Langtangen, H.P., Tveito, A.: Systems of PDEs and block preconditioning. In: Langtangen, H.P., Tveito, A. (eds.) Advanced Topics in Computational Partial Differential Equations. LNCSE, vol. 33, chap. 5, pp. 200–236. Springer, Berlin (2004)

319. Mardal, K.-A., Nielsen, B.F., Cai, X., Tveito, A.: An order optimal solver for the discretized bidomain equations. Numer. Linear Algebr. Appl. **14**(2), 83–98 (2007)

320. Markowich, P.A.: The Stationary Semiconductor Device Equations. Springer, Berlin (1986)

321. Mascagni, M.: The backward euler method for numerical solution of the Hodgkin–Huxley equations of nerve conduction. SIAM J. Numer. Anal. **27**(4), 941–962 (1990)

322. Matta, R.J., Verrier, R.L., Lown, B.: Repetitive extrasystole as an index of vulnerability to ventricular fibrillation. Am. J. Physiol. **230**, 1469–1473 (1976)

323. McAllister, R.E., Noble, D., Tsien, R.W.: Reconstruction of the electrical activity of cardiac Purkinje fibres. J. Physiol. **251**, 1–59 (1975)

324. Mehra, R., Furman, S.: Comparison of cathodal, anodal, and bipolar strength-interval curves with temporary and permanent pacing electrodes. Br. Heart J. **41**, 468–476 (1979)

325. Messnarz, B., Seger, M., Modre, R., Fischer, G., Hanser, F., Tilg, B.: A comparison of noninvasive reconstruction of epicarial versus transmembrane potentials in consideration of the null space. IEEE Trans. Biomed. Eng. **51**(9), 1609–1618 (2004)

326. Messnarz, B., Tilg, B., Modre, R., Fischer, G., Hanser, F.: A new spatiotemporal regularization approach for reconstruction of cardiac transmembrane potential patterns. IEEE Trans. Biomed. Eng. **51**(2), 273–281 (2004)

327. Metaxas, D.N., Axel, L. (eds.): Proceedings of the 6th International Conference on Functional Imaging and Modeling of the Heart, FIMH'11, New York City, 25–27 May 2011. LNCS, vol. 6666. Springer, Berlin (2011)

328. Millar, C.K., Kralios, F.A., Lux, R.L.: Correlation between refractory periods and activation-recovery intervals from electrograms – effects of rate and adrenergic interventions. Circulation **72**, 1372–1379 (1985)

329. Miller, W.T., Geselowitz, D.B.: Simulation studies of the electrocardiogram I. The normal heart. Circ. Res. **43**(2), 301–315 (1978)

330. Miragoli, M., Gaudesius, G., Rohr, S.: Electrotonic modulation of cardiac impulse conduction by myofibroblasts. Circ. Res. **98**, 801–810 (2006)

331. Mirams, G.R., et al.: Chaste: an open source C plus plus library for computational physiology and biology. PLoS Comput. Biol. **9**(3), e100297 (2013)

332. Miranda, C.: Partial Differential Equations of Elliptic Type. Springer, Berlin (1970)

333. Mitchell, C.C., Schaeffer, D.G.: A two-current model for the dynamics of cardiac membrane. Bull. Math. Biol. **65**(5), 767–793 (2003)

334. Miura, R.H.: Accurate computation of stable solitary waves for the FitzHugh–Nagumo equations. J. Math. Biol. **13**, 247–269 (1982)

335. Modre, R., Tilg, B., Fischer, G., Wach, P.: Noninvasive myocardial activation time imaging: a novel inverse algorithm applied to clinical ECG mapping data. IEEE Trans. Biomed. Eng. **49**(10), 1153–1161 (2002)

336. Moore, P.K.: An adaptive finite element method for parabolic differential systems: some algorithmic considerations in solving in three space dimensions. SIAM J. Sci. Comput. **21**(4), 1567–1586 (2000)

337. Morris, C., Lecar, H.: Voltage oscillations in the barnacle giant muscle. Biophys. J. **35**, 193–213 (1981)

338. Munteanu, M.: Overlapping additive Schwarz methods for nonlinear parabolic reaction-diffusion problems. Ph.D. thesis, Department of Mathematics, University of Milano (2008)

339. Munteanu, M., Pavarino, L.F.: Implicit parallel solvers in computational electrocardiology. In: Carja, O., Vrabie, I.I. (eds.) Applied Analysis and Differential Equations, pp. 255–266. World Scientific, Singapore (2007)

340. Munteanu, M., Pavarino, L.F.: Decoupled Schwarz algorithms for implicit discretization of nonlinear Monodomain and Bidomain systems. Math. Model Methods Appl. Sci. **19**(7), 1065–1097 (2009)

341. Munteanu, M., Pavarino, L.F., Scacchi, S.: A scalable Newton-Krylov-Schwarz method for the Bidomain reaction-diffusion system. SIAM J. Sci. Comput. **31**(5), 3861–3883 (2009)

342. Murillo, M., Cai, X.: A fully implicit parallel algorithm for simulating the nonlinear electrical activity of the heart. Numer. Linear Algebr. Appl. **11**, 261–277 (2004)

343. Murthy, M.K.V., Stampacchia, G.: Le problème de Dirichlet pour les équations elliptiques du second ordre à coefficients discontinus. Ann. Ist. Fourier **XV**, 189–258 (1965)

344. Muzikant, A., Hsu, E.W., Wolf, P.D., Henriquez, C.S.: Region specific modeling of cardiac muscle: comparison of simulated and experimental potentials. Ann. Biomed. Eng. **30**, 867–883 (2002)

345. Nayak, A.R., Shajahan, T.K., Panfilov, A.V., Pandit, R.: Spiral-wave dynamics in a mathematical model of human ventricular tissue with myocytes and fibroblasts. PLoS One **8**(9), e72950 (2013)

346. Nelson, C.V., Gezelowitz, D.B.: The Theoretical Basis of Electrocardiology. Clarendon, Oxford (1976)

347. Nesterenko, V.V., Kondo, M., Antzelevitch, C.: Biophysical basis for monophasic action potential. Cardiovasc. Res. **65**, 942–944 (2005)

348. Neu, J.S., Krassowska, W.: Homogenization of syncitial tissues. CRC Crit. Rev. Biomed. Eng. **21**(2), 137–199 (1993)

349. Neunlist, M., Tung, L.: Spatial distribution of cardiac transmembrane potentials around an extracellular electrode: dependence on fiber orientation. Biophys. J. **68**, 2310–2311 (1995)

350. Ni, Q., MacLeod, R.S., Punske, B.B., Taccardi, B.: Computing and visualizing electric potentials and current pathways in the Thorax. J. Electrocard. **33**, 189–197 (2000)

351. Niederer, S., Smith, N.: A mathematical model of the slow force response to stretch in rat ventricular myocytes. Biophys. J. **92**, 4030–4044 (2007)

352. Nielsen, I.J., Le Grice, P.M.F., Hunter, P.J., Smaill, B.H.: Mathematical model of geometry and fibrous structure of the heart. Am. J. Physiol. Heart Circ. Physiol. **260**, H1365–H1378 (1991)

353. Nielsen, B.F., Cai, X., Sundnes, J., Tveito, A.: Toward a computational method for imaging the extracellular potassium concentration during regional ischemia. Math. Biosci. **220**, 118–130 (2009)

354. Nielsen, B.F., Lysaker, M., Grøttum, P.: Computing ischemic regions in the heart with the bidomain model: first step toward validation. IEEE Trans. Med. Imag. **32**(6), 1085–1096 (2013)

355. Noble, D.: A modification of the Hodgkin-Huxley equations applicable to Purkinje fibre action and pacemaker potentials. J. Physiol. **160**, 317–352 (1962)

356. Noble, D., Rudy, Y.: Models of cardiac ventricular action potentials: iterative interaction between experiment and simulation. Philos. Trans. R. Soc. Lond. A **359**, 1127–1142 (2001)

357. Noble, D., Noble, S., Bett, C., Earm, Y.E., Ko, W.K., So, I.K.: The role of sodium-calcium exchange during the cardiac action potential. Ann. NY Acad. Sci. **639**, 334–354 (1991)

358. Noble, D., Varghese, A., Kohl, P., Noble, P.J.: Improved guinea-pig ventricular cell model incorporating a diadic space, iKr & iKs, and lenght- & tension-dependent processes. Can. J. Cardiol. **14**, 123–134 (1998)

359. Nochetto, R.H., Savarè, G., Verdi, C.: A posteriori error estimates for variable time-step discretizations of nonlinear evolution equations. Commun. Pure Appl. Math. **53**(5), 525–589 (2000)

360. Nygren, A., Fiset, C., Firek, L., Clark, J.W., Lindblad, D.S., Clark, R.B., Giles, W.R.: Mathematical Model of an Adult Human Atrial Cell. Circ. Res. **82**, 63–81 (1998)

361. O'Hara, T., Virag, L., Varro, A., Rudy, Y.: Simulation of the undiseased human cardiac ventricular action potential: model formulation and experimental validation. PLoS Comput. Biol. **7**(5), 1–29 (2011)

362. Oleinik, O.A., Shamaev, A.S., Yosifian, G.A.: Mathematical Problems in Elasticity and Homogenization. North-Holland, Amsterdam (1992)

363. Opthof, T., Coronel, R., Wilms-Schopman, F.J.G., Plotnikov, A.N., Shlapakova, I.N., Danilo, P., Rosen, M.R., Janse, M.J.: Dispersion of repolarization in canine ventricle and the electrocardiographic T wave: T_{p-e} interval does not reflect transmural dispersion. Heart Rhythm **4**, 341–348 (2007)

364. Osaka, T., Kodama, I., Tsuboi, N., Toyama, J., Yamada, K.: Effects of activation sequence and anisotropic cellular geometry on the repolarization phase of action potential of dog ventricular muscle. Circulation **76**(1), 226–236 (1987)

365. Osher, S., Fedkin, R.: Level Set Methods and Dynamic Implicit Surfaces. Applied Mathematical Sciences, vol. 153. Springer, New York (2003)

366. Ourselin, S., Rueckert, D., Smith, N. (eds.): Proceedings of the 7th International Conference on Functional Imaging and Modeling of the Heart, FIMH'13, London, 20–22 June 2013. LNCS, vol. 7945. Springer, Berlin (2013)

367. Pandit, S.V., Clark, R.B., Giles, W.R., Demir, S.S.: A mathematical model of action potential heterogeneity in adult rat left ventricular myocytes. Biophys. J. **81**(6), 3029–3051 (2001)

368. Panfilov, A.V.: Spiral breakup as a model of ventricular fibrillation. Chaos **8**, 57–64 (1998)

369. Panfilov, A.V., Holden, A.V.: Computational Biology of the Heart. Wiley, New York (1997)

370. Park, J.-H., Jerome, J.W.: Qualitative properties of steady-state Poisson-Nernst-Planck systems: mathematical study. SIAM J. Appl. Math. **57**(3), 609–630 (1997)

371. Pavarino, L.F., Colli Franzone, P.: Parallel solution of cardiac reaction-diffusion models. In: Kornhuber, R., et al. (eds.) Domain Decomposition Methods in Science and Engineering. LNCSE, vol. 40, pp. 669–676. Springer, Berlin (2004)

372. Pavarino, L.F., Scacchi, S.: Multilevel additive Schwarz preconditioners for the Bidomain reaction-diffusion system. SIAM J. Sci. Comput. **31**(1), 420–443 (2008)

373. Pavarino, L.F., Scacchi, S.: Parallel multilevel Schwarz and block preconditioners for the Bidomain parabolic-parabolic and parabolic-elliptic formulations. SIAM J. Sci. Comput. **33**(4), 1897–1919 (2011)

374. Payne, L.E.: Improperly Posed Problems in Partial Differential Equations. PA Saunders, Philadelphia (1975)

375. Penland, R., Harrild, D., Henriquez, C.: Modeling impulse propagation and extracellular potential distributions in anisotropic cardiac tissue using a finite volume element discretization. Comput. Vis. Sci. **4**, 215–226 (2002)

376. Pennacchio, M.: A nonconforming domain decomposition method for the cardiac potential problem. In: Proceedings of IEEE Computers in Cardiology, Rotterdam, 23–26 Sept 2001, vol. 28, pp. 537–540 (2001)

377. Pennacchio, M.: The mortar finite element method for the cardiac "bidomain" model of extracellular potential. J. Sci. Comput. **20**(2), 191–210 (2004)

378. Pennacchio, M., Savarè, G., Colli Franzone, P.: Multiscale modeling for the electrical activity of the heart. SIAM J. Math. Anal. **37**(4), 1333–1370 (2006)

379. Pennacchio, M., Simoncini, V.: Efficient algebraic solution of reaction-diffusion systems for the cardiac excitation process. J. Comput. Appl. Math. **145**, 49–70 (2002)

380. Pennacchio, M., Simoncini, V.: Substructuring preconditioners for mortar discretization of degenerate evolution problem. J. Sci. Comput. **36**, 391–419 (2008)

381. Pennacchio, M., Simoncini, V.: Algebraic multigrid preconditioners for the bidomain reaction–diffusion system. Appl. Numer. Math. **59**, 3033–3050 (2009)

382. Pennacchio, M., Simoncini, V.: Fast structured AMG preconditioning for the bidomain model in electrocadiology. SIAM J. Sci. Comput. **33**, 721–745 (2011)

383. Peskin, C.S.: Mathematical Aspects of Heart Physiology. Lecture Notes of the Courant Institute of Mathematical Sciences, New York University, New York (1975)

384. Peskin, C.S.: Numerical analysis of blood flow in the heart. J. Comput. Phys. **25**(3), 220–252 (1977)

385. Peskin, C.S., McQueen, D.M.: Cardiac fluid dynamics. Crit. Rev. Biomed. Eng. **20**, 451–459 (1992)

386. Pilkington, T.C., Plonsey, R.: Engineering Contributions to Biophysical Electrocardiography. IEEE, New York (1982)

387. Pilkington, T.C., Loftis, B., Palmer, T., Budinger, T.F.: High-Performance Computing in Biomedical Research. CRC, Boca Raton (1993)

388. Plank, G., Burton, R.A.B., Hales, P., Bishop, M., Mansoori, T., Bernabeu, M.O., Garny, A., Prassl, A.J., Bollendorsff, C., Mason, F., Mahmood, F., Rodriguez, B., Grau, V., Schneider, J.E., Gavaghan, D., Kohl, P.: Generation of histo-anatomically representative models of the individual heart: tools and application. Philos. Trans. R. Soc. A **367**(1895), 2257–2292 (2009)

389. Plank, G., Liebmann, M., Weber dos Santos, M.O., Vigmond, E.J., Haase, G.: Algebraic Multigrid Preconditioner for the Cardiac Bidomain Model. IEEE Trans. Biomed. Eng. **54**(4), 585–596 (2007)

390. Plank, G., Prassl, A., Hofer, E., Trayanova, N.A.: Evaluating intramural virtual electrodes in the myocardial wedge preparation: simulations of experimental conditions. Biophys. J. **94**, 1904–1915 (2008)

391. Plonsey, R.: Bioelectric sources arising in excitable fibers (Alza lecture). Ann. Biomed. Eng. **16**, 519–546 (1988)

392. Plonsey, R., Barr, R.C.: Current flow patterns in two-dimensional anisotropic bisyncitia with normal and extreme conductivities. Biophys. J. **45**, 557–571 (1984)

393. Plonsey, R., Barr, R.C.: Bioelectricity: A Quantitative Approach. Springer, New York (2007)

394. Plonsey, R., Heppner, D.: Consideration of quasi-stationarity in electrophysiological systems. Bull. Math. Biophys. **29**, 657–664 (1967)

395. Poelzing, S., Rosenbaum, D.S.: Heterogeneous connexin43 expression produces electrophysiological heterogeneities across ventricular wall. Am J. Physiol. Heart Circ. Physiol. **286**, H2001–H2009 (2004)

396. Poelzing, S., Rosenbaum, D.S.: Altered connexin43 expression produces arrhythmia substrate in heart failure. Am. J. Physiol (Heart Circ. Physiol) **287**, H1762–H1770 (2004)

397. Pollard, A.E., Hooke, N., Henriquez, C.S.: Cardiac propagation simulation. CRC Crit. Rev. Biomed. Eng. **20**(3–4), 171–210 (1992)

398. Pollard, A.E., Burgess, M.J., Spitzer, K.W.: Computer simulations of three-dimensional propagation in ventricular myocardium. Circ. Res. **72**(4), 744–756 (1993)

399. Potse, M., Dubè, B., Richer, J., Vinet, A., Gulrajani, R.: A comparison of Monodomain and Bidomain reaction–diffusion models for action potential propagation in the human heart. IEEE Trans. Biomed. Eng. **53**(12), 2425–2434 (2006)

400. Potse, M., Vinet, A., Opthof, T., Coronel, R.: Validation of a simple model for the morphology of the T wave in unipolar electrograms. Am. J. Physiol. Heart Circ. Physiol. **297**(2), H792–H801 (2009)

401. Pressler, M.L., Munster, P.N., Huang, X.-D.: Gap junction distribution in the heart: functional relevance. In: Zipes, D., Jalife, J. (eds.) Cardiac Electrophysiology, chap. 16, pp. 144–151. W. B. Sauders, Philadelphia (1995)

402. Priebe, L., Beuckelmann, D.J.: Simulation study of cellular electrical properties in heart failure. Circ. Res. **82**, 1206–1223 (1998)

403. Prinzmetal, M., Toyoshima, A., Ekmekci, Y., Mizumo, Y., Nagaya, T.: Myocardial ischemia. Nature of ischemic electrocardiographic patterns in the mammalian ventricles as determined by intracellular electrographic and metabolic changes. Am. J. Cardiol. **8**, 493–503 (1961)

404. Prior, P., Roth, B.J.: Calculation of optical signal using three-dimensional bidomain/diffusion model reveals distortion of the transmembrane potential. Biophys. J. **95**, 2097–2102 (2008)

405. Puglisi, J.L., Bers, D.M.: LabHEART: an interactive computer model of rabbit ventricular myocyte ion channels and Ca transport. Am. J. Physiol. Cell Physiol. **281**(6), C2049–C2060 (2001)

406. Pullan, A.J., Buist, M.L., Cheng, L.K.: Mathematically Modelling the Electrical Activity of the Heart. World Scientific, Singapore (2005)

407. Pullan, A.J., Cheng, L.K., Nash, M.P., Ghodrati, A., MacLeod, R.S., Brooks, D.H.: The inverse problem of electrocardiography. In: Comprehensive Electrocardiology, pp. 299–344. Springer, New York (2010)

408. Punske, B.B., Ni, Q., Lux, R.L., MacLeod, R.S., Ershler, P.R., Dustman, T.J., Allison, M.J., Taccardi, B.: Spatial methods of epicardial activation time determination in normal hearts. Ann. Biomed. Eng. **31**(7), 781–792 (2003)

409. Puwal, S., Roth, B.J.: Forward Euler stability of the bidomain model of cardiac tissue. IEEE Trans. Biomed. Eng. **54**(5), 951–953 (2007)

410. Qu, Z., Garfinkel, A.: An advanced algorithm for solving partial differential equation in cardiac conduction. IEEE Trans. Biomed. Eng. **46**(9), 1166–1168 (1999)

411. Qu, Z., Kill, J., Xie, F., Garfinkel, A., Weiss, J.N.: Scroll wave dynamics in a three-dimensional cardiac tissue model: roles of restitution, thickness, and fiber rotation. Biophys. J. **78**, 2761–2775 (2000)

412. Qu, Z., Xie, F., Garfinkel, A., Weiss, J.N.: Origins of spiral wave meander and breakup in a two-dimensional cardiac tissue model. Ann. Biomed. Eng. **28**, 755–771 (2000)

413. Quan, W., Evans, S.J., Hastings, H.M.: Efficient integration of a realistic two-dimensional cardiac tissue model by domain decomposition. IEEE Trans. Biomed. Eng. **45**, 372–385 (1998)

414. Quarteroni, A., Valli, A.: Numerical Approximation of Partial Differential Equations. Springer, Berlin (1994)

415. Ramanathan, C., Ghanem, R.N., Jia, P., Ryu, K., Rudy, Y.: Noninvasive electrocardiographic imaging for cardiac electrophysiology and arrhythmia. Nat. Med. **10**(4), 422–428 (2004)

416. Ranjan, R., Tomaselli, G.F., Marban, E.: A novel mechanism of anode-break stimulation predicted by bidomain modeling. Circ. Res. **84**, 153–156 (1999)

417. Rappel, W.J.: Filament instability and rotational tissue anisotropy: a numerical study using detailed cardiac models. Chaos **11**(1), 71–80 (2001)

418. Rasmusson, R.I., Clark, J.W., Giles, W.R., Robinson, K., Clark, R.B., Shibata, E.F., Campbell, D.L.: A mathematical model of electrophysiological activity in a bullfrog atrial cell. Am. J. Physiol. **259**, H370–H389 (1990)

419. Rinzel, J., Ermentrout, B.: Analysis of neural excitability and oscillations. In: Kock, C., et al. (eds.) Methods in Neuronal Modelling: From Synapses to Networks. MIT, Boston (1998)

420. Roberts, D., Scher, A.M.: Effect of tissue anisotropy on extracellular potential fields in canine myocardium in situ. Circ. Res. **50**, 342–351 (1982)

421. Roberts, D., Hersch, L.T., Scher, A.M.: Influence of cardiac fiber orientation on wave front voltage, conduction velocity and tissue resistivity. Circ. Res. **44**, 701–712 (1979)

422. Rogers, J.M., McCulloch, A.D.: A collocation-Galerkin finite element model of cardiac action potential propagation. IEEE Trans. Biomed. Eng. **41**, 743–757 (1994)

423. Rohr, S.: Role of gap junctions in the propagation of the cardiac action potential. Cardiovasc. Res. **62**, 309–322 (2004)

424. Rohr, S.: Cardiac fibroblasts in cell culture systems: myofibroblasts all along? J. Cardiovasc. Pharmacol. **57**(4), 389–399 (2011)

425. Romero, D., Sebastian, R., Bijnens, B.H., et al.: Effects of the Purkinje system and cardiac geometry on biventricular pacing: a model study. Ann. Biomed. Eng. **38**(4), 1388–1398 (2010)

426. Roth, B.J.: The electrical potential produced by a strand of cardiac muscle: a bidomain analysis. Ann. Biomed. Eng. **16**, 609–637 (1988)

427. Roth, B.J.: A mathematical model of make and break electrical stimulation of cardiac tissue by a unipolar anode or cathode. IEEE Trans. Biomed. Eng. **42**, 1174–1184 (1995)

428. Roth, B.J.: Strength-Interval curve for cardiac tissue predicted using the bidomain model. J. Cardiovasc. Electrophysiol. **7**, 722–737 (1996)

429. Roth, B.J.: Nonsustained reentry following successive stimulation of cardiac tissue through a unipolar electrode. J. Cardiovasc. Electrophysiol. **8**, 768–778 (1997)

430. Roth, B.J., Chen, J.: Mechanism of anode break excitation in the heart: the relative influence of membrane and electrotonic factors. J. Biol. Syst. **7**(4), 541–552 (1999)

431. Roth, B.J., Krassowska, W.: The induction of reentry in cardiac tissue. The missing link: how electric fields alter transmembrane potential. Chaos **8**, 204–220 (1998)

432. Roth, B.J., Patel, S.G.: Effects of elevated extracellular potassium ion concentration on anodal excitation of cardiac tissue. J. Cardiovasc. Electrophysiol. **14**, 1351–1355 (2003)

433. Roth, B.J., Pertsov, A.M.: Hybrid modeling of electrical and optical behavior in the heart. Physica D **238**, 1019–1027 (2009)

434. Roth, B.J., Wikswo, J.P., Jr.: A bidomain model for the extracellular potential and magnetic field of cardiac tissue. IEEE Trans. Biomed. Eng. **33**(4), 467–469 (1986)

435. Roth, B.J., Wikswo, J.P., Jr.: Electrical stimulation of cardiac tissue: a bidomain model with active membrane properties. IEEE Trans. Biomed. Eng. **41**(3), 232–240 (1994)

436. Roth, B.J., Lin, S.-F., Wikswo, J.P., Jr.: Unipolar stimulation of cardiac tissue. J. Electrocardiol. **31**(Suppl), 6–12 (1998)

437. Roux, B., Allen, T., Berneche, S.: Theoretical and computational models of biological ion channels. Q. Rev. Biophys. **37**(1), 15–103 (2001)

438. Rubinstein, I.: Electro-Diffusion of Ions. SIAM, Philadelphia (1990)

439. Rudy, Y.: The electrocardiogram and its relationship to excitation of the heart. In: Sperelakis, N. (ed.) Physiology and Pathophysiology of the Heart, 3rd edn., chap. 11, pp. 201–239. Kluwer Academic, Dordrecht (1995)

440. Rudy, Y.: Noninvasive electrocardiographic imaging of arrhythmogenic substrates in humans. Circ. Res. **112**, 863–874 (2013)

441. Rudy, Y., Messinger-Rapport, B.J.: The inverse problem in electrocardiography: solutions in terms of epicardial potentials. CRC Crit. Rev. Biomed. Eng. **16**(3), 215–268 (1988)

442. Rudy, Y., Oster, H.S.: The electrocardiographic inverse problem. CRC Crit. Rev. Biomed. Eng. **20**, 25–45 (1992)

443. Rudy, Y., Silva, J.R.: Computational biology in the study of cardiac ion channels and cell electrophysiology. Q. Rev. Biophys. **39**(1), 57–116 (2006)

444. Rushmer, R.F.: Structure and Function of the Cardiovascular System, 2nd edn. W. B. Saunders, Philadelphia (1976)

445. Saad, Y.: Iterative Methods for Sparse Linear Systems, 2nd edn. SIAM, Philadelphia (2003)

446. Sachse, F.B.: Computational Cardiology. Modeling of Anatomy, Electrophysiology, and Mechanics. LNCS, vol. 2966. Springer, Berlin (2004)

447. Sachse, F.B., Seemann, G. (eds.): Proceedings of the 4th International Conference on Functional Imaging and Modeling of the Heart, FIMH'07, Salt Lake City, 7–9 June 2007. LNCS, vol. 4466. Springer, Berlin (2007)

448. Saffitz, J.E., Kanter, H.L., Green, K.G., Tolley, T.K., Beyer, E.C.: Tissue-specific determinants of anisotropic conduction velocity in canine atrial and ventricular myocardium. Circ. Res. **74**, 1065–1070 (1994)

449. Saleheen, H.I., Ng, K.T.: A new three-dimensional finite-difference bidomain formulation for inhomogeneous anisotropic cardiac tissues. IEEE Trans. Biomed. Eng. **45**(1), 15–25 (1998)

450. Sambelashvili, A., Efimov, I.R.: Dynamics of virtual electrode-induced scroll-wave reentry in a 3D bidomain model. Am. J. Physiol Heart Circ. Physiol. **287**, H1570–H1581 (2004)

451. Sambelashvili, A., Nikolsky, V.P., Efimov, I.R.: Virtual electrode theory explains pacing threshold increase caused by cardiac tissue damage. Am. J. Physiol Heart Circ. Physiol. **286**, H2183–H2194 (2004)

452. Sampson, K.J., Henriquez, C.S.: Electrotonic influences on action potential duration dispersion in small hearts: a simulation study. Am. J. Physiol. Heart Circ. Physiol. **289**, H350–H360 (2005)

453. Samson, W., Scher, A.: Mechanism of ST-segment alteration during acute myocardial injury. Circ. Res. **8**, 780–787 (1960)

454. Sanchez-Palencia, E., Zaoui, A.: Homogenization Techniques for Composite Media. Lectures Notes in Physics, vol. 272. Springer, Berlin (1987)

455. Sanfelici, S.: Convergence of the Galerkin approximation of a degenerate evolution problem in electrocardiology. Numer. Methods Part. Differ. Equ. **18**, 218–240 (2002)

456. Sanfelici, S.: Numerical simulations of fractioned electrograms and pathological cardiac action potential. J. Theor. Med. **4**(3), 167–181 (2002)

457. Savaré, G.: Weak solutions and maximal regularity for abstract evolution inequalities. Adv. Math. Sci. Appl. **6**, 377–418 (1996)

458. Scacchi, S.: A hybrid multilevel Schwarz method for the bidomain model. Comput. Methods Appl. Mech. Eng. **197**(45–48), 4051–4061 (2008)

459. Scacchi, S.: A multilevel hybrid Newton-Krylov-Schwarz method for the Bidomain model of electrocardiology. Comput. Methods Appl. Mech. Eng. **200**(5–8), 717–725 (2011)

460. Scacchi, S., Colli Franzone, P., Pavarino, L.F., Taccardi, B.: A reliability analysis of cardiac repolarization time markers. Math. Biosci. **219**(2), 113–128 (2009)

461. Scacchi, S., Colli Franzone, P., Pavarino, L.F., Taccardi, B.: Computing cardiac recovery maps from electrograms and monophasic action potentials under heterogeneous and ischemic conditions. Math. Model Methods Appl. Sci. **20**(7), 1089–1127 (2010)

462. Scher, A.M.: Excitation of the heart. In: Nelson, C.V., Geselowitz, D.B. (eds.) The Theoretical Basis of Electrocardiology, pp. 44–67. Clarendon, Oxford (1976)

463. Schmitt, O.H.: Biological information processing using the concept of interpenetrating domains. In: Leibovich, K.N. (ed.) Information Processing in the Nervous System, pp. 325–331. Springer, New York (1969)

464. Schuss, Z., Nadler, B., Eisenberg, R.S.: Derivation of Poisson and Nernst-Planck equations in a bath and channel from a molecular model. Phys. Rev. E **64**, 036116 (2001)

465. Scollan, D.F., Holmes, A., Zhang, J., Winslow, R.L.: Reconstruction of cardiac ventricular geometry and fiber orientation using magnetic resonance imaging. Ann. Biomed. Eng. **28**(8), 934–944 (2000)

466. Seemann, G., Hoeper, C., Sachse, F.B., Doessel, O., Holden, A.V.: Heterogeneous three-dimensional anatomical and electrophysiological model of human atria. Philos. Trans. R. Soc. A **364**, 1465–1481 (2006)

467. Seemann, G., Sachse, F.B., Weiss, D.L., Dossel, O.: Quantitative reconstruction of cardiac electromechanics in human myocardium: regional heterogeneity. J. Cardiovasc. Electrophysiol. **14**(10), S219–S228 (2003)

468. Seger, M., Fischer, G., Modre, R., Messnarz, B., Hanser, F., Tilg, B.: Lead field computation for the electrocardiographic inverse problem – finite element versus boundary elements. Comput. Methods Prog. Biomed. **77**, 241–252 (2005)

469. Sepulveda, N.G., Roth, B.J., Wikswo, J.P., Jr.: Current injection into a two-dimensional anisotropic bidomain. Biophys. J. **55**, 987–999 (1989)

470. Sermesant, M., Konukoglu, E., Delingette, H., Coudiere, Y., Khinchapatnam, P., Rhode, K.S., Razzavi, R., Ayache, N.: An anisotropic multi-front fast marching method for real-time simulation in cardiac electrophysiology. In: Sachse, F.B., Seemann, G. (eds.) FIMH'07, Salt Lake City, 7–9 June 2007. LNCS, vol. 4466, pp. 160–169. Springer, Berlin (2007)

471. Sethian, J.A.: Level Set Methods: Evolving Interfaces in Geometry, Fluid Mechanics, Computer Vision and Material Sciences, 2nd edn. Cambridge University Press, Cambridge (1999)

472. Severi, S., Fantini, M., Charawi, L.A., Di Francesco, D.: An updated computational model of rabbit sinoatrial action potential to investigate the mechanisms of heart rate modulation. J. Physiol. **590**, 4483–4499 (2012)

473. Shannon, T.R., Wang, F., Puglisi, J., Weber, C., Bers, D.M.: A mathematical treatment of integrated Ca dynamics within the ventricular myocyte. Biophys. J. **87**(5), 3351–3357 (2004); Erratum Biophys. J. **102**(8), 1996–2001 (2012)

474. Shaw, R.M., Rudy, Y.: Ionic mechanisms of propagation in cardiac tissue. Role of the sodium and L-type calcium currents during reduced excitability and decreased gap junction coupling. Circ. Res. **81**(5), 727–741 (1997)

475. Shenasa, M., Hindricks, G., Borggrefe, M., Breithardt, G., Josephson, M.E.: Cardiac Mapping, 4th edn. Wiley-Blackwell, Chichester (2012)

476. Shibata, N., Chen, P.S., Dixon, E.G., Wolf, P.D., Danieley, N.D., Smith, W.M., Ideker, R.E.: Influence of shock strength and timing on induction of ventricular arrhythmias in dogs. Am. J. Physiol. **255**, H891–H901 (1988)

477. Shou, G., Xia, L., Jiang, M.: Total variation regularization in electrocardiographic mapping. In: Li, K., et al. (eds.) Life System Modeling and Intelligence Computing. LNMI, vol. 6330, pp. 51–59. Springer, Berlin (2010)

478. Skipa, O., Nalbach, M., Sachse, F., Werner, C., Dossel, O.: Transmembrane potential reconstruction in anisotropic heart model. Int. J. Bioelectromagn. **4**(2), 17–18 (2002)

479. Sicouri, S., Antzelevich, C.: A subpopulation of cells with unique electrophysiological properties in the deep subepicardium of the canine ventricle. The M cell. Circ. Res. **68**, 1729–1741 (1991)

480. Sidorov, V.Y., Woods, M.C., Baudenbacher, P., Baudenbacher, F.: Examination of stimulation mechanism and strength-interval curve in cardiac tissue. Am. J. Physiol. Heart Circ. Physiol. **289**, H2602–H2615 (2005)

481. Sigg, D.C., Iaizzo, P.A., Xiao, Y.-F., He, B.: Cardiac Electrophysiology Methods and Models. Springer, New York (2010)

482. Silva, J.R., Pan, H., Wu, D., Nekouzadeh, A., Decker, K.F., Cui, J., Baker, N.A., Sept, D., Rudy, Y.: A multiscale model linking ion-channel molecular dynamics and electrostatics to the cardiac action potential. Proc. Nat. Acad. Sci. **106**(27), 11102–11106 (2009)

483. Simms, H.D., Geselowitz, D.B.: Computation of heart surface potentials using the surface source model. J. Cardiovasc. Electrophysiol. **6**, 522–531 (1995)

484. Singer, A., Gillespie, D., Norbury, J., Eisenberg, R.S.: Singular perturbation analysis of the steady-state Poisson-Nernst-Planck system: applications to ion channels. Eur. J. Appl. Math. **19**, 541–560 (2008)

485. Skouibine, K., Krassowska, W.: Increasing the computational efficiency of a bidomain model of defibrillation using a time-dependent activating function. Ann. Biomed. Eng. **28**, 772–780 (2000)

486. Skouibine, K., Trayanova, N., Moore, P.: Anode/cathode make and break phenomena in a model of defibrillation. IEEE Trans. Biomed. Eng. **46**(7), 769–777 (1999)

487. Skouibine, K., Trayanova, N., Moore, P.: A numerically efficient model for the simulation of defibrillation in an active bidomain sheet of myocardium. Math. Biosci. **166**(1), 85–100 (2000)

488. Smaill, B.H., Zhao, J., Trew, M.L.: Three-dimensional impulse propagation in myocardium. Arrhythmogenic mechanisms at the tissue level. Circ. Res. **112**, 834–848 (2013)

489. Smith, B.F., Bjørstad, P., Gropp, W.D.: Domain Decomposition: Parallel Multilevel Methods for Elliptic Partial Differential Equations. Cambridge University Press, Cambridge (1996)

490. Smith, N.P., Pullan, A.J., Hunter, P.J.: An anatomically based model of transient coronary blood flow in the heart. SIAM J. Appl. Math. **62**(3), 990–1018 (2002)

491. Smith, N.P., Nickerson, D.P., Crampin, E.J., Hunter, P.J.: Multiscale computational modelling of the heart. Acta Numer. 371–431 (2004)

492. Soravia, J.P., Souganidis, P.E.: Phase-field theory for Fitzhugh-Nagumo type systems. SIAM J. Math. Anal. **27**(5), 1341–1359 (1996)

493. Spach, M.S., Dolber, P.C.: Relating extracellular potentials and their derivatives to anisotropic propagation at microscopic level in human cardiac muscle. Evidence for electrical uncoupling of side-to-side fiber connections with increasing age. Circ. Res. **58**, 356–371 (1986)

494. Spiteri, R.J., Dean, R.C.: On the performance of an implicit-explicit Runge-Kutta method in models of cardiac electrical activity. IEEE Trans. Biomed. Eng. **55**(5), 1488–1495 (2008)

495. Stampacchia, G.: Boundary value problems for some degenerate-elliptic operators. Ann. Math. Pura Appl. **LXXX**(IV), 1–122 (1968)

496. Steinhaus, B.M.: Estimating cardiac transmembrane activation and recovery times from unipolar and bipolar extracellular electrograms: a simulation study. Circ. Res. **64**(3), 449–462 (1989)

497. Steinhaus, B.M., Spitzer, K.W., Isomura, S.: Action potential collision in heart tissue. Computer simulations and tissue experiments. IEEE Trans. Biomed. Eng. **32**(10), 731–742 (1985)

498. Streeter, D.: Gross morphology and fiber geometry in the heart. In: Berne, R.M. (ed.) Handbook of Physiology, vol. 1, sect. 2, pp. 61–112. Williams & Wilkins, Philadelphia (1979)

499. Sundnes, J., Lines, G.T., Mardal, K., Tveito, A.: Multigrid block preconditioning for a coupled system of partial differential equations modeling the electrical activity in the heart. Comput. Methods Biomech. Biomed. Eng. **5**, 397–409 (2002)

500. Sundnes, J., Lines, G., Lines, G.T., Grottum, P., Tveito, A.: Electrical activity in the human heart. In: Langtangen, H.P., Tveito, A. (eds.) Advanced Topics in Computational Partial Differential Equations. LNCSE, vol. 33, chap. 10, pp. 401–449. Springer, Berlin (2004)

501. Sundnes, J., Lines, G.T., Tveito, A.: An operator splitting method for solving the bidomain equations coupled to a volume conductor model for the torso. Math. Biosci. **194**(2), 233–248 (2005)

502. Sundnes, J., Lines, G.T., Cai, X., Nielsen, B.F., Mardal, K.-A., Tveito, A.: Computing the Electrical Activity of the Heart. Springer, Berlin (2006)

503. Sundnes, J., Nielsen, B.F., Mardal, K.A., Lines, G.T., Mardal, K.A., Tveito, A.: On the computational complexity of the bidomain and the monodomain models of electrophysiology. Ann. Biomed. Eng. **34**(7), 1088–1097 (2006)

504. Taccardi, B., Punske, B.B.: Body surface potential mapping. In: Zipes, D., Jalife, J. (eds.) Cardiac Electrophysiology. From cell to Bedside, 4th edn., pp. 803–811. W. B. Saunders, Philadelphia (2004)

505. Taccardi, B., de Ambroggi, L., Viganotti, C.: Body surface mapping of heart potentials. In: Nelson, C.V., Geselowitz, D.B. (eds.) The Theoretical Basis of Electrocardiology, pp. 436–466. Clarendon, Oxford (1976)

506. Taccardi, B., Lux, R.L., Ershler, P.R., MacLeod, R.S., Vyhmeister, Y.: Effect of myocardial fiber direction on 3-D shape of excitation wavefronts and associated potential distributions in ventricular walls. Circulation **86**, I-752 (1992)

507. Taccardi, B., Macchi, E., Lux, R.L., Ershler, P.R., Spaggiari, S., Baruffi, S., Vyhmeister, Y.: Effect of myocardial fiber direction on epicardial potentials. Circulation **90**, 3076–3090 (1994)

508. Taccardi, B., Lux, R.L., Ershler, P.R., MacLeod, R.S., Vyhmeister, Y.: Modern views on the spread of excitation in anisotropic heart muscle. Jpn. Heart J. **35**, 31–35 (1994)

509. Taccardi, B., Lux, R.L., Ershler, P.R., MacLeod, R.S., Dustman, T.J., Ingebrigtsen, N.: Anatomical architecture and electrical activity of the heart. Acta Cardiol. **52**, 91–105 (1997)

510. Taccardi, B., Veronese, S., Colli Franzone, P., Guerri, L.: Multiple components in the unipolar electrocardiogram: a simulation study in a three-dimensional model of ventricular myocardium. J. Cardiovasc. Electrophysiol. **9**, 1062–1084 (1998)

511. Taccardi, B., Punske, B., Lux, R., MacLeod, R., Ershler, P., Dustman, T., Vyhmeister, Y.: Useful lesson from body surface mapping on body. J. Cardiovasc. Electrophysiol. **9**(7), 773–786 (1998)

512. Taccardi, B., Punske, B., Helie, F., MacLeod, R., Lux, R., Ershler, P., Dustman, T., Vyhmeister, Y.: Epicardial recovery sequences and excitation recovery intervals during paced beats. Role of myocardial architecture. PACE **22**(4), part II: 833 (1999)

513. Taccardi, B., Punske, B.B., MacLeod, R.S., Ni, Q.: Visualization, analysis and physiological interpretation of three-dimensional cardiac electric fields. In: Proceedings of the 2nd Joint EMBS/BMSE Conference, Houston, Oct 2002. vol. 2, pp. 1366–1367 (2002)

514. Taccardi, B., Punske, B.B., Colli Franzone, P.: Cardiac potential mapping. In: Proceedings of EMBS/25th IEEE Annual International Conference, Cancun, 17–21 Sept 2003. vol. 4, pp. 3749–3752 (2003)

515. Taccardi, B., Punske, B.B., Sachse, F., Tricoche, X., Colli Franzone, P., Pavarino, L.F., Zabawa, C.: Intramural activation and repolarization sequences in canine ventricles. Experimental and simulation studies. J. Electrocardiol. **38**, 131–137 (2005)

516. Taccardi, B., Punske, B., Macchi, E., MacLeod, R.S., Ershler, P.R.: Epicardial and intramural excitation during ventricular pacing: effects of myocardial structure. Am. J. Physiol. Heart. Circ. Physiol. **294**, H1753–H1766 (2008)

517. Taggart, P., Sutton, P., Opthof, T., Coronel, R., Trimlett, R., Pugsley, W., Kallis, P.: Transmural repolarization in the left ventricle in humans during normoxia and ischemia. Cardiovasc. Res. **50**, 454–462 (2001)

518. Tarkhanov, N.N.: The Cauchy Problem for Solutions of Elliptic Equations. Akademic Verlag Gmbh, Berlin (1995)

519. ten Tusscher, K.H.W.J., Panfilov, A.V.: Alternans and spiral breakup in a human ventricular tissue model. Am. J. Physiol. Heart Circ. Physiol. **291**(3), H1088–H1100 (2006)

520. ten Tusscher, K.H.W.J., Panfilov, A.V.: Modelling of the ventricular conduction system. Prog. Biophys. Mol. Biol. **96**(1–3), 152–170 (2008)

521. ten Tusscher, K., Noble, D., Noble, P.J., Panfilov, A.V.: A model for human ventricular tissue. Am. J. Phys. Heart. Circ. Physiol. **286**(4), H1573–H1589 (2004)

522. Tomlinson, K.A., Hunter, P.J., Pullan, A.J.: A finite element method for an eikonal equation model of myocardial excitation wavefront propagation. SIAM J. Appl. Math. **63**(1), 324–350 (2002)

523. Toselli, A., Widlund, O.B.: Domain Decomposition Methods: Algorithms and Theory. Computational Mathematics, vol. 34. Springer, Berlin (2004)

524. Transgenstein, J.A., Kim, C.: Operator splitting and adaptive mesh refinement for the Luo–Rudy I model. J. Comput. Phys. **196**, 645–679 (2004)

525. Trayanova, N.A.: Defibrillation of the heart: insights into mechanisms from modelling studies. Exp. Physiol. **91**(2), 323–337 (2006)

526. Trayanova, N., Eason, J., Aguel, F.: Computer simulations of cardiac defibrillation: a look inside the heart. Comput. Vis. Sci. **4**, 259–270 (2002)

527. Trayanova, N.A., Constantino, J., Gurev, V.: Electromechanical models of the ventricles. Am. J. Physiol. Heart Circ. Physiol. **301**(2), H279–H286 (2011)

528. Trew, M., Le Grice, I., Smaill, B., Pullan, A.: A finite volume method for modeling discontinuous electrical activation in cardiac tissue. Ann. Biomed. Eng. **33**(5), 590–602 (2005)

529. Trew, M., Smaill, B., Bullivant, D., Hunter, P., Pullan, A.: A generalized finite difference method for modeling cardiac electrical activation on arbitrary, irregular computational meshes. Math. Biosci. **198**(2), 169–189 (2005)

530. Trew, M.L., Caldwell, B.J., Sands, G.B., Hooks, D.A., Tai, D.C.-S., Austin, T.M., LeGrice, I.J., Pullan, A.J., Smaill, B.H.: Cardiac electrophysiology and tissue structure: bridging the scale gap with a joint measurement and modelling paradigm. Exp. Physiol. **91**(2), 355–370 (2006)

531. Tung, L.: A bidomain model for describing ischemic myocardial D.C. potentials. Ph.D. dissertation, MIT, Cambridge, MA (1978)

532. Tyson, J.J., Keener, J.P.: Singular perturbation theory of traveling waves in excitable media. (A review). Physica D **32**, 327–361 (1988)

533. Ueda, N., Zipes, D.P., Wu, J.: Functional and transmural modulation of M cell behavior in canine ventricular wall. Am. J. Physiol. (Heart Circ. Physiol) **287**, H2569–H2575 (2004)

534. van Dam, P.M., Oostendorp, T.F., Linnenbank, A.C., van Oosterom, A.: Non-invasive imaging of cardiac activation and recovery. Ann. Biomed. Eng. **37**(9), 1739–1756 (2009)

535. van Oosterom, A.: Cell models–Macroscopic source descriptions. In: Macfarlane, P.W., Lawrie, T.D.V. (eds.) Comprehensive Electrocardiology, pp. 155–179. Pergamon, Oxford (1989)

536. van Oosterom, A.: Forward and inverse problems in electrocardiography. In: Panfilov, A.V., Holden, A.V. (eds.) Computational Biology of the Heart. Wiley, New York (1997)

537. van Oosterom, A.: Genesis of the T wave as based on an equivalent surface source model. J. Electrocardiol. **34**(Suppl), 217–227 (2001)

538. van Oosterom, P.: Genesis of the T wave as based on an equivalent surface source model. J. Electrocardiol. **34**, 217–227 (2001)

539. Varghese, A., Sell, G.R.: A conservation principle and its effect on the formulation of Na–Ca exchanger current in cardiac cells. J. Theor. Biol. **189**, 33–40 (1997)

540. Veneroni, M.: Reaction-diffusion systems for the microscopic cellular model of the cardiac electric field. Math. Methods Appl. Sci. **29**, 1631–1661 (2006)

541. Veneroni, M.: Reaction-Diffusion systems for the macroscopic Bidomain model of the cardiac electric field. Nonlinear Anal. Real World Appl. **10**(2), 849–868 (2009)

542. Vigmond, E.J.: The electrophysiologic basis of MAP recordings. Cardiovasc. Res. **68**, 502–503 (2005)

543. Vigmond, E.J., Leon, L.J.: Computational efficient model for simulating electrical activity in cardiac tissue with fiber rotation. Ann. Biomed. Eng. **27**, 160–170 (1999)

544. Vigmond, E.J., Aguel, F., Trayanova, N.A.: Computational techniques for solving the bidomain equations in three dimensions. IEEE Trans. Biomed. Eng. **49**(11), 1260–1269 (2002)

545. Vigmond, E.J., Weber dos Santos, R., Prassl, A.J., Deo, M., Plank, G.: Solvers for the cardiac bidomain equations. Prog. Biophys. Mol. Biol. **96**, 3–18 (2008)

546. Viswanathan, P.C., Shaw, R.M., Rudy, Y.: Effects of I_{Kr} and I_{Ks} heterogeneity on action potential duration and its rate dependence. A simulation study. Circulation **99**(18), 2466–2474 (1999)

547. Wagner, J., Keizer, J.: Effects of rapid buffers on Ca^{2+} diffusion and Ca^{+2} oscillations. Biophys. J. **67**, 447–456 (1994)

548. Wang, Y., Rudy, Y.: Action potential propagation in inhomogeneous cardiac tissue: safety factor considerations and ionic mechanism. Am. J. Physiol. Heart Circ. Physiol. **278**, H1019–H1029 (2000)

549. Wang, D., Kirby, R.M., Johnson, C.R.: Finite-element-based discretization and regularization strategies for 3-D inverse electrocardiography. IEEE Trans. Biomed. Eng. **58**(6), 1827–1838 (2011)

550. Wang, L., Wong, K.C., Zhang, H., Liu, H., Shi, P.: Noninvasive computational imaging of cardiac electrophysiology for 3-D infarct. IEEE Trans. Biomed. Eng. **58**(4), 1033–1043 (2011)

551. Wang, L., Dawoud, F., Yeung, S.-K., Shi, P., Wong, K., Lardo, A.: Transmural imaging of ventricular action potential and post-infarction scars in swine hearts. IEEE Trans. Med. Image **32**(4), 731–747 (2013)

552. Weber dos Santos, R., Plank, G., Bauer, S., Vigmond, E.J.: Parallel multigrid preconditioner for the cardiac bidomain model. IEEE Trans. Biomed. Eng. **51**(11), 1960–1968 (2004)

553. Weissenburger, J., Nesterenko, V., Antzelevitch, C.: Transmural heterogeneity of ventricular repolarization under baseline and long QT conditions in the canine heart in vivo: torsade de Pointes develops with halotane but not pentobarbital anesthesia. J. Cardiovasc. Electrophysiol. **11**, 290–304 (2000)

554. White, C.S., Haramati, L.B., Jen-Sho Chen, J., Levsky, J.M.: Cardiac Imaging. Oxford University Press, Oxford (2014)

555. Whiteley, J.P.: An efficient numerical technique for the solution of the monodomain and bidomain equations. IEEE Trans. Biomed. Eng. **53**(11), 2139–2147 (2006)

556. Whiteley, J.P.: Physiology driven adaptivity for the numerical solution of the bidomain equations. Ann. Biomed. Eng. **35**(9), 1510–1520 (2007)

557. Wikswo, J.P., Jr.: Tissue anisotropy, the cardiac bidomain, and the virtual cathode effect. In: Zipes D.P., Jalife J. (eds.) Cardiac Electrophysiology: From Cell to Bedside, 2nd edn., pp. 348–361. W. B. Saunders, Philadelphia (1994)

558. Wikswo, J.P., Jr., Roth, B.J.: Virtual electrode theory of pacing. In: Efimov, I.R., Kroll, M.W., Tchou, P.J. (eds.) Cardiac Bioelectric Therapy, Chap. 4.3, pp. 283–330. Springer, New York (2009)

559. Wikswo, J.P., Jr., Lin, S.-F., Abbas, R.A.: Virtual electrodes in cardiac tissue: a common mechanism for anodal and cathodal stimulation. Biophys. J. **69**, 2195–2210 (1995)

560. Wilson, L.D., Jeyaraj, D.: Controversies in measuring repolarization using extracellular recordings: why should be care. Heart Rhythm **3**(9), 1051–1052 (2006)

561. Winfree, A.T.: Sudden cardiac death: a problem in topology. Sci. Am. **248**, 144–161 (1983)

562. Winfree, A.T.: The Geometry of Biological Time, 2nd edn. Springer, New York (2001)

563. Winslow, R.L., Rice, J., Jafri, S., Marban, E., O'Rourke, B.: Mechanisms of altered excitation-contraction coupling in canine tachycardia-induced heart failure, II – model studies. Circ. Res. **84**(5), 571–586 (1999)

564. Wit, A.L., Janse, M.J.: The Ventricular Arrhythmias of Ischemia and Infarction: Electrophysiological Mechanisms. Futura Publishing Co., New York (1993)

565. Wolferth, C.C., Bettet, S., Livezey, M.M., Murphy, F.: Negative displacement of the RS-T segment in the electrocardiogram and its relationships to positive displacement: an experimental study. Am. Heart J. **29**, 220–244 (1945)

566. Wyatt, R.P.: Comparison of estimates of activation and recovery times from bipolar and unipolar electrograms to in vivo transmembrane action potential durations. In: Proceedings of IEEE Engineering in Medicine and Biology Society, 2nd Annual Conference, Washington, DC, pp. 22–25 (1980)

567. Xia, Y., Kongstad, O., Hertvig, E., Li, Z., Holm, M., Olsson, B., Yuan, S.: Activation recovery time measurements in evaluation of global sequence and dispersion of ventricular repolarization. J. Electrocardiol. **38**, 28–35 (2005)

568. Xie, F., Qu, Z.L., Yang, J., Baher, A., Weiss, J.N., Garfinkel, A.: A simulation study of the effects of cardiac anatomy in ventricular fibrillation. J. Clin. Invest. **113**, 686–693 (2004)

569. Xu, A., Guevara, M.R.: Two forms of spiral-wave reentry in an ionic model of ischemic ventricular myocardium. Chaos **8**(1), 157–174 (1998)

570. Yamashita, Y., Geselowitz, D.B.: Source–field relationships for cardiac generators on the heart surface based on their transfer coefficients. IEEE Trans. Biomed. Eng. **32**, 964–970 (1985)

571. Yan, G.-X., Antzelevitch, C.: Cellular basis for the normal T wave and the electrocardiographic manifestations of the Long-QT syndrome. Circulation **98**, 1928–1936 (1998)

572. Yan, G.X., Shimizu, W., Antzelevitch, C.: Characteristics and distribution of M cells in arterially perfused canine left ventricular wedge preparations. Circulation **98**(18), 1921–1927 (1998)

573. Yehia, A.R., Jeandupeaux, D., Alonso, F., Guevara, M.R.: Hysteresis and bistability in the direct transition from 1:1 to 2:1 rhythm in periodically driven single ventricular cells. Chaos **9**, 916–931 (1999)

574. Ying, W.J., Rose, D.J., Henriquez, C.S.: Efficient fully implicit time integration methods for modeling cardiac dynamics. IEEE Trans. Biomed. Eng. **55**(12), 2701–2711 (2008)

575. Young, R.J., Panfilov, A.: Anisotropy of wave propagation in the heart can be modeled by a Riemannian electrophysiological metric. Proc. Natl. Acad. Sci. **107**(34), 15063–15068 (2010)

576. Young, A.A., LeGrice, I.J., Young, M.A., Smaill, B.H.: Extended confocal microscopy of myocardial laminae and collagen network. J. Microscop. **192**, 139–150 (1998)

577. Yu, H.: Solving parabolic problems with different time steps in different regions in space based on domain decomposition methods. Appl. Numer. Math. **30**(4), 475–491 (1999)

578. Yu, H.: A local space-time adaptive scheme in solving two-dimensional parabolic problems based on domain decomposition methods. SIAM J. Sci. Comput. **23**(1), 304–322 (2001)

579. Yu, H., Chang, F., Cohen, I.S.: Pacemaker i(f) in adult canine cardiac ventricular myocytes. J. Physiol. **485**, 469–483 (1995)

580. Yue, A.M., Betts, T.R., Roberts, P.R., Morgan, J.M.: Global dynamic coupling of activation and repolarization in human ventricle. Circulation **112**, 2592–2601 (2005)

581. Zampini, S.: Balancing Neumann-Neumann methods for the cardiac Bidomain model. Numer. Math. **123**, 363–393 (2013)

582. Zampini, S.: Dual-primal methods for the cardiac bidomain model. Math. Model Methods Appl. Sci. **24**(4), 667–696 (2014)

583. Zeng, J., Laurita, K.R., Rosenbaum, D.S., Rudy, Y.: Two Components of the delayed rectifier K^+ current in ventricular myocytes of the guinea pig type. Theoretical formulation and their role in repolarization. Circ. Res. **77**, 140–152 (1995)

584. Zhang, X.: Multilevel Schwarz methods. Numer. Math. **63**(4), 521–539 (1992)

585. Zhang, H., Holden, A.V., Kodama, I., Honjo, H., Lei, M., Varghese, T., Boyett, M.R.: Mathematical models of action potentials in the periphery and center of the rabbit sinoatrial node. Am. J. Physiol. Heart. Circ. Physiol. **279**, H397–H421 (2000)

586. Zipes, D., Jalife, J.: Cardiac Electrophysiology, 2nd edn. W. B. Saunders, Philadelphia (1995)

587. Zipes, D., Jalife, J.: Cardiac Electrophysiology, 3rd edn. W. B. Saunders, Philadelphia (2000)

588. Zipes, D., Jalife, J.: Cardiac Electrophysiology: From Cell to Bedside, 4th edn. W. B. Saunders, Philadelphia (2004)

589. Zipes, D., Jalife, J.: Cardiac Electrophysiology, 5th edn. W. B. Saunders, Philadelphia (2009)

590. Zipes, D., Jalife, J.: Cardiac Electrophysiology: From Cell to Bedside, 6th edn. W. B. Saunders, Philadelphia (2013)

591. Zozor, S., Blanc, O., Jacquemet, V., Virag, N., Vesin, J., Pruvot, E., Kappenberger, L., Henriquez, C.: A numerical scheme for modeling wavefront propagation on a monolayer of arbitrary geometry. IEEE Trans. Biomed. Eng. **50**(4), 412–420 (2003)

Index

MS&A – Modeling, Simulation and Applications

Series Editors:

Alfio Quarteroni
École Polytechnique Fédérale
de Lausanne (Switzerland)

Anthony T. Patera
Massachusetts Institute of Technology
Cambridge, MA (USA)

Tom Hou
California Institute of Technology
Pasadena, CA (USA)

Enrique Zuazua
Basque Center for Applied
Mathematics
Bilbao (Spain)

Claude Le Bris
École des Ponts Paris Tech
Paris (France)

Editor at Springer:

Francesca Bonadei
francesca.bonadei@springer.com

1. L. Formaggia, A. Quarteroni, A. Veneziani (Eds.)
   Cardiovascular Mathematics
   2009, XIV+522 pp, ISBN 978-88-470-1151-9

2. A. Quarteroni
   Numerical Models for Differential Problems
   2009, XVI+602 pp, ISBN 978-88-470-1070-3

3. M. Emmer, A. Quarteroni (Eds.)
   MATHKNOW
   2009, XII+264 pp, ISBN 978-88-470-1121-2

4. A. Alonso Rodríguez, A. Valli
   Eddy Current Approximation of Maxwell Equations
   2010, XIV+348 pp, ISBN 978-88-470-1934-8

5. D. Ambrosi, A. Quarteroni, G. Rozza (Eds.)
   Modeling of Physiological Flows
   2012, X+414 pp, ISBN 978-88-470-1934-8

6. W. Liu
   Introduction to Modeling Biological Cellular Control Systems
   2012, XII+268 pp, ISBN 978-88-470-2489-2

7. B. Maury
   The Respiratory System in Equations
   2013, XVIII+276 pp, ISBN 978-88-470-5213-0

8. A. Quarteroni
   Numerical Models for Differential Problems, 2nd Edition
   2014, XX+656pp, ISBN 978-88-470-5521-6

9. A. Quarteroni, G. Rozza (Eds.)
   Reduced Order Methods for modeling and computational reduction
   2014, X+332pp, ISBN 978-3-319-02089-1

10. J. Xin, Y. Qi
    An Introduction to Mathematical Modeling and Signal Processing in Speech
    and Hearing Sciences
    2014, XII+208pp, ISBN 978-3-319-03085-2

11. L. Beirão da Veiga, K. Lipnikov, G. Manzini
    The Mimetic Finite Difference Method for Elliptic Problems
    2014, XVI+392pp, ISBN 978-3-319-02662-6

12. E. Cristiani, B. Piccoli, A.Tosin
    Multiscale Modeling of Pedestrian Dynamics
    2014, XVI+260pp, ISBN 978-3-319-06619-6

13. P. Colli Franzone, L.F. Pavarino, S. Scacchi
    Mathematical Cardiac Electrophysiology
    2014, XIV+399pp, ISBN 978-3-319-04800-0

For further information, please visit the following link:
http://www.springer.com/series/8377